

Advanced Structured Materials

Bilen Emek Abali
Ivan Giorgio *Editors*

Developments and Novel Approaches in Nonlinear Solid Body Mechanics

 Springer


Advanced Structured Materials

Volume 130

Series Editors

Andreas Öchsner, Faculty of Mechanical Engineering, Esslingen University of Applied Sciences, Esslingen, Germany

Lucas F. M. da Silva, Department of Mechanical Engineering, Faculty of Engineering, University of Porto, Porto, Portugal

Holm Altenbach , Faculty of Mechanical Engineering, Otto von Guericke University Magdeburg, Magdeburg, Sachsen-Anhalt, Germany

Common engineering materials reach in many applications their limits and new developments are required to fulfil increasing demands on engineering materials. The performance of materials can be increased by combining different materials to achieve better properties than a single constituent or by shaping the material or constituents in a specific structure. The interaction between material and structure may arise on different length scales, such as micro-, meso- or macroscale, and offers possible applications in quite diverse fields.

This book series addresses the fundamental relationship between materials and their structure on the overall properties (e.g. mechanical, thermal, chemical or magnetic etc.) and applications.

The topics of *Advanced Structured Materials* include but are not limited to

- classical fibre-reinforced composites (e.g. glass, carbon or Aramid reinforced plastics)
- metal matrix composites (MMCs)
- micro porous composites
- micro channel materials
- multilayered materials
- cellular materials (e.g., metallic or polymer foams, sponges, hollow sphere structures)
- porous materials
- truss structures
- nanocomposite materials
- biomaterials
- nanoporous metals
- concrete
- coated materials
- smart materials

Advanced Structured Materials is indexed in Google Scholar and Scopus.

More information about this series at <http://www.springer.com/series/8611>

Bilen Emek Abali · Ivan Giorgio
Editors

Developments and Novel Approaches in Nonlinear Solid Body Mechanics

 Springer

Editors

Bilen Emek Abali
Institute of Mechanics
Technische Universität Berlin
Berlin, Germany

Ivan Giorgio
Department of Mechanical
and Aerospace Engineering
University of Rome La Sapienza
Latina, Italy

ISSN 1869-8433

Advanced Structured Materials

ISBN 978-3-030-50459-5

<https://doi.org/10.1007/978-3-030-50460-1>

ISSN 1869-8441 (electronic)

ISBN 978-3-030-50460-1 (eBook)

© Springer Nature Switzerland AG 2020

This work is subject to copyright. All rights are reserved by the Publisher, whether the whole or part of the material is concerned, specifically the rights of translation, reprinting, reuse of illustrations, recitation, broadcasting, reproduction on microfilms or in any other physical way, and transmission or information storage and retrieval, electronic adaptation, computer software, or by similar or dissimilar methodology now known or hereafter developed.

The use of general descriptive names, registered names, trademarks, service marks, etc. in this publication does not imply, even in the absence of a specific statement, that such names are exempt from the relevant protective laws and regulations and therefore free for general use.

The publisher, the authors and the editors are safe to assume that the advice and information in this book are believed to be true and accurate at the date of publication. Neither the publisher nor the authors or the editors give a warranty, expressed or implied, with respect to the material contained herein or for any errors or omissions that may have been made. The publisher remains neutral with regard to jurisdictional claims in published maps and institutional affiliations.

This Springer imprint is published by the registered company Springer Nature Switzerland AG
The registered company address is: Gewerbestrasse 11, 6330 Cham, Switzerland

Preface

The ICoNSOM 2019, International Conference on Nonlinear Solid Mechanics, took place at Palazzo Argiletum, Rome, Italy, from June 16 to June 19, 2019. Over 200 participation from the whole globe, the urge of this proceedings became clear. With the aid of the organizers, Marco Amabili, Francesco dell’Isola, Ivan Giorgio, Nicola Rizzi, and Luca Placidi, the scientific community did show a great interest allowing us to bring together this proceedings collected in two volumes:

- Developments and Novel Approaches in Nonlinear Solid Body Mechanics
- Developments and Novel Approaches in Biomechanics and Metamaterials

ICoNSoM 2019 Conference has been intended to provide an international opportunity for communicating recent developments in various areas of nonlinear solid mechanics. This monograph consists theory, experiments, and applications in mechanics, thermodynamics, and multiphysics simulation in many length scales.

As editors, we intend to thank all authors for their crucial contributions as well as all reviewers for their invaluable time and effort. We delightedly acknowledge Dr. Christoph Baumann (Springer Publisher) for initiating the book project. In addition, we have to thank Dr. Mayra Castro (Senior Editor Applied Sciences; Materials Science; Materials Engineering; Nanotechnology and Nanomedicine) and Mr. Ashok Arumairaj (Production Administrator) giving their support in the process of publication.

Brussels, Rome
May 2020

*Bilen Emek Abali
Ivan Giorgio*

Contents

| | | |
|----------|--|----------|
| 1 | International Conference on Nonlinear Solid Mechanics 2019: General Topics and Review of Plenary Lectures | 1 |
| | Marco Laudato, Daria Scerrato, Chuong Anthony Tran, and Emilio Barchiesi | |
| 1.1 | Why Nonlinear Solid Mechanics Deserves an International Conference? | 1 |
| 1.2 | Plenary Lectures | 4 |
| 1.2.1 | Nonlinear Mechanics of Drilling – B. Balachandran | 4 |
| 1.2.2 | Surface Elasticity with Applications to Material Modeling at the Nano- and Micro-Scales – V. A. Eremeyev | 5 |
| 1.2.3 | Ten Years of Global Digital Volume Correlation: What Has Been Achieved? – F. Hild | 6 |
| 1.2.4 | Granular Micromechanics: Bridging Grain Interactions and Continuum Descriptions – A. Misra | 6 |
| 1.2.5 | On Seven- and Twelve-Parameter Shell Finite Elements and Non-Local Theories for Composite Structures – J. N. Reddy | 7 |
| 1.2.6 | Exploiting Global Dynamics to Unveil the Nonlinear Response and Actual Safety of Systems and Structures – G. Rega | 8 |
| 1.2.7 | Vibrations of Nonlinear Continua Subject to Combined Harmonic and Stochastic Forces: Linearization Approximations and Monte Carlo Simulations – P. D. Spanos | 9 |
| 1.3 | Conclusions | 9 |
| | References | 10 |

Part I Mathematical Tools for Mechanics

| | | |
|----------|---|----|
| 2 | Asymptotic Construction of Solutions of Ordinary Differential Equations with Holomorphic Coefficients in the Neighborhood of an Irregular Singular Point | 17 |
| | Maria V. Korovina & Vladimir Yu. Smirnov | |
| | References | 21 |
| 3 | Poincare Problem and Classification of Irregular Singular Points for Linear Differential Equations with Holomorphic Coefficients | 23 |
| | Maria V. Korovina & Vladimir Yu. Smirnov | |
| | References | 26 |
| 4 | Behavior of Solutions of the Cauchy Problem and the Mixed Initial Boundary Value Problem for an Inhomogeneous Hyperbolic Equation with Periodic Coefficients | 29 |
| | Hovik A. Matevossian, Giorgio Nardo, and Anatoly V. Vestyak | |
| | 4.1 Introduction | 29 |
| | 4.2 Notation and Preliminaries | 31 |
| | 4.3 Main Results | 33 |
| | References | 34 |
| 5 | A Soft Embedding Theorem for Soft Topological Spaces | 37 |
| | Giorgio Nardo | |
| | 5.1 Introduction | 37 |
| | 5.2 Preliminaries | 39 |
| | 5.3 Soft Embedding Theorem | 48 |
| | 5.4 Conclusion | 54 |
| | References | 54 |
| 6 | The Diffusion–Vortex Problems in Terms of Stresses for Bingham Materials | 59 |
| | Dimitri Georgievskii | |
| | 6.1 The Generalized Diffusion of Vortex | 59 |
| | 6.2 Diffusion of Plane Vortex Layer. Extraction of a Plane out of Visco-Plastic Space | 62 |
| | 6.3 Diffusion of Axially Symmetric Vortex Layer. Extraction of a Thread out of Visco-Plastic Space | 63 |
| | 6.4 Diffusion of Vortex Thread | 64 |
| | References | 65 |
| 7 | On the Behavior of Solutions of Quasilinear Elliptic Inequalities Near a Boundary Point | 67 |
| | Andrej A. Kon'kov | |
| | 7.1 Introduction | 67 |
| | 7.2 Estimates of Solutions near a Boundary Point | 70 |
| | References | 76 |

8 Integrable Dissipative Dynamical Systems with Three and Four Degrees of Freedom 77
 Maxim V. Shamolin
 8.1 Introduction 77
 8.2 Equations of Geodesic Lines 78
 8.3 A Fairly General Case 79
 8.4 Potential Field of Force 81
 8.5 Force Field with Dissipation 82
 8.6 Structure of Transcendental First Integrals 84
 8.7 Conclusions 84
 8.8 Important Example: Case of Four-Dimensional Manifold 85
 8.8.1 Equations of Motion in a Potential Force Field and First Integrals 88
 8.8.2 Equations of Motion in a Force Field with Dissipation and First Integrals 89
 References 91

Part II Modeling, Design, and Computation of Nonlinear Structures

9 A Variational Formulation of Classical Nonlinear Beam Theories 95
 Simon R. Eugster & Jonas Harsch
 9.1 Introduction 95
 9.2 Notation and Kinematics 97
 9.3 Strain Energy Functional 101
 9.4 Virtual Work Contributions 103
 9.5 Principle of Virtual Work and Equations of Motion 107
 9.6 Constrained Beam Theories 109
 9.6.1 Nonlinear Euler–Bernoulli Beam 109
 9.6.2 Nonlinear Inextensible Euler–Bernoulli Beam 110
 9.7 Constrained and Unconstrained Planar Beam Theories 110
 9.7.1 Timoshenko Beam 111
 9.7.2 Euler–Bernoulli Beam 115
 9.7.3 Inextensible Euler–Bernoulli Beam 117
 9.8 Conclusion 118
 References 119

10 Finite Element Analysis of Planar Nonlinear Classical Beam Theories 123
 Jonas Harsch & Simon R. Eugster
 10.1 Introduction 123
 10.2 Notation 125
 10.3 Virtual Work Contributions in Parameter Space 125
 10.3.1 Timoshenko Beam 127
 10.3.2 Euler–Bernoulli Beam 128
 10.3.3 Constraint Virtual Work Contributions 129
 10.4 B-Spline Shape Functions 130

| | | |
|-----------|---|------------|
| 10.5 | Discrete Kinematics, Semidiscrete Virtual Work, and Equations of Motion | 133 |
| 10.5.1 | Timoshenko Beam | 134 |
| 10.5.2 | Euler–Bernoulli Beam | 136 |
| 10.5.3 | Constraint Forces | 138 |
| 10.5.4 | Equations of Motion and Bilateral Constraints | 140 |
| 10.6 | Numerical Examples | 142 |
| 10.6.1 | Pure Bending of a Cantilever Beam | 142 |
| 10.6.2 | Cantilever Beam Subjected to Constant End Load | 143 |
| 10.6.3 | Cantilever Beam Subject to Follower End Load | 145 |
| 10.6.4 | Clamped-Hinged Circular Arch Subject to Point Load | 147 |
| 10.6.5 | Buckling of a Hinged Right-Angle Frame under Follower Point Load | 150 |
| 10.6.6 | Natural Frequencies of a Two Sided Pinned Euler–Bernoulli Beam | 152 |
| 10.7 | Conclusion | 155 |
| | References | 156 |
| 11 | Modelling of Two-dimensional Timoshenko Beams in Hencky Fashion | 159 |
| | Emilio Turco | |
| 11.1 | Introduction | 159 |
| 11.2 | Modelling of Two-Dimensional Timoshenko Beams | 160 |
| 11.3 | Numerically Driven Drawing of the Equilibrium Path | 164 |
| 11.4 | Quantitative Analysis of the Influence of the Shear Stiffness Parameter | 166 |
| 11.4.1 | Tip Deflection of a Cantilever Beam | 167 |
| 11.4.2 | Buckling of a Simply Supported Beam | 169 |
| 11.5 | Concluding Remarks and Future Challenges | 172 |
| | References | 173 |
| 12 | Nonlinear Phenomena in Granular Solids: Modeling and Experiments | 179 |
| | Marco Laudato | |
| 12.1 | Introduction | 179 |
| 12.2 | Nonlinear Phenomena in Granular Solids: Modeling and Experiments | 180 |
| 12.2.1 | Deformation and Destruction at Deformation Rate of Order 10^3 s^{-1} Wood of Hardwood Trees - Tatiana Yuzhina | 181 |
| 12.2.2 | Experimental Study of the Dynamic Properties of Concrete under Compressive Load - Mikhail Gonov | 181 |
| 12.2.3 | Damage Probing in Cemented Granular Materials with Ultrasound - Ioan Ionescu | 182 |
| 12.2.4 | The Role of Fabric in the Behavior of Granular Material - Niels Kruyt | 182 |

| | | |
|-----------|---|------------|
| 12.2.5 | Grain-Scale Description of Higher-Order Continuum Model for Granular Solid - Takashi Matsushima | 182 |
| 12.2.6 | Validation of a Simple Model Using the Distinct Element Method for Numerical Simulations of Slope Collapse - Nakase Hitoshi | 183 |
| 12.2.7 | Damage and Plastic Evolution of Second Gradient Effective Elastic Moduli of Heterogeneous Granular Materials - Luca Placidi | 183 |
| 12.2.8 | Micro-Macro Identification: Continuum Parameters from Grain Properties - Payam Poorsolhjoui | 184 |
| 12.2.9 | Electromagnetic Microcontinuum Approach to Granular Media - Maurizio Romeo | 184 |
| 12.2.10 | Strain Localization from a Mesoscale Point of View - Antoine Wautier | 185 |
| 12.3 | Conclusions | 185 |
| | References | 186 |
| 13 | A Tool to Describe Particle System Evolution from Swarm Robotics Behavior | 191 |
| | Ramiro dell’Erba | |
| 13.1 | Introduction | 191 |
| 13.2 | Method | 193 |
| 13.3 | Results | 197 |
| 13.3.1 | Case a) Tensile Test | 197 |
| 13.3.2 | Case b) Shear Test with Poisson Effect | 199 |
| 13.3.3 | Case c) Fracture Test | 201 |
| 13.3.4 | Case d) The Importance of the Frame Rules | 202 |
| 13.3.5 | Case e) The Importance of the Lattice | 203 |
| 13.3.6 | Case f) Fracture the Importance of the Lattice and of the Neighbors | 204 |
| 13.3.7 | Case g) ASTM Test | 206 |
| 13.3.8 | The Beam | 208 |
| | 13.3.8.1 Case h) Short Beam | 208 |
| | 13.3.8.2 Case i) Long Beam | 211 |
| 13.4 | Future Work and Conclusion | 212 |
| | References | 214 |
| 14 | Characterization of Polystyrene under Shear Deformation Using Molecular Dynamics | 219 |
| | Maximilian Ries, Paul Steinmann, and Sebastian Pfaller | |
| 14.1 | Introduction and Methodology | 220 |
| 14.2 | Preparation of MD Systems | 222 |
| 14.3 | Pure Shear Deformation within MD | 222 |
| 14.4 | Simulation Results | 224 |
| 14.5 | Relaxation Tests | 227 |
| 14.6 | Summary and Outlook | 228 |

| | |
|--|------------|
| References | 228 |
| 15 Manufacturing and Morphing Behavior of High-Amplitude Corrugated Laminates | 231 |
| Gerald Rolf Kress & Daniel Thomas Filipovic | |
| 15.1 Introduction | 232 |
| 15.1.1 Research on Morphing-Wing Applications | 232 |
| 15.1.2 Manufacturing Methods for Corrugated Laminates | 233 |
| 15.1.3 Substitute-Plate Modeling | 234 |
| 15.1.4 Stresses in Corrugated Laminates | 235 |
| 15.1.5 Deformation Limits of Corrugated Laminates | 235 |
| 15.1.6 Large Deformation of Corrugated Laminates | 235 |
| 15.1.7 Structure of the Paper | 236 |
| 15.2 Geometry and Classical Theory of Laminated Plates Recall | 236 |
| 15.2.1 Circular-Sections Corrugation Shape Geometry | 237 |
| 15.2.2 Excerpts of the Classical Theory of Laminated Plates | 239 |
| 15.3 Feasibility Study | 241 |
| 15.3.1 Materials | 241 |
| 15.3.2 Laminate Thermal Deformation Coefficients | 241 |
| 15.3.3 Residual Stresses | 243 |
| 15.4 Design Procedure | 244 |
| 15.5 Mold-Less Manufacturing | 245 |
| 15.6 Process Simulations | 246 |
| 15.6.1 Simulation Tools and Verification | 246 |
| 15.6.2 FEM Residual Stress Evaluations | 247 |
| 15.7 Aerodynamic Sliding Overlaps Design | 248 |
| 15.8 Corrugated Laminate Demonstrator | 249 |
| 15.8.1 Autoclave-Table Size | 249 |
| 15.8.2 Material | 249 |
| 15.8.3 Prototype for Measuring Thermal Curvature | 249 |
| 15.8.4 Corrugated-Laminate Sample with Three Unit Cells | 250 |
| 15.9 Morphing Model | 251 |
| 15.9.1 Geometric and Mechanical Unit Cells | 251 |
| 15.9.2 Reference Configuration | 252 |
| 15.9.3 Cylindrical Bending and Constitutive Equations | 252 |
| 15.9.4 Mechanical Unit-Cell Equilibrium | 253 |
| 15.9.5 Curvature and Rotation | 254 |
| 15.9.6 Deformed Configuration | 254 |
| 15.9.6.1 Stretch of Line Elements | 254 |
| 15.9.6.2 Integration of the Rotation | 255 |
| 15.9.6.3 Displacements in Reference Coordinates | 255 |
| 15.10 Morphing Solution Algorithm | 255 |
| 15.10.1 Inner Process | 256 |
| 15.10.2 Outer Process | 258 |
| 15.11 Morphing Simulations | 259 |

- 15.11.1 Material, Laminates, and Reference Shape 259
- 15.11.2 Deformed Configurations 259
- 15.11.3 Stretch-Line-Force Diagrams 260
- 15.12 Discussion 260
- 15.13 Conclusion 261
- References 262

Part III Applications of Nonlinear Dynamics

16 An FE-BE Method for the Hydroelastic Vibration Analysis of Plates and Shells Partially in Contact with Fluid 267

I. Tugrul Ardic, M. Erden Yildizdag, and Ahmet Ergin

- 16.1 Introduction 267
- 16.2 Mathematical Model 271
 - 16.2.1 In-Vacuo (Dry) Structural Analysis 271
 - 16.2.2 Wet Analysis 273
 - 16.2.2.1 Formulation of the Fluid Problem 273
 - 16.2.2.2 Numerical Evaluation of Perturbation Potential 273
 - 16.2.2.3 Generalized Fluid-Structure Interaction Forces 275
 - 16.2.2.4 Calculation of Wet Frequencies and Mode Shapes 276
- 16.3 Numerical Examples 276
 - 16.3.1 Vertical Rectangular Plate in Contact with Fluid on One Side 276
 - 16.3.2 Horizontal Cylindrical Shell Partially Filled with Fluid . . 283
- 16.4 Conclusions 288
- References 297

17 A Multimodal Approach for Automation of Mechanical Design 301

Klaus Hoschke, Konstantin Kappe, Werner Riedel, and Stefan Hiermaier

- 17.1 Introduction 301
- 17.2 Theoretical Framework 304
 - 17.2.1 Linear, Elastic, and Static Problem Description 304
 - 17.2.2 Nonlinear, Plastic, and Transient Problem Description . . . 305
 - 17.2.3 Topology Optimization 307
- 17.3 Multimodal Approach for the Mechanical Design 310
- 17.4 Save, Lightweight Design Scheme 311
- 17.5 Implementation and Demonstration 313
 - 17.5.1 Multiple-Model Topology Optimization 313
 - 17.5.2 Conversion of Analysis Modes 315
 - 17.5.3 Conversion of the Analysis Domain and Spatial Discretization 316
 - 17.5.4 Nonlinear Analysis and Nonlinear Optimization 317
- 17.6 Experimental Validation by Testing of 3D Printed Structures 318
- 17.7 Conclusion 320
- References 322

| | | |
|-----------|---|-----|
| 18 | Forced Longitudinal Fractional Type Vibrations of a Rod with Variable Cross Section | 325 |
| | Katica R. (Stevanović) Hedrih | |
| 18.1 | Introduction | 326 |
| 18.2 | Fundamentals of Mechanics of Hereditary and Fractional Type Materials and Systems | 327 |
| 18.3 | Constitutive Relation of the Fractional Type Material of the Rod .. | 327 |
| 18.4 | Partial Fractional Order Differential Equation of Longitudinal Fractional Type Vibrations of a Rod with Variable Cross Section .. | 328 |
| 18.5 | Solution of Partial Fractional Order Differential Equation | 330 |
| 18.5.1 | Free Longitudinal Fractional Type Oscillation | 330 |
| 18.5.2 | Forced Longitudinal Fractional Type Oscillation | 331 |
| 18.6 | Energy Analysis | 336 |
| 18.7 | Concluding Remarks | 342 |
| | References | 342 |
| 19 | Comparative Numerical Analysis of Composites in the Aspect of Contact Algorithm | 345 |
| | Agnieszka Derewonko | |
| 19.1 | Introduction | 345 |
| 19.2 | The Contact Problems | 346 |
| 19.3 | Research Object | 350 |
| 19.4 | Validation of Numerical Models | 352 |
| 19.5 | Results of Numerical Simulations | 353 |
| 19.6 | Summary and Conclusions | 356 |
| | References | 360 |
| 20 | Vibration Analysis Based Spalling Defect Severity Assessment of Spur Gearbox Using a Dynamic Model | 363 |
| | Vishwadeep C. Handikherkar & Vikas M. Phalle | |
| 20.1 | Introduction | 363 |
| 20.2 | Evaluation of Gear-Mesh Stiffness | 365 |
| 20.3 | Dynamical Model and Simulation | 367 |
| 20.4 | Results and Discussion | 370 |
| 20.5 | Conclusion | 373 |
| | References | 374 |
| 21 | Simulation of Self Compensating Hydrostatic Bearing Using Finite Element Analysis | 377 |
| | Sumit J. Patil, Abhishek N. Khairnar, Vikas M. Phalle, and Praveen K. Limaye | |
| 21.1 | Introduction | 378 |
| 21.2 | Methodology | 379 |
| 21.3 | Steps in Implementation of FEM | 379 |
| 21.3.1 | Step 1 - Setting up the Governing Equation | 379 |
| 21.3.2 | Step 2 - Mathematical Formulation of FEM | 381 |

21.3.3 Step 3 - Meshing of the Solution Domain 383

21.3.4 Step 4 - Boundary Conditions on the Solution Domain . . 384

21.3.5 Step 5 - Computer Implementation 384

21.4 Results 384

21.5 Conclusion 387

References 388

Part IV Experimental and Numerical Techniques

22 An Experimental-Numerical Procedure for the Determination of “True” Stress-Strain Tensile Curve in Ductile Materials 391
 Anatoliy M. Bragov, Aleksander Y. Konstantinov, and Andrey K. Lomunov

22.1 Introduction 391

22.2 Split Hopkinson Bar Technique 393

22.3 True Stresses and Strains in the Tension Experiments 393

22.4 Experimental and Numerical Procedure of Construction a True Strain Curve According to Experiment on High-Speed Tension . . . 395

22.5 Conclusions 398

References 400

23 Experimental Study of the Dynamic Properties of Concrete under Compressive Load 403
 Anatoliy M. Bragov, Mikhail E. Gonov, Andrey K. Lomunov, and Vladimir VI. Balandin

23.1 Introduction 404

23.2 The Method of Manufacturing Concrete Samples 404

23.3 Test Results of Samples of Fine-Grained Concrete under Compressive Load 406

23.4 Conclusion 409

References 411

24 FE-Analysis of Deformation and Failure of Structural Elements under Quasistatic Multifactor Effects 413
 Vasilii Gorokhov, Dmitrii Zhegalov, Dmitrii Kazakov, Sergei Kapustin, and Yuriy Churilov

24.1 Introduction 413

24.2 Technique of Numerical Modeling of Deformation and Accumulation of Damages in Structural Elements under Quasi-Static Loading 414

24.3 Technique of Modeling the Processes of Nucleation and Propagation of Cracks 417

24.4 Numerical Modeling of Elastoplastic Fracture of a Flat Specimen with a Notch under Conditions of Plane Bending 418

24.5 Numerical Modeling of the Crack Propagation Process in a Cylindrical Specimen with a Notch in the High-Temperature Creep 420

| | | |
|----------------------------------|--|------------|
| 24.6 | Numerical Modeling of Corrosion Failure of a Tubular Specimen under axial Tension | 422 |
| 24.7 | Conclusion | 425 |
| | References | 426 |
| 25 | Numerical Analysis of Permeability Coefficient Influence on Dynamic Responses in Poroviscoelastic Solids Using BEM | 429 |
| | Leonid A. Igumnov, Aleksander A. Ipatov, and Svetlana Yu. Litvinchuk | |
| 25.1 | Introduction | 429 |
| 25.2 | Mathematical Model | 431 |
| | 25.2.1 Poroelastic Formulation | 431 |
| | 25.2.2 Poroviscoelastic Formulation | 432 |
| 25.3 | Solution Method | 432 |
| | 25.3.1 Boundary-Element Approach | 432 |
| | 25.3.2 Laplace Transform Inversion | 434 |
| 25.4 | Numerical Results | 435 |
| | 25.4.1 Test Example | 435 |
| | 25.4.2 Poroviscoelastic Solutions | 436 |
| 25.5 | Conclusion | 439 |
| | References | 440 |
| 26 | Deformation and Destruction at Deformation Rate of Order 10^3 s^{-1} in Wood of Hardwood Trees | 443 |
| | Anatoliy Bragov, Mikhail Gonov, Aleksander Konstantinov, Andrey Lomunov, and Tatiana Yuzhina | |
| 26.1 | Introduction | 443 |
| 26.2 | Experimental Methods and Investigated Samples | 445 |
| 26.3 | Conclusion | 449 |
| | References | 450 |
| Part V Masonry Structures | | |
| 27 | Effect of Shape Uncertainties on the Collapse Condition of the Circular Masonry Arch | 455 |
| | Nicola Cavalagli, Vittorio Gusella, and Riccardo Liberotti | |
| 27.1 | Introduction | 455 |
| 27.2 | Generative Modelling of Masonry Arches with Uncertain Shape | 457 |
| | 27.2.1 Geometrical hypotheses | 457 |
| | 27.2.2 The Random Defined Polycentric Arch | 458 |
| 27.3 | Limit Equilibrium Analysis | 460 |
| 27.4 | Analysis of the Results | 462 |
| 27.5 | Conclusion | 465 |
| | References | 466 |

28 Challenging Mathematical Insights into Masonry Domes over the Centuries 469
 Raffaella Pavani

28.1 Introduction 469

28.2 Parabola vs. Catenary 470

28.3 Case Study: Santa Maria del Fiore in Florence 475

28.4 Some More Ancient Masonry Domes 477

 28.4.1 St. Peter’s Dome in Rome 477

 28.4.2 St. Gaudenzio’s Dome in Novara 478

28.5 Conclusions 479

References 479

29 Innovative Voxel Approach for Homogenized Out-of-Plane Analysis of Non-Periodic Masonry Walls 481
 Simone Tiberti & Gabriele Milani

29.1 Introduction 481

29.2 Voxel Procedure for Homogenized Out-of-Plane Failure Surfaces . 482

29.3 Numerical Validation of the Voxel Procedure 484

29.4 Application of the Voxel Procedure to Single Curvature Masonry Cells 486

29.5 Application of the Voxel Procedure to a Double Curvature Masonry Cell 488

29.6 Conclusion 490

References 491

List of Contributors

I. T. Ardic

Department of Naval Architecture and Ocean Engineering, Istanbul Technical University, Maslak, 34469, Istanbul, Turkey
e-mail: ardici@itu.edu.tr

V. VI. Balandin

Research Institute for Mechanics, National Research Lobachevsky State University of Nizhni Novgorod, av. Gagarin 23b6, Nizhny Novgorod, 603950, Russia
e-mail: rustydog2007@yandex.ru

E. Barchiesi

International Research Centre on Mathematics and Mechanics of Complex Systems, Università degli Studi dell'Aquila, Via Giovanni Gronchi 18 - Zona industriale di Pile, 67100 L'Aquila, Italy.
e-mail: barchiesiemilio@gmail.com

A. M. Bragov

Research Institute for Mechanics, National Research Lobachevsky State University of Nizhni Novgorod, av. Gagarin 23b6, Nizhny Novgorod, 603950, Russia
e-mail: bragov@mech.unn.ru

N. Cavalagli

Department of Civil and Environmental Engineering, University of Perugia, Perugia, Italy
e-mail: nicola.cavalagli@unipg.it

Yu. A. Churilov

Research Institute for Mechanics, National Research Lobachevsky State University of Nizhni Novgorod, av. Gagarin 23b6, Nizhny Novgorod, 603950, Russia
e-mail: chyuan@rambler.ru

R. dell'Erba

ENEA Technical Unit technologies for energy and industry - Robotics Laboratory
e-mail: ramiro.dellerba@enea.it

A. Derewonko

Department of Mechanics and Applied Computer Science, Faculty of Mechanical Engineering, Military University of Technology, Sylwestra Kaliskiego Street 2, 00-908 Warsaw, Poland
e-mail: agnieszka.derewonko@wat.edu.pl

A. Ergin

Department of Naval Architecture and Ocean Engineering, Istanbul Technical University, Maslak, 34469, Istanbul, Turkey
e-mail: ergina@itu.edu.tr

S. R. Eugster

Institute for Nonlinear Mechanics, University of Stuttgart, Stuttgart, Germany
e-mail: eugster@inm.uni-stuttgart.de

D.T. Filipovic

ETH Zürich, Tannenstr. 3, Zurich, Switzerland
e-mail: fidaniel@ethz.ch

D. Georgievskii

Mechanical and Mathematical Department, Moscow State University, Moscow 119991, Russia
e-mail: georgiev@mech.math.msu.su

M. Gonov

Research Institute for Mechanics, National Research Lobachevsky State University of Nizhni Novgorod, av. Gagarin 23b6, Nizhny Novgorod, 603950, Russia
e-mail: gonov_mikhail@mech.unn.ru

V. A. Gorokhov

Research Institute for Mechanics, National Research Lobachevsky State University of Nizhni Novgorod, av. Gagarin 23b6, Nizhny Novgorod, 603950, Russia
e-mail: vas-gor@rambler.ru

V. Gusella

Department of Civil and Environmental Engineering, University of Perugia, Perugia, Italy
e-mail: vittorio.gusella@unipg.it

V. C. Handikherkar

Veerмата Jijabai Technological Institute, Mumbai.
e-mail: vishwadeepch@gmail.com

J. Harsch

Institute for Nonlinear Mechanics, University of Stuttgart, Stuttgart, Germany
e-mail: harsch@inm.uni-stuttgart.de

K. R. (Stevanović) Hedrih

Mathematical Institute of Serbian Academy of Sciences and Arts, Belgrade, Serbia.
e-mail: khedrih@sbb.rs

S. Hiermaier

Fraunhofer Institute for High-Speed Dynamics, Ernst-Zermelo-Straße 4, 79104
Freiburg, Germany
e-mail: Stefan.Hiermaier@emi.fraunhofer.de

K. Hoschke

Fraunhofer Institute for High-Speed Dynamics, Ernst-Zermelo-Straße 4, 79104
Freiburg, Germany
e-mail: Klaus.Hoschke@emi.fraunhofer.de

L. A. Igumnov

Research Institute for Mechanics, National Research Lobachevsky State University
of Nizhny Novgorod, Nizhny Novgorod, Russia
e-mail: igumnov@mech.unn.ru

A. A. Ipatov

Research Institute for Mechanics, National Research Lobachevsky State University
of Nizhny Novgorod, Nizhny Novgorod, Russia
e-mail: ipatov@mech.unn.ru

K. Kappe

Fraunhofer Institute for High-Speed Dynamics, Ernst-Zermelo-Straße 4, 79104
Freiburg, Germany
e-mail: Konstantin.Kappe@emi.fraunhofer.de

S. A. Kapustin

Research Institute for Mechanics, National Research Lobachevsky State University
of Nizhny Novgorod, av. Gagarin 23b6, Nizhny Novgorod, 603950, Russia
e-mail: sergei.kapustin@mail.ru

D. A. Kazakov

Research Institute for Mechanics, National Research Lobachevsky State University
of Nizhny Novgorod, av. Gagarin 23b6, Nizhny Novgorod, 603950, Russia
e-mail: kazakov@mech.unn.ru

A. N. Khairnar

Veer mata Jijabai Technological Institute, Mumbai.
e-mail: ankhairnar_b15@me.vjti.ac.in

A. A. Kon'kov

Department of Differential Equations, Faculty of Mechanics and Mathematics,
Moscow Lomonosov State University, Vorobyovy Gory, Moscow, 119992 Russia
e-mail: konkov@mech.math.msu.su

A. Yu. Konstantinov

Research Institute for Mechanics, National Research Lobachevsky State University of Nizhni Novgorod, av. Gagarin 23b6, Nizhny Novgorod, 603950, Russia
e-mail: bconstantinov.al@yandex.ru

M. V. Korovina

Lomonosov Moscow State University, Moscow, Russia
e-mail: betelgeuser@yandex.ru

G.R. Kress

ETH Zürich, Tannenstr. 3, Zurich, Switzerland
e-mail: gkress@ethz.ch

M. Laudato

Dipartimento di Ingegneria e Scienze dell'Informazione e Matematica, Università degli Studi dell'Aquila. Via Vetoio, Coppito, 67100 L'Aquila, Italy.
e-mail: marco.laudato@graduate.univaq.it

R. Liberotti

Department of Civil and Environmental Engineering, University of Perugia, Perugia, Italy
e-mail: riccardo.liberotti@unipg.it

P. K. Limaye

Bhabha Atomic Research Centre (BARC), Mumbai
e-mail: pklimaye@barc.gov.in

S. Yu. Litvinchuk

Research Institute for Mechanics, National Research Lobachevsky State University of Nizhny Novgorod, Nizhny Novgorod, Russia
e-mail: litvinchuk@mech.unn.ru

A. K. Lomunov

Research Institute for Mechanics, National Research Lobachevsky State University of Nizhni Novgorod, av. Gagarin 23b6, Nizhny Novgorod, 603950, Russia
e-mail: lomunov@mech.unn.ru

H. A. Matevossian

Federal Research Center "Computer Science and Control", Russian Academy of Sciences,
Vavilov str., 40, Moscow 119333 Russia;
Steklov Mathematical Institute, Russian Academy of Sciences, Gubkin str., 8,
Moscow 119991 Russia;
Moscow Aviation Institute (National Research University),
Volokolomskoe shosse, 4, Moscow 125993 Russia;
e-mail: hmatevossian@graduate.org

G. Milani

Technical University of Milan, Piazza Leonardo da Vinci 32, 20133 Milan
e-mail: gabriele.milani@polimi.it

G. Nordo

MIFT - Dipartimento di Scienze Matematiche e Informatiche, Scienze Fisiche e Scienze della Terra,
Università di Messina, Viale F. Stagno D'Alcontres, 31 – Contrada Papardo, salita Sperone,
98166 Sant'Agata – Messina, Italy;
e-mail: giorgio.nordo@unime.it

S. J. Patil

Veerмата Jijabai Technological Institute, Mumbai.
e-mail: sjpatil_b15@me.vjti.ac.in

R. Pavani

Department of Mathematics, Politecnico di Milano, Piazza L. da Vinci 32 - 20133 Milano, Italy
e-mail: raffaella.pavani@polimi.it

S. Pfaller

Chair of Applied Mechanics, Friedrich-Alexander-Universität Erlangen-Nürnberg
e-mail: sebastian.pfaller@fau.de

V. M. Phalle

Veerмата Jijabai Technological Institute, Mumbai.
e-mail: vmphalle@me.vjti.ac.in

W. Riedel

Fraunhofer Institute for High-Speed Dynamics, Ernst-Zermelo-Straße 4, 79104 Freiburg, Germany
e-mail: Werner.Riedel@emi.fraunhofer.de

M. Ries

Chair of Applied Mechanics, Friedrich-Alexander-Universität Erlangen-Nürnberg
e-mail: maximilian.ries@fau.de

D. Scerrato

International Research Centre on Mathematics and Mechanics of Complex Systems,
Università degli Studi dell'Aquila, Via Giovanni Gronchi 18 - Zona industriale di Pile, 67100 L'Aquila, Italy.
e-mail: daria.scerrato@gmail.com

M. V. Shamolin

Institute of Mechanics, Lomonosov Moscow State University, 1 Michurinskii Ave., 119192, Moscow, Russian Federation
e-mail: shamolin@imec.msu.ru

V. Yu. Smirnov

Moscow Aviation Institute (National Research University), Moscow, Russia
e-mail: vl-smirnov@mail.ru

P. Steinmann

Chair of Applied Mechanics, Friedrich-Alexander-Universität Erlangen-Nürnberg
e-mail: paul.steinmann@fau.de

S. Tiberti

Technical University of Milan, Piazza Leonardo da Vinci 32, 20133 Milan
e-mail: simone.tiberti@polimi.it

C. A. Tran

International Research Centre on Mathematics and Mechanics of Complex Systems,
Università degli Studi dell'Aquila, Via Giovanni Gronchi 18 - Zona industriale di
Pile, 67100 L'Aquila, Italy.
e-mail: tcanth@outlook.com

E. Turco

Department of Architecture, Design and Urban planning (DADU), University of
Sassari, Italy
e-mail: emilio.turco@uniss.it

A. V. Vestyak

Moscow Aviation Institute (National Research University), Moscow, Russia.
e-mail: vestyak2016@mail.ru

M. E. Yildizdag

Department of Naval Architecture and Ocean Engineering, Istanbul Technical
University, Maslak, 34469, Istanbul, Turkey
e-mail: yildizdag@itu.edu.tr

T. Yuzhina

Research Institute for Mechanics, National Research Lobachevsky State University
of Nizhni Novgorod, av. Gagarin 23b6, Nizhny Novgorod, 603950, Russia
e-mail: yuzhina_tatiana@mech.unn.ru

D. V. Zhegalov

Research Institute for Mechanics, National Research Lobachevsky State University
of Nizhni Novgorod, av. Gagarin 23b6, Nizhny Novgorod, 603950, Russia
e-mail: zhegalov@mech.unn.ru



Chapter 1

International Conference on Nonlinear Solid Mechanics 2019: General Topics and Review of Plenary Lectures

Marco Laudato, Daria Scerrato, Chuong Anthony Tran, and Emilio Barchiesi

Abstract The International Conference on Nonlinear Solid Mechanics (ICoN-SoM) 2019, held in Rome from June 16th through 19th of 2019, had as its main goal to gather together researchers in the field of nonlinear Solid Mechanics in a stimulating research environment. This work accounts for the plenary lectures held during the conference. It is mainly aimed at providing interested researchers with a track of the contents discussed during the conference and with the relevant bibliography of the plenary lectures. Additional information, such as the abstracts of all the talks, can be found on the official web-site of the conference: <http://www.memocsevents.eu/iconsom2019>.

Keywords: Nonlinear mechanics · Surface elasticity · Digital volume correlation · Composite structures

1.1 Why Nonlinear Solid Mechanics Deserves an International Conference?

Nonlinearity is one of the key-features shared by the majority of the fast-growing sectors of Solid Mechanics. Thanks to the recent development of efficient numerical methods and reliable fast-prototyping techniques, researchers and engineers are

M. Laudato

Dipartimento di Ingegneria e Scienze dell'Informazione e Matematica,
Università degli Studi dell'Aquila. Via Vetoio, Coppito, 67100 L'Aquila, Italy.
e-mail: marco.laudato@graduate.univaq.it

D. Scerrato, C. A. Tran, E. Barchiesi

International Research Centre on Mathematics and Mechanics of Complex Systems,
Università degli Studi dell'Aquila, Via Giovanni Gronchi 18 - Zona industriale di Pile, 67100
L'Aquila, Italy.
e-mail: daria.scerrato@gmail.com, tcanth@outlook.com, barchiesiemilio@gmail.com

© Springer Nature Switzerland AG 2020

B. E. Abali and I. Giorgio (eds.), *Developments and Novel Approaches in Nonlinear Solid Body Mechanics*, Advanced Structured Materials 130,
https://doi.org/10.1007/978-3-030-50460-1_1

nowadays enabled to explore experimentally and mathematically new methods for the analysis of nonlinear phenomena. One of the most relevant examples is provided by mechanical metamaterials Barchiesi et al (2019b); Milton et al (2017a). Researchers working in different areas of Mechanics worldwide are sharing efforts trying to understand and control the behaviours of multi-scale systems, where nonlinearity related to the intrinsic complexity of such systems can exhibit phenomena of notable engineering interest Misra et al (2018); Milton et al (2017b).

When considering systems with a kinematics given – at so-called micro-scale – in terms of extremely many degrees of freedom, one of the amenable approaches for an efficient description is to devise an equivalent macroscopic continuum field theory Steigmann and dell’Isola (2015); Steigmann (1996), for instance via homogenization techniques Rahali et al (2015); Seppecher et al (2011); Boutin et al (2017); Mandadapu et al (2018). Owing to the complexity of the system in terms of mechanics and topology of the microstructure, it might happen that the resulting continuous description cannot be framed in the setting of standard Cauchy elasticity Alibert et al (2003). Generalizations of Cauchy elasticity, often in non-linear regimes, have to be considered in these cases, namely *generalized continua* dell’Isola et al (2015); dell’Isola et al (2015). A paradigmatic example of generalized continua – particularly second gradient continua – is given by so-called pantographic metamaterials dell’Isola et al (2019a,b); Placidi et al (2016a).

In Solid Mechanics, nonlinearity can arise also in the study of systems where the mechanical behaviour is coupled with other physical interactions, as electromagnetic ones Andreaus et al (2004); Alessandrini et al (2004); Giorgio et al (2009); Los-souarn et al (2016), and also when the considered system is composite and made up of different (and interacting) materials Lekszycki and dell’Isola (2012); Madeo et al (2012); Giorgio et al (2017a); Abali et al (2019). Clearly, nonlinearities arise naturally when a material undergoes large deformations dell’Isola et al (2016). There are many phenomena which are intrinsically nonlinear, both in a statics Giorgio et al (2016, 2017b); Abali et al (2015) and dynamics Baroudi et al (2019); Laudato and Barchiesi (2019). The message that emerges clearly from the above-reported evidence is that mathematical descriptions needed to obtain wholesome forecasts should not be limited by linearity.

In addition to developments in mathematical Placidi et al (2016b); Giorgio et al (2017c) and numerical Turco et al (2016a,b); Niiranen et al (2016); Khakalo and Niiranen (2017); Abali et al (2017, 2015) aspects, the fast growth of nonlinear Solid Mechanics is undoubtedly due to the improvements in fast-prototyping and experimental methods: 3D-printing techniques, for instance, allow to reach the accuracy needed to fabricate complex microstructures at engineering scales Golaszewski et al (2019); dell’Isola et al (2019c). Furthermore, the time required for specimens fabrication, thanks to improvements in many of the involved technologies Spagnuolo et al (2019), has been reduced as to make a trial-and-error approach feasible. Nevertheless, complex microstructures designed to undergo large deformations still require new and more advanced experimental techniques to obtain reliable and wholesome data. This has pushed researchers to enhance existing experimental and data acquisition techniques, and even to invent new ones. One of the most successful examples is

given by Digital Image Correlation techniques Barchiesi et al (2019a); Hild and Roux (2006), where a panoply of enhancements and new concepts have been introduced for taking into account heterogeneous materials and extremely large deformations.

It is therefore concluded that Nonlinear Solid Mechanics represents the ideal meeting point for researchers working within all the different areas of Mechanics to share points of view and know-how. This has been the main motivation behind the establishment of the International Conference of Nonlinear Solid Mechanics (ICoNSoM) 2019, held in Rome from June 16th through 19th of 2019. ICoNSoM has been purposely conceived to provide a stimulating opportunity of discussion in the community of nonlinear Solid Mechanics. Following the path established by the Canadian Conference on Nonlinear Solid Mechanics held in 2013 at McGill University, the International Research Centre on Mathematics and Mechanics of Complex System (M&MoCS) and the McGill University have started this series of international conferences on the topic. The conference was organized in collaboration with the Laboratoire International Associé Coss&Vita and the Department of Architecture of the University ROMA TRE. ICoNSoM 2019 has been an occasion to foster an effective exchange of knowledge and ideas between scientists from different expertise areas. A series of plenary lectures has been held by acknowledged experts in the various fields related to nonlinear Solid Mechanics. The content of these lectures, that are discussed in detail successively, has been designed to give a smooth introduction to the relevant topics of the conference and, at the same time, to provide a reliable idea of the state of the art progresses.

The talks and the keynote lectures have been organized in a series of thematic mini symposia. The following list of symposia can be therefore considered as a reliable overview of the main topics analyzed during the conference:

- Nonlinear dynamics and wave motion
- Micro and nano systems
- Nonlinear vibrations of continuous systems
- Nonlinear mechanics with singularities
- Dynamics and control of MEMS and NEMS
- Nonlinear phenomena in granular solid: modeling and experiments
- Nonlinear dynamics and control of advanced materials and structures
- Mathematical models and numerical methods for hysteretic mechanical systems and materials
- Unusual dynamics and active control
- Asymptotic approaches in nonlinear of mechanics of solids
- Novel computational methods with applications in continuum mechanics
- Ten years of global digital volume correlations: what has been achieved?
- Nonlinear fluid-structure interactions
- Buckling and post-buckling of laminated structures
- Contact mechanics of interfaces
- Topology optimization and structures
- Advanced experimental solid mechanics and optical field measurement
- Computational fracture mechanics

- Nonlinear mechanics of lattice metamaterials
- Acoustic metamaterials: recent developments and challenges
- Structural models with high continuity: theoretical and numerical aspects
- Nonlinear biomechanics of soft tissue
- Complex structures and microarchitectures of metamaterials
- Advanced modeling in mechanobiology
- Generalized models of solids including surface-related phenomena
- Perspectives in generalized continua
- Multiscale modeling of plasticity, viscoelasticity, viscoplasticity of heterogeneous materials
- New frontiers in regularized damage modeling
- Multiscale and multi-physics modeling for complex materials
- Additive manufacturing and characterization of metamaterials
- Numerical methods for stochastic mechanics and dynamical systems
- Recent advances in the mechanical modeling of architected materials and periodic structures
- Modeling natural and engineered materials with internal microstructure
- Nonlinear static and dynamic instability of thin-walled structures
- Mechanical friction, wear, lubrication and condition monitoring
- Mathematical physics, theory of capillarity and composite materials
- Advanced mechanical modeling of composite materials and structures
- Multiscale modeling of polymers and elastomers
- Nonlinear behavior of vaulted masonry structures
- Modeling and computational strategies for masonry structures

Since a complete report of such a populated list of symposia is not suitable within a single paper, in the following we will discuss in details the content (with a list of relevant bibliographic references) of all the plenary lectures. We are planning to produce similar reports for other relevant symposia of the ICoNSoM conference in a close future. For further details, the interested reader can visit the official web-site of the conference.

1.2 Plenary Lectures

In this section, the topic of the plenary lectures held during the conference will be reviewed, aimed at giving a rapid link with the relevant bibliography.

1.2.1 Nonlinear Mechanics of Drilling – B. Balachandran

Balakumar Balachandran, is Minta Martin Professor of Engineering at the University of Maryland since 1993. Nonlinear phenomena, control, vibration and dynamics

have been the main topic explored during his research career. He is the author of the successful Wiley textbook *Applied Nonlinear Mechanics: Analytical, Computational, and Experimental Methods*, a Cambridge University Press textbook titled *Vibrations*, and he was the editor of the Springer book *Delay Differential Equations, Recent Advances and New Directions*. Prof. Balachandran holds five different patents on atomic force microscopy and fiber optics.

In his lecture titled *Nonlinear mechanics of drilling*, he discussed the nonlinearity sources when modeling drilling operations, with special focus on the petro-chemical sector. Prof. Balachandran provided technical background supporting that these nonlinearities are often the reason of harmful vibrations in drill-strings and are mainly related to the contact between the drill string and bore hole, to coupling between axial, torsional and lateral motions, and to drag-bit cutting mechanics Liao et al (2011); Liu et al (2013, 2014). The role of delay effects in cutting action operations such as milling, and their relation to nonlinear behavior of this kind of systems, was one of the key concepts of his talk. During the lecture, some of the consequent phenomena such as forward and backward whirling motions and stick-slip dynamics have been discussed and a combination of analytical, numerical, and experimental results on drill-string dynamics have been presented.

1.2.2 Surface Elasticity with Applications to Material Modeling at the Nano- and Micro-Scales – V. A. Eremeyev

Victor A. Eremeyev is professor at Gdańsk University of Technology. His main research interests are related to the theory of elastic and inelastic shells. Moreover, he has studied the behavior of continuum media with microstructure and generalized media such as Cosserat continua. Finally, he is involved in the analysis of surface stresses, nonlinear elasticity nano- and micro-mechanics, and phase transformations. His research had a remarkable impact in these topics and he has been author of more than 160 publications and 13 edited or written books.

He presented a lecture titled *Surface elasticity with applications to material modeling at the nano- and micro-scales*. The main aim of the lecture was to present material modeling strategies within the framework of surface elasticity models. The first part of his lecture was focused on the formulation of surface elasticity models. The strategy is to model body boundaries as elastic membranes or shells. From the mathematical point of view, this assumption corresponds to define a dynamical generalization of the Laplace-Young equation from capillarity theory. Following this scheme, the influence of the surface stresses on the parametrization of layered plates and shallow shells was discussed. However, the essential effect on the surface properties is related to the propagation of anti-plane surface waves Eremeyev and Sharma (2019); Eremeyev et al (2019); Eremeyev (2019). Finally, in the last part of the talk a new class of surface metamaterials, called metasurface and based on coatings, has been presented. In particular, strategies for the definition of a

homogenized continuum model obtained by replacing thin coating with an effective material surface have been outlined.

1.2.3 Ten Years of Global Digital Volume Correlation: What Has Been Achieved? – F. Hild

François Hild is CNRS research professor at the Laboratoire de Mécanique et Technologie, ENS Paris-Saclay. His research interests have been initially related to brittle fracture, where he gave fundamental contributions in renewing the then-classical approach. After that, he focused on the application of image processing techniques to experimental mechanics as full-field measuring tool, i.e. digital image correlation. He was one of the pioneers in this field, whose output has been diffusely transferred – also thanks to his continuous efforts in collaborative projects with industrial partners – into commercial solutions. The impact of his work onto the scientific community granted him the CNRS 2017 silver medal.

In the lecture *Ten years of global digital volume correlation: What has been achieved?*, François Hild reviewed the major developments in global digital volume correlation over the past ten years. So-called global approaches to digital volume correlation were carefully described, underlying particularly how they can be tailored to exploit the utilization of kinematic fields obtained from finite element simulations Hild et al (2019); Mendoza et al (2019); Hild and Roux (2006): one of the breakthrough of François Hild’s research is the introduction of model-based mechanical content into the optical measurement of displacement fields to enhance the quality of results. In the final part of his presentation several case-studies were presented, highlighting how the various features of global digital volume correlation were tailored to overtake some of the most challenging problems in today’s experimental mechanics.

1.2.4 Granular Micromechanics: Bridging Grain Interactions and Continuum Descriptions – A. Misra

Anil Misra is professor in the Civil, Environmental and Architectural Engineering Department of the University of Kansas. His research interests span a wide range, from fundamental topics in generalized mechanics to applications in geo-materials and bio-materials, passing through computational and experimental aspects in granular mechanics. His scientific production of more than 300 papers in journals, edited books and conference proceedings, has a vast recognition. For the impact of his research he was awarded in 2017 the Eugenio Beltrami Senior Scientist Prize.

In his lecture *Granular micromechanics: bridging grain interactions and continuum descriptions*, Prof. Misra analyzed relations between continuum and discrete descriptions for granular materials. Kinematic measurements of disk assemblies,

with and without controlled grain interactions Misra and Jiang (1997), were presented as phenomenological basis to introduce the micromechanics approach, i.e. a modeling strategy based on the interplay between a discrete micro-scale description and a suitable macro-scale continuum description Misra and Poursolhjoui (2017); NejadSadeghi and Misra (2019); Misra and NejadSadeghi (2019). Since interactions between grains play a fundamental role on the overall behavior of granular systems, any modeling scheme should strongly rely on the specification of these interactions. Within the approach devised by Prof. Misra, the mechanical properties of the target micromorphic continuum model can be derived without needing full knowledge of mechano-morphological properties at micro-scale, which current measurement techniques cannot provide satisfactorily. During the lecture, the main advantages of this approach were shown by means of examples and computations. In particular, promising results in the study of damage and failure in cementitious materials Poursolhjoui and Misra (2017), wave dispersions and frequency band gaps Misra and Poursolhjoui (2016); NejadSadeghi et al (2019), and in the design of granular metamaterials Jia et al (2017); Misra and NejadSadeghi (2019) have been outlined. Finally, some specific applications of continuum models based on granular micromechanics were discussed Yang and Misra (2012); Misra et al (2017); Misra and Poursolhjoui (2015).

1.2.5 On Seven- and Twelve-Parameter Shell Finite Elements and Non-Local Theories for Composite Structures – J. N. Reddy

Junuthula N. Reddy is a Distinguished Professor, Regents' Professor, and inaugural holder of the Oscar S. Wyatt Endowed Chair in Mechanical Engineering at Texas A&M University in College Station. He authored pioneering works on the theory and finite element analysis of shear-deformable plates and shells, with special focus on the analysis of interlaminar stresses in composite structures. During his successful career he received several honors and awards. He is an elected member of the US National Academy of Engineering, a Foreign Fellow of the Canadian Academy of Engineering, a member of the Indian National Academy of Engineering, and of the Brazilian National Academy of Engineering.

In the first part of his lecture *On seven- and twelve-parameter shell finite elements and non-local theories for composite structures*, finite element methods for large deformation analyses of composite shell structures were discussed. In particular, the differences between the seven parameters and twelve parameters finite elements were analyzed Payette and Reddy (2014); Rivera et al (2016); Rivera and Reddy (2016). The seven-parameter shell elements are defined as a generalization of the first-order shell theory by means of a seven-parameter expansion of the displacement field. On the other hand, the twelve-parameter shell elements are obtained by means of a third-order thickness stretch kinematics. In the second part of the lecture, some recent results in non-local elasticity – especially on the role of couple-stresses in the modeling of functionally graded beams and plates – were analyzed Reddy and Srinivasa

(2014). Two modeling schemes were discussed, the first being based on the modified couple-stress theory by Mindlin, taking into account geometric nonlinearities, and the second being based on the Srinivasa-Reddy gradient elasticity theory Srinivasa and Reddy (2013), which takes into account microstructure-dependent size effects. In the final part of his presentation, Prof. Reddy presented the finite element scheme GraFEA, aimed at studying damage and fracture in brittle materials Khodabakhshi et al (2016).

1.2.6 Exploiting Global Dynamics to Unveil the Nonlinear Response and Actual Safety of Systems and Structures – G. Rega

Giuseppe Rega is Professor Emeritus at the Sapienza University of Rome. During his career, he gave fundamental contributions to several fields of Mechanics such as nonlinear oscillations, cable dynamics, macro-to-micro scale analysis of structural mechanics, chaos and bifurcation phenomena in applied mechanics, exploitation of global dynamics for engineering safety and many others. He was awarded the ASME Lyapunov Award 2017 and he has been honored with the Birthday anniversary Special Issue of Nonlinear Dynamics and of International Journal of Nonlinear Mechanics.

In his lecture *Exploiting global dynamics to unveil the nonlinear response and actual safety of systems and structures* he carefully discussed the role played by global dynamics in unveiling the nonlinear response and actual safety of engineering structures in different environments Lenci and Rega (2019). A first successful example of the use of this approach is the modeling of thermo-mechanical laminated plates with von Kármán nonlinearities in presence of mechanical excitations and body and boundary thermal sources Saetta and Rega (2017). Indeed, the complementary information given by local bifurcation analyses and the study of the global dynamics allow to detect particular conditions under which the thermal transient strongly influences the steady (buckled and unbuckled) responses of the system. In such situations, it is observed a different dynamical behavior of the system with respect to the case when the mechanical system is directly subjected to steady thermal excitations Settini et al (2018). Other interesting examples were discussed, as a minimal order model of atomic force micro-cantilever for the non-contact detection of sample surface properties Settini and Rega (2016b,a). Finally, the great potential of global dynamics analyses in the evaluation of dynamical integrity and its consequences on an aware, safe, and less-conservative design of systems and structures were discussed.

1.2.7 Vibrations of Nonlinear Continua Subject to Combined Harmonic and Stochastic Forces: Linearization Approximations and Monte Carlo Simulations – P. D. Spanos

Pol D. Spanos is L.B. Ryon Endowed Chair in Engineering at Rice University in Houston, Texas. His research interests focus on the dynamics and vibrations analysis of structural and mechanical nonlinear systems under different loads in hazard/risk inducing conditions. Moreover, he has given seminal contributions in fatigue and fracture mechanics for composite materials, and developed algorithms for the study of dynamic phenomena in biomedical applications. His research efforts have enabled major improvements in these subjects and, for this reason, he has received several honors and awards.

He presented a lecture titled *Vibrations of Nonlinear continua subject to combined harmonic and stochastic forces: linearization approximations and Monte Carlo simulations*. The main aim of the lecture was to present an efficient modeling scheme to estimate the second order statistics of the response of a continuum system undergoing a combination of random and harmonics loads. The main advantage of this scheme is that it can successfully describe systems in which the harmonic load is affected by a significant noise that cannot be neglected when computing the response statistics. The systems considered during the talk were beams and plates endowed with fractional derivative elements undergoing nonlinear vibrations. In the modeling approach the system response is represented by linear modes of vibrations, obtaining in this way a system of nonlinear fractional ordinary differential equations for the time dependent variation of the modes amplitude. The stochastic ordinary differential equations which arise in the description are analyzed by combining the harmonic balance and statistical linearization techniques in order to derive the coupled nonlinear algebraic equations which describe the second-order statistical behavior of the response. In the final part of the lecture, some relevant Monte Carlo simulations were shown to highlight the reliability of the presented modeling approach Kougoumtzoglou and Spanos (2009, 2012, 2013).

1.3 Conclusions

ICoNSoM 2019 has been a valuable opportunity for researchers from different backgrounds to share ideas and establish new collaborations. The relaxing atmosphere provided by the venue, Palazzo Argiletum in Rome, and the proposed social events have contributed to build a stimulating research environment. Moreover, the excellent work made by the chairmen of the several mini symposia, has facilitated spontaneous debates during the talks. From the discussions generated during and after all the plenary lectures it is evident that the nonlinear Solid Mechanics framework has a true prospective future. Several crucial problems are still open and will require the shared efforts of all the community. In the the opinion of the authors, it is worth to be noted

that ICoNSoM 2019 has also given to several young researchers the opportunity to present their own research projects during a populated poster session, and to attend the presentations of eminent scientists in their fields. The hope of the organizers is that new scientific collaborations will start following the interesting discussions originated during the conference and, most importantly, that the exposure to variegated ideas provided by the conference will inspire scientists to develop new approaches progressing the whole field of nonlinear Solid Mechanics.

References

- Abali BE, Müller WH, Eremeyev VA (2015) Strain gradient elasticity with geometric nonlinearities and its computational evaluation. *Mechanics of Advanced Materials and Modern Processes* 1(1):4, DOI 10.1186/s40759-015-0004-3
- Abali BE, Müller WH, dell'Isola F (2017) Theory and computation of higher gradient elasticity theories based on action principles. *Archive of Applied Mechanics* 87(9):1495–1510
- Abali BE, Yang H, Papadopoulos P (2019) A computational approach for determination of parameters in generalized mechanics. In: Altenbach H, Müller WH, Abali BE (eds) *Higher Gradient Materials and Related Generalized Continua, Advanced Structured Materials*, vol. 120, Springer, Cham, chap 1, pp 1–18, DOI 10.1007/978-3-030-30406-5_1
- Alessandroni S, Andreaus U, dell'Isola F, Porfiri M (2004) Piezo-electromechanical (pem) Kirchhoff–Love plates. *European Journal of Mechanics-A/Solids* 23(4):689–702
- Alibert JJ, Seppecher P, dell'Isola F (2003) Truss modular beams with deformation energy depending on higher displacement gradients. *Mathematics and Mechanics of Solids* 8(1):51–73
- Andreaus U, dell'Isola F, Porfiri M (2004) Piezoelectric passive distributed controllers for beam flexural vibrations. *Journal of Vibration and Control* 10(5):625–659
- Barchiesi E, Bouterf A, Hild F, dell'Isola F, Misra A, Neggers J, Pawlikowski M, Spagnuolo M, Turco E (2019a) On the use of fe-based dic to measure the kinematics of metamaterials at different scales
- Barchiesi E, Spagnuolo M, Placidi L (2019b) Mechanical metamaterials: a state of the art. *Mathematics and Mechanics of Solids* 24(1):212–234
- Baroudi D, Giorgio I, Battista A, Turco E, Igumnov LA (2019) Nonlinear dynamics of uniformly loaded elastica: Experimental and numerical evidence of motion around curled stable equilibrium configurations. *ZAMM-Journal of Applied Mathematics and Mechanics/Zeitschrift für Angewandte Mathematik und Mechanik* p e201800121
- Boutin C, Giorgio I, Placidi L, et al (2017) Linear pantographic sheets: Asymptotic micro-macro models identification. *Mathematics and Mechanics of Complex Systems* 5(2):127–162
- dell'Isola F, Andreaus U, Placidi L (2015) At the origins and in the vanguard of peridynamics, non-local and higher-gradient continuum mechanics: An underestimated and still topical contribution of Gabrio Piola. *Mathematics and Mechanics of Solids* 20(8):887–928
- dell'Isola F, Giorgio I, Pawlikowski M, Rizzi NL (2016) Large deformations of planar extensible beams and pantographic lattices: heuristic homogenization, experimental and numerical examples of equilibrium. *Proc R Soc A* 472(2185)
- dell'Isola F, Seppecher P, Alibert JJ, et al (2019a) Pantographic metamaterials: an example of mathematically driven design and of its technological challenges. *Continuum Mechanics and Thermodynamics* 31(4):851–884
- dell'Isola F, Seppecher P, Spagnuolo M, et al (2019b) Advances in Pantographic Structures: Design, Manufacturing, Models, Experiments and Image Analyses. *Continuum Mechanics and Thermodynamics* 31(4):1231–1282

- dell'Isola F, Turco E, Misra A, Vangelatos Z, Grigoropoulos C, Melissinaki V, Farsari M (2019c) Force–displacement relationship in micro-metric pantographs: Experiments and numerical simulations. *Comptes Rendus Mécanique* 347(5):397–405
- Eremeyev VA (2019) On anti-plane surface waves considering highly anisotropic surface elasticity constitutive relations. In: *Wave Dynamics, Mechanics and Physics of Microstructured Metamaterials*, Springer, pp 1–9
- Eremeyev VA, Sharma BL (2019) Anti-plane surface waves in media with surface structure: Discrete vs. continuum model. *International Journal of Engineering Science* 143:33–38
- Eremeyev VA, Rosi G, Naili S (2019) Comparison of anti-plane surface waves in strain-gradient materials and materials with surface stresses. *Mathematics and mechanics of solids* 24(8):2526–2535
- Giorgio I, Culla A, Del Vescovo D (2009) Multimode vibration control using several piezoelectric transducers shunted with a multiterminal network. *Archive of Applied Mechanics* 79(9):859–879, DOI 10.1007/s00419-008-0258-x
- Giorgio I, Della Corte A, dell'Isola F, Steigmann DJ (2016) Buckling modes in pantographic lattices. *Comptes rendus Mécanique* 344(7):487–501
- Giorgio I, Andreaus U, dell'Isola F, Lekszycki T (2017a) Viscous second gradient porous materials for bones reconstructed with bio-resorbable grafts. *Extreme Mechanics Letters* 13:141–147, DOI 10.1016/j.eml.2017.02.008
- Giorgio I, Della Corte A, dell'Isola F (2017b) Dynamics of 1d nonlinear pantographic continua. *Nonlinear Dynamics* 88(1):21–31
- Giorgio I, Rizzi N, Turco E (2017c) Continuum modelling of pantographic sheets for out-of-plane bifurcation and vibrational analysis. *Proceedings of the Royal Society A: Mathematical, Physical and Engineering Sciences* 473(2207):20170,636
- Golaszewski M, Grygoruk R, Giorgio I, Laudato M, Di Cosmo F (2019) Metamaterials with relative displacements in their microstructure: technological challenges in 3d printing, experiments and numerical predictions. *Continuum Mechanics and Thermodynamics* 31(4):1015–1034
- Hild F, Roux S (2006) Digital image correlation: from displacement measurement to identification of elastic properties—a review. *Strain* 42(2):69–80
- Hild F, Bouterf A, Roux S (2019) Measurement of kinematic fields via dic for impact engineering applications. *International Journal of Impact Engineering* 130:163–171
- dell'Isola F, Seppecher P, Della Corte A (2015) The postulations à la D'Alembert and à la Cauchy for higher gradient continuum theories are equivalent: a review of existing results. In: *Proc. R. Soc. A, The Royal Society*, vol 471
- Jia H, Misra A, Poorolajjouy P, Liu C (2017) Optimal structural topology of materials with micro-scale tension-compression asymmetry simulated using granular micromechanics. *Materials & Design* 115:422–432
- Khakalo S, Niiranen J (2017) Isogeometric analysis of higher-order gradient elasticity by user elements of a commercial finite element software. *Computer-Aided Design* 82:154–169
- Khodabakhshi P, Reddy J, Srinivasa A (2016) Grafea: a graph-based finite element approach for the study of damage and fracture in brittle materials. *Meccanica* 51(12):3129–3147
- Kougioumtzoglou IA, Spanos PD (2009) An approximate approach for nonlinear system response determination under evolutionary stochastic excitation. *Current science* pp 1203–1211
- Kougioumtzoglou IA, Spanos PD (2012) Response and first-passage statistics of nonlinear oscillators via a numerical path integral approach. *Journal of Engineering Mechanics* 139(9):1207–1217
- Kougioumtzoglou IA, Spanos PD (2013) Nonlinear mdof system stochastic response determination via a dimension reduction approach. *Computers & Structures* 126:135–148
- Laudato M, Barchiesi E (2019) Non-linear dynamics of pantographic fabrics: Modelling and numerical study. In: *Wave Dynamics, Mechanics and Physics of Microstructured Metamaterials*, Springer, pp 241–254
- Lekszycki T, dell'Isola F (2012) A mixture model with evolving mass densities for describing synthesis and resorption phenomena in bones reconstructed with bio-resorbable materials. *ZAMM-Zeitschrift für Angewandte Mathematik und Mechanik* 92(6):426–444

- Lenci S, Rega G (2019) *Global Nonlinear Dynamics for Engineering Design and System Safety*. Springer
- Liao CM, Balachandran B, Karkoub M, Abdel-Magid YL (2011) Drill-string dynamics: reduced-order models and experimental studies. *Journal of Vibration and Acoustics* 133(4):041,008
- Liu X, Vlajic N, Long X, Meng G, Balachandran B (2013) Nonlinear motions of a flexible rotor with a drill bit: stick-slip and delay effects. *Nonlinear Dynamics* 72(1-2):61–77
- Liu X, Vlajic N, Long X, Meng G, Balachandran B (2014) State-dependent delay influenced drill-string oscillations and stability analysis. *Journal of Vibration and Acoustics* 136(5):051,008
- Lossouarn B, Deü JF, Aucejo M, Cunefare KA (2016) Multimodal vibration damping of a plate by piezoelectric coupling to its analogous electrical network. *Smart Materials and Structures* 25(11):115,042
- Madeo A, George D, Lekszycki T, Nierenberger M, Remond Y (2012) A second gradient continuum model accounting for some effects of micro-structure on reconstructed bone remodelling. *Comptes Rendus Mecanique* 340(8):575–589
- Mandadapu KK, Abali BE, Papadopoulos P (2018) On the polar nature and invariance properties of a thermomechanical theory for continuum-on-continuum homogenization. 1808.02540
- Mendoza A, Neggers J, Hild F, Roux S (2019) Complete mechanical regularization applied to digital image and volume correlation. *Computer Methods in Applied Mechanics and Engineering* 355:27–43
- Milton G, Briane M, Harutyunyan D (2017a) On the possible effective elasticity tensors of 2-dimensional and 3-dimensional printed materials. *Math and Mech of Comp Sys* 5(1):41–94
- Milton G, Harutyunyan D, Briane M (2017b) Towards a complete characterization of the effective elasticity tensors of mixtures of an elastic phase and an almost rigid phase. *Mathematics and Mechanics of Complex Systems* 5(1):95–113
- Misra A, Jiang H (1997) Measured kinematic fields in the biaxial shear of granular materials. *Computers and Geotechnics* 20(3-4):267–285
- Misra A, Nejjadsadeghi N (2019) Longitudinal and transverse elastic waves in 1d granular materials modeled as micromorphic continua. *Wave Motion* 90:175–195
- Misra A, Poursolhjouy P (2015) Identification of higher-order elastic constants for grain assemblies based upon granular micromechanics. *Mathematics and Mechanics of Complex Systems* 3(3):285–308
- Misra A, Poursolhjouy P (2016) Granular micromechanics based micromorphic model predicts frequency band gaps. *Continuum Mechanics and Thermodynamics* 28(1-2):215–234
- Misra A, Poursolhjouy P (2017) Grain-and macro-scale kinematics for granular micromechanics based small deformation micromorphic continuum model. *Mechanics Research Communications* 81:1–6
- Misra A, Singh V, Darabi MK (2017) Asphalt pavement rutting simulated using granular micromechanics-based rate-dependent damage-plasticity model. *International Journal of Pavement Engineering* pp 1–14
- Misra A, Lekszycki T, Giorgio I, Ganzo G, Müller WH, dell’Isola F (2018) Pantographic metamaterials show atypical Poynting effect reversal. *Mech Res Commun* 89:6–10
- Nejjadsadeghi N, Misra A (2019) Axially moving materials with granular microstructure. *International Journal of Mechanical Sciences* 161:105,042
- Nejjadsadeghi N, Placidi L, Romeo M, Misra A (2019) Frequency band gaps in dielectric granular metamaterials modulated by electric field. *Mechanics Research Communications* 95:96–103
- Niiranen J, Khakalo S, Balobanov V, Niemi AH (2016) Variational formulation and isogeometric analysis for fourth-order boundary value problems of gradient-elastic bar and plane strain/stress problems. *Computer Methods in Applied Mechanics and Engineering* 308:182–211
- Payette G, Reddy J (2014) A seven-parameter spectral/hp finite element formulation for isotropic, laminated composite and functionally graded shell structures. *Computer methods in applied mechanics and engineering* 278:664–704
- Placidi L, Barchiesi E, Turco E, Rizzi NL (2016a) A review on 2d models for the description of pantographic fabrics. *Zeitschrift für angewandte Mathematik und Physik* 67(5):121

- Placidi L, Greco L, Bucci S, Turco E, Rizzi NL (2016b) A second gradient formulation for a 2d fabric sheet with inextensible fibres. *Zeitschrift für angewandte Mathematik und Physik* 67(5):114
- Poorsohjoui P, Misra A (2017) Effect of intermediate principal stress and loading-path on failure of cementitious materials using granular micromechanics. *International Journal of Solids and Structures* 108:139–152
- Rahali Y, Giorgio I, Ganghoffer J, dell’Isola F (2015) Homogenization à la Piola produces second gradient continuum models for linear pantographic lattices. *International Journal of Engineering Science* 97:148–172
- Reddy J, Srinivasa A (2014) Non-linear theories of beams and plates accounting for moderate rotations and material length scales. *International Journal of Non-Linear Mechanics* 66:43–53
- Rivera MG, Reddy J (2016) Stress analysis of functionally graded shells using a 7-parameter shell element. *Mechanics Research Communications* 78:60–70
- Rivera MG, Reddy J, Amabili M (2016) A new twelve-parameter spectral/hp shell finite element for large deformation analysis of composite shells. *Composite Structures* 151:183–196
- Saetta E, Rega G (2017) Third order thermomechanically coupled laminated plate: 2d nonlinear modeling, minimal reduction, and transient/post-buckled dynamics under different thermal excitations. *Composite Structures* 174:420–441
- Sepecher P, Alibert JJ, Isola FD (2011) Linear elastic trusses leading to continua with exotic mechanical interactions. In: *Journal of Physics: Conference Series*, IOP Publishing, vol 319, p 012018
- Settimi V, Rega G (2016a) Exploiting global dynamics of a noncontact atomic force microcantilever to enhance its dynamical robustness via numerical control. *International Journal of Bifurcation and Chaos* 26(07):1630,018
- Settimi V, Rega G (2016b) Global dynamics and integrity in noncontacting atomic force microscopy with feedback control. *Nonlinear Dynamics* 86(4):2261–2277
- Settimi V, Rega G, Saetta E (2018) Avoiding/inducing dynamic buckling in a thermomechanically coupled plate: a local and global analysis of slow/fast response. *Proceedings of the Royal Society A: Mathematical, Physical and Engineering Sciences* 474(2213):20180,206
- Spagnuolo M, Peyre P, Dupuy C (2019) Phenomenological aspects of quasi-perfect pivots in metallic pantographic structures. *Mechanics Research Communications*
- Srinivasa A, Reddy J (2013) A model for a constrained, finitely deforming, elastic solid with rotation gradient dependent strain energy, and its specialization to von kármán plates and beams. *Journal of the Mechanics and Physics of Solids* 61(3):873–885
- Steigmann D, dell’Isola F (2015) Mechanical response of fabric sheets to three-dimensional bending, twisting, and stretching. *Acta Mechanica Sinica* 31(3):373–382
- Steigmann DJ (1996) The variational structure of a nonlinear theory for spatial lattices. *Meccanica* 31(4):441–455
- Turco E, dell’Isola F, Cazzani A, Rizzi NL (2016a) Hencky-type discrete model for pantographic structures: numerical comparison with second gradient continuum models. *Zeitschrift für angewandte Mathematik und Physik* 67(4):85
- Turco E, Golaszewski M, Cazzani A, Rizzi NL (2016b) Large deformations induced in planar pantographic sheets by loads applied on fibers: experimental validation of a discrete lagrangian model. *Mechanics Research Communications* 76:51–56
- Yang Y, Misra A (2012) Micromechanics based second gradient continuum theory for shear band modeling in cohesive granular materials following damage elasticity. *International Journal of Solids and Structures* 49(18):2500–2514

Part I
Mathematical Tools for Mechanics



Chapter 2

Asymptotic Construction of Solutions of Ordinary Differential Equations with Holomorphic Coefficients in the Neighborhood of an Irregular Singular Point

Maria V. Korovina & Vladimir Yu. Smirnov

Abstract The aim of this article is constructing asymptotics of solution of ordinary differential equations with holomorphic coefficients in neighborhood of infinity. Since infinity in general is irregular singular point then problem of representing asymptotics of solution of an equation is a special case of Poincare problem.

Keywords: Asymptotics · Irregular singular point · Ordinary differential equations

In this paper we construct asymptotics of solutions of ordinary differential equations with holomorphic coefficients in vicinities of irregular singular points. We consider ordinary differential equations with holomorphic coefficients of the form

$$b_n(r) \left(\frac{d}{dr}\right)^n u(r) + b_{n-1}(r) \left(\frac{d}{dr}\right)^{n-1} u(r) + \dots + b_i(r) \left(\frac{d}{dr}\right)^i u(r) + \dots + b_0(r) u(r) = 0 \quad (2.1)$$

here $b_i(r)$ are holomorphic functions.

If the coefficient at the high derivative $b_n(r)$ vanishes at some point, without loss of generality we can take this point to be $r = 0$, and equation (2.1) has a singularity at zero. In this case zero can be either regular or irregular singular point. The problem of representing asymptotics of solution of an equation with holomorphic coefficients in the vicinity of irregular singular point was first formulated by H. Poincare in papers (Poincare, 1886, 1974). He was the first who demonstrated that solution of an equation with holomorphic coefficients in the vicinity of an irregular singular point in certain cases can be expanded into asymptotic series. One of possible techniques of summing up these generally divergent series with the aid of integral transforms

M. V. Korovina

Lomonosov Moscow State University, Moscow, Russia

e-mail: betelgeuser@yandex.ru

V. Yu. Smirnov

Moscow Aviation Institute (National Research University), Moscow, Russia

e-mail: vl-smirnov@mail.ru

was formulated also by Poincare (1974). Poincare used Laplace integral transform; however, it is applicable only in particular cases. In this paper for summing up asymptotic series we will use the Laplace-Borel transform introduced by Ecalle (1984).

One of the first papers devoted to the problem of constructing asymptotics in the vicinity of an irregular singular point is the work of Thome (1871). The author considered an equation with holomorphic coefficients

$$\begin{aligned} & \left(\frac{d}{dx}\right)^n u(x) + a_{n-1}(x) \left(\frac{d}{dx}\right)^{n-1} u(x) + \dots \\ & + a_i(x) \left(\frac{d}{dx}\right)^i u(x) + \dots + a_0(x) u(x) = 0 \end{aligned} \quad (2.2)$$

Here coefficients $a_i(x)$ are regular at infinity. This means, that there exists an exterior of the circle $|x| > a$, that functions $a_i(x)$, $i = 0, 1, \dots, n-1$ can be expanded in it into convergent power series $a_i(x) = \sum_{j=0}^{\infty} \frac{b_i^j}{x^j}$. The aim of our study is constructing asymptotics of solution of equation (2.2) in the vicinity of infinity. Later the subject was studied by many authors. We should note papers by Sternberg (1920) who considered the problem of constructing asymptotics of solution in the neighborhood of infinity and also works by Sternin and Shatalov (2002) who tried to apply Laplace-Borel transform to this problem.

Authors of this papers derived asymptotic expansions of solutions of ordinary differential equations. These had the form of products of corresponding exponents by divergent power series, namely

$$u = \sum_{i=1}^n e^{\alpha_i/r} r^{\sigma_i} \sum_{k=0}^{\infty} a_i^k r^k \quad (2.3)$$

where α_i , $i = 1, \dots, n$ are roots of polynomial $H_0(p)$, σ_i and a_i^k are some complex numbers. However, the issue of interpretation of the obtained divergent series remained unclear, in other words, there is no method of summing up these series. Such asymptotics later got the name of WKB (Wentzel-Kramers-Brillouin) asymptotics. This name appeared in solution of some problems of quantum mechanics where asymptotics of such type were obtained. Similar problems are found in other areas of mechanics. For example, a Laplace operator written in spherical coordinates has a irregular singular point at zero (Korovina, 2017). They can also be used in many other tasks, for example equation of this type is used to solve the planar problem of finding the stress-strain state of a rectangular cross section body with a cylindrical cavity along an ideal incompressible fluid moves (Sciarra et al, 2005).

In the case when an asymptotic expansion

$$\begin{aligned} u & \approx u_1 + u_2 + \dots + u_n = \\ & = e^{\lambda_1/r} r^{\sigma_1} \sum_{k=0}^{\infty} a_1^k r^k + e^{\lambda_2/r} r^{\sigma_2} \sum_{k=0}^{\infty} a_2^k r^k + \dots \\ & + e^{\lambda_n/r} r^{\sigma_n} \sum_{k=0}^{\infty} a_n^k r^k \end{aligned} \quad (2.4)$$

has at least two addends corresponding to the values λ_1 and λ_2 with distinct real parts (for definitiveness let $Re\lambda_1 > Re\lambda_2$) a significant complication in interpretation of

the obtained expansion arises. All addends of the first WKB element corresponding to the value λ_1 (*dominant* WKB element) are of larger order at $r > 0$ than any of the addends of the second (*recessive*) WKB element. That's why to interpret expansion (2.4) one should sum up (generally, divergent) series, corresponding to the dominant WKB-element. Analysis of recessive components of solution u of equation (2.1) is important, in particular, for derivation of uniform asymptotics of solutions in the complex case, when point r is moving in the complex plane and roles of dominant and recessive components of expansions can swap. In other words, plane is conditionally subdivided into sectors in each of that one of the components is main and the other one is recessive, and after transition from one sector to the other swap of leadership occurs (the recessive component becomes the main one and vice versa). However, in the vicinities of boundaries of these sectors several components are of the same order and neither of them can be neglected. This phenomenon arises, e.g., in consideration of the Euler example (Sternin and Shatalov, 1996) and in derivation of asymptotics at infinity for the problem (2.1) and generally for all WKB asymptotics (2.2). So, study of asymptotic expansions of equation (2.1) requires a regular method of summing up divergent series for construction of uniform asymptotics of solutions in variable r .

Later a technique for summing up such series based on the methods of resurgent analysis was developed. The method of summing up divergent series is the Laplace-Borel transform. This technique was used in works by B.-W. Schulze, B. Yu. Sternin and V.E. Shatalov in studies of degenerating equations, arising in studies of elliptic equations on manifolds with cusp-like singularities, and also for derivation of asymptotics of equation with a small parameter. In several cases these authors managed to derive asymptotics for equations with parameter and equations with cuspidal degeneration in Sobolev weight spaces (Sternin and Shatalov, 1996; Schulze et al, 1996).

However, later consideration of asymptotics in Sobolev weight spaces was laid aside.

Later, another approach was selected. Asymptotics of solutions are derived using Laplace-Borel transform in the space of functions of exponential growth.

The technique for interpretation and derivation of asymptotic expansions of the form (2.4), based on Laplace-Borel transform, is called *resurgent analysis*. Its main idea is as follows. Formal Borel transforms $\tilde{u}_1(p)$, $\tilde{u}_2(p)$... are power series in dual variable p convergent in the vicinities of points $p = \lambda_i$. At that, the inverse Borel transform provides a regular way of summing up series (2.4). However, here one should prove infinite continuability of functions $\tilde{u}_j(p)$, i.e., continuability along any path on Riemannian surface $\tilde{u}_j(p)$ not passing through some discrete set depending on the function (exact definition of infinite continuability will be given later). Proof of this fact, as a rule, was very complicated in application of resurgent analysis to construction of asymptotics of solutions of differential equations. Proof of infinite continuability for equations with degenerations was given in Korovina and Shatalov (2010); Korovina (2011b). This result enables one to construct asymptotics of solutions of linear differential equations with holomorphic coefficients.

Thanks to this result, in Sternin and Shatalov (1996); Korovina (2011a) uniform asymptotics for the case, when roots of the high symbol $H_0(p) = H(0, p)$ are of the first order, were derived.

However, methods used in derivation of asymptotics of solutions in the case when the main symbol had simple roots appeared inapplicable in the case of multiple roots except second-order equations. In Korovina (2017), the problem of constructing asymptotics of solutions for second-order equations with arbitrary holomorphic coefficients was solved for a general case. The author also constructed asymptotics of solutions for Laplace equation on a manifold with a cuspidal singularity.

For solving problem of multiple roots, the method of re-quantization was developed (Korovina, 2016). This method is applied in the case, when the integral-differential equation in dual space cannot be solved by the method of successive approximations and is reduced to an equation with cuspidal degenerations. In this case, we prove theorem of infinite continuability of solution (for ordinary differential equations it has already been proved) and once again apply the Laplace-Borel transform. For the obtained equation we construct asymptotics with which we can find asymptotics of the original equation. Using this method, many problems for equations with degenerations in the case of multiple roots were solved.

The aim of this paper is derivation of asymptotics of equation (2.2) at infinity. Problem (2.2) by change of variable $x = \frac{1}{r}$ is reduced to the equation with cuspidal degeneration of the second order at zero, which can be written as

$$H\left(r, -r^2 \frac{d}{dr}\right) u = 0 \quad (2.5)$$

where

$$H\left(r, -r^2 \frac{d}{dr}\right) = \left(-r^2 \frac{d}{dr}\right)^n + \sum_{i=0}^{n-1} a_i(r) \left(-r^2 \frac{d}{dr}\right)^i \quad (2.6)$$

The main symbol $H_0(p)$ of operator \hat{H} is $H_0(p) = H(0, p)$.

The question arises: which form takes the asymptotics in the vicinity of a multiple root.

First consider the case when the main symbol of differential operator has just one root. Without loss of generality assume that this root is zero. Write equation (2.5) in the form

$$\begin{aligned} & \left(-r^2 \frac{d}{dr}\right)^n u + a_0 r^m \left(-r^2 \frac{d}{dr}\right)^k u + a_1 r^{m+1} \left(-r^2 \frac{d}{dr}\right)^{k-1} u + \\ & \quad a_2 r^{m+2} \left(-r^2 \frac{d}{dr}\right)^{k-2} u + \dots + a_{k+1} r^{m+k} u + \dots \\ & + \sum_{j=1}^h r^j \sum_{i=h_j}^{n-1} a_j^i \left(-r^2 \frac{d}{dr}\right)^i u + r^{h+1} \sum_{i=0}^{n-1} a^i(r) \left(-r^2 \frac{d}{dr}\right)^i u = 0 \end{aligned} \quad (2.7)$$

Here $h_j + j > m + k$. Let us call $h = m + k$ the singularity index. We will call terms of the form $a_j^i r^j \left(r^2 \frac{d}{dr}\right)^i$, under condition $j + i > h$, the lowest terms of equation (2.7). Let us subdivide lowest terms into two types. To the first type belong terms for which $h \geq j$ and to the second type those where $h < j$. Our goal

is derivation of asymptotics of solutions of equation (2.7) in the vicinity of infinity. For singularity index equal to $1 + k$ this problem was solved in Korovina (2019).

Let inequality

$$h_i + i - h > (m - i) \frac{n - h}{m} \quad (2.8)$$

be fulfilled. Then the following theorem holds

THEOREM. Asymptotics of solution of equations (2.2) in the vicinity of infinity have the form

$$u(x) \approx \sum_{j=1}^{n-k} \exp\left(\sum_{i=1}^{n-k-m} \alpha_i^j x^{\frac{i}{n-k}}\right) x^{-\frac{\sigma_j}{n-k}} \sum_l^\infty A_l^j x^{-\frac{l}{n-k}} + \sum_{j=0}^{k_0} \left(\ln \frac{1}{x}\right)^j x^{\alpha_j} \sum_{i=0}^\infty b_i^j x^{-i}, \quad (2.9)$$

where $\alpha_{n-k-m}^j, j = 1, \dots, n-k$ are roots of polynomials $p^{n-k} + \left(\frac{n-k}{n-k-m}\right)^{n-k} a_0, A_l^j, \sigma_i, b_i^j, k_0$ and $\alpha_i^j, j = 1, \dots, n-k-1$ are some numbers.

If the main symbol has several multiple roots, after Laplace-Borel transform we move one of the roots to zero and find asymptotics of solution in the vicinity of zero, then move the second root to zero and so on. In the result we find asymptotics of solution in dual space in vicinities of all roots of the polynomial. Then, applying the inverse Laplace-Borel transform, we get asymptotics of the original equation in the vicinity of zero. Details are explained in Korovina (2019).

References

- Ecalle J (1984) Cinq applications des fonctions resurgentes. Prepub Math p 110
- Korovina MV (2011a) Asymptotics solutions of equations with higher-order degeneracies. Doklady Mathematics 83(2):182–184
- Korovina MV (2011b) Existence of resurgent solutions for equations with higher-order degeneration. Differential Equations 47(3):346–354
- Korovina MV (2016) Repeated quantization method and its applications to the construction of asymptotics of solutions of equations with degeneration. Differential Equations 52(1):58–75
- Korovina MV (2017) Asymptotic solutions of second order equations with holomorphic coefficients with degeneracies and laplace's equations on a manifold with a cuspidal singularity. Global Journal of Science Frontier Research (GJSFR): F Mathematics and Decision Sciences 17(6):57–71
- Korovina MV (2019) Application of the repeated quantization method to the problem of making asymptotic solutions of equations with holomorphic coefficients. International Journal of Open Information Technologies 7(9):14–22
- Korovina MV, Shatalov VE (2010) Differential equations with degeneration and resurgent analysis. Differential Equations 46(9):1267–1286
- Poincare H (1886) Sur les integrales irregulieres des equations lineaires. Acta math 8:295–344
- Poincare H (1974) Selected works in three volumes. Volume 3. Mathematics. Theoretical physics. Analysis of the mathematical and natural works of Henri Poincare. "Nauka" publishing house

- Schulze BW, Sternin B, Shatalov V (1996) Asymptotic solutions to differential equations on manifolds with cusps. Preprint MPI 96-89
- Sciarra G, dell'Isola F, Hutter K (2005) Dilatational and compacting behavior around a cylindrical cavern leached out in a solid–fluid elastic rock salt. *International Journal of Geomechanics* 5(3):233–243
- Sternberg W (1920) *Über die asymptotische integration von differentialgleichungen*
- Sternin B, Shatalov V (1996) *Borel-Laplace Transform and Asymptotic Theory. Introduction to Resurgent Analysis*. CRC Press
- Sternin BY, Shatalov VE (2002) Differential equations in spaces with asymptotics on manifolds with cusp singularities. *Differential Equations* 38(12):1764–1773
- Thome LW (1871) *Zur Theorie der linearen differentialgleichungen*



Chapter 3

Poincare Problem and Classification of Irregular Singular Points for Linear Differential Equations with Holomorphic Coefficients

Maria V. Korovina & Vladimir Yu. Smirnov

Abstract In the paper we study the Poincare problem for second-order linear differential equations and also classification of asymptotic expansions of solutions in vicinities of irregular singular points for linear differential equations with holomorphic coefficients

Keywords: Asymptotics · Irregular singular point · Ordinary Differential Equations

The problem of representing asymptotics of solution of an equation with holomorphic coefficients was first formulated by Poincare (1886). The author demonstrated that the solution of an equation with holomorphic coefficients in several cases can be represented in the form of asymptotic series. The Poincare problem is formulated as follows: Find asymptotic expansions for solutions of arbitrary linear equations with holomorphic coefficients. In the presented article the authors solve the Poincare problem for second-order equations. We also give classification of singular points and study corresponding asymptotic expansions.

Second-order differential equations with singular points are used in various fields of mechanics. For example Laplace operator written in spherical coordinates has a singular point in zero (Korovina, 2017). Also second-order equation of this type is used to solve the planar problem of finding the stress-strain state of a rectangular cross section body with a cylindrical cavity along an ideal incompressible fluid moves (Sciarra et al, 2005). In this case equations with irregular singular point arises. Another example of second-order equation with singular point is DPE (Density Profile Equation). They are studied in dell'Isola et al (1995, 1996).

Consider ordinary differential equations

M. V. Korovina
Lomonosov Moscow State University, Moscow, Russia
e-mail: betelgeuser@yandex.ru

V.Yu. Smirnov
Moscow Aviation Institute (National Research University), Moscow, Russia
e-mail: vl-smirnov@mail.ru

$$\begin{aligned}
& b_n(r) \left(\frac{d}{dr}\right)^n u(r) + b_{n-1}(r) \left(\frac{d}{dr}\right)^{n-1} u(r) + \\
& \dots + b_i(r) \left(\frac{d}{dr}\right)^i u(r) + \dots + b_0(r) u(r) = 0
\end{aligned} \tag{3.1}$$

here $b_i(r)$ are holomorphic functions.

If the coefficient at high derivative $b_n(r)$ vanishes at some point, without loss of generality we can assume that this point is $r = 0$, so equation (3.1) has a singularity at zero. In this case, zero can be either regular or irregular singular point. Equation (3.1) can be reduced to equation of the form

$$\hat{H}u = H\left(r, -r^{k+1} \frac{d}{dr}\right)u = 0, \tag{3.2}$$

where \hat{H} is a differential operator with holomorphic coefficients

$$H(r, p) = \sum_{i=0}^n b'_i(r) p^i. \tag{3.3}$$

Here $b'_i(r)$ are corresponding holomorphic functions. The minimal value of k was calculated in Kats (2015). Depending on the minimal value of k we can subdivide equations into three types and each of them is associated with different types of asymptotics. Equations with $k = -1$ belong to the first type. In this case we have non-degenerate differential equations without singularity at zero. When $k=0$, equation is degenerated. The singular point is regular, we have an equation of Fuchs type and asymptotics of solution in this case are conormal.

A special type of asymptotics arises when $k \in \mathbb{N}$. This corresponds to the case of irregular singularities. The equation is of non-Fuchs type. An example of non-Fuchs asymptotics are those of the form

$$\sum_{j=1}^n \exp\left(\frac{p_j}{r^k} + \sum_{i=1}^{k-1} \frac{\alpha_{k-i}^j}{r^{k-i}}\right) r^{\sigma_j} \sum_{i=0}^{\infty} b_i^j r^i \tag{3.4}$$

Non-Fuchs asymptotics of the form (3.4) correspond to the case when the main symbol of operator $H_0(p) = H(0, p)$ has only simple roots $p_j, j = 1, \dots, n$. Here $\sum_{i=0}^{\infty} b_i^j r^i$ is an asymptotic series and α_{k-i}^j, σ_j are some numbers. Korovina and Shatalov (2011); Korovina (2011) derived uniform non-Fuchs asymptotics for this case. Consider equation

$$H\left(r, -r^2 \frac{d}{dr}\right)u = f. \tag{3.5}$$

Let the right-hand side of the equation can be represented in the form of WKB (Wentzel-Kramers-Brillouin) asymptotics, in other words,

$$f = \sum_{i=1}^n e^{\lambda_i/r} r^{\sigma_i} \sum_{k=0}^{\infty} a_i^k r^k$$

Hence, the Laplace-Borel transform of function f has singularities at points $\lambda_i, i = 1, \dots, n$. If the numbers $\lambda_i, i = 1, \dots, n$ do not coincide with the roots of polynomial $H_0(p)$, this case is called non-resonance. Let roots of polynomial $H_0(p)$ be of the first order and the equation be non-resonance. Then the following theorem holds.

THEOREM *Let function $u(r)$ be a solution of equation (3.5), then under formulated above conditions for any positive A the resurgent function $u(r)$ can be represented in the form*

$$u(r) = \sum_j u_j(r) + O\left(e^{-\frac{A}{r}}\right) \tag{3.6}$$

The sum is taken over union $\{p_j\}$ of roots of the polynomial $H_0(p)$ and singularities of Laplace-Borel transformation of the right-hand side $\tilde{f}(p)$ located in the half-plane $\text{Re } p > -A$, and functions $u_j(r)$ are inverse Laplace-Borel transforms of functions $\tilde{u}_j(p)$ with singularities at points p_j and their asymptotic expansions are

$$u_j(r) = e^{\frac{p_j}{r}} r^{\sigma_j} \sum_{k=0}^{\infty} a_k^{(j)} r^k, \tag{3.7}$$

here $\sigma_j a_k^{(j)}$ – are some numbers.

These coefficients were calculated in Kats (2015, 2016).

When the equation has order higher than two, asymptotics of solution has the form (3.4).

If polynomial $H(0, p)$ has multiple roots, the problem of constructing asymptotics of solutions of corresponding non-Fuchs equations becomes much more complicated. In a general case, the Poincare problem has not been solved yet. The question arises: Do non-Fuchs asymptotics of the form (3.4) represent the general form of asymptotics for all linear differential equations with holomorphic coefficients?

To answer this question, consider linear second-order differential equations

$$H\left(r, \frac{1}{n}r^{n+1} \frac{d}{dr}\right)u(r) = 0, \tag{3.8}$$

where symbol $H(r, p)$ is a second-order polynomial with respect to p with holomorphic coefficients. Earlier we proved that solutions of equations like this are resurgent functions. We will assume that the main symbol has a multiple root. If it is not the case, asymptotics of solutions will have the form of non-Fuchs asymptotics (3.4). So, consider equation

$$\left(\frac{1}{n}r^{n+1} \frac{d}{dr}\right)^2 u + a_1(r) \left(\frac{1}{n}r^{n+1} \frac{d}{dr}\right) u + a_0(r) u + r v(r) \left(\frac{1}{n}r^{n+1} \frac{d}{dr}\right)^2 u = 0, \tag{3.9}$$

where $a_i(r)$ and $v(r)$ are holomorphic coefficients. Represent coefficients $a_i(r)$ in the form

$$\begin{aligned} a_1(r) &= br^k + r^{k+1}b_1(r), \\ a_0(r) &= cr^p + r^{p+1}c_1(r) \end{aligned} \tag{3.10}$$

Here $b_1(r)$, $c_1(r)$ are corresponding holomorphic functions, b and c are nonzero constants. Since the main symbol of the differential operator has second multiplicity at zero, neither k nor p can vanish, so $k \in \mathbb{N}$ and $p \in \mathbb{N}$.

Korovina (2014) demonstrated that if $k > n$ or $\frac{p}{2} > n$, equation (3.9) is reduced to an equation with conical degeneration and asymptotics of its solution, as was written above, have conormal form. When p is odd and inequality $k > \frac{p}{2}$ holds, asymptotics have the form

$$\begin{aligned} & \exp\left(-\frac{\alpha_0}{r^{n-\frac{p}{2}}} + \sum_{i=1}^{2n-p-1} \frac{\alpha_i^1}{r^{n-\frac{p}{2}-\frac{i}{2}}}\right) r^{\sigma_1} \sum_{i=0}^{\infty} b_i^1 r^{\frac{i}{2}} + \\ & + \exp\left(\frac{\alpha_0}{r^{n-\frac{p}{2}}} + \sum_{i=1}^{2n-p-1} \frac{\alpha_i^2}{r^{n-\frac{p}{2}-\frac{i}{2}}}\right) r^{\sigma_2} \sum_{i=0}^{\infty} b_i^2 r^{\frac{i}{2}} \end{aligned} \tag{3.11}$$

here $\alpha_0 = \frac{2ni\sqrt{c}}{2n-p}$. In other cases, asymptotics of solutions are non-Fuchs asymptotics of the form (3.4). Notice that asymptotics (3.11) differ from non-Fuchs asymptotics in the following: Powers of variable r in exponents of asymptotics (3.11) unlike asymptotics (3.4) can be non-integral.

Asymptotics like this also arise in the case when asymptotics of equation

$$\begin{aligned} & \left(\frac{d}{dx}\right)^n u(x) + a_{n-1}(x) \left(\frac{d}{dx}\right)^{n-1} u(x) + \dots \\ & + a_i(x) \left(\frac{d}{dx}\right)^i u(x) + \dots + a_0(x) u(x) = 0 \end{aligned}$$

are constructed in the vicinity of infinitely distant point which, generally speaking, is an irregular singular point. Asymptotics of solutions have the form

$$u(r) \approx \sum_{j=1}^m \exp\left(\sum_{i=1}^{n-h} \alpha_i^j r^{-\frac{i}{m}}\right) x^{\sigma_j} \sum_l^{\infty} A_l^j r^{\frac{l}{m}} + \sum_{j=0}^{k_0} (\ln r)^j x^{\alpha_j} \sum_{i=0}^{\infty} b_i^j r^i \tag{3.12}$$

Here $h, m, A_i^j, j = 0, 1, 2$ are corresponding numbers. Details of the problem are exposed in Korovina (2019). Let us call asymptotics of the type (3.12) generalized asymptotics of non-Fuchs type. It is evident that asymptotics of non-Fuchs type represent a particular case of the generalized non-Fuchs asymptotics.

We can suppose that

Asymptotics of solution of equation (3.1) can be represented as a sum of a generalized non-Fuchs asymptotics and a conormal asymptotics.

References

dell’Isola F, Gouin H, Seppecher P (1995) Radius and surface tension of microscopic bubbles by second gradient theory. *Comptes rendus de l’Académie des sciences* 320(5):211–216
 dell’Isola F, Gouin H, Rotoli G (1996) Nucleation of spherical shell-like interfaces by second gradient theory: numerical simulations. *European journal of mechanics B, Fluids* 15(4):545–568

- Kats DS (2015) Computation of the asymptotics of solutions for equations with polynomial degeneration of the coefficients. *Differential Equations* 51(12):1589–1594
- Kats DS (2016) Coefficients of series in asymptotic expansions of solutions of equations with degenerations. *International Journal of Open Information Technologies* 4(9):1–7
- Korovina MV (2011) Asymptotics solutions of equations with higher-order degeneracies. *Doklady Mathematics* 83(2):182–184
- Korovina MV (2014) The asymptotic behavior of solutions to second-order equations with higher-order degeneracies and the laplace equation on a manifold with a cuspidal singularity. *Doklady Mathematics* 89(3):328–330
- Korovina MV (2017) Asymptotic solutions of second order equations with holomorphic coefficients with degeneracies and laplace's equations on a manifold with a cuspidal singularity. *Global Journal of Science Frontier Research (GJSFR): F Mathematics and Decision Sciences* 17(6):57–71
- Korovina MV (2019) Application of the repeated quantization method to the problem of making asymptotic solutions of equations with holomorphic coefficients. *International Journal of Open Information Technologies* 7(9):14–22
- Korovina MV, Shatalov VE (2011) Differential equations with degeneracies. *Doklady Mathematics* 437(1):16–19
- Poincare H (1886) Sur les integrales irregulieres des equations lineaires. *Acta math* 8:295–344
- Sciara G, dell'Isola F, Hutter K (2005) Dilatational and compacting behavior around a cylindrical cavern leached out in a solid–fluid elastic rock salt. *International Journal of Geomechanics* 5(3):233–243



Chapter 4

Behavior of Solutions of the Cauchy Problem and the Mixed Initial Boundary Value Problem for an Inhomogeneous Hyperbolic Equation with Periodic Coefficients

Hovik A. Matevossian, Giorgio Nordo, and Anatoly V. Vestyak

Abstract We study the asymptotic as $t \rightarrow \infty$ behavior of solutions $u(x, t)$ of the Cauchy problem and the mixed initial boundary value problem for a second-order hyperbolic equation with periodic coefficients in \mathbb{R}^1 and on the semi-axis. In the case of non-homogeneous equation, initial and boundary data are zero, and the right-hand side of the equation is of the form $f(x) \exp(-i\omega t)$, where $\omega > 0$ is real.

Keywords: Asymptotic behavior · Hyperbolic equation · Cauchy problem · Mixed initial boundary value problem · Periodic coefficients

4.1 Introduction

PROBLEM A. Let $u(x, t)$ be a solution of the Cauchy problem

$$u_{tt}(x, t) - (p(x) u_x(x, t))_x + q(x) u(x, t) = f(x) e^{-i\omega t}, \quad (x, t) \in \mathbb{R}^1 \times \{t > 0\}, \quad (4.1)$$

with the initial conditions

H. A. Matevossian

Federal Research Center “Computer Science and Control”, Russian Academy of Sciences, Moscow;
Steklov Mathematical Institute, Russian Academy of Sciences, Moscow;
e-mail: hmatevossian@graduate.org

G. Nordo

MIFT - Dipartimento di Scienze Matematiche e Informatiche, Scienze Fisiche e Scienze della Terra,
Università di Messina, Viale F. Stagno D’Alcontres, 31 – Contrada Papardo, salita Sperone,
98166 Sant’Agata – Messina, Italy;
e-mail: giorgio.nordo@unime.it

H. A. Matevossian, A. V. Vestyak

Moscow Aviation Institute (National Research University), Moscow, Russia.
e-mail: hmatevossian@graduate.org, vestyak2016@mail.ru

$$u(x, t)|_{t=0} = 0, \quad u_t(x, t)|_{t=0} = 0, \quad x \in \mathbb{R}^1. \quad (4.2)$$

PROBLEM B. Let $u(x, t)$ be a solution of the mixed initial boundary value problem

$$u_{tt}(x, t) - (p(x) u_x(x, t))_x + q(x) u(x, t) = f(x) e^{-i\omega t}, \quad x > 0, t > 0, \quad (4.3)$$

with zero initial and boundary conditions

$$\begin{aligned} u(x, t)|_{t=0} = 0, \quad u_t(x, t)|_{t=0} = 0, \quad x \geq 0; \\ u(x, t)|_{x=0} = 0, \quad t \geq 0. \end{aligned} \quad (4.4)$$

Here the functions $p(x)$ and $q(x)$ are 1-periodic:

$$p(x+1) = p(x) \geq \text{const} > 0, \quad q(x+1) = q(x) > \text{const} \geq 0. \quad (4.5)$$

Moreover, the functions $p(x)$ and $q(x)$ are continuous, the function $q(x)$ has a finite number of discontinuities of the first kind on the period, $\psi \in C_0^\infty(\mathbb{R}^1)$ and $\text{supp}\psi \subset [0, 1]$. Equation (4.1) (or (4.3)) describes the oscillation driven by a force periodic in t , and $\omega > 0$ is real.

The behavior as $t \rightarrow \infty$ of solutions of problems similar to PROBLEMS A and B, and the corresponding multi-dimensional problems under the condition that the potential either differs from a constant by a compactly supported function or sufficiently rapidly tends to a constant at infinity, has been studied in many papers (see, e.g., Laptev, 1975; Matevossian and V, 2017; Peržan, 1978; Surguladze, 1989; Topiler, 1983; Vainberg, 1989; Vestyak and Matevossian, 2016; Vestyak and Matevosyan, 2017).

In particular, in article of Laptev (1975), an asymptotic expansion as $t \rightarrow \infty$ of the solution $u(x, t)$ of the Cauchy problem for the equation

$$\begin{aligned} u_{tt}(x, t) - u_{xx}(x, t) + (\alpha_0 + q(x))u = 0, \quad (x, t) \in \mathbb{R}^1 \times \{t > 0\}, \\ u(x, t)|_{t=0} = \varphi(x), \quad u_t(x, t)|_{t=0} = \psi(x), \quad x \in \mathbb{R}^1. \end{aligned} \quad (4.6)$$

with compactly supported initial functions $\varphi(x) \in C^2(\mathbb{R}^1)$ and $\psi(x) \in C^1(\mathbb{R}^1)$, and under weaker constraints on the potential $\alpha_0 + q(x)$, where $\alpha_0 = \text{const}$, and $q(x)$ for some $k \geq 1$ satisfies to the condition

$$\int_{-\infty}^{+\infty} |x|^k |q(x)| < \infty. \quad (4.7)$$

In Peržan (1978), the following Cauchy problem was considered for the string oscillation equation:

$$\begin{aligned} u_{tt}(x, t) = (a(x) u_x(x, t))_x, \quad 0 < a_0 \leq a(x) \leq A_0 < +\infty, \quad (x, t) \in \mathbb{R}^1 \times \{t > 0\}, \\ u(x, t)|_{t=0} = \varphi(x), \quad u_t(x, t)|_{t=0} = 0, \quad x \in \mathbb{R}^1. \end{aligned} \quad (4.8)$$

Sufficient conditions for the stabilization of the solution $u(x, t)$ as $t \rightarrow +\infty$ uniformly in x on any compact set and necessary and sufficient conditions for the stabilization of the solution $u(x, t)$ in the mean were obtained under certain assumptions on the tension rate $a(x)$. In Topiler (1983), the behavior of the solution of the Cauchy problem

$$\begin{aligned} u_{xx} - q(x)u_{tt} = 0, \quad 0 < q_0 \leq q(x) \leq q_\infty < +\infty, \quad (x, t) \in \mathbb{R}^1 \times \{t > 0\}, \\ u(x, t)|_{t=0} = \varphi(x), \quad u_t(x, t)|_{t=0} = \psi(x), \quad x \in \mathbb{R}^1, \end{aligned} \quad (4.9)$$

for the hyperbolic equation was studied for large values of t , and the rate of decrease as $t \rightarrow \infty$ of solutions related to the rate of stabilization of $q(x)$ as $x \rightarrow \pm\infty$ was estimated under the assumption that the function $q(x)$ tends to a limit as $x \rightarrow \pm\infty$ in a certain way. The behavior of the solution of the Cauchy problem for the one-dimensional hyperbolic equation with periodic potential $q(x)$ for large values of t was studied in article of Surguladze (1989), and the Bloch principle for elliptic equations with periodic coefficients was obtained in article of Zhikov and Pastukhova (2016). In the case of periodic $p(x)$ and $q(x)$, the asymptotic behavior as $t \rightarrow \infty$ of the solution of the Cauchy problem for a hyperbolic equation was first studied in papers of Vestyak and Matevossian (2016); Vestyak and Matevosyan (2017).

4.2 Notation and Preliminaries

Let $L_2(\Omega)$ be the space of measurable functions on Ω satisfying the condition

$$\|u; L_2(\Omega)\| = \left(\int_{\Omega} |u|^2 dx \right)^{1/2} < \infty. \quad (4.10)$$

Let H_0 denote the Hill operator

$$H_0 = -\frac{d}{dx} \left(p(x) \frac{d}{dx} \right) + q(x) \quad (4.11)$$

on the space $L_2(\mathbb{R}^1)$.

The Hill operator has a continuous spectrum only, which is located on the real axis and is bounded on the left (Titchmarsh, 1958).

Let $y_n(x, \lambda_n)$ be eigenfunctions of the periodic Sturm–Liouville problem normalized by the condition $\|y_n; L_2([0, 1])\| = 1$:

$$\begin{aligned} -(p(x)y')' + q(x)y = \lambda_n y, \quad x \in [0, 1], \\ y(0) = y(1), \quad y'(0) = y'(1), \end{aligned} \quad (4.12)$$

and let $y_n(x, \mu_n)$ be eigenfunctions of the anti-periodic Sturm–Liouville problem normalized in $L_2([0, 1])$:

$$\begin{aligned} -(p(x)y')' + q(x)y &= \mu_n y, & x \in [0, 1], \\ y(0) &= -y(1), & y'(0) = -y'(1). \end{aligned} \quad (4.13)$$

where the λ_n and $\mu_n, n = 0, 1, 2, \dots$ are eigenvalues of the corresponding problems numbered in ascending order with multiplicities taken into account.

Let $\varphi(x, \lambda)$ and $\theta(x, \lambda)$ are the fundamental system of solutions of the equation

$$(p(x)y')' + (\lambda - q(x))y = 0, \quad p(x) \geq \text{const} > 0, \quad q(x) > \text{const} \geq 0, \quad (4.14)$$

with condition

$$\begin{aligned} \theta(0, \lambda) &= 1, & \varphi(0, \lambda) &= 0, \\ \theta'(0, \lambda) &= 0, & \varphi'(0, \lambda) &= 1, \end{aligned} \quad (4.15)$$

where $\varphi'(x, \lambda)$ is the derivative of the function $\varphi(x, \lambda)$ of the variable x .

Let \mathcal{L}^* be the operator on $L_2(0, +\infty)$ generated by the differential operation

$$\mathcal{L}y = -(p(x)y')' + q(x)y \quad (4.16)$$

and the condition $y(0) = 0$.

The properties of the spectrum of the operator \mathcal{L}^* and the eigenvalue problem

$$\begin{aligned} -(p(x)y')' + q(x)y &= \mu_n y, & x \in (0, 1), \\ y(0) &= y(1) = 0 \end{aligned} \quad (4.17)$$

are well known (see, e.g., Coddington and Levinson, 1955). The continuous spectrum of the operator \mathcal{L}^* coincides with that of the operator H_0 , and the eigenvalues $\lambda = \lambda_m, m = 1, 2, \dots$, of \mathcal{L}^* coincide with those zeros of the function $\varphi(1, \lambda)$ at which

$$\text{sign} \left((\varphi'(1, \lambda) - \theta(1, \lambda)) \sqrt{(\varphi'(1, \lambda) + \theta(1, \lambda))^2 - 4} \right) = -1, \quad (4.18)$$

where the branch of the root $\sqrt{(\varphi'(1, \lambda) + \theta(1, \lambda))^2 - 4}$ determinate by the condition

$$\sqrt{(\varphi'(1, \lambda) + \theta(1, \lambda))^2 - 4} > 0 \quad \text{with} \quad \lambda < \lambda_0. \quad (4.19)$$

The eigenvalues $\lambda = \mu_n, n = 1, 2, \dots$, of the problem (4.17) coincide with the zeros of the function $\varphi(1, \lambda)$ and, therefore, $\{\lambda_m\} \subseteq \{\mu_n\}$. The values λ_m and μ_n are numbered in ascending order with multiplicities taken into account. By $v_n(x, \lambda_m)$ ($v_n(x, \mu_n)$) we denote the eigenfunction of problem (4.17) with eigenvalue λ_m (μ_n) normalized by the condition $\|v; L_2([0, 1])\| = 1$.

Let

$$h(x, \omega) = \begin{cases} (H_0 - \omega^2)^{-1}(f), & \text{if } \omega^2 \notin \sigma(H_0), \\ \lim_{\text{Im } k > 0, k \rightarrow \omega} (H_0 - k^2)^{-1}(f), & \text{if } \omega^2 \in \sigma(H_0), \text{ and } \omega^2 \\ & \text{does not lie on the boundary} \\ & \text{of the spectrum } \sigma(H_0), \end{cases} \quad (4.20)$$

where the limit is regarded in the uniform metric on each closed interval in \mathbb{R}^1 . The function $h(x, \omega)$ is the solution of the equation

$$(p(x)y')' + (\omega^2 - q(x))y = f(x), \quad (4.21)$$

and belongs to $L_2(\mathbb{R}^1)$ if ω^2 does not belong to the spectrum $\sigma(H_0)$ of the operator H_0 . Further, let $C > 0$ be an arbitrary fixed constant.

4.3 Main Results

Theorem 4.1. *If the Hill operator H_0 is positive, $p(x) \geq \text{const} > 0$, $q(x) \geq 0$, and the point ω^2 does not lie on the boundary of the spectrum $\sigma(H_0)$ of the operator H_0 , then, for $|x| < C$ and $t > 0$, the solution of the PROBLEMS A and B has the form*

$$u(x, t) = -ie^{-i\omega t}h(x, \omega) + \frac{1}{\sqrt{t}}\{u_1(x, t) + u_2(x, t)\} + v(x, t), \quad (4.22)$$

where $u_1(x, t)$ is the periodic solution of the PROBLEMS A and B,

$$u_1(x, t) = \sum_{n=0}^{\infty} a_{\lambda_n} \psi_{\lambda_n} v_n(x, \lambda_n) \sin(\sqrt{\lambda_n}t + (-1)^n \frac{\pi}{4} + b_{\lambda_n}), \quad (4.23)$$

$u_2(x, t)$ is an anti-periodic solution of the PROBLEMS A and B,

$$u_2(x, t) = \sum_{n=0}^{\infty} a_{\mu_n} \psi_{\mu_n} v_n(x, \mu_n) \sin(\sqrt{\mu_n}t + (-1)^{n+1} \frac{\pi}{4} + b_{\mu_n}), \quad (4.24)$$

and for $|x| < C$ and $t > 0$, the function $v(x, t)$ satisfies the estimates

$$|v(x, t)| \leq \frac{C_0}{t} \|f; L_2(\mathbb{R}^1)\|, \quad C_0 = \text{const}(C). \quad (4.25)$$

where ψ_{λ_n} (or ψ_{μ_n}) are the coefficients of the Fourier series expansion of the function $\psi(x)$ with respect to the system $\{v_n(x, \lambda_n)\}_{n=0}^{\infty}$, (or $\{v_n(x, \mu_n)\}_{n=0}^{\infty}$), and $a_{\lambda_n}, a_{\mu_n}, b_{\lambda_n}, b_{\mu_n}$ are constants, where a_{λ_n} and a_{μ_n} are of order $o(1/n^2)$ as $n \rightarrow \infty$.

Here the sums are taken over only those n for which λ_n (μ_n) are simple eigenvalues of the periodic (anti-periodic) Sturm–Liouville problem, and each

$v_n(x, \lambda_n)(v_n(x, \lambda_n))$ is the periodic (anti-periodic) function on \mathbb{R}^1 whose restriction to $[0, 1]$ coincides with $y_n(x, \lambda_n)(y_n(x, \mu_n))$.

Let $\varepsilon > 0$ be a sufficiently small number, and let the point ω^2 lie on the boundary on the spectrum $\sigma(H_0)$ of the operator H_0 . Then, in the domain

$$\Omega_k \equiv \{k : \text{Im } k > 0, |k - \omega| < \varepsilon\} \quad (4.26)$$

the following equality holds:

$$(H_0 - k^2)^{-1}(f) = h_1(x, \omega)(k - \omega)^{-1/2} + h_2(x, \omega) + h_3(x, \omega)(k - \omega)^{1/2} + O(k - \omega). \quad (4.27)$$

Theorem 4.2. *If the Hill operator H_0 is positive, $p(x) \geq \text{const} > 0$, $q(x) \geq 0$, and the point ω^2 lies on the boundary of the spectrum $\sigma(H_0)$ of the operator H_0 , then, for $|x| < C$ and $t > 0$, the solution of the PROBLEMS A and B has the form*

$$u(x, t) = C_1 \sqrt{t} e^{-i\omega t} h_1(x, \omega) - C_2 i e^{-i\omega t} h_2(x, \omega) + \frac{1}{\sqrt{t}} \{u_1(x, t) + u_2(x, t) + C_3 e^{-i\omega t} h_3(x, \omega)\} + v(x, t), \quad (4.28)$$

where the functions $u_1(x, t)$ and $u_2(x, t)$ have the same form as in Theorem 4.1 with the only difference that the expansions of $u_1(x, t)$ and $u_2(x, t)$ don't contain the term corresponding to ω^2 and, as in Theorem 4.1, the function $v(x, t)$ satisfies the estimate (4.25) for $|x| < C$, $t > 0$, and $C_i = \text{const}$, $i = 0, 1, 2, 3$.

The main idea of the proofs of these theorems is the same as in the case of a compactly supported function $q(x)$ (Vainberg, 1989). Problems A and B are solved using the Fourier transform with the contour of integration in the inverse Fourier transform shifted onto the “non-physical sheet” of the Riemannian surface of the spectral parameter, after which the integral defining the solution is studied, i.e., the principal term of the asymptotics is chosen and the remainder estimated.

Note that the integral under consideration and the methods of its study strongly differ from those in the case of a compactly supported function $q(x)$. The study of the integral is based essentially on the properties of the resolvent of the Hill operator H_0 (see Firsova, 1984, 1987, 1989; Hochstadt, 1965; Korotyaev, 2000).

References

- Coddington E, Levinson N (1955) Theory of ordinary differential equations. Tata McGraw-Hill Education
- Firsova N (1984) Resonances of a Hill operator, perturbed by an exponentially decreasing additive potential. Mathematical Notes 36(5):854–861
- Firsova N (1987) The direct and inverse scattering problems for the one-dimensional perturbed hill operator. Math USSR–Sbornik 58(2):351–388

- Firsova N (1989) On solution of the cauchy problem for the korteweg-de vries equation with initial data the sum of a periodic and a rapidly decreasing function. *Math USSR–Sbornik* 63(1):257–265
- Hochstadt H (1965) On the determination of a hill's equation from its spectrum. *Arch Rational Mech Anal* 19(5):353–362
- Korotyaev E (2000) Estimates for the hill operator, I. *Journal of Differential Equations* 162(1):1–26
- Lapteva SA (1975) On the behaviour for large values of the time of the solution of the Cauchy problem for the equation $\frac{\partial^2 u}{\partial t^2} - \frac{\partial^2 u}{\partial x^2} + \alpha(x)u = 0$. *Matematicheskii Sbornik* 139(3):435–461
- Matevosian HA, V VA (2017) Behavior of the solution of the cauchy problem for an inhomogeneous hyperbolic equation with periodic coefficients. *Journal of Physics (JPCS)* 936(012097):5 pages
- Peržan A (1978) Stabilization of the solution of the Cauchy problem for a hyperbolic equation. *Differentsial'nye Uravneniya* 14(6):1065–1075
- Surguladze TA (1989) The behavior, for large time values, of solutions of a one-dimensional hyperbolic equation with periodic coefficients. *USSR Doklady Math* 38(1):79–83
- Titchmarsh EC (1958) *Eigenfunction expansions: associated with second-order differential equations, vol 2*. Oxford: Clarendon Press
- Topiler NG (1983) Behavior of the solution of the Cauchy problem for the equation $u_{xx} - q(x)u_{tt} = 0$ for large time values t . *Differentsial'nye Uravneniya* 19(2):347–353
- Vainberg B (1989) *Asymptotic methods in equations of mathematical physics*. CRC Press
- Vestyak AV, Matevosian OA (2016) On the behavior of the solution of the Cauchy problem for the hyperbolic equation with periodic coefficients. *Mathematical notes* 100(5-6):751–755
- Vestyak AV, Matevosyan OA (2017) On the behavior of the solution of the Cauchy problem for an inhomogeneous hyperbolic equation with periodic coefficients. *Mathematical Notes* 102(3-4):424–428
- Zhikov VV, Pastukhova SE (2016) Bloch principle for elliptic differential operators with periodic coefficients. *Russian Journal of Mathematical Physics* 23(2):257–277



Chapter 5

A Soft Embedding Theorem for Soft Topological Spaces

Giorgio Nordo

Abstract In this paper, based on the researches on soft set theory and soft topology, we introduce the notions of soft separation between soft points and soft closed sets in order to obtain a generalization of the well-known Embedding Theorem to the class of soft topological spaces.

Keywords: Soft set · Soft topology · Soft mapping · Soft slab · Embedding theorem

5.1 Introduction

Almost every branch of sciences and many practical problems in engineering, economics, computer science, physics, meteorology, statistics, medicine, sociology, etc. have its own uncertainties and ambiguities because they depend on the influence of many parameters and, due to the inadequacy of the existing theories of parameterization in dealing with uncertainties, it is not always easy to model such a kind of problems by using classical mathematical methods. In Molodtsov (1999) initiated the novel concept of Soft Sets Theory as a new mathematical tool and a completely different approach for dealing with uncertainties while modelling problems in a large class of applied sciences. Indeed, dealing with uncertainties becomes of the utmost importance, especially when complex systems must be studied. This is particularly true for some mechanical systems, for example, in studying the new conceived materials, so-called metamaterials (Barchiesi et al, 2019; dell’Isola et al, 2019b,a) which are ad hoc designed to provide a specific behaviour, micro-devices that show a “size effect” (Abali et al, 2015), biological applications (Lekszycki and dell’Isola,

G. Nordo

MIFT - Dipartimento di Scienze Matematiche e Informatiche, Scienze Fisiche e Scienze della Terra, Università di Messina, Viale F. Stagno D’Alcontres, 31 – Contrada Papardo, salita Sperone, 98166 Sant’Agata – Messina, Italy.
e-mail: giorgio.nordo@unime.it

© Springer Nature Switzerland AG 2020

B. E. Abali and I. Giorgio (eds.), *Developments and Novel Approaches in Nonlinear Solid Body Mechanics*, Advanced Structured Materials 130, https://doi.org/10.1007/978-3-030-50460-1_5

37

2012; Giorgio et al, 2019; Sheidaei et al, 2019) characterized by an evolution of their mechanical behaviour, energy harvesting and vibration control (Giorgio et al, 2009; Lossouarn et al, 2015; dell'Isola and Vidoli, 1998), and robotics (Giorgio and Del Vecovo, 2018, 2019) and so on.

In the past few years, the fundamentals of soft set theory have been studied by many researchers. Starting from Maji et al (2002, 2003) studied the theory of soft sets initiated by Molodtsov, defining notion as the equality of two soft sets, the subset and super set of a soft set, the complement of a soft set, the union and the intersection of soft sets, the null soft set and absolute soft set, and they gave many examples. In Pei and Miao (2005); Chen et al (2005) improved the work of Maji. Further contributions to the Soft Sets Theory were given by Yang (2008); Ali et al (2009); Li (2011); Qin and Hong (2010); Sezgin and Atagün (2011); Neog and Sut (2011); Ahmad and Kharal (2009); Babitha and Sunil (2010); Ibrahim and Yusuf (2012); Singh and Onyeozili (2012); Feng and Li (2013); Onyeozili and Gwary (2014); Çağman (2014).

In Shabir and Naz (2011) introduced the concept of soft topological spaces, also defining and investigating the notions of soft closed sets, soft closure, soft neighborhood, soft subspace and some separation axioms. Some other properties related to soft topology were studied by Çağman et al (2011). In the same year Hussain and Ahmad (2011) investigated the properties of soft closed sets, soft neighbourhoods, soft interior, soft exterior and soft boundary, while Kharal and Ahmad (2011) defined the notion of a mapping on soft classes and studied several properties of images and inverse images. The notion of soft interior, soft neighborhood and soft continuity were also object of study by Zorlutuna et al (2012). Some other relations between these notions was proved by Ahmad and Hussain (2012). The neighbourhood properties of a soft topological space were investigated in Nazmul and Samanta (2013). The class of soft Hausdorff spaces was extensively studied by Varol and Aygün (2013). In Aygünoğlu and Aygün (2012) defined and studied the notions of soft continuity and soft product topology. Some years later, Zorlutuna and Çaku (2015) gave some new characterizations of soft continuity, soft openness and soft closedness of soft mappings, also generalizing the Pasting Lemma to the soft topological spaces. Soft first countable and soft second countable spaces were instead defined and studied by Rong (2012). Furthermore, the notion of soft continuity between soft topological spaces was independently introduced and investigated by Hazra et al (2012). Soft connectedness was also studied in Al-Khafaj and Mahmood (2014); Hussain (2015). In the same year, Das and Samanta (2013b,a) introduced and extensively studied the soft metric spaces. In Hussain and Ahmad (2015) redefined and explored several properties of soft T_i (with $i = 0, 1, 2, 3, 4$) separation axioms and discuss some soft invariance properties namely soft topological property and soft hereditary property. Xie (2015) introduced the concept of soft points and proved that soft sets can be translated into soft points so that they may conveniently dealt as same as ordinary sets. Tantawy et al (2016) continued the study of soft T_i -spaces (for $i = 0, 1, 2, 3, 4, 5$) also discussing the hereditary and topological properties for such spaces. Fu et al (2017) investigated some basic properties concerning the soft topological product space. Further contributions to the theory of soft sets and that

of soft topology were added by Min (2011); Janaki and Sredja (2012); Varol et al (2012); Peyghan (2013); Wardowski (2013); Nazmul and Samanta (2014); Peyghan et al (2014); Georgiou et al (2013); Georgiou and Megaritis (2014); Uluçay et al (2016); Wadkar et al (2016); Matejdes (2016); Fu et al (2017); Bdaiwi (2017), and, more recently, by Bayramov and Aras (2018); El-Shafei et al (2018); Al-Shami et al (2018); Nordo (2018, 2019a).

In the present paper we will present the notions of family of soft mappings soft separating soft points and soft points from soft closed sets in order to give a generalization of the well-known Embedding Theorem for soft topological spaces.

5.2 Preliminaries

In this section we present some basic definitions and results on soft sets and suitably exemplify them. Terms and undefined concepts are used as in Engelking (1989).

Definition 5.1. (Molodtsov, 1999) Let \mathbb{U} be an initial universe set and \mathbb{E} be a nonempty set of parameters (or abstract attributes) under consideration with respect to \mathbb{U} and $A \subseteq \mathbb{E}$, we say that a pair (F, A) is a **soft set** over \mathbb{U} if F is a set-valued mapping $F : A \rightarrow \mathbb{P}(\mathbb{U})$ which maps every parameter $e \in A$ to a subset $F(e)$ of \mathbb{U} .

In other words, a soft set is not a real (crisp) set but a parameterized family $\{F(e)\}_{e \in A}$ of subsets of the universe \mathbb{U} . For every parameter $e \in A$, $F(e)$ may be considered as the set of *e-approximate elements* of the soft set (F, A) .

Remark 5.1. Ma et al (2010) proved that every soft set (F, A) is equivalent to the soft set (F, \mathbb{E}) related to the whole set of parameters \mathbb{E} , simply considering empty every approximations of parameters which are missing in A , that is extending in a trivial way its set-valued mapping, i.e. setting $F(e) = \emptyset$, for every $e \in \mathbb{E} \setminus A$.

For such a reason, in this paper we can consider all the soft sets over the same parameter set \mathbb{E} as in Chiney and Samanta (2016) and we will redefine all the basic operations and relations between soft sets originally introduced in Maji et al (2002, 2003); Molodtsov (1999) as in Nazmul and Samanta (2013), that is by considering the same parameter set.

Definition 5.2. (Zorlutuna et al, 2012) The set of all the soft sets over a universe \mathbb{U} with respect to a set of parameters \mathbb{E} will be denoted by $\mathcal{SS}(\mathbb{U})_{\mathbb{E}}$.

Definition 5.3. (Nazmul and Samanta, 2013) Let $(F, \mathbb{E}), (G, \mathbb{E}) \in \mathcal{SS}(\mathbb{U})_{\mathbb{E}}$ be two soft sets over a common universe \mathbb{U} and a common set of parameters \mathbb{E} , we say that (F, \mathbb{E}) is a **soft subset** of (G, \mathbb{E}) and we write $(F, \mathbb{E}) \underline{\subseteq} (G, \mathbb{E})$ if $F(e) \subseteq G(e)$ for every $e \in \mathbb{E}$.

Definition 5.4. (Nazmul and Samanta, 2013) Let $(F, \mathbb{E}), (G, \mathbb{E}) \in \mathcal{SS}(\mathbb{U})_{\mathbb{E}}$ be two soft sets over a common universe \mathbb{U} , we say that (F, \mathbb{E}) and (G, \mathbb{E}) are **soft equal** and we write $(F, \mathbb{E}) \underline{\cong} (G, \mathbb{E})$ if $(F, \mathbb{E}) \underline{\subseteq} (G, \mathbb{E})$ and $(G, \mathbb{E}) \underline{\subseteq} (F, \mathbb{E})$.

Definition 5.5. (Nazmul and Samanta, 2013) A soft set (F, \mathbb{E}) over a universe \mathbb{U} is said to be the **null soft set** and it is denoted by $(\tilde{\emptyset}, \mathbb{E})$ if $F(e) = \emptyset$ for every $e \in \mathbb{E}$.

Definition 5.6. (Nazmul and Samanta, 2013) A soft set $(F, \mathbb{E}) \in \mathcal{SS}(\mathbb{U})_{\mathbb{E}}$ over a universe \mathbb{U} is said to be the **absolute soft set** and it is denoted by $(\tilde{\mathbb{U}}, \mathbb{E})$ if $F(e) = \mathbb{U}$ for every $e \in \mathbb{E}$.

Definition 5.7. Let $(F, \mathbb{E}) \in \mathcal{SS}(\mathbb{U})_{\mathbb{E}}$ be a soft set over a universe \mathbb{U} and V be a nonempty subset of U , the **constant soft set** of V , denoted by (\tilde{V}, \mathbb{E}) (or, sometimes, by \tilde{V}), is the soft set $(\underline{V}, \mathbb{E})$, where $\underline{V} : \mathbb{E} \rightarrow \mathcal{P}(U)$ is the constant set-valued mapping defined by $\underline{V}(e) = V$, for every $e \in \mathbb{E}$.

Definition 5.8. (Nazmul and Samanta, 2013) Let $(F, \mathbb{E}) \in \mathcal{SS}(\mathbb{U})_{\mathbb{E}}$ be a soft set over a universe \mathbb{U} , the **soft complement** (or more exactly the **soft relative complement**) of (F, \mathbb{E}) , denoted by $(F, \mathbb{E})^c$, is the soft set (F^c, \mathbb{E}) where $F^c : \mathbb{E} \rightarrow \mathcal{P}(U)$ is the set-valued mapping defined by $F^c(e) = F(e)^c = \mathbb{U} \setminus F(e)$, for every $e \in \mathbb{E}$.

Definition 5.9. (Nazmul and Samanta, 2013) Let $(F, \mathbb{E}), (G, \mathbb{E}) \in \mathcal{SS}(\mathbb{U})_{\mathbb{E}}$ be two soft sets over a common universe \mathbb{U} , the **soft difference** of (F, \mathbb{E}) and (G, \mathbb{E}) , denoted by $(F, \mathbb{E}) \tilde{\setminus} (G, \mathbb{E})$, is the soft set $(F \setminus G, \mathbb{E})$ where $F \setminus G : \mathbb{E} \rightarrow \mathcal{P}(U)$ is the set-valued mapping defined by $(F \setminus G)(e) = F(e) \setminus G(e)$, for every $e \in \mathbb{E}$.

Clearly, for every soft set $(F, \mathbb{E}) \in \mathcal{SS}(\mathbb{U})_{\mathbb{E}}$, it results $(F, \mathbb{E})^c \doteq (\tilde{\mathbb{U}}, \mathbb{E}) \tilde{\setminus} (F, \mathbb{E})$.

Definition 5.10. (Nazmul and Samanta, 2013) Let $(F, \mathbb{E}), (G, \mathbb{E}) \in \mathcal{SS}(\mathbb{U})_{\mathbb{E}}$ be two soft sets over a universe \mathbb{U} , the **soft union** of (F, \mathbb{E}) and (G, \mathbb{E}) , denoted by $(F, \mathbb{E}) \tilde{\cup} (G, \mathbb{E})$, is the soft set $(F \cup G, \mathbb{E})$ where $F \cup G : \mathbb{E} \rightarrow \mathcal{P}(U)$ is the set-valued mapping defined by $(F \cup G)(e) = F(e) \cup G(e)$, for every $e \in \mathbb{E}$.

Definition 5.11. (Nazmul and Samanta, 2013) Let $(F, \mathbb{E}), (G, \mathbb{E}) \in \mathcal{SS}(\mathbb{U})_{\mathbb{E}}$ be two soft sets over a universe \mathbb{U} , the **soft intersection** of (F, \mathbb{E}) and (G, \mathbb{E}) , denoted by $(F, \mathbb{E}) \tilde{\cap} (G, \mathbb{E})$, is the soft set $(F \cap G, \mathbb{E})$ where $F \cap G : \mathbb{E} \rightarrow \mathcal{P}(U)$ is the set-valued mapping defined by $(F \cap G)(e) = F(e) \cap G(e)$, for every $e \in \mathbb{E}$.

Definition 5.12. (Al-Khafaj and Mahmood, 2014) Two soft sets (F, \mathbb{E}) and (G, \mathbb{E}) over a common universe \mathbb{U} are said to be **soft disjoint** if their soft intersection is the soft null set, i.e. if $(F, \mathbb{E}) \tilde{\cap} (G, \mathbb{E}) \doteq (\tilde{\emptyset}, \mathbb{E})$. If two soft sets are not soft disjoint, we also say that they **soft meet** each other. In particular, if $(F, \mathbb{E}) \tilde{\cap} (G, \mathbb{E}) \not\dot{=} (\tilde{\emptyset}, \mathbb{E})$ we say that (F, \mathbb{E}) **soft meets** (G, \mathbb{E}) .

Definition 5.13. (Xie, 2015) A soft set $(F, \mathbb{E}) \in \mathcal{SS}(\mathbb{U})_{\mathbb{E}}$ over a universe \mathbb{U} is said to be a **soft point** over U if it has only one non-empty approximation which is a singleton, i.e. if there exists some parameter $\alpha \in \mathbb{E}$ and an element $p \in \mathbb{U}$ such that $F(\alpha) = \{p\}$ and $F(e) = \emptyset$ for every $e \in \mathbb{E} \setminus \{\alpha\}$. Such a soft point is usually denoted by (p_{α}, \mathbb{E}) . The singleton $\{p\}$ is called the **support set** of the soft point and α is called the **expressive parameter** of (p_{α}, \mathbb{E}) .

Definition 5.14. (Xie, 2015) The set of all the soft points over a universe \mathbb{U} with respect to a set of parameters \mathbb{E} will be denoted by $\mathcal{SP}(\mathbb{U})_{\mathbb{E}}$.

Since any soft point is a particular soft set, it is evident that $\mathcal{SP}(\mathbb{U})_{\mathbb{E}} \subseteq \mathcal{SS}(\mathbb{U})_{\mathbb{E}}$.

Definition 5.15. (Xie, 2015) Let $(p_{\alpha}, \mathbb{E}) \in \mathcal{SP}(\mathbb{U})_{\mathbb{E}}$ and $(F, \mathbb{E}) \in \mathcal{SS}(\mathbb{U})_{\mathbb{E}}$ be a soft point and a soft set over a common universe \mathbb{U} , respectively. We say that *the soft point* (p_{α}, \mathbb{E}) *soft belongs to the soft set* (F, \mathbb{E}) and we write $(p_{\alpha}, \mathbb{E}) \tilde{\in} (F, \mathbb{E})$, if the soft point is a soft subset of the soft set, i.e. if $(p_{\alpha}, \mathbb{E}) \tilde{\subseteq} (F, \mathbb{E})$ and hence if $p \in F(\alpha)$. We also say that *the soft point* (p_{α}, \mathbb{E}) *does not belongs to the soft set* (F, \mathbb{E}) and we write $(p_{\alpha}, \mathbb{E}) \tilde{\notin} (F, \mathbb{E})$, if the soft point is not a soft subset of the soft set, i.e. if $(p_{\alpha}, \mathbb{E}) \tilde{\not\subseteq} (F, \mathbb{E})$ and hence if $p \notin F(\alpha)$.

Definition 5.16. (Das and Samanta, 2013b) Let $(p_{\alpha}, \mathbb{E}), (q_{\beta}, \mathbb{E}) \in \mathcal{SP}(\mathbb{U})_{\mathbb{E}}$ be two soft points over a common universe \mathbb{U} , we say that (p_{α}, \mathbb{E}) and (q_{β}, \mathbb{E}) are *soft equal*, and we write $(p_{\alpha}, \mathbb{E}) \tilde{=} (q_{\beta}, \mathbb{E})$, if they are equals as soft sets and hence if $p = q$ and $\alpha = \beta$.

Definition 5.17. (Das and Samanta, 2013b) We say that two soft points (p_{α}, \mathbb{E}) and (q_{β}, \mathbb{E}) are *soft distincts*, and we write $(p_{\alpha}, \mathbb{E}) \tilde{\neq} (q_{\beta}, \mathbb{E})$, if and only if $p \neq q$ or $\alpha \neq \beta$.

The notion of soft point allows us to express the soft inclusion in a more familiar way.

Proposition 5.1. Let $(F, \mathbb{E}), (G, \mathbb{E}) \in \mathcal{SS}(\mathbb{U})_{\mathbb{E}}$ be two soft sets over a common universe \mathbb{U} respect to a parameter set \mathbb{E} , then $(F, \mathbb{E}) \tilde{\subseteq} (G, \mathbb{E})$ if and only if for every soft point $(p_{\alpha}, \mathbb{E}) \tilde{\in} (F, \mathbb{E})$ it follows that $(p_{\alpha}, \mathbb{E}) \tilde{\in} (G, \mathbb{E})$.

Definition 5.18. (Hussain and Ahmad, 2011) Let $(F, \mathbb{E}) \in \mathcal{SS}(\mathbb{U})_{\mathbb{E}}$ be a soft set over a universe \mathbb{U} and V be a nonempty subset of \mathbb{U} , the *sub soft set* of (F, \mathbb{E}) over V , is the soft set $({}^V F, \mathbb{E})$, where ${}^V F : \mathbb{E} \rightarrow \mathbb{P}(\mathbb{U})$ is the set-valued mapping defined by ${}^V F(e) = F(e) \cap V$, for every $e \in \mathbb{E}$.

Remark 5.2. Using Definitions 5.7 and 5.11, it is a trivial matter to verify that a sub soft set of (F, \mathbb{E}) over V can also be expressed as $({}^V F, \mathbb{E}) \tilde{=} (F, \mathbb{E}) \tilde{\cap} (\tilde{V}, \mathbb{E})$.

Furthermore, it is evident that the sub soft set $({}^V F, \mathbb{E})$ above defined belongs to the set of all the soft sets over V with respect to the set of parameters \mathbb{E} , which is contained in the set of all the soft sets over the universe \mathbb{U} with respect to \mathbb{E} , that is $({}^V F, \mathbb{E}) \in \mathcal{SS}(V)_{\mathbb{E}} \subseteq \mathcal{SS}(\mathbb{U})_{\mathbb{E}}$.

Definition 5.19. (Babitha and Sunil, 2010; Kazancı et al, 2010) Let $\{(F_i, \mathbb{E}_i)\}_{i \in I}$ be a family of soft sets over a universe set \mathbb{U}_i with respect to a set of parameters \mathbb{E}_i (with $i \in I$), respectively. Then the *soft product* (or, more precisely, the *soft cartesian product*) of $\{(F_i, \mathbb{E}_i)\}_{i \in I}$, denoted by $\tilde{\prod}_{i \in I} (F_i, \mathbb{E}_i)$, is the soft set $(\prod_{i \in I} F_i, \prod_{i \in I} \mathbb{E}_i)$ over the (usual) cartesian product $\prod_{i \in I} \mathbb{U}_i$ and with respect to the set of parameters $\prod_{i \in I} \mathbb{E}_i$, where $\prod_{i \in I} F_i : \prod_{i \in I} \mathbb{E}_i \rightarrow \mathbb{P}(\prod_{i \in I} \mathbb{U}_i)$ is the set-valued mapping defined by $\prod_{i \in I} F_i (\langle e_i \rangle_{i \in I}) = \prod_{i \in I} F_i(e_i)$, for every $\langle e_i \rangle_{i \in I} \in \prod_{i \in I} \mathbb{E}_i$.

Proposition 5.2. (Nordo, 2019b) *Let $\widetilde{\prod}_{i \in I} (F_i, \mathbb{E}_i)$ be the soft product of a family $\{(F_i, \mathbb{E}_i)\}_{i \in I}$ of soft sets over a universe set \mathbb{U}_i with respect to a set of parameters \mathbb{E}_i (with $i \in I$), and let $(p_\alpha, \prod_{i \in I} \mathbb{E}_i) \in \mathcal{SP}(\prod_{i \in I} \mathbb{U}_i)_{\prod_{i \in I} \mathbb{E}_i}$ be a soft point of the product $\prod_{i \in I} \mathbb{U}_i$, where $p = \langle p_i \rangle_{i \in I} \in \prod_{i \in I} \mathbb{U}_i$ and $\alpha = \langle \alpha_i \rangle_{i \in I} \in \prod_{i \in I} \mathbb{E}_i$, then $(p_\alpha, \prod_{i \in I} \mathbb{E}_i) \tilde{\in} \widetilde{\prod}_{i \in I} (F_i, \mathbb{E}_i)$ if and only if $((p_i)_{\alpha_i}, \mathbb{E}_i) \tilde{\in} (F_i, \mathbb{E}_i)$ for every $i \in I$.*

Corollary 5.1. (Nordo, 2019b) *The soft product of a family $\{(F_i, \mathbb{E}_i)\}_{i \in I}$ of soft sets over a universe set \mathbb{U}_i with respect to a set of parameters \mathbb{E}_i (with $i \in I$) is null if and only if at least one of its soft sets is null, that is $\widetilde{\prod}_{i \in I} (F_i, \mathbb{E}_i) \tilde{=} (\tilde{\emptyset}, \prod_{i \in I} \mathbb{E}_i)$ iff there exists some $j \in I$ such that $(F_j, \mathbb{E}_j) \tilde{=} (\tilde{\emptyset}, \mathbb{E}_j)$.*

Proposition 5.3. (Kazancı et al, 2010) *Let $\{(F_i, \mathbb{E}_i)\}_{i \in I}$ and $\{(G_i, \mathbb{E}_i)\}_{i \in I}$ be two families of soft sets over a universe set \mathbb{U}_i with respect to a set of parameters \mathbb{E}_i (with $i \in I$), then it results:*

$$\widetilde{\prod}_{i \in I} ((F_i, \mathbb{E}_i) \tilde{\cap} (G_i, \mathbb{E}_i)) \tilde{=} \widetilde{\prod}_{i \in I} (F_i, \mathbb{E}_i) \tilde{\cap} \widetilde{\prod}_{i \in I} (G_i, \mathbb{E}_i).$$

According to Remark 5.1 the following notions by Kharal and Ahmad have been simplified and slightly modified for soft sets defined on a common parameter set.

Definition 5.20. (Kharal and Ahmad, 2011) Let $\mathcal{SS}(\mathbb{U})_{\mathbb{E}}$ and $\mathcal{SS}(\mathbb{U}')_{\mathbb{E}'}$ be two sets of soft open sets over the universe sets \mathbb{U} and \mathbb{U}' with respect to the sets of parameters \mathbb{E} and \mathbb{E}' , respectively. and consider a mapping $\varphi : \mathbb{U} \rightarrow \mathbb{U}'$ between the two universe sets and a mapping $\psi : \mathbb{E} \rightarrow \mathbb{E}'$ between the two set of parameters. The mapping $\varphi_\psi : \mathcal{SS}(\mathbb{U})_{\mathbb{E}} \rightarrow \mathcal{SS}(\mathbb{U}')_{\mathbb{E}'}$, which maps every soft set (F, \mathbb{E}) of $\mathcal{SS}(\mathbb{U})_{\mathbb{E}}$ to a soft set $(\varphi_\psi(F), \mathbb{E}')$ of $\mathcal{SS}(\mathbb{U}')_{\mathbb{E}'}$, denoted by $\varphi_\psi(F, \mathbb{E})$, where $\varphi_\psi(F) : \mathbb{E}' \rightarrow \mathcal{P}(\mathbb{U}')$ is the set-valued mapping defined by $\varphi_\psi(F)(e') = \bigcup \{\varphi(F(e)) : e \in \psi^{-1}(\{e'\})\}$ for every $e' \in \mathbb{E}'$, is called a **soft mapping** from \mathbb{U} to \mathbb{U}' induced by the mappings φ and ψ , while the soft set $\varphi_\psi(F, \mathbb{E}) \tilde{=} (\varphi_\psi(F), \mathbb{E}')$ is said to be the **soft image** of the soft set (F, \mathbb{E}) under the soft mapping $\varphi_\psi : \mathcal{SS}(\mathbb{U})_{\mathbb{E}} \rightarrow \mathcal{SS}(\mathbb{U}')_{\mathbb{E}'}$. The soft mapping $\varphi_\psi : \mathcal{SS}(\mathbb{U})_{\mathbb{E}} \rightarrow \mathcal{SS}(\mathbb{U}')_{\mathbb{E}'}$ is said **injective** (respectively **surjective**, **bijective**) if the mappings $\varphi : \mathbb{U} \rightarrow \mathbb{U}'$ and $\psi : \mathbb{E} \rightarrow \mathbb{E}'$ are both injective (resp. surjective, bijective).

It is worth noting that soft mappings between soft sets behaves similarly to usual (crisp) mappings in the sense that they maps soft points to soft points, as proved in the following property.

Proposition 5.4. *Let $\varphi_\psi : \mathcal{SS}(\mathbb{U})_{\mathbb{E}} \rightarrow \mathcal{SS}(\mathbb{U}')_{\mathbb{E}'}$ be a soft mapping induced by the mappings $\varphi : \mathbb{U} \rightarrow \mathbb{U}'$ and $\psi : \mathbb{E} \rightarrow \mathbb{E}'$ between the two sets $\mathcal{SS}(\mathbb{U})_{\mathbb{E}}$, $\mathcal{SS}(\mathbb{U}')_{\mathbb{E}'}$ of soft sets. and consider a soft point (p_α, \mathbb{E}) of $\mathcal{SP}(\mathbb{U})_{\mathbb{E}}$. Then the soft image $\varphi_\psi(p_\alpha, \mathbb{E})$ of the soft point (p_α, \mathbb{E}) under the soft mapping φ_ψ is the soft point $(\varphi(p)_{\psi(\alpha)}, \mathbb{E}')$, i.e. $\varphi_\psi(p_\alpha, \mathbb{E}) \tilde{=} (\varphi(p)_{\psi(\alpha)}, \mathbb{E}')$.*

Corollary 5.2. Let $\varphi_\psi : \mathbb{S}\mathbb{S}(\mathbb{U})_{\mathbb{E}} \rightarrow \mathbb{S}\mathbb{S}(\mathbb{U}')_{\mathbb{E}'}$ be a soft mapping induced by the mappings $\varphi : \mathbb{U} \rightarrow \mathbb{U}'$ and $\psi : \mathbb{E} \rightarrow \mathbb{E}'$ between the two sets $\mathbb{S}\mathbb{S}(\mathbb{U})_{\mathbb{E}}, \mathbb{S}\mathbb{S}(\mathbb{U}')_{\mathbb{E}'}$ of soft sets, then φ_ψ is injective if and only if its soft images of every distinct pair of soft points are distinct too, i.e. if for every $(p_\alpha, \mathbb{E}), (q_\beta, \mathbb{E}) \in \mathbb{S}\mathcal{P}(\mathbb{U})_{\mathbb{E}}$ such that $(p_\alpha, \mathbb{E}) \not\tilde{=} (q_\beta, \mathbb{E})$ it follows that $\varphi_\psi(p_\alpha, \mathbb{E}) \not\tilde{=} \varphi_\psi(q_\beta, \mathbb{E})$.

Definition 5.21. (Kharal and Ahmad, 2011) Let $\varphi_\psi : \mathbb{S}\mathbb{S}(\mathbb{U})_{\mathbb{E}} \rightarrow \mathbb{S}\mathbb{S}(\mathbb{U}')_{\mathbb{E}'}$ be a soft mapping induced by the mappings $\varphi : \mathbb{U} \rightarrow \mathbb{U}'$ and $\psi : \mathbb{E} \rightarrow \mathbb{E}'$ between the sets $\mathbb{S}\mathbb{S}(\mathbb{U})_{\mathbb{E}}, \mathbb{S}\mathbb{S}(\mathbb{U}')_{\mathbb{E}'}$ of soft sets and consider a soft set (G, \mathbb{E}') of $\mathbb{S}\mathbb{S}(\mathbb{U}')_{\mathbb{E}'}$. The **soft inverse image** of (G, \mathbb{E}') under the soft mapping $\varphi_\psi : \mathbb{S}\mathbb{S}(\mathbb{U})_{\mathbb{E}} \rightarrow \mathbb{S}\mathbb{S}(\mathbb{U}')_{\mathbb{E}'}$, denoted by $\varphi_\psi^{-1}(G, \mathbb{E}')$ is the soft set $(\varphi_\psi^{-1}(G), \mathbb{E}')$ of $\mathbb{S}\mathbb{S}(\mathbb{U})_{\mathbb{E}}$ where $\varphi_\psi^{-1}(G) : \mathbb{E} \rightarrow \mathbb{P}(\mathbb{U})$ is the set-valued mapping defined by $\varphi_\psi^{-1}(G)(e) = \varphi^{-1}(G(\psi(e)))$ for every $e \in \mathbb{E}$.

Corollary 5.3. Let $\varphi_\psi : \mathbb{S}\mathbb{S}(\mathbb{U})_{\mathbb{E}} \rightarrow \mathbb{S}\mathbb{S}(\mathbb{U}')_{\mathbb{E}'}$ be a soft mapping induced by the mappings $\varphi : \mathbb{U} \rightarrow \mathbb{U}'$ and $\psi : \mathbb{E} \rightarrow \mathbb{E}'$. If $(F, \mathbb{E}) \in \mathbb{S}\mathbb{S}(\mathbb{U})_{\mathbb{E}}$ and $(F', \mathbb{E}') \in \mathbb{S}\mathbb{S}(\mathbb{U}')_{\mathbb{E}'}$ are soft sets over \mathbb{U} and \mathbb{U}' , respectively and $(p_\alpha, \mathbb{E}) \in \mathbb{S}\mathcal{P}(\mathbb{U})_{\mathbb{E}}$ and $(q_\beta, \mathbb{E}') \in \mathbb{S}\mathcal{P}(\mathbb{U}')_{\mathbb{E}'}$ are soft points over \mathbb{U} and \mathbb{U}' , respectively, then the following hold:

- (1) $(p_\alpha, \mathbb{E}) \tilde{\in} (F, \mathbb{E})$ implies $\varphi_\psi(p_\alpha, \mathbb{E}) \tilde{\in} \varphi_\psi(F, \mathbb{E})$.
- (2) $(q_\beta, \mathbb{E}') \tilde{\in} (F', \mathbb{E}')$ implies $\varphi_\psi^{-1}(q_\beta, \mathbb{E}') \tilde{\subseteq} \varphi_\psi^{-1}(F', \mathbb{E}')$.

Definition 5.22. Let $\varphi_\psi : \mathbb{S}\mathbb{S}(\mathbb{U})_{\mathbb{E}} \rightarrow \mathbb{S}\mathbb{S}(\mathbb{U}')_{\mathbb{E}'}$ be a bijective soft mapping induced by the mappings $\varphi : \mathbb{U} \rightarrow \mathbb{U}'$ and $\psi : \mathbb{E} \rightarrow \mathbb{E}'$. The **soft inverse mapping** of φ_ψ , denoted by φ_ψ^{-1} , is the soft mapping $\varphi_\psi^{-1} = (\varphi^{-1})_{\psi^{-1}} : \mathbb{S}\mathbb{S}(\mathbb{U}')_{\mathbb{E}'} \rightarrow \mathbb{S}\mathbb{S}(\mathbb{U})_{\mathbb{E}}$ induced by the inverse mappings $\varphi^{-1} : \mathbb{U}' \rightarrow \mathbb{U}$ and $\psi^{-1} : \mathbb{E}' \rightarrow \mathbb{E}$ of the mappings φ and ψ , respectively.

Remark 5.3. Evidently, the soft inverse mapping $\varphi_\psi^{-1} : \mathbb{S}\mathbb{S}(\mathbb{U}')_{\mathbb{E}'} \rightarrow \mathbb{S}\mathbb{S}(\mathbb{U})_{\mathbb{E}}$ of a bijective soft mapping $\varphi_\psi : \mathbb{S}\mathbb{S}(\mathbb{U})_{\mathbb{E}} \rightarrow \mathbb{S}\mathbb{S}(\mathbb{U}')_{\mathbb{E}'}$ is also bijective and its soft image of a soft set in $\mathbb{S}\mathbb{S}(\mathbb{U}')_{\mathbb{E}'}$ coincides with the soft inverse image of the corresponding soft set under the soft mapping φ_ψ .

Definition 5.23. (Aygünoğlu and Aygün, 2012) Let $\mathbb{S}\mathbb{S}(\mathbb{U})_{\mathbb{E}}, \mathbb{S}\mathbb{S}(\mathbb{U}')_{\mathbb{E}'}$ and $\mathbb{S}\mathbb{S}(\mathbb{U}'')_{\mathbb{E}''}$ be three sets of soft open sets over the universe sets $\mathbb{U}, \mathbb{U}', \mathbb{U}''$ with respect to the sets of parameters $\mathbb{E}, \mathbb{E}', \mathbb{E}''$, respectively, and $\varphi_\psi : \mathbb{S}\mathbb{S}(\mathbb{U})_{\mathbb{E}} \rightarrow \mathbb{S}\mathbb{S}(\mathbb{U}')_{\mathbb{E}'}$, $\gamma_\delta : \mathbb{S}\mathbb{S}(\mathbb{U}')_{\mathbb{E}'} \rightarrow \mathbb{S}\mathbb{S}(\mathbb{U}'')_{\mathbb{E}''}$ be two soft mappings between such sets, then the **soft composition** of the soft mappings φ_ψ and γ_δ , denoted by $\gamma_\delta \tilde{\circ} \varphi_\psi$ is the soft mapping $(\gamma \circ \varphi)_{\delta \circ \psi} : \mathbb{S}\mathbb{S}(\mathbb{U})_{\mathbb{E}} \rightarrow \mathbb{S}\mathbb{S}(\mathbb{U}'')_{\mathbb{E}''}$ induced by the compositions $\gamma \circ \varphi : \mathbb{U} \rightarrow \mathbb{U}''$ of the mappings φ and γ between the universe sets and $\delta \circ \psi : \mathbb{E} \rightarrow \mathbb{E}''$ of the mappings ψ and δ between the parameter sets.

The notion of soft topological spaces as topological spaces defined over a initial universe with a fixed set of parameters was introduced by Shabir and Naz (2011).

Definition 5.24. (Shabir and Naz, 2011) Let X be an initial universe set, \mathbb{E} be a nonempty set of parameters with respect to X and $\mathcal{T} \subseteq \mathbb{S}\mathbb{S}(X)_{\mathbb{E}}$ be a family of soft sets over X , we say that \mathcal{T} is a **soft topology** on X with respect to \mathbb{E} if the following four conditions are satisfied:

- (i) the null soft set belongs to \mathcal{T} , i.e. $(\tilde{\emptyset}, \mathbb{E}) \in \mathcal{T}$.
- (ii) the absolute soft set belongs to \mathcal{T} , i.e. $(\tilde{X}, \mathbb{E}) \in \mathcal{T}$.
- (iii) the soft intersection of any two soft sets of \mathcal{T} belongs to \mathcal{T} , i.e. for every $(F, \mathbb{E}), (G, \mathbb{E}) \in \mathcal{T}$ then $(F, \mathbb{E}) \tilde{\cap} (G, \mathbb{E}) \in \mathcal{T}$.
- (iv) the soft union of any subfamily of soft sets in \mathcal{T} belongs to \mathcal{T} , i.e. for every $\{(F_i, \mathbb{E})\}_{i \in I} \subseteq \mathcal{T}$ then $\tilde{\bigcup}_{i \in I} (F_i, \mathbb{E}) \in \mathcal{T}$.

The triplet $(X, \mathcal{T}, \mathbb{E})$ is called a **soft topological space** (or soft space, for short) over X with respect to \mathbb{E} .

In some case, when it is necessary to better specify the universal set and the set of parameters, the topology will be denoted by $\mathcal{T}(X, \mathbb{E})$.

Definition 5.25. (Shabir and Naz, 2011) Let $(X, \mathcal{T}, \mathbb{E})$ be a soft topological space over X with respect to \mathbb{E} , then the members of \mathcal{T} are said to be **soft open set** in X .

Definition 5.26. (Hazra et al, 2012) Let \mathcal{T}_1 and \mathcal{T}_2 be two soft topologies over a common universe set X with respect to a set of paramters \mathbb{E} . We say that \mathcal{T}_2 is **finer** (or stronger) than \mathcal{T}_1 if $\mathcal{T}_1 \subseteq \mathcal{T}_2$ where \subseteq is the usual set-theoretic relation of inclusion between crisp sets. In the same situation, we also say that \mathcal{T}_1 is **coarser** (or weaker) than \mathcal{T}_2 .

Definition 5.27. (Shabir and Naz, 2011) Let $(X, \mathcal{T}, \mathbb{E})$ be a soft topological space over X and (F, \mathbb{E}) be a soft set over X . We say that (F, \mathbb{E}) is **soft closed set** in X if its complement $(F, \mathbb{E})^c$ is a soft open set, i.e. if $(F, \mathbb{E})^c \in \mathcal{T}$.

Notation 5.2.1 *The family of all soft closed sets of a soft topological space $(X, \mathcal{T}, \mathbb{E})$ over X with respect to \mathbb{E} will be denoted by σ , or more precisely with $\sigma(X, \mathbb{E})$ when it is necessary to specify the universal set X and the set of parameters \mathbb{E} .*

Definition 5.28. (Aygünöglu and Aygün, 2012) Let $(X, \mathcal{T}, \mathbb{E})$ be a soft topological space over X and $\mathcal{B} \subseteq \mathcal{T}$ be a non-empty subset of soft open sets. We say that \mathcal{B} is a **soft open base** for $(X, \mathcal{T}, \mathbb{E})$ if every soft open set of \mathcal{T} can be expressed as soft union of a subfamily of \mathcal{B} , i.e. if for every $(F, \mathbb{E}) \in \mathcal{T}$ there exists some $\mathcal{A} \subset \mathcal{B}$ such that $(F, \mathbb{E}) = \tilde{\bigcup} \{(A, \mathbb{E}) : (A, \mathbb{E}) \in \mathcal{A}\}$.

Proposition 5.5. (Nazmul and Samanta, 2013) *Let $(X, \mathcal{T}, \mathbb{E})$ be a soft topological space over X and $\mathcal{B} \subseteq \mathcal{T}$ be a family of soft open sets of X . Then \mathcal{B} is a soft open base for $(X, \mathcal{T}, \mathbb{E})$ if and only if for every soft open set $(F, \mathbb{E}) \in \mathcal{T}$ and any soft point $(x_\alpha, \mathbb{E}) \tilde{\in} (F, \mathbb{E})$ there exists some soft open set $(B, \mathbb{E}) \in \mathcal{B}$ such that $(x_\alpha, \mathbb{E}) \tilde{\in} (B, \mathbb{E}) \tilde{\subseteq} (F, \mathbb{E})$.*

Definition 5.29. (Zorlutuna et al, 2012) Let $(X, \mathcal{T}, \mathbb{E})$ be a soft topological space, $(N, \mathbb{E}) \in \mathcal{SS}(X)_{\mathbb{E}}$ be a soft set and $(x_\alpha, \mathbb{E}) \in \mathcal{SP}(X)_{\mathbb{E}}$ be a soft point over a common universe X . We say that (N, \mathbb{E}) is a **soft neighbourhood** of the soft point (x_α, \mathbb{E}) if there is some soft open set soft containing the soft point and soft contained in the soft set, that is if there exists some soft open set $(A, \mathbb{E}) \in \mathcal{T}$ such that $(x_\alpha, \mathbb{E}) \tilde{\in} (A, \mathbb{E}) \tilde{\subseteq} (N, \mathbb{E})$.

Notation 5.2.2 *The family of all soft neighbourhoods (sometimes also called soft neighbourhoods system) of a soft point $(x_\alpha, \mathbb{E}) \in \mathcal{SP}(X)_\mathbb{E}$ in a soft topological space $(X, \mathcal{T}, \mathbb{E})$ will be denoted by $\mathcal{N}_{(x_\alpha, \mathbb{E})}$ (or more precisely with $\mathcal{N}_{(x_\alpha, \mathbb{E})}^{\mathcal{T}}$ if it is necessary to specify the topology).*

Definition 5.30. (Shabir and Naz, 2011) Let $(X, \mathcal{T}, \mathbb{E})$ be a soft topological space over X and (F, \mathbb{E}) be a soft set over X . Then the **soft closure** of the soft set (F, \mathbb{E}) with respect to the soft space $(X, \mathcal{T}, \mathbb{E})$, denoted by $s\text{-cl}_X(F, \mathbb{E})$, is the soft intersection of all soft closed set over X soft containing (F, \mathbb{E}) , that is

$$s\text{-cl}_X(F, \mathbb{E}) \doteq \widetilde{\bigcap} \{ (C, \mathbb{E}) \in \sigma(X, \mathbb{E}) : (F, \mathbb{E}) \widetilde{\subseteq} (C, \mathbb{E}) \}.$$

Proposition 5.6. (Shabir and Naz, 2011) *Let $(X, \mathcal{T}, \mathbb{E})$ be a soft topological space over X , and (F, \mathbb{E}) be a soft set over X . Then the following hold:*

- (1) $s\text{-cl}_X(\tilde{\emptyset}, \mathbb{E}) \doteq (\tilde{\emptyset}, \mathbb{E})$.
- (2) $s\text{-cl}_X(\tilde{X}, \mathbb{E}) \doteq (\tilde{X}, \mathbb{E})$.
- (3) $(F, \mathbb{E}) \widetilde{\subseteq} s\text{-cl}_X(F, \mathbb{E})$.
- (4) (F, \mathbb{E}) is a soft closed set over X if and only if $s\text{-cl}_X(F, \mathbb{E}) \doteq (F, \mathbb{E})$.
- (5) $s\text{-cl}_X(s\text{-cl}_X(F, \mathbb{E})) \doteq s\text{-cl}_X(F, \mathbb{E})$.

Proposition 5.7. (Shabir and Naz, 2011) *Let $(X, \mathcal{T}, \mathbb{E})$ be a soft topological space and $(F, \mathbb{E}), (G, \mathbb{E}) \in \mathcal{SS}(X)_\mathbb{E}$ be two soft sets over a common universe X . Then the following hold:*

- (1) $(F, \mathbb{E}) \widetilde{\subseteq} (G, \mathbb{E})$ implies $s\text{-cl}_X(F, \mathbb{E}) \widetilde{\subseteq} s\text{-cl}_X(G, \mathbb{E})$.
- (2) $s\text{-cl}_X((F, \mathbb{E}) \tilde{\cup} (G, \mathbb{E})) \doteq s\text{-cl}_X(F, \mathbb{E}) \tilde{\cup} s\text{-cl}_X(G, \mathbb{E})$.
- (3) $s\text{-cl}_X((F, \mathbb{E}) \tilde{\cap} (G, \mathbb{E})) \widetilde{\subseteq} s\text{-cl}_X(F, \mathbb{E}) \tilde{\cap} s\text{-cl}_X(G, \mathbb{E})$.

Definition 5.31. (Xie, 2015) Let $(X, \mathcal{T}, \mathbb{E})$ be a soft topological space, $(F, \mathbb{E}) \in \mathcal{SS}(X)_\mathbb{E}$ and $(x_\alpha, \mathbb{E}) \in \mathcal{SP}(X)_\mathbb{E}$ be a soft set and a soft point over the common universe X with respect to the sets of parameters \mathbb{E} , respectively. We say that (x_α, \mathbb{E}) is a **soft adherent point** (sometimes also called **soft closure point**) of (F, \mathbb{E}) if it soft meets every soft neighbourhood of the soft point, that is if for every $(N, \mathbb{E}) \in \mathcal{N}_{(x_\alpha, \mathbb{E})}$, $(F, \mathbb{E}) \tilde{\cap} (N, \mathbb{E}) \not\widetilde{\subseteq} (\tilde{\emptyset}, \mathbb{E})$.

As in the classical topological space, it is possible to prove that the soft closure of a soft set coincides with the set of all its soft adherent points.

Proposition 5.8. (Xie, 2015) *Let $(X, \mathcal{T}, \mathbb{E})$ be a soft topological space, $(F, \mathbb{E}) \in \mathcal{SS}(X)_\mathbb{E}$ and $(x_\alpha, \mathbb{E}) \in \mathcal{SP}(X)_\mathbb{E}$ be a soft set and a soft point over the common universe X with respect to the sets of parameters \mathbb{E} , respectively. Then $(x_\alpha, \mathbb{E}) \tilde{\in} s\text{-cl}_X(F, \mathbb{E})$ if and only if (x_α, \mathbb{E}) is a soft adherent point of (F, \mathbb{E}) .*

Having in mind the Definition 5.18 we can recall the following proposition.

Proposition 5.9. (Hussain and Ahmad, 2011) *Let $(X, \mathcal{T}, \mathbb{E})$ be a soft topological space over X , and Y be a nonempty subset of X , then the family \mathcal{T}_Y of all sub soft sets of \mathcal{T} over Y , i.e.*

$$\mathcal{T}_Y = \{({}^Y F, \mathbb{E}) : (F, \mathbb{E}) \in \mathcal{T}\}$$

is a soft topology on Y .

Definition 5.32. (Hussain and Ahmad, 2011) *Let $(X, \mathcal{T}, \mathbb{E})$ be a soft topological space over X , and let Y be a nonempty subset of X , the soft topology $\mathcal{T}_Y = \{({}^Y F, \mathbb{E}) : (F, \mathbb{E}) \in \mathcal{T}\}$ is said to be the **soft relative topology** of \mathcal{T} on Y and $(Y, \mathcal{T}_Y, \mathbb{E})$ is called the **soft topological subspace** of $(X, \mathcal{T}, \mathbb{E})$ on Y .*

Definition 5.33. (Zorlutuna et al, 2012) *Let $\varphi_\psi : \mathbb{S}\mathbb{S}(X)_{\mathbb{E}} \rightarrow \mathbb{S}\mathbb{S}(X')_{\mathbb{E}'}$, be a soft mapping between two soft topological spaces $(X, \mathcal{T}, \mathbb{E})$ and $(X', \mathcal{T}', \mathbb{E}')$ induced by the mappings $\varphi : X \rightarrow X'$ and $\psi : \mathbb{E} \rightarrow \mathbb{E}'$ and $(x_\alpha, \mathbb{E}) \in \mathbb{S}\mathcal{P}(X)_{\mathbb{E}}$ be a soft point over X . We say that the soft mapping φ_ψ is **soft continuous at the soft point** (x_α, \mathbb{E}) if for each soft neighbourhood (G, \mathbb{E}') of $\varphi_\psi(x_\alpha, \mathbb{E})$ in $(X', \mathcal{T}', \mathbb{E}')$ there exists some soft neighbourhood (F, \mathbb{E}) of (x_α, \mathbb{E}) in $(X, \mathcal{T}, \mathbb{E})$ such that $\varphi_\psi(F, \mathbb{E}) \subseteq (G, \mathbb{E}')$. If φ_ψ is soft continuous at every soft point $(x_\alpha, \mathbb{E}) \in \mathbb{S}\mathcal{P}(X)_{\mathbb{E}}$, then $\varphi_\psi : \mathbb{S}\mathbb{S}(X)_{\mathbb{E}} \rightarrow \mathbb{S}\mathbb{S}(X')_{\mathbb{E}'}$ is called **soft continuous** on X .*

Proposition 5.10. (Zorlutuna et al, 2012) *Let $\varphi_\psi : \mathbb{S}\mathbb{S}(X)_{\mathbb{E}} \rightarrow \mathbb{S}\mathbb{S}(X')_{\mathbb{E}'}$, be a soft mapping between two soft topological spaces $(X, \mathcal{T}, \mathbb{E})$ and $(X', \mathcal{T}', \mathbb{E}')$ induced by the mappings $\varphi : X \rightarrow X'$ and $\psi : \mathbb{E} \rightarrow \mathbb{E}'$. Then the soft mapping φ_ψ is soft continuous if and only if every soft inverse image of a soft open set in X' is a soft open set in X , that is, if for each $(G, \mathbb{E}') \in \mathcal{T}'$ we have that $\varphi_\psi^{-1}(G, \mathbb{E}') \in \mathcal{T}$.*

Proposition 5.11. (Zorlutuna et al, 2012) *Let $\varphi_\psi : \mathbb{S}\mathbb{S}(X)_{\mathbb{E}} \rightarrow \mathbb{S}\mathbb{S}(X')_{\mathbb{E}'}$, be a soft mapping between two soft topological spaces $(X, \mathcal{T}, \mathbb{E})$ and $(X', \mathcal{T}', \mathbb{E}')$ induced by the mappings $\varphi : X \rightarrow X'$ and $\psi : \mathbb{E} \rightarrow \mathbb{E}'$. Then the soft mapping φ_ψ is soft continuous if and only if every soft inverse image of a soft closed set in X' is a soft closed set in X , that is, if for each $(C, \mathbb{E}') \in \sigma(X', \mathbb{E}')$ we have that $\varphi_\psi^{-1}(C, \mathbb{E}') \in \sigma(X, \mathbb{E})$.*

Definition 5.34. (Zorlutuna et al, 2012) *Let $\varphi_\psi : \mathbb{S}\mathbb{S}(X)_{\mathbb{E}} \rightarrow \mathbb{S}\mathbb{S}(X')_{\mathbb{E}'}$, be a soft mapping between two soft topological spaces $(X, \mathcal{T}, \mathbb{E})$ and $(X', \mathcal{T}', \mathbb{E}')$ induced by the mappings $\varphi : X \rightarrow X'$ and $\psi : \mathbb{E} \rightarrow \mathbb{E}'$, and let Y be a nonempty subset of X , the **restriction** of the soft mapping φ_ψ to Y , denoted by $\varphi_\psi|_Y$, is the soft mapping $(\varphi|_Y)_\psi : \mathbb{S}\mathbb{S}(Y)_{\mathbb{E}} \rightarrow \mathbb{S}\mathbb{S}(X')_{\mathbb{E}'}$ induced by the restriction $\varphi|_Y : Y \rightarrow X'$ of the mapping φ between the universe sets and by the same mapping $\psi : \mathbb{E} \rightarrow \mathbb{E}'$ between the parameter sets.*

Proposition 5.12. (Zorlutuna et al, 2012) *If $\varphi_\psi : \mathbb{S}\mathbb{S}(X)_{\mathbb{E}} \rightarrow \mathbb{S}\mathbb{S}(X')_{\mathbb{E}'}$ is a soft continuous mapping between two soft topological spaces $(X, \mathcal{T}, \mathbb{E})$ and $(X', \mathcal{T}', \mathbb{E}')$, then its restriction $\varphi_\psi|_Y : \mathbb{S}\mathbb{S}(Y)_{\mathbb{E}} \rightarrow \mathbb{S}\mathbb{S}(X')_{\mathbb{E}'}$ to a nonempty subset Y of X is soft continuous too.*

Proposition 5.13. *If $\varphi_\psi : \mathbb{S}\mathbb{S}(X)_{\mathbb{E}} \rightarrow \mathbb{S}\mathbb{S}(X')_{\mathbb{E}'}$ is a soft continuous mapping between two soft topological spaces $(X, \mathcal{T}, \mathbb{E})$ and $(X', \mathcal{T}', \mathbb{E}')$, then its corestriction $\varphi_\psi : \mathbb{S}\mathbb{S}(X)_{\mathbb{E}} \rightarrow \varphi_\psi(\mathbb{S}\mathbb{S}(X)_{\mathbb{E}})$ is soft continuous too.*

Proof. It easily follows from Definitions 5.20 and 5.21, and Proposition 5.10.

Definition 5.35. (Aygünoğlu and Aygün, 2012) Let $(X, \mathcal{T}, \mathbb{E})$ be a soft topological space over X and $\mathcal{S} \subseteq \mathcal{T}$ be a non-empty subset of soft open sets. We say that \mathcal{S} is a **soft open subbase** for $(X, \mathcal{T}, \mathbb{E})$ if the family of all finite soft intersections of members of \mathcal{S} forms a soft open base for $(X, \mathcal{T}, \mathbb{E})$.

Proposition 5.14. (Aygünoğlu and Aygün, 2012) *Let $\mathcal{S} \subseteq \mathbb{S}\mathbb{S}(X)_{\mathbb{E}}$ be a family of soft sets over X , containing both the null soft set $(\tilde{\emptyset}, \mathbb{E})$ and the absolute soft set (\tilde{X}, \mathbb{E}) . Then the family $\mathcal{T}(\mathcal{S})$ of all soft union of finite soft intersections of soft sets in \mathcal{S} is a soft topology having \mathcal{S} as soft open subbase.*

Definition 5.36. (Aygünoğlu and Aygün, 2012) Let $\mathcal{S} \subseteq \mathbb{S}\mathbb{S}(X)_{\mathbb{E}}$ be a family of soft sets over X respect to a set of parameters \mathbb{E} and such that $(\tilde{\emptyset}, \mathbb{E}), (\tilde{X}, \mathbb{E}) \in \mathcal{S}$, then the soft topology $\mathcal{T}(\mathcal{S})$ of the above Proposition 5.14 is called the **soft topology generated** by the soft open subbase \mathcal{S} over X and $(X, \mathcal{T}(\mathcal{S}), \mathbb{E})$ is said to be the **soft topological space generated by \mathcal{S}** over X .

Definition 5.37. (Aygünoğlu and Aygün, 2012) Let $\mathbb{S}\mathbb{S}(X)_{\mathbb{E}}$ be the set of all the soft sets over a universe set X with respect to a set of parameter \mathbb{E} and consider a family of soft topological spaces $\{(Y_i, \mathcal{T}_i, \mathbb{E}_i)\}_{i \in I}$ and a corresponding family $\{(\varphi_\psi)_i\}_{i \in I}$ of soft mappings $(\varphi_\psi)_i = (\varphi_i)_{\psi_i} : \mathbb{S}\mathbb{S}(X)_{\mathbb{E}} \rightarrow \mathbb{S}\mathbb{S}(Y_i)_{\mathbb{E}_i}$ induced by the mappings $\varphi_i : X \rightarrow Y_i$ and $\psi_i : \mathbb{E} \rightarrow \mathbb{E}_i$ (with $i \in I$). Then the soft topology $\mathcal{T}(\mathcal{S})$ generated by the soft open subbase $\mathcal{S} = \{(\varphi_\psi)_i^{-1}(G, \mathbb{E}_i) : (G, \mathbb{E}_i) \in \mathcal{T}_i, i \in I\}$ of all soft inverse images of soft open sets of \mathcal{T}_i under the soft mappings $(\varphi_\psi)_i$ is called the **initial soft topology** induced on X by the family of soft mappings $\{(\varphi_\psi)_i\}_{i \in I}$ and it is denoted by $\mathcal{T}_{ini}(X, \mathbb{E}, Y_i, \mathbb{E}_i, (\varphi_\psi)_i; i \in I)$.

Proposition 5.15. (Aygünoğlu and Aygün, 2012) *The initial soft topology $\mathcal{T}_{ini}(X, \mathbb{E}, Y_i, \mathbb{E}_i, (\varphi_\psi)_i; i \in I)$ induced on X by the family of soft mappings $\{(\varphi_\psi)_i\}_{i \in I}$ is the coarsest soft topology on $\mathbb{S}\mathbb{S}(X)_{\mathbb{E}}$ for which all the soft mappings $(\varphi_\psi)_i : \mathbb{S}\mathbb{S}(X)_{\mathbb{E}} \rightarrow \mathbb{S}\mathbb{S}(Y_i)_{\mathbb{E}_i}$ (with $i \in I$) are soft continuous.*

Definition 5.38. (Aygünoğlu and Aygün, 2012) Let $\{(X_i, \mathcal{T}_i, \mathbb{E}_i)\}_{i \in I}$ be a family of soft topological spaces over the universe sets X_i with respect to the sets of parameters \mathbb{E}_i , respectively. For every $i \in I$, the soft mapping

$(\pi_i)_{\rho_i} : \mathbb{S}\mathbb{S}(\prod_{i \in I} X_i)_{\prod_{i \in I} \mathbb{E}_i} \rightarrow \mathbb{S}\mathbb{S}(X_i)_{\mathbb{E}_i}$ induced by the canonical projections

$\pi_i : \prod_{i \in I} X_i \rightarrow X_i$ and $\rho_i : \prod_{i \in I} \mathbb{E}_i \rightarrow \mathbb{E}_i$ is said the **i -th soft projection mapping**

and, by setting $(\pi_\rho)_i = (\pi_i)_{\rho_i}$, it will be denoted by

$(\pi_\rho)_i : \mathbb{S}\mathbb{S}(\prod_{i \in I} X_i)_{\prod_{i \in I} \mathbb{E}_i} \rightarrow \mathbb{S}\mathbb{S}(X_i)_{\mathbb{E}_i}$.

Definition 5.39. (Aygünoğlu and Aygün, 2012) Let $\{(X_i, \mathcal{T}_i, \mathbb{E}_i)\}_{i \in I}$ be a family of soft topological spaces and let $\{(\pi_\rho)_i\}_{i \in I}$ be the corresponding family of soft projection mappings $(\pi_\rho)_i : \mathbb{S}\mathbb{S}(\prod_{i \in I} X_i)_{\prod_{i \in I} \mathbb{E}_i} \rightarrow \mathbb{S}\mathbb{S}(X_i)_{\mathbb{E}_i}$ (with $i \in I$). Then, the

initial soft topology $\mathcal{T}_{ini}(\prod_{i \in I} X_i, \mathbb{E}, X_i, \mathbb{E}_i, (\pi_\rho)_i; i \in I)$ induced on $\prod_{i \in I} X_i$ by the family of soft projection mappings $\{(\pi_\rho)_i\}_{i \in I}$ is called the **soft product topology** of the soft topologies \mathcal{T}_i (with $i \in I$) and denoted by $\mathcal{T}(\prod_{i \in I} X_i)$.

The triplet $(\prod_{i \in I} X_i, \mathcal{T}(\prod_{i \in I} X_i), \prod_{i \in I} \mathbb{E}_i)$ will be said the **soft topological product space** of the soft topological spaces $(X_i, \mathcal{T}_i, \mathbb{E}_i)$.

The following statement easily derives from Definition 5.39 and Proposition 5.15.

Corollary 5.4. *The soft product topology $\mathcal{T}(\prod_{i \in I} X_i)$ is the coarsest soft topology over $\mathcal{SS}(\prod_{i \in I} X_i)_{\prod_{i \in I} \mathbb{E}_i}$ for which all the soft projection mappings $(\pi_\rho)_i : \mathcal{SS}(\prod_{i \in I} X_i)_{\prod_{i \in I} \mathbb{E}_i} \rightarrow \mathcal{SS}(X_i)_{\mathbb{E}_i}$ (with $i \in I$) are soft continuous.*

Proposition 5.16. (Aygünoğlu and Aygün, 2012) *Let $\{(X_i, \mathcal{T}_i, \mathbb{E}_i)\}_{i \in I}$ be a family of soft topological spaces, $(X, \mathcal{T}(X), \mathbb{E})$ be the soft topological product of such soft spaces induced on the product $X = \prod_{i \in I} X_i$ of universe sets with respect to the product $\mathbb{E} = \prod_{i \in I} \mathbb{E}_i$ of the sets of parameters, $(Y, \mathcal{T}', \mathbb{E}')$ be a soft topological space and $\varphi_\psi : \mathcal{SS}(Y)_{\mathbb{E}'} \rightarrow \mathcal{SS}(X)_{\mathbb{E}}$ be a soft mapping induced by the mappings $\varphi : Y \rightarrow X$ and $\psi : \mathbb{E}' \rightarrow \mathbb{E}$. Then the soft mappings φ_ψ is soft continuous if and only if, for every $i \in I$, the soft compositions $(\pi_\rho)_i \tilde{\circ} \varphi_\psi$ with the soft projection mappings $(\pi_\rho)_i : \mathcal{SS}(X)_{\mathbb{E}} \rightarrow \mathcal{SS}(X_i)_{\mathbb{E}_i}$ are soft continuous mappings.*

Let us note that the soft cartesian product $\tilde{\prod}_{i \in I} (F_i, \mathbb{E}_i)$ of a family $\{(F_i, \mathbb{E}_i)\}_{i \in I}$ of soft sets over a set X_i with respect to a set of parameters \mathbb{E}_i , respectively, as introduced in Definition 5.19, is a soft set of the soft topological product space $(\prod_{i \in I} X_i, \mathcal{T}(\prod_{i \in I} X_i), \prod_{i \in I} \mathbb{E}_i)$ i.e. that $\tilde{\prod}_{i \in I} (F_i, \mathbb{E}_i) \in \mathcal{SS}(\prod_{i \in I} X_i)_{\prod_{i \in I} \mathbb{E}_i}$ and the following statement holds.

Proposition 5.17. (Nordo, 2019b) *Let $(\prod_{i \in I} X_i, \mathcal{T}(\prod_{i \in I} X_i), \prod_{i \in I} \mathbb{E}_i)$ be the soft topological product space of a family $\{(X_i, \mathcal{T}_i, \mathbb{E}_i)\}_{i \in I}$ of soft topological spaces and let $\tilde{\prod}_{i \in I} (F_i, \mathbb{E}_i)$ be the soft product in $\mathcal{SS}(\prod_{i \in I} X_i)_{\prod_{i \in I} \mathbb{E}_i}$ of a family $\{(F_i, \mathbb{E}_i)\}_{i \in I}$ of soft sets of $\mathcal{SS}(X_i)_{\mathbb{E}_i}$, for every $i \in I$. Then the soft closure of $\tilde{\prod}_{i \in I} (F_i, \mathbb{E}_i)$ in the soft topological product $(\prod_{i \in I} X_i, \mathcal{T}(\prod_{i \in I} X_i), \prod_{i \in I} \mathbb{E}_i)$ coincides with the soft product of the corresponding soft closures of the soft sets (F_i, \mathbb{E}_i) in the corresponding soft topological spaces $(X_i, \mathcal{T}_i, \mathbb{E}_i)$, that is:*

$$\text{s-cl}_{\prod_{i \in I} X_i} \left(\tilde{\prod}_{i \in I} (F_i, \mathbb{E}_i) \right) \cong \tilde{\prod}_{i \in I} \text{s-cl}_{X_i} (F_i, \mathbb{E}_i).$$

5.3 Soft Embedding Theorem

Definition 5.40. (Aras et al, 2013) Let $(X, \mathcal{T}, \mathbb{E})$ and $(X', \mathcal{T}', \mathbb{E}')$ be two soft topological spaces over the universe sets X and X' with respect to the sets of parameters \mathbb{E} and \mathbb{E}' , respectively. We say that a soft mapping $\varphi_\psi : \mathcal{SS}(X)_{\mathbb{E}} \rightarrow \mathcal{SS}(X')_{\mathbb{E}'}$ is a

soft homeomorphism if it is soft continuous, bijective and its soft inverse mapping $\varphi_\psi^{-1} : \mathbb{S}\mathbb{S}(X')_{\mathbb{E}'} \rightarrow \mathbb{S}\mathbb{S}(X)_{\mathbb{E}}$ is soft continuous too. In such a case, the soft topological spaces $(X, \mathcal{T}, \mathbb{E})$ and $(X', \mathcal{T}', \mathbb{E}')$ are said **soft homeomorphic** and we write that $(X, \mathcal{T}, \mathbb{E}) \approx (X', \mathcal{T}', \mathbb{E}')$.

Definition 5.41. Let $(X, \mathcal{T}, \mathbb{E})$ and $(X', \mathcal{T}', \mathbb{E}')$ be two soft topological spaces. We say that a soft mapping $\varphi_\psi : \mathbb{S}\mathbb{S}(X)_{\mathbb{E}} \rightarrow \mathbb{S}\mathbb{S}(X')_{\mathbb{E}'}$ is a **soft embedding** if its corestriction $\varphi_\psi : \mathbb{S}\mathbb{S}(X)_{\mathbb{E}} \rightarrow \varphi_\psi(\mathbb{S}\mathbb{S}(X)_{\mathbb{E}})$ is a soft homeomorphism.

Definition 5.42. (Aras et al, 2013) Let $(X, \mathcal{T}, \mathbb{E})$ and $(X', \mathcal{T}', \mathbb{E}')$ be two soft topological spaces. We say that a soft mapping $\varphi_\psi : \mathbb{S}\mathbb{S}(X)_{\mathbb{E}} \rightarrow \mathbb{S}\mathbb{S}(X')_{\mathbb{E}'}$ is a **soft closed mapping** if the soft image of every soft closed set of $(X, \mathcal{T}, \mathbb{E})$ is a soft closed set of $(X', \mathcal{T}', \mathbb{E}')$, that is if for any $(C, \mathbb{E}) \in \sigma(X, \mathbb{E})$, we have $\varphi_\psi(C, \mathbb{E}) \in \sigma(X', \mathbb{E}')$.

Proposition 5.18. Let $\varphi_\psi : \mathbb{S}\mathbb{S}(X)_{\mathbb{E}} \rightarrow \mathbb{S}\mathbb{S}(X')_{\mathbb{E}'}$ be a soft mapping between two soft topological spaces $(X, \mathcal{T}, \mathbb{E})$ and $(X', \mathcal{T}', \mathbb{E}')$. If φ_ψ is a soft continuous, injective and soft closed mapping then it is a soft embedding.

Proof. If we consider the soft mapping $\varphi_\psi : \mathbb{S}\mathbb{S}(X)_{\mathbb{E}} \rightarrow \varphi_\psi(\mathbb{S}\mathbb{S}(X)_{\mathbb{E}})$, by hypothesis and Proposition 5.13, it immediately follows that it is a soft continuous bijective mapping and so we have only to prove that its soft inverse mapping $\varphi_\psi^{-1} = (\varphi_\psi^{-1})_{\psi^{-1}} : \varphi_\psi(\mathbb{S}\mathbb{S}(X)_{\mathbb{E}}) \rightarrow \mathbb{S}\mathbb{S}(X)_{\mathbb{E}}$ is continuous too. In fact, because the bijectiveness of the corestriction and Remark 5.3, for every soft closed set $(C, \mathbb{E}) \in \sigma(X, \mathbb{E})$, the soft inverse image of the (C, \mathbb{E}) under the soft inverse mapping φ_ψ^{-1} coincides with the soft image of the same soft set under the soft mapping φ_ψ , that is $(\varphi_\psi^{-1})^{-1}(C, \mathbb{E}) \cong \varphi_\psi(C, \mathbb{E})$ and since by hypothesis φ_ψ is soft closed, it follows that $(\varphi_\psi^{-1})^{-1}(C, \mathbb{E}) \in \sigma(X', \mathbb{E}')$ which, by Proposition 5.11, proves that $\varphi_\psi^{-1} : \mathbb{S}\mathbb{S}(X')_{\mathbb{E}'} \rightarrow \mathbb{S}\mathbb{S}(X)_{\mathbb{E}}$ is a soft continuous mapping, and so, by Proposition 5.12, we finally have that $\varphi_\psi^{-1} : \varphi_\psi(\mathbb{S}\mathbb{S}(X)_{\mathbb{E}}) \rightarrow \mathbb{S}\mathbb{S}(X)_{\mathbb{E}}$ is a soft continuous mapping.

Definition 5.43. Let $(X, \mathcal{T}, \mathbb{E})$ be a soft topological space over a universe set X with respect to a set of parameter \mathbb{E} , let $\{(X_i, \mathcal{T}_i, \mathbb{E}_i)\}_{i \in I}$ be a family of soft topological spaces over a universe set X_i with respect to a set of parameters \mathbb{E}_i , respectively and consider a family $\{(\varphi_\psi)_i\}_{i \in I}$ of soft mappings $(\varphi_\psi)_i = (\varphi_i)_{\psi_i} : \mathbb{S}\mathbb{S}(X)_{\mathbb{E}} \rightarrow \mathbb{S}\mathbb{S}(X_i)_{\mathbb{E}_i}$ induced by the mappings $\varphi_i : X \rightarrow X_i$ and $\psi_i : \mathbb{E} \rightarrow \mathbb{E}_i$ (with $i \in I$). Then the soft mapping $\Delta = \varphi_\psi : \mathbb{S}\mathbb{S}(X)_{\mathbb{E}} \rightarrow \mathbb{S}\mathbb{S}(\prod_{i \in I} X_i)_{\prod_{i \in I} \mathbb{E}_i}$ induced by the diagonal mappings (in the classical meaning) $\varphi = \Delta_{i \in I} \varphi_i : X \rightarrow \prod_{i \in I} X_i$ on the universes sets and $\psi = \Delta_{i \in I} \psi_i : \mathbb{E} \rightarrow \prod_{i \in I} \mathbb{E}_i$ on the sets of parameters (respectively defined by $\varphi(x) = \langle \varphi_i(x) \rangle_{i \in I}$ for every $x \in X$ and by $\psi(e) = \langle \psi_i(e) \rangle_{i \in I}$ for every $e \in \mathbb{E}$) is called the **soft diagonal mapping** of the soft mappings $(\varphi_\psi)_i$ (with $i \in I$) and it is denoted by $\Delta = \Delta_{i \in I} (\varphi_\psi)_i : \mathbb{S}\mathbb{S}(X)_{\mathbb{E}} \rightarrow \mathbb{S}\mathbb{S}(\prod_{i \in I} X_i)_{\prod_{i \in I} \mathbb{E}_i}$.

The following proposition establishes a useful relation about the soft image of a soft diagonal mapping.

Proposition 5.19. (Nordo, 2019b) *Let $(X, \mathcal{T}, \mathbb{E})$ be a soft topological space over a universe set X with respect to a set of parameter \mathbb{E} , let $(F, \mathbb{E}) \in \mathcal{SS}(X)_{\mathbb{E}}$ be a soft set of X , let $\{(X_i, \mathcal{T}_i, \mathbb{E}_i)\}_{i \in I}$ be a family of soft topological spaces over a universe set X_i with respect to a set of parameters \mathbb{E}_i , respectively and let $\Delta = \Delta_{i \in I}(\varphi_{\psi})_i : \mathcal{SS}(X)_{\mathbb{E}} \rightarrow \mathcal{SS}(\prod_{i \in I} X_i)_{\prod_{i \in I} \mathbb{E}_i}$ be the soft diagonal mapping of the soft mappings $(\varphi_{\psi})_i$, with $i \in I$. Then the soft image of the soft set (F, \mathbb{E}) under the soft diagonal mapping Δ is soft contained in the soft product of the soft images of the same soft set under the soft mappings $(\varphi_{\psi})_i$, that is*

$$\Delta(F, \mathbb{E}) \tilde{\subseteq} \widetilde{\prod}_{i \in I} (\varphi_{\psi})_i(F, \mathbb{E}).$$

Proof. Set $\varphi = \Delta_{i \in I} \varphi_i : X \rightarrow \prod_{i \in I} X_i$ and $\psi = \Delta_{i \in I} \psi_i : \mathbb{E} \rightarrow \prod_{i \in I} \mathbb{E}_i$, by Definition 5.43, we know that $\Delta = \Delta_{i \in I} (\varphi_{\psi})_i = \varphi_{\psi}$. Suppose, by contradiction, that there exists some soft point $(x_{\alpha}, \mathbb{E}) \tilde{\in} (F, \mathbb{E})$ such that

$$\Delta(x_{\alpha}, \mathbb{E}) \tilde{\notin} \widetilde{\prod}_{i \in I} (\varphi_{\psi})_i(F, \mathbb{E}).$$

Set $(y_{\beta}, \prod_{i \in I} \mathbb{E}_i) \tilde{=} \Delta(x_{\alpha}, \mathbb{E}) \tilde{=} \varphi_{\psi}(x_{\alpha}, \mathbb{E})$, by Proposition 5.4, it follows that

$$\left(y_{\beta}, \prod_{i \in I} \mathbb{E}_i \right) \tilde{=} \left(\varphi(x)_{\psi(\alpha)}, \prod_{i \in I} \mathbb{E}_i \right)$$

where

$$y = \langle y_i \rangle_{i \in I} = \varphi(x) = (\Delta_{i \in I} \varphi_i)(x) = \langle \varphi_i(x) \rangle_{i \in I}$$

and

$$\beta = \langle \beta_i \rangle_{i \in I} = \psi(\alpha) = (\Delta_{i \in I} \psi_i)(\alpha) = \langle \psi_i(\alpha) \rangle_{i \in I}.$$

So, set $(G_i, \mathbb{E}_i) \tilde{=} (\varphi_{\psi})_i(F, \mathbb{E})$ for every $i \in I$, we have that

$$\left(y_{\beta}, \prod_{i \in I} \mathbb{E}_i \right) \tilde{\notin} \widetilde{\prod}_{i \in I} (G_i, \mathbb{E}_i)$$

hence, by Proposition 5.2, it follows that there exists some $j \in I$ such that

$$((y_j)_{\beta_j}, \mathbb{E}_j) \tilde{\notin} (G_j, \mathbb{E}_j)$$

that, by Definition 5.15, means

$$y_j \notin G_j(\beta_j)$$

i.e.

$$\varphi_j(x) \notin G_j(\psi_j(\alpha))$$

and so, by using again Definition 5.15, we have

$$\left(\varphi_j(x)_{\psi_j(\alpha), \mathbb{E}_j} \right) \not\tilde{\in} (G_j, \mathbb{E}_j)$$

that, by Proposition 5.4, is equivalent to

$$(\varphi_\psi)_j(x_\alpha, \mathbb{E}) \not\tilde{\in} (G_j, \mathbb{E}_j)$$

which is a contradiction because we know that $(x_\alpha, \mathbb{E}) \tilde{\in} (F, \mathbb{E})$ and by Corollary 5.3(1) it follows $(\varphi_\psi)_j(x_\alpha, \mathbb{E}) \tilde{\in} (\varphi_\psi)_j(F, \mathbb{E}) \tilde{=} (G_j, \mathbb{E}_j)$.

Definition 5.44. Let $\{(\varphi_\psi)_i\}_{i \in I}$ be a family of soft mappings $(\varphi_\psi)_i : \mathbb{S}\mathbb{S}(X)_{\mathbb{E}} \rightarrow \mathbb{S}\mathbb{S}(X_i)_{\mathbb{E}_i}$ between a soft topological space $(X, \mathcal{T}, \mathbb{E})$ and the members of a family of soft topological spaces $\{(X_i, \mathcal{T}_i, \mathbb{E}_i)\}_{i \in I}$. We say that the family $\{(\varphi_\psi)_i\}_{i \in I}$ **soft separates soft points** of $(X, \mathcal{T}, \mathbb{E})$ if for every $(x_\alpha, \mathbb{E}), (y_\beta, \mathbb{E}) \in \mathcal{S}\mathcal{P}(X)_{\mathbb{E}}$ such that $(x_\alpha, \mathbb{E}) \not\tilde{=} (y_\alpha, \mathbb{E})$ there exists some $j \in I$ such that $(\varphi_\psi)_j(x_\alpha, \mathbb{E}) \not\tilde{=} (\varphi_\psi)_j(y_\beta, \mathbb{E})$.

Definition 5.45. Let $\{(\varphi_\psi)_i\}_{i \in I}$ be a family of soft mappings $(\varphi_\psi)_i : \mathbb{S}\mathbb{S}(X)_{\mathbb{E}} \rightarrow \mathbb{S}\mathbb{S}(X_i)_{\mathbb{E}_i}$ between a soft topological space $(X, \mathcal{T}, \mathbb{E})$ and the members of a family of soft topological spaces $\{(X_i, \mathcal{T}_i, \mathbb{E}_i)\}_{i \in I}$. We say that the family $\{(\varphi_\psi)_i\}_{i \in I}$ **soft separates soft points from soft closed sets** of $(X, \mathcal{T}, \mathbb{E})$ if for every $(C, \mathbb{E}) \in \sigma(X, \mathbb{E})$ and every $(x_\alpha, \mathbb{E}) \in \mathcal{S}\mathcal{P}(X)_{\mathbb{E}}$ such that $(x_\alpha, \mathbb{E}) \tilde{\in} (\tilde{X}, \mathbb{E}) \tilde{\cap} (C, \mathbb{E})$ there exists some $j \in I$ such that $(\varphi_\psi)_j(x_\alpha, \mathbb{E}) \not\tilde{\in} \text{s-cl}_{X_j}((\varphi_\psi)_j(C, \mathbb{E}))$.

Proposition 5.20 (Soft Embedding Theorem). *Let $(X, \mathcal{T}, \mathbb{E})$ be a soft topological space, $\{(X_i, \mathcal{T}_i, \mathbb{E}_i)\}_{i \in I}$ be a family of soft topological spaces and $\{(\varphi_\psi)_i\}_{i \in I}$ be a family of soft continuous mappings $(\varphi_\psi)_i : \mathbb{S}\mathbb{S}(X)_{\mathbb{E}} \rightarrow \mathbb{S}\mathbb{S}(X_i)_{\mathbb{E}_i}$ that separates both the soft points and the soft points from the soft closed sets of $(X, \mathcal{T}, \mathbb{E})$. Then the soft diagonal mapping $\Delta = \Delta_{i \in I}(\varphi_\psi)_i : \mathbb{S}\mathbb{S}(X)_{\mathbb{E}} \rightarrow \mathbb{S}\mathbb{S}(\prod_{i \in I} X_i)_{\prod_{i \in I} \mathbb{E}_i}$ of the soft mappings $(\varphi_\psi)_i$ is a soft embedding.*

Proof. Let $\varphi = \Delta_{i \in I} \varphi_i$, $\psi = \Delta_{i \in I} \psi_i$ and $\Delta = \Delta_{i \in I} (\varphi_\psi)_i = \varphi_\psi$ as in Definition 5.43, for every $i \in I$, by using Definition 5.23, we have that every corresponding soft composition is given by

$$(\pi_\rho)_i \tilde{\circ} \Delta = ((\pi_i)_{\rho_i}) \tilde{\circ} \varphi_\psi = (\pi_i \circ \varphi)_{\rho_i \circ \psi} = (\varphi_i)_{\psi_i} = (\varphi_\psi)_i$$

which, by hypothesis, is a soft continuous mapping. Hence, by Proposition 5.16, it follows that the soft diagonal mapping $\Delta : \mathbb{S}\mathbb{S}(X)_{\mathbb{E}} \rightarrow \mathbb{S}\mathbb{S}(\prod_{i \in I} X_i)_{\prod_{i \in I} \mathbb{E}_i}$ is a soft continuous mapping.

Now, let (x_α, \mathbb{E}) and (y_β, \mathbb{E}) be two distinct soft points of $\mathcal{S}\mathcal{P}(X)_{\mathbb{E}}$. Since, by hypothesis, the family $\{(\varphi_\psi)_i\}_{i \in I}$ of soft mappings soft separates soft points, by Definition 5.44, we have that there exists some $j \in I$ such that

$$(\varphi_\psi)_j(x_\alpha, \mathbb{E}) \not\tilde{=} (\varphi_\psi)_j(y_\beta, \mathbb{E})$$

that is

$$(\varphi_j)_{\psi_j}(x_\alpha, \mathbb{E}) \not\approx (\varphi_j)_{\psi_j}(y_\beta, \mathbb{E}).$$

Hence, by Proposition 5.4, we have that:

$$\left((\varphi_j(x)_{\psi_i(\alpha)}, \mathbb{E}_j) \right) \not\approx \left((\varphi_j(y)_{\psi_i(\beta)}, \mathbb{E}_j) \right)$$

and so, by the Definition 5.17 of distinct soft points, it necessarily follows that:

$$\varphi_j(x) \neq \varphi_j(y) \quad \text{or} \quad \psi_j(\alpha) \neq \psi_j(\beta).$$

Since $\varphi = \Delta_{i \in I} \varphi_i : X \rightarrow \prod_{i \in I} X_i$ and $\psi = \Delta_{i \in I} \psi_i : \mathbb{E} \rightarrow \prod_{i \in I} \mathbb{E}_i$ are usual diagonal mappings, we have that:

$$\varphi(x) \neq \varphi(y) \quad \text{or} \quad \psi(\alpha) \neq \psi(\beta)$$

and, by Definition 5.17, it follows that:

$$\left(\varphi(x)_{\psi(\alpha)}, \prod_{i \in I} \mathbb{E}_i \right) \not\approx \left(\varphi(y)_{\psi(\beta)}, \prod_{i \in I} \mathbb{E}_i \right)$$

hence, applying again Proposition 5.4, we get:

$$\varphi_\psi(x_\alpha, \mathbb{E}) \not\approx \varphi_\psi(y_\beta, \mathbb{E})$$

that is:

$$\Delta_{i \in I} (\varphi_\psi)_i(x_\alpha, \mathbb{E}) \not\approx \Delta_{i \in I} (\varphi_\psi)_i(y_\beta, \mathbb{E})$$

i.e. that $\Delta(x_\alpha, \mathbb{E}) \not\approx \Delta(y_\beta, \mathbb{E})$ which, by Corollary 5.2, proves the injectivity of the soft diagonal mapping $\Delta : \mathcal{SS}(X)_{\mathbb{E}} \rightarrow \mathcal{SS}(\prod_{i \in I} X_i)_{\prod_{i \in I} \mathbb{E}_i}$.

Finally, let $(C, \mathbb{E}) \in \sigma(X, \mathbb{E})$ be a soft closed set in X and, in order to prove that the soft image $\Delta(C, \mathbb{E})$ is a soft closed set of $\sigma(\prod_{i \in I} X_i, \prod_{i \in I} \mathbb{E}_i)$, consider a soft point $(x_\alpha, \mathbb{E}) \in \mathcal{SP}(X)_{\mathbb{E}}$ such that $\Delta(x_\alpha, \mathbb{E}) \not\in \Delta(C, \mathbb{E})$ and, hence, by Corollary 5.3(1), such that $(x_\alpha, \mathbb{E}) \not\in (C, \mathbb{E})$. Since, by hypothesis, the family $\{(\varphi_\psi)_i\}_{i \in I}$ of soft mappings soft separates soft points from soft closed sets, by Definition 5.45, we have that there exists some $j \in I$ such that

$$(\varphi_\psi)_j(x_\alpha, \mathbb{E}) \not\in \text{s-cl}_{X_j}((\varphi_\psi)_j(C, \mathbb{E}))$$

that is:

$$(\varphi_j)_{\psi_j}(x_\alpha, \mathbb{E}) \not\in \text{s-cl}_{X_j}((\varphi_\psi)_j(C, \mathbb{E}))$$

that, by Proposition 5.4, corresponds to:

$$\left(\varphi_j(x)_{\psi_j(\alpha)}, \mathbb{E}_j \right) \not\in \text{s-cl}_{X_j}((\varphi_\psi)_j(C, \mathbb{E})) .$$

So, set $(C_i, \mathbb{E}_i) \cong \text{s-cl}_{X_i}((\varphi\psi)_i(C, \mathbb{E}))$ for every $i \in I$, we have in particular for $i = j$ that

$$\left(\varphi_j(x)_{\psi_j(\alpha)}, \mathbb{E}_j \right) \not\cong (C_j, \mathbb{E}_j)$$

which, by Definition 5.15, is equivalent to say that:

$$\varphi_j(x) \notin C_j(\psi_j(\alpha))$$

and since the diagonal mapping $\varphi = \Delta_{i \in I} \varphi_i : X \rightarrow \prod_{i \in I} X_i$ on the universes sets is defined by $\varphi(x) = \langle \varphi_i(x) \rangle_{i \in I}$, it follows that:

$$\varphi(x) \notin \prod_{i \in I} C_i(\psi_i(\alpha)).$$

Now, since the diagonal mapping $\psi = \Delta_{i \in I} \psi_i : X \rightarrow \prod_{i \in I} X_i$ on the sets of parameters is defined by $\psi(\alpha) = \Delta_{i \in I} \psi_i(\alpha) = \langle \psi_i(\alpha) \rangle_{i \in I}$, using Definition 5.19, we obtain:

$$\prod_{i \in I} C_i(\psi_i(\alpha)) = \left(\prod_{i \in I} C_i \right) (\psi(\alpha))$$

and hence that

$$\varphi(x) \notin \left(\prod_{i \in I} C_i \right) (\psi(\alpha))$$

which, by Definitions 5.15 and 5.19, is equivalent to say that:

$$\left(\varphi(x)_{\psi(\alpha)}, \prod_{i \in I} \mathbb{E}_i \right) \not\cong \widetilde{\prod}_{i \in I} (C_i, \mathbb{E}_i)$$

that, by Proposition 5.4, means:

$$\varphi_\psi(x_\alpha, \mathbb{E}) \not\cong \widetilde{\prod}_{i \in I} (C_i, \mathbb{E}_i)$$

i.e.

$$\Delta(x_\alpha, \mathbb{E}) \not\cong \widetilde{\prod}_{i \in I} \text{s-cl}_{X_i}((\varphi\psi)_i(C, \mathbb{E})).$$

So, recalling, by Proposition 5.17, that

$$\text{s-cl}_{\prod_{i \in I} X_i} \left(\widetilde{\prod}_{i \in I} (\varphi\psi)_i(C, \mathbb{E}) \right) \cong \widetilde{\prod}_{i \in I} \text{s-cl}_{X_i}((\varphi\psi)_i(C, \mathbb{E}))$$

it follows that:

$$\Delta(x_\alpha, \mathbb{E}) \not\cong \text{s-cl}_{\prod_{i \in I} X_i} \left(\widetilde{\prod}_{i \in I} (\varphi\psi)_i(C, \mathbb{E}) \right).$$

Since, by Propositions 5.19 and 5.6(3) we have

$$\Delta(C, \mathbb{E}) \subseteq \widetilde{\prod}_{i \in I} (\varphi_\psi)_i(C, \mathbb{E}) \subseteq \text{s-cl}_{\prod_{i \in I} X_i} \left(\widetilde{\prod}_{i \in I} (\varphi_\psi)_i(C, \mathbb{E}) \right)$$

and, by applying Propositions 5.7(1) and 5.6(5), we obtain

$$\text{s-cl}_{\prod_{i \in I} X_i} (\Delta(C, \mathbb{E})) \subseteq \text{s-cl}_{\prod_{i \in I} X_i} \left(\widetilde{\prod}_{i \in I} (\varphi_\psi)_i(C, \mathbb{E}) \right)$$

it follows, a fortiori, that

$$\Delta(x_\alpha, \mathbb{E}) \not\subseteq \text{s-cl}_{\prod_{i \in I} X_i} (\Delta(C, \mathbb{E})).$$

So, it is proved by contradiction that $\text{s-cl}_{\prod_{i \in I} X_i} (\Delta(C, \mathbb{E})) \subseteq \Delta(C, \mathbb{E})$ and hence, by Proposition 5.6(4) and Definition 5.42, that $\Delta : \mathbb{S}\mathbb{S}(X)_\mathbb{E} \rightarrow \mathbb{S}\mathbb{S}(\prod_{i \in I} X_i)_{\prod_{i \in I} \mathbb{E}_i}$ is a soft closed mapping.

Thus, we finally have that the soft diagonal mapping $\Delta = \Delta_{i \in I} (\varphi_\psi)_i : \mathbb{S}\mathbb{S}(X)_\mathbb{E} \rightarrow \mathbb{S}\mathbb{S}(\prod_{i \in I} X_i)_{\prod_{i \in I} \mathbb{E}_i}$ is a soft continuous, injective and soft closed mapping and so, by Proposition 5.18, it is a soft embedding.

5.4 Conclusion

In this paper we have introduced the notions of family of soft mappings separating points and points from closed sets and that of soft diagonal mapping and we have proved a generalization to soft topological spaces of the well-known Embedding Theorem for classical (crisp) topological spaces. Such a result could be the start point for extending and investigating other important topics such as extension and compactifications theorems, metrization theorems etc. in the context of soft topology.

Acknowledgements The author is grateful and thankful to the Editors and to the anonymous reviewers for their valuable suggestions and comments which were precious for the successful revision of the paper.

References

Abali BE, Müller WH, Eremeyev VA (2015) Strain gradient elasticity with geometric nonlinearities and its computational evaluation. *Mechanics of Advanced Materials and Modern Processes* 1(1):1–11

Ahmad B, Hussain S (2012) On some structures of soft topology. *Mathematical Sciences* 6(1):64

Ahmad B, Kharal A (2009) On fuzzy soft sets. *Advances in Fuzzy Systems* 2009:586,507–6

Al-Khafaj MAK, Mahmood MH (2014) Some properties of soft connected spaces and soft locally connected spaces. *IOSR Journal of Mathematics* 10(5):102–107

Al-Shami TM, El-Shafei ME, Abo-Elhamayel M (2018) Almost soft compact and approximately soft Lindelöf spaces. *Journal of Taibah University for Science* 12(5):620–630

- Ali MI, Feng F, Liu X, Min WK, Shabir M (2009) On some new operations in soft set theory. *Computers & Mathematics with Applications* 57(9):1547–1553
- Aras CG, Sonmez A, Çakallı H (2013) On soft mappings. *Proceedings of CMMSE 2013 - 13th International Conference on Computational and Mathematical Methods in Science and Engineering* p 11
- Aygünoğlu A, Aygün H (2012) Some notes on soft topological spaces. *Neural computing and Applications* 21(1):113–119
- Babitha KV, Sunil JJ (2010) Soft set relations and functions. *Computers & Mathematics with Applications* 60(7):1840–1849
- Barchiesi E, Spagnuolo M, Placidi L (2019) Mechanical metamaterials: a state of the art. *Mathematics and Mechanics of Solids* 24(1):212–234
- Bayramov S, Aras CG (2018) A new approach to separability and compactness in soft topological spaces. *TWMS J Pure Appl Math* 9(1):82–93
- Bdaiwi AJ (2017) Generalized soft filter and soft net. *International Journal of Innovative Science, Engineering & Technology* 4(3):195–200
- Çağman N (2014) Contributions to the theory of soft sets. *Journal of New Results in Science* 3(4):33–41
- Çağman N, Karataş S, Enginoglu S (2011) Soft topology. *Computers & Mathematics with Applications* 62(1):351–358
- Chen D, Tsang E, Yeung DS, Wang X (2005) The parameterization reduction of soft sets and its applications. *Computers & Mathematics with Applications* 49(5-6):757–763
- Chiney M, Samanta SK (2016) Soft topology redefined. *arXiv preprint arXiv:170100466* p 18
- Das S, Samanta S (2013a) On soft metric spaces. *J Fuzzy Math* 21(3):707–734
- Das S, Samanta SK (2013b) Soft metric. *Annals of Fuzzy Mathematics and Informatics* 6(1):77–94
- dell'Isola F, Vidoli S (1998) Damping of bending waves in truss beams by electrical transmission lines with PZT actuators. *Archive of Applied Mechanics* 68(9):626–636
- dell'Isola F, Seppecher P, et al (2019a) Advances in pantographic structures: design, manufacturing, models, experiments and image analyses. *Continuum Mechanics and Thermodynamics* 31(4):1231–1282
- dell'Isola F, Seppecher P, et al (2019b) Pantographic metamaterials: an example of mathematically driven design and of its technological challenges. *Continuum Mechanics and Thermodynamics* 31(4):851–884
- El-Shafei ME, Abo-Elhamayel M, Al-shami TM (2018) Partial soft separation axioms and soft compact spaces. *Filomat* 32(13):4755–4771
- Engelking R (1989) *General topology*. Berlin: Heldermann Verlag
- Feng F, Li Y (2013) Soft subsets and soft product operations. *Information Sciences* 232:44–57
- Fu L, Fu H, You F (2017) Soft topological product space. In: *2017 4th International Conference on Systems and Informatics (ICSAI)*, IEEE, pp 1610–1615
- Georgiou DN, Megaritis AC (2014) Soft set theory and topology. *Applied General Topology* 15(1):93–109
- Georgiou DN, Megaritis AC, Petropoulos VI (2013) On soft topological spaces. *Applied Mathematics & Information Sciences* 7(5):1889–1901
- Giorgio I, Del Vescovo D (2018) Non-linear lumped-parameter modeling of planar multi-link manipulators with highly flexible arms. *Robotics* 7(4):60
- Giorgio I, Del Vescovo D (2019) Energy-based trajectory tracking and vibration control for multilink highly flexible manipulators. *Mathematics and Mechanics of Complex Systems* 7(2):159–174
- Giorgio I, Culla A, Del Vescovo D (2009) Multimode vibration control using several piezoelectric transducers shunted with a multiterminal network. *Archive of Applied Mechanics* 79(9):859
- Giorgio I, dell'Isola F, Andreus U, Alzahrani F, Hayat T, Lekszycki T (2019) On mechanically driven biological stimulus for bone remodeling as a diffusive phenomenon. *Biomechanics and modeling in mechanobiology* 18(6):1639–1663
- Hazra H, Majumdar P, Samanta SK (2012) Soft topology. *Fuzzy information and Engineering* 4(1):105–115

- Hussain S (2015) A note on soft connectedness. *Journal of the Egyptian Mathematical Society* 23(1):6–11
- Hussain S, Ahmad B (2011) Some properties of soft topological spaces. *Computers & Mathematics with Applications* 62(11):4058–4067
- Hussain S, Ahmad B (2015) Soft separation axioms in soft topological spaces. *Hacettepe Journal of Mathematics and Statistics* 44(3):559–568
- Ibrahim AM, Yusuf AO (2012) Development of soft set theory. *American International Journal of Contemporary Research* 2(9):205–210
- Janaki C, Sredja D (2012) A new class of homeomorphisms in soft topological spaces. *International Journal of Science and Research* 3(6):810–814
- Kazancı O, Yılmaz S, Yamak S (2010) Soft sets and soft BCH-algebras. *Hacettepe Journal of Mathematics and Statistics* 39(2):205–217
- Kharal A, Ahmad B (2011) Mappings on soft classes. *New Mathematics and Natural Computation* 7(03):471–481
- Lekszycki T, dell'Isola F (2012) A mixture model with evolving mass densities for describing synthesis and resorption phenomena in bones reconstructed with bio-resorbable materials. *ZAMM-Zeitschrift für Angewandte Mathematik und Mechanik* 92(6):426–444
- Li F (2011) Notes on the soft operations. *ARNP Journal of Systems and software* 1(6):205–208
- Lossouarn B, Deü JF, Aucejo M (2015) Multimodal vibration damping of a beam with a periodic array of piezoelectric patches connected to a passive electrical network. *Smart Materials and Structures* 24(11):115,037
- Ma Zm, Yang W, Hu BQ (2010) Soft set theory based on its extension. *Fuzzy Information and Engineering* 2(4):423–432
- Maji P, Roy AR, Biswas R (2002) An application of soft sets in a decision making problem. *Computers & Mathematics with Applications* 44(8-9):1077–1083
- Maji PK, Biswas R, Roy AR (2003) Soft set theory. *Computers & Mathematics with Applications* 45(4-5):555–562
- Matejdes M (2016) Soft topological space and topology on the cartesian product. *Hacettepe Journal of Mathematics and Statistics* 45(4):1091–1100
- Min WK (2011) A note on soft topological spaces. *Computers & Mathematics with Applications* 62(9):3524–3528
- Molodtsov D (1999) Soft set theory—first results. *Computers & Mathematics with Applications* 37(4-5):19–31
- Nazmul S, Samanta SK (2013) Neighbourhood properties of soft topological spaces. *Ann Fuzzy Math Inform* 6(1):1–15
- Nazmul S, Samanta SK (2014) Some properties of soft topologies and group soft topologies. *Ann Fuzzy Math Inform* 8(4):645–661
- Neog TJ, Sut DK (2011) A new approach to the theory of soft sets. *International Journal of Computer Applications* 32(2):0975–8887
- Nordo G (2018) An embedding lemma in soft topological spaces. In: *Proceedings of the International Scientific Conference on Related Problems of Continuum Mechanics*, Kutaisi, Georgia, pp 194–199
- Nordo G (2019a) Soft n -topological spaces. *Mechanics, Materials Science & Engineering Journal* 20
- Nordo G (2019b) Some notes on soft topological product. preprint
- Onyeozili IA, Gwary TM (2014) A study of the fundamentals of soft set theory. *International Journal of Scientific and Technology Research* 3(4):132–143
- Pei D, Miao D (2005) From soft sets to information systems. In: *2005 IEEE international conference on granular computing, IEEE*, vol 2, pp 617–621
- Peyghan E (2013) About soft topological spaces. *Journal of New Results in Science* 2(2):60–75
- Peyghan E, Samadi B, Tayebi A (2014) Some results related to soft topological spaces. *Facta Universitatis, Series: Mathematics and Informatics* 29(4):325–336
- Qin K, Hong Z (2010) On soft equality. *Journal of Computational and Applied Mathematics* 234(5):1347–1355

- Rong W (2012) The countabilities of soft topological spaces. *International Journal of Computational and Mathematical Sciences* 6:159–162
- Sezgin A, Atagün AO (2011) On operations of soft sets. *Computers & Mathematics with Applications* 61(5):1457–1467
- Shabir M, Naz M (2011) On soft topological spaces. *Computers & Mathematics with Applications* 61(7):1786–1799
- Sheidaei A, Kazempour M, Hasanabadi A, Nosouhi F, Pithioux M, Baniassadi M, Rémond Y, George D (2019) Influence of bone microstructure distribution on developed mechanical energy for bone remodeling using a statistical reconstruction method. *Mathematics and Mechanics of Solids* 24(10):3027–3041
- Singh D, Onyeozili IA (2012) Some conceptual misunderstandings of the fundamentals of soft set theory. *ARNP Journal of Systems and Software* 2(9):251–254
- Tantawy O, El-Sheikh SA, Hamde S (2016) Separation axioms on soft topological spaces. *Annals of Fuzzy Mathematics and Informatics* 11(4):511–525
- Uluçay V, Sahin M, Olgun N, Kilicman A (2016) On soft expert metric spaces. *Malaysian Journal of Mathematical Sciences* 10(2):221–231
- Varol BP, Aygün H (2013) On soft hausdorff spaces. *Annals of Fuzzy Mathematics and Informatics* 5(1):15–24
- Varol BP, Shostak A, Aygün H (2012) A new approach to soft topology. *Hacettepe Journal of Mathematics and Statistics* 41(5):731–741
- Wadkar BR, Bhardwaj R, Mishra VN, Singh B (2016) Fixed point results related to soft sets. *Australian Journal of Basic and Applied Sciences* 10(16):128–137
- Wardowski D (2013) On a soft mapping and its fixed points. *Fixed Point Theory and Applications* 2013(1):182–11
- Xie N (2015) Soft points and the structure of soft topological spaces. *Annals of Fuzzy Mathematics and Informatics* 10(2):309–322
- Yang CF (2008) A note on “soft set theory”[comput. math. appl. 45 (4–5)(2003) 555–562]. *Computers & Mathematics with Applications* 56(7):1899–1900
- Zorlutuna I, Çaku H (2015) On continuity of soft mappings. *Applied Mathematics & Information Sciences* 9(1):403–409
- Zorlutuna I, Akdag M, Min WK, Atmaca S (2012) Remarks on soft topological spaces. *Annals of fuzzy Mathematics and Informatics* 3(2):171–185



Chapter 6

The Diffusion–Vortex Problems in Terms of Stresses for Bingham Materials

Dimitri Georgievskii

Abstract The formulations and the new exact self-similar solutions of the diffusion-vortex problems in terms of stresses simulating a non-steady one-dimensional shear in some curvilinear orthogonal coordinate system of two-constant rigid visco-plastic medium (the Bingham solid), are analyzed. Both the diffusion of plane and axisymmetric vortex layers as and the diffusion of vortex thread belong to these type of incompressible flows. A shear is realized inside the certain expanding in time sub-domains of infinite space with beforehand unknown bounds. Herewith one possible way for formulation of additional condition at infinity is described. We introduce into consideration the generalized diffusion of vortex which contains several material parameters and an order of stress irregularity in zero. The self-similar solutions where an order of irregularity corresponds or does not correspond to the kind of shear in the selected coordinate system are constructed.

Keywords: Bingham solid · Visco-plastic medium

6.1 The Generalized Diffusion of Vortex

Let us consider the non-steady flows of incompressible homogeneous rigid visco-plastic medium with linear viscosity (the Bingham solids) such that they represent one-dimensional shear in some orthogonal coordinate system. We should present the material in dimensionless form including the density ρ , the dynamical viscosity μ , and the parameter $\sigma_s/\sqrt{2}$ in the dimension basis. Here σ_s is yield stress of the Bingham material according to the Mises–Hencky criterion of plasticity (Klimov et al, 2005).

D. Georgievskii

Mechanical and Mathematical Department, Moscow State University, Moscow 119991, Russia
e-mail: georgiev@mech.math.msu.su

© Springer Nature Switzerland AG 2020

B. E. Abali and I. Giorgio (eds.), *Developments and Novel Approaches in Nonlinear Solid Body Mechanics*, Advanced Structured Materials 130,
https://doi.org/10.1007/978-3-030-50460-1_6

Let in some orthogonal coordinate system at any time moment the domain Ω occupied by medium is described by the inequality $\Omega = \{x > 0\}$ where x is one of curvilinear coordinates the dimension analog of which possesses a length dimension. The domain Ω consists of two beforehand unknown subdomains —the zone of visco-plastic flow $\Omega_f = \{0 < x < \xi(t)\}$, $\xi(0) = 0$, and the immovable rigid zone $\Omega_r = \{\xi(t) < x\}$. The stress intensity is equal to the yield stress on the moving interface of Ω_f and Ω_r . Mass forces are assumed to be absent.

The non-steady one-dimensional shear flow is characterized (Georgievskii, 2007) by the only nonzero component $v(x, t)$ of the velocity vector, and two tangent components $d(x, t)$ and $s(x, t)$ of the strain rate tensor and the stress tensor:

$$d = \frac{1}{2} \left(\frac{\partial v}{\partial x} - \frac{a_2 v}{x} \right), \quad v_u = \sqrt{\text{tr} \mathbf{d}^2} = \sqrt{2} |d|, \quad \sigma_u = \sqrt{\text{tr} \mathbf{s}^2} = \sqrt{2} |s| \quad (6.1)$$

where v_u and σ_u are the quadratic invariants of \mathbf{d} and \mathbf{s} named by intensities of strain rate and stresses respectively; \mathbf{s} is the stress deviator tensor.

In the domain Ω_f (where $\sigma_u > \sqrt{2}$ or in other words $|s| > 1$) the constitutive relations of the Bingham material

$$\mathbf{x} \in \Omega_f : \quad s = \frac{\sigma_u}{v_u} d, \quad \sigma_u = \sqrt{2} + 2v_u \quad (6.2)$$

are fulfilled. By virtue of (6.1) they reduce to the connection of the functions s and v :

$$\mathbf{x} \in \Omega_f : \quad s = \text{sign} d + 2d = \text{sign} \left(\frac{\partial v}{\partial x} - \frac{a_2 v}{x} \right) + \frac{\partial v}{\partial x} - \frac{a_2 v}{x} \quad (6.3)$$

Everywhere in Ω the equation of motion

$$\mathbf{x} \in \Omega = \Omega_f \cup \Omega_r : \quad \frac{\partial s}{\partial x} + \frac{a_1 s}{x} = \frac{\partial v}{\partial t} \quad (6.4)$$

is correct.

In the rigid zone Ω_r (where $\sigma_u \leq \sqrt{2}$ or in other words $|s| \leq 1$) the constitutive relations are not given. Instead of it we require that the domain Ω_r moves as absolutely rigid body or in particular is in rest.

On the boundary of the domain Ω_f the following conditions are given

$$x \rightarrow +0 : \quad x^\alpha s \rightarrow Sh(t), \quad S = \text{const}; \quad x = \xi(t) : \quad \sigma_u = \sqrt{2} \iff |s| = 1 \quad (6.5)$$

where $h(t)$ is the Heaviside function; S is the given intensity of tangent stresses; α is the order of peculiarity of the function s in zero; the real-valued parameters a_1 and a_2 depend on a choice of the orthogonal coordinate system as well as on a kind of a shear in this system.

Since $\xi(0) = 0$, i.e. the domain of visco-plastic flow is missing when $t = 0$, there are no any initial conditions in the formulation of problem. This fact leads to

insufficiency of the system (6.5) for obtaining of all unknown functions. Further the additional condition for a solvability of the problem will be stated.

Thus in all the domain Ω occupied by the Bingham material we search two functions $s(x, t)$ and $v(x, t)$ such that $s \in C_2(\Omega_f)$, $s \in C(\Omega)$, $v \in C_2(\Omega_f)$, $v \in C_1(\Omega)$ as well as the function $\xi(t)$ complying with the equations (6.3), (6.4) and the boundary conditions (6.5). Without loss of generality, the constant S is assumed to be positive so we can be determined with signs:

$$\mathbf{x} \in \Omega_f : \quad s > 1, \quad d > 0; \quad \mathbf{x} \in \Omega_r : \quad s \leq 1, \quad d = 0$$

Using the equations (6.3) and (6.4) it is not difficult to derive the following parabolic equation for $s(x, t)$:

$$\mathbf{x} \in \Omega_f : \quad \frac{\partial^2 s}{\partial x^2} + \frac{1}{x}(a_1 - a_2) \frac{\partial s}{\partial x} - \frac{1}{x^2} a_1(a_2 + 1) s = \frac{\partial s}{\partial t} \quad (6.6)$$

It is naturally to search its solution in self-similar form $s(x, t) = \tilde{s}(\eta)/x^\alpha$; $\eta = x/(2\sqrt{t})$. Then

$$\tilde{s}'' + \left[2\eta + \frac{1}{\eta}(a_1 - a_2 - 2\alpha) \right] \tilde{s}' + \frac{1}{\eta^2}(\alpha - a_1)(\alpha + a_2 + 1) \tilde{s} = 0 \quad (6.7)$$

$$\tilde{s}|_{\eta \rightarrow 0} \rightarrow S \quad (6.8)$$

Let us turn our attention to the important particular case realizable in the applications under consideration below when $\alpha = a_1$. This means a correspondence of the order of peculiarity in zero and kind of shear. Then the equation (6.7) with the only boundary condition (6.8) has the exact analytical solution

$$\tilde{s}(\eta) = S \left(1 - c \int_0^\eta \zeta^{a_1+a_2 - \zeta^2} d\zeta \right) \quad (6.9)$$

with unknown constant c . It is necessary to require that $a_1 + a_2 > -1$ for integrability of (6.9) in zero (and moreover $\alpha \geq 0 \iff a_1 \geq 0$). The integral in (6.9) can be expressed in terms of elementary functions if the number $a_1 + a_2$ is odd.

For the unknown function $\xi(t)$ we can write the following equation resulting of the solution (6.9) as well as the second boundary condition (6.5):

$$\xi^\alpha = S \left(1 - c \int_0^{\xi/(2\sqrt{t})} \zeta^{a_1+a_2 - \zeta^2} d\zeta \right) \quad (6.10)$$

How to find the coefficient value c ? One of possible ways consists of the following (see also Kruzhkov, 1969; Ogibalov and Mirzadzhanzade, 1977; Tikhonov and Samarskii, 2013; Iannacci et al, 1998; Andres et al, 2001). We rewrite the equation (6.10) in terms of dimension variables:

$$\left(\frac{\sqrt{\rho\sigma_s/\sqrt{2}}}{\mu} \right)^\alpha \xi_{\text{dim}}^\alpha = \frac{S_{\text{dim}}}{\sigma_s/\sqrt{2}} \left(1 - c \int_0^{\eta_0} \zeta^{a_1+a_2} - \zeta^2 d\zeta \right), \quad \eta_0 = \frac{\xi_{\text{dim}}}{2\sqrt{\mu t_{\text{dim}}/\rho}} \quad (6.11)$$

$$[\sigma_s] = [S_{\text{dim}}] = \text{ML}^{-1}\text{T}^{-2}, \quad [\xi_{\text{dim}}] = \text{L}, \quad [t_{\text{dim}}] = \text{T}$$

and require that the value c should not depend on the material constant of the medium, in particular should be fixed by passage to the limit $\sigma_s \rightarrow 0$. This limit means a transition to Newtonian viscous fluid where rigid zones are absent generally, i.e. $\eta_0 = \infty$. Realizing passage to the limit $\sigma_s \rightarrow 0$, $\eta_0 \rightarrow \infty$ in (6.11) we receive

$$c = \left(\int_0^\infty \zeta^{a_1+a_2} - \zeta^2 d\zeta \right)^{-1} \quad (6.12)$$

It follows from (6.10) when $t \rightarrow \infty$ that the interface $x = \xi(t)$ of the domains Ω_f and Ω_r approaches to the value $\xi_\infty = S^{1/\alpha}$ if $\alpha > 0$ and to infinity if $\alpha = 0$.

Inside the immovable rigid zone Ω_r :

$$\mathbf{x} \in \Omega_r : \quad s(x, t) = \left(\frac{\xi(t)}{x} \right)^{a_1} \quad (6.13)$$

The function $s(x, t)$ has a break on the moving bound $x = \xi(t)$ but this break disappears over time so that

$$\mathbf{x} \in \Omega, \quad t \rightarrow \infty : \quad s(x, t) \rightarrow \frac{S}{x^{a_1}} \quad (6.14)$$

It is not difficulty to obtain analytically the velocity $v(x, t)$. For that purpose it is necessary to integrate the equation

$$\frac{\partial}{\partial x} \frac{v}{x^{a_2}} = \frac{S}{x^{a_1+a_2}} - \frac{1}{x^{a_2}} - \frac{Sc}{x^{a_1+a_2}} \int_0^{x/(2\sqrt{t})} \zeta^{a_1+a_2} - \zeta^2 d\zeta \quad (6.15)$$

with the condition $v(\xi(t), t) = 0$.

6.2 Diffusion of Plane Vortex Layer. Extraction of a Plane out of Visco-Plastic Space

We consider several important particular cases of the investigated above problem simulating nonsteady shear flows by diffusion-vortex type of the Bingham material (Georgievskii, 2006, 2018). Let us at first turn out attention to a plane flow and set that Ω is the half-plane described by the inequality $x > 0$ in the Cartesian coordinate system (x_1, x_2) , $x_2 \equiv x$. Herewith the component $v_1(x, t)$ of the velocity vector,

the component $d_{12}(x, t)$ of the strain rate tensor and the component $\sigma_{12}(x, t)$ of the stress tensor play a part in the function v , d and s respectively. Both the kinematics and shear geometry such that $a_1 = a_2 = 0$, $\alpha = 0$.

It should be noted that if $a_1 = a_2 = 0$ then the constant c in (6.12) is equal to $2/\sqrt{\pi}$ (the Euler–Poisson integral). The solution (6.9) in terms of stresses can be written as

$$\tilde{s}(\eta) = S \left(1 - \frac{2}{\sqrt{\pi}} \int_0^\eta e^{-\zeta^2} d\zeta \right) \equiv S \operatorname{erfc} \eta; \quad s(x, t) = \tilde{s}(\eta) \quad (6.16)$$

where $\operatorname{erfc} \eta$ is the additional error function. The interface bound $\xi(t) = 2\eta_0\sqrt{t}$ is determined from the equation (6.10):

$$\int_0^{\eta_0} e^{-\zeta^2} d\zeta = \frac{\sqrt{\pi}(S-1)}{2S} \quad (6.17)$$

Using the constitutive relation (6.3) where $a_2 = 0$ or directly the equation (6.15) we can obtain v after integrating:

$$v(x, t) = -(S-1)(\xi(t) - x) + \frac{2S}{\sqrt{\pi}} \int_x^{\xi(t)} \int_0^{\tilde{x}/(2\sqrt{t})} e^{-\zeta^2} d\zeta d\tilde{x} \quad (6.18)$$

Here it is taken into account that $v(\xi(t), t) = 0$ what corresponds to immovability of the rigid zone Ω_r . It follows from the equation of equilibrium (6.4) in Ω_r (where $a_1 = 0$) that $s \equiv 1$ in Ω_r . Thus, a continuity of s by x as well as a smoothness of v by x in all the space Ω are ensured.

The solution relevant to diffusion of plane vortex layer (or extraction of a plane out of the Bingham material) is such that the domain of visco-plastic flow Ω_f spreads during infinite time at all the domain Ω penetrating into the depths with decreasing velocity inversely proportional to \sqrt{t} .

6.3 Diffusion of Axially Symmetric Vortex Layer. Extraction of a Thread out of Visco-Plastic Space

Let now in the cylindrical coordinate system (r, θ, z) a (rz) -shear is realized in all three-dimensional space Ω without the axis z , i.e. $\Omega = \{r > 0\}$. The components $v_z(r, t)$, $d_{rz}(r, t)$ and $s_{rz}(r, t)$ are the only nonzero components of the velocity vector, the strain rate tensor and the stress tensor respectively. In this case $a_1 = 1$, $a_2 = 0$, $\alpha = 1$.

The general solution in terms of stresses (6.9) leads to the following shear stress in the domain $\Omega_f = \{0 < r < \xi(t)\}$:

$$\tilde{s}(\eta) = S e^{-\eta^2} \iff s(r, t) = \frac{S}{r} \exp\left(-\frac{r^2}{4t}\right) \quad (6.19)$$

The interface bound of Ω_f and $\Omega_r = \{r > \xi(t)\}$ may be found from the transcendental equation

$$\xi = S \exp\left(-\frac{\xi^2}{4t}\right) \quad (6.20)$$

which easily allows to express the inverse function $t = t(\xi)$.

The velocity of flow $v(r, t)$ in Ω_f has a logarithmic peculiarity when $r \rightarrow 0$:

$$v(r, t) = \xi(t) - r - S \int_r^{\xi(t)} \exp\left(-\frac{\tilde{r}^2}{4t}\right) \frac{d\tilde{r}}{\tilde{r}} \quad (6.21)$$

The equation of equilibrium in rigid zone arising from (6.4) by $\partial v / \partial t \equiv 0$ leads to the stress distribution in Ω_r : $s(r, t) = \xi(t)/r$ guaranteeing necessary classes of smoothness for s and v in Ω . The function $s(r, t)$ has a break in the point $r = \xi(t)$ but this break disappears over time and $\lim_{t \rightarrow \infty} s(r, t) = S/r$ in all the domain Ω .

It should be noted that according to (6.20) the interface bound $\xi(t)$ approaches to the value $\xi_\infty = S$ when $t \rightarrow \infty$, i.e. exterior part of the cylinder by the radius S is at rest for any time.

6.4 Diffusion of Vortex Thread

The third typical diffusion-vortex problem in terms of stresses is connected with analysis of non-steady $(r\theta)$ -shear (rotation or torsion) in the cylindrical coordinate system (r, θ, z) realizable in all the space without the axis z : $\Omega = \{r > 0\}$. Unlike the axial longitudinal shear (section 6.3) the nonzero components $v_\theta(r, t)$, $d_{r\theta}(r, t)$ and $s_{r\theta}(r, t)$ correspond to the functions v , d and s . The parameters a_1 , a_2 and α take the values $a_1 = 2$, $a_2 = 1$ and $\alpha = 2$ for $(r\theta)$ -shear.

The solution in terms of stresses (6.9), (6.12) in the domain $\Omega_f = \{0 < r < \xi(t)\}$ by such values of a_1 and a_2 has a form

$$\tilde{s} = C(1 + \eta^2)e^{-\eta^2} \iff s(r, t) = S\left(\frac{1}{r^2} + \frac{1}{4t}\right) \exp\left(-\frac{r^2}{4t}\right) \quad (6.22)$$

so that the interface bound $r = \xi(t)$ is obtained from the following transcendent equation

$$\xi^2 = C\left(1 + \frac{\xi^2}{4t}\right) \exp\left(-\frac{\xi^2}{4t}\right) \quad (6.23)$$

Rotation velocity of the material in the domain Ω_f may be found after substitution of (6.22) into the constitutive relation (6.3) and integrating over $x \equiv r$ with the same boundary condition $v(\xi(t), t) = 0$:

$$v(r, t) = -r \ln \frac{r}{\xi(t)} - Cr \int_r^{\xi(t)} \left(\frac{1}{\tilde{r}^3} + \frac{1}{4\tilde{r}t} \right) \exp\left(-\frac{\tilde{r}^2}{4t}\right) d\tilde{r} \quad (6.24)$$

As is obvious, it has a peculiarity by order $1/r$ when $r \rightarrow 0$.

The equation of equilibrium in the rigid zone $\Omega_r = \{r > \xi(t)\}$ arising from (6.4) by $\partial v / \partial t \equiv 0$ gives the usual in $(r\theta)$ -shear problems distribution of tangent stresses: $s(r, t) = \xi^2(t)/r^2$. Then the function $s(r, t)$ is continuous in all the space Ω as well as the function $v(r, t)$ is continuously differentiable.

We emphasize the typical property of the solution (6.22)–(6.24) highly similar to the noted one in section 6.3. The interface bound $\xi(t)$ of the domains Ω_f and Ω_r approaches to the value $\xi_\infty = \sqrt{S}$ when $t \rightarrow \infty$, i.e. exterior part of the cylinder by the radius \sqrt{S} is at rest and is not subjected to rotation. Therefore, neither extracting a thread (the axis z) out of visco-plastic space by the aid of longitudinal shear nor realizing a vortex motion around this thread it is impossible to deform all the space. The domain of visco-plastic flow should be bounded by some cylinder with the radius depending on the shear intensity. It is worth noticing that Bingham solid is very interesting in mechanical applications. Indeed, It can be used as a damping material, especially in the framework of the newly conceived metamaterials (see, e.g., dell’Isola et al, 2019a,b).

References

- Andres J, Bersani AM, Leśniak K (2001) On some almost-periodicity problems in various metrics. *Acta Applicandae Mathematica* 65(1-3):35–57
- dell’Isola F, Seppecher P, Alibert JJ, et al (2019a) Pantographic metamaterials: an example of mathematically driven design and of its technological challenges. *Continuum Mechanics and Thermodynamics* 31(4):851–884
- dell’Isola F, Seppecher P, Spagnuolo M, et al (2019b) Advances in pantographic structures: design, manufacturing, models, experiments and image analyses. *Continuum Mechanics and Thermodynamics* 31(4):1231–1282
- Georgievskii DV (2006) Break diffusion of the tangential strain on the boundary of a viscoplastic half-plane. *Prikl Mat Mekh* 70:884–892
- Georgievskii DV (2007) Self-similar solutions in the problem of generalized vortex diffusion. *Fluid Dynamics* 42:151–159
- Georgievskii DV (2018) Selected problems of continuum mechanics. LENAND, Moscow
- Iannacci R, Bersani AM, Dell’Acqua G, Santucci P (1998) Embedding theorems for Sobolev–Besicovitch spaces of almost periodic functions. *Zeitschrift für Analysis und ihre Anwendungen* 17(2):443–457
- Klimov DM, Petrov AG, Georgievskii DV (2005) Viscoplastic flows: dynamic chaos, stability, mixing. Nauka, Moscow
- Kruzhkov SN (1969) Nonlinear partial differential equations, Part 1: Elliptic and parabolic equations of second order. Moscow University Press, Moscow
- Ogibalov PM, Mirzadzhanzade KA (1977) Unsteady flows of viscoplastic media. Moscow University Press, Moscow
- Tikhonov AN, Samarskii AA (2013) Equations of mathematical physics. Courier Corporation



Chapter 7

On the Behavior of Solutions of Quasilinear Elliptic Inequalities Near a Boundary Point

Andrej A. Kon'kov

Abstract Assume that $p > 1$ and $p - 1 \leq \alpha \leq p$ are real numbers and Ω is a non-empty open subset of \mathbb{R}^n , $n \geq 2$. We consider the inequality

$$\operatorname{div} A(x, Du) + b(x)|Du|^\alpha \geq 0,$$

where $D = (\partial/\partial x_1, \partial/\partial x_2, \dots, \partial/\partial x_n)$ is the gradient operator and, moreover, $A : \Omega \times \mathbb{R}^n \rightarrow \mathbb{R}^n$ and $b : \Omega \rightarrow [0, \infty)$ are some functions with

$$C_1|\xi|^p \leq \xi A(x, \xi), \quad |A(x, \xi)| \leq C_2|\xi|^{p-1}, \quad C_1, C_2 = \text{const} > 0,$$

for almost all $x \in \Omega$ and for all $\xi \in \mathbb{R}^n$. For solutions of this inequality we obtain estimates depending on the geometry of Ω . In particular, these estimates imply regularity conditions of a boundary point.

Keywords: Quasilinear Elliptic Inequalities · Boundary conditions

7.1 Introduction

Let Ω be an open subset of \mathbb{R}^n , $n \geq 2$. By B_r^x and S_r^x we mean the open ball and the sphere in \mathbb{R}^n of radius $r > 0$ and center at a point x . In the case of $x = 0$, we write B_r and S_r instead of B_r^0 and S_r^0 , respectively. Let us denote $B_{r_1, r_2} = \{x \in \mathbb{R}^n : r_1 < |x| < r_2\}$ and $\Omega_{r_1, r_2} = B_{r_1, r_2} \cap \Omega$, $0 < r_1 < r_2$. Through out the paper, we assume that $S_r \cap \Omega \neq \emptyset$ for any $r \in (0, R)$, where $R > 0$ is some real number.

We are interested in the behavior of solutions of the problem

A. A. Kon'kov
Department of Differential Equations, Faculty of Mechanics and Mathematics, Moscow Lomonosov State University, Vorobyovy Gory, Moscow, 119992 Russia
e-mail: konkov@mech.math.msu.su

$$\operatorname{div} A(x, Du) + b(x)|Du|^\alpha \geq 0 \quad \text{in } B_R \cap \Omega, \quad u|_{B_R \cap \partial\Omega} = 0, \quad (7.1)$$

where $D = (\partial/\partial x_1, \partial/\partial x_2, \dots, \partial/\partial x_n)$ is the gradient operator and the function $A : \Omega \times \mathbb{R}^n \rightarrow \mathbb{R}^n$ satisfies the ellipticity conditions

$$C_1|\xi|^p \leq \xi A(x, \xi), \quad |A(x, \xi)| \leq C_2|\xi|^{p-1}$$

with some constants $C_1 > 0$, $C_2 > 0$, and $p > 1$ for almost all $x \in \Omega$ and for all $\xi \in \mathbb{R}^n$. It is also assumed that $p - 1 \leq \alpha \leq p$ is a real number and b is a non-negative function such that $b \in L_\nu(\Omega_{r,R})$ for all $r \in (0, R)$, where ν satisfies the following requirements:

- (i) if $\alpha = p$, then $\nu = \infty$;
- (ii) if $\alpha = p - 1$ and $1 < p \leq n$, then $\nu > n$;
- (iii) if $\alpha = p - 1$ and $p > n$, then $\nu = p$;
- (iv) if $p - 1 < \alpha < p$ and $n \neq p$, then $\nu = \max\{n, p\}/(p - \alpha)$;
- (v) if $p - 1 < \alpha < p$ and $n = p$, then $\nu > p/(p - \alpha)$.

We say that $u \in W_p^1(B_R \cap \Omega) \cap L_\infty(B_R \cap \Omega)$ is a solution of problem (7.1) if $A(x, Du) \in L_{p/(p-1)}(B_R \cap \Omega)$,

$$-\int_\Omega A(x, Du)D\varphi \, dx + \int_\Omega b(x)|Du|^\alpha \varphi \, dx \geq 0$$

for any non-negative function $\varphi \in C_0^\infty(B_R \cap \Omega)$, and $u\psi \in \mathring{W}_p^1(\Omega)$ for any $\psi \in C_0^\infty(B_R)$.

In his classical papers, Wiener (1924b,a) obtained a boundary point regularity criteria for solutions of the Dirichlet problem for the Laplace equation. In other words, he found necessary and sufficient conditions for solutions of the Dirichlet problem for the Laplace equation to be continuous at a boundary point. The criteria was formulated in terms of capacity which is very similar to the one that arises in electrostatics. This approach proved to be very productive and was subsequently used by many authors (Björn, 2001; Gariepy and Ziemer, 1977; Kon'kov, 2014, 2004; Landis, 1997; Littman et al, 1963; Maz'ya, 1970; Iannacci et al, 1998; Andres et al, 2001; dell'Isola et al, 2019a,b). Maz'ya (1970) managed to get sufficient regularity conditions for solutions of the Dirichlet problem for the p-Laplace equation. The results of V.G. Maz'ya were generalized for quasilinear equations containing term with lower-order derivatives by Gariepy and Ziemer (1977) and for systems of quasilinear equations by Björn (2001). In doing that, Björn (2001); Gariepy and Ziemer (1977) imposed essential restrictions on coefficients of the lower-order derivatives. In the case of problem (7.1), this restrictions take the form $b^{1/(p-\alpha)} \in L_n(B_R \cap \Omega)$ if $1 < p < n$ and $b^{1/(p-\alpha)} \in L_\lambda(B_R \cap \Omega)$, $\lambda > n$, if $p = n$. Therefore, the results of Björn (2001); Gariepy and Ziemer (1977) can not be applied if $b(x)$ grows fast enough as $x \rightarrow 0$ (see Examples 1–3). Below we present Theorems 1–10 that are free from this shortcoming.

We use the following notations. For every solution of (7.1) we put

$$M(r; u) = \operatorname{ess\,sup}_{S_r \cap \Omega} u, \tag{7.2}$$

where the restriction of u to $S_r \cap \Omega$, $r \in (0, R)$, is understood in the sense of the trace and the essential supremum in (7.2) is taken with respect to $(n - 1)$ -dimensional Lebesgue measure on the sphere S_r . In accordance with the maximum principle either $M(\cdot; u)$ is a monotonic function on the whole interval $(0, R)$ or there exists $R_* \in (0, R)$ such that $M(\cdot; u)$ does not increase on $(0, R_*)$ and does not decrease on (R_*, R) .

Let E be a non-empty open subset of the sphere S_r . We denote

$$\lambda_{\min}(E) = \inf_{\psi \in C_0^\infty(E)} \frac{\int_E |\nabla \psi|^p dS_r}{\int_E |\psi|^p dS_r},$$

where $|\nabla \psi| = (g^{ij} \nabla_i \psi \nabla_j \psi)^{1/2}$, g^{ij} is the dual metric tensor on S_r induced by the standard euclidean metric on \mathbb{R}^n , and dS_r is the $(n - 1)$ -dimensional volume element of S_r . By the variational principle, $\lambda_{\min}(E)$ is the first eigenvalue of the problem

$$\Delta_p v = -\lambda |v|^{p-2} v \quad \text{in } E, \quad v|_{\partial E} = 0,$$

for the p -Laplace–Beltrami operator $\Delta_p v = \nabla_i (|\nabla v|^{p-2} g^{ij} \nabla_j v)$.

The capacity of a compact set $K \subset \omega$ relative to a non-empty open set $\omega \subset \mathbb{R}^n$ is defined as

$$\operatorname{cap}(K, \omega) = \inf_{\varphi} \int_{\omega} |D\varphi|^p dx,$$

where the infimum is taken over all functions $\varphi \in C_0^\infty(\omega)$ that are identically equal to one in a neighborhood of K . By definition, the capacity of the empty set is equal to zero. In the case of $\omega = \mathbb{R}^n$, we write $\operatorname{cap}(K)$ instead of $\operatorname{cap}(K, \omega)$. If $p = 2$ and $n \geq 3$, then $\operatorname{cap}(K)$ coincides with the well-known Wiener capacity.

It can be shown that $\operatorname{cap}(K, \omega)$ has the following natural properties.

(a) *Monotonicity*: If $K_1 \subset K_2$ and $\omega_2 \subset \omega_1$, then

$$\operatorname{cap}(K_1, \omega_1) \leq \operatorname{cap}(K_2, \omega_2).$$

(b) *Similarity property*: If $K' = \lambda K$ and $\omega' = \lambda \omega$, where $\lambda > 0$ is a real number, then

$$\operatorname{cap}(K', \omega') = \lambda^{n-p} \operatorname{cap}(K, \omega).$$

(c) *Semiadditivity*: Assume that K_1 and K_2 are compact subsets of an open set ω , then

$$\operatorname{cap}(K_1 \cup K_2, \omega) \leq \operatorname{cap}(K_1, \omega) + \operatorname{cap}(K_2, \omega).$$

By the ε -essential inner diameter of an open set ω , where $0 < \varepsilon < 1$ is a real number, we mean the value

$$\operatorname{diam}_\varepsilon \omega = \sup \left\{ r \in (0, \infty) : \exists x \in \omega \frac{\operatorname{cap}(\overline{B_r^x} \setminus \omega, B_{2r}^x)}{\operatorname{cap}(\overline{B_r}, B_{2r})} < \varepsilon \right\}.$$

In this way, if $\omega = \emptyset$, then $\text{diam}_\varepsilon \omega = 0$.

The ε -essential inner diameter is a monotone set function, i.e. $\text{diam}_\varepsilon \omega_1 \leq \text{diam}_\varepsilon \omega_2$ if $\omega_1 \subset \omega_2$. It also is a monotone function of ε . In other words, $\text{diam}_{\varepsilon_1} \omega \leq \text{diam}_{\varepsilon_2} \omega$ if $\varepsilon_1 \leq \varepsilon_2$.

We say that $f \in \mathcal{L}_{\nu,\varepsilon}(\omega)$, where $\nu \geq 1$ and $0 < \varepsilon < 1$ are real numbers and ω is an open set, if $f \in L_{\nu,loc}(\omega)$ and

$$\sup_{x \in \omega} \|f\|_{L_\nu(\omega \cap B_{\text{diam}_\varepsilon}^x \omega)} < \infty.$$

It can be seen that $\mathcal{L}_{\nu,\varepsilon}(\omega)$ is a Banach space with the norm

$$\|f\|_{\mathcal{L}_{\nu,\varepsilon}(\omega)} = |S_1|^{-1/\nu} \sup_{x \in \omega} \|f\|_{L_\nu(\omega \cap B_{\text{diam}_\varepsilon}^x \omega)},$$

where $|S_1|$ is the $(n-1)$ -dimensional volume of S_1 . In the case of $f \in L_\infty(\omega)$, we obviously have

$$\|f\|_{\mathcal{L}_{\nu,\varepsilon}(\omega)} \leq (\text{diam}_\varepsilon \omega)^{n/\nu} \|f\|_{L_\infty(\omega)}. \quad (7.3)$$

7.2 Estimates of Solutions near a Boundary Point

Below we assume by default that Λ , q , and \mathcal{D} are non-negative measurable functions such that

$$\Lambda(r) \leq \inf_{t \in (r/\theta, r\theta) \cap (0, R)} \lambda_{\min}(S_t \cap \Omega), \quad (7.4)$$

$$q(r) \geq (\text{diam}_\varepsilon \Omega_{r/\theta, r\theta})^{p-\alpha-n/\nu} \|b\|_{\mathcal{L}_{\nu,\varepsilon}(\Omega_{r/\theta, r\theta})}, \quad (7.5)$$

and

$$\mathcal{D}(r) \leq \frac{1}{\text{diam}_\varepsilon \Omega_{r/\theta, r\theta}}$$

for almost all $r \in (0, R)$, where $\theta > 1$ and $0 < \varepsilon < 1$ are some real numbers.

Remark 1 In view of (7.3), if $b \in L_\infty(\Omega_{r,R})$ for any $r \in (0, R)$, then to perform (7.5) it is sufficient to require that

$$q(r) \geq (\text{diam}_\varepsilon \Omega_{r/\theta, r\theta})^{p-\alpha} \text{esssup}_{\Omega_{r/\theta, r\theta}} b$$

for almost all $r \in (0, R)$.

Theorem 1 Let $p-1 < \alpha \leq p$ and

$$\int_0^R \frac{\min\{(r\Lambda(r))^{1/(p-1)}, \Lambda^{1/p}(r)\}}{1 + q^{1/(\alpha-p+1)}(r)} dr = \infty.$$

Then every non-negative solution of (7.1) satisfies the estimate

$$M(r; u) \leq M(R; u) \exp \left(-C \int_r^R \frac{\min\{(t\Lambda(t))^{1/(p-1)}, \Lambda^{1/p}(t)\}}{1 + q^{1/(\alpha-p+1)}(t)} dt \right) \quad (7.6)$$

for all sufficiently small $r > 0$, where the constant $C > 0$ depends only on $n, p, \alpha, \varepsilon, \theta$, and the ellipticity constants C_1 and C_2 .

Example 1 Assume that $p - 1 < \alpha \leq p$, $\{(x', x_n) \in \mathbb{R}^n : |x'| < k_1 x_n, 0 < x_n < R\} \subset B_R \setminus \Omega$, and

$$b(x) \leq k_2 |x|^l \quad (7.7)$$

for almost all $x \in B_R \cap \Omega$, where k_1 and k_2 are positive constants and $l \in \mathbb{R}$.

If $l \geq \alpha - p$, then Theorem 1 implies that $M(r; u) \rightarrow 0$ as $r \rightarrow +0$ for any non-negative solution of (7.1). In addition, the estimate

$$M(r; u) \leq M(R; u) r^k$$

is valid for all sufficiently small $r > 0$, where the constant $k > 0$ does not depend on u . Really, we can take the function Λ such that

$$\Lambda(r) \sim r^{-p} \quad \text{as } r \rightarrow +0 \quad (7.8)$$

or, in other words,

$$\varkappa_1 r^{-p} \leq \Lambda(r) \leq \varkappa_2 r^{-p}$$

with some constants $\varkappa_1 > 0$ and $\varkappa_2 > 0$ for all $r > 0$ from a neighborhood of zero. In so doing, as the q , we can take a bounded function.

We note that, from paper *Gariepy and Ziemer (1977)*, the required regularity follows only for $l > \alpha - p$. In the case of the critical exponent $l = \alpha - p$, the results of *Gariepy and Ziemer (1977)* are inapplicable.

Now, let the inequality

$$b(x) \leq k_2 |x|^{\alpha-p} \left(\log \frac{1}{|x|} \right)^\sigma$$

be fulfilled instead of (7.7). In other words, we examine the case of the critical exponent $l = \alpha - p$. If $\sigma \leq \alpha - p + 1$, then in accordance with Theorem 1, where Λ satisfies (7.8) and

$$q(r) \sim \left(\log \frac{1}{r} \right)^\sigma \quad \text{as } r \rightarrow +0,$$

we have $M(r; u) \rightarrow 0$ as $r \rightarrow +0$ for any non-negative solution of (7.1). In addition, it can be shown that

$$M(r; u) \leq M(R; u) e^{-Cf(r)} \quad (7.9)$$

for all sufficiently small $r > 0$, where

$$f(r) = \begin{cases} \log \frac{1}{r}, & \sigma \leq 0, \\ \left(\log \frac{1}{r} \right)^{(\alpha-p+1-\sigma)/(\alpha-p+1)}, & 0 < \sigma < \alpha - p + 1, \\ \log \log \frac{1}{r}, & \sigma = \alpha - p + 1, \end{cases}$$

and $C > 0$ is a constant independent of u .

Theorem 2 Let $p - 1 < \alpha \leq p$,

$$\int_0^R \frac{\Lambda^{1/p}(r)}{1 + q^{1/(\alpha-p+1)}(r)} dr = \infty$$

and, moreover,

$$\liminf_{r \rightarrow +0} r^{p-n} \operatorname{cap} (\overline{B_{r\theta^{-2/3}, r\theta^{-1/3}}} \setminus \Omega, B_{r/\theta, r}) > 0. \quad (7.10)$$

Then every non-negative solution of (7.1) satisfies the estimate

$$M(r; u) \leq M(R; u) \exp \left(-C \int_r^R \frac{\Lambda^{1/p}(t)}{1 + q^{1/(\alpha-p+1)}(t)} dt \right) \quad (7.11)$$

for all sufficiently small $r > 0$, where the constant $C > 0$ depends only on $n, p, \alpha, \varepsilon, \theta, C_1, C_2$, and on the limit in the left-hand side of (7.10).

Remark 2 Condition (7.11) is obviously fulfilled if we can touch zero by a cone that lies entirely outside the set Ω . This condition is also fulfilled if

$$\lim_{r \rightarrow +0} \frac{\operatorname{diam}_\varepsilon \Omega_{r/\theta, r\theta}}{r} = 0.$$

Theorem 3 Let $p - 1 < \alpha \leq p$,

$$\int_0^R \frac{\mathcal{D}(r)}{1 + q^{1/(\alpha-p+1)}(r)} dr = \infty$$

and, moreover, (7.10) holds. Then every non-negative solution of (7.1) satisfies the estimate

$$M(r; u) \leq M(R; u) \exp \left(-C \int_r^R \frac{\mathcal{D}(t)}{1 + q^{1/(\alpha-p+1)}(t)} dt \right)$$

for all sufficiently small $r > 0$, where the constant $C > 0$ depends only on $n, p, \alpha, \varepsilon, \theta, C_1, C_2$, and on the limit in the left-hand side of (7.10).

Example 2 Assume that $p - 1 < \alpha \leq p$, $B_R \cap \Omega \subset \{(x', x_n) \in \mathbb{R}^n : |x_n| < k_1|x'|^s, |x'| < R\}$, and (7.7) is valid, where $k_1 > 0$, $k_2 > 0$, and $s > 1$ are some constants.

In the case of $l \geq \alpha - p + 1 - s$, applying Theorem 3 with

$$\mathcal{D}(r) \sim r^{-s} \quad \text{and} \quad q(r) \sim r^{s(p-\alpha)+l} \quad \text{as } r \rightarrow +0,$$

we obtain that $M(r; u) \rightarrow 0$ as $r \rightarrow +0$ for any non-negative solution of (7.1). In so doing, Theorem 3 implies estimate (7.9), where

$$f(r) = \begin{cases} r^{1-s}, & s(\alpha - p) \leq l, \\ r^{(\alpha-p+1-s-l)/(\alpha-p+1)}, & \alpha - p + 1 - s < l < s(\alpha - p), \\ \log \frac{1}{r}, & l = \alpha - p + 1 - s. \end{cases}$$

We note that the results of paper Gariepy and Ziemer (1977) yields the required regularity for $l > (\alpha - p)(n + s - 1)/n$. It does not present any particular problem to verify that $(\alpha - p)(n + s - 1)/n > \alpha - p + 1 - s$ for all positive integers n . Thus, Theorem 3 provides us with a regularity condition that is better than the analogous condition given in Gariepy and Ziemer (1977).

Now, let the inequality

$$b(x) \leq k_2|x|^{\alpha-p+1-s} \left(\log \frac{1}{|x|} \right)^\sigma$$

be fulfilled instead of (7.7).

If $\sigma \leq \alpha - p + 1$, then $M(r; u) \rightarrow 0$ as $r \rightarrow +0$ for any non-negative solution of (7.1). In addition, the function $M(\cdot; u)$ satisfies estimate (7.9), where

$$f(r) = \begin{cases} \left(\log \frac{1}{r} \right)^{(\alpha-p+1-\sigma)/(\alpha-p+1)}, & \sigma < \alpha - p + 1, \\ \log \log \frac{1}{r}, & \sigma = \alpha - p + 1. \end{cases}$$

To show this, it is sufficient to apply Theorem 3 with

$$\mathcal{D}(r) \sim r^{-s} \quad \text{and} \quad q(r) \sim r^{s(p-\alpha)+\alpha-p+1-s} \left(\log \frac{1}{r} \right)^\sigma \quad \text{as } r \rightarrow +0.$$

Theorem 4 Estimate (7.6) remains valid if, under the assumptions of Theorem 1, the function Λ satisfies the inequality

$$\Lambda(r) \leq \inf_{\Omega_{r\theta^{-1/3}, r\theta^{1/3}}} \mu_\delta^p + r^{-n} \text{cap}(\overline{B_{r\theta^{-2/3}, r\theta^{-1/3}}} \setminus \Omega, B_{r/\theta, r}) \quad (7.12)$$

instead of (7.4), where $\theta > 1$ and $0 < \delta < 1 - \theta^{-1/3}$ are some real numbers and

$$\mu_\delta(x) = \sup_{r \in (0, \delta|x|)} (r^{1-n} \text{cap}(\overline{B_r^x} \setminus \Omega, B_{2r}^x))^{1/(p-1)}.$$

In this case, the constant $C > 0$ in (7.6) depends also on δ .

Corollary 1 *Let the inequality*

$$A(r) \leq r^{-n} \text{cap}(\overline{B_{r\theta^{-2/3}, r\theta^{-1/3}} \setminus \Omega, B_{r/\theta, r}})$$

be fulfilled instead of (7.4) and, moreover,

$$\int_0^R \frac{(rA(r))^{1/(p-1)}}{1 + q^{1/(\alpha-p+1)}(r)} dr = \infty.$$

Then every non-negative solution of (7.1) satisfies the estimate

$$M(r; u) \leq M(R; u) \exp\left(-C \int_r^R \frac{(tA(t))^{1/(p-1)}}{1 + q^{1/(\alpha-p+1)}(t)} dt\right)$$

for all sufficiently small $r > 0$, where the constant $C > 0$ depends only on n, p, α, θ , and the ellipticity constants C_1 and C_2 .

Theorem 5 *Estimate (7.11) remains valid if, in the assumptions of Theorem 2, the function Λ satisfies inequality (7.12) instead of (7.4). In this case, the constant $C > 0$ in (7.11) depends also on δ .*

Theorem 6 *Let u be a non-negative solution of (7.1), where $\alpha = p - 1$. Then there exist constants $k > 0$ and $C > 0$ depending only on $n, p, \varepsilon, \theta$, and the ellipticity constants C_1 and C_2 such that the condition*

$$\int_0^R e^{-kq(r)} \min\{(rA(r))^{1/(p-1)}, A^{1/p}(r)\} dr = \infty \quad (7.13)$$

implies the estimate

$$M(r; u) \leq M(R; u) \exp\left(-C \int_r^R e^{-kq(t)} \min\{(rA(r))^{1/(p-1)}, A^{1/p}(r)\} dt\right) \quad (7.14)$$

for all sufficiently small $r > 0$.

Theorem 7 *Let u be a non-negative solution of (7.1) with $\alpha = p - 1$ and, moreover, (7.10) holds. Then there exist constants $k > 0$ and $C > 0$ depending only on $n, p, \alpha, \varepsilon, \theta, C_1, C_2$, and on the limit in the left-hand side of (7.10) such that the condition*

$$\int_0^R e^{-kq(r)} A^{1/p}(r) dr = \infty \quad (7.15)$$

implies the estimate

$$M(r; u) \leq M(R; u) \exp \left(-C \int_r^R e^{-kq(t)} \Lambda^{1/p}(t) dt \right) \quad (7.16)$$

for all sufficiently small $r > 0$.

Theorem 8 *Let u be a non-negative solution of (7.1) with $\alpha = p - 1$ and, moreover, (7.10) holds. Then there exist constants $k > 0$ and $C > 0$ depending only on $n, p, \alpha, \varepsilon, \theta, C_1, C_2$, and on the limit in the left-hand side of (7.10) such that the condition*

$$\int_0^R e^{-kq(r)} \mathcal{D}(r) dr = \infty$$

implies the estimate

$$M(r; u) \leq M(R; u) \exp \left(-C \int_r^R e^{-kq(t)} \mathcal{D}(t) dt \right)$$

for all sufficiently small $r > 0$.

Example 3 *Assume that $\alpha = p - 1$, $B_R \cap \Omega \subset \{(x', x_n) \in \mathbb{R}^n : |x_n| < k_1|x'|^s, |x'| < R\}$, and (7.7) is valid, where $k_1 > 0, k_2 > 0$, and $s > 1$ are some constants.*

In the case of $l \geq -s$, taking

$$\mathcal{D}(r) \sim r^{-s} \quad \text{and} \quad q(r) \sim 1 \quad \text{as } r \rightarrow +0$$

in Theorem 8, we obtain $M(r; u) \rightarrow 0$ as $r \rightarrow +0$ for any non-negative solution of (7.1). In so doing, estimate (7.9) is valid, where

$$f(r) = r^{1-s}.$$

Note that the results of paper Gariepy and Ziemer (1977) guarantee the required regularity for $l > -(n + s - 1)/n$. It is easy to see that $-s < -(n + s - 1)/n$ for all integers $n \geq 2$. Thus, Theorem 8 gives us a better regularity condition than the results of paper Gariepy and Ziemer (1977).

Theorem 9 *In the hypotheses of Theorem 6, let the function Λ satisfies inequality (7.12) instead of (7.4). Then there exist constants $k > 0$ and $C > 0$ depending only on $n, p, \delta, \varepsilon, \theta$, and the ellipticity constants C_1 and C_2 such that the condition (7.13) implies estimate (7.14).*

Theorem 10 *In the hypotheses of Theorem 7, let the function Λ satisfies inequality (7.12) instead of (7.4). Then there exist constants $k > 0$ and $C > 0$ depending only on $n, p, \delta, \alpha, \varepsilon, \theta, C_1, C_2$, and on the limit in the left-hand side of (7.10) such that the condition (7.15) implies estimate (7.16).*

References

- Andres J, Bersani AM, Leśniak K (2001) On some almost-periodicity problems in various metrics. *Acta Applicandae Mathematica* 65(1-3):35–57
- Björn J (2001) Boundedness and differentiability for nonlinear elliptic systems. *Transactions of the American Mathematical Society* 353(11):4545–4565
- dell'Isola F, Seppecher P, Alibert JJ, et al (2019a) Pantographic metamaterials: an example of mathematically driven design and of its technological challenges. *Continuum Mechanics and Thermodynamics* 31(4):851–884
- dell'Isola F, Seppecher P, Spagnuolo M, et al (2019b) Advances in pantographic structures: design, manufacturing, models, experiments and image analyses. *Continuum Mechanics and Thermodynamics* 31(4):1231–1282
- Gariepy R, Ziemer WP (1977) A regularity condition at the boundary for solutions of quasilinear elliptic equations. *Archive for Rational Mechanics and Analysis* 67(1):25–39
- Iannacci R, Bersani AM, Dell'Acqua G, Santucci P (1998) Embedding theorems for Sobolev–Besicovitch spaces of almost periodic functions. *Zeitschrift für Analysis und ihre Anwendungen* 17(2):443–457
- Kon'kov AA (2004) Comparison theorems for second-order elliptic inequalities. *Nonlinear Analysis: Theory, Methods & Applications* 59(4):583–608
- Kon'kov AA (2014) On comparison theorems for quasi-linear elliptic inequalities with a special account of the geometry of the domain. *Izvestiya: Mathematics* 78(4):758
- Landis EM (1997) Second order equations of elliptic and parabolic type. *American Mathematical Soc.*
- Littman W, Stampacchia G, Weinberger HF (1963) Regular points for elliptic equations with discontinuous coefficients. *Annali della Scuola Normale Superiore di Pisa-Classe di Scienze* 17(1-2):43–77
- Maz'ya VG (1970) On the continuity at a boundary point of the solution of quasi-linear elliptic equations. *Vestnik Leningrad Univ* 25:42–55
- Wiener N (1924a) Certain notions in potential theory. *Journal of Mathematics and Physics* 3(1):24–51
- Wiener N (1924b) The Dirichlet problem. *Journal of Mathematics and Physics* 3(3):127–146



Chapter 8

Integrable Dissipative Dynamical Systems with Three and Four Degrees of Freedom

Maxim V. Shamolin

Abstract In this work, the integrability of some classes of dynamic systems on tangent bundles of three-dimensional manifolds is demonstrated. The corresponding force fields possess the so-called variable dissipation and generalize those considered earlier.

Keywords: Dynamic systems · Tangent bundles

8.1 Introduction

In many problems of dynamics, there appear mechanical systems with three-dimensional manifolds as position spaces. Tangent bundles of such manifolds naturally become phase spaces of such systems. For example, study of a four-dimensional generalized spherical pendulum in a nonconservative force field leads to a dynamic system on the tangent bundle of a three-dimensional sphere, and the metric of special form on it is induced by an additional symmetry group (Bogoyavlenskii, 1986; Bogoyavlenskii and Ivakh, 1985). In this case, dynamic systems describing the motion of such a pendulum possess alternating dissipation and the complete list of first integrals consists of transcendental functions that can be expressed in terms of a finite combination of elementary functions (Bogoyavlenskii and Ivakh, 1985; Dubrovin and Novikov, 1984).

The class of problems about the motion of a point on a three-dimensional surface is also known; the metric on it is induced by the Euclidean metric of the ambient space. In some cases of systems with dissipation, it is also possible to find a complete list of first integrals; the list consists of transcendental functions. The results obtained

M. V. Shamolin
Institute of Mechanics, Lomonosov Moscow State University, 1 Michurinskii Ave., 119192,
Moscow, Russian Federation
e-mail: shamolin@imec.msu.ru

are especially important in the aspect of the presence of just a nonconservative force field in the system (see, e.g., Giorgio and Scerrato, 2017; Baroudi et al, 2019; dell'Isola et al, 2019a,b).

8.2 Equations of Geodesic Lines

It is well known that, in the case of a three-dimensional Riemannian manifold M^3 with coordinates (α, β) , $\beta = (\beta_1, \beta_2)$, and affine connection $\Gamma_{jk}^i(x)$ the equations of geodesic lines on the tangent bundle $T_*M^3\{\dot{\alpha}, \dot{\beta}_1, \dot{\beta}_2; \alpha, \beta_1, \beta_2\}$, $\alpha = x^1$, $\beta_1 = x^2$, $\beta_2 = x^3$, $x = (x^1, x^2, x^3)$, have the following form (the derivatives are taken with respect to the natural parameter):

$$\ddot{x}^i + \sum_{j,k=1}^3 \Gamma_{jk}^i(x) \dot{x}^j \dot{x}^k = 0, \quad i = 1, 2, 3. \quad (8.1)$$

Let us study the structure of Eqs. (8.1) under a change of coordinates on the tangent bundle T_*M^3 . Consider a change of coordinates of the tangent space:

$$\dot{x}^i = \sum_{j=1}^3 R^{ij}(x) z_j, \quad (8.2)$$

which can be inverted:

$$z_j = \sum_{i=1}^3 T_{ji}(x) \dot{x}^i,$$

herewith R^{ij} , T_{ji} , $i, j = 1, 2, 3$, are functions of x^1, x^2, x^3 , and

$$RT = E,$$

$$R = R^{ij}, \quad T = T_{ji}.$$

We also call Eqs. (8.2) new kinematic relations, i.e., relations on the tangent bundle T_*M^3 .

The following equalities are valid:

$$\dot{z}_j = \sum_{i=1}^3 \dot{T}_{ji} \dot{x}^i + \sum_{i=1}^3 T_{ji} \ddot{x}^i, \quad \dot{T}_{ji} = \sum_{k=1}^3 T_{ji,k} \dot{x}^k, \quad (8.3)$$

$$T_{ji,k} = \frac{\partial T_{ji}}{\partial x^k}, \quad j, i, k = 1, 2, 3.$$

If we substitute Eqs. (8.1) to Eqs. (8.3), we have:

$$\dot{z}_i = \sum_{j,k=1}^3 T_{ij,k} \dot{x}^j \dot{x}^k - \sum_{j,p,q=1}^3 T_{ij} \Gamma_{pq}^j \dot{x}^p \dot{x}^q, \tag{8.4}$$

in the last system, one should substitute formulas (8.2) instead of \dot{x}^i , $i = 1, 2, 3$.

Furthermore, Eq. (8.4) we can rewrite:

$$\dot{z}_i + \sum_{j,k=1}^3 Q_{ijk} \dot{x}^j \dot{x}^k |_{(8.2)} = 0, \tag{8.5}$$

$$Q_{ijk}(x) = \sum_{s=1}^3 T_{is}(x) \Gamma_{jk}^s(x) - T_{ij,k}(x). \tag{8.6}$$

Proposition 1 *System (8.1) is equivalent to compound system (8.2), (8.4) in a domain where $\det R(x) \neq 0$.*

Therefore, the result of the passage from equations of geodesic lines (8.1) to an equivalent system of equations (8.2), (8.4) depends both on the change of variables (8.2) (i.e., introduced kinematic relations) and on the affine connection $\Gamma_{jk}^i(x)$.

8.3 A Fairly General Case

Consider next a sufficiently general case of specifying kinematic relations in the following form:

$$\begin{cases} \dot{\alpha} = -z_3, \\ \dot{\beta}_1 = z_2 f_1(\alpha), \\ \dot{\beta}_2 = z_1 f_2(\alpha) g(\beta_1), \end{cases} \tag{8.7}$$

where $f_1(\alpha)$, $f_2(\alpha)$, $g(\beta_1)$ are smooth functions on their domain of definition. Such coordinates z_1, z_2, z_3 in the tangent space are introduced when the following equations of geodesic lines are considered (Kozlov, 1983; Shamolin, 2015c) (in particular, on surfaces of revolution):

$$\begin{cases} \ddot{\alpha} + \Gamma_{11}^\alpha(\alpha, \beta) \dot{\beta}_1^2 + \Gamma_{22}^\alpha(\alpha, \beta) \dot{\beta}_2^2 = 0, \\ \ddot{\beta}_1 + 2\Gamma_{\alpha 1}^1(\alpha, \beta) \dot{\alpha} \dot{\beta}_1 + \Gamma_{22}^1(\alpha, \beta) \dot{\beta}_2^2 = 0, \\ \ddot{\beta}_2 + 2\Gamma_{\alpha 2}^2(\alpha, \beta) \dot{\alpha} \dot{\beta}_2 + 2\Gamma_{12}^2(\alpha, \beta) \dot{\beta}_1 \dot{\beta}_2 = 0, \end{cases} \tag{8.8}$$

i.e., other connection coefficients are zero. In case (8.7), Eqs. (8.4) take the form

$$\begin{cases} \dot{z}_1 = \left[2\Gamma_{\alpha 2}^2(\alpha, \beta) + \frac{d \ln |f_2(\alpha)|}{d\alpha} \right] z_1 z_3 - \left[2\Gamma_{12}^2(\alpha, \beta) + \frac{d \ln |g(\beta_1)|}{d\beta_1} \right] f_1(\alpha) z_1 z_2, \\ \dot{z}_2 = \left[2\Gamma_{\alpha 1}^1(\alpha, \beta) + \frac{d \ln |f_1(\alpha)|}{d\alpha} \right] z_2 z_3 - \Gamma_{22}^1(\alpha, \beta) \frac{f_2^2(\alpha)}{f_1(\alpha)} g^2(\beta_1) z_1^2, \\ \dot{z}_3 = \Gamma_{11}^\alpha f_1^2(\alpha) z_2^2 + \Gamma_{22}^\alpha f_2^2(\alpha) g^2(\beta_1) z_1^2, \end{cases} \tag{8.9}$$

and Eqs. (8.8) are almost everywhere equivalent to compound system (8.7), (8.9) on the manifold $T_*M^3\{z_3, z_2, z_1; \alpha, \beta_1, \beta_2\}$.

To integrate system (8.7), (8.9) completely, it is necessary to know, generally speaking, five independent first integrals.

Proposition 2 *If the system of equalities*

$$\left\{ \begin{array}{l} 2\Gamma_{\alpha 1}^1(\alpha, \beta) + \frac{d \ln |f_1(\alpha)|}{d\alpha} + \Gamma_{11}^\alpha(\alpha, \beta) f_1^2(\alpha) \equiv 0, \\ 2\Gamma_{\alpha 2}^2(\alpha, \beta) + \\ + \frac{d \ln |f_2(\alpha)|}{d\alpha} + \Gamma_{22}^\alpha(\alpha, \beta) f_2^2(\alpha) g^2(\beta_1) \equiv 0, \\ \left[2\Gamma_{12}^2(\alpha, \beta) + \frac{d \ln |g(\beta_1)|}{d\beta_1} \right] f_1^2(\alpha) + \Gamma_{22}^1(\alpha, \beta) f_2^2(\alpha) g^2(\beta_1) \equiv 0, \end{array} \right. \quad (8.10)$$

is valid everywhere in its domain of definition, system (8.7), (8.9) has an analytic first integral of the form

$$\Phi_1(z_3, z_2, z_1) = z_1^2 + z_2^2 + z_3^2 = C_1^2 = \text{const}. \quad (8.11)$$

We suppose that the condition

$$f_1(\alpha) = f_2(\alpha) = f(\alpha), \quad (8.12)$$

is satisfied in Eqs. (8.7); the function $g(\beta_1)$ must satisfy the transformed third equality from (8.10):

$$2\Gamma_{12}^2(\alpha, \beta) + \frac{d \ln |g(\beta_1)|}{d\beta_1} + \Gamma_{22}^1(\alpha, \beta) g^2(\beta_1) \equiv 0. \quad (8.13)$$

Proposition 3 *If properties (8.12) and (8.13) are valid and the equalities*

$$\Gamma_{\alpha 1}^1(\alpha, \beta) = \Gamma_{\alpha 2}^2(\alpha, \beta) = \Gamma_1(\alpha), \quad (8.14)$$

are satisfied, system (8.7), (8.9) has a smooth first integral of the following form:

$$\Phi_2(z_2, z_1; \alpha) = \sqrt{z_1^2 + z_2^2} \Phi_0(\alpha) = C_2 = \text{const}, \quad (8.15)$$

$$\Phi_0(\alpha) = f(\alpha) \exp \left\{ 2 \int_{\alpha_0}^{\alpha} \Gamma_1(b) db \right\}.$$

Proposition 4 *If property (8.12) is valid and the equality*

$$\Gamma_{12}^2(\alpha, \beta) = \Gamma_2(\beta_1), \quad (8.16)$$

and the second equality from (8.14) ($\Gamma_{\alpha 2}^2(\alpha, \beta) = \Gamma_1(\alpha)$) are satisfied, system (8.7), (8.9) has a smooth first integral of the following form:

$$\Phi_3(z_1; \alpha, \beta_1) = z_1 \Phi_0(\alpha) \Phi(\beta_1) = C_3 = \text{const}, \quad (8.17)$$

$$\Phi(\beta_1) = g(\beta_1) \exp \left\{ 2 \int_{\beta_{10}}^{\beta_1} \Gamma_2(b) db \right\}.$$

Proposition 5 *If conditions (8.12), (8.13), (8.14), (8.16) are satisfied, system (8.7), (8.9) has a first integral of the following form:*

$$\Phi_4(z_2, z_1; \beta) = \beta_2 \pm \int_{\beta_{10}}^{\beta_1} \frac{C_3 g(b)}{\sqrt{C_2^2 \Phi^2(b) - C_3^2}} db = C_4 = \text{const}, \quad (8.18)$$

where, after taking integral (8.18), one should substitute the left-hand sides of equalities (8.15), (8.17) instead of the constants C_2, C_3 , respectively.

Under the conditions listed above, system (8.7), (8.9) has a complete set (four) of independent first integrals of the form (8.11), (8.15), (8.17), (8.18).

8.4 Potential Field of Force

Let us now somewhat modify system (8.7), (8.9) under conditions (8.12), (8.13), (8.14), (8.16), which yields a conservative system. Namely, the presence of the force field is characterized by the coefficient $F(\alpha)$ in the second equation of system (8.19) at $b = 0$. The system under consideration on the tangent bundle $T_*M^3\{z_3, z_2, z_1; \alpha, \beta_1, \beta_2\}$ takes the form

$$\left\{ \begin{array}{l} \dot{\alpha} = -z_3 + b\delta(\alpha), \\ \dot{z}_3 = F(\alpha) + \Gamma_{11}^\alpha(\alpha, \beta) f^2(\alpha) z_2^2 + \Gamma_{22}^\alpha(\alpha, \beta) f^2(\alpha) g^2(\beta_1) z_1^2, \\ \dot{z}_2 = \left[2\Gamma_1(\alpha) + \frac{d \ln |f(\alpha)|}{d\alpha} \right] z_2 z_3 - \Gamma_{22}^1(\beta_1) f(\alpha) g^2(\beta_1) z_1^2, \\ \dot{z}_1 = \left[2\Gamma_1(\alpha) + \frac{d \ln |f(\alpha)|}{d\alpha} \right] z_1 z_3 - \left[2\Gamma_2(\beta_1) + \frac{d \ln |g(\beta_1)|}{d\beta_1} \right] f(\alpha) z_1 z_2, \\ \dot{\beta}_1 = z_2 f(\alpha), \\ \dot{\beta}_2 = z_1 f(\alpha) g(\beta_1), \end{array} \right. \quad (8.19)$$

and at $b = 0$ it is almost everywhere equivalent to the following system:

$$\left\{ \begin{array}{l} \ddot{\alpha} + F(\alpha) + \Gamma_{11}^\alpha(\alpha, \beta) \dot{\beta}_1^2 + \Gamma_{22}^\alpha(\alpha, \beta) \dot{\beta}_2^2 = 0, \\ \ddot{\beta}_1 + 2\Gamma_1(\alpha) \dot{\alpha} \dot{\beta}_1 + \Gamma_{22}^1(\beta_1) \dot{\beta}_2^2 = 0, \\ \ddot{\beta}_2 + 2\Gamma_1(\alpha) \dot{\alpha} \dot{\beta}_2 + 2\Gamma_2(\beta_1) \dot{\beta}_1 \dot{\beta}_2 = 0. \end{array} \right.$$

Proposition 6 *If the conditions of Proposition 2 are satisfied, system (8.19) at $b = 0$ has a smooth first integral of the following form:*

$$\begin{aligned} \Phi_1(z_3, z_2, z_1; \alpha) &= z_1^2 + z_2^2 + z_3^2 + F_1(\alpha) = \\ &= C_1 = \text{const}, \quad F_1(\alpha) = 2 \int_{\alpha_0}^{\alpha} F(a) da. \end{aligned} \quad (8.20)$$

Proposition 7 *If the conditions of Propositions 3, 4 are satisfied, system (8.19) at $b = 0$ has two smooth first integrals of form (8.15), (8.17).*

Proposition 8 *If the conditions of Proposition 5 are satisfied, system (8.19) at $b = 0$ has a first integral of form (8.18).*

Under the conditions listed above, system (8.19) at $b = 0$ has a complete set of (four) independent first integrals of form (8.20), (8.15), (8.17), (8.18).

8.5 Force Field with Dissipation

Let us now consider system (8.19) at $b \neq 0$. In doing this, we obtain a system with dissipation. Namely, the presence of dissipation (generally speaking, sign-alternating) is characterized by the coefficient $b\delta(\alpha)$ in the first equation of system (8.19), which is almost everywhere equivalent to the following system:

$$\begin{cases} \ddot{\alpha} - b\dot{\alpha}\delta'(\alpha) + F(\alpha) + \Gamma_{11}^\alpha(\alpha, \beta)\dot{\beta}_1^2 + \Gamma_{22}^\alpha(\alpha, \beta)\dot{\beta}_2^2 = 0, \\ \ddot{\beta}_1 - b\dot{\beta}_1\delta(\alpha) \left[2\Gamma_1(\alpha) + \frac{d \ln |f(\alpha)|}{d\alpha} \right] + 2\Gamma_1(\alpha)\dot{\alpha}\dot{\beta}_1 + \Gamma_{22}^1(\beta_1)\dot{\beta}_2^2 = 0, \\ \ddot{\beta}_2 - b\dot{\beta}_2\delta(\alpha) \left[2\Gamma_1(\alpha) + \frac{d \ln |f(\alpha)|}{d\alpha} \right] + 2\Gamma_1(\alpha)\dot{\alpha}\dot{\beta}_2 + 2\Gamma_2(\beta_1)\dot{\beta}_1\dot{\beta}_2 = 0. \end{cases}$$

Now we pass to integration of the sought six-order system (8.19) under condition (8.13), as well as under the equalities

$$\Gamma_{11}^\alpha(\alpha, \beta) = \Gamma_{22}^\alpha(\alpha, \beta)g^2(\beta_1) = \Gamma_3(\alpha). \quad (8.21)$$

We also introduce (by analogy with (8.13)) a restriction on the function $f(\alpha)$. It must satisfy the transformed first equality from (8.10):

$$2\Gamma_1(\alpha) + \frac{d \ln |f(\alpha)|}{d\alpha} + \Gamma_3(\alpha)f^2(\alpha) \equiv 0. \quad (8.22)$$

To integrate it completely, one should know, generally speaking, five independent first integrals. However, after the following change of variables,

$$z_1, z_2 \rightarrow z, z_*, z = \sqrt{z_1^2 + z_2^2}, z_* = \frac{z_2}{z_1},$$

system (8.19) decomposes as follows:

$$\begin{cases} \dot{\alpha} = -z_3 + b\delta(\alpha), \\ \dot{z}_3 = F(\alpha) + \Gamma_3(\alpha)f^2(\alpha)z^2, \\ \dot{z} = \left[2\Gamma_1(\alpha) + \frac{d \ln |f(\alpha)|}{d\alpha} \right] z z_3, \end{cases} \quad (8.23)$$

$$\begin{cases} \dot{z}_* = \pm z \sqrt{1 + z_*^2} f(\alpha) \left[2\Gamma_2(\beta_1) + \frac{d \ln |g(\beta_1)|}{d\beta_1} \right], \\ \dot{\beta}_1 = \pm \frac{z z_*}{\sqrt{1 + z_*^2}} f(\alpha), \end{cases} \tag{8.24}$$

$$\dot{\beta}_2 = \pm \frac{z}{\sqrt{1 + z_*^2}} f(\alpha) g(\beta_1). \tag{8.25}$$

It is seen that to integrate system (8.23)–(8.25) completely, it is sufficient to determine two independent first integrals of system (8.23), one integral of system (8.24), and an additional first integral attaching Eq. (8.25) (i.e., four integrals in total).

Theorem 11 *Let the equalities*

$$\Gamma_3(\alpha) f^2(\alpha) = \kappa \frac{d}{d\alpha} \ln |\delta(\alpha)|, \quad F(\alpha) = \lambda \frac{d}{d\alpha} \frac{\delta^2(\alpha)}{2} \tag{8.26}$$

be valid for some $\kappa, \lambda \in \mathbf{R}$. Then system (8.19) under equalities (8.13), (8.21), (8.22) has a complete set of (four) independent, generally speaking, transcendental first integrals.

In the general case, the first integrals are written awkwardly. In particular, if $\kappa = -1$, the explicit form of one of first integrals for system (8.23) is as follows:

$$\Theta_1(z_3, z; \alpha) = G_1 \left(\frac{z_3}{\delta(\alpha)}, \frac{z}{\delta(\alpha)} \right) = \frac{z_3^2 + z^2 - bz_3\delta(\alpha) + \lambda\delta^2(\alpha)}{z\delta(\alpha)} = C_1 = \text{const.} \tag{8.27}$$

Here, the additional first integral for system (8.23) has the following structural form:

$$\Theta_2(z_3, z; \alpha) = G_2 \left(\delta(\alpha), \frac{z_3}{\delta(\alpha)}, \frac{z}{\delta(\alpha)} \right) = C_2 = \text{const.} \tag{8.28}$$

Here, after taking the integral, one should substitute the left-hand side of equality (8.27) for C_1 . The right-hand side of this equality is expressed through a finite combination of elementary functions; the left-hand part, depending on the function $\delta(\alpha)$. Therefore, expressing first integrals (8.27), (8.28) through a finite combination of elementary functions depends not only on calculation of quadratures but also on the explicit form of the function $\delta(\alpha)$.

The first integral for system (8.24) has the form

$$\Theta_3(z_*; \beta_1) = \frac{\sqrt{1 + z_*^2}}{\Phi(\beta_1)} = C_3 = \text{const}, \tag{8.29}$$

as for the function $\Phi(\beta_1)$, see (8.17). The additional first integral attaching Eq. (8.25) is found by analogy with (8.18):

$$\Theta_4(z_*; \beta) = \beta_2 \pm \int_{\beta_{10}}^{\beta_1} \frac{g(b)}{\sqrt{C_3^2 \Phi^2(b) - 1}} db = C_4 = \text{const},$$

here, after taking this integral, one should substitute the left-hand side of equality (8.29) for C_3 .

8.6 Structure of Transcendental First Integrals

If α is a periodic coordinate with a period of 2π , system (8.23) becomes a dynamic system with variable dissipation with a zero mean (Shamolin, 2015a,b, 2016a). At $b = 0$, it turns into a conservative system having two smooth first integrals of form (8.20), (8.15). By virtue of (8.26),

$$\Phi_1(z_3, z_2, z_1; \alpha) = z_1^2 + z_2^2 + z_3^2 + 2 \int_{\alpha_0}^{\alpha} F(a) da \cong z^2 + z_3^2 + \lambda \delta^2(\alpha), \quad (8.30)$$

where “ \cong ” means equality up to an additive constant. At the same time, by virtue of (8.22) and (8.26),

$$\Phi_2(z_2, z_1; \alpha) = \sqrt{z_1^2 + z_2^2} f(\alpha) \exp \left\{ 2 \int_{\alpha_0}^{\alpha} \Gamma_1(b) db \right\} \cong z \delta(\alpha) = C_2 = \text{const}, \quad (8.31)$$

where “ \cong ” now means equality up to a multiplicative additive constant.

It is evident that the ratio of the two first integrals (8.30) and (8.31) (or, (8.20) and (8.15)) is also a first integral of system (8.23) for $b = 0$. However, at $b \neq 0$, each of the functions

$$z^2 + z_3^2 - bz_3 \delta(\alpha) + \lambda \delta^2(\alpha) \quad (8.32)$$

and (8.31) taken individually is not a first integral of system (8.23). However, the ratio of functions (8.32) and (8.31) is a first integral of system (8.23) (at $\kappa = -1$) for any b .

Generally, for systems with dissipation, transcendence of functions (in the aspect of the presence of essentially singular points) as first integrals is inherited from the existence of attracting and repelling limit sets in the system (Shamolin, 2016b, 2017a).

8.7 Conclusions

By analogy with low-dimensional cases, we pay special attention to two important cases for the function $f(\alpha)$ defining the metric on a sphere:

$$f(\alpha) = \frac{\cos \alpha}{\sin \alpha}, \quad (8.33)$$

$$f(\alpha) = \frac{1}{\cos \alpha \sin \alpha}. \quad (8.34)$$

Case (8.33) forms a class of systems corresponding to the motion of a dynamically symmetric four-dimensional solid body at zero levels of cyclic integrals, generally speaking, in a nonconservative field of forces (Shamolin, 2017b,c). Case (8.34) forms a class of systems corresponding to the motion of a material point on a three-dimensional sphere also, generally speaking, in a nonconservative field of forces. In particular, at

$$\delta(\alpha) \equiv F(\alpha) \equiv 0,$$

the system under consideration describes a geodesic flow on a three-dimensional sphere. In case (8.33), the system describes the spatial motion of a four-dimensional solid body in the force field under the action of a tracking force (Shamolin, 2017c). In particular, if

$$\delta(\alpha) = \frac{F(\alpha)}{\cos \alpha},$$

and

$$\delta(\alpha) = \sin \alpha,$$

the system also describes a generalized four-dimensional spherical pendulum in a nonconservative force field and has a complete set of transcendental first integrals that can be expressed in terms of a finite combination of elementary functions.

If the function $\delta(\alpha)$ is not periodic, the dissipative system under consideration is a system with variable dissipation with a zero mean (i.e., it is properly dissipative). Nevertheless, an explicit form of transcendental first integrals that can be expressed in terms of a finite combination of elementary functions can be obtained even in this case. This is a new nontrivial case of integrability of dissipative systems in an explicit form.

8.8 Important Example: Case of Four-Dimensional Manifold

We consider the rather general case of introducing the kinematic relations in the form

$$\dot{\alpha} = -z_4, \quad \dot{\beta}_1 = z_3 f_1(\alpha), \quad \dot{\beta}_2 = z_2 f_2(\alpha) g_1(\beta_1), \quad \dot{\beta}_3 = z_1 f_3(\alpha) g_2(\beta_1) h(\beta_2), \quad (8.35)$$

where $f_k(\alpha)$, $k = 1, 2, 3$, $g_l(\beta_1)$, $l = 1, 2$, $h(\beta_2)$, are smooth functions. Such coordinates z_1, z_2, z_3, z_4 are introduced in the tangent space if the following classes of geodesic equations are considered (in particular, on spheres or more general surfaces of revolution):

$$\begin{cases} \ddot{\alpha} + \Gamma_{11}^\alpha(\alpha, \beta) \dot{\beta}_1^2 + \Gamma_{22}^\alpha(\alpha, \beta) \dot{\beta}_2^2 + \Gamma_{33}^\alpha(\alpha, \beta) \dot{\beta}_3^2 = 0, \\ \ddot{\beta}_1 + 2\Gamma_{\alpha 1}^1(\alpha, \beta) \dot{\alpha} \dot{\beta}_1 + \Gamma_{22}^1(\alpha, \beta) \dot{\beta}_2^2 + \Gamma_{33}^1(\alpha, \beta) \dot{\beta}_3^2 = 0, \\ \ddot{\beta}_2 + 2\Gamma_{\alpha 2}^2(\alpha, \beta) \dot{\alpha} \dot{\beta}_2 + 2\Gamma_{12}^2(\alpha, \beta) \dot{\beta}_1 \dot{\beta}_2 + \Gamma_{33}^2(\alpha, \beta) \dot{\beta}_3^2 = 0, \\ \ddot{\beta}_3 + 2\Gamma_{\alpha 3}^3(\alpha, \beta) \dot{\alpha} \dot{\beta}_3 + 2\Gamma_{13}^3(\alpha, \beta) \dot{\beta}_1 \dot{\beta}_3 + 2\Gamma_{23}^3(\alpha, \beta) \dot{\beta}_2 \dot{\beta}_3 = 0, \end{cases} \quad (8.36)$$

i.e., the remaining connection coefficients vanish. In the case (8.35), we can write (8.4) as

$$\begin{aligned}
\dot{z}_1 &= \left[2\Gamma_{\alpha 3}^3(\alpha, \beta) + \frac{d \ln |f_3(\alpha)|}{d\alpha} \right] z_1 z_4 - \left[2\Gamma_{13}^3(\alpha, \beta) + \frac{d \ln |g_2(\beta_1)|}{d\beta_1} \right] f_1(\alpha) z_1 z_3 - \\
&\quad - \left[2\Gamma_{23}^3(\alpha, \beta) + \frac{d \ln |h(\beta_2)|}{d\beta_2} \right] f_2(\alpha) g_1(\beta_1) z_1 z_2, \\
\dot{z}_2 &= \left[2\Gamma_{\alpha 2}^2(\alpha, \beta) + \frac{d \ln |f_2(\alpha)|}{d\alpha} \right] z_2 z_4 - \left[2\Gamma_{12}^2(\alpha, \beta) + \frac{d \ln |g_1(\beta_1)|}{d\beta_1} \right] f_1(\alpha) z_2 z_3 - \\
&\quad - \Gamma_{33}^2(\alpha, \beta) \frac{f_3^2(\alpha)}{f_2(\alpha)} \frac{g_2^2(\beta_1)}{g_1(\beta_1)} h^2(\beta_2) z_1^2, \\
\dot{z}_3 &= \left[2\Gamma_{\alpha 1}^1(\alpha, \beta) + \frac{d \ln |f_1(\alpha)|}{d\alpha} \right] z_3 z_4 - \Gamma_{22}^1(\alpha, \beta) \frac{f_2^2(\alpha)}{f_1(\alpha)} g_1^2(\beta_1) z_2^2 - \\
&\quad - \Gamma_{33}^1(\alpha, \beta) \frac{f_3^2(\alpha)}{f_1(\alpha)} g_2^2(\beta_1) h^2(\beta_2) z_1^2, \\
\dot{z}_4 &= \Gamma_{11}^\alpha f_1^2(\alpha) z_3^2 + \Gamma_{22}^\alpha f_2^2(\alpha) g_1^2(\beta_1) z_2^2 + \Gamma_{33}^\alpha f_3^2(\alpha) g_2^2(\beta_1) h^2(\beta_2) z_1^2,
\end{aligned} \tag{8.37}$$

and the system (8.36) is almost everywhere equivalent to the composite system (8.35), (8.37) on the tangent bundle $T_*M^4\{z_4, z_3, z_2, z_1; \alpha, \beta_1, \beta_2, \beta_3\}$.

Generally speaking, for the complete integrability of the system (8.35), (8.37) we need to know seven independent first integrals. However, a less number of first integrals is required in the case under consideration, which will be shown in the study of systems with dissipation below.

Proposition 9 *If the following identities hold everywhere on their domain:*

$$\left\{ \begin{array}{l}
2\Gamma_{\alpha 1}^1(\alpha, \beta) + \frac{d \ln |f_1(\alpha)|}{d\alpha} + \Gamma_{11}^\alpha(\alpha, \beta) f_1^2(\alpha) \equiv 0, \\
2\Gamma_{\alpha 2}^2(\alpha, \beta) + \frac{d \ln |f_2(\alpha)|}{d\alpha} + \Gamma_{22}^\alpha(\alpha, \beta) f_2^2(\alpha) g_1^2(\beta_1) \equiv 0, \\
\left[2\Gamma_{12}^2(\alpha, \beta) + \frac{d \ln |g_1(\beta_1)|}{d\beta_1} \right] f_1^2(\alpha) + \Gamma_{22}^1(\alpha, \beta) f_2^2(\alpha) g_1^2(\beta_1) \equiv 0, \\
2\Gamma_{\alpha 3}^3(\alpha, \beta) + \frac{d \ln |f_3(\alpha)|}{d\alpha} + \Gamma_{33}^\alpha(\alpha, \beta) f_3^2(\alpha) g_2^2(\beta_1) h^2(\beta_2) \equiv 0, \\
\left[2\Gamma_{13}^3(\alpha, \beta) + \frac{d \ln |g_2(\beta_1)|}{d\beta_1} \right] f_1^2(\alpha) + \Gamma_{33}^1(\alpha, \beta) f_3^2(\alpha) g_2^2(\beta_1) h^2(\beta_2) \equiv 0, \\
\left[2\Gamma_{23}^3(\alpha, \beta) + \frac{d \ln |h(\beta_2)|}{d\beta_2} \right] f_2^2(\alpha) g_1^2(\beta_1) + \Gamma_{33}^2(\alpha, \beta) f_3^2(\alpha) g_2^2(\beta_1) h^2(\beta_2) \equiv 0,
\end{array} \right. \tag{8.38}$$

then the system (8.35), (8.37) has an analytic first integral of the form

$$\Phi_1(z_4, \dots, z_1) = z_1^2 + \dots + z_4^2 = C_1^2 = \text{const}. \tag{8.39}$$

We apply an approach allowing us to find successfully the complete list of first integrals of systems with dissipation by using the solutions to the system (8.38). We assume that in (8.35) the following conditions are satisfied:

$$f_1(\alpha) = f_2(\alpha) = f_3(\alpha) = f(\alpha), \tag{8.40}$$

moreover, $g_l(\beta_1)$, $l = 1, 2$, $h(\beta_2)$ satisfy the transformed equations from (8.38):

$$\left\{ \begin{array}{l}
2\Gamma_{12}^2(\alpha, \beta) + \frac{d \ln |g_1(\beta_1)|}{d\beta_1} + \Gamma_{22}^1(\alpha, \beta) g_1^2(\beta_1) \equiv 0, \\
2\Gamma_{13}^3(\alpha, \beta) + \frac{d \ln |g_2(\beta_1)|}{d\beta_1} + \Gamma_{33}^1(\alpha, \beta) g_2^2(\beta_1) h^2(\beta_2) \equiv 0, \\
2\Gamma_{23}^3(\alpha, \beta) + \frac{d \ln |h(\beta_2)|}{d\beta_2} + \Gamma_{33}^2(\alpha, \beta) h^2(\beta_2) \equiv 0.
\end{array} \right. \tag{8.41}$$

Proposition 10 *If (8.40) and (8.41), hold and*

$$\Gamma_{\alpha_1}^1(\alpha, \beta) = \Gamma_{\alpha_2}^2(\alpha, \beta) = \Gamma_{\alpha_3}^3(\alpha, \beta) = \Gamma_1(\alpha), \quad (8.42)$$

then the system (8.35), (8.37) has a smooth first integral of the form

$$\Phi_2(z_3, z_2, z_1; \alpha) = \sqrt{z_1^2 + z_2^2 + z_3^2} \Phi_0(\alpha) = C_2 = \text{const}, \quad (8.43)$$

$$\Phi_0(\alpha) = f(\alpha) \exp \left\{ 2 \int_{\alpha_0}^{\alpha} \Gamma_1(b) db \right\}.$$

Proposition 11 *Under the assumptions of Proposition 10, if*

$$g_1(\beta_1) = g_2(\beta_1) = g(\beta_1), \quad (8.44)$$

$$\Gamma_{12}^2(\alpha, \beta) = \Gamma_{13}^3(\alpha, \beta) = \Gamma_2(\beta_1), \quad (8.45)$$

then the system (8.35), (8.37) has a smooth first integral of the form

$$\Phi_3(z_2, z_1; \alpha, \beta_1) = \sqrt{z_1^2 + z_2^2} \Phi_0(\alpha) \Psi_1(\beta_1) = C_3 = \text{const}, \quad (8.46)$$

where

$$\Psi_1(\beta_1) = g(\beta_1) \exp \left\{ 2 \int_{\beta_{10}}^{\beta_1} \Gamma_2(b) db \right\}.$$

The following two assertions are proved in the same way as Propositions 10 and 11.

Proposition 12 *Under the assumptions of Propositions 10 and 11, if*

$$\Gamma_{23}^3(\alpha, \beta) = \Gamma_3(\beta_2), \quad (8.47)$$

then the system (8.35), (8.37) has a smooth first integral of the form

$$\Phi_4(z_1; \alpha, \beta_1, \beta_2) = z_1 \Phi_0(\alpha) \Psi_1(\beta_1) \Psi_2(\beta_2) = C_4 = \text{const}, \quad (8.48)$$

where

$$\Psi_2(\beta_2) = h(\beta_2) \exp \left\{ 2 \int_{\beta_{20}}^{\beta_2} \Gamma_3(b) db \right\}.$$

Proposition 13 *Under the assumptions of Propositions 10, 11, and 12, the system (8.35), (8.37) has a first integral of the form*

$$\Phi_5(z_2, z_1; \alpha, \beta) = \beta_3 \pm \int_{\beta_{20}}^{\beta_2} \frac{C_4 h(b)}{\sqrt{C_3^2 \Phi_2^2(b) - C_4^2}} db = C_5 = \text{const}. \quad (8.49)$$

The first integrals (8.39), (8.43), (8.46), (8.48), (8.49) form the complete list of independent first integrals of the system (8.35), (8.37) under the above conditions

(the fact that only five (instead of seven) first integrals are included into the complete list will be justified below).

8.8.1 Equations of Motion in a Potential Force Field and First Integrals

Modifying the system (8.35), (8.37) under the conditions (8.40)–(8.42), (8.44), (8.45), (8.47), we obtain a conservative system. Namely, the presence of a force field is characterized by a sufficiently smooth coefficient $F(\alpha)$ in the second equation of the system (8.50). The system under consideration on the tangent bundle $T_*M^4\{z_4, z_3, z_2, z_1; \alpha, \beta_1, \beta_2, \beta_3\}$ takes the form

$$\left\{ \begin{array}{l} \dot{\alpha} = -z_4, \\ \dot{z}_4 = F(\alpha) + \Gamma_{11}^\alpha f_1^2(\alpha) z_3^2 + \Gamma_{22}^\alpha f_2^2(\alpha) g_1^2(\beta_1) z_2^2 + \Gamma_{33}^\alpha f_3^2(\alpha) g_2^2(\beta_1) h^2(\beta_2) z_1^2, \\ \dot{z}_3 = \left[2\Gamma_{\alpha 1}^1(\alpha, \beta) + \frac{d \ln |f_1(\alpha)|}{d\alpha} \right] z_3 z_4 - \Gamma_{22}^1(\alpha, \beta) \frac{f_2^2(\alpha)}{f_1(\alpha)} g_1^2(\beta_1) z_2^2 - \\ \quad - \Gamma_{33}^1(\alpha, \beta) \frac{f_3^2(\alpha)}{f_1(\alpha)} g_2^2(\beta_1) h^2(\beta_2) z_1^2, \\ \dot{z}_2 = \left[2\Gamma_{\alpha 2}^2(\alpha, \beta) + \frac{d \ln |f_2(\alpha)|}{d\alpha} \right] z_2 z_4 - \left[2\Gamma_{12}^2(\alpha, \beta) + \frac{d \ln |g_1(\beta_1)|}{d\beta_1} \right] f_1(\alpha) z_2 z_3 - \\ \quad - \Gamma_{33}^2(\alpha, \beta) \frac{f_3^2(\alpha)}{f_2(\alpha)} \frac{g_2^2(\beta_1)}{g_1(\beta_1)} h^2(\beta_2) z_1^2, \\ \dot{z}_1 = \left[2\Gamma_{\alpha 3}^3(\alpha, \beta) + \frac{d \ln |f_3(\alpha)|}{d\alpha} \right] z_1 z_4 - \left[2\Gamma_{13}^3(\alpha, \beta) + \frac{d \ln |g_2(\beta_1)|}{d\beta_1} \right] f_1(\alpha) z_1 z_3 - \\ \quad - \left[2\Gamma_{23}^3(\alpha, \beta) + \frac{d \ln |h(\beta_2)|}{d\beta_2} \right] f_2(\alpha) g_1(\beta_1) z_1 z_2, \\ \dot{\beta}_1 = z_3 f(\alpha), \\ \dot{\beta}_2 = z_2 f(\alpha) g(\beta_1), \\ \dot{\beta}_3 = z_1 f(\alpha) g(\beta_1) h(\beta_2), \end{array} \right. \quad (8.50)$$

which is almost everywhere equivalent to the system

$$\left\{ \begin{array}{l} \ddot{\alpha} + F(\alpha) + \Gamma_{11}^\alpha(\alpha, \beta) \dot{\beta}_1^2 + \Gamma_{22}^\alpha(\alpha, \beta) \dot{\beta}_2^2 + \Gamma_{33}^\alpha(\alpha, \beta) \dot{\beta}_3^2 = 0, \\ \ddot{\beta}_1 + 2\Gamma_1(\alpha) \dot{\alpha} \dot{\beta}_1 + \Gamma_{22}^1(\alpha, \beta) \dot{\beta}_2^2 + \Gamma_{33}^1(\alpha, \beta) \dot{\beta}_3^2 = 0, \\ \ddot{\beta}_2 + 2\Gamma_1(\alpha) \dot{\alpha} \dot{\beta}_2 + 2\Gamma_2(\beta_1) \dot{\beta}_1 \dot{\beta}_2 + \Gamma_{33}^2(\alpha, \beta) \dot{\beta}_3^2 = 0, \\ \ddot{\beta}_3 + 2\Gamma_1(\alpha) \dot{\alpha} \dot{\beta}_3 + 2\Gamma_2(\beta_1) \dot{\beta}_1 \dot{\beta}_3 + 2\Gamma_3(\beta_2) \dot{\beta}_2 \dot{\beta}_3 = 0. \end{array} \right.$$

Proposition 14 *Under the assumptions of Proposition 9, the system (8.50) has a smooth first integral of the form*

$$\Phi_1(z_4, \dots, z_1; \alpha) = z_1^2 + \dots + z_4^2 + F_1(\alpha) = C_1 = \text{const}, \quad F_1(\alpha) = 2 \int_{\alpha_0}^{\alpha} F(a) da. \quad (8.51)$$

The following two assertions are proved in the same way as Propositions 10–13.

Proposition 15 *Under the assumptions of Propositions 10, 11, 12, the system (8.50) has three smooth first integrals of the form (8.43), (8.46), (8.48).*

Proposition 16 *Under the assumptions of Proposition 13, the system (8.50) has a first integral of the form (8.49).*

The first integrals (8.51), (8.43), (8.46), (8.48), (8.49) form the complete list of independent first integrals of the system (8.50) under the above conditions (we will show below that the complete list consists of five (not seven) first integrals).

8.8.2 Equations of Motion in a Force Field with Dissipation and First Integrals

We consider a more complicated system of the form (8.50) with dissipation. Namely, the presence of dissipation (generally speaking, alternating) is characterized by a sufficiently smooth coefficient $b\delta(\alpha)$ in the first equation of the system

$$\left\{ \begin{array}{l} \dot{\alpha} = -z_4 + b\delta(\alpha), \\ \dot{z}_4 = F(\alpha) + \Gamma_{11}^\alpha f_1^2(\alpha) z_3^2 + \Gamma_{22}^\alpha f_2^2(\alpha) g_1^2(\beta_1) z_2^2 + \Gamma_{33}^\alpha f_3^2(\alpha) g_2^2(\beta_1) h^2(\beta_2) z_1^2, \\ \dot{z}_3 = \left[2\Gamma_{\alpha 1}^1(\alpha, \beta) + \frac{d \ln |f_1(\alpha)|}{d\alpha} \right] z_3 z_4 - \Gamma_{22}^1(\alpha, \beta) \frac{f_2^2(\alpha)}{f_1(\alpha)} g_1^2(\beta_1) z_2^2 - \\ \quad - \Gamma_{33}^1(\alpha, \beta) \frac{f_3^2(\alpha)}{f_1(\alpha)} g_2^2(\beta_1) h^2(\beta_2) z_1^2, \\ \dot{z}_2 = \left[2\Gamma_{\alpha 2}^2(\alpha, \beta) + \frac{d \ln |f_2(\alpha)|}{d\alpha} \right] z_2 z_4 - \left[2\Gamma_{12}^2(\alpha, \beta) + \frac{d \ln |g_1(\beta_1)|}{d\beta_1} \right] f_1(\alpha) z_2 z_3 - \\ \quad - \Gamma_{33}^2(\alpha, \beta) \frac{f_3^2(\alpha)}{f_2(\alpha)} \frac{g_2^2(\beta_1)}{g_1(\beta_1)} h^2(\beta_2) z_1^2, \\ \dot{z}_1 = \left[2\Gamma_{\alpha 3}^3(\alpha, \beta) + \frac{d \ln |f_3(\alpha)|}{d\alpha} \right] z_1 z_4 - \left[2\Gamma_{13}^3(\alpha, \beta) + \frac{d \ln |g_2(\beta_1)|}{d\beta_1} \right] f_1(\alpha) z_1 z_3 - \\ \quad - \left[2\Gamma_{23}^3(\alpha, \beta) + \frac{d \ln |h(\beta_2)|}{d\beta_2} \right] f_2(\alpha) g_1(\beta_1) z_1 z_2, \\ \dot{\beta}_1 = z_3 f(\alpha), \\ \dot{\beta}_2 = z_2 f(\alpha) g(\beta_1), \\ \dot{\beta}_3 = z_1 f(\alpha) g(\beta_1) h(\beta_2), \end{array} \right. \quad (8.52)$$

which is almost everywhere equivalent to the system

$$\left\{ \begin{array}{l} \ddot{\alpha} - b\dot{\alpha}\delta'(\alpha) + F(\alpha) + \Gamma_{11}^\alpha(\alpha, \beta)\dot{\beta}_1^2 + \Gamma_{22}^\alpha(\alpha, \beta)\dot{\beta}_2^2 + \Gamma_{33}^\alpha(\alpha, \beta)\dot{\beta}_3^2 = 0, \\ \ddot{\beta}_1 - b\dot{\beta}_1\delta(\alpha)W(\alpha) + 2\Gamma_1(\alpha)\dot{\alpha}\dot{\beta}_1 + \Gamma_{22}^1(\alpha, \beta)\dot{\beta}_2^2 + \Gamma_{33}^1(\alpha, \beta)\dot{\beta}_3^2 = 0, \\ \ddot{\beta}_2 - b\dot{\beta}_2\delta(\alpha)W(\alpha) + 2\Gamma_1(\alpha)\dot{\alpha}\dot{\beta}_2 + 2\Gamma_2(\beta_1)\dot{\beta}_1\dot{\beta}_2 + \Gamma_{33}^2(\alpha, \beta)\dot{\beta}_3^2 = 0, \\ \ddot{\beta}_3 - b\dot{\beta}_3\delta(\alpha)W(\alpha) + 2\Gamma_1(\alpha)\dot{\alpha}\dot{\beta}_3 + 2\Gamma_2(\beta_1)\dot{\beta}_1\dot{\beta}_3 + 2\Gamma_3(\beta_2)\dot{\beta}_2\dot{\beta}_3 = 0, \end{array} \right.$$

$$W(\alpha) = \left[2\Gamma_1(\alpha) + \frac{d \ln |f(\alpha)|}{d\alpha} \right].$$

We proceed by integrating the eighth order system (8.52) under the conditions (8.40), (8.41), (8.44), provided that the following identities hold:

$$\Gamma_{11}^\alpha(\alpha, \beta) = \Gamma_{22}^\alpha(\alpha, \beta)g^2(\beta_1) = \Gamma_{33}^\alpha(\alpha, \beta)g^2(\beta_1)h^2(\beta_2) = \Gamma_4(\alpha). \quad (8.53)$$

We also impose the condition on the function $f(\alpha)$: it should satisfy the transformed first identity in (8.38):

$$2\Gamma_1(\alpha) + \frac{d \ln |f(\alpha)|}{d\alpha} + \Gamma_4(\alpha) f^2(\alpha) \equiv 0. \quad (8.54)$$

In general, for the complete integrability of the system (8.52) it is necessary to know seven independent first integrals. However, after the change of variables

$$w_4 = z_4, \quad w_3 = \sqrt{z_1^2 + z_2^2 + z_3^2}, \quad w_2 = \frac{z_2}{z_1}, \quad w_1 = \frac{z_3}{\sqrt{z_1^2 + z_2^2}},$$

the system (8.52) splits:

$$\begin{cases} \dot{\alpha} = -w_4 + b\delta(\alpha), \\ \dot{w}_4 = F(\alpha) + \Gamma_4(\alpha) f^2(\alpha) w_3^2, \\ \dot{w}_3 = \left[2\Gamma_1(\alpha) + \frac{d \ln |f(\alpha)|}{d\alpha} \right] w_3 w_4, \end{cases} \quad (8.55)$$

$$\begin{cases} \dot{w}_2 = \pm w_3 \sqrt{1 + w_2^2} f(\alpha) g(\beta_1) \left[2\Gamma_3(\beta_2) + \frac{d \ln |h(\beta_2)|}{d\beta_2} \right], \\ \dot{\beta}_2 = \pm \frac{w_2 w_3}{\sqrt{1 + w_2^2}} f(\alpha) g(\beta_1), \end{cases} \quad (8.56)$$

$$\begin{cases} \dot{w}_1 = \pm w_3 \sqrt{1 + w_1^2} f(\alpha) \left[2\Gamma_2(\beta_1) + \frac{d \ln |g(\beta_1)|}{d\beta_1} \right], \\ \dot{\beta}_1 = \pm \frac{w_1 w_3}{\sqrt{1 + w_1^2}} f(\alpha), \end{cases} \quad (8.57)$$

$$\dot{\beta}_3 = \pm \frac{w_3}{\sqrt{1 + w_2^2}} f(\alpha) g(\beta_1) h(\beta_2). \quad (8.58)$$

It is clear that for the complete integrability of the system (8.55)–(8.58) it suffices to have two independent first integrals of the system (8.55), one first integral of the system (8.56), one first integral of the system (8.57) (exchanging independent variables), and the additional first integral, “binding” Equation (8.58) (i.e., five first integrals in total).

Theorem 8.1. *Let for some $\kappa, \lambda \in \mathbf{R}$*

$$\Gamma_4(\alpha) f^2(\alpha) = \kappa \frac{d}{d\alpha} \ln |\delta(\alpha)|, \quad F(\alpha) = \lambda \frac{d}{d\alpha} \frac{\delta^2(\alpha)}{2}. \quad (8.59)$$

Then the system (8.52) under the conditions (8.40), (8.41), (8.44), (8.53), (8.54) possesses the complete list of (five) independent, generally speaking, transcendental first integrals.

References

- Baroudi D, Giorgio I, Battista A, Turco E, Igumnov LA (2019) Nonlinear dynamics of uniformly loaded elastica: Experimental and numerical evidence of motion around curled stable equilibrium configurations. *ZAMM-Zeitschrift für Angewandte Mathematik und Mechanik* 99(7):e201800,121
- Bogoyavlenskii OI (1986) Some integrable cases of euler equation. *Dokl Akad Nauk SSSR* 285(5):1105–1108
- Bogoyavlenskii OI, Ivakh GF (1985) Topological analysis of Steklov's integrable cases. *Uspekhi Mat Nauk* 40(4):145–146
- dell'Isola F, Seppecher P, Alibert JJ, et al (2019a) Pantographic metamaterials: an example of mathematically driven design and of its technological challenges. *Continuum Mechanics and Thermodynamics* 31(4):851–884
- dell'Isola F, Seppecher P, Spagnuolo M, et al (2019b) Advances in pantographic structures: design, manufacturing, models, experiments and image analyses. *Continuum Mechanics and Thermodynamics* 31(4):1231–1282
- Dubrovin BA, Novikov SP (1984) On Poisson brackets of hydrodynamic type. *Dokl Akad Nauk SSSR* 279(2):294–297
- Giorgio I, Scerrato D (2017) Multi-scale concrete model with rate-dependent internal friction. *European Journal of Environmental and Civil Engineering* 21(7-8):821–839
- Kozlov VV (1983) Integrability and nonintegrability in Hamiltonian Mechanics. *Usp Mat Nauk* 38(1):3–67
- Shamolin MV (2015a) Complete list of first integrals of dynamic equations for a multidimensional solid in a nonconservative field. *Doklady Physics* 60(4):183–187
- Shamolin MV (2015b) Complete list of the first integrals of dynamic equations of a multidimensional solid in a nonconservative field under the assumption of linear damping. *Doklady Physics* 60(10):471–475
- Shamolin MV (2015c) A multidimensional pendulum in a nonconservative force field. *Doklady Physics* 60(1):34–38
- Shamolin MV (2016a) A multidimensional pendulum in a nonconservative force field under the presence of linear damping. *Doklady Physics* 61(9):476–480
- Shamolin MV (2016b) New cases of integrable systems with dissipation on tangent bundles of two- and three-dimensional spheres. *Doklady Physics* 61(12):625–629
- Shamolin MV (2017a) New cases of integrable systems with dissipation on a tangent bundle of a multidimensional sphere. *Doklady Physics* 62(5):262–265
- Shamolin MV (2017b) New cases of integrable systems with dissipation on a tangent bundle of a two-dimensional manifold. *Doklady Physics* 62(8):392–396
- Shamolin MV (2017c) New cases of integrable systems with dissipation on the tangent bundle of a three-dimensional manifold. *Doklady Physics* 62(11):517–521

Part II
Modeling, Design, and Computation of
Nonlinear Structures



Chapter 9

A Variational Formulation of Classical Nonlinear Beam Theories

Simon R. Eugster & Jonas Harsch

Abstract This article intends to present a concise theory of spatial nonlinear classical beams followed by a special treatment of the planar case. Hereby the considered classical beams are understood as generalized one-dimensional continua that model the mechanical behavior of three-dimensional beam-like objects. While a one-dimensional continuum corresponds to a deformable curve in space, parametrized by a single material coordinate and time, a generalized continuum is augmented by further kinematical quantities depending on the very same parameters. We introduce the following three nonlinear spatial beams: The Timoshenko beam, the Euler–Bernoulli beam and the inextensible Euler–Bernoulli beam. In the spatial theory, the Euler–Bernoulli beam and its inextensible companion are presented as constrained theories. In the planar case, both constrained theories are additionally described using an alternative kinematics that intrinsically satisfies the defining constraints of these theories.

9.1 Introduction

One particular reason for confusion in beam theory is the lack of a consistent naming in literature. Hence, whenever talking and writing about beam theory, it is crucial to clarify this ambiguity by defining the kinematics of the discussed theory. In this article, a *Timoshenko beam* is considered as a generalized one-dimensional continuum described by a spatial curve, its centerline, augmented in each point of the curve by an orthonormal director triad. For beam-like three-dimensional elastic bodies the director triads model the cross sections, which remain plane and rigid for all configurations. Alternative names given in literature are “special Cosserat rod”, see Antman (2005), “Simo–Reissner beam” referring to Simo (1985) and Reissner

Simon R. Eugster, J. Harsch
Institute for Nonlinear Mechanics, University of Stuttgart, Stuttgart, Germany
e-mail: eugster@inm.uni-stuttgart.de, harsch@inm.uni-stuttgart.de

(1981), “geometrically exact beam”, see (Betsch and Steinmann, 2003; Eugster et al, 2014), or “poutres naturelle” (“natural beam”) in French literature as for instance in Ballard and Millard (2009). If the director triad is constrained such that one of the directors always aligns with the centerline’s tangent, we call the beam an *Euler–Bernoulli beam* (Eugster, 2015; Eugster and Steigmann, 2020). Also here alternative names are around, i.e., “Kirchhoff–Clebsch rod” (Steigmann and Faulkner, 1993), “Kirchhoff–Love rod” (Greco and Cuomo, 2013), “Kirchhoff rod” (Meier et al, 2014), or “Navier–Bernoulli beam” (Ballard and Millard, 2009). We call the beam an *inextensible Euler–Bernoulli beam* if in addition the norm of the centerline’s tangent remains unchanged throughout the motion.

Since the beginning of continuum mechanics, beam theory has been an omnipresent research field that has newly received its attention not only in soft robotics (Deutschmann et al, 2018; Eugster and Deutschmann, 2018; Till et al, 2019) but also in the field of mechanical metamaterials (Barchiesi et al, 2019b). Many metamaterials are composed of networks of beams such as the class of pantographic materials (dell’Isola et al, 2019a,b, 2020b), which were analyzed in various forms, see among others (Alibert et al, 2003; Andreus et al, 2018; Barchiesi et al, 2019a, 2020; Boutin et al, 2017; Capobianco et al, 2018; dell’Isola et al, 2016a,c; dell’Isola and Steigmann, 2015; Giorgio et al, 2017; Maurin et al, 2019; Rahali et al, 2015; Shirani et al, 2019; Steigmann and dell’Isola, 2015). The presented beam theories are formulated in a variational setting, where the principle of virtual work plays the role of the fundamental postulate in mechanics, see (Eugster and Glocker, 2017; dell’Isola et al, 2020a; dell’Isola and Placidi, 2011; dell’Isola and Seppecher, 1995; Eugster and dell’Isola, 2017, 2018). The principle states that the sum of all virtual work contributions of the modeled mechanical effects must vanish for all virtual displacements. For static problems, the total virtual work is composed of internal and external virtual work contributions, which model, respectively, mechanical interactions of material points of the beam among themselves as well as mechanical interactions of material points of the beam and the environment. For dynamic problems, virtual work contributions incorporating inertial effects of the beam have to be added. Moreover, the principle of virtual work must then hold for all time instants. The main task in the development of a beam theory is the definition of each virtual work contribution. This task is by no means unique and can be considered as the modeling procedure in mechanics. Since the (inextensible) Euler–Bernoulli beam can be considered as a constrained Timoshenko beam, the virtual work contributions thereof are formulated first in Sections 9.2–9.5. We pursue the following strategy for the internal and external virtual work contributions. The internal virtual work contributions are related to the variation of a strain energy function that depends on the kinematical quantities describing the beam (Section 9.2). The set of strain energy functions is reduced in Section 9.3 by the requirement of an invariance principle. More precisely, we postulate the invariance under superimposed rigid body motions of the strain energy function. Similar invariance conditions are obtained when advocating for a change of observer as discussed in Steigmann (2017). This leads us not only to the most general strain energy function that guarantees the invariance principle, but also to the internal virtual work of the Timoshenko beam.

The suitable external virtual work contributions are subsequently obtained by an integration by parts procedure. Accordingly, the form of the internal virtual work defines the external force effects that the beam can resist. These are for the classical theories, distributed forces and couples as well as point forces and couples at both ends of the beam. The virtual work contributions of the inertial effects are derived in the sense of an induced theory in which the beam is considered as a constrained three-dimensional body, see (Antman, 2005; Eugster, 2015). The total virtual work of the (inextensible) Euler–Bernoulli beam is obtained in Section 9.6 by augmenting the strain energy function in the sense of a Lagrange multiplier method (Bersani et al, 2019; dell’Isola et al, 2016b). In Section 9.7, the motion of the beams are restricted to be planar. For the Timoshenko beam, the parametrization of the required rotation fields becomes trivial. For both the Euler–Bernoulli beam and the inextensible Euler–Bernoulli beam, a minimal set of kinematical descriptors can be found. In these minimal formulations, the virtual work contributions of the constraints vanish.

9.2 Notation and Kinematics

We regard tensors as linear transformations from a three-dimensional vector space \mathbb{E}^3 to itself and use standard notation such as \mathbf{A}^T , \mathbf{A}^{-1} , $\det(\mathbf{A})$. These are, respectively, the transpose, the inverse, and the determinant of a tensor \mathbf{A} . The set of tensors is denoted by $L(\mathbb{E}^3; \mathbb{E}^3)$. The tensor $\mathbf{1}$ stands for the identity tensor, which leaves every vector $\mathbf{a} \in \mathbb{E}^3$ unchanged, i.e. $\mathbf{a} = \mathbf{1}\mathbf{a}$. We use *Skw* to denote the linear subspace of skew tensors and $Orth^+ = \{\mathbf{A} \in L(\mathbb{E}^3; \mathbb{E}^3) \mid \mathbf{A}^T \mathbf{A} = \mathbf{A} \mathbf{A}^T = \mathbf{1} \wedge \det(\mathbf{A}) = +1\}$ to identify the group of rotation tensors. The tensor product of three-vectors is indicated by interposing the symbol \otimes . Latin and Greek indices take values in $\{1, 2, 3\}$ and $\{2, 3\}$, respectively, and, when repeated, are summed over their ranges. Furthermore, we abbreviate the arguments in functions depending on the three components (a_1, a_2, a_3) or merely on the last two components (a_2, a_3) of a vector $\mathbf{a} \in \mathbb{E}^3$ by (a_i) or (a_α) , respectively. Derivatives of functions $f = f(s, t)$ with respect to s and t are denoted by a prime $f' = \partial f / \partial s$ and a dot $\dot{f} = \partial f / \partial t$, respectively. The variation of a function $f = f(s, t)$, denoted by a delta, is the derivative with respect to the parameter ε of a one-parameter family $\hat{f} = \hat{f}(s, t; \varepsilon)$ evaluated at $\varepsilon = 0$, i.e. $\delta f(s, t) = \partial \hat{f} / \partial \varepsilon(s, t; 0)$. The one-parameter family satisfies $f(s, t) = \hat{f}(s, t; 0)$.

Next, we introduce the required kinematical quantities for the spatial nonlinear Timoshenko beam theory. The motion of the *centerline* is the mapping $\mathbf{r}: I \times \mathbb{R} \rightarrow \mathbb{E}^3$, $(s, t) \mapsto \mathbf{r}(s, t)$, where, for each instant of time $t \in \mathbb{R}$, the closed interval $I = [l_1, l_2] \subset \mathbb{R}$ parametrizes the set of beam points. We make the convenient choice to use as material coordinate the arc length parameter s of the *reference centerline* $\mathbf{r}_0: I \rightarrow \mathbb{E}^3$. To capture cross-sectional orientations of beam-like bodies, the kinematics of the centerline is augmented by the motion of positively oriented director triads $\mathbf{d}_i: I \times \mathbb{R} \rightarrow \mathbb{E}^3$. The directors $\mathbf{d}_\alpha(s, t)$ span the plane and rigid cross section of the beam for the material coordinate s at time t . The positively

oriented director triads in the reference configuration are given by the mappings $\mathbf{D}_i : I \rightarrow \mathbb{E}^3$. While \mathbf{D}_1 is identified with the unit tangent to the reference centerline \mathbf{r}_0 , i.e., $\mathbf{D}_1 = \mathbf{r}'_0$, the vectors $\mathbf{D}_2(s)$ and $\mathbf{D}_3(s)$ are identified with the geometric principal axes of the cross sections.

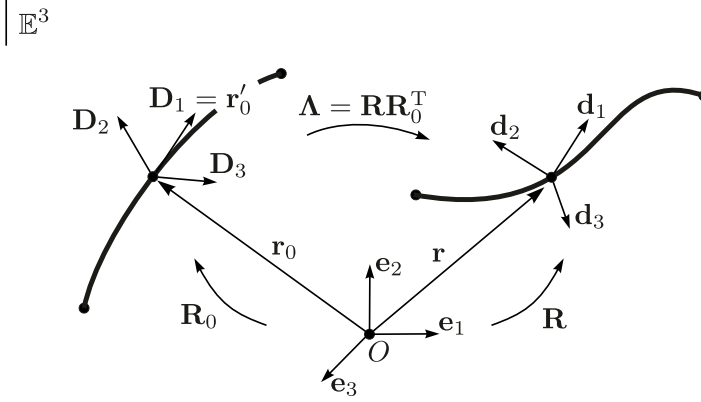


Fig. 9.1 Kinematics of a spatial Timoshenko beam.

With the reference and current rotation fields $\mathbf{R}_0 : I \rightarrow Orth^+$ and $\mathbf{R} : I \times \mathbb{R} \rightarrow Orth^+$, respectively, the reference and current director triads are related to a fixed right-handed inertial frame $\{\mathbf{e}_1, \mathbf{e}_2, \mathbf{e}_3\}$ by

$$\mathbf{D}_i(s) = \mathbf{R}_0(s)\mathbf{e}_i, \quad \mathbf{d}_i(s, t) = \mathbf{R}(s, t)\mathbf{e}_i. \quad (9.1)$$

Using the identity tensor in the form $\mathbf{1} = \mathbf{e}_i \otimes \mathbf{e}_i$ together with the relations (9.1), the current and reference rotation fields can be expressed as

$$\mathbf{R}_0 = \mathbf{R}_0\mathbf{1} = \mathbf{R}_0(\mathbf{e}_i \otimes \mathbf{e}_i) = (\mathbf{R}_0\mathbf{e}_i) \otimes \mathbf{e}_i = \mathbf{D}_i \otimes \mathbf{e}_i, \quad (9.2)$$

$$\mathbf{R} = \mathbf{R}\mathbf{1} = \mathbf{R}(\mathbf{e}_i \otimes \mathbf{e}_i) = (\mathbf{R}\mathbf{e}_i) \otimes \mathbf{e}_i = \mathbf{d}_i \otimes \mathbf{e}_i. \quad (9.3)$$

With the inverse relations of (9.1) at hand and exploiting the equivalence of the inverse and the transpose for rotations, we can relate all bases by

$$\mathbf{e}_i = \mathbf{R}_0^T(s)\mathbf{D}_i(s) = \mathbf{R}^T(s, t)\mathbf{d}_i(s, t). \quad (9.4)$$

To capture the deformation between the reference and the current configuration, we introduce the rotation field $\mathbf{\Lambda} : I \times \mathbb{R} \rightarrow Orth^+$, $(s, t) \mapsto \mathbf{\Lambda}(s, t) = \mathbf{R}(s, t)\mathbf{R}_0^T(s)$, which rotates the reference director triads to the current director triads, i.e.,

$$\mathbf{d}_i(s, t) = \mathbf{\Lambda}(s, t)\mathbf{D}_i(s). \quad (9.5)$$

Using the identity tensor in the form $\mathbf{1} = \mathbf{D}_i \otimes \mathbf{D}_i$ and repeating the steps as in (9.3), we can represent the rotation between reference and current configuration as

$$\mathbf{\Lambda} = \mathbf{\Lambda} \mathbf{1} = \mathbf{\Lambda}(\mathbf{D}_i \otimes \mathbf{D}_i) = (\mathbf{\Lambda} \mathbf{D}_i) \otimes \mathbf{D}_i \stackrel{(9.5)}{=} \mathbf{d}_i \otimes \mathbf{D}_i . \quad (9.6)$$

Using (9.1) and (9.4), the rate of change of the reference director triad with respect to the arc length s is expressed as

$$\mathbf{D}'_i(s) = (\mathbf{R}_0(s) \mathbf{e}_i)' = \mathbf{R}'_0(s) \mathbf{e}_i \stackrel{(9.4)}{=} \mathbf{R}'_0(s) \mathbf{R}_0^T(s) \mathbf{D}_i(s) = \tilde{\boldsymbol{\kappa}}_0(s) \mathbf{D}_i(s) , \quad (9.7)$$

where we have introduced the *reference curvature* $\tilde{\boldsymbol{\kappa}}_0(s) = \mathbf{R}'_0(s) \mathbf{R}_0^T(s)$. Taking the derivative with respect to s of (9.2), the reference curvature can be expressed with respect to the $\mathbf{D}_i \otimes \mathbf{D}_j$ -basis as

$$\tilde{\boldsymbol{\kappa}}_0 = \tilde{\kappa}_{ij}^0 \mathbf{D}_i \otimes \mathbf{D}_j = (\mathbf{D}_i \otimes \mathbf{e}_i)' (\mathbf{D}_j \otimes \mathbf{e}_j)^T = \mathbf{D}'_i \otimes \mathbf{D}_j = (\mathbf{D}_i \cdot \mathbf{D}'_j) \mathbf{D}_i \otimes \mathbf{D}_j . \quad (9.8)$$

The reference curvature $\tilde{\boldsymbol{\kappa}}_0$ is skew-symmetric, i.e., $\tilde{\boldsymbol{\kappa}}_0^T = -\tilde{\boldsymbol{\kappa}}_0$. This follows straightforwardly from

$$\mathbf{0} = (\mathbf{1})' = (\mathbf{R}_0 \mathbf{R}_0^T)' = \mathbf{R}'_0 \mathbf{R}_0^T + \mathbf{R}_0 \mathbf{R}'_0^T = \mathbf{R}'_0 \mathbf{R}_0^T + (\mathbf{R}'_0 \mathbf{R}_0^T)^T . \quad (9.9)$$

Thus $\tilde{\boldsymbol{\kappa}}_0(s)$ has an associated axial vector $\text{ax}(\tilde{\boldsymbol{\kappa}}_0(s)) = \boldsymbol{\kappa}_0(s) \in \mathbb{E}^3$ defined by the relation $\tilde{\boldsymbol{\kappa}}_0(s) \mathbf{a} = \boldsymbol{\kappa}_0(s) \times \mathbf{a} \forall \mathbf{a} \in \mathbb{E}^3$. The reference curvature can thus also be expressed by the vector valued function

$$\boldsymbol{\kappa}_0 = \kappa_i^0 \mathbf{D}_i = \text{ax}(\tilde{\boldsymbol{\kappa}}_0) = \frac{1}{2} \varepsilon_{ijk} \kappa_{kj}^0 \mathbf{D}_i = \frac{1}{2} \varepsilon_{ijk} (\mathbf{D}_k \cdot \mathbf{D}'_j) \mathbf{D}_i , \quad (9.10)$$

where ε_{ijk} denotes the Levi-Civita permutation symbol, which is ± 1 for even and odd permutations of $\{1, 2, 3\}$, respectively, and zero otherwise.

The *current curvature* $\tilde{\boldsymbol{w}}(s, t) = \mathbf{R}'(s, t) \mathbf{R}^T(s, t) \in Skw$ and its axial representation $\mathbf{w}(s, t) \in \mathbb{E}^3$ capture the rate of change of the current director triad with respect to the arc length parameter s and emerge in the relation

$$\mathbf{d}'_i = (\mathbf{R} \mathbf{e}_i)' = \mathbf{R}' \mathbf{e}_i \stackrel{(9.4)}{=} \mathbf{R}' \mathbf{R}^T \mathbf{d}_i = \tilde{\boldsymbol{w}} \mathbf{d}_i = \mathbf{w} \times \mathbf{d}_i . \quad (9.11)$$

The skew symmetry of $\tilde{\boldsymbol{w}}(s, t)$ follows from the analogous computations as carried out in (9.9). The current curvature can be represented with respect to the $\mathbf{d}_i \otimes \mathbf{d}_j$ -basis as

$$\tilde{\boldsymbol{w}} = \tilde{w}_{ij} \mathbf{d}_i \otimes \mathbf{d}_j = (\mathbf{d}_i \otimes \mathbf{e}_i)' (\mathbf{d}_j \otimes \mathbf{e}_j)^T = \mathbf{d}'_i \otimes \mathbf{d}_j = (\mathbf{d}_i \cdot \mathbf{d}'_j) \mathbf{d}_i \otimes \mathbf{d}_j , \quad (9.12)$$

or as vector-valued function

$$\mathbf{w} = w_i \mathbf{d}_i = \text{ax}(\tilde{\boldsymbol{w}}) = \frac{1}{2} \varepsilon_{ijk} \tilde{w}_{kj} \mathbf{d}_i = \frac{1}{2} \varepsilon_{ijk} (\mathbf{d}_k \cdot \mathbf{d}'_j) \mathbf{d}_i . \quad (9.13)$$

The rate of change of the current directors with respect to time t is described by the *angular velocity* $\tilde{\boldsymbol{\omega}}(s, t) = \dot{\mathbf{R}}(s, t) \mathbf{R}^T(s, t) = \dot{\mathbf{\Lambda}}(s, t) \mathbf{\Lambda}^T(s, t) \in Skw$, which appears together with the corresponding axial vector $\boldsymbol{\omega}(s, t) \in \mathbb{E}^3$ in

$$\dot{\mathbf{d}}_i = (\mathbf{R}\mathbf{e}_i)^\cdot = \dot{\mathbf{R}}\mathbf{e}_i \stackrel{(9.4)}{=} \dot{\mathbf{R}}\mathbf{R}^T\mathbf{d}_i = \tilde{\boldsymbol{\omega}}\mathbf{d}_i = \boldsymbol{\omega} \times \mathbf{d}_i . \quad (9.14)$$

The angular velocity can thus be represented as

$$\tilde{\boldsymbol{\omega}} = \tilde{\omega}_{ij}\mathbf{d}_i \otimes \mathbf{d}_j = (\mathbf{d}_i \otimes \mathbf{e}_i)(\mathbf{d}_j \otimes \mathbf{e}_j)^T = \dot{\mathbf{d}}_i \otimes \mathbf{d}_i = (\mathbf{d}_i \cdot \dot{\mathbf{d}}_j)\mathbf{d}_i \otimes \mathbf{d}_j , \quad (9.15)$$

or as vector-valued function in the form

$$\boldsymbol{\omega} = \omega_i\mathbf{d}_i = \text{ax}(\tilde{\boldsymbol{\omega}}) = \frac{1}{2}\varepsilon_{ijk}\tilde{\omega}_{kj}\mathbf{d}_i = \frac{1}{2}\varepsilon_{ijk}(\mathbf{d}_k \cdot \dot{\mathbf{d}}_j)\mathbf{d}_i . \quad (9.16)$$

The skew-symmetry of $\tilde{\boldsymbol{\omega}}$ can be verified similar to (9.9).

The rate of change of the current directors under a variation of the current configuration is captured by the skew symmetric *virtual rotation* $\delta\tilde{\boldsymbol{\phi}} = \delta\mathbf{R}\mathbf{R}^T = \delta\boldsymbol{\Lambda}\boldsymbol{\Lambda}^T$ with its axial vector $\delta\boldsymbol{\phi}(s, t) \in \mathbb{E}^3$. Both representations can be recognized in

$$\delta\mathbf{d}_i = \delta(\mathbf{R}\mathbf{e}_i) = \delta\mathbf{R}\mathbf{e}_i = \delta\mathbf{R}\mathbf{R}^T\mathbf{d}_i = \delta\tilde{\boldsymbol{\phi}}\mathbf{d}_i = \delta\boldsymbol{\phi} \times \mathbf{d}_i . \quad (9.17)$$

As before, the virtual rotation can be represented either as the tensor function

$$\delta\tilde{\boldsymbol{\phi}} = \delta\tilde{\phi}_{ij}\mathbf{d}_i \otimes \mathbf{d}_j = \delta(\mathbf{d}_i \otimes \mathbf{e}_i)(\mathbf{d}_j \otimes \mathbf{e}_j)^T = \delta\mathbf{d}_i \otimes \mathbf{d}_i = (\mathbf{d}_i \cdot \delta\mathbf{d}_j)\mathbf{d}_i \otimes \mathbf{d}_j , \quad (9.18)$$

or as the vector-valued function

$$\delta\boldsymbol{\phi} = \delta\phi_i\mathbf{d}_i = \text{ax}(\delta\tilde{\boldsymbol{\phi}}) = \frac{1}{2}\varepsilon_{ijk}\delta\tilde{\phi}_{kj}\mathbf{d}_i = \frac{1}{2}\varepsilon_{ijk}(\mathbf{d}_k \cdot \delta\mathbf{d}_j)\mathbf{d}_i . \quad (9.19)$$

Due to the symmetry of second derivatives, the partial derivative with respect to s and the variation δ commute, i.e., $\delta(\mathbf{d}'_i) = (\delta\mathbf{d}_i)' = \delta\mathbf{d}'_i$. This identity can be reformulated by using (9.11), (9.17) and subtracting the left-hand side from the right-hand side, yielding $\delta(\mathbf{w} \times \mathbf{d}_i) - (\delta\boldsymbol{\phi} \times \mathbf{d}_i)' = 0$. Application of the product rule, applying once again (9.11) and (9.17) as well as making use of the skew-symmetry of the cross product, i.e., $\mathbf{a} \times \mathbf{b} = -\mathbf{b} \times \mathbf{a}$, $\forall \mathbf{a}, \mathbf{b} \in \mathbb{E}^3$, we get

$$\delta\mathbf{w} \times \mathbf{d}_i + \mathbf{w} \times (\delta\boldsymbol{\phi} \times \mathbf{d}_i) - \delta\boldsymbol{\phi}' \times \mathbf{d}_i + \delta\boldsymbol{\phi} \times (\mathbf{d}_i \times \mathbf{w}) = 0 . \quad (9.20)$$

Using the Jacobi identity $\mathbf{a} \times (\mathbf{b} \times \mathbf{c}) + \mathbf{b} \times (\mathbf{c} \times \mathbf{a}) = -\mathbf{c} \times (\mathbf{a} \times \mathbf{b}) \forall \mathbf{a}, \mathbf{b}, \mathbf{c} \in \mathbb{E}^3$ and applying twice the skew-symmetry of the cross-product, the above equation reduces to

$$(\delta\mathbf{w} - \delta\boldsymbol{\phi}' - \delta\boldsymbol{\phi} \times \mathbf{w}) \times \mathbf{d}_i = 0 . \quad (9.21)$$

Since (9.21) must hold for arbitrary $\mathbf{d}_i \in \mathbb{E}^3$, we can conclude that

$$\delta\boldsymbol{\phi}' = \delta\mathbf{w} - \delta\boldsymbol{\phi} \times \mathbf{w} . \quad (9.22)$$

9.3 Strain Energy Functional

Following Shirani et al (2019), we assume the strain energy E stored in a beam segment $[s_1, s_2] \subset I$ to be expressed as

$$E = \int_{s_1}^{s_2} U \, ds, \quad (9.23)$$

where U , the strain energy function per unit reference arc length s , is a function of the list $\{\mathbf{r}, \mathbf{r}', \mathbf{\Lambda}, \mathbf{\Lambda}'\}$ and possibly depends explicitly on s , i.e.,

$$U = U(\mathbf{r}, \mathbf{r}', \mathbf{\Lambda}, \mathbf{\Lambda}'; s). \quad (9.24)$$

The explicit s -dependence may arise from an initial curvature of the beam, or from nonuniform material properties.

By the requirement that strain energy functions must ensure invariance under superimposed rigid body motions, we can reduce the set of possible strain energy functions. Thus, for $\mathbf{Q}(t) \in Orth^+$ and $\mathbf{c}(t) \in \mathbb{E}^3$, the strain energy function U must be invariant under the transformations

$$\begin{aligned} \mathbf{r} &\mapsto \mathbf{r}^+ = \mathbf{Q}\mathbf{r} + \mathbf{c}, & \mathbf{r}' &\mapsto (\mathbf{r}^+)' = \mathbf{Q}\mathbf{r}', \\ \mathbf{\Lambda} &\mapsto \mathbf{\Lambda}^+ = \mathbf{Q}\mathbf{\Lambda}, & \mathbf{\Lambda}' &\mapsto (\mathbf{\Lambda}^+)' = \mathbf{Q}\mathbf{\Lambda}'. \end{aligned} \quad (9.25)$$

By choosing $\mathbf{Q}(t) = \mathbf{1}$ and $\mathbf{c}(t) \in \mathbb{E}^3$ arbitrary, we get the condition

$$U(\mathbf{r}, \mathbf{r}', \mathbf{\Lambda}, \mathbf{\Lambda}'; s) = U(\mathbf{r}^+, (\mathbf{r}^+)', \mathbf{\Lambda}^+, (\mathbf{\Lambda}^+)' ; s) = U(\mathbf{r} + \mathbf{c}, \mathbf{r}', \mathbf{\Lambda}, \mathbf{\Lambda}'; s), \quad (9.26)$$

from which we conclude that $U(\mathbf{r}, \mathbf{r}', \mathbf{\Lambda}, \mathbf{\Lambda}'; s) = \tilde{U}(\mathbf{r}', \mathbf{\Lambda}, \mathbf{\Lambda}'; s)$ has to be independent of the centerline \mathbf{r} . For a particular material coordinate $s \in I$, we choose the rotation $\mathbf{Q}(t) = \mathbf{\Lambda}^T(s, t)$ together with a vanishing displacement $\mathbf{c}(t) = \mathbf{0}$, which yields the condition

$$\tilde{U}(\mathbf{r}', \mathbf{\Lambda}, \mathbf{\Lambda}'; s) = \tilde{U}(\mathbf{\Lambda}^T \mathbf{r}', \mathbf{\Lambda}^T \mathbf{\Lambda}, \mathbf{\Lambda}^T \mathbf{\Lambda}'; s) = \tilde{U}(\mathbf{\Lambda}^T \mathbf{r}', \mathbf{1}, \mathbf{\Lambda}^T \mathbf{\Lambda}'; s). \quad (9.27)$$

Due to $\mathbf{\Lambda}^T \mathbf{\Lambda} = \mathbf{1}$, the strain energy per unit arc length \tilde{U} may not depend on the argument $\mathbf{\Lambda}$ either. Hence, we conclude that if the strain energy function U is invariant under superimposed rigid body motions then there is a strain energy function \tilde{W} which is related to U by

$$U(\mathbf{r}, \mathbf{r}', \mathbf{\Lambda}, \mathbf{\Lambda}'; s) = \tilde{W}(\mathbf{\Lambda}^T \mathbf{r}', \mathbf{\Lambda}^T \mathbf{\Lambda}'; s). \quad (9.28)$$

The reverse direction, which implies from condition (9.28) the invariance of U , is obtained immediately since the kinematic quantities $\mathbf{\Lambda}^T \mathbf{r}' = (\mathbf{\Lambda}^+)^T (\mathbf{r}^+)'$ and $\mathbf{\Lambda}^T \mathbf{\Lambda}' = (\mathbf{\Lambda}^+)^T (\mathbf{\Lambda}^+)'$ are invariant under the transformations (9.25). For that reason, we take these kinematic quantities as generalized strain measures of the beam, where

$$\Gamma(s, t) = I_i(s, t) \mathbf{D}_i(s) = \mathbf{\Lambda}^\top(s, t) \mathbf{r}'(s, t) = (\mathbf{r}'(s, t) \cdot \mathbf{d}_i(s, t)) \mathbf{D}_i(s) \quad (9.29)$$

incorporates in its \mathbf{D}_i -components the projection of the centerline's tangent \mathbf{r}' onto the current directors \mathbf{d}_i . Identifying $\mathbf{R}' = \tilde{\mathbf{w}} \mathbf{R}$ in (9.11), the second generalized strain measure $\mathbf{\Lambda}^\top(s, t) \mathbf{\Lambda}'(s, t) \in Skw$ can be related to the reference and current curvature by

$$\begin{aligned} \mathbf{\Lambda}^\top \mathbf{\Lambda}' &= (\mathbf{R} \mathbf{R}_0^\top)^\top (\mathbf{R} \mathbf{R}_0^\top)' = \mathbf{R}_0 \mathbf{R}^\top \mathbf{R}' \mathbf{R}_0^\top + \mathbf{R}_0 \mathbf{R}_0^{\top\prime} \\ &= \mathbf{\Lambda}^\top \tilde{\mathbf{w}} \mathbf{\Lambda} - \tilde{\boldsymbol{\kappa}}_0 = \tilde{\boldsymbol{\kappa}} - \tilde{\boldsymbol{\kappa}}_0, \end{aligned} \quad (9.30)$$

where we have introduced the current curvature pulled-back to the reference configuration $\tilde{\boldsymbol{\kappa}} = \mathbf{\Lambda}^\top \tilde{\mathbf{w}} \mathbf{\Lambda}$. Making use of (9.6) and the definition of $\tilde{\mathbf{w}}$ given in (9.12), $\tilde{\boldsymbol{\kappa}}$ can be represented as

$$\tilde{\boldsymbol{\kappa}} = \tilde{\kappa}_{ij} \mathbf{D}_i \otimes \mathbf{D}_j = \mathbf{\Lambda}^\top \tilde{\mathbf{w}} \mathbf{\Lambda} = \tilde{w}_{ij} \mathbf{\Lambda}^\top (\mathbf{d}_i \otimes \mathbf{d}_j) \mathbf{\Lambda} = \tilde{w}_{ij} \mathbf{D}_i \otimes \mathbf{D}_j, \quad (9.31)$$

which shows that the components of $\tilde{\boldsymbol{\kappa}}$ in the $\mathbf{D}_i \otimes \mathbf{D}_j$ -basis and $\tilde{\mathbf{w}}$ in the $\mathbf{d}_i \otimes \mathbf{d}_j$ -basis coincide, i.e., $\tilde{\kappa}_{ij} = \tilde{w}_{ij}$. The skew symmetry of $\mathbf{\Lambda}^\top \mathbf{\Lambda}'$ allows us to write the strain measure also as the vector-valued function

$$\boldsymbol{\kappa} - \boldsymbol{\kappa}_0 = (\kappa_i - \kappa_i^0) \mathbf{D}_i = \text{ax}(\tilde{\boldsymbol{\kappa}}) - \text{ax}(\tilde{\boldsymbol{\kappa}}_0) \quad (9.32)$$

with their corresponding components in the \mathbf{D}_i -basis given by

$$\kappa_i = \frac{1}{2} \varepsilon_{ijk} \tilde{\kappa}_{kj} = \frac{1}{2} \varepsilon_{ijk} (\mathbf{d}_k \cdot \mathbf{d}_j'), \quad \kappa_i^0 = \frac{1}{2} \varepsilon_{ijk} \tilde{\kappa}_{kj}^0 = \frac{1}{2} \varepsilon_{ijk} (\mathbf{D}_k \cdot \mathbf{D}_j'). \quad (9.33)$$

Replacing $\mathbf{\Lambda}^\top \mathbf{\Lambda}'$ with its axial vector (9.32) and putting the dependence of the strain energy function on a pre-curved reference configuration indicated by a non-vanishing $\boldsymbol{\kappa}_0$ into the explicit s -dependence, we obtain the final form of the objective strain energy function per unit arc length

$$U(\mathbf{r}, \mathbf{r}', \mathbf{\Lambda}, \mathbf{\Lambda}'; s) = W(\boldsymbol{\Gamma}, \boldsymbol{\kappa}; s) \quad (9.34)$$

which solely depends on (9.29) and the current parts of (9.32).

Whenever an explicit strain energy function is required in the following, we choose the quadratic strain energy function of the form

$$W(\boldsymbol{\Gamma}, \boldsymbol{\kappa}; s) = \sum_{i=1}^3 \left\{ \frac{1}{2} E_i (\Gamma_i - \delta_{i1})^2 + \frac{1}{2} F_i (\kappa_i - \kappa_i^0)^2 \right\}. \quad (9.35)$$

Note that there is a possible s -dependence in the axial stiffness E_1 , the shear stiffnesses E_2 and E_3 , the torsional stiffness F_1 as well as the flexural stiffnesses F_2 and F_3 .

If the beam models a body that could also be described as a three-dimensional continuous body with isotropic material, the stiffnesses are often related to the material properties and the geometry of the body. Then, the axial stiffness E_1 is given by the

Young's modulus times the cross-sectional area, the shear stiffnesses E_2 and E_3 are shear modulus times the cross-sectional area multiplied with an appropriate shear correction factor (Timoshenko and Goodier, 1951; Cowper, 1966), the torsional stiffness F_1 is shear modulus times the polar moment of the cross section and the flexural stiffnesses F_2 and F_3 are Young's modulus times the appropriate second moment of area of the cross section.

9.4 Virtual Work Contributions

With the objective strain energy function (9.34), we define the internal virtual work contributions of the beam using the first variation of the beam's total strain energy E in accordance with

$$\delta W^{\text{int}} = -\delta E = - \int_{l_1}^{l_2} \delta W \, ds = - \int_{l_1}^{l_2} \left\{ \frac{\partial W}{\partial \Gamma_i} \delta \Gamma_i + \frac{\partial W}{\partial \kappa_i} \delta \kappa_i \right\} ds. \quad (9.36)$$

In the following, the variations of the generalized strain measures are derived. The variations of the components of (9.29) can be computed using (9.17) together with the invariance of the triple product with respect to even permutations, i.e., $\mathbf{a} \cdot (\mathbf{b} \times \mathbf{c}) = \mathbf{b} \cdot (\mathbf{c} \times \mathbf{a}) = \mathbf{c} \cdot (\mathbf{a} \times \mathbf{b}) \forall \mathbf{a}, \mathbf{b}, \mathbf{c} \in \mathbb{E}^3$, and the skew-symmetry of the cross product

$$\delta \Gamma_i = \delta(\mathbf{r}' \cdot \mathbf{d}_i) = (\delta \mathbf{r}' - \delta \boldsymbol{\phi} \times \mathbf{r}') \cdot \mathbf{d}_i. \quad (9.37)$$

Again using the properties of the triple product, the relation of the permutation symbol and the Kronecker delta $\varepsilon_{ijk}\varepsilon_{jkl} = \varepsilon_{ijk}\varepsilon_{ljk} = 2\delta_{il}$ as well as (9.17), the variation of the first equation in (9.33) is given as

$$\begin{aligned} \delta \kappa_i &= \frac{1}{2} \varepsilon_{ijk} \delta(\mathbf{d}_k \cdot \mathbf{d}'_j) \stackrel{(9.17)}{=} \frac{1}{2} \varepsilon_{ijk} [(\delta \boldsymbol{\phi} \times \mathbf{d}_k) \cdot \mathbf{d}'_j + \mathbf{d}_k \cdot (\delta \boldsymbol{\phi} \times \mathbf{d}'_j)] \\ &= \frac{1}{2} \varepsilon_{ijk} [(\delta \boldsymbol{\phi} \times \mathbf{d}_k) \cdot \mathbf{d}'_j + \mathbf{d}_k \cdot (\delta \boldsymbol{\phi}' \times \mathbf{d}_j + \delta \boldsymbol{\phi} \times \mathbf{d}'_j)] \\ &= \frac{1}{2} \varepsilon_{ijk} \mathbf{d}_k \cdot (\delta \boldsymbol{\phi}' \times \mathbf{d}_j) = \frac{1}{2} \varepsilon_{ijk} \delta \boldsymbol{\phi}' \cdot (\mathbf{d}_j \times \mathbf{d}_k) \\ &= \frac{1}{2} \varepsilon_{ijk} \varepsilon_{jkl} (\delta \boldsymbol{\phi}' \cdot \mathbf{d}_l) = \delta \boldsymbol{\phi}' \cdot \mathbf{d}_i. \end{aligned} \quad (9.38)$$

Substituting (9.22) and the variation of the two generalized strain measures (9.37) and (9.38) into the internal virtual work (9.36), their final form is given by

$$\begin{aligned}
\delta W^{\text{int}} &= - \int_{l_1}^{l_2} \left\{ \frac{\partial W}{\partial \Gamma_i} \delta \Gamma_i + \frac{\partial W}{\partial \kappa_i} \delta \kappa_i \right\} ds \\
&= - \int_{l_1}^{l_2} \{ (\delta \mathbf{r}' - \delta \boldsymbol{\phi} \times \mathbf{r}') \cdot \mathbf{n} + \delta \boldsymbol{\phi}' \cdot \mathbf{m} \} ds \\
&= - \int_{l_1}^{l_2} \{ (\delta \mathbf{r}' - \delta \boldsymbol{\phi} \times \mathbf{r}') \cdot \mathbf{n} + (\delta \mathbf{w} - \delta \boldsymbol{\phi} \times \mathbf{w}) \cdot \mathbf{m} \} ds ,
\end{aligned} \tag{9.39}$$

where the generalized internal forces $\mathbf{n} = \frac{\partial W}{\partial \Gamma_i} \mathbf{d}_i$ and $\mathbf{m} = \frac{\partial W}{\partial \kappa_i} \mathbf{d}_i$ have been introduced. The interpretation of these generalized forces is postponed to the next section. However, note that in the case of inelastic behavior, where no strain energy function might be available, the internal virtual work could be defined by (9.39) in which the generalized forces \mathbf{n} and \mathbf{m} follow different constitutive laws than here. According to Germain (1973) or Eugster and Glocker (2017), the internal virtual work must vanish for all rigid virtual displacements, i.e., for $\delta \mathbf{r}(s, t) = \delta \mathbf{c}(t) + \delta \boldsymbol{\varphi}(t) \times \mathbf{r}(s, t)$ and $\delta \boldsymbol{\phi}(s, t) = \delta \boldsymbol{\varphi}(t)$, where $\delta \mathbf{c}(t), \delta \boldsymbol{\varphi}(t) \in \mathbb{E}^3$. Independent of the constitutive assumption, this is granted when using the internal virtual work (9.39).

Using integration by parts in the second line of (9.39), we can rewrite the internal virtual work as

$$\begin{aligned}
\delta W^{\text{int}} &= \int_{l_1}^{l_2} \{ \delta \mathbf{r} \cdot \mathbf{n}' + \delta \boldsymbol{\phi} \cdot (\mathbf{m}' + \mathbf{r}' \times \mathbf{n}) \} ds \\
&\quad - \sum_{i=1}^2 (-1)^i \{ \delta \mathbf{r} \cdot \mathbf{n} + \delta \boldsymbol{\phi} \cdot \mathbf{m} \} |_{s=l_i} .
\end{aligned} \tag{9.40}$$

For the static case, where only the internal virtual work contributions equilibrate the external virtual work contributions, (9.40) gives us the form of the external forces that we allow in our beam theory. These are *distributed external forces* $\bar{\mathbf{n}} : I \times \mathbb{R} \rightarrow \mathbb{E}^3$ and *distributed external couples* $\bar{\mathbf{m}} : I \times \mathbb{R} \rightarrow \mathbb{E}^3$. In addition we allow point-wise defined *external forces* $\bar{\mathbf{n}}_1, \bar{\mathbf{n}}_2 : \mathbb{R} \rightarrow \mathbb{E}^3$ and *couples* $\bar{\mathbf{m}}_1, \bar{\mathbf{m}}_2 : \mathbb{R} \rightarrow \mathbb{E}^3$ to be applied on the boundaries l_1 and l_2 of the beam. This leads to the virtual work contributions of the external forces of the form

$$\delta W^{\text{ext}} = \int_{l_1}^{l_2} \{ \delta \mathbf{r} \cdot \bar{\mathbf{n}} + \delta \boldsymbol{\phi} \cdot \bar{\mathbf{m}} \} ds + \sum_{i=1}^2 \{ \delta \mathbf{r} \cdot \bar{\mathbf{n}}_i + \delta \boldsymbol{\phi} \cdot \bar{\mathbf{m}}_i \} |_{s=l_i} . \tag{9.41}$$

If we want to allow countable many point forces inside the beam, the open set (l_1, l_2) has to be divided into further open sets, where the point forces are applied on the corresponding boundaries.

In order to formulate the virtual work contributions of inertial effects, we proceed differently as before. For a meanwhile, we assume that the beam is a three-dimensional continuous body whose points in the reference configuration occupy the positions

$$\mathbf{X}(s, \theta_\alpha) = \mathbf{r}_0(s) + \theta_\alpha \mathbf{D}_\alpha(s). \quad (9.42)$$

Hence, every material point in the reference configuration is addressed by the coordinates $(s, \theta_2, \theta_3) \in B \subset \mathbb{R}^3$. We assume that the cross sections of the beam are spanned by the reference directors \mathbf{D}_2 and \mathbf{D}_3 such that θ_2 and θ_3 are the cross section coordinates. In the sense of an induced theory, we assume the beam to be a constrained three-dimensional continuum whose current configuration is restricted to

$$\mathbf{x}(s, \theta_\alpha, t) = \mathbf{r}(s, t) + \theta_\alpha \mathbf{d}_\alpha(s, t). \quad (9.43)$$

In fact the kinematical ansatz (9.43) restricts the motion of the cross sections to remain plane and rigid for any motion. The virtual work of the inertial forces of a three-dimensional continuum is commonly defined as

$$\delta W^{\text{dyn}} = - \int_B \delta \mathbf{x} \cdot \ddot{\mathbf{x}} \, dm = - \int_B \delta \mathbf{x} \cdot \ddot{\mathbf{x}} \, \rho_0 \, dA ds, \quad (9.44)$$

where $\rho_0 : B \rightarrow \mathbb{R}$ is the beam's *mass density* per unit volume in its reference configuration and dA is the cross-sectional surface element in the beam's reference configuration. For convenience, we introduce $\boldsymbol{\rho}(s, \theta_\alpha, t) = \theta_\alpha \mathbf{d}_\alpha(s, t)$ with its corresponding skew-symmetric tensor $\tilde{\boldsymbol{\rho}}(s, \theta_\alpha, t) \in \text{Skw}$. Using (9.17), the virtual displacements admissible with respect to the position field (9.43) are obtained as

$$\delta \mathbf{x} = \delta \mathbf{r} + \delta \boldsymbol{\phi} \times \theta_\alpha \mathbf{d}_\alpha = \delta \mathbf{r} + \delta \boldsymbol{\phi} \times \boldsymbol{\rho} = \delta \mathbf{r} - \tilde{\boldsymbol{\rho}} \delta \boldsymbol{\phi}. \quad (9.45)$$

Making use of the kinematic relation (9.14) and by taking the first and second time derivative of the position field (9.43), the *velocity* and *acceleration fields* are

$$\begin{aligned} \dot{\mathbf{x}} &= \dot{\mathbf{r}} + \boldsymbol{\omega} \times \theta_\alpha \mathbf{d}_\alpha = \dot{\mathbf{r}} + \boldsymbol{\omega} \times \boldsymbol{\rho}, \\ \ddot{\mathbf{x}} &= \ddot{\mathbf{r}} + \dot{\boldsymbol{\omega}} \times \boldsymbol{\rho} + \boldsymbol{\omega} \times (\boldsymbol{\omega} \times \boldsymbol{\rho}) = \ddot{\mathbf{r}} - \tilde{\boldsymbol{\rho}} \dot{\boldsymbol{\omega}} + \tilde{\boldsymbol{\omega}} \tilde{\boldsymbol{\rho}} \boldsymbol{\rho}. \end{aligned} \quad (9.46)$$

For the next steps, we introduce some abbreviations for integral expressions that will appear in the upcoming derivation and which are related to the zeroth, first and second moment with respect to the mass density ρ_0 . The *cross section mass density* per unit of s is defined as

$$A_{\rho_0}(s) := \int_{A(s)} \rho_0 \, dA, \quad (9.47)$$

where $A(s) = \{(\theta_2, \theta_3) \in \mathbb{R}^2 \mid (s, \theta_2, \theta_3) \in B\}$. In case that the centerline does not coincide with the *line of centroids* $\mathbf{r}_c : I \times \mathbb{R} \rightarrow \mathbb{E}^3, (s, t) \mapsto \mathbf{r}_c(s, t)$ a *coupling term*

$$\mathbf{c} = A_{\rho_0}(\mathbf{r}_c - \mathbf{r}) = \int_{A(s)} \boldsymbol{\rho} \rho_0 \, dA = \int_{A(s)} \theta_\alpha \mathbf{d}_\alpha \rho_0 \, dA \quad (9.48)$$

will remain. Using (9.14) and (9.48), the second time derivative of the coupling term is

$$\ddot{\mathbf{c}} = (\boldsymbol{\omega} \times \mathbf{c})' = \dot{\boldsymbol{\omega}} \times \mathbf{c} + \boldsymbol{\omega} \times (\boldsymbol{\omega} \times \mathbf{c}) = -\tilde{\mathbf{c}} \dot{\boldsymbol{\omega}} + \tilde{\boldsymbol{\omega}} \tilde{\boldsymbol{\omega}} \mathbf{c}. \quad (9.49)$$

Note that we denoted the skew-symmetric tensor corresponding to \mathbf{c} by $\tilde{\mathbf{c}}$. The last required integrated quantity is the *cross section inertia density* defined as

$$\mathbf{I}_{\rho_0} = \int_{A(s)} \tilde{\boldsymbol{\rho}} \tilde{\boldsymbol{\rho}}^T \rho_0 \, dA . \quad (9.50)$$

Furthermore, the time derivative of $\mathbf{h} = \mathbf{I}_{\rho_0} \boldsymbol{\omega}$, i.e., the product of the cross section inertia density \mathbf{I}_{ρ_0} and the angular velocity $\boldsymbol{\omega}$ is

$$\dot{\mathbf{h}}(s, t) = (I_{ij}^{\rho_0} \omega_j \mathbf{d}_i)' = I_{ij}^{\rho_0} (\dot{\omega}_j \mathbf{d}_i + \omega_j \dot{\mathbf{d}}_i) . \quad (9.51)$$

Note that the components of cross section inertia density $\mathbf{I}_{\rho_0} = I_{ij}^{\rho_0} \mathbf{d}_i \otimes \mathbf{d}_j$ in the $\mathbf{d}_i \otimes \mathbf{d}_j$ -basis are constant with respect to time t . Since the cross product of two collinear vectors vanishes, i.e., $0 = \boldsymbol{\omega} \times \boldsymbol{\omega} = \boldsymbol{\omega} \times \omega_k \mathbf{d}_k$, we can extend the above equation, which leads together with (9.14) to the compact form

$$\dot{\mathbf{h}} = I_{ij}^{\rho_0} \mathbf{d}_i \otimes \mathbf{d}_j (\dot{\omega}_k \mathbf{d}_k + \boldsymbol{\omega} \times \omega_k \mathbf{d}_k) + \boldsymbol{\omega} \times I_{ij}^{\rho_0} \omega_j \mathbf{d}_i = \mathbf{I}_{\rho_0} \dot{\boldsymbol{\omega}} + \tilde{\boldsymbol{\omega}} \mathbf{I}_{\rho_0} \boldsymbol{\omega} . \quad (9.52)$$

With the acceleration vector (9.46) and the virtual displacements (9.45), the contributions of the inertial forces to the virtual work are given by

$$\delta W^{\text{dyn}} = - \int_B \delta \mathbf{x} \cdot \ddot{\mathbf{x}} \, dm = - \int_B (\delta \mathbf{r} - \tilde{\boldsymbol{\rho}} \delta \phi) \cdot (\ddot{\mathbf{r}} - \tilde{\boldsymbol{\rho}} \dot{\boldsymbol{\omega}} + \tilde{\boldsymbol{\omega}} \tilde{\boldsymbol{\rho}}) \rho_0 \, dA ds . \quad (9.53)$$

The integration over the body B can be split in an integration over the cross section $A(s)$ and an integration along the arc length s . Together with the integrated quantities defined above, the properties of the triple product, the skew symmetry $\tilde{\boldsymbol{\rho}} = -\tilde{\boldsymbol{\rho}}^T$, as well as the relation $\tilde{\mathbf{a}} \tilde{\mathbf{b}} \tilde{\mathbf{b}} \tilde{\mathbf{a}} = -\tilde{\mathbf{b}} \tilde{\mathbf{a}} \tilde{\mathbf{a}} \tilde{\mathbf{b}}$ for $\tilde{\mathbf{a}}, \tilde{\mathbf{b}} \in \text{Skw}$, where $\mathbf{a} = \text{ax}(\tilde{\mathbf{a}})$, $\mathbf{b} = \text{ax}(\tilde{\mathbf{b}})$, we obtain

$$\begin{aligned} \delta W^{\text{dyn}} &= - \int_{l_1}^{l_2} \left\{ \delta \mathbf{r} \cdot \left(\ddot{\mathbf{r}} \int_{A(s)} \rho_0 \, dA - \int_{A(s)} \tilde{\boldsymbol{\rho}} \rho_0 \, dA \dot{\boldsymbol{\omega}} + \tilde{\boldsymbol{\omega}} \tilde{\boldsymbol{\rho}} \int_{A(s)} \boldsymbol{\rho} \rho_0 \, dA \right) \right. \\ &\quad \left. + \delta \phi \cdot \left(\int_{A(s)} \tilde{\boldsymbol{\rho}} \rho_0 \, dA \ddot{\mathbf{r}} + \int_{A(s)} \tilde{\boldsymbol{\rho}} \tilde{\boldsymbol{\rho}}^T \rho_0 \, dA \dot{\boldsymbol{\omega}} + \tilde{\boldsymbol{\omega}} \int_{A(s)} \tilde{\boldsymbol{\rho}} \tilde{\boldsymbol{\rho}}^T \rho_0 \, dA \boldsymbol{\omega} \right) \right\} ds \\ &= - \int_{l_1}^{l_2} \left\{ \delta \mathbf{r} \cdot (A_{\rho_0} \ddot{\mathbf{r}} - \tilde{\mathbf{c}} \dot{\boldsymbol{\omega}} + \tilde{\boldsymbol{\omega}} \tilde{\boldsymbol{\omega}} \mathbf{c}) + \delta \phi \cdot (\tilde{\mathbf{c}} \ddot{\mathbf{r}} + \mathbf{I}_{\rho_0} \dot{\boldsymbol{\omega}} + \tilde{\boldsymbol{\omega}} \mathbf{I}_{\rho_0} \boldsymbol{\omega}) \right\} ds . \end{aligned} \quad (9.54)$$

Using (9.49) and (9.52), the virtual work contributions of the inertial terms can be written in the compact form

$$\delta W^{\text{dyn}} = - \int_{l_1}^{l_2} \left\{ \delta \mathbf{r} \cdot (A_{\rho_0} \ddot{\mathbf{r}} + \ddot{\mathbf{c}}) + \delta \phi \cdot (\mathbf{c} \times \ddot{\mathbf{r}} + \dot{\mathbf{h}}) \right\} ds . \quad (9.55)$$

9.5 Principle of Virtual Work and Equations of Motion

The principle of virtual work can be stated as following. For all admissible virtual displacements and for any instant of time t , the total virtual work of the beam must vanish, i.e.,

$$\delta W^{\text{tot}} = \delta W^{\text{dyn}} + \delta W^{\text{int}} + \delta W^{\text{ext}} = 0 \quad \forall \delta \mathbf{r}, \delta \boldsymbol{\phi}, t. \quad (9.56)$$

Inserting the individual contributions of the virtual work (9.39), (9.41) and (9.55) into the principle of virtual work (9.56) leads to the *weak variational formulation* of the spatial nonlinear Timoshenko beam

$$\begin{aligned} \delta W^{\text{tot}} = & \int_{l_1}^{l_2} \{ \delta \mathbf{r} \cdot (\bar{\mathbf{n}} - A_{\rho_0} \ddot{\mathbf{r}} - \ddot{\mathbf{c}}) + \delta \boldsymbol{\phi} \cdot (\bar{\mathbf{m}} - \mathbf{c} \times \ddot{\mathbf{r}} - \dot{\mathbf{h}}) - (\delta \mathbf{r}' - \delta \boldsymbol{\phi} \times \mathbf{r}') \cdot \mathbf{n} \\ & - \delta \boldsymbol{\phi}' \cdot \mathbf{m} \} ds + \sum_{i=1}^2 \{ \delta \mathbf{r} \cdot \bar{\mathbf{n}}_i + \delta \boldsymbol{\phi} \cdot \bar{\mathbf{m}}_i \} |_{s=l_i} = 0 \quad \forall \delta \mathbf{r}, \delta \boldsymbol{\phi}, t. \end{aligned} \quad (9.57)$$

Using the internal virtual work in the form (9.40), i.e., after integration by parts, we end up with the *strong variational formulation* of the spatial nonlinear Timoshenko beam

$$\begin{aligned} \delta W^{\text{tot}} = & \int_{l_1}^{l_2} \{ \delta \mathbf{r} \cdot (\mathbf{n}' + \bar{\mathbf{n}} - A_{\rho_0} \ddot{\mathbf{r}} - \ddot{\mathbf{c}}) \\ & + \delta \boldsymbol{\phi} \cdot (\mathbf{m}' + \mathbf{r}' \times \mathbf{n} + \bar{\mathbf{m}} - \mathbf{c} \times \ddot{\mathbf{r}} - \dot{\mathbf{h}}) \} ds \\ & + \sum_{i=1}^2 \{ \delta \mathbf{r} \cdot (\bar{\mathbf{n}}_i - (-1)^i \mathbf{n}) + \delta \boldsymbol{\phi} \cdot (\bar{\mathbf{m}}_i - (-1)^i \mathbf{m}) \} |_{s=l_i} = 0, \quad \forall \delta \mathbf{r}, \delta \boldsymbol{\phi}, t. \end{aligned} \quad (9.58)$$

By the fundamental lemma of calculus of variations, (9.58) can only be fulfilled if the equations of motion of the Timoshenko beam

$$\begin{aligned} \mathbf{n}' + \bar{\mathbf{n}} &= A_{\rho_0} \ddot{\mathbf{r}} + \ddot{\mathbf{c}} \\ \mathbf{m}' + \mathbf{r}' \times \mathbf{n} + \bar{\mathbf{m}} &= \mathbf{c} \times \ddot{\mathbf{r}} + \dot{\mathbf{h}} \end{aligned} \quad (9.59)$$

are satisfied in the interior of the beam, $s \in (l_1, l_2)$, together with the boundary conditions $\mathbf{n}(l_1, t) = -\bar{\mathbf{n}}_1(t)$, $\mathbf{m}(l_1, t) = -\bar{\mathbf{m}}_1(t)$ and $\mathbf{n}(l_2, t) = \bar{\mathbf{n}}_2(t)$, $\mathbf{m}(l_2, t) = \bar{\mathbf{m}}_2(t)$, see also (Antman, 2005; Dill, 1992). Certainly appropriate initial conditions in time have to be stated.

For getting an interpretation of the generalized internal forces \mathbf{n} and \mathbf{m} introduced in the internal virtual work contributions (9.39), we consider the static problem of a cantilever beam with reference length L , i.e., $I = [0, L]$. The beam is clamped at $s = 0$ and subjected to distributed forces $\bar{\mathbf{n}}$ and couples $\bar{\mathbf{m}}$ as well as a point force and a couple $\bar{\mathbf{n}}_2$, $\bar{\mathbf{m}}_2$ at $s = L$. For the clamped end, the boundary conditions and

the admissible virtual displacements and rotations read

$$\mathbf{r}(0) = 0, \quad \delta \mathbf{r}(0) = 0, \quad \phi(0) = 0, \quad \delta \phi(0) = 0. \quad (9.60)$$

Disregarding inertial effects and applying the admissible virtual displacements at the boundary (9.60), the equations of motion (9.59) turn into the equilibrium conditions

$$\begin{aligned} \mathbf{n}' + \bar{\mathbf{n}} &= 0 \\ \mathbf{m}' + \mathbf{r}' \times \mathbf{n} + \bar{\mathbf{m}} &= 0, \end{aligned} \quad (9.61)$$

together with the force boundary conditions $\mathbf{n}(L) = \bar{\mathbf{n}}_2$ and $\mathbf{m}(L) = \bar{\mathbf{m}}_2$ at the end of the beam. The boundary condition $\mathbf{n}(L) = \bar{\mathbf{n}}_2$ identifies $\mathbf{n}(L)$ as the force applied at the end $s = L$; the same holds for the couple.

For $\bar{s} \in I$, the fundamental theorem of calculus allows us to write $\int_{\bar{s}}^L \mathbf{n}' ds = \mathbf{n}(L) - \mathbf{n}(\bar{s})$. Using the first equilibrium equation in (9.61) together with the boundary condition $\mathbf{n}(L) = \bar{\mathbf{n}}_2$, we get

$$\mathbf{n}(\bar{s}) = \mathbf{n}(L) - \int_{\bar{s}}^L \mathbf{n}' ds = \bar{\mathbf{n}}_2 + \int_{\bar{s}}^L \bar{\mathbf{n}} ds. \quad (9.62)$$

Accordingly, $\mathbf{n}(\bar{s})$ corresponds to the force exerted by the segment $(\bar{s}, L]$ on the part $[0, \bar{s}]$. We consequently identify $\mathbf{n} = N\mathbf{d}_1 + Q_2\mathbf{d}_2 + Q_3\mathbf{d}_3$ as the *resultant contact force*, where $N = \partial W / \partial \Gamma_1$ and $Q_\alpha = \partial W / \partial \Gamma_\alpha$ correspond to the axial force and the shear forces, respectively.

Using the relation $\int_{\bar{s}}^L \mathbf{m}' ds = \mathbf{m}(L) - \mathbf{m}(\bar{s})$ together with the second equilibrium equation in (9.61), the boundary condition $\mathbf{m}(L) = \bar{\mathbf{m}}_2$ and subsequent integration by parts, we obtain

$$\begin{aligned} \mathbf{m}(\bar{s}) &= \mathbf{m}(L) + \int_{\bar{s}}^L \{\mathbf{r}' \times \mathbf{n} + \bar{\mathbf{m}}\} ds \\ &= \bar{\mathbf{m}}_2 + \mathbf{r}(L) \times \mathbf{n}(L) - \mathbf{r}(\bar{s}) \times \mathbf{n}(\bar{s}) + \int_{\bar{s}}^L \{\bar{\mathbf{m}} - \mathbf{r} \times \mathbf{n}'\} ds. \end{aligned} \quad (9.63)$$

For a fixed $\bar{s} \in I$, let $\Delta \mathbf{r}(s) = \mathbf{r}(s) - \mathbf{r}(\bar{s})$ be the vector connecting the point $\mathbf{r}(\bar{s})$ with $\mathbf{r}(s)$ for an arbitrary $s \in I$. Substituting $\mathbf{r}(s) = \mathbf{r}(\bar{s}) + \Delta \mathbf{r}(s)$ in the above equation, using the first equilibrium equation in (9.61) and the identity (9.62), the terms with $\mathbf{r}(\bar{s})$ cancel and we get

$$\mathbf{m}(\bar{s}) = \bar{\mathbf{m}}_2 + \Delta \mathbf{r}(L) \times \bar{\mathbf{n}}_2 + \int_{\bar{s}}^L \{\bar{\mathbf{m}} + \Delta \mathbf{r} \times \bar{\mathbf{n}}\} ds. \quad (9.64)$$

From (9.64), it becomes apparent that $\mathbf{m}(\bar{s})$ is the couple exerted by the segment $(\bar{s}, L]$ on the part $[0, \bar{s}]$. We identify $\mathbf{m} = T\mathbf{d}_1 + M_2\mathbf{d}_2 + M_3\mathbf{d}_3$ as the *resultant contact couple*, where $T = \partial W / \partial \kappa_1$ and $M_\alpha = \partial W / \partial \kappa_\alpha$ correspond to the twisting couple and the bending couples, respectively.

9.6 Constrained Beam Theories

In the preceding sections, we have established the governing equations for a spatial nonlinear Timoshenko beam. To end up with an Euler–Bernoulli or an inextensible Euler–Bernoulli beam, we have to prescribe further constraints. For the Euler–Bernoulli beam, the current director \mathbf{d}_1 must align with the centerline’s tangent \mathbf{r}' . For an inextensible Euler–Bernoulli beam, also the norm of the centerline’s tangent must remain constant, i.e., $\|\mathbf{r}'\| = \|\mathbf{r}'_0\| = 1$. All required constraint conditions can be formulated in the form $g(s, t) = 0$. To incorporate such a constraint into the variational formulation, i.e., in the principle of virtual work (9.56), we augment the strain energy functional of the whole beam (9.23) in accordance with

$$E^* = E + \bar{E}, \quad \bar{E} = - \int_{l_1}^{l_2} g(s, t) \sigma(s, t) ds, \quad (9.65)$$

where the Lagrange multiplier field $\sigma : I \times \mathbb{R} \rightarrow \mathbb{R}$ has been introduced. Again, the internal virtual work is obtained by the variation of the strain energy functional, which in the constrained case reads as

$$\begin{aligned} \delta W^{\text{int},*} &= -\delta E^* = -\delta E - \delta \bar{E} = \delta W^{\text{int}} + \delta W_c^{\text{int}}, \quad \delta W_c^{\text{int}} = \delta W_{c,1}^{\text{int}} + \delta W_{c,2}^{\text{int}}, \\ \delta W_{c,1}^{\text{int}} &= \int_{l_1}^{l_2} g(s, t) \delta \sigma(s, t) ds, \quad \delta W_{c,2}^{\text{int}} = \int_{l_1}^{l_2} \delta g(s, t) \sigma(s, t) ds. \end{aligned} \quad (9.66)$$

The first additional internal virtual work contribution $\delta W_{c,1}^{\text{int}}$ corresponds to the weak form of the constraint condition, which is important for a later numerical treatment. The second contribution $\delta W_{c,2}^{\text{int}}$ represents the virtual work of the constraint forces. For multiple constraints, the contributions are just summed up.

9.6.1 Nonlinear Euler–Bernoulli Beam

If the current director \mathbf{d}_1 aligns with the centerline’s tangent \mathbf{r}' , then the cross sections spanned by the directors \mathbf{d}_α remain orthogonal to \mathbf{r}' . This restriction can be formulated by the two conditions

$$g_\alpha(s, t) = \Gamma_\alpha(s, t) = \mathbf{d}_\alpha(s, t) \cdot \mathbf{r}'(s, t) = 0. \quad (9.67)$$

For this case, the constraint conditions coincide with vanishing shear deformations, see (9.29). Identifying $\delta g_\alpha = \delta \Gamma_\alpha = \mathbf{d}_\alpha \cdot (\delta \mathbf{r}' - \delta \phi \times \mathbf{r}')$, together with its definition given in (9.37), the virtual work contributions of the constraints are

$$\begin{aligned}\delta W_{c,1}^{\text{int}} &= \int_{l_1}^{l_2} \delta \sigma_\alpha g_\alpha \, ds = \int_{l_1}^{l_2} \delta \sigma_\alpha (\mathbf{d}_\alpha \cdot \mathbf{r}') \, ds , \\ \delta W_{c,2}^{\text{int}} &= \int_{l_1}^{l_2} \sigma_\alpha \delta g_\alpha \, ds = \int_{l_1}^{l_2} (\delta \mathbf{r}' - \delta \boldsymbol{\phi} \times \mathbf{r}') \cdot \mathbf{n}_C \, ds ,\end{aligned}\tag{9.68}$$

where we have introduced $\mathbf{n}_C = \sigma_\alpha \mathbf{d}_\alpha$. Hence, the two Lagrange multiplier fields σ_α act as shear constraint forces to enforce the vanishing shear deformations Γ_α in the Euler–Bernoulli beam.

9.6.2 Nonlinear Inextensible Euler–Bernoulli Beam

If, in addition to (9.67), we further prescribe an inextensibility constraint, the constraint condition

$$g_1(s, t) = \Gamma_1(s, t) - 1 = \mathbf{d}_1(s, t) \cdot \mathbf{r}'(s, t) - 1 = 0 \tag{9.69}$$

must hold. For the physically reasonable situation that $\mathbf{d}_1 \cdot \mathbf{r}' > 0$ and since $\mathbf{d}_\alpha \cdot \mathbf{r}' = 0$, the constraint condition (9.69) coincides with the condition that the centerline's tangent has unit length. Indeed $0 = \|\mathbf{r}'\| - 1 = [(\mathbf{d}_i \cdot \mathbf{r}')(\mathbf{d}_i \cdot \mathbf{r}')]^{1/2} - 1 \stackrel{(9.67)}{=} [(\mathbf{d}_1 \cdot \mathbf{r}')(\mathbf{d}_1 \cdot \mathbf{r}')]^{1/2} - 1 = \mathbf{d}_1 \cdot \mathbf{r}' - 1$. Identifying $\delta g_1 = \delta \Gamma_1$, together with its definition given in (9.37), the virtual work contributions of the constraints (9.67) and (9.69) are

$$\begin{aligned}\delta W_{c,1}^{\text{int}} &= \int_{l_1}^{l_2} \delta \sigma_i g_i \, ds = \int_{l_1}^{l_2} \delta \sigma_i (\mathbf{d}_i \cdot \mathbf{r}' - \delta_{i1}) \, ds , \\ \delta W_{c,2}^{\text{int}} &= \int_{l_1}^{l_2} \sigma_i \delta g_i \, ds = \int_{l_1}^{l_2} (\delta \mathbf{r}' - \delta \boldsymbol{\phi} \times \mathbf{r}') \cdot \mathbf{n}_C \, ds ,\end{aligned}\tag{9.70}$$

with $\mathbf{n}_C = \sigma_i \mathbf{d}_i$. For the inextensible Euler–Bernoulli beam, the resultant contact forces are pure reaction forces that guarantee unshearability and inextensibility of the beam.

9.7 Constrained and Unconstrained Planar Beam Theories

In the previous section, we have shown how to augment the principle of virtual work to also treat the Euler–Bernoulli beam theory and its inextensible version as a constrained theory in a variational setting. In this section, we will restrict the motion of the beams to be planar. Furthermore, we will work out the virtual work contributions of the constrained theories in detail for a possible finite element analysis as it is presented in Harsch and Eugster (2020). For the (inextensible)

Euler–Bernoulli beam, we will also choose kinematical descriptions that satisfy the constraint conditions intrinsically. These formulations are then called minimal formulations referring to the terminology of minimal coordinates in finite degree of freedom mechanics.

9.7.1 Timoshenko Beam

For the planar case, the kinematics of the beam’s centerline is restricted to the \mathbf{e}_1 - \mathbf{e}_2 -plane. The position vector of the centerline, the tangent vector and its derivative with respect to the arc length parameter s for the reference and current configurations are given by

$$\begin{aligned} \mathbf{r}_0(s) &= X(s)\mathbf{e}_1 + Y(s)\mathbf{e}_2, & \mathbf{r}(s,t) &= x(s,t)\mathbf{e}_1 + y(s,t)\mathbf{e}_2, \\ \mathbf{r}'_0(s) &= X'(s)\mathbf{e}_1 + Y'(s)\mathbf{e}_2, & \mathbf{r}'(s,t) &= x'(s,t)\mathbf{e}_1 + y'(s,t)\mathbf{e}_2, \\ \mathbf{r}''_0(s) &= X''(s)\mathbf{e}_1 + Y''(s)\mathbf{e}_2, & \mathbf{r}''(s,t) &= x''(s,t)\mathbf{e}_1 + y''(s,t)\mathbf{e}_2, \end{aligned} \tag{9.71}$$

using the coordinate functions $X, Y : I \rightarrow \mathbb{R}$ and $x, y : I \times \mathbb{R} \rightarrow \mathbb{R}$. Planar rotations are given by rotations around $\mathbf{D}_3 = \mathbf{d}_3 = \mathbf{e}_3$. As depicted in Fig. 9.2, the reference

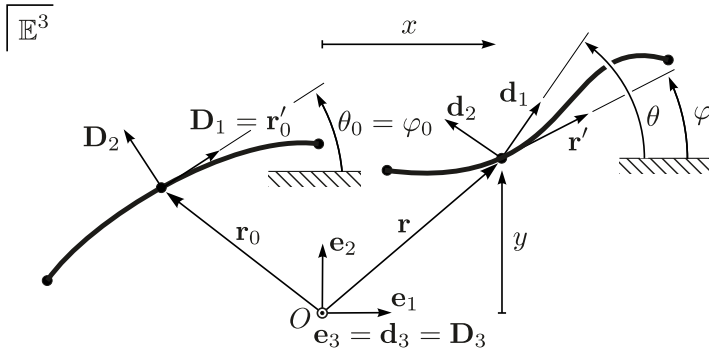


Fig. 9.2 Graphic illustration of planar position and rotation fields.

and current director triads are

$$\begin{aligned} \mathbf{D}_1 &= \cos \theta_0(s)\mathbf{e}_1 + \sin \theta_0(s)\mathbf{e}_2, & \mathbf{D}_2 &= -\sin \theta_0(s)\mathbf{e}_1 + \cos \theta_0(s)\mathbf{e}_2, \\ \mathbf{d}_1 &= \cos \theta(s,t)\mathbf{e}_1 + \sin \theta(s,t)\mathbf{e}_2, & \mathbf{d}_2 &= -\sin \theta(s,t)\mathbf{e}_1 + \cos \theta(s,t)\mathbf{e}_2, \end{aligned} \tag{9.72}$$

where $\theta_0 : I \rightarrow \mathbb{R}$ parameterizes the absolute angle of the reference director \mathbf{D}_1 with respect to the vector \mathbf{e}_1 and $\theta : I \times \mathbb{R} \rightarrow \mathbb{R}$ the absolute angle of the current director \mathbf{d}_1 .

The rotation of the reference configuration is given by $\mathbf{R}_0 = R_{ij}^0 \mathbf{e}_i \otimes \mathbf{e}_j$, with the components $R_{ij}^0 = \mathbf{e}_i \cdot \mathbf{D}_j$. The current rotation field is given analogously by $\mathbf{R} = R_{ij} \mathbf{e}_i \otimes \mathbf{e}_j$ with $R_{ij} = \mathbf{e}_i \cdot \mathbf{d}_j$. Both components can be written in matrix notation as

$$[R_{ij}^0] = \begin{pmatrix} \cos \theta_0 & -\sin \theta_0 & 0 \\ \sin \theta_0 & \cos \theta_0 & 0 \\ 0 & 0 & 1 \end{pmatrix}, \quad [R_{ij}] = \begin{pmatrix} \cos \theta & -\sin \theta & 0 \\ \sin \theta & \cos \theta & 0 \\ 0 & 0 & 1 \end{pmatrix}. \quad (9.73)$$

The rotation field $\mathbf{\Lambda} = \mathbf{R}\mathbf{R}_0^T = R_{ik}R_{jk}^0 \mathbf{e}_i \otimes \mathbf{e}_j = \Lambda_{ij} \mathbf{e}_i \otimes \mathbf{e}_j$ has the components in matrix form given by

$$[\Lambda_{ij}] = [R_{ik}][R_{kj}^0]^T = \begin{pmatrix} \cos(\theta - \theta_0) & -\sin(\theta - \theta_0) & 0 \\ \sin(\theta - \theta_0) & \cos(\theta - \theta_0) & 0 \\ 0 & 0 & 1 \end{pmatrix}. \quad (9.74)$$

Computing the derivatives of the directors (9.72) with respect to s , we get

$$\mathbf{D}'_1 = \theta'_0 \mathbf{D}_2, \quad \mathbf{D}'_2 = -\theta'_0 \mathbf{D}_1, \quad \mathbf{d}'_1 = \theta' \mathbf{d}_1, \quad \mathbf{d}'_2 = -\theta' \mathbf{d}_1, \quad \mathbf{D}'_3 = \mathbf{d}'_3 = 0. \quad (9.75)$$

The curvatures $\tilde{\boldsymbol{\kappa}} - \tilde{\boldsymbol{\kappa}}_0 = (\tilde{\kappa}_{ij} - \tilde{\kappa}_{ij}^0) \mathbf{D}_i \otimes \mathbf{D}_j$ and their associated axial vectors $\boldsymbol{\kappa} - \boldsymbol{\kappa}_0 = (\kappa_i - \kappa_i^0) \mathbf{d}_i$, together with their components are given in (9.33). The components can be obtained by inserting the directors (9.72) and their partial derivatives (9.75). This yields the very simple planar curvatures

$$[\tilde{\kappa}_{ij}] = \begin{pmatrix} 0 & -\theta' & 0 \\ \theta' & 0 & 0 \\ 0 & 0 & 0 \end{pmatrix}, \quad [\tilde{\kappa}_{ij}^0] = \begin{pmatrix} 0 & -\theta'_0 & 0 \\ \theta'_0 & 0 & 0 \\ 0 & 0 & 0 \end{pmatrix}, \quad (9.76)$$

$$\boldsymbol{\kappa} = \kappa_3 \mathbf{e}_3 = \theta' \mathbf{e}_3, \quad \boldsymbol{\kappa}_0 = \kappa_3^0 \mathbf{e}_3 = \theta'_0 \mathbf{e}_3.$$

The generalized strain measure $\mathbf{\Gamma}$ from (9.29) is computed using (9.71) together with (9.72) and reads

$$\mathbf{\Gamma} = \Gamma_1 \mathbf{D}_1 + \Gamma_2 \mathbf{D}_2 = (\mathbf{r}' \cdot \mathbf{d}_1) \mathbf{D}_1 + (\mathbf{r}' \cdot \mathbf{d}_2) \mathbf{D}_2. \quad (9.77)$$

The third component Γ_3 of the strain measure vanishes, because the current tangential vector has no component in \mathbf{d}_3 -direction.

The velocities and accelerations of the beam's centerline are easily computed from (9.71) as

$$\dot{\mathbf{r}} = \dot{x} \mathbf{e}_1 + \dot{y} \mathbf{e}_2, \quad \ddot{\mathbf{r}} = \ddot{x} \mathbf{e}_1 + \ddot{y} \mathbf{e}_2. \quad (9.78)$$

The rate of change of the director triad $\dot{\mathbf{d}}_i$ is obtained by replacing the derivative with respect to s in (9.75) by the time derivative. The angular velocity (9.15) can be easily computed in the $\mathbf{e}_i \otimes \mathbf{e}_j$ -basis as

$$\tilde{\boldsymbol{\omega}} = \dot{\mathbf{R}}\mathbf{R}^T = \tilde{\omega}_{ij}\mathbf{e}_i \otimes \mathbf{e}_j, \quad [\tilde{\omega}_{ij}] = [\dot{R}_{ik}][R_{kj}]^T = \begin{pmatrix} 0 & -\dot{\theta} & 0 \\ \dot{\theta} & 0 & 0 \\ 0 & 0 & 0 \end{pmatrix}. \quad (9.79)$$

Since $\mathbf{d}_3 = \mathbf{e}_3$, the associated axial vector $\boldsymbol{\omega}$ can be represented as

$$\boldsymbol{\omega} = \text{ax}(\tilde{\boldsymbol{\omega}}) = \dot{\theta}\mathbf{e}_3. \quad (9.80)$$

The variation of the beam's centerline and the variation of the tangent vector are

$$\delta\mathbf{r} = \delta x\mathbf{e}_1 + \delta y\mathbf{e}_2, \quad \delta\mathbf{r}' = \delta x'\mathbf{e}_1 + \delta y'\mathbf{e}_2. \quad (9.81)$$

Also for the virtual rotation $\delta\tilde{\boldsymbol{\phi}}$ given in (9.18), it is easiest to compute its components in the $\mathbf{e}_i \otimes \mathbf{e}_j$ -basis as

$$\delta\tilde{\boldsymbol{\phi}} = \delta\boldsymbol{\Lambda}\boldsymbol{\Lambda}^T = \delta\tilde{\phi}_{ij}\mathbf{e}_i \otimes \mathbf{e}_j, \quad [\delta\tilde{\phi}_{ij}] = [\delta\Lambda_{ik}][\Lambda_{kj}]^T = \begin{pmatrix} 0 & -\delta\theta & 0 \\ \delta\theta & 0 & 0 \\ 0 & 0 & 0 \end{pmatrix}. \quad (9.82)$$

The associated axial vector and its partial derivative with respect to the arc length parameter s read

$$\delta\boldsymbol{\phi} = \text{ax}(\delta\tilde{\boldsymbol{\phi}}) = \delta\theta\mathbf{e}_3, \quad \delta\boldsymbol{\phi}' = \delta\theta'\mathbf{e}_3. \quad (9.83)$$

Dropping the index in the shear force Q_2 and the bending couple M_3 , the planar form of the resultant contact forces and couples defined in (9.39) are

$$\begin{aligned} \mathbf{n} &= N\mathbf{d}_1 + Q\mathbf{d}_2 = (N \cos \theta - Q \sin \theta)\mathbf{e}_1 + (N \sin \theta + Q \cos \theta)\mathbf{e}_2 \\ &= n_1\mathbf{e}_1 + n_2\mathbf{e}_2, \\ \mathbf{m} &= M\mathbf{d}_3 = M\mathbf{e}_3. \end{aligned} \quad (9.84)$$

Note the just introduced abbreviations $n_1 = N \cos \theta - Q \sin \theta$ and $n_2 = N \sin \theta + Q \cos \theta$.

For the sake of compact notation, we define the mapping

$$\perp: \mathbb{E}^3 \rightarrow \mathbb{E}^3, \quad \mathbf{a} \mapsto \mathbf{a}^\perp = \mathbf{A}\mathbf{a}, \quad \mathbf{A} = \mathbf{e}_2 \otimes \mathbf{e}_1 - \mathbf{e}_1 \otimes \mathbf{e}_2, \quad (9.85)$$

which rotates a vector in the \mathbf{e}_1 - \mathbf{e}_2 plane around the \mathbf{e}_3 -axis by $\pi/2$ in the mathematically positive sense. Accordingly, we can write

$$\delta\mathbf{r}' - \delta\boldsymbol{\phi} \times \mathbf{r}' = \delta x'\mathbf{e}_1 + \delta y'\mathbf{e}_2 + \delta\theta y'\mathbf{e}_1 - \delta\theta x'\mathbf{e}_2 = \delta\mathbf{r}' - \delta\theta\mathbf{r}'^\perp. \quad (9.86)$$

Inserting the variation of the tangent vector (9.81), the above computed expression, the variation of the virtual rotation (9.83) and the planar contact forces and couples given in (9.84) into the internal virtual work contributions (9.39), we obtain its planar form

$$\delta W^{\text{int}} = - \int_{l_1}^{l_2} \{(\delta \mathbf{r}' - \delta \theta \mathbf{r}'^\perp) \cdot \mathbf{n} + \delta \theta' M\} ds. \quad (9.87)$$

The external forces $\bar{\mathbf{n}} = \bar{n}_1 \mathbf{e}_1 + \bar{n}_2 \mathbf{e}_2$ only act in the \mathbf{e}_1 - \mathbf{e}_2 -plane and external couples are of the form $\bar{\mathbf{m}} = \bar{M} \mathbf{e}_3$. Same holds for the external forces $\bar{\mathbf{n}}_i = \bar{n}_1^i \mathbf{e}_1 + \bar{n}_2^i \mathbf{e}_2$ and couples $\bar{\mathbf{m}}_i = \bar{M}_i \mathbf{e}_3$ at the boundaries of the beam. The virtual work contributions of the external forces are straightforwardly obtained by inserting (9.81) and (9.83) into (9.41), i.e.,

$$\delta W^{\text{ext}} = \int_{l_1}^{l_2} \{\delta \mathbf{r} \cdot \bar{\mathbf{n}} + \delta \theta \bar{M}\} ds + \sum_{i=1}^2 \{\delta \mathbf{r} \cdot \bar{\mathbf{n}}_i + \delta \theta \bar{M}_i\} |_{s=l_i}. \quad (9.88)$$

For the sake of brevity, we assume that the centerline \mathbf{r} corresponds with the line of centroids \mathbf{r}_c . Hence, the coupling term $\mathbf{c} = A_{\rho_0}(\mathbf{r}_c - \mathbf{r})$ and its time derivatives vanish. Moreover, we assume a homogeneous mass distribution in the cross section such that the directors \mathbf{d}_α coincide with the geometric principal axes of the beam's cross section. Thus, the components of the cross section inertia density $\mathbf{I}_{\rho_0} = I_{ij}^{\rho_0} \mathbf{d}_i \otimes \mathbf{d}_j$ can be arranged in matrix form given by the diagonal matrix

$$[I_{ij}^{\rho_0}] = \text{Diag}[I_1, I_2, I_3] = \begin{pmatrix} I_1 & 0 & 0 \\ 0 & I_2 & 0 \\ 0 & 0 & I_3 \end{pmatrix}. \quad (9.89)$$

The product of the cross section inertia density with the angular velocity and its time derivative (9.52) are given by

$$\mathbf{h} = \mathbf{I}_{\rho_0} \boldsymbol{\omega} = I_3 \dot{\theta} \mathbf{e}_3, \quad \dot{\mathbf{h}} = \mathbf{I}_{\rho_0} \dot{\boldsymbol{\omega}} + \boldsymbol{\omega} \times \mathbf{I}_{\rho_0} \boldsymbol{\omega} = I_3 \ddot{\theta} \mathbf{e}_3. \quad (9.90)$$

Using the above derived simplifications, together with the variation and acceleration of the centerline given in (9.81) and (9.78), respectively, the virtual work contributions of the inertial forces (9.55) reduce to

$$\delta W^{\text{dyn}} = - \int_{l_1}^{l_2} \left\{ \delta \mathbf{r} \cdot A_{\rho_0} \ddot{\mathbf{r}} + \delta \theta I_3 \ddot{\theta} \right\} ds. \quad (9.91)$$

The total virtual work of the planar Timoshenko beam is given by assembling the individual contributions from (9.87), (9.88) and (9.91) which yields

$$\begin{aligned} \delta W^{\text{tot}} = \int_{l_1}^{l_2} \{ \delta \mathbf{r} \cdot (\bar{\mathbf{n}} - A_{\rho_0} \ddot{\mathbf{r}}) + \delta \theta (\bar{M} - I_3 \ddot{\theta} + \mathbf{r}'^\perp \cdot \mathbf{n}) - \delta \mathbf{r}' \cdot \mathbf{n} - \delta \theta' M \} ds \\ + \sum_{i=1}^2 \{ \delta \mathbf{r} \cdot \bar{\mathbf{n}}_i + \delta \theta \bar{M}_i \} |_{s=l_i}. \end{aligned} \quad (9.92)$$

By identifying the first set of constraint conditions (9.67) with the quantities given in (9.77), we get

$$g_2(s, t) = \Gamma_2 = \mathbf{r}' \cdot \mathbf{d}_2 = 0, \quad g_3(s, t) = \Gamma_3 = \mathbf{r}' \cdot \mathbf{d}_3 = 0, \quad (9.93)$$

where the constraint g_3 is trivially fulfilled. With $\delta g_2 = \delta \Gamma_2 = \delta \mathbf{r}' \cdot \mathbf{d}_2 - \delta \theta \mathbf{r}' \cdot \mathbf{d}_1$, the spatial virtual work contributions given in (9.68) reduces to

$$\delta W_{c,1}^{\text{int}} = \int_{l_1}^{l_2} \delta \sigma_2 (\mathbf{r}' \cdot \mathbf{d}_2) ds, \quad \delta W_{c,2}^{\text{int}} = \int_{l_1}^{l_2} \sigma_2 (\delta \mathbf{r}' \cdot \mathbf{d}_2 - \delta \theta \mathbf{r}' \cdot \mathbf{d}_1) ds. \quad (9.94)$$

Adding the virtual work contributions above to the unconstrained total virtual work of the Timoshenko beam (9.92), the Euler–Bernoulli beam model is obtained.

In addition to (9.93), the inextensibility condition (9.69) can be met in the form

$$g_1(s, t) = \Gamma_1(s, t) - 1 = \mathbf{d}_1 \cdot \mathbf{r}' - 1 = \|\mathbf{r}'\| - 1 = g - 1 = 0, \quad (9.95)$$

where we have introduced the abbreviation $g = \|\mathbf{r}'\|$. The variation of the current stretch is given by

$$\delta \Gamma_1 = \delta g = \frac{\delta \mathbf{r}' \cdot \mathbf{r}'}{g}, \quad (9.96)$$

which leads for the inextensible Euler–Bernoulli beam to the additional virtual work contributions

$$\delta W_{c,1}^{\text{int}} = \int_{l_1}^{l_2} \delta \sigma_1 (g - 1) ds, \quad \delta W_{c,2}^{\text{int}} = \int_{l_1}^{l_2} \sigma_1 \frac{\delta \mathbf{r}' \cdot \mathbf{r}'}{g} ds. \quad (9.97)$$

Adding the virtual work contributions above, together with (9.94) to the unconstrained total virtual work of the planar Timoshenko beam (9.92), the inextensible planar Euler–Bernoulli beam model is obtained.

9.7.2 Euler–Bernoulli Beam

In this section, we show how to formulate the planar Euler–Bernoulli beam theory with coordinates that meet the required constraint conditions and for which the constraint forces become obsolete. By inserting the planar versions for the tangent vector (9.71) and the second director (9.72) into the first equality given in (9.93), we can express the absolute angle of the current cross section as

$$\theta = \arctan \left(\frac{y'}{x'} \right). \quad (9.98)$$

Recapitulating the abbreviation $g = \|\mathbf{r}'\| = [(x')^2 + (y')^2]^{1/2}$, the variation and the partial derivative with respect to s of (9.98) are given by

$$\delta \theta = \frac{x' \delta y' - y' \delta x'}{g^2} = \frac{\mathbf{r}'^\perp \cdot \delta \mathbf{r}'}{g^2}, \quad \theta' = \frac{x' y'' - y' x''}{g^2} = \frac{\mathbf{r}'^\perp \cdot \mathbf{r}''}{g^2}, \quad (9.99)$$

where we have used $\frac{d}{dx} \arctan(x) = (1 + x^2)^{-1}$ and the chain rule of differential calculus. With the same arguments, the first and second time derivative of (9.98) are given by

$$\dot{\theta} = \frac{\mathbf{r}'^\perp \cdot \dot{\mathbf{r}}'}{g^2}, \quad \ddot{\theta} = \frac{\mathbf{r}'^\perp \cdot \ddot{\mathbf{r}}'}{g^2} - \frac{2\dot{\theta}\mathbf{r}' \cdot \dot{\mathbf{r}}'}{g^2}, \quad (9.100)$$

where, for the second identity, we have used the property $\mathbf{a}^\perp \cdot \mathbf{a} = 0 \forall \mathbf{a} \in \mathbb{E}^3$. Using the skew symmetry of the rotation operation (9.85)¹ and the linearity of the dot product, the variation of θ' is computed straightforwardly as

$$\delta\theta' = \frac{1}{g^2} (\delta\mathbf{r}'' \cdot \mathbf{r}'^\perp - \delta\mathbf{r}' \cdot [2\theta'\mathbf{r}' + \mathbf{r}''^\perp]). \quad (9.101)$$

With the above derived relations at hand, we are able to replace all quantities depending on θ in the virtual work of the Euler–Bernoulli beam. After minor rearrangements, this leads to the compact internal virtual work contributions of the Euler–Bernoulli beam

$$\begin{aligned} \delta W^{\text{int}} &= - \int_{l_1}^{l_2} \{ \delta\Gamma_1 N + \delta\theta' M \} ds \\ &= - \int_{l_1}^{l_2} \left\{ \frac{1}{g} \delta\mathbf{r}' \cdot \left(\mathbf{r}' N - \frac{M}{g} [2\theta'\mathbf{r}' + \mathbf{r}''^\perp] \right) + \delta\mathbf{r}'' \cdot \mathbf{r}'^\perp \frac{M}{g^2} \right\} ds. \end{aligned} \quad (9.102)$$

Note, that the integral of the virtual work has to exist, thus we require the beam's centerline to be at least C^1 -continuous. This has to be kept in mind for a later discretization.

Inserting the first identity of (9.99) into the planar virtual work contributions of the external forces, given in (9.88), we get

$$\begin{aligned} \delta W^{\text{ext}} &= \int_{l_1}^{l_2} \left\{ \delta\mathbf{r} \cdot \bar{\mathbf{n}} + \frac{\mathbf{r}'^\perp \cdot \delta\mathbf{r}'}{g^2} \bar{M} \right\} ds \\ &\quad + \sum_{i=1}^2 \left\{ \delta\mathbf{r} \cdot \bar{\mathbf{n}}_i + \frac{\mathbf{r}'^\perp \cdot \delta\mathbf{r}'}{g^2} \bar{M}_i \right\} \Big|_{s=l_i}. \end{aligned} \quad (9.103)$$

Using the relations given in (9.99) and (9.100), the virtual work contributions of the inertial forces (9.91) are given by

$$\delta W^{\text{dyn}} = - \int_{l_1}^{l_2} \left\{ \delta\mathbf{r} \cdot A_{\rho_0} \ddot{\mathbf{r}} + I_3 \frac{\mathbf{r}'^\perp \cdot \delta\mathbf{r}'}{g^4} \left(\mathbf{r}'^\perp \cdot \ddot{\mathbf{r}}' - 2\dot{\theta}\mathbf{r}' \cdot \dot{\mathbf{r}}' \right) \right\} ds. \quad (9.104)$$

Note that very often the cumbersome contribution containing I_3 is omitted, see Elishakoff et al (2015) for a discussion about that issue.

¹ Using the property that \mathbf{A} in (9.85) is skew symmetric, i.e., $\mathbf{A}^T = -\mathbf{A}$, we get $\mathbf{a} \cdot \mathbf{b}^\perp = \mathbf{a} \cdot \mathbf{A}\mathbf{b} = (\mathbf{A}^T \mathbf{a}) \cdot \mathbf{b} = -(\mathbf{A}\mathbf{a}) \cdot \mathbf{b} = -\mathbf{a}^\perp \cdot \mathbf{b}$ and thus the variation of the rotated tangential vector and the centerline's second derivative can be swapped by a sign change, i.e., $\delta\mathbf{r}'^\perp \cdot \mathbf{r}'' = -\delta\mathbf{r}' \cdot \mathbf{r}''^\perp$.

Additionally, the inextensibility (9.96) can be enforced by adding the planar version of the constraint virtual work contributions (9.97) to the total planar virtual work, which leads to the mixed formulation (minimal formulation and inextensibility constraint) of the planar inextensible Euler–Bernoulli beam.

9.7.3 Inextensible Euler–Bernoulli Beam

The third constraint condition (9.69) can also be satisfied by choosing a new set of coordinates. Computing the components of the current tangent vector in the \mathbf{d}_i -basis yields

$$\mathbf{r}' = (\mathbf{r}' \cdot \mathbf{d}_i) \mathbf{d}_i \stackrel{(9.93)}{=} (\mathbf{r}' \cdot \mathbf{d}_1) \mathbf{d}_1 = \Gamma_1 \mathbf{d}_1 \stackrel{(9.95, 9.72)}{=} \cos \theta \mathbf{e}_1 + \sin \theta \mathbf{e}_2, \quad (9.105)$$

which necessarily fulfills (9.69). In what follows, $\mathbf{r}' = \mathbf{r}'(\theta)$ is considered as function of θ . The position vector at (s, t) is obtained as the integrated quantity

$$\mathbf{r}(s, t) = \int_{l_1}^s \mathbf{r}'(\theta(\bar{s}, t)) \, d\bar{s} + \bar{\mathbf{r}}(t), \quad (9.106)$$

where $\bar{\mathbf{r}}(t)$ is the time dependent reference point at $s = l_1$. Computing the time derivative of the above equation, we get the velocity vector

$$\dot{\mathbf{r}}(s, t) = \int_{l_1}^s \frac{\partial \mathbf{r}'}{\partial \theta}(\theta(\bar{s}, t)) \dot{\theta}(\bar{s}, t) \, d\bar{s} + \dot{\bar{\mathbf{r}}}(t). \quad (9.107)$$

Accordingly, the acceleration vector is obtained as

$$\ddot{\mathbf{r}}(s, t) = \int_{l_1}^s \left\{ \frac{\partial^2 \mathbf{r}'}{\partial \theta^2}(\theta(\bar{s}, t)) \dot{\theta}^2(\bar{s}, t) + \frac{\partial \mathbf{r}'}{\partial \theta}(\theta(\bar{s}, t)) \ddot{\theta}(\bar{s}, t) \right\} d\bar{s} + \ddot{\bar{\mathbf{r}}}(t). \quad (9.108)$$

The variation of the position vector is given as

$$\delta \mathbf{r}(s, t) = \int_{l_1}^s \frac{\partial \mathbf{r}'}{\partial \theta}(\theta(\bar{s}, t)) \delta \theta(\bar{s}, t) \, d\bar{s} + \delta \bar{\mathbf{r}}(t). \quad (9.109)$$

Using the last identity of (9.95) and inserting its variation $\delta \Gamma_1 = 0$ into the internal virtual work of the Euler–Bernoulli beam given in (9.102), we get

$$\delta W^{\text{int}} = - \int_{l_1}^{l_2} \delta \theta' M \, ds. \quad (9.110)$$

The external virtual work contributions of the inextensible Euler–Bernoulli beam in minimal formulation are given as

$$\begin{aligned} \delta W^{\text{ext}} = & \int_{l_1}^{l_2} \left\{ \left(\int_{l_1}^s \frac{\partial \mathbf{r}'}{\partial \theta} \delta \theta \, d\bar{s} + \delta \bar{\mathbf{r}} \right) \cdot \bar{\mathbf{n}} + \delta \theta \bar{M} \right\} ds \\ & + \sum_{i=1}^2 \left\{ \left(\int_{l_1}^s \frac{\partial \mathbf{r}'}{\partial \theta} \delta \theta \, d\bar{s} + \delta \bar{\mathbf{r}} \right) \cdot \bar{\mathbf{n}}_i + \delta \theta \bar{M}_i \right\} \Big|_{s=l_i} . \end{aligned} \quad (9.111)$$

Inserting (9.108) and (9.109) into the virtual work contributions of the inertial forces given in (9.55) we obtain the cumbersome relation

$$\begin{aligned} \delta W^{\text{dyn}} = & - \int_{l_1}^{l_2} \left\{ \delta \mathbf{r} \cdot A_{\rho_0} \ddot{\mathbf{r}} + \delta \theta I_3 \ddot{\theta} \right\} ds \\ = & - \int_{l_1}^{l_2} A_{\rho_0} \left\{ \int_{l_1}^s \delta \theta \frac{\partial \mathbf{r}'}{\partial \theta} \cdot \frac{\partial^2 \mathbf{r}'}{\partial \theta^2} \dot{\theta}^2 \, d\bar{s} + \int_{l_1}^s \delta \theta \frac{\partial \mathbf{r}'}{\partial \theta} \, d\bar{s} \cdot \ddot{\mathbf{r}} \right. \\ & + \int_{l_1}^s \delta \theta \frac{\partial \mathbf{r}'}{\partial \theta} \cdot \frac{\partial \mathbf{r}'}{\partial \theta} \ddot{\theta} \, d\bar{s} + \delta \bar{\mathbf{r}} \cdot \int_{l_1}^s \frac{\partial^2 \mathbf{r}'}{\partial \theta^2} \dot{\theta}^2 \, d\bar{s} \\ & \left. + \delta \bar{\mathbf{r}} \cdot \int_{l_1}^s \frac{\partial \mathbf{r}'}{\partial \theta} \ddot{\theta} \, d\bar{s} + \delta \bar{\mathbf{r}} \cdot \ddot{\mathbf{r}} + \delta \theta \frac{I_3}{A_{\rho_0}} \ddot{\theta} \right\} ds . \end{aligned} \quad (9.112)$$

If we apply this theory of the planar inextensible Euler–Bernoulli beam to the static consideration of a clamped straight cantilever subjected to a force or a couple at the end, the principle of virtual work leads us directly to the equations known from the elastica theory.

Even though this minimal formulation of the inextensible Euler–Bernoulli beam would be suitable for a subsequent finite element analysis, we will not pursue this any further in Harsch and Eugster (2020). The double integral expressions that appear in the virtual work expressions of distributed forces and couples (9.111) as well as in the inertia terms (9.112) make a numerical treatment extremely cumbersome and not to strive for. Just think about the numerical error of the position (9.106) that cumulates with increasing beam length.

9.8 Conclusion

In this article we presented the derivation of the equations of motion describing the three classical beams, i.e., the Timoshenko beam, the Euler–Bernoulli beam as well as its inextensible companion. The governing equations for the beams were obtained within the variational framework of the principle of virtual work. The applied variational formulation is beneficial not only to add constraints in the sense of the Lagrange multiplier method but also for a subsequent finite element formulation as shown in Harsch and Eugster (2020) for the planar theories. Therefore we additionally elaborated all virtual work contributions of the classical planar theories both as constrained and as unconstrained theories. The corresponding virtual work contributions are ready for a Bubnov–Galerkin discretization.

Acknowledgements This research has been funded by the Deutsche Forschungsgemeinschaft (DFG, German Research Foundation) under Grant No. 405032572 as part of the priority program 2100 Soft Material Robotic Systems.

References

- Alibert JJ, Seppecher P, dell'Isola F (2003) Truss modular beams with deformation energy depending on higher displacement gradients. *Mathematics and Mechanics of Solids* 8(1):51–73
- Andreas U, Spagnuolo M, Lekszycki T, Eugster SR (2018) A Ritz approach for the static analysis of planar pantographic structures modeled with nonlinear Euler–Bernoulli beams. *Continuum Mechanics and Thermodynamics* 30(5):1103–1123
- Antman SS (2005) *Nonlinear Problems of Elasticity*, Applied Mathematical Sciences, vol 107, 2nd edn. Springer
- Ballard P, Millard A (2009) *Poutres et Arcs Élastiques*. Les Éditions de l'École Polytechnique
- Barchiesi E, Eugster SR, Placidi L, dell'Isola F (2019a) Pantographic beam: a complete second gradient 1D-continuum in plane. *Zeitschrift für angewandte Mathematik und Physik* 70(5):135
- Barchiesi E, Spagnuolo M, Placidi L (2019b) Mechanical metamaterials: a state of the art. *Mathematics and Mechanics of Solids* 24(1):212–234
- Barchiesi E, Eugster SR, dell'Isola F, Hild F (2020) Large in-plane elastic deformations of bipantographic fabrics: asymptotic homogenization and experimental validation. *Mathematics and Mechanics of Solids* 25(3):739–767
- Bersani A, dell'Isola F, Seppecher P (2019) Lagrange multipliers in infinite dimensional spaces, examples of application. In: Altenbach H, Öchsner A (eds) *Encyclopedia of Continuum Mechanics*, Springer, pp 1–8
- Betsch P, Steinmann P (2003) Constrained dynamics of geometrically exact beams. *Computational Mechanics* 31:49–59
- Boutin C, dell'Isola F, Giorgio I, Placidi L (2017) Linear pantographic sheets: asymptotic micro-macro models identification. *Mathematics and Mechanics of Complex Systems* 5(2):127–162
- Capobianco G, Eugster SR, Winandy T (2018) Modeling planar pantographic sheets using a nonlinear Euler–Bernoulli beam element based on B-spline functions. *Proceedings in Applied Mathematics and Mechanics* 18(1):1–2
- Cowper GR (1966) The Shear Coefficient in Timoshenko's Beam Theory. *Journal of Applied Mechanics* 33(2):335–340
- dell'Isola F, Placidi L (2011) Variational principles are a powerful tool also for formulating field theories. In: dell'Isola F, Gavriluk S (eds) *Variational models and methods in solid and fluid mechanics*. CISM Courses and Lectures, vol 535, Springer, pp 1–15
- dell'Isola F, Seppecher P (1995) The relationship between edge contact forces, double forces and interstitial working allowed by the principle of virtual power. *Comptes Rendus de l'Académie des Sciences Série II, Mécanique, physique, chimie, astronomie* 321(8):303–308
- dell'Isola F, Steigmann D (2015) A two-dimensional gradient-elasticity theory for woven fabrics. *Journal of Elasticity* 118(1):113–125
- dell'Isola F, Della Corte A, Giorgio I, Scerrato D (2016a) Pantographic 2D sheets: Discussion of some numerical investigations and potential applications. *International Journal of Non-Linear Mechanics* 80:200–208
- dell'Isola F, Della Corte A, Greco L, Luongo A (2016b) Plane bias extension test for a continuum with two inextensible families of fibers: A variational treatment with Lagrange multipliers and a perturbation solution. *International Journal of Solids and Structures* 81:1–12
- dell'Isola F, Giorgio I, Pawlikowski M, Rizzi NL (2016c) Large deformations of planar extensible beams and pantographic lattices: heuristic homogenization, experimental and numerical examples of equilibrium. *Proceedings of the Royal Society of London A: Mathematical, Physical and Engineering Sciences* 472(2185):1–23

- dell'Isola F, Seppecher P, et al (2019a) Advances in pantographic structures: design, manufacturing, models, experiments and image analyses. *Continuum Mechanics and Thermodynamics* 31(4):1231–1282
- dell'Isola F, Seppecher P, et al (2019b) Pantographic metamaterials: an example of mathematically driven design and of its technological challenges. *Continuum Mechanics and Thermodynamics* 31(4):851–884
- dell'Isola F, Seppecher P, Placidi L, Barchiesi E, Misra A (2020a) Least Action and Virtual Work Principles for the Formulation of Generalized Continuum Models, Cambridge University Press, chap 8, pp 327–394
- dell'Isola F, Spagnuolo M, Barchiesi E, Giorgio I, Seppecher P (2020b) Pantographic Metamaterial: A (Not So) Particular Case, Cambridge University Press, chap 3, pp 103–138
- Deutschmann B, Eugster SR, Ott C (2018) Reduced models for the static simulation of an elastic continuum mechanism. *IFAC-PapersOnLine* 51(2):403 – 408
- Dill EH (1992) Kirchhoff's theory of rods. *Archive for History of Exact Sciences* 44(1):1–23
- Elishakoff I, Kaplunov J, Nolde E (2015) Celebrating the centenary of Timoshenko's study of effects of shear deformation and rotary inertia. *Applied Mechanics Reviews* 67(6):060,802
- Eugster SR (2015) Geometric Continuum Mechanics and Induced Beam Theories, Lecture Notes in Applied and Computational Mechanics, vol 75. Springer
- Eugster SR, dell'Isola F (2017) Exegesis of the introduction and sect. I from "Fundamentals of the mechanics of continua" by E. Hellinger. *Zeitschrift für angewandte Mathematik und Mechanik* 97(4):477–506
- Eugster SR, dell'Isola F (2018) Exegesis of sect. II and III.A from "Fundamentals of the mechanics of continua" by E. Hellinger. *Zeitschrift für angewandte Mathematik und Mechanik* 98(1):31–68
- Eugster SR, Deutschmann B (2018) A nonlinear Timoshenko beam formulation for modeling a tendon-driven compliant neck mechanism. *Proceedings in Applied Mathematics and Mechanics* 18(1):1–2
- Eugster SR, Glocker Ch (2017) On the notion of stress in classical continuum mechanics. *Mathematics and Mechanics of Complex Systems* 5(3-4):299–338
- Eugster SR, Steigmann DJ (2020) Variational methods in the theory of beams and lattices. In: Altenbach H, Öchsner A (eds) *Encyclopedia of Continuum Mechanics*, Springer, pp 1–9
- Eugster SR, Hesch C, Betsch P, Glocker Ch (2014) Director-based beam finite elements relying on the geometrically exact beam theory formulated in skew coordinates. *International Journal for Numerical Methods in Engineering* 97(2):111–129
- Germain P (1973) The method of virtual power in continuum mechanics. Part 2: Microstructure. *SIAM Journal on Applied Mathematics* 25:556–575
- Giorgio I, Rizzi NL, Turco E (2017) Continuum modelling of pantographic sheets for out-of-plane bifurcation and vibrational analysis. *Proceedings of the Royal Society of London A: Mathematical, Physical and Engineering Sciences* 473(2207)
- Greco L, Cuomo M (2013) B-spline interpolation of Kirchhoff-Love space rods. *Computer Methods in Applied Mechanics and Engineering* 256(0):251–269
- Harsch J, Eugster SR (2020) Finite element analysis of planar nonlinear classical beam theories. In: Abali BE, Giorgio I (eds) *Developments and Novel Approaches in Nonlinear Solid Body Mechanics, Advanced Structured Materials*, Springer
- Maurin F, Greco F, Desmet W (2019) Isogeometric analysis for nonlinear planar pantographic lattice: discrete and continuum models. *Continuum Mechanics and Thermodynamics* 31(4):1051–1064
- Meier C, Popp A, Wall WA (2014) An objective 3D large deformation finite element formulation for geometrically exact curved Kirchhoff rods. *Computer Methods in Applied Mechanics and Engineering* 278(0):445–478
- Rahali Y, Giorgio I, Ganghoffer J, dell'Isola F (2015) Homogenization à la Piola produces second gradient continuum models for linear pantographic lattices. *International Journal of Engineering Science* 97:148 – 172
- Reissner E (1981) On finite deformations of space-curved beams. *Zeitschrift für Angewandte Mathematik und Physik* 32(6):734–744

- Shirani M, Luo C, Steigmann DJ (2019) Cosserat elasticity of lattice shells with kinematically independent flexure and twist. *Continuum Mechanics and Thermodynamics* 31:1087–1097
- Simo JC (1985) A finite strain beam formulation. the three-dimensional dynamic problem. part I. *Computer Methods in Applied Mechanics and Engineering* 49:55–70
- Steigmann DJ (2017) *Finite Elasticity Theory*. Oxford University Press
- Steigmann DJ, dell’Isola F (2015) Mechanical response of fabric sheets to three-dimensional bending, twisting, and stretching. *Acta Mechanica Sinica* 31(3):373–382
- Steigmann DJ, Faulkner MG (1993) Variational theory for spatial rods. *Journal of Elasticity* 33(1):1–26
- Till J, Aloï V, Rucker C (2019) Real-time dynamics of soft and continuum robots based on Cosserat rod models. *The International Journal of Robotics Research* 38(6):723–746
- Timoshenko S, Goodier JN (1951) *Theory of Elasticity*, 2nd edn. McGraw-Hill book Company



Chapter 10

Finite Element Analysis of Planar Nonlinear Classical Beam Theories

Jonas Harsch & Simon R. Eugster

Abstract This article is based on the planar beam theories presented in Eugster and Harsch (2020) and deals with the finite element analysis of their presented beam models. A Bubnov-Galerkin method, where B-splines are chosen for both ansatz and test functions, is applied for discretizing the variational formulation of the beam theories. Five different planar beam finite element formulations are presented: The Timoshenko beam, the Euler–Bernoulli beam obtained by enforcing the cross-section’s orthogonality constraint as well as the inextensible Euler–Bernoulli beam by additionally blocking the beam’s extension. Furthermore, the Euler–Bernoulli beam is formulated with a minimal set of kinematical descriptors together with a constrained version that satisfies inextensibility. Whenever possible, the numerical results of the different formulations are compared with analytical and semi-analytical solutions. Additionally, numerical results reported in classical beam finite element literature are collected and reproduced.

10.1 Introduction

The finite element discretization relies on the variational formulation of the planar classical beam theories given in Eugster and Harsch (2020). With the mere choice of ansatz and test functions, the discretization of the virtual work contributions directly leads to the corresponding beam finite element formulations. Besides the time t , the virtual work contributions presented in Eugster and Harsch (2020) are parametrized by a single material coordinate s , the arc length parameter of the reference curve. With the subsequent discretization in mind, it is convenient to express the individual virtual work contributions in terms of a non arc length coordinate ξ given in the unit interval. This reparametrization is presented in Section 10.3 and yields the total

J. Harsch, S. R. Eugster
Institute for Nonlinear Mechanics, University of Stuttgart, Stuttgart, Germany
e-mail: harsch@inm.uni-stuttgart.de, eugster@inm.uni-stuttgart.de

virtual work of the different beam formulations given in the so-called parameter space.

The minimal formulation of the Euler–Bernoulli beam, which can be found in (Eugster and Harsch, 2020, Section 9.7.2), requires shape functions that are at least C^1 -continuous. Hence, the well-known Lagrangian shape functions, being only C^0 -continuous, can not be used here. Gontier and Vollmer (1995) proposed the usage of computer aided design (CAD) curve representation, such as Béziers curves, Basis splines (B-splines) or non rational B-splines (NURBS), for implementing beam finite elements. More recently, Hughes et al (2005) and Cottrell et al (2009) established the name isogeometric analysis, which unifies the fields of CAD and finite element analysis. They show the power of combining both tools for numerical analysis of partial differential equations. Led by these ideas, (Greco and Cuomo, 2013, 2014) used B-spline shape functions, which meet the above-mentioned C^1 -continuity requirements, to implement a spatial Euler–Bernoulli beam. B-spline curves, which go back to the pioneering works of Schöneberg (1946) and de Boor (1972), are introduced in Section 10.4, based on the comprehensive monographs (Piegl and Tiller, 1997; Farin, 1997).

Section 10.5 shows that substituting the B-spline curves into the virtual work contributions in parameter space leads to the semi-discrete equations of motion, which are still continuous in time. If the discretized model additionally contains geometric bilateral constraints, either stemming from the constrained beam models or from enforcing boundary conditions, this leads to a set of differential algebraic equations. Although the formulations based on the Timoshenko beam model are not restricted to the above-mentioned continuity requirement, B-splines or NURBS can again be used for their discretization (Cazzani et al, 2016a,b). Another advantage over standard shape functions is, by using B-spline shape functions the global polynomial degree can be chosen arbitrarily. Thus, besides the standard h -refinement (decreasing the element length), also a p -refinement (increasing the polynomial degree) can easily be carried out. The combination of h - and p -refinement is called k -refinement (Cottrell et al, 2009; Greco and Cuomo, 2013). The discretization and all associated algorithms are generalized for any polynomial degree, which will later prove to be advantageous when studying normal modes.

Exclusive numerical examples are studied in Section 10.6. First, the presented beam formulations together with their finite element approximations are verified using analytical and semi-analytical problems from literature. Second, numerical examples of more advanced problems are treated, e.g., tracing the post-buckling equilibrium path of precurved beams. The numerical outcomes are compared with results reported in classical beam finite element literature. The article closes with conclusions and suggestions for future work.

10.2 Notation

Let \mathbb{E}^3 denote a three-dimensional Euclidean vector space with an orthonormal basis $\{\mathbf{e}_1, \mathbf{e}_2, \mathbf{e}_3\}$. For the discretization, all arising vector quantities from Eugster and Harsch (2020) will be expressed in this basis. For that, we collect the components of vectors $\mathbf{a} = a_1\mathbf{e}_1 + a_2\mathbf{e}_2 + a_3\mathbf{e}_3 \in \mathbb{E}^3$ in the tuple ${}_I\mathbf{a} = (a_1, a_2, a_3)^T \in \mathbb{R}^3$. If not stated otherwise, \mathbb{R}^f -tuples are considered in the sense of matrix multiplication as $\mathbb{R}^{f \times 1}$ -matrices, i.e., as "column vectors". Its transposed will be given by a $\mathbb{R}^{1 \times f}$ -matrix, i.e., a "row vector". The components of a vector rotated around \mathbf{e}_3 by $\frac{\pi}{2}$ is denoted by ${}_I\mathbf{a}^\perp = (-a_2, a_1, a_3)^T$. Partial derivatives of vector valued functions $f: \mathbb{R}^f \rightarrow \mathbb{R}, \mathbf{q} \mapsto f(\mathbf{q})$, are introduced as "row vectors" $\partial f / \partial \mathbf{q} = (\partial f / \partial q^1 \dots \partial f / \partial q^f) \in \mathbb{R}^{1 \times f}$. Derivatives of functions $f = f(s, t)$ with respect to the first argument and t are denoted by a prime $f' = \partial f / \partial s$ and a dot $\dot{f} = \partial f / \partial t$, respectively. The variation of a function $f = f(s, t)$, denoted by a delta, is the derivative with respect to the parameter ε of a one-parameter family $\hat{f} = \hat{f}(s, t; \varepsilon)$ evaluated at $\varepsilon = 0$, i.e., $\delta f(s, t) = \partial \hat{f} / \partial \varepsilon(s, t; 0)$. The one-parameter family satisfies $f(s, t) = \hat{f}(s, t; 0)$.

10.3 Virtual Work Contributions in Parameter Space

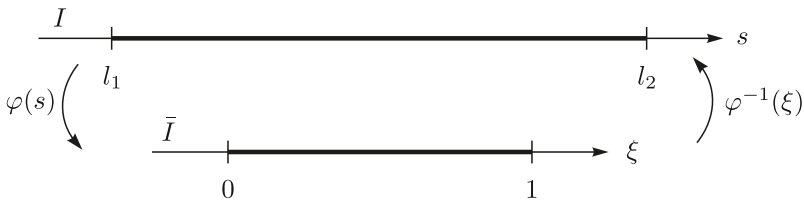


Fig. 10.1 Mapping from the material domain I to the parameter space \bar{I} .

As mentioned in the introduction, the parameter domain can be defined as $\bar{I} = [0, 1] \subset \mathbb{R}$. Points $\xi \in \bar{I}$ belonging to the parameter domain are obtained from material points $s \in I = [l_1, l_2] \subset \mathbb{R}$ by a mapping $\varphi: I \rightarrow \bar{I}$. This new parametrization can be understood in the sense of a non arc length parametrization. We can introduce the strictly increasing function

$$\varphi: I \rightarrow \bar{I}, \quad s \mapsto \xi = \varphi(s), \tag{10.1}$$

depicted in Fig. 10.1. Using the monotonicity property of (10.1), there exists an inverse function $\varphi^{-1}: \bar{I} \rightarrow I$, which is defined on the set $\bar{I} = \varphi(I)$, given by

$$\varphi^{-1}: \bar{I} \rightarrow I, \quad \xi \mapsto s = \varphi^{-1}(\xi). \tag{10.2}$$

Let V denote some linear space, e.g., \mathbb{R} . With the above mappings at hand we can express an arbitrary function $f: I \times \mathbb{R} \rightarrow V$, e.g., the fields x , y , and θ introduced in (Eugster and Harsch, 2020), by a new function $\bar{f}: \bar{I} \times \mathbb{R} \rightarrow V$, defined on the parameter space \bar{I} .

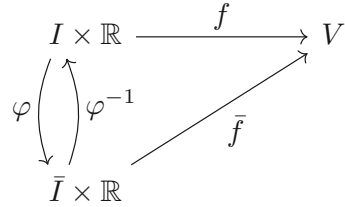


Fig. 10.2 Commutative diagram for the relations of the material coordinate s and non arc length coordinate ξ .

Since the diagram in Fig. 10.2 commutes, we find the relation

$$f(s, t) = \bar{f}(\varphi(s), t) . \quad (10.3)$$

Using (10.3) together with the chain rule of differential calculus, the first and second derivatives of f with respect to s are given by

$$\begin{aligned} f'(s, t) &= \frac{\partial \bar{f}}{\partial \xi}(\varphi(s), t) \frac{d\varphi}{ds}(s) = \bar{f}'(\varphi(s), t) \varphi'(s) , \\ f''(s, t) &= \frac{\partial^2 \bar{f}}{\partial \xi^2}(\varphi(s), t) \left(\frac{d\varphi}{ds}(s) \right)^2 + \frac{\partial \bar{f}}{\partial \xi}(\varphi(s), t) \frac{d^2\varphi}{ds^2}(s) \\ &= \bar{f}''(\varphi(s), t) (\varphi'(s))^2 + \bar{f}'(\varphi(s), t) \varphi''(s) , \end{aligned} \quad (10.4)$$

where a prime $(\cdot)'$ denotes the derivative with respect to the first argument, i.e., either s or ξ . The arc length parametrization of the reference curve $\mathbf{r}_0 = \mathbf{r}_0(s)$ is defined such that the arc length of a curve can be written as

$$l_2 - l_1 = \int_{l_1}^{l_2} \|\mathbf{r}'_0(s)\| \, ds = \int_{l_1}^{l_2} ds , \quad (10.5)$$

from which we identify $\|\mathbf{r}'_0(s)\| = 1$. This can be further manipulated using (10.4) and yields the relation for the Euclidean norm of the reference tangential vector

$$1 = \|\mathbf{r}'_0(s)\| = \|\bar{\mathbf{r}}'_0(\varphi(s))\| |\varphi'(s)| . \quad (10.6)$$

By using the property that φ is a strictly increasing function, its derivative with respect to s is positive and $\varphi'(s)$ coincides with its absolute value. Inserting these observations into (10.6), we obtain

$$\varphi'(s) = \frac{1}{\|\bar{\mathbf{r}}'_0(\varphi(s))\|} = \frac{1}{\bar{G}(\varphi(s))} , \quad (10.7)$$

where we have introduced $\bar{G}(\xi) = \|\bar{\mathbf{r}}'_0(\xi)\|$. The inverse function theorem yields the relation

$$(\varphi^{-1})'(\xi) = \frac{1}{\varphi'(\varphi^{-1}(\xi))} = \bar{G}(\xi) . \quad (10.8)$$

By repeated differentiation, the second derivative of φ is given by

$$\varphi''(s) = -\frac{\bar{\mathbf{r}}'_0(\varphi(s)) \cdot \bar{\mathbf{r}}''_0(\varphi(s))}{\bar{G}^4(\varphi(s))} . \quad (10.9)$$

Using the abbreviation $\mathfrak{G}(\xi) = \frac{\bar{\mathbf{r}}'_0(\xi) \cdot \bar{\mathbf{r}}''_0(\xi)}{\bar{G}^2(\xi)}$, we can insert (10.7) and (10.9) into (10.4), to get

$$\begin{aligned} f'(s, t) &= \frac{\bar{f}'(\varphi(s), t)}{\bar{G}(\varphi(s))} , \\ f''(s, t) &= \frac{1}{\bar{G}^2(\varphi(s))} (\bar{f}''(\varphi(s), t) - \bar{f}'(\varphi(s), t)\mathfrak{G}(\varphi(s))) . \end{aligned} \quad (10.10)$$

In the individual virtual work contributions presented by Eugster and Harsch (2020), integral expressions with respect to the material coordinate s occur. In order to formulate the total virtual work in the parameter space, all functions depending on the pair (s, t) have to be replaced with the overlined functions depending on $(\varphi(s), t)$, as shown in (10.3), together with their derivatives given in (10.10). With the help of (10.3), these integrals can be expressed by the overlined functions according to

$$\int_{l_1}^{l_2} f(s, t) \, ds = \int_{l_1}^{l_2} \bar{f}(\varphi(s), t) \, ds , \quad (10.11)$$

where derivatives with respect to s have to be computed in accordance with (10.4). Using integration by substitution, together with (10.8), the integral expression over the material domain can be computed by an integral over the parameter space given as

$$\int_{l_1=\varphi^{-1}(0)}^{l_2=\varphi^{-1}(1)} \bar{f}(\varphi(s), t) \, ds = \int_0^1 \bar{f}(\xi, t)(\varphi^{-1})'(\xi) \, d\xi = \int_0^1 \bar{f}(\xi, t)\bar{G}(\xi) \, d\xi , \quad (10.12)$$

where in the first step the identity map $\xi = \varphi(\varphi^{-1}(\xi))$ was identified.

10.3.1 Timoshenko Beam

Next, we express the components of the beam's centerline \mathbf{r} and the rotation angle θ by the overlined functions $\bar{\mathbf{r}}$ and $\bar{\theta}$. Moreover, we can collect their components given in the \mathbf{e}_i -basis in the generalized state tuple

$$\mathbf{s}(\xi, t) = (\bar{x}(\xi, t), \bar{y}(\xi, t), \bar{\theta}(\xi, t))^T \in \mathbb{R}^3. \quad (10.13)$$

By substituting the mapping φ into all arising functions, we reformulate the virtual work contributions of the inertia forces (Eugster and Harsch, 2020, (9.91)) in the following compact form

$$\delta W^{\text{dyn}} = - \int_0^1 \delta \mathbf{s}^T \bar{\Theta} \bar{\mathbf{s}} \bar{G} \, d\xi, \quad \bar{\Theta} = \begin{pmatrix} \bar{A}_{\rho_0} & 0 & 0 \\ 0 & \bar{A}_{\rho_0} & 0 \\ 0 & 0 & \bar{I}_3 \end{pmatrix}. \quad (10.14)$$

The virtual work contributions of the internal forces (Eugster and Harsch, 2020, (9.87)) can be computed by

$$\begin{aligned} \delta W^{\text{int}} &= \int_0^1 \{ \delta \mathbf{s}^T \bar{\mathbf{t}}_1 - \delta \mathbf{s}'^T \bar{\mathbf{t}}_2 \} \, d\xi, \\ \bar{\mathbf{t}}_1 &= (0, 0, ({}_I \bar{\mathbf{n}} \times {}_I \mathbf{e}_3)^T \mathbf{s}')^T, \quad \bar{\mathbf{t}}_2 = (\bar{n}_1, \bar{n}_2, \bar{M})^T, \end{aligned} \quad (10.15)$$

where we have used $\bar{x}'\bar{n}_2 - \bar{y}'\bar{n}_1 = {}_I \mathbf{e}_3^T (\mathbf{s}' \times {}_I \bar{\mathbf{n}}) = ({}_I \bar{\mathbf{n}} \times {}_I \mathbf{e}_3)^T \mathbf{s}'$. Note that in both terms of the sum, \bar{G} cancels with the substituted change of integration domain. In the same way the external virtual work contributions (Eugster and Harsch, 2020, (9.88)) can be expressed in the parameter domain as

$$\begin{aligned} \delta W^{\text{ext}} &= \int_0^1 \delta \mathbf{s}^T \bar{\mathbf{t}} \bar{G} \, d\xi + \sum_{i=1}^2 \delta \mathbf{s}^T \bar{\mathbf{t}}_i |_{\xi=\varphi(l_i)}, \\ \bar{\mathbf{t}} &= (\bar{n}_1, \bar{n}_2, \bar{M})^T, \quad \bar{\mathbf{t}}_i = (\bar{n}_1^i, \bar{n}_2^i, \bar{M}_i)^T. \end{aligned} \quad (10.16)$$

10.3.2 Euler–Bernoulli Beam

Also for the Euler–Bernoulli beam, the overlined expressions have to be inserted. From (10.10) and the fact that the variation and the partial derivative with respect to s can be interchanged, we get

$$\mathbf{r}' = \frac{\bar{\mathbf{r}}'}{\bar{G}}, \quad \mathbf{r}'' = \frac{\bar{\mathbf{r}}'' - \bar{\mathbf{r}}' \mathcal{G}}{\bar{G}^2}, \quad \delta \mathbf{r}' = \frac{\delta \bar{\mathbf{r}}'}{\bar{G}}, \quad \delta \mathbf{r}'' = \frac{\delta \bar{\mathbf{r}}'' - \delta \bar{\mathbf{r}}' \mathcal{G}}{\bar{G}^2}. \quad (10.17)$$

The kinematical quantities defined in (Eugster and Harsch, 2020, (9.95) and (9.99)) are of the form

$$g = \frac{\|\bar{\mathbf{r}}'\|}{\bar{G}} = \frac{\bar{g}}{\bar{G}}, \quad \theta' = \frac{\bar{\mathbf{r}}'^{\perp} \cdot \bar{\mathbf{r}}''}{\bar{g}^2 \bar{G}} = \frac{\bar{\theta}'}{\bar{G}}, \quad (10.18)$$

where for the second identity we have used the property $\mathbf{a}^{\perp} \cdot \mathbf{a} = 0 \, \forall \mathbf{a} \in \mathbb{E}^3$.

Carrying out an integration by substitution, we obtain the virtual work contributions of the internal forces (Eugster and Harsch, 2020, (9.102)) given in parameter space

$$\delta W^{\text{int}} = - \int_0^1 \left\{ {}_I \delta \bar{\mathbf{r}}'^{\text{T}} \left(\frac{{}_I \bar{\mathbf{r}}' \bar{N}}{\bar{g}} - \frac{\bar{M}}{\bar{g}^2} [2\bar{\theta}' {}_I \bar{\mathbf{r}}' + {}_I \bar{\mathbf{r}}''^{\perp}] \right) + {}_I \delta \bar{\mathbf{r}}''^{\text{T}} {}_I \bar{\mathbf{r}}'^{\perp} \frac{\bar{M}}{\bar{g}^2} \right\} d\xi. \quad (10.19)$$

It is remarkable that all terms involving \mathcal{G} cancel.

Next we can express the variation of the angle θ , its velocity and acceleration (Eugster and Harsch, 2020, (9.99) and (9.100)) by

$$\delta\theta = \frac{\bar{\mathbf{r}}'^{\perp} \cdot \delta \bar{\mathbf{r}}'}{\bar{g}^2}, \quad \dot{\theta} = \frac{\bar{\mathbf{r}}'^{\perp} \cdot \dot{\bar{\mathbf{r}}}'}{\bar{g}^2}, \quad \ddot{\theta} = \frac{\bar{\mathbf{r}}'^{\perp} \cdot \ddot{\bar{\mathbf{r}}}'}{\bar{g}^2} - \frac{2\dot{\theta} \bar{\mathbf{r}}' \cdot \dot{\bar{\mathbf{r}}}'}{\bar{g}^2}. \quad (10.20)$$

Inserting the above relations into (Eugster and Harsch, 2020, (9.104)), the virtual work contributions of the inertia forces in parameter space are transformed to

$$\delta W^{\text{dyn}} = - \int_0^1 \left\{ \bar{I}_3 \frac{{}_I \bar{\mathbf{r}}'^{\perp \text{T}} {}_I \delta \bar{\mathbf{r}}'}{\bar{g}^4} \left({}_I \bar{\mathbf{r}}'^{\perp \text{T}} {}_I \ddot{\bar{\mathbf{r}}}' - 2\dot{\theta} {}_I \bar{\mathbf{r}}'^{\text{T}} {}_I \dot{\bar{\mathbf{r}}}' \right) + \bar{A}_{\rho_0} {}_I \delta \bar{\mathbf{r}}^{\text{T}} {}_I \ddot{\bar{\mathbf{r}}} \right\} \bar{G} d\xi. \quad (10.21)$$

Finally, the virtual work contributions for the external forces (Eugster and Harsch, 2020, (9.103)) have to be expressed in parameter space. This can be done analogously to the above procedure and yields

$$\delta W^{\text{ext}} = \int_0^1 \left\{ {}_I \delta \bar{\mathbf{r}}^{\text{T}} {}_I \bar{\mathbf{n}} + \frac{{}_I \bar{\mathbf{r}}'^{\perp \text{T}} {}_I \delta \bar{\mathbf{r}}'}{\bar{g}^2} \bar{M} \right\} \bar{G} d\xi + \sum_{i=1}^2 \left\{ {}_I \delta \bar{\mathbf{r}}^{\text{T}} {}_I \bar{\mathbf{n}}_i + \frac{{}_I \bar{\mathbf{r}}'^{\perp \text{T}} {}_I \delta \bar{\mathbf{r}}'}{\bar{g}^2} \bar{M}_i \right\} \Big|_{\xi=\varphi(l_i)}. \quad (10.22)$$

10.3.3 Constraint Virtual Work Contributions

Next, also the virtual work contributions of the constraint forces are expressed in parameter space, using the same procedure as above. The planar virtual work contributions of the orthogonality constraint (Eugster and Harsch, 2020, (9.94)) are expressed in parameter space

$$\delta W_{c,1}^{\text{int}} = \int_0^1 \delta \bar{\sigma}_2 (\mathbf{s}'^{\text{T}} {}_I \bar{\mathbf{d}}_2) d\xi, \quad (10.23)$$

$$\delta W_{c,2}^{\text{int}} = \int_0^1 \bar{\sigma}_2 \{ \delta \mathbf{s}'^{\text{T}} {}_I \bar{\mathbf{d}}_2 - \delta \mathbf{s}^{\text{T}} {}_I \mathbf{e}_3 (\mathbf{s}'^{\text{T}} {}_I \bar{\mathbf{d}}_1) \} d\xi.$$

Accordingly, the virtual work contributions of the inextensibility constraint (Eugster and Harsch, 2020, (9.97)) can be transformed to the integrals over the parameter space given by

$$\delta W_{c,1}^{\text{int}} = \int_0^1 \delta \bar{\sigma}_1 (\bar{g} - \bar{G}) \, d\xi, \quad \delta W_{c,2}^{\text{int}} = \int_0^1 \bar{\sigma}_1 \frac{I \delta \bar{\mathbf{r}}'^T I \bar{\mathbf{r}}'}{\bar{g}} \, d\xi. \quad (10.24)$$

10.4 B-Spline Shape Functions

The excellent monograph of Piegler and Tiller (1997) gives a comprehensive introduction to the topic. They introduce B-spline shape functions and B-spline curves, together with a myriad of important properties. For this, the *knot vector* Ξ with its elements ξ_i , $i = 1, \dots, m$ will be introduced as a non-decreasing sequence, i.e., $\xi_i \leq \xi_{i+1}$. The total number of knots is determined by the chosen polynomial degree p of the target B-spline curve and the total number n of curve sections aka elements. It can be computed as $m = n + 2p + 1$. In the subsequent treatment we restrict ourselves to

- *open* knot vectors, i.e., the multiplicity of the first and last knot is $p + 1$
- knot vectors in the unit interval $[0, 1]$
- equally spaced, so called *uniform* knot vectors, i.e., $\Delta \xi = \xi_{i+1} - \xi_i = \frac{1}{n}$ for $i = p+1, \dots, n+p$ belonging to the interior of the knot vector

These restrictions lead to knot vectors of the form

$$\Xi = \underbrace{\{0, \dots, 0\}}_{p+1}, \underbrace{\{\xi_{p+2}, \dots, \xi_{m-p-1}\}}_{n-1}, \underbrace{\{1, \dots, 1\}}_{p+1}. \quad (10.25)$$

According to (Cox, 1972; de Boor, 1972; Piegler and Tiller, 1997) the i th of total $N = n+p$ B-spline shape functions is recursively defined as

$$N_0^i(\xi) = \begin{cases} 1, & \xi \in [\xi_i, \xi_{i+1}) \\ 0, & \xi \notin [\xi_i, \xi_{i+1}) \end{cases}, \quad (10.26)$$

$$N_p^i(\xi) = \frac{\xi - \xi_i}{\xi_{i+p} - \xi_i} N_{p-1}^i(\xi) + \frac{\xi_{i+p+1} - \xi}{\xi_{i+p+1} - \xi_{i+1}} N_{p-1}^{i+1}(\xi),$$

where in the last line possibly arising quotients of the form $\frac{0}{0}$ are defined as zero. In Fig. 10.3 all non-zero cubic shape functions for a uniform open knot vector, built of four elements, are shown.

The first derivative of a B-spline shape function can be computed from two lower order B-spline shape functions as

$$\frac{d}{d\xi} N_p^i(\xi) = N_{p,\xi}^i(\xi) = \frac{p}{\xi_{i+p} - \xi_i} N_{p-1}^i(\xi) - \frac{p}{\xi_{i+p+1} - \xi_{i+1}} N_{p-1}^{i+1}(\xi). \quad (10.27)$$

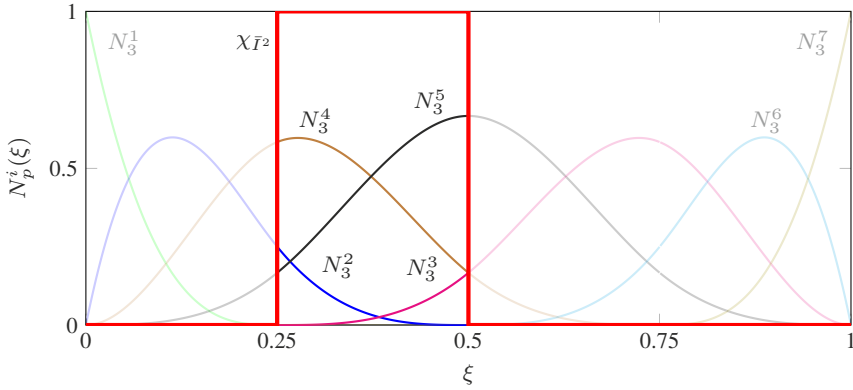


Fig. 10.3 Non-zero cubic B-spline shape functions N_3^1 to N_3^7 for a given uniform and open knot vector $\Xi = \{0, 0, 0, 0, 0.25, 0.5, 0.75, 1, 1, 1, 1\}$ which builds $n = 4$ elements. The indicator function $\chi_{\bar{T}2}$ of the second element, defined in (10.34), picks the corresponding cubic shape functions N_3^2 to N_3^5 .

Denoting the k th derivative of $N_p^i(\xi)$ by $\frac{d^k}{d\xi^k} N_p^i(\xi)$, repeated differentiation of (10.27) leads to the general formula

$$\begin{aligned} \frac{d^k}{d\xi^k} N_p^i(\xi) &= \frac{p}{\xi_{i+p} - \xi_i} \left(\frac{d^{k-1}}{d\xi^{k-1}} N_{p-1}^i(\xi) \right) \\ &\quad - \frac{p}{\xi_{i+p+1} - \xi_{i+1}} \left(\frac{d^{k-1}}{d\xi^{k-1}} N_{p-1}^{i+1}(\xi) \right). \end{aligned} \tag{10.28}$$

Another generalization computes the k th derivative of $N_p^i(\xi)$ by the use of the basis functions $N_{p-k}^i, \dots, N_{p-k}^{i+k}$, namely

$$\begin{aligned} \frac{d^k}{d\xi^k} N_p^i(\xi) &= \frac{p!}{(p-k)!} \sum_{j=0}^k a_{k,j} N_{p-k}^{i+j}(\xi), \\ a_{k,k} &= \begin{cases} 1 & k = 0 \\ \frac{a_{k-1,0}}{\xi_{i+p-k+1} - \xi_i} & k \neq 0 \end{cases}, \\ a_{k,j} &= \begin{cases} \frac{a_{k-1,0}}{\xi_{i+p-k+1} - \xi_i} & j = 0 \\ \frac{a_{k-1,j} - a_{k-1,j-1}}{\xi_{i+p+j-k+1} - \xi_{i+j}} & j = 1, \dots, k-1 \end{cases}. \end{aligned} \tag{10.29}$$

Some knot differences in the denominator of $a_{k,j}$ given in (10.29) can be zero, the arising quotient $\frac{\bullet}{0}$ is defined as zero in these cases.¹

¹ Piegl and Tiller (1997) present an efficient algorithm that is based on (10.29) and that computes for a given knot value ξ the value of the B-spline shape functions together with all $k = 1, \dots, p$ non-zero derivatives. The pseudocode is given in (Piegl and Tiller, 1997, Chap. 2, p. 71, algorithm

In the following some important properties of B-spline shape functions, presented by Piegl and Tiller (1997), are listed.

- P1 $N_0^i(\xi)$ is a step function, which is only non-zero in the half open interval $\bar{I}_i = [\xi_i, \xi_{i+1})$, the so called *ith knot span*.
- P2 $N_p^i(\xi) = 0$ for ξ outside the knot span, which is called the *local support* property. Note that the knot vector contains $m - 1 = n + 2p$ intervals, but only n of them are non-zero. These non-zero intervals are called *element intervals* $\bar{I}^e = \bar{I}_{e+p} = [\xi_{e+p}, \xi_{e+p+1})$ and are addressed by the element number $e = i - p$. Note that we distinguish the knot span and the element interval by using a subscript and a superscript, respectively.
- P3 For positive p the shape function $N_p^i(\xi)$ is a linear combination of two lower order shape functions with polynomial degree $p - 1$. This leads to a truncated triangular table which is exemplary depicted in Fig. 10.4 for B-spline shape functions up to a polynomial degree of $p = 2$. The arrows denote the influence of the current shape function on shape functions of higher polynomial degree.

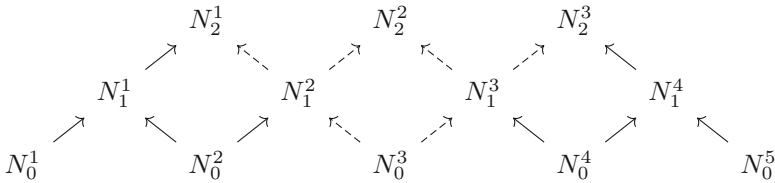


Fig. 10.4 Truncated triangular table for B-spline shape functions up to a polynomial degree of $p = 2$.

- P4 For a given knot span, $\bar{I}_i = [\xi_i, \xi_{i+1})$ at most $p + 1$ shape functions N_p^i are non-zero, namely the functions N_p^{i-p}, \dots, N_p^i . Using again the triangular table depicted in Fig. 10.4, we recognize that on the third knot span $\bar{I}_3 = [\xi_3, \xi_4)$, the only non-zero zeroth-degree shape function is N_0^3 . Hence, the only linear and quadratic shape functions not being zero on \bar{I}^3 are N_1^2, N_1^3 and N_2^1, N_2^2, N_2^3 , respectively. In Fig. 10.4, the dashed arrows point from or to the non-zero shape functions for the third knot span. In Fig. 10.3 the cubic shape functions for a knot vector $\Xi = \{0, 0, 0, 0, 0.25, 0.5, 0.75, 1, 1, 1, 1\}$ are visualized. This defines a B-spline curve given by $n = 4$ elements. For the fifth knot span (second element interval) $\bar{I}_5 = \bar{I}^2 = [0.25, 0.5)$ solely four of the total seven shape functions are non-zero.
- P5 All shape functions are positive, i.e., $N_p^i(\xi) \geq 0$ for all i, p, ξ . This is called the *non-negativity* property.
- P6 *Partition of unity*, for all $\xi \in [\xi_i, \xi_{i+1})$ in an arbitrary knot span $\bar{I}_i = [\xi_i, \xi_{i+1})$, we have $\sum_{j=i-p}^i N_p^j(\xi) = 1$.

A2.3). This algorithm can be vectorized easily in order to compute all shape functions and their derivatives for a set of knot values.

P7 In the interior of a knot span, (ξ_i, ξ_{i+1}) , the B-spline curve is a polynomial of degree p and thus there exist all derivatives $N_p^i(\xi)$. At a knot ξ_i , the shape function $N_p^i(\xi)$ is $p-k$ times continuously differentiable, where k is the multiplicity of the knot.² Hence, increasing the polynomial degree globally increases the continuity of the B-spline curve.

For uniform, open knot vectors $\Xi \in [0, 1]$, on which we confined ourselves in the beginning of this section, a p th degree B-spline curve is defined as

$$\mathbf{c}(\xi, t) = \sum_{i=1}^N N_p^i(\xi) \mathbf{q}^i(t), \quad 0 \leq \xi < 1, \quad (10.30)$$

where the tuple \mathbf{q}^i are denoted as control points. In the sense of a Galerkin method in mechanics the N control points \mathbf{q}^i are called *generalized coordinates*. The B-spline shape functions $N_p^i(\xi)$ are computed according to (10.26). A computational algorithm for evaluating (10.30) is given in (Piegl and Tiller, 1997, Chap. 3, p. 82, algorithm A3.1).

Computing the k th derivative of $\mathbf{c}(\xi, t)$, namely $\frac{d^k}{d\xi^k} \mathbf{c}(\xi, t)$, is done analogously to (10.30) and reads

$$\frac{d^k}{d\xi^k} \mathbf{c}(\xi) = \sum_{i=1}^N \frac{d^k}{d\xi^k} N_p^i(\xi) \mathbf{q}^i, \quad 0 \leq \xi < 1. \quad (10.31)$$

The derivatives of the shape functions have to be computed by (10.28) or (10.29). A computational algorithm for the evaluation of (10.31) is given in (Piegl and Tiller, 1997, Chap. 3, p. 93, algorithm A3.2).

10.5 Discrete Kinematics, Semidiscrete Virtual Work, and Equations of Motion

In the subsequent, treatment the continuous fields \mathbf{s} and ${}_I \bar{\mathbf{r}}$ will be approximated by p th order B-spline curves. Thus the infinite-dimensional beam models are projected to finite dimensional discretized systems. Depending on the approximated field, the i th control point \mathbf{q}^i is given by the tuples $\mathbf{q}^i(t) = (x^i(t), y^i(t), \theta^i(t))^T \in \mathbb{R}^3$ or $\mathbf{q}^i(t) = (x^i(t), y^i(t))^T \in \mathbb{R}^2$.

² This property is of crucial importance for the discretization of the presented Euler–Bernoulli beam. The evaluation of the internal virtual work contributions require the existence of the integral (10.19). Since this integral includes terms of second derivative, C^1 -continuity of the chosen interpolation polynomial is required. For polynomial degrees $p \geq 2$ this continuity requirement is unconditionally fulfilled.

10.5.1 Timoshenko Beam

The generalized coordinates are collected in the tuple of generalized coordinates

$$\mathbf{q} = (x^1, \dots, x^N, y^1, \dots, y^N, \theta^1, \dots, \theta^N)^T \in \mathbb{R}^{3N}. \quad (10.32)$$

Thus, the generalized state tuple (10.13) can be approximated by the p th order B-spline curve

$$\mathbf{s}(\xi, t) \approx \mathbf{c}(\xi, \mathbf{q}(t)) = \sum_{i=1}^N N_p^i(\xi) \mathbf{q}^i(t). \quad (10.33)$$

In a Galerkin method, it is convenient to evaluate the kinematic quantities in an element-wise setting. As mentioned in P4, for a given element e and its corresponding element interval $\bar{I}^e = [\xi_{e+p}, \xi_{e+p+1})$, several B-spline shape functions are non-zero. Thus, we have to partly consider multiple shape functions. In order to extract the correct parts of the shape functions and to not consider the same parts multiple times, the indicator function

$$\chi_{\bar{I}^e} : \mathbb{R} \rightarrow \mathbb{R}, \quad \chi_{\bar{I}^e}(\xi) = \begin{cases} 1, & \xi \in \bar{I}^e \\ 0, & \xi \notin \bar{I}^e \end{cases} \quad (10.34)$$

is introduced. See Fig. 10.3 for a graphical visualization. With the above definition at hand, (10.33) can be written as

$$\mathbf{c}(\xi, \mathbf{q}(t)) = \sum_{e=1}^n \sum_{i=1}^N \chi_{\bar{I}^e}(\xi) N_p^i(\xi) \mathbf{q}^i(t). \quad (10.35)$$

As written in P4, for a given knot span $\bar{I}_i = \bar{I}^{i-p}$, only $p + 1$ B-spline shape functions are non-zero, namely N_p^{i-p}, \dots, N_p^i . Thus instead of summing over all N shape functions, we can equivalently write

$$\mathbf{c}(\xi, \mathbf{q}(t)) = \sum_{e=1}^n \sum_{i=e}^{e+p} \chi_{\bar{I}^e}(\xi) N_p^i(\xi) \mathbf{q}^i(t), \quad (10.36)$$

where we have shifted the shape function index using the relation between knot span and element number given by $i = e + p$. The inner sum can be computed by the matrix tuple product

$$\mathbf{c}(\xi, \mathbf{q}(t)) = \sum_{e=1}^n \chi_{\bar{I}^e}(\xi) \mathbf{c}^e, \quad \mathbf{c}^e = \mathbf{N}_p^e(\xi) \mathbf{q}^e(t). \quad (10.37)$$

It is composed of the element matrix of the B-spline shape functions $\mathbf{N}_p^e \in \mathbb{R}^{3 \times 3(p+1)}$ and the element generalized coordinate tuple $\mathbf{q}^e \in \mathbb{R}^{3(p+1)}$, each of which is defined as

$$\mathbf{N}_p^e = \begin{pmatrix} N_p^e & N_p^{e+1} & \dots & N_p^{e+p} & 0 & 0 & \dots & 0 & 0 & 0 & \dots & 0 \\ 0 & 0 & \dots & 0 & N_p^e & N_p^{e+1} & \dots & N_p^{e+p} & 0 & 0 & \dots & 0 \\ 0 & 0 & \dots & 0 & 0 & 0 & \dots & 0 & N_p^e & N_p^{e+1} & \dots & N_p^{e+p} \end{pmatrix},$$

$$\mathbf{q}^e = (x^e, x^{e+1}, \dots, x^{e+p}, y^e, y^{e+1}, \dots, y^{e+p}, \theta^e, \theta^{e+1}, \dots, \theta^{e+p})^T. \quad (10.38)$$

Using the Boolean allocation matrix $\mathbf{C}^e \in \mathbb{R}^{3(p+1) \times 3N}$, the relationship of the element coordinates \mathbf{q}^e and the global nodal coordinates \mathbf{q} is given by

$$\mathbf{q}^e = \mathbf{C}^e \mathbf{q}. \quad (10.39)$$

Let the generalized velocities $\dot{\mathbf{q}}$, generalized accelerations $\ddot{\mathbf{q}}$ and the first variation of the generalized coordinates $\delta \mathbf{q}$ be of the same form as (10.32). By transferring the relation between the element coordinates and the global ones from (10.39), we are able to approximate the first and second spatial derivatives, the acceleration, as well as the variation of the generalized state tuple by

$$\begin{aligned} \mathbf{s}'(\xi, t) &\approx \mathbf{c}'(\xi, \mathbf{q}(t)) = \sum_{e=1}^n \chi_{\bar{I}^e}(\xi) \mathbf{N}_p^{e'}(\xi) \mathbf{C}^e \mathbf{q}(t), \\ \mathbf{s}''(\xi, t) &\approx \mathbf{c}''(\xi, \mathbf{q}(t)) = \sum_{e=1}^n \chi_{\bar{I}^e}(\xi) \mathbf{N}_p^{e''}(\xi) \mathbf{C}^e \mathbf{q}(t), \\ \ddot{\mathbf{s}}(\xi, t) &\approx \ddot{\mathbf{c}}(\xi, \mathbf{q}(t)) = \sum_{e=1}^n \chi_{\bar{I}^e}(\xi) \mathbf{N}_p^e(\xi) \mathbf{C}^e \ddot{\mathbf{q}}(t), \\ \delta \mathbf{s}(\xi, t) &\approx \delta \mathbf{c}(\xi, \mathbf{q}(t)) = \sum_{e=1}^n \chi_{\bar{I}^e}(\xi) \mathbf{N}_p^e(\xi) \mathbf{C}^e \delta \mathbf{q}(t). \end{aligned} \quad (10.40)$$

Furthermore, we can substitute the approximations for the variation and acceleration of the generalized state tuple given in (10.40), into the planar virtual work of the inertia contributions in parameter space (10.14). Recapitulating that the characteristic function is non-zero only if $\xi \in \bar{I}^e$, either one of the characteristic functions vanishes if the two arising sums have not the same index, thus the product of two sums reduces to a single one and we get

$$\delta W^{\text{dyn}} \approx - \int_0^1 \sum_{e=1}^n \chi_{\bar{I}^e} \delta \mathbf{q}^T \mathbf{C}^{eT} \mathbf{N}_p^{eT} \bar{\Theta} \mathbf{N}_p^e \mathbf{C}^e \ddot{\mathbf{q}} \bar{G} \, d\xi. \quad (10.41)$$

For a given element e , the characteristic function extracts the element interval $\bar{I}^e = [\xi_e, \xi_{e+1}]$ from the parameter space $\bar{I} = [0, 1]$. Thus, the integral over the whole parameter space \bar{I} reduces to an integral over the element interval \bar{I}^e . Accordingly, we obtain after minor rearrangements

$$\delta W^{\text{dyn}} \approx - \delta \mathbf{q}^T \sum_{e=1}^n \mathbf{C}^{eT} \int_{\xi_e}^{\xi_{e+1}} \mathbf{N}_p^{eT} \bar{\Theta} \mathbf{N}_p^e \bar{G} \, d\xi \mathbf{C}^e \ddot{\mathbf{q}} = - \delta \mathbf{q}^T \mathbf{M} \ddot{\mathbf{q}}. \quad (10.42)$$

The global and elemental mass matrices \mathbf{M} and \mathbf{M}^e , respectively, are obtained as

$$\mathbf{M} = \sum_{e=1}^n \mathbf{C}^{eT} \mathbf{M}^e \mathbf{C}^e, \quad \mathbf{M}^e = \int_{\xi_e}^{\xi_{e+1}} \mathbf{N}_p^{eT} \bar{\Theta} \mathbf{N}_p^e \bar{G} \, d\xi. \quad (10.43)$$

Further we used that $\delta \mathbf{q}$ and $\ddot{\mathbf{q}}$ are independent of ξ and therefore can be pulled out the integral.

Accordingly, the internal virtual work contributions in the parameter space, given in (10.15), can be approximated by

$$\begin{aligned} \delta W^{\text{int}} &\approx \delta \mathbf{q}^T \mathbf{f}^{\text{int}}, \quad \mathbf{f}^{\text{int}} = \sum_{e=1}^n \mathbf{C}^{eT} \mathbf{f}^{\text{int},e}, \\ \mathbf{f}^{\text{int},e} &= \int_{\xi_e}^{\xi_{e+1}} \{ \mathbf{N}_p^{eT} \bar{\mathbf{t}}_1 - \mathbf{N}_p^{eT} \bar{\mathbf{t}}_2 \} \, d\xi, \end{aligned} \quad (10.44)$$

where we have introduced the global internal forces \mathbf{f}^{int} and their elemental contributions $\mathbf{f}^{\text{int},e}$. With some straightforward computations, the internal stiffness matrix $\mathbf{K} = \frac{\partial \mathbf{f}^{\text{int}}}{\partial \mathbf{q}}$ can be computed as

$$\begin{aligned} \mathbf{K} &= \sum_{e=1}^n \mathbf{C}^{eT} \mathbf{K}^e \mathbf{C}^e, \quad \mathbf{K}^e = \int_{\xi_e}^{\xi_{e+1}} \left\{ \mathbf{N}_p^{eT} \frac{\partial \bar{\mathbf{t}}_1}{\partial \mathbf{q}^e} - \mathbf{N}_p^{eT} \frac{\partial \bar{\mathbf{t}}_2}{\partial \mathbf{q}^e} \right\} \, d\xi, \\ \frac{\partial \bar{\mathbf{t}}_1}{\partial \mathbf{q}^e} &= \left(\frac{\partial 0}{\partial \mathbf{q}^e}, \frac{\partial 0}{\partial \mathbf{q}^e}, (I \bar{\mathbf{n}} \times I \mathbf{e}_3)^T \mathbf{N}_p^{e'} + (I \mathbf{e}_3 \times \mathbf{c}^{e'})^T \frac{\partial I \bar{\mathbf{n}}}{\partial \mathbf{q}^e} \right)^T, \\ \frac{\partial \bar{\mathbf{t}}_2}{\partial \mathbf{q}^e} &= \left(\frac{\partial \bar{n}_1}{\partial \mathbf{q}^e}, \frac{\partial \bar{n}_2}{\partial \mathbf{q}^e}, \frac{\partial \bar{M}}{\partial \mathbf{q}^e} \right)^T. \end{aligned} \quad (10.45)$$

Using the same procedure as for the inertia and internal virtual work contributions, we obtain the discretized form of the external virtual work contributions in parameter space (10.16) given by

$$\begin{aligned} \delta W^{\text{ext}} &\approx \delta \mathbf{q}^T (\mathbf{f}^{\text{ext}} + \sum_{i=1}^2 \mathbf{f}_i^{\text{ext}}), \quad \mathbf{f}^{\text{ext}} = \sum_{e=1}^n \mathbf{C}^{eT} \mathbf{f}^{\text{ext},e}, \\ \mathbf{f}^{\text{ext},e} &= \int_{\xi_e}^{\xi_{e+1}} \mathbf{N}_p^{eT} \bar{\mathbf{t}} \bar{G} \, d\xi, \quad \mathbf{f}_i^{\text{ext}} = \sum_{e=1}^n \mathbf{C}^{eT} \chi_{I^e} \mathbf{N}_p^{eT} \bar{\mathbf{t}}_i |_{\xi=\varphi(l_i)}. \end{aligned} \quad (10.46)$$

10.5.2 Euler–Bernoulli Beam

For the discretization of the Euler–Bernoulli beam, only the first $2N$ generalized coordinates of (10.32) are collected in a new generalized coordinate tuple

$$\mathbf{q} = (x^1, \dots, x^N, y^1, \dots, y^N)^T \in \mathbb{R}^{2N}. \quad (10.47)$$

Similarly to (10.37), the components of the position vector given in the \mathbf{e}_i -basis can be approximated by

$${}_I\bar{\mathbf{r}}(\xi, t) \approx \mathbf{c}(\xi, \mathbf{q}(t)) = \sum_{e=1}^n \chi_{I^e}(\xi) \mathbf{c}^e, \quad \mathbf{c}^e = \mathbf{N}_p^e(\xi) \mathbf{q}^e(t). \quad (10.48)$$

The element matrix of the B-spline shape functions $\mathbf{N}_p^e \in \mathbb{R}^{2 \times 2(p+1)}$ and the element generalized coordinate tuple $\mathbf{q}^e \in \mathbb{R}^{2(p+1)}$ are defined as

$$\begin{aligned} \mathbf{N}_p^e &= \begin{pmatrix} N_p^e & N_p^{e+1} & \dots & N_p^{e+p} & 0 & 0 & \dots & 0 \\ 0 & 0 & \dots & 0 & N_p^e & N_p^{e+1} & \dots & N_p^{e+p} \end{pmatrix}, \\ \mathbf{q}^e &= (x^e, x^{e+1}, \dots, x^{e+p}, y^e, y^{e+1}, \dots, y^{e+p})^T. \end{aligned} \quad (10.49)$$

Using a new Boolean allocation matrix $\mathbf{C}^e \in \mathbb{R}^{2(p+1) \times 2N}$, the relationship of the element coordinates \mathbf{q}^e and global nodal coordinates \mathbf{q} is again given by $\mathbf{q}^e = \mathbf{C}^e \mathbf{q}$. Inserting the approximations for all required kinematic quantities into (10.21), we get the approximated virtual work contributions of the inertia forces

$$\begin{aligned} \delta W^{\text{dyn}} &\approx -\delta \mathbf{q}^T \mathbf{M} \ddot{\mathbf{q}} + \delta \mathbf{q}^T \mathbf{h}, \quad \mathbf{M} = \sum_{e=1}^n \mathbf{C}^{eT} \mathbf{M}^e \mathbf{C}^e, \quad \mathbf{h} = \sum_{e=1}^n \mathbf{C}^{eT} \mathbf{h}^e, \\ \mathbf{M}^e &= \int_{\xi_e}^{\xi_{e+1}} \left(\bar{A}_{\rho_0} \mathbf{N}_p^{eT} \mathbf{N}_p^e + \frac{\bar{I}_3}{\bar{g}^4} (\mathbf{N}_p^{e/T} \mathbf{c}^{e/\perp}) (\mathbf{c}^{e/\perp T} \mathbf{N}_p^e) \right) \bar{G} \, d\xi, \\ \mathbf{h}^e &= \int_{\xi_e}^{\xi_{e+1}} \frac{2\dot{\theta} \bar{I}_3}{\bar{g}^4} (\mathbf{N}_p^{e/T} \mathbf{c}^{e/\perp}) (\mathbf{c}^{e/T} \dot{\mathbf{c}}^{e'}) \bar{G} \, d\xi. \end{aligned} \quad (10.50)$$

Note, that in addition to the mass matrix \mathbf{M} , a gyroscopic force \mathbf{h} and its elemental counterpart \mathbf{h}^e appears. Both \mathbf{h} and \mathbf{h}^e are quadratic in $\dot{\mathbf{q}}$ and $\dot{\mathbf{q}}^e$, respectively.

Accordingly, the internal virtual work contributions (10.19) can be approximated by

$$\begin{aligned} \delta W^{\text{int}} &\approx \delta \mathbf{q}^T \mathbf{f}^{\text{int}}, \quad \mathbf{f}^{\text{int}} = \sum_{e=1}^n \mathbf{C}^{eT} \mathbf{f}^{\text{int},e}, \\ \mathbf{f}^{\text{int},e} &= - \int_{\xi_e}^{\xi_{e+1}} \left\{ \mathbf{N}_p^{e/T} \left(\frac{\mathbf{c}^{e'} \bar{N}}{\bar{g}} - \frac{\bar{M}}{\bar{g}^2} [2\dot{\theta}' \mathbf{c}^{e'} + \mathbf{c}^{e''\perp}] \right) \right. \\ &\quad \left. + \mathbf{N}_p^{e''T} \mathbf{c}^{e'\perp} \frac{\bar{M}}{\bar{g}^2} \right\} d\xi. \end{aligned} \quad (10.51)$$

Using basic rules of calculus, the stiffness matrix can be derived as

$$\begin{aligned} \mathbf{K} &= \frac{\partial \mathbf{f}^{\text{int}}}{\partial \mathbf{q}} = \sum_{e=1}^n \mathbf{C}^{e\text{T}} \mathbf{K}^e \mathbf{C}^e, \\ \mathbf{K}^e &= \int_{\xi_e}^{\xi_{e+1}} \left\{ \mathbf{N}_p^{e'\text{T}} \left(k_2 \frac{\partial \mathbf{c}^{e'\perp}}{\partial \mathbf{q}^e} + \mathbf{c}^{e'\perp} \frac{\partial k_2}{\partial \mathbf{q}^e} \right) \right. \\ &\quad \left. + \mathbf{N}_p^{e'\text{T}} \left[\frac{\partial \mathbf{k}_1}{\partial \mathbf{q}^e} - (\mathbf{k}_3 + \mathbf{c}^{e'\perp}) \frac{\partial k_2}{\partial \mathbf{q}^e} - k_2 \left(\frac{\partial \mathbf{k}_3}{\partial \mathbf{q}^e} + \frac{\partial \mathbf{c}^{e'\perp}}{\partial \mathbf{q}^e} \right) \right] \right\} d\xi. \end{aligned} \quad (10.52)$$

The introduced auxiliary functions and their partial derivatives with respect to the generalized coordinates are given by

$$\begin{aligned} \mathbf{k}_1 &= \frac{\mathbf{c}^{e'} \bar{N}}{\bar{g}}, \quad \frac{\partial \mathbf{k}_1}{\partial \mathbf{q}^e} = -\frac{\mathbf{k}_1}{\bar{g}} \frac{\partial \bar{g}}{\partial \mathbf{q}^e} + \frac{1}{\bar{g}} \left(\bar{N} \mathbf{N}_p^{e'} + \mathbf{c}^{e'} \frac{\partial \bar{N}}{\partial \mathbf{q}^e} \right), \\ k_2 &= \frac{\bar{M}}{\bar{g}^2}, \quad \frac{\partial k_2}{\partial \mathbf{q}^e} = -2 \frac{k_2}{\bar{g}} \frac{\partial \bar{g}}{\partial \mathbf{q}^e} + \frac{1}{\bar{g}^2} \frac{\partial \bar{M}}{\partial \mathbf{q}^e}, \\ \mathbf{k}_3 &= 2 \bar{\theta}' \mathbf{c}^{e'}, \quad \frac{\partial \mathbf{k}_3}{\partial \mathbf{q}^e} = 2 \left(\mathbf{c}^{e'} \frac{\partial \bar{\theta}'}{\partial \mathbf{q}^e} + \bar{\theta}' \mathbf{N}_p^{e'} \right), \\ \frac{\partial \bar{g}}{\partial \mathbf{q}^e} &= \frac{\mathbf{c}^{e'}}{\bar{g}} \mathbf{N}_p^{e'}, \quad \frac{\partial \bar{\theta}'}{\partial \mathbf{q}^e} = \frac{1}{\bar{g}^2} \left(\mathbf{c}^{e'\perp\text{T}} \mathbf{N}_p^{e''} - \mathbf{c}^{e''\text{T}} \frac{\partial \mathbf{c}^{e'\perp}}{\partial \mathbf{q}^e} \right) - 2 \frac{\bar{\theta}'}{\bar{g}} \frac{\partial \bar{g}}{\partial \mathbf{q}^e}. \end{aligned} \quad (10.53)$$

Finally, the external virtual work contributions in parameter space given in (10.22) can be discretized by

$$\begin{aligned} \delta W^{\text{ext}} &\approx \delta \mathbf{q}^{\text{T}} (\mathbf{f}^{\text{ext}} + \sum_{i=1}^2 \mathbf{f}_i^{\text{ext}}), \quad \mathbf{f}^{\text{ext}} = \sum_{e=1}^n \mathbf{C}^{e\text{T}} \mathbf{f}^{\text{ext},e}, \\ \mathbf{f}^{\text{ext},e} &= \int_{\xi_e}^{\xi_{e+1}} \left\{ \mathbf{N}_p^{e\text{T}} \bar{\mathbf{n}} + \mathbf{N}_p^{e'\text{T}} \mathbf{c}^{e'\perp} \frac{\bar{M}}{\bar{g}^2} \right\} \bar{G} d\xi, \\ \mathbf{f}_i^{\text{ext}} &= \sum_{e=1}^n \mathbf{C}^{e\text{T}} \chi_{\bar{I}^e} \left\{ \mathbf{N}_p^{e\text{T}} \bar{\mathbf{n}}_i + \mathbf{N}_p^{e'\text{T}} \mathbf{c}^{e'\perp} \frac{\bar{M}_i}{\bar{g}^2} \right\} \Big|_{\xi=\varphi(l_i)}. \end{aligned} \quad (10.54)$$

10.5.3 Constraint Forces

In addition to the discretization of the position and rotation fields, the contributions of the constraint forces (10.23) and (10.24) have to be discretized. This is done by approximating the Lagrange multiplier fields $\bar{\sigma}_1$ and $\bar{\sigma}_2$ using B-spline curves in accordance with (10.37), i.e., the same element distribution for the Lagrange multiplier fields and the kinematic quantities is chosen. Two new sets of generalized coordinates can be introduced

$$\mathbf{q}_{\sigma_1} = (\bar{\sigma}_1^1, \dots, \bar{\sigma}_1^N)^{\text{T}} \in \mathbb{R}^N, \quad \mathbf{q}_{\sigma_2} = (\bar{\sigma}_2^1, \dots, \bar{\sigma}_2^N)^{\text{T}} \in \mathbb{R}^N. \quad (10.55)$$

Thus for $k = 1, 2$, both Lagrange multipliers can be approximated by the B-spline curve of polynomial degree p_{σ_k} given as

$$\begin{aligned}\bar{\sigma}_k(\xi, t) &\approx c_k(\xi, \mathbf{q}_{\sigma_k}(t)) = \sum_{e=1}^n \chi_{\bar{I}^e}(\xi) c_k^e, \\ c_k^e &= \mathbf{N}_{p_{\sigma_k}}^e(\xi) \mathbf{q}_{\sigma_k}^e(t), \quad \mathbf{q}_{\sigma_k}^e = \mathbf{C}_{\sigma_k}^e \mathbf{q}_{\sigma_k}.\end{aligned}\quad (10.56)$$

The element tuple of the B-spline shape functions $\mathbf{N}_{p_{\sigma_k}}^e \in \mathbb{R}^{1 \times p_{\sigma_k} + 1}$ and the element generalized coordinate tuple $\mathbf{q}_{\sigma_k}^e \in \mathbb{R}^{p_{\sigma_k} + 1}$ are defined as

$$\mathbf{N}_{p_{\sigma_k}}^e = (N_{p_{\sigma_k}}^e, N_{p_{\sigma_k}}^{e+1}, \dots, N_{p_{\sigma_k}}^{e+p_{\sigma_k}}), \quad \mathbf{q}_{\sigma_k}^e = (\bar{\sigma}_k^e, \bar{\sigma}_k^{e+1}, \dots, \bar{\sigma}_k^{e+p_{\sigma_k}})^T. \quad (10.57)$$

The question arises, which polynomial degree p_{σ_k} for the approximation of the Lagrange multipliers is compatible with the polynomial degree p of the approximated kinematic quantities. Without further investigations, we chose the polynomial degree $p_{\sigma_k} = p - 1$ in the subsequent treatment. Numerical experiments have shown, that such a polynomial degree leads to good convergence and accuracy of the constraint beam models. By substituting the approximation of the Lagrange multiplier fields given in (10.56) into the constraint virtual work contributions (10.23), the approximated version reads

$$\begin{aligned}\delta W_{c,1}^{\text{int}} &= \delta \mathbf{q}_{\sigma_2}^T \mathbf{g}_{\sigma_2}, \quad \mathbf{g}_{\sigma_2} = \sum_{e=1}^n \mathbf{C}_{\sigma_2}^{eT} \mathbf{g}_{\sigma_2}^e, \quad \mathbf{g}_{\sigma_2}^e = \int_{\xi_e}^{\xi_{e+1}} \mathbf{N}_{p_{\sigma_2}}^{eT} (\mathbf{c}^{e/T} {}_I \bar{\mathbf{d}}_2) d\xi, \\ \delta W_{c,2}^{\text{int}} &= \delta \mathbf{q}^T \mathbf{f}_c^{\text{int}} = \delta \mathbf{q}^T \mathbf{W}_{\sigma_2} \mathbf{q}_{\sigma_2}, \quad \mathbf{W}_{\sigma_2} = \sum_{e=1}^n \mathbf{C}^{eT} \mathbf{W}_{\sigma_2}^e \mathbf{C}_{\sigma_2}^e, \\ \mathbf{W}_{\sigma_2}^e &= \int_{\xi_e}^{\xi_{e+1}} \{ \mathbf{N}_{p_{\sigma_2}}^{e/T} {}_I \bar{\mathbf{d}}_2 - \mathbf{N}_p^{eT} {}_I \mathbf{e}_3 (\mathbf{c}^{e/T} {}_I \bar{\mathbf{d}}_1) \} \mathbf{N}_{p_{\sigma_2}}^e d\xi.\end{aligned}\quad (10.58)$$

From the above we can identify the generalized force directions by the partial derivative of the discretized constraint function, i.e., $\mathbf{W}_{\sigma_2}^T = \partial \mathbf{g}_{\sigma_2} / \partial \mathbf{q}$ and $\mathbf{W}_{\sigma_2}^{eT} = \partial \mathbf{g}_{\sigma_2}^e / \partial \mathbf{q}^e$.

For the inextensibility condition introduced in (10.24), the same steps as above can be performed which yields

$$\begin{aligned}\delta W_{c,1}^{\text{int}} &= \delta \mathbf{q}_{\sigma_1}^T \mathbf{g}_{\sigma_1}, \quad \mathbf{g}_{\sigma_1} = \sum_{e=1}^n \mathbf{C}_{\sigma_1}^{eT} \mathbf{g}_{\sigma_1}^e, \quad \mathbf{g}_{\sigma_1}^e = \int_{\xi_e}^{\xi_{e+1}} \mathbf{N}_{p_{\sigma_1}}^{eT} (\bar{g} - \bar{G}) d\xi, \\ \delta W_{c,2}^{\text{int}} &= \delta \mathbf{q}^T \mathbf{f}_c^{\text{int}} = \delta \mathbf{q}^T \mathbf{W}_{\sigma_1} \mathbf{q}_{\sigma_1}, \quad \mathbf{W}_{\sigma_1} = \sum_{e=1}^n \mathbf{C}^{eT} \mathbf{W}_{\sigma_1}^e \mathbf{C}_{\sigma_1}^e, \\ \mathbf{W}_{\sigma_1}^e &= \int_{\xi_e}^{\xi_{e+1}} \mathbf{N}_p^{e/T} \frac{\mathbf{c}^{e/T}}{\bar{g}} \mathbf{N}_{p_{\sigma_1}}^e d\xi.\end{aligned}\quad (10.59)$$

Again, the generalized force directions can be identified with the partial derivative of the discretized constraint functions with respect to the generalized coordinates, i.e. $\mathbf{W}_{\sigma_1}^T = \partial \mathbf{g}_{\sigma_1} / \partial \mathbf{q}$ and $\mathbf{W}_{\sigma_1}^{eT} = \partial \mathbf{g}_{\sigma_1}^e / \partial \mathbf{q}^e$.

10.5.4 Equations of Motion and Bilateral Constraints

The principle of virtual work, stated in (Eugster and Harsch, 2020, (9.56)), can be formulated in a discrete way by inserting the discrete virtual work contributions presented in the previous section. The total virtual work has to vanish for all admissible variations $\delta \mathbf{q}$ of the generalized coordinates and for any instant of time t , i.e.

$$\delta W = \delta W^{\text{dyn}} + \delta W^{\text{int}} + \delta W^{\text{ext}} = 0, \quad \forall \delta \mathbf{q}, \forall t. \quad (10.60)$$

Substituting the generalized forces introduced in Section 10.5.1 and demanding it to hold for arbitrary variations $\delta \mathbf{q}$ for all time t , we get

$$\begin{aligned} -\delta \mathbf{q}^T (\mathbf{M}(\mathbf{q})\ddot{\mathbf{q}} - \mathbf{f}^{\text{int}}(\mathbf{q}) - \mathbf{f}^{\text{ext}}(\mathbf{q}, \dot{\mathbf{q}}, t)) &= 0, \quad \forall \delta \mathbf{q}, \forall t \\ \Rightarrow \mathbf{M}(\mathbf{q})\ddot{\mathbf{q}} - \mathbf{f}^{\text{int}}(\mathbf{q}) - \mathbf{f}^{\text{ext}}(\mathbf{q}, \dot{\mathbf{q}}, t) &= 0, \end{aligned} \quad (10.61)$$

which are the semidiscrete equations of motion of the planar Timoshenko beam, which hold for all time instants t .

Similarly, the semidiscrete equations of motion of the planar Euler–Bernoulli beam are obtained by substituting the discrete counterparts of the virtual work contributions given in Section 10.5.2 into the principle of virtual work, which leads to

$$\mathbf{M}(\mathbf{q})\ddot{\mathbf{q}} - \mathbf{h}(\mathbf{q}, \dot{\mathbf{q}}) - \mathbf{f}^{\text{int}}(\mathbf{q}) - \mathbf{f}^{\text{ext}}(\mathbf{q}, \dot{\mathbf{q}}, t) = 0. \quad (10.62)$$

Furthermore, the virtual work contributions of the constraint forces can be added to both discrete virtual work principles given above. The constrained Euler–Bernoulli beam is obtained by incorporating the angle constraint (10.58) in the total virtual work of the Timoshenko beam. Further the inextensibility condition (10.59) can be added, which yields the constrained inextensible Euler–Bernoulli beam formulation. The discretized minimal formulated Euler–Bernoulli beam can be made inextensible by the very same constraint condition. Next, depending on the desired constrained beam formulation, the generalized vector of constraints \mathbf{g}_{σ_1} , respectively \mathbf{g}_{σ_2} are named \mathbf{g}_σ when only one constraint condition is applied. Or both constraints \mathbf{g}_{σ_1} and \mathbf{g}_{σ_2} are stacked in the tuple \mathbf{g}_σ . In an analogous fashion, the corresponding generalized coordinates tuple \mathbf{q}_σ is built. Similarly, one of the generalized force directions \mathbf{W}_{σ_1} and \mathbf{W}_{σ_2} is named \mathbf{W}_σ when only a single set of constraints is required, or we can assemble \mathbf{W}_{σ_1} and \mathbf{W}_{σ_2} in a matrix \mathbf{W}_σ , when both sets of constraints are imposed. Thus, independent of the chosen set of constraints, the equations of motion for the constrained beam models are given by

$$\begin{aligned} \mathbf{M}(\mathbf{q})\ddot{\mathbf{q}} - \mathbf{f}^{\text{int}}(\mathbf{q}) - \mathbf{f}^{\text{ext}}(\mathbf{q}, \dot{\mathbf{q}}, t) - \mathbf{W}_\sigma(\mathbf{q})\mathbf{q}_\sigma &= 0 \\ \mathbf{g}_\sigma(\mathbf{q}) &= 0. \end{aligned} \quad (10.63)$$

It is convenient to introduce another set of perfect bilateral constraints $\mathbf{g}(\mathbf{q}, t) \in \mathbb{R}^f$ which enforce the prescribed kinematic boundary conditions. Their associated generalized force directions are $\mathbf{W}^T = \partial \mathbf{g} / \partial \mathbf{q}$ with $\mathbf{W} \in \mathbb{R}^{3N \times f}$ or $\mathbf{W} \in \mathbb{R}^{2N \times f}$ for the Timoshenko and Euler–Bernoulli beam model, respectively. The corresponding tuple of Lagrange multipliers is $\boldsymbol{\lambda} \in \mathbb{R}^f$. The discrete equations of motion are extended with the constraint force contributions $\mathbf{W}(\mathbf{q}, t)\boldsymbol{\lambda}$, together with the additional constraint conditions $\mathbf{g}(\mathbf{q}, t)$ and read

$$\begin{aligned} \mathbf{M}(\mathbf{q})\ddot{\mathbf{q}} - \mathbf{f}^{\text{int}}(\mathbf{q}) - \mathbf{f}^{\text{ext}}(\mathbf{q}, \dot{\mathbf{q}}, t) - \mathbf{W}_\sigma(\mathbf{q})\mathbf{q}_\sigma - \mathbf{W}(\mathbf{q}, t)\boldsymbol{\lambda} &= 0 \\ \mathbf{g}_\sigma(\mathbf{q}) &= 0 \\ \mathbf{g}(\mathbf{q}, t) &= 0. \end{aligned} \quad (10.64)$$

They have to be solved for the unknowns $\{\mathbf{q}, \mathbf{q}_\sigma, \boldsymbol{\lambda}\}$. In case of the Euler–Bernoulli beam model the gyroscopic force vector \mathbf{h} has to be subtracted from the left-hand side of the first equality in (10.63) and (10.64).

Both (10.63) and (10.64) are sets of differential algebraic equations (DAE) of index 3. A general introduction to DAE solvers is given in Hairer and Wanner (2002), including the standard methods like *Shake*, *Rattle* and *backward differentiation formula (BDF)*. In structural dynamics the generalized- α method is a well-established solver, not only because of its simple implementation, but also because of its ability to eliminate the contribution of non-physical high-frequency modes. Variants of the generalized α -method for constraint mechanical systems are introduced in (Lunk and Simeon, 2006; Arnold and Brüls, 2007; Jay and Negrut, 2009). In order to include unilateral constraints (Leine and van de Wouw, 2007), a more recent variant of the generalized- α method is proposed by Brüls et al (2014, 2018).

The static equilibrium problem is obtained by omitting the inertia terms and allowing the external forces and the bilateral constraints to depend only on the generalized coordinates \mathbf{q} . This leads to the static residual equation

$$\mathbf{R}(\mathbf{q}, \mathbf{q}_\sigma, \boldsymbol{\lambda}) = (\mathbf{f}^{\text{int}}(\mathbf{q}) + \mathbf{f}^{\text{ext}}(\mathbf{q}) + \mathbf{W}_\sigma(\mathbf{q})\mathbf{q}_\sigma + \mathbf{W}(\mathbf{q})\boldsymbol{\lambda}, \mathbf{g}_\sigma(\mathbf{q}), \mathbf{g}(\mathbf{q}))^T. \quad (10.65)$$

Application of a truncated Taylor-series expansion of (10.65) around a given point $\{\mathbf{q}_0, \mathbf{q}_{\sigma_0}, \boldsymbol{\lambda}_0\}$ yields a Newton–Raphson type iteration scheme, which solves for the unknowns $\{\mathbf{q}, \mathbf{q}_\sigma, \boldsymbol{\lambda}\}$.

Finally, the arising element integrals over the domain $\bar{I}^e = [\xi_e, \xi_{e+1}]$ in the individual parts of the equations of motion have to be computed. This is done by using a numerical integration scheme. The basic idea of numerical quadrature is the approximation of the integral $\int_a^b f(\xi) \, d\xi$ in a given interval $I = [a, b]$ by evaluating the function f at some discrete values $\xi_i \in I$ and multiplication with the so-called integration weights w_i . Since numerical quadrature rules are well known in literature, the reader is referred to basic textbooks about numerical analysis, e.g., (Stoer et al, 2002, Chap. 3) and (Quarteroni et al, 2000, Chap. 9-10). The

numerical examples, presented in the subsequent section are computed using the Gauss-Legendre quadrature rule, whereby the number of quadrature points within one element are chosen such that they equal the polynomial degree p of the B-spline curves.

10.6 Numerical Examples

The subsequent section deals with the performed numerical examples. At first, we present some static benchmark problems that show the differences of the finite element implementations of all beam models and their numerical accuracy with respect to analytical solutions. Afterwards more advanced problems are investigated, including buckling problems, which are compared to numerical and semi-analytical solutions found in literature. Finally, the natural frequencies of the presented Euler-Bernoulli beam formulation will be compared to the analytically derived ones.

All presented beam models are implemented in an in-house object oriented multi-body dynamics code written in Python. The data found in literature is digitalized using the amazing Webplotdigitizer tool developed by Rohatgi (2019).

10.6.1 Pure Bending of a Cantilever Beam

In the first example a straight beam of length $L = 2\pi$, axial stiffness $E_1 = 5$, shear stiffness $E_2 = 1$, and bending stiffness $F_3 = 2$ is subjected to a concentrated end couple $\bar{M}_2 = 2\pi F_3/L$. The exact solution for this problem is given by a closed circle of radius $r = 1$. This static boundary condition (pure bending) leads to a homogenous flexural deformation. There should be neither extensional nor shear effects, thus we expect all beam models leading to the very same solution. By regarding the computed configurations depicted in Fig. 10.5, this expectation has come true.

Next, the convergence behavior of all five presented beam formulations were investigated, namely the Timoshenko beam (T_1), the Euler-Bernoulli beam obtained by adding the corresponding constraint (T_2), the inextensible Euler-Bernoulli beam given by additionally adding the inextensibility condition (T_3), the minimal formulation of the Euler-Bernoulli beam (E_1) and the inextensible Euler-Bernoulli beam obtained by adding the corresponding constraint condition (E_2). All beam formulations presented in the previous sections were computed with different number of elements $n \in \{8, 16, 32, 64, 128\}$ (h -refinement) and polynomial degrees $p \in \{2, 3, 5\}$ (p -refinement). The Lagrange multiplier fields for the constrained beam models were discretized with B-splines of polynomial degree $p_{\sigma_k} = p - 1$. Further information regarding the different refinement strategies, including combinations of h - and p -refinement, the so-called k -refinement, can be found in (Cottrell et al, 2009; Greco and Cuomo, 2013). For each refinement level, 50 iterations of a force controlled Newton-Raphson method were performed using a convergence

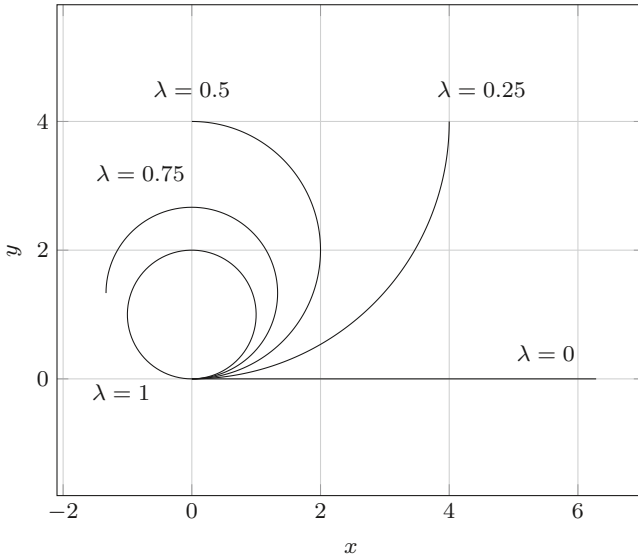


Fig. 10.5 Same configurations for all presented beam models with load increments $\lambda \in \{0, 0.25, 0.5, 0.75, 1\}$.

tolerance of 10^{-12} with respect to the maximum absolute error of the static residual (10.65). Let e be the Euclidean error of the point of applied couple with respect to the analytical solution, given by the origin. In Fig. 10.6, the normalized error e/L is depicted. By increasing the polynomial degree or the number of used finite elements, the error decreases. Two more remarkable observations can be made. The minimal formulations of the Timoshenko and Euler–Bernoulli beam led to the same errors as their constrained counterparts. This is due to the absence of axial and shear deformations in this problem. Thus, the constraints have no influence on the convergence behavior. For the finest discretization ($n = 128$ and $p = 5$), all beam models converge to an error of $\mathcal{O}(10^{-12})$, which coincides with the given tolerance of the underlying Newton–Raphson scheme.

Henceforth, we restrict the presentation to the three kinematically different beam models. For computational efficiency the models with the smallest number of degrees of freedom are chosen. These are the Timoshenko beam model (T_1), the minimal formulation of the Euler–Bernoulli beam (E_1) and its inextensible version (E_2).

10.6.2 Cantilever Beam Subjected to Constant End Load

Let us consider an initially straight beam of length $L = 2\pi$, axial stiffness $E_1 = 5$, shear stiffness $E_2 = 1$, and bending stiffness $F_3 = 2$ which is subjected to a constant end load in negative vertical direction. For the inextensible Euler–Bernoulli beam,

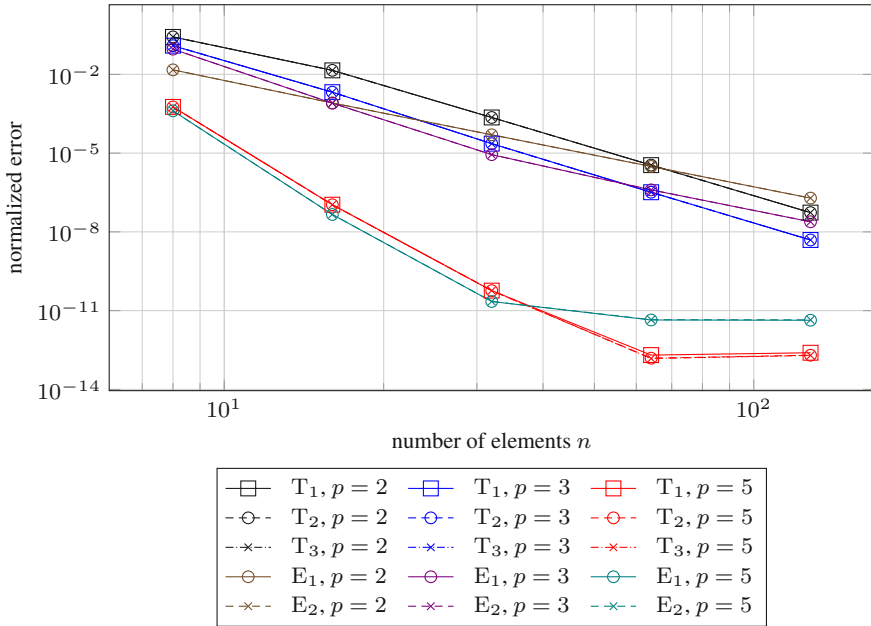


Fig. 10.6 Normalized Euclidean error of the point of applied couple with respect to the analytical solution, given by the origin, for all different beam models using different levels of refinement.

this kind of problem is solved analytically using the first and second elliptic integrals, defined as

$$F(\theta, k) = \int_0^\theta (1 - k^2 \sin^2 \tilde{\theta})^{-\frac{1}{2}} d\tilde{\theta}, \quad E(\theta, k) = \int_0^\theta (1 - k^2 \sin^2 \tilde{\theta})^{\frac{1}{2}} d\tilde{\theta}. \tag{10.66}$$

Byrd and Friedman (1954) give a general introduction to elliptic integrals. Let

$${}_I \mathbf{F} = -P_I \mathbf{e}_2, \quad P = \left(\frac{\alpha}{L}\right)^2 F_3, \tag{10.67}$$

be an external point force at the beam's end $s = L$ depending on a force parameter α^2 . Bisshopp and Drucker (1945) derived the solution for the horizontal and vertical deflection of the cantilever beam in terms of the elliptic integrals given in (10.66), i.e.,

$$\begin{aligned} x(L) &= \frac{L\sqrt{2}}{\alpha} \sqrt{\sin \phi_0}, \quad \sin \phi_0 = 2k^2 - 1, \\ y(L) &= L \left(1 - \frac{2}{\alpha} [E(\pi/2, k) - E(\theta_1, k)] \right), \quad \sin \theta_1 = \frac{\sqrt{2}}{2k}. \end{aligned} \tag{10.68}$$

The deflections solely depend on the parameter k . Bisshopp and Drucker (1945) showed that the inextensibility condition leads to

$$\alpha = F(\pi/2, k) - F(\theta_1, k) . \quad (10.69)$$

By using a root-finding method, e.g., a bisection method, for a given load value α^2 , the corresponding k value can be obtained. This completely determines the displacement of the beam tip of the inextensible Euler–Bernoulli beam.

For the discretization of the used finite element models, $n = 20$ quadratic B-spline elements ($p = 2, p_{\sigma_1} = 1$) were used. The numerical solution was obtained by application of a load controlled Newton–Raphson method with 10 load steps and a convergence tolerance of 10^{-8} with respect to the maximum absolute error of the static residual (10.65).

In Fig. 10.7, the configurations for the different beam models are compared with the solution found by using elliptic integrals. For the inextensible Euler–Bernoulli beam model all configurations are in excellent accordance with the elliptic integral solution. The Euler–Bernoulli beam model leads to the same curvature but due to its extensibility the end points do not coincide with the elliptic integral solution. For the Timoshenko beam additionally shear deformation is allowed. Thus also the curvatures do not coincide with those of the inextensible Euler–Bernoulli beam solutions.

In Fig. 10.8, the normalized horizontal and vertical displacements given by $\delta = -y(L)/L$ and $\Delta = x(L)/L$ are depicted for given load parameters α^2 . It can be observed that the inextensible Euler–Bernoulli beam model can reproduce the results obtained by using elliptic integrals. The Timoshenko and Euler–Bernoulli beam models lead to slightly different results, due to presence of extensional and shear deformations.

10.6.3 Cantilever Beam Subject to Follower End Load

In this example the large deflection of a cantilever beam of length $L = 1$, axial stiffness $E_1 = EA$ ($E = 2100, A = 20 \cdot 10^{-4}$), shear stiffness $E_2 = GA$ ($G = E/(2 + 2\nu), \nu = 0.3$), flexural stiffness $F_3 = EI$ ($I = 1,667 \cdot 10^{-8}$) under non-conservative transverse force is investigated. This problem was examined by (Argyris and Symeonidis, 1981; Simo and Vu-Quoc, 1986). The beam is clamped on the left-hand side and on the right-hand side a transverse follower force \mathbf{F} with $\|\mathbf{F}\| = \lambda 3 \cdot 10^{-3}$ is applied. The force is applied perpendicular to the beam tip. The angle between the free end and the applied force thus always remains $\pi/2$.

For the discretization of the used finite element models, $n = 20$ quadratic B-spline elements ($p = 2, p_{\sigma_1} = 1$) were used. The numerical solution was obtained by application of a load controlled Newton–Raphson method with 100 load steps and a convergence tolerance of 10^{-8} with respect to the maximum absolute error of the static residual (10.65).

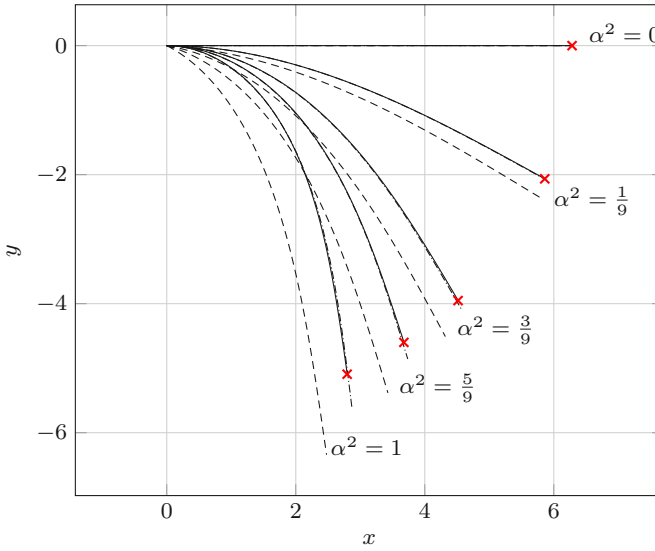


Fig. 10.7 Configurations for different load parameters $\alpha^2 \in \{0, \frac{1}{9}, \frac{3}{9}, \frac{5}{9}, 1\}$. The Timoshenko beam is depicted by dashed lines, the Euler–Bernoulli beam by dashdotted lines and the inextensible Euler–Bernoulli beam model by solid lines. The elliptic integral solutions given in Bisshopp and Drucker (1945) are indicated by red crosses.

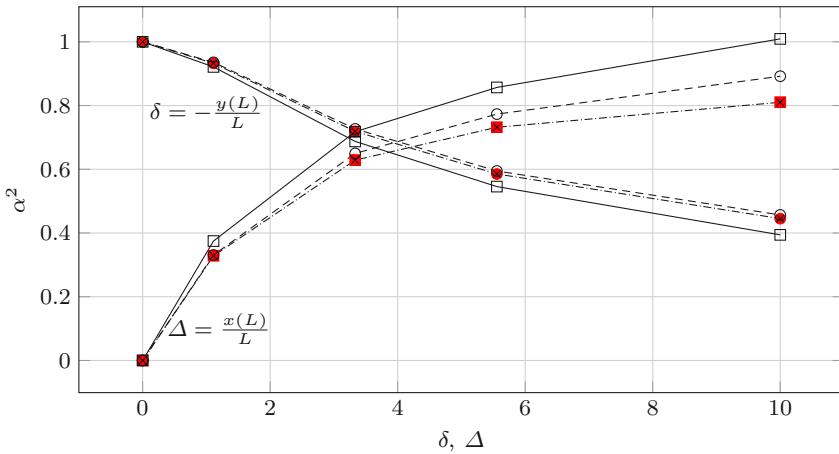


Fig. 10.8 Force displacement curves for the cantilever beam. The analytical solutions using elliptic integrals are depicted by red bullets and squares for the δ and Δ values, respectively. The finite element solutions of the Timoshenko beam are depicted by solid lines, the Euler–Bernoulli beam by dashed lines and the inextensible Euler–Bernoulli beam model by dashdotted lines.

For small load increments, the configurations of the different beam formulations, depicted in Fig 10.9, can't be distinguished. For increasing load increments, the configurations obtained by the Timoshenko beam model differ from the ones obtained by the two Euler–Bernoulli beams. The effect of the inextensibility can not be recognized.

In Fig. 10.10 the load deflection curve is compared with the results obtained by Argyris and Symeonidis (1981). There is a good overall accordance. For the loads between $\lambda = 0.1$ and $\lambda = 0.2$ the horizontal displacement curves are separated for all beam models. In contrast to Argyris and Symeonidis (1981), larger load increments were computed, in order to see slightly differences of the Timoshenko and Euler–Bernoulli beam models. Again the inextensible Euler–Bernoulli beam can not be distinguished from the extensible one.

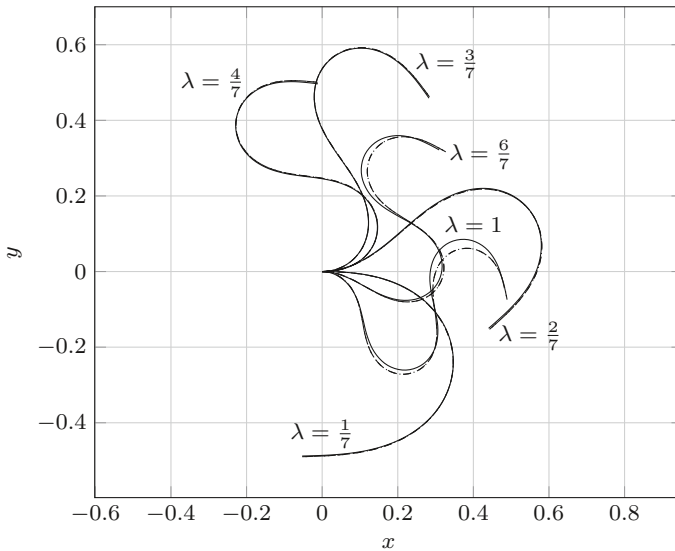


Fig. 10.9 Deformed configurations of the different beam models under a non-conservative follower force with load parameters $\lambda \in \{\frac{1}{7}, \frac{2}{7}, \frac{3}{7}, \frac{4}{7}, \frac{6}{7}, 1\}$. The Timoshenko beam model is depicted by solid lines, the Euler–Bernoulli beam by dashed lines and the inextensible Euler–Bernoulli beam model by dashdotted lines.

10.6.4 Clamped-Hinged Circular Arch Subject to Point Load

In this example, we investigated the buckling and post-buckling behavior of a circular arch of radius $R = 100$ clamped on the right end and hinged on the left, see Fig. 10.11. This problem is also discussed in (Dadeppo and Schmidt, 1975; Simo and Vu-Quoc, 1986), both of which are using an inextensible Euler–Bernoulli beam model, either

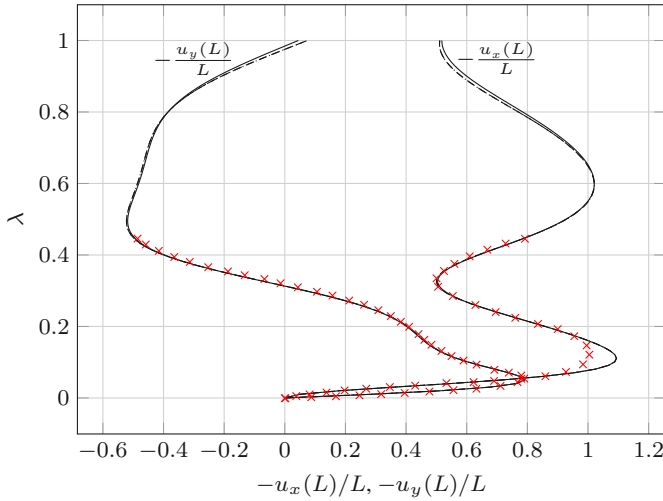


Fig. 10.10 Load deflection curves for the horizontal displacement $u_x = x(L) - L$ and vertical displacement $u_y = -y(L)$ of the point of applied load. The Timoshenko beam model is depicted by solid lines, the Euler–Bernoulli beam with dashed lines and the inextensible Euler–Bernoulli beam model by dashdotted lines. The results found in Argyris and Symeonidis (1981) are depicted by red crosses.

by direct formulation or by utilizing a penalty approach, for their investigations. The inner angle of the arc is $2\alpha = 205^\circ$. The arch is represented by two beams of axial stiffness $E_1 = 50$, shear stiffness $E_2 = 10$ and flexural stiffness $F_3 = 1000$. The beams are connected by the use of bilateral constraints that guarantee the same position and angle at the connection point. Both beams are of undeformed length $L_1 = L_2 = 100 \frac{180^\circ}{\alpha}$. A constant external force ${}_I\mathbf{F} = -\lambda_I \mathbf{e}_2$ is applied at the crown of the circle.

B-spline shape functions are not able to represent perfect archs. In order to obtain a pre-curved reference configuration an optimization technique was developed. Let $\{\mathbf{p}_i\}$, $i = 1, \dots, k$ be a given set of points $\mathbf{p}_i \in \mathbb{R}^2$, which describe the target curve of the reference configuration. Next a set of evaluation points ξ_i is collected in a knot vector $\Xi \in \mathbb{R}^f$. There are several possibilities found in literature (Piegl and Tiller, 1997, Chap. 9.2, p. 364). The most simple method is choosing equally spaced knots in the interval $[0, 1]$. Next a p th order B-spline curve divided into n elements, which depends on the chosen polynomial degree p and the $N = n + p$ generalized coordinates $\{\mathbf{q}_j\}$, $j = 1, \dots, N$, can be introduced. The generalized coordinates $\mathbf{q}_j \in \mathbb{R}^2$ are collected in a tuple $\mathbf{q} \in \mathbb{R}^N$. Solving the optimization problem

$$K = \sum_{i=1}^k \frac{1}{2} \|\mathbf{c}(\xi_i, \mathbf{q}) - \mathbf{p}_i\|^2 \rightarrow \min, \quad (10.70)$$

leads to an optimal fit of the B-spline curve \mathbf{c} , defined in (10.48), to the points \mathbf{p}_i in a least squares sense. The necessary condition for solving the minimization problem (10.70) reads $\partial K/\partial \mathbf{q} = 0$. Inserting the definition of the B-spline curve given in (10.48) and after carrying out minor rearrangements, we obtain the linear system of equations

$$\begin{aligned} \mathbf{A}\mathbf{q} = \mathbf{b}, \quad \mathbf{A} &= \sum_{i=1}^k \sum_{e=1}^n \chi_{\bar{I}^e}(\xi_i) \mathbf{C}^{eT} \mathbf{N}_p^{eT}(\xi_i) \mathbf{N}_p^e(\xi_i) \mathbf{C}^e, \\ \mathbf{b} &= \sum_{i=1}^k \sum_{e=1}^n \chi_{\bar{I}^e}(\xi_i) \mathbf{C}^{eT} \mathbf{N}_p^{eT}(\xi_i) \mathbf{p}_i. \end{aligned} \quad (10.71)$$

This can be solved for the unknown generalized coordinates \mathbf{q} of the reference configuration. As a requirement for \mathbf{A} to be well-conditioned, every knot span must contain at least one ξ_i , see (Piegl and Tiller, 1997, Chap. 9.4.1, p. 412) and (de Boor, 1978, Chap. 14.4, p. 223).

In order to obtain the B-spline curve representing the angle, i.e., ${}_I \mathbf{e}_3^T \mathbf{c}(\xi, \mathbf{q})$, with \mathbf{c} from (10.37), in a second step an analogous minimization problem has to be solved. The angle of the target curve can be computed by $\bar{\theta}_i = \arctan(\bar{y}'(\xi_i, \mathbf{q})/\bar{x}'(\xi_i, \mathbf{q}))$. The values for \bar{x}' and \bar{y}' are obtained as the first and second component of the B-spline curve's derivative \mathbf{c}' given in (10.70). The new minimization problem reads

$$K^* = \sum_{i=1}^k \frac{1}{2} \| {}_I \mathbf{e}_3^T \mathbf{c}(\xi_i, \mathbf{q}) - \bar{\theta}_i \|^2 \rightarrow \min. \quad (10.72)$$

In the discretization, presented in the previous section, we restricted ourselves to open knot vectors, thus we had to ensure that the first and last point \mathbf{p}_1 and \mathbf{p}_k , respectively exactly match with the generalized coordinates \mathbf{q}_1 and \mathbf{q}_N . Analogously, the angles have to coincide with angles of the target curve. This was obtained by additionally imposing constraints onto (10.70) and (10.72). These constraints are met by extending the system with a Lagrange multiplier method, see (Piegl and Tiller, 1997, Chap. 9.4.2).

In order to obtain post-buckling solutions, i.e., configurations after exceeding a critical force value, a numerical path following algorithm was used instead of the classical Newton–Raphson method. The most simple methods are the so-called linear arc length methods. The first solution method was published by Riks (1979), followed by others, e.g., Crisfield (1981). A general introduction to the topic of path-following and arc length methods can be found in Crisfield (1991). In order to use these solvers, together with bilateral constraints, some modifications are required. The basic ideas are sketched below. First, in contrast to a load incremented solution technique, the load parameter λ becomes an additional degree of freedom. Thus, one additional equation has to be found, in order to close the static equilibrium problem. This is done by introducing a new scalar function $f(\mathbf{q}, \lambda)$, limiting the incremental displacements. As proposed by Crisfield (1991) the simple function $f(\mathbf{q}, \lambda) = (\mathbf{q} - \mathbf{q}_0)^T (\mathbf{q} - \mathbf{q}_0) - \Delta s^2$, with \mathbf{q}_0 being the last converged set of

generalized coordinates lying on the equilibrium path and Δs some given incremental length leads to good convergence. Next the extended residual equation

$$\mathbf{R}(\mathbf{q}, \mathbf{q}_\sigma, \lambda, \lambda) = \begin{pmatrix} \mathbf{f}^{\text{int}}(\mathbf{q}) + \lambda \mathbf{f}^{\text{ext}}(\mathbf{q}) + \mathbf{W}_\sigma(\mathbf{q})\mathbf{q}_\sigma + \mathbf{W}(\mathbf{q})\lambda \\ \mathbf{g}_\sigma(\mathbf{q}) \\ \mathbf{g}(\mathbf{q}) \\ f(\mathbf{q}, \lambda) \end{pmatrix} \quad (10.73)$$

has to be linearized around the last converged set of generalized coordinates, i.e., around $\{\mathbf{q}_0, \mathbf{q}_{\sigma 0}, \lambda_0, \lambda_0\}$. This directly yields the modified Newton–Raphson iteration scheme. The choice of a predictor solution, in the beginning of each increment, has to be made with special care, see Crisfield (1991) for an extensive discussion.

In the present example each of the two beam finite element models was build by using $n = 20$ quadratic B-spline elements ($p = 2, p_{\sigma_1} = 1$). The numerical solution was obtained by using the linear arc length solver presented above with an incremental length $\Delta s = 0.08$, together with a convergence tolerance of 10^{-6} with respect to the maximum absolute error of the extended residual (10.73).

In Fig. 10.11, five pre- and post-buckling configurations of the different beam models are depicted, where the post-buckling configurations are forming a loop. In contrast to Dadeppo and Schmidt (1975), the post-buckling configurations are also computed. It can be seen that for increasing load parameters the three beam models lead to slightly different configurations. The Timoshenko beam, as the softest beam, yields the largest deflection for $\lambda = 1$. The Euler–Bernoulli beam and its inextensible version are stiffer and thus the deformation for the total external force are smaller compared to the Timoshenko beam.

The load deflection curves for the horizontal and vertical deflection of the circles apex are depicted in Fig. 10.12. For the inextensible Euler–Bernoulli beam, the results found in (Dadeppo and Schmidt, 1975) and (Simo and Vu-Quoc, 1986) are in good accordance. The buckling load for the different beam models are $\lambda_b = 0.8297$ (Timoshenko), $\lambda_b = 0.8805$ (Euler–Bernoulli), $\lambda_b = 0.9102$ (inextensible Euler–Bernoulli). For the inextensible Euler–Bernoulli beam the buckling load is in good agreement with the values reported by (Simo and Vu-Quoc, 1986, $\lambda_b = 0.90528$) and (Dadeppo and Schmidt, 1975, $\lambda_b = 0.897$). In (Simo and Vu-Quoc, 1986) a second limit point is identified with the load value $\lambda_b = -0.0771$, which only slightly differs from the value $\lambda_b = -0.0807$ obtained by the presented inextensible Euler–Bernoulli beam model.

10.6.5 Buckling of a Hinged Right-Angle Frame under Follower Point Load

In this example the buckling of a both sided hinged right-angle frame of height and length 120 under non-conservative transverse force is investigated, see Fig. 10.13. Three beams are used for this problem. One vertical beam of length $L_1 = 120$ and two

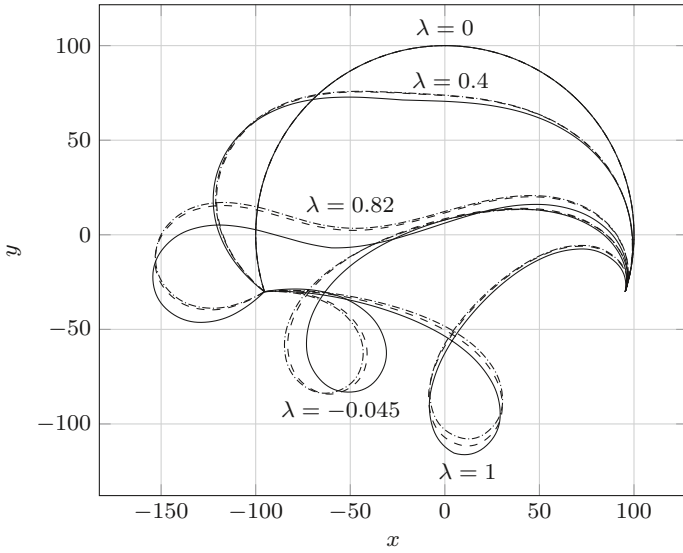


Fig. 10.11 Deformed configurations of the different beam models for load parameters $\lambda \in \{0, 0.4, 0.82, -0.045, 1\}$. The Timoshenko beam model is depicted by solid lines, the Euler-Bernoulli beam by dashed lines and the inextensible Euler-Bernoulli beam model by dashdotted lines.

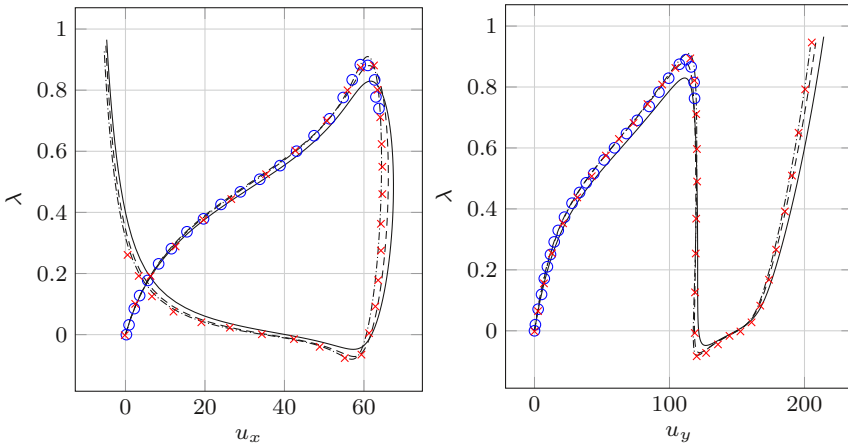


Fig. 10.12 Load deflection curves for the horizontal displacement $u_x = x(L_1)$ and vertical displacement $u_y = -(y(L_1) - 100)$ of the point of applied load. The Timoshenko beam model is depicted by solid lines, the Euler-Bernoulli beam by dashed lines and the inextensible Euler-Bernoulli beam model by dashdotted lines. The results of Dadeppo and Schmidt (1975) are depicted by blue circles, the ones computed by Simo and Vu-Quoc (1986) by red crosses.

horizontal ones, the first of length $L_2 = \frac{1}{5}L_1$, the second one of length $L_3 = \frac{4}{5}L_1$. The three beams are connected using bilateral constraints for the corresponding positions and angles. At the point where the two horizontal beams meet, a non-conservative load $P = \lambda 40 \cdot 10^3$ is applied under the angle $\pi/2$. The three beams are build with Young's modulus $E = 7.2 \cdot 10^6$, shear modulus $G = E/(2 + 2\nu)$, Poisson's ratio $\nu = 0.3$, cross section area $A = 6$, moment of inertia $I_3 = 2$, axial stiffness $E_1 = EA$, shear stiffness $E_2 = GA$ and flexural stiffness $F_3 = EI_3$.

The vertical beam was discretized using $n = 20$ quadratic B-spline elements ($p = 2$, $p_{\sigma_1} = 1$), the small and large horizontal parts were discretized with 4 and 16 quadratic B-spline elements, respectively. The numerical solutions were obtained using the previously presented linear arc length solver with $\Delta s = 600$ and a convergence tolerance of 10^{-6} with respect to the maximum absolute error of the extended residual (10.73).

Fig. 10.13 shows five representative configurations of the different beam models. Only for the force increments $\lambda = 0.885$ and $\lambda = -0.345$ minor differences between the Timoshenko beam model and the two Euler–Bernoulli beams can be noted. This is due to the large axial and shear stiffness parameters introduced by Argyris and Symeonidis (1981), which were taken for comparative purposes.

In Fig. 10.14, the load deflection curves for the horizontal and vertical deflections are depicted. The computed results are in good accordance with the ones reported by (Argyris and Symeonidis, 1981) and (Simo and Vu-Quoc, 1986), both of which present Timoshenko beam models. In the magnified areas small differences between the Timoshenko beam and the two Euler–Bernoulli beams can be recognized. The configurations for both Euler–Bernoulli beam models cannot be distinguished.

10.6.6 Natural Frequencies of a Two Sided Pinned Euler–Bernoulli Beam

In this example the natural frequencies of a two sided pinned beam of length $L = 2\pi$, axial stiffness $E_1 = 0.1$, flexural stiffness $F_3 = 1$ and mass density $\rho_0 = 1$ are compared with the ones computed using the Euler–Bernoulli beam finite element model. For the numerical computation different polynomial degrees $p \in \{2, 3, 5\}$ and element numbers $n \in \{32, 128, 512\}$ were compared and their influence on the accuracy was investigated.

The analytic solutions for the eigenvalues are well known in literature, e.g., Graff (1975). They can be derived from the governing equation

$$a^2 y''''(s, t) + \ddot{y}(s, t) = 0, \quad a^2 = EI/\rho A. \quad (10.74)$$

By substituting the separation ansatz $y(s, t) = Y(s)T(t)$ into (10.74) and separating the spatial and time dependent variables we get

$$a^2 \frac{Y''''}{Y} = \frac{\ddot{T}}{T} = \omega^2. \quad (10.75)$$

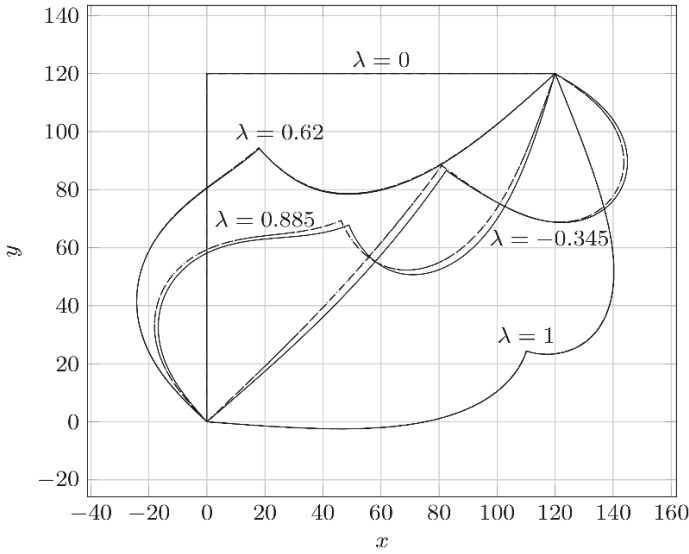


Fig. 10.13 Deformed configurations of the different beam models for load parameters $\lambda \in \{0, 0.62, 0.885, -0.345, 1\}$. The Timoshenko beam model is depicted by solid lines, the Euler–Bernoulli beam by dashed lines and the inextensible Euler–Bernoulli beam model by dashdotted lines.

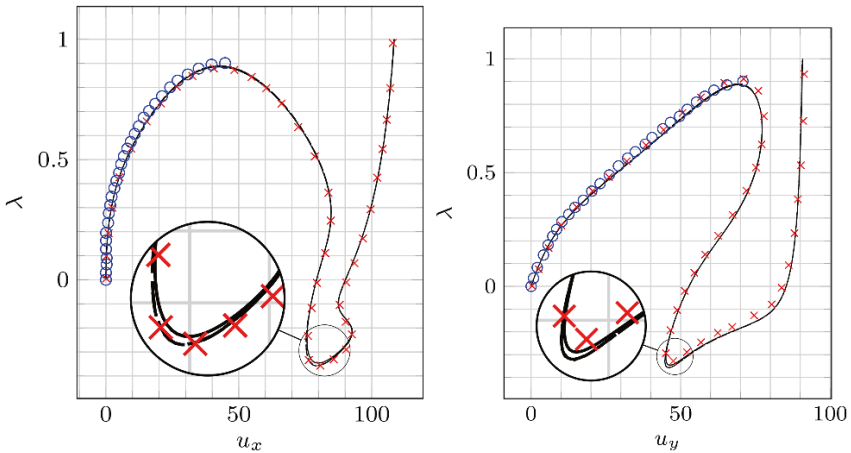


Fig. 10.14 Load deflection curves of the point of applied force for the horizontal displacement $u_x = x(L_2) - 120$ and the vertical displacement $u_y = -(y(L_2) - 120)$. The Timoshenko beam model is depicted by solid lines, the Euler–Bernoulli beam by dashed lines and the inextensible Euler–Bernoulli beam model by dashdotted lines. The results of Argyris and Symeonidis (1981) are depicted by blue circles, the ones reported by Simo and Vu-Quoc (1986) using red crosses.

The solution of the left hand side, a fourth order ordinary differential equation, is given by

$$Y(s) = C_1 \sin(\beta s) + C_2 \cos(\beta s) + C_3 \sinh(\beta s) + C_4 \cosh(\beta s), \quad \beta^4 = \frac{\omega^2}{a^2}. \quad (10.76)$$

The second order ordinary differential equation of the right hand side is fulfilled by

$$T(t) = A \cos(\omega t) + B \sin(\omega t). \quad (10.77)$$

For a two sided pinned beam, the boundary conditions in terms of $Y(s)$, are given by $Y(0) = Y''(0) = Y(L) = Y''(L) = 0$. Inserting these boundary conditions into (10.76), the constants $C_2 = C_3 = C_4 = 0$ can be identified. Thus, the frequency equation

$$\sin(\beta L) = 0, \quad \beta L = n\pi, \quad n = 1, 2, \dots \quad (10.78)$$

is obtained. The radial and cyclical frequencies for the two sided pinned beam are given by

$$\omega_n = a \left(\frac{n\pi}{L} \right)^2, \quad f_n = \frac{a\pi n^2}{2L^2}, \quad n = 1, 2, \dots \quad (10.79)$$

The corresponding normal modes read

$$Y_n(s) = \sin(\beta_n s), \quad \beta_n = \frac{n\pi}{L}, \quad n = 1, 2, \dots \quad (10.80)$$

The numerical eigenfrequencies were computed using the linearized equilibrium equation

$$\mathbf{M}\ddot{\mathbf{q}} - \mathbf{K}\mathbf{q} = \mathbf{0}, \quad (10.81)$$

with stiffness matrix in (10.52). For the mass matrix (10.50), the term involving I_3 was omitted. This is in accordance with the linearized partial differential equation (10.74), where rotatory effects of the cross sections are not included. Substituting the solution ansatz $\mathbf{q} = \phi e^{\lambda t}$, $\ddot{\mathbf{q}} = \lambda^2 \phi e^{\lambda t}$, the corresponding eigenvalue problem is obtained by multiplying $e^{-\lambda t}$ from the right and using $\lambda = i\omega$

$$(-\mathbf{K} - \omega^2 \mathbf{M}) \phi = \mathbf{0}. \quad (10.82)$$

This can be solved numerically for the normal values ω_n and their corresponding normal modes ϕ_n .

In Fig. 10.15 the absolute errors of the first 21 numerically computed natural frequencies with respect to the analytical ones are depicted using a semi-logarithmic axis. It can be observed that both refinement strategies lead to better agreements of the finite element approximation with the analytical normal frequencies. For the reported normal frequencies, the influence of the polynomial degree elevation of the chosen B-spline shape functions is larger than increasing the number of elements. For the finest refinement level ($p = 5$, $n = 512$) all shown normal frequencies are computed up to machine precision.

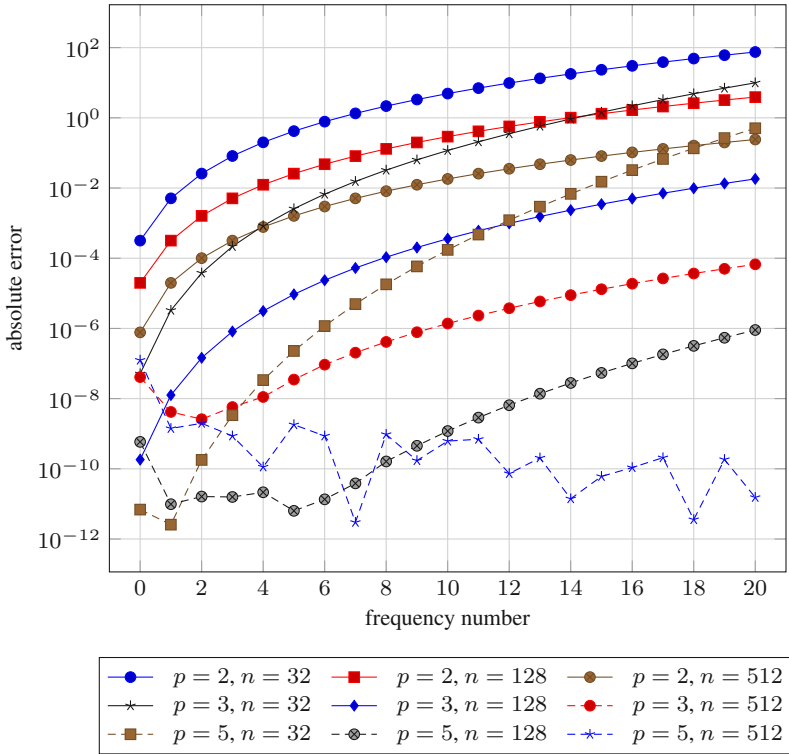


Fig. 10.15 Error in the first 21 natural frequencies of the finite element implementation of the Euler–Bernoulli beam model.

10.7 Conclusion

Starting from a variational framework, this article presents a finite element analysis of planar nonlinear classical beam theories. For discretizing the total virtual work, B-splines are chosen for both ansatz and test functions. This led to three kinematically different beam finite element models, either by finding a minimal set of kinematical descriptors, or by imposing additional constraint equations. All different beam models were studied in a variety of numerical experiments. Reproduction of analytical solutions and numerical results reported in classical beam finite element literature show the power and versatility of the presented numerical implementations.

Thus, the investigated discretization approach is well-suited for application to large systems of beams, e.g., pantographic structures (Andreaus et al, 2018; dell’Isola et al, 2018, 2019). Due to the lack of ready-to-use beam finite element models (dell’Isola et al, 2016), or because of their simple but performant implementation (Turco et al, 2016; Giorgio, 2020), discrete Hencky-type beam models are often used in literature.

Further research should include a finite element discretization approach for spatial beam models. This leads to a variety of applications, including out of plane deformation of the above-mentioned pantographic structures and their buckling and post-buckling behavior (Giorgio et al, 2017).

Acknowledgements This research has been funded by the Deutsche Forschungsgemeinschaft (DFG, German Research Foundation) under Grant No. 405032572 as part of the priority program 2100 Soft Material Robotic Systems.

References

- Andreas U, Spagnuolo M, Lekszycki T, Eugster SR (2018) A Ritz approach for the static analysis of planar pantographic structures modeled with nonlinear Euler-Bernoulli beams. *Continuum Mechanics and Thermodynamics* 30(5):1103–1123
- Argyris JH, Symeonidis S (1981) Nonlinear finite element analysis of elastic systems under non-conservative loading-natural formulation. part I. quasistatic problems. *Computer Methods in Applied Mechanics and Engineering* 26(1):75 – 123
- Arnold M, Brüls O (2007) Convergence of the generalized- α scheme for constrained mechanical systems. *Multibody System Dynamics* 18(2):185–202
- Bisshopp KE, Drucker DC (1945) Large deflection of cantilever beams. *Quart Appl Math* 3 (1945), 272-275
- de Boor C (1972) On calculating with B-splines. *Journal of Approximation Theory* 6(1):50 – 62
- de Boor C (1978) *A Practical Guide to Splines*. Applied Mathematical Sciences, Springer New York
- Brüls O, Acary V, Cardona A (2014) Simultaneous enforcement of constraints at position and velocity levels in the nonsmooth generalized- α scheme. *Computer Methods in Applied Mechanics and Engineering* 281:131–161
- Brüls O, Acary V, Cardona A (2018) On the constraints formulation in the nonsmooth generalized- α method. In: *Advanced Topics in Nonsmooth Dynamics*, Springer, pp 335–374
- Byrd PF, Friedman MD (1954) *Handbook of Elliptic Integrals for Engineers and Physicists*. Die Grundlehren der mathematischen Wissenschaften, Springer
- Cazzani A, Malagù M, Turco E (2016a) Isogeometric analysis of plane-curved beams. *Mathematics and Mechanics of Solids* 21(5):562–577
- Cazzani A, Malagù M, Turco E, Stochino F (2016b) Constitutive models for strongly curved beams in the frame of isogeometric analysis. *Mathematics and Mechanics of Solids* 21(2):182–209
- Cottrell JA, Hughes TJR, Bazilevschij JJ (2009) *Isogeometric analysis: toward integration of CAD and FEA*. Wiley, Chichester
- Cox MG (1972) The numerical evaluation of B-splines. *IMA Journal of Applied Mathematics* 10(2):134–149
- Crisfield MA (1981) A fast incremental/iterative solution procedure that handles "snap-through". *Computers & Structures* 13(1):55 – 62
- Crisfield MA (1991) *Non-linear Finite Element Analysis of Solids and Structures: Essentials*. *Non-Linear Finite Element Analysis of Solids and Structures*, Wiley
- Dadeppo DA, Schmidt R (1975) Instability of Clamped-Hinged Circular Arches Subjected to a Point Load. *Journal of Applied Mechanics* 42:894
- dell'Isola F, Giorgio I, Pawlikowski M, Rizzi N (2016) Large deformations of planar extensible beams and pantographic lattices: Heuristic homogenisation, experimental and numerical examples of equilibrium. *Proceedings of The Royal Society A* 472

- dell'Isola F, Seppecher P, et al (2018) Pantographic metamaterials: an example of mathematically driven design and of its technological challenges. *Continuum Mechanics and Thermodynamics* pp 1–34
- dell'Isola F, Seppecher P, et al (2019) Advances in pantographic structures: Design, manufacturing, models, experiments and image analyses. *Continuum Mechanics and Thermodynamics* 31:1231–1282
- Eugster SR, Harsch J (2020) A variational formulation of classical nonlinear beam theories. In: Abali BE, Giorgio I (eds) *Developments and Novel Approaches in Nonlinear Solid Body Mechanics, Advanced Structured Materials*, Springer
- Farin GE (1997) *Curves and Surfaces for Computer-aided Geometric Design: A Practical Guide*. No. Bd. 1 in *Computer science and scientific computing*, Academic Press
- Giorgio I (2020) A discrete formulation of Kirchhoff rods in large-motion dynamics. *Mathematics and Mechanics of Solids* 25(5):1081–1100
- Giorgio I, Rizzi N, Turco E (2017) Continuum modelling of pantographic sheets for out-of-plane bifurcation and vibrational analysis. *Proceedings of the Royal Society A: Mathematical, Physical and Engineering Science* 473:20170,636
- Gontier C, Vollmer C (1995) A large displacement analysis of a beam using a CAD geometric definition. *Computers & Structures* 57(6):981 – 989
- Graff KF (1975) *Wave motion in elastic solids*. Clarendon Press, Oxford
- Greco L, Cuomo M (2013) B-spline interpolation of Kirchhoff-Love space rods. *Computer Methods in Applied Mechanics and Engineering* 256(0):251–269
- Greco L, Cuomo M (2014) An implicit G^1 multi patch B-spline interpolation for Kirchhoff-Love space rod. *Computer Methods in Applied Mechanics and Engineering* 269:173 – 197
- Hairer E, Wanner G (2002) *Solving Ordinary Differential Equations II*, 2nd edn. Springer
- Hughes T, Cottrell J, Bazilevs Y (2005) Isogeometric analysis: CAD, finite elements, NURBS, exact geometry and mesh refinement. *Computer Methods in Applied Mechanics and Engineering* 194(39):4135 – 4195
- Jay OL, Negrut D (2009) *A Second Order Extension of the Generalized- α Method for Constrained Systems in Mechanics*, Springer, pp 143–158
- Leine R, van de Wouw N (2007) *Stability and Convergence of Mechanical Systems with Unilateral Constraints*. *Lecture Notes in Applied and Computational Mechanics*, Springer
- Lunk C, Simeon B (2006) Solving constrained mechanical systems by the family of newmark and α -methods. *Zeitschrift für Angewandte Mathematik und Mechanik* 86(10):772–784
- Piegl LA, Tiller W (1997) *The NURBS Book*, 2nd edn. Springer
- Quarteroni A, Sacco R, Saleri F (2000) *Numerical Mathematics*. *Texts in applied mathematics*, Springer
- Riks E (1979) An incremental approach to the solution of snapping and buckling problems. *International Journal of Solids and Structures* 15(7):529 – 551
- Rohatgi A (2019) Webplotdigitizer. <https://automeris.io/WebPlotDigitizer>
- Schöneberg IJ (1946) Contributions to the problem of approximation of equidistant data by analytic functions: Part a.—on the problem of smoothing or graduation. A first class of analytic approximation formulae. *Quarterly of Applied Mathematics* 4(1):45–99
- Simo JC, Vu-Quoc L (1986) A three-dimensional finite-strain rod model. part II: Computational aspects. *Computer Methods in Applied Mechanics and Engineering* 58:79–116
- Stoer J, Bartels R, Gautschi W, Bulirsch R, Witzgall C (2002) *Introduction to Numerical Analysis*. *Texts in Applied Mathematics*, Springer New York
- Turco E, dell'Isola F, Cazzani A, Rizzi NL (2016) Hencky-type discrete model for pantographic structures: numerical comparison with second gradient continuum models. *Zeitschrift für angewandte Mathematik und Physik* 67(4):85



Chapter 11

Modelling of Two-dimensional Timoshenko Beams in Hencky Fashion

Emilio Turco

Abstract We describe a novel mechanical model of planar Timoshenko beam for large displacements analysis in elastic regime following Hencky beam model guidelines. More precisely, we model the strain energy of the beam in a discrete form by considering, besides the bending contribution, both the stretching and the sliding contributions. In this way a discrete model of Timoshenko beam is generated. This model, besides to be interesting *di per sé* has strong applications in the study of metamaterials based on beam lattices where, sometimes, the approximations introduced by the use of Euler–Bernoulli beam model are too rough for capturing some desired details. In addition, this is an intermediate step toward the construction of discrete three-dimensional Timoshenko beam models.

Keywords: Two-dimensional Timoshenko beam · Large displacements in elastic regime · Buckling of beams

11.1 Introduction

The Timoshenko beam model is the object of several scientific studies of historical kind (see, e.g., Elishakoff, 2020), of mathematical kind (see, e.g., Della Corte et al, 2019), both for static (Balobanov and Niiranen, 2018; Kiendl et al, 2015; Turco et al, 2020) and dynamic problems (Luu et al, 2015; Cazzani et al, 2016b,c,a). All these studies prove the great interest about this model both *di per sé* and also from the point of view of the technical applications. This interest is increased in last years for the large use of this model in the analysis of metamaterials when their internal structure requires beam models richer than the so-called Euler–Bernoulli beam (see, e.g., Meza et al, 2017, 2014; Gross et al, 2019; Vangelatos et al, 2019a,b).

E. Turco

Department of Architecture, Design and Urban planning (DADU), University of Sassari, Italy
e-mail: emilio.turco@uniss.it

By considering, for instance, pantographic metamaterials as described in the recent papers (dell'Isola et al, 2019b,a), the beams forming the pantographic sheet might have dimensions which suggest to consider the shear deformability instead of neglecting it *a priori* choosing the Euler–Bernoulli model. The Timoshenko beam model is obviously more expensive than Euler–Bernoulli model since the former requires to describe the rotations which are independent from displacements. However, this extra computational cost could balance, at least partially, a richer – therefore more accurate in principle – model.

The discrete form used for modelling the Timoshenko beam which will be described in this work is largely inspired by the work of Hencky (1921), although here both the stretching and the sliding terms of the strain are considered. Starting from the guidelines reported in Eremeyev and Altenbach (2017); Turco (2018); Eremeyev (2019) for describing the bending strain for three-dimensional beams, here, limiting ourselves to two-dimensional beams, we introduce in a simple way the stretching and the sliding strain measures. Since the discrete model presented here uses, besides Lagrangian parameters for describing the rotation field, also the nodal displacements, it makes simpler the treatment of systems of beams when the kinematical constraints on the nodes have to be imposed, as is necessary for pantographic structures.

After this brief Introduction, it will be presented the discrete model of a two-dimensional Timoshenko beam in the framework of Hencky approach, Section 11.2, defining completely the strain energy and, therefore, both the structural reaction and the stiffness matrix which are the main tools used in a path-following strategy such as proposed by Riks (1972), Section 11.3. Some numerical results showing the influence of the shear deformability are presented and discussed in Sec. 11.4. Finally, some concluding remarks along with a list of forthcoming issues are presented in Section 11.5.

11.2 Modelling of Two-Dimensional Timoshenko Beams

We consider a planar rectilinear beam¹ discretized by means of a series of links of equal length ℓ (for the sake of simplicity) connected by joints, see Fig. 11.1 sketched as black circles.

The position of j -th joint in the reference and in the current configuration is P_j and p_j , respectively. In the spirit of Cosserat brothers for one-dimensional continuum and of the Timoshenko beam model, each joint is also equipped, in the reference configuration, with a unit vector D_j which is transformed in the current configuration in the unit vector $\mathbf{d}_j = \mathbf{Q}_j D_j$ being \mathbf{Q}_j a proper orthogonal tensor which represents a rotation. Reference and current configurations are described by the sets $\{P_j, D_j\}$ and $\{p_j, \mathbf{d}_j\}$, respectively. We remark that using the immediately above hypotheses the Lagrangian parameters used for describing the motion is the displacement of

¹ The rectilinear hypothesis can easily be removed to represent broken lines approximating curves.

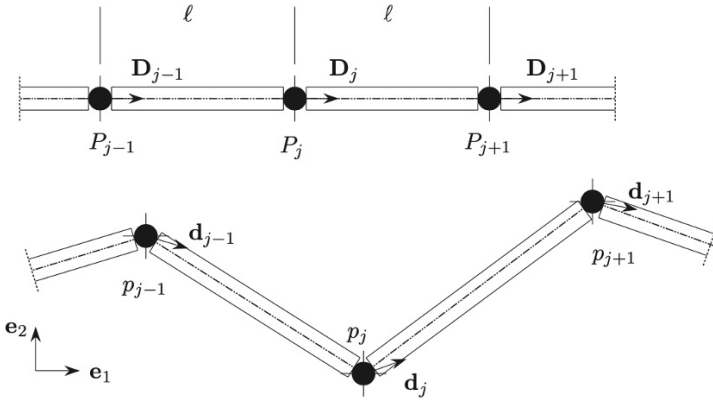


Fig. 11.1 Reference and current configuration of a segment of planar Timoshenko beam discretized à la Hencky.

j -th joint $w_j = p_j - P_j$ and the rotation associated with the j -th proper orthogonal tensor \mathbf{Q}_j .

Looking again at Fig. 11.1, we can define as strain measures the vector Δw_{j+1}

$$\Delta w_{j+1} = (p_{j+1} - p_j) - \ell \mathbf{Q}_j \mathbf{D}_j, \tag{11.1}$$

and the tensor $\Delta \mathbf{P}_{j+1}$

$$\Delta \mathbf{P}_{j+1} = \mathbf{Q}_j^T \mathbf{Q}_{j+1}. \tag{11.2}$$

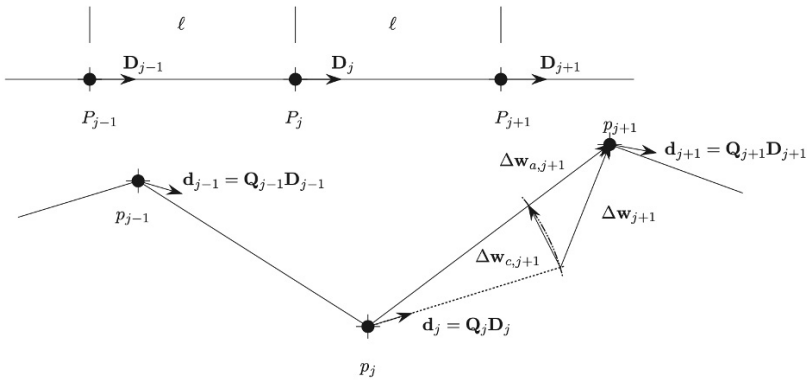


Fig. 11.2 Strain measures for a planar Timoshenko beam discretized à la Hencky.

The vector $\Delta \mathbf{w}_{j+1}$, i.e. the difference between $p_{j+1} - p_j$ (the vector which connects the j -th and $(j + 1)$ -th current positions) and $\ell \mathbf{Q}_j \mathbf{D}_j$ (that is the vector having ℓ norm obtained rotating \mathbf{D}_j by \mathbf{Q}_j). The just defined strain vector $\Delta \mathbf{w}_{j+1}$, can be decomposed in two parts:

$$\Delta \mathbf{w}_{a,j+1} = (p_{j+i} - p_j) \left(1 - \frac{\ell}{\|p_{j+i} - p_j\|} \right), \quad (11.3)$$

$$\Delta \mathbf{w}_{c,j+1} = \Delta \mathbf{w}_{j+1} - \Delta \mathbf{w}_{a,j+1}, \quad (11.4)$$

being the graphic representation of each one sketched in Fig. 11.2.

The norms of these two vectors describe the stretching and the sliding, respectively, of the link in-between j and $j + 1$ joints.

The proper orthogonal tensor $\Delta \mathbf{P}_{j+1}$ describes the bending that is the relative rotation between the two considered links. In details, as reported in Turco (2018) for the case of three-dimensional inextensible Euler–Benoulli beams, from Rodrigues’ formula, see Rodrigues (1840), the relation between a rotation of amplitude φ about the rotation axis depicted by the unit vector \mathbf{e} is represented by the proper orthogonal tensor \mathbf{Q} expressed by²

$$\mathbf{Q} = \cos \varphi \mathbf{I} + (1 - \cos \varphi) \mathbf{e} \otimes \mathbf{e} + \sin \varphi \mathbf{E}, \quad (11.5)$$

being \mathbf{I} and \mathbf{E} the identity tensor and the skew tensor defined by the equivalence $\mathbf{E} \mathbf{u} = \mathbf{e} \times \mathbf{u}$, respectively.

Equation (11.5) define the rotation tensor as function of the rotation angle φ and the rotation axis \mathbf{e} . If we are interested to the rotation angle and to the rotation axis starting from the rotation tensor, taking into account that \mathbf{E} is skew so $\text{tr}(\mathbf{E}) = 0$ and $\mathbf{E}^T = -\mathbf{E}$, we can simply evaluate the trace of \mathbf{Q} :

$$\text{tr}(\mathbf{Q}) = 2 \cos \varphi + 1, \quad (11.6)$$

and the difference

$$\mathbf{Q} - \mathbf{Q}^T = 2 \sin \varphi \mathbf{E}, \quad (11.7)$$

from which we can compute the vectorial invariant \mathbf{Q}_\times of \mathbf{Q} , in formula:

$$\mathbf{Q}_\times = \sin \varphi \mathbf{e}. \quad (11.8)$$

From Eqs. (11.6) and (11.8) we have

$$\frac{\sin \varphi \mathbf{e}}{1 + \cos \varphi} = \frac{2 \mathbf{Q}_\times}{1 + \text{tr}(\mathbf{Q})}, \quad (11.9)$$

and finally, by using the bisection formula, we obtain

² It is better to treat the problem in 3D and successively simplify the results to the considered two-dimensional case, i.e. $\mathbf{e} = \mathbf{e}_3$.

$$2 \tan \frac{\varphi}{2} \mathbf{e} = \frac{4\mathbf{Q}_{\times}}{1 + \text{tr}(\mathbf{Q})}. \quad (11.10)$$

Formula (11.10) suggest the use of variable $2 \tan \frac{\varphi}{2}$, instead of φ , to describe the rotation angle. With this change of variable, Rodrigues formula can be written as

$$\mathbf{Q} = \frac{1}{4 + \vartheta^2} ((4 - \vartheta^2)\mathbf{I} + 2\boldsymbol{\theta} \otimes \boldsymbol{\theta} + 4\vartheta\mathbf{E}), \quad (11.11)$$

where $\boldsymbol{\theta} = \vartheta \mathbf{e}$ and $\vartheta^2 = \boldsymbol{\theta} \cdot \boldsymbol{\theta}$.

For two-dimensional Timoshenko beams, the kinematics is simpler since the rotation axis is always directed along the unit vector \mathbf{e}_3 . For example, the skew tensor \mathbf{E} and the rotation tensor \mathbf{Q} become

$$\mathbf{E} = \begin{bmatrix} 0 & -1 & 0 \\ 1 & 0 & 0 \\ 0 & 0 & 0 \end{bmatrix}, \quad (11.12)$$

and

$$\mathbf{Q} = \begin{bmatrix} \cos \varphi & -\sin \varphi & 0 \\ \sin \varphi & \cos \varphi & 0 \\ 0 & 0 & 1 \end{bmatrix} \quad \text{or} \quad \mathbf{Q} = \frac{1}{4 + \vartheta^2} \begin{bmatrix} 4 - \vartheta^2 & -4\vartheta & 0 \\ 4\vartheta & 4 - \vartheta^2 & 0 \\ 0 & 0 & 4 + \vartheta^2 \end{bmatrix}, \quad (11.13)$$

respectively.

In the foregoing we have described the relationships between Lagrangian parameters used to describe the motion, i.e. the displacements of joints and the rotations of the links which, following the Timoshenko guidelines have to be independent, and the chosen strain measures $\Delta \mathbf{w}_{a,j}$, $\Delta \mathbf{w}_{c,j}$ and $\Delta \mathbf{P}_{j+1}$. Correspondingly, we can write the strain energy of the beam just summing the following elementary contributions:

$$2E_a = a \|\Delta \mathbf{w}_{a,j+1}\|^2, \quad (11.14)$$

$$2E_b = b \|\Delta \boldsymbol{\phi}_{j+1}\|^2, \quad (11.15)$$

$$2E_c = c \|\Delta \mathbf{w}_{c,j+1}\|^2, \quad (11.16)$$

where, besides the quantities already defined, we use $\Delta \boldsymbol{\phi}_{j+1}$ which is the finite relative rotation vector associated to $\Delta \mathbf{P}_{j+1}$ by using the link defined by Eq. (11.10) and a , b and c are the stiffness parameters related to stretching, bending and sliding. We remark that in the considered case $\Delta \boldsymbol{\phi}_{j+1}$ has only one component different from zero, i.e. the third.

Finally we observe that in the case of \mathbf{d}_j directed as the segment in-between j and $j + 1$ there is not sliding and we come back to the Hencky approximation of the Euler–Bernoulli model as described, e.g., in Turco et al (2016).

11.3 Numerically Driven Drawing of the Equilibrium Path

Enforcing the stationarity condition for the potential energy with respect to nodal displacements vector \mathbf{u} , the nonlinear system of equilibrium equations can be written as

$$\mathbf{s}[\mathbf{u}] - \mathbf{p}[\lambda] = \mathbf{0}, \quad (11.17)$$

being the vector \mathbf{s} the structural reaction, depending upon nodal displacement vector \mathbf{u} , and $\mathbf{p}[\lambda]$ the external load vector ruled by the dimensionless load parameter λ . The structural reaction \mathbf{s} can be computed starting from the total strain energy E of the system, i.e. adding the contributions deriving from (11.14), (11.15) and (11.16), as

$$\mathbf{s} = \frac{dE}{d\mathbf{u}}, \quad (11.18)$$

while, the external load is expressed in the form

$$\mathbf{p}[\lambda] = \mathbf{p}_0 + \lambda \hat{\mathbf{p}}, \quad (11.19)$$

able to represent both external loads $\lambda \hat{\mathbf{p}}$ which increase with the dimensionless parameter λ and external loads independent from λ , i.e. \mathbf{p}_0 . This load representation is useful to model the so-called load imperfections.

The solution of the nonlinear system of equations (11.17) could be obtained by using a stepwise procedure which uses the Newton's method. Starting from the pair $(\mathbf{u}_i, \lambda_i)$ which represents the i -th equilibrium point, the next one, and nearby, $(\mathbf{u}_i + \Delta\mathbf{u}, \lambda_i + \Delta\lambda)$ can be computed, by linearizing Eq. (11.17)

$$\mathbf{s}[\mathbf{u}_i] + \mathbf{K}\Delta\mathbf{u} - (\mathbf{p}_0 + (\lambda_i + \Delta\lambda)\hat{\mathbf{p}}) \approx \mathbf{0}, \quad (11.20)$$

which uses the stiffness matrix \mathbf{K} defined as

$$\mathbf{K} = \frac{d\mathbf{s}}{d\mathbf{u}}, \quad (11.21)$$

computed in \mathbf{u}_i . Newton's method, starting from the linearization (11.20), gives the recurrent formula to compute $\Delta\mathbf{u}$ when the value of $\Delta\lambda$ is fixed in advance:

$$\Delta\mathbf{u} = -\Delta\lambda \mathbf{K}^{-1} \hat{\mathbf{p}}. \quad (11.22)$$

As is well documented in technical literature, Newton's method does not converge when \mathbf{K} is singular or nearly-singular. In order to bypass this limitation, Riks (1972) proposed the parametrization of the equilibrium path by means its arc-length instead of the dimensionless load parameter λ . The consequent integration scheme is not affected by the convergence problems intrinsic in the Newton's method, but it has to be completed by an additional equation.

In some detail, Riks' arc-length scheme proposes a correction on the extrapolation obtained from Newton formula (11.22). If the pair $(\mathbf{u}_i, \lambda_i)$ is an equilibrium point and $(\Delta\mathbf{u}, \Delta\lambda)$ is a Newton extrapolation, the Riks correction $(\hat{\mathbf{u}}, \hat{\lambda})$ can be evaluated

from the linearization (11.17) in the point $(\mathbf{u}_i + \Delta\mathbf{u}, \lambda_i + \Delta\lambda)$

$$\mathbf{s}[\mathbf{u}_i + \Delta\mathbf{u}] + \mathbf{K}\dot{\mathbf{u}} - (\mathbf{p}_0 + (\lambda_i + \Delta\lambda + \dot{\lambda})\hat{\mathbf{p}}) \approx \mathbf{0}, \quad (11.23)$$

where the stiffness matrix \mathbf{K} is now computed in $\mathbf{u}_i + \Delta\mathbf{u}$. From (11.23) $\dot{\mathbf{u}}$ can be computed from

$$\dot{\mathbf{u}} = -\mathbf{K}^{-1} \left(\mathbf{s}[\mathbf{u}_i + \Delta\mathbf{u}] - (\mathbf{p}_0 + (\lambda_i + \Delta\lambda + \dot{\lambda})\hat{\mathbf{p}}) \right), \quad (11.24)$$

The additional equation required to compensate the unknown $\dot{\lambda}$ can be chosen in several different ways. One producing a very simple formula, also computationally convenient, is

$$\Delta\mathbf{u} \cdot \mathbf{K}\dot{\mathbf{u}} = 0, \quad (11.25)$$

which enforces the \mathbf{K} -orthogonality between the Newton extrapolation $\Delta\mathbf{u}$ and the Riks correction $\dot{\mathbf{u}}$. Substituting (11.24) in (11.25) and taking also into account (11.22), simple calculations give the straightforward expression

$$\dot{\lambda} = \frac{\hat{\mathbf{u}} \cdot \mathbf{r}}{\hat{\mathbf{u}} \cdot \hat{\mathbf{p}}}, \quad (11.26)$$

being $\mathbf{r} = \mathbf{s}[\mathbf{u}_i + \Delta\mathbf{u}] - (\mathbf{p}_0 + (\lambda_i + \Delta\lambda)\hat{\mathbf{p}})$ the rest of equilibrium equations and $\hat{\mathbf{u}} = \mathbf{K}^{-1}\hat{\mathbf{p}}$ (from (11.22)). Finally, from (11.24), the Riks correction $\dot{\mathbf{u}}$ can be computed making use of Newton extrapolation $\Delta\mathbf{u}$.

Formulae (11.26), (11.24) and (11.22) fully define the Riks-based algorithm once the first extrapolation is defined:

$$\Delta\lambda = \mu(\lambda_i - \lambda_{i-1}), \quad (11.27)$$

$$\Delta\mathbf{u} = \mu(\mathbf{u}_i - \mathbf{u}_{i-1}), \quad (11.28)$$

here, μ is an adaptive coefficient used to vary the arc-length during the stepwise procedure and the pairs $(\lambda_i, \mathbf{u}_i)$ and $(\lambda_{i-1}, \mathbf{u}_{i-1})$ the last and the second last computed point of the equilibrium path, respectively. Synthetically, the adaptive coefficient μ drives the step-length of each step on the nonlinearity of the equilibrium path. A straightforward expression for computing μ , is suggested in Wriggers (2008); Clarke and Hancock (1990):

$$\mu = 1 - \frac{r_l - n_l}{r_l + n_l}, \quad (11.29)$$

it uses the number of required loops r_l to reach the convergence in the current step and the number of needed loops n_l (the usual choiche is $n_l = 5$). At the beginning of the analysis process $\mu = 1$ is assumed, whereas the value of $\Delta\lambda$ is estimated by some auxiliary analysis. The initial settings of $\Delta\lambda$ and of $\Delta\mathbf{u}$ fix, implicitly, the curve arc-length.

11.4 Quantitative Analysis of the Influence of the Shear Stiffness Parameter

The quantitative difference between the discrete form of the Euler–Bernoulli and Timoshenko beam models can be estimated in a simple way by referring to a cantilever beam ℓ long loaded with a transversal force F on the free end. If we compute, in the case of linear elasticity and for small displacements, the transversal displacement of the free end, neglecting the deformation due to the shear, we have $F\ell^3/3EI$ being E and I the Young modulus of the material and the inertia of the cross-section, respectively. Therefore, the bending stiffness is $3EI/\ell^3$. Conversely, the contribution related to the shear deformability is $F\ell/GA^*$ being G and A^* the shear modulus of the material and the reduced area of the cross-section, respectively. The corresponding shear stiffness is GA^*/ℓ . If we compute the ratio between the displacement of the free end due to the shear and to the bending contributions we have

$$\frac{w_s}{w_b} = \frac{\frac{3EI}{\ell^3}}{\frac{GA^*}{\ell}}, \tag{11.30}$$

from which we deduce that this ratio is inversely proportional to the square of the beam length. If we consider a beam with rectangular cross-section b depth and h height, the ratio becomes

$$\frac{w_s}{w_b} \propto \left(\frac{h}{\ell}\right)^2, \tag{11.31}$$

besides to be dependent from the Poisson’s ratio. For example, for $h/\ell = 0.5$ the shear term is equal to the 25% of bending term and so surely not negligible.

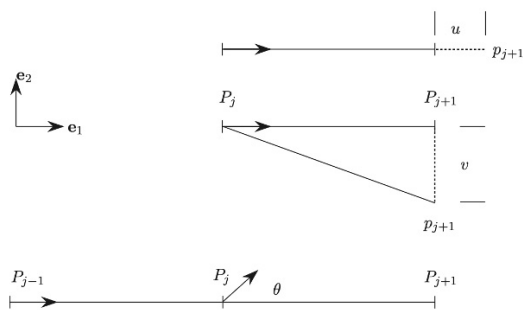


Fig. 11.3 Deformation modes: stretching (on the top), sliding (on the middle) and bending (on the bottom).

Starting from this simple analysis, we can compute numerically the values of the energy related to stretching, bending and sliding following Eqs. (11.14), (11.15) and (11.16). Therefore, for large displacements, we consider the three representative deformation modes sketched in Fig. 11.3:

1. the first one considers the points P_j and P_{j+1} and the deformation corresponding to $p_{j+1} = P_{j+1} + ue_1$ keeping $p_j = P_j$;
2. the second one, always for the points P_j and P_{j+1} , considers the deformation corresponding to $p_{j+1} = P_{j+1} + ve_2$ keeping $p_j = P_j$;
3. the third one considers for the links in-between three consecutive points P_{j-1} , P_j and P_{j+1} the rotations θ_j keeping $\theta_{j-1} = 0$.

Figure 11.4 reports the dimensionless strain energy split in stretching, bending and sliding contributions as function of the parameters u , v and θ_j . We remark that the parameter u influences only the stretching energy, v stretching and sliding and, finally, θ_j stretching, bending and sliding. Figure 11.5 reports the sliding-stretching strain energy ratio *versus* the dimensionless displacement v_j/ℓ varying the c/a ratio from 0.1 to 10 keeping unchanged b . Figure 11.6 shows as the sliding-bending strain energy ratio varies when the non-dimensional stiffness ratio $c\ell^2/b$ increases from 0.1 to 10 keeping unchanged a .

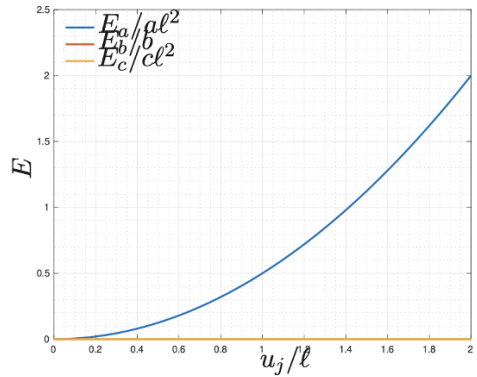
The last two plots show, also quantitatively, the influence of the sliding part of the energy, respect to the stretching and the bending part, when the stiffness parameter c increases. In addition, we notice that the sliding part of the strain energy decreases when the displacement parameter of the considered deformation mode increases.

11.4.1 Tip Deflection of a Cantilever Beam

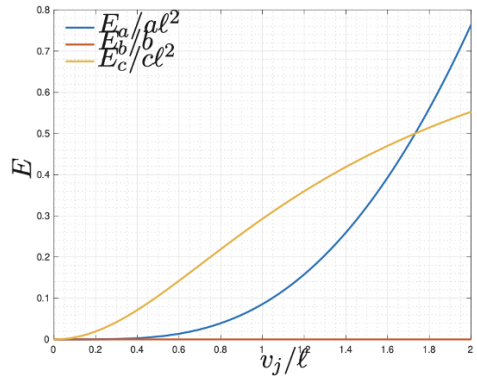
By referring to the cantilever beam reported in Fig. 11.7 loaded with a transversal force on the tip, Figure 11.8 shows as the cantilever beam tip displacement varies when the load parameter λ increases varying the stiffness ratio c/b . As can be noticed from the plots, for large displacements the influence of the parameter c is relevant and surely it can not be neglected.

Figure 11.9 reports two deformations corresponding to the end of the loading path. They correspond to the values $c/b = 0.005$, on the left, and $c/b = 5$, on the right, respectively. Colors red and blue distinguish the current positions of nodes and of rotations, respectively. It can be noticed that the two deformations are very different. In the first one, see Fig. 11.9(a), the effect of sliding is clearly visible and it is described by the blue segments sharply distinct from the red line which describes the displacements. In the second one, see Fig. 11.9(b), blue segments and red line are overlapped showing that for the used c/b ratio the sliding is practically negligible and the Euler–Bernoulli beam model could be profitably used.

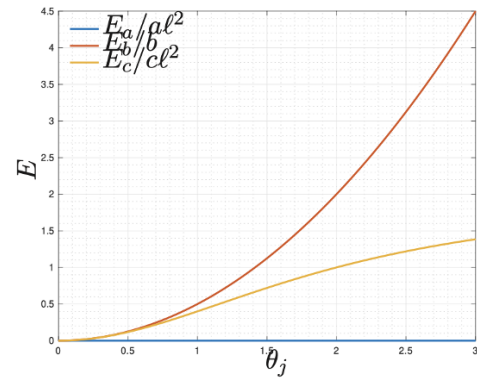
Figure 11.10 shows the strain energy evolution, when λ increases, for two limit cases, $c/b = 0.005$ on the left and $c/b = 5$ on the right. Small values of the sliding stiffness c , respect to bending stiffness b , give non-negligible values of the sliding strain energy, respect to the bending strain energy, whereas for higher values of c the relative contribution E_c is negligible, respect to the bending strain energy.



(a) Stretching deformation mode



(b) Sliding deformation mode



(c) Bending deformation mode

Fig. 11.4 Dimensionless strain energy, split in stretching, bending and sliding contributions, corresponding to deformation modes associated to u_j/l , v_j/l and θ_j .

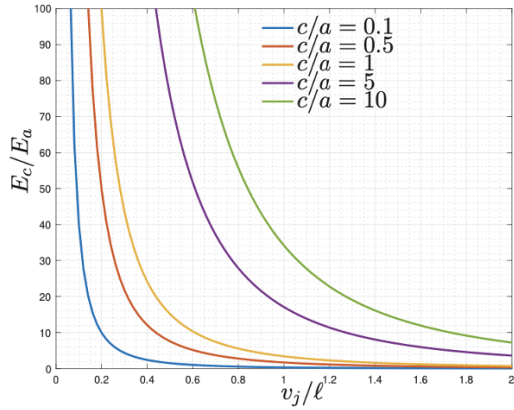


Fig. 11.5 Sliding-stretching strain energy ratio corresponding to the deformation modes associated to v_j/l varying the c/a ratio from 0.1 to 10.

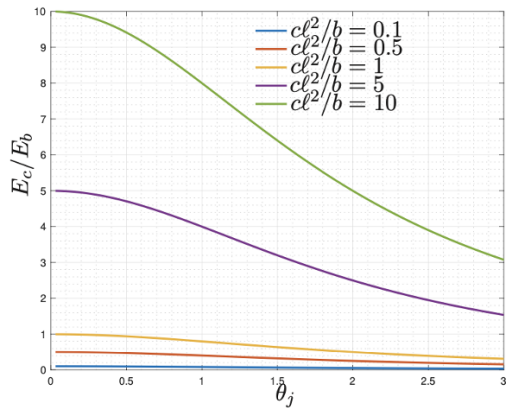


Fig. 11.6 Sliding-bending strain energy ratio corresponding to the deformation modes associated to θ_j varying the cl^2/b ratio.

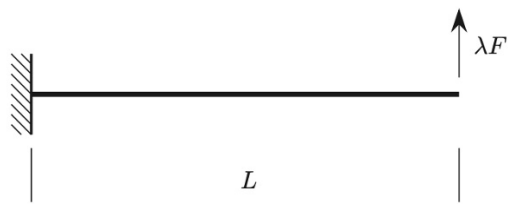
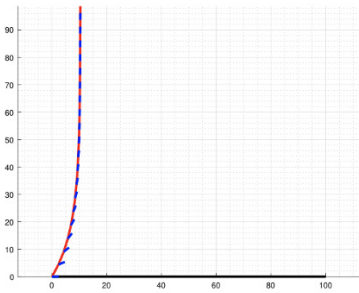
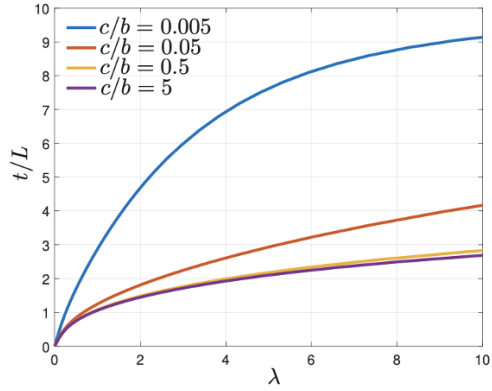


Fig. 11.7 Cantilever beam under a shear force on the tip.

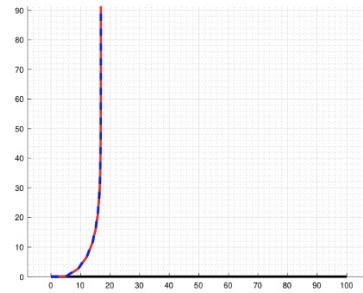
11.4.2 Buckling of a Simply Supported Beam

By referring to the simply-supported beam depicted in Fig. 11.11 loaded with a compression force ruled by the load parameter λ and a transversal force on the beam midpoint mimicking an imperfection load, Figure 11.12 shows as the dimensionless transversal displacement t/L of the midpoint varies when the load parameter λ

Fig. 11.8 Dimensionless cantilever beam tip displacement t/L loaded by a transversal force on the tip (L is the length of the beam) vs. the load parameter λ varying c/b ratio.

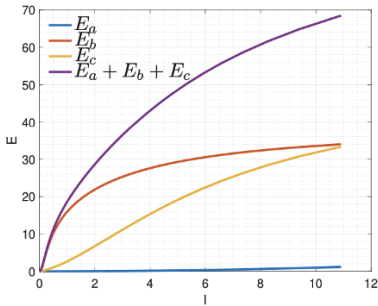


(a) $c/b = 0.005$

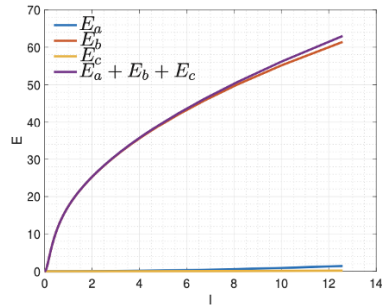


(b) $c/b = 5$

Fig. 11.9 Deformation for $c/b = 0.005$, on the left, and $c/b = 5$, on the right, (red color is used for current positions of nodes blue color for rotations).



(a) $c/b = 0.005$



(b) $c/b = 5$

Fig. 11.10 Strain energy (total and split in stretching E_a , bending E_b and sliding E_c parts) for $c/b = 0.005$ (on the left) and $c/b = 5$ (on the right).

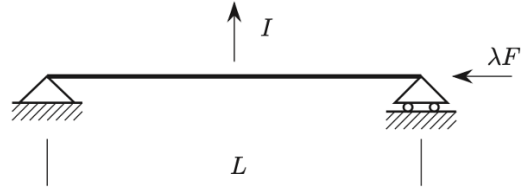


Fig. 11.11 Simply supported beam under compression load and transversal imperfection.

increases varying the stiffness ratio c/b . From the plots, we can guess, at least approximatively, the strong influence of c/b ratio on the buckling loads and on the first part of the secondary branches while last parts of the equilibrium paths are practically indistinguishable.

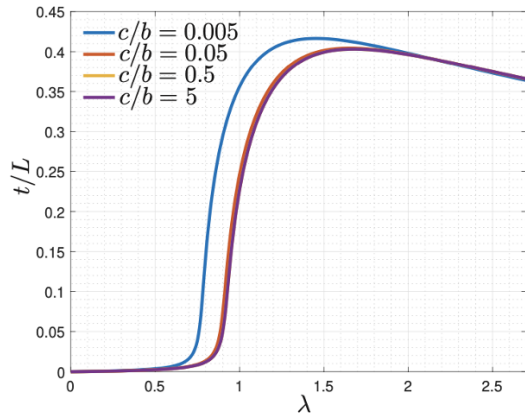


Fig. 11.12 Buckling of a simply supported beam: dimensionless midpoint displacement t/L (L is the length of the beam) vs. load parameter λ varying c/b ratio.

Figure 11.13 reports two deformations corresponding to the end of the loading path.³ They correspond to the values $c/b = 0.005$, on the left, and $c/b = 5$, on the right, respectively. As in the foregoing, red and blue colors distinguish current positions of nodes and rotations, respectively. It can be noticed that the two deformations are very different. In the first one, see Fig. 11.13(a), the sliding effect, described by the blue segments sharply distinct from the red line which describes the displacements, is clearly visible. In the second one, see Fig. 11.13(b), blue segments and red line are overlapped showing that the used c/b ratio the sliding is practically negligible and the Euler–Bernoulli beam model could be profitably used.

Figure 11.14 shows the strain energy evolution, when λ increases, for two limit cases, $c/b = 0.005$ on the left and $c/b = 5$ on the right. Small values of the sliding stiffness c , respect to bending stiffness b , give non-negligible values of the sliding

³ The Author is aware that these solutions are admissible only if the overlapping of the beam is allowed.

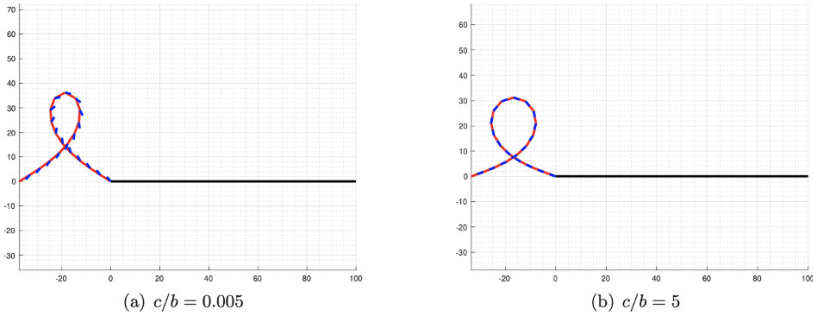


Fig. 11.13 Buckling of a simply supported beam: deformation for $c/b = 0.005$, on the left, and $c/b = 5$, on the right, (red color is used for current positions of nodes whereas in blue color for rotations).

strain energy, respect to the bending strain energy, whereas for higher values of c the relative contribution E_c is negligible, respect to the bending strain energy.

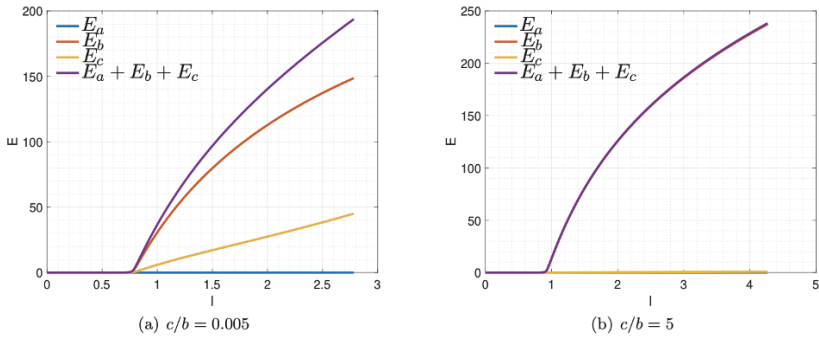


Fig. 11.14 Buckling of a simply supported beam: strain energy (total and split in stretching E_a , bending E_b and sliding E_c parts) for $c/b = 0.005$ (on the left) and $c/b = 5$ (on the right).

11.5 Concluding Remarks and Future Challenges

This work has presented and discussed a novel discrete mechanical model, largely inspired by the Hencky work, devoted to study two-dimensional Timoshenko beam. After the model presentation and a brief sketch of the algorithm used for reconstructing the equilibrium path, the results of some numerical simulations are used for evaluating the sensitivity of results respect to the shear stiffness parameter. In some detail, numerical simulations have shown that neglecting the shear deformation

can produce results almost far from those produced taking into account the shear contribution. This result is confirmed also when buckling problems for simple beams are considered.

After this preliminary work, there are several open problems to tackle, in particular: *i*) it is necessary a further careful analysis on the stiffness parameters used to model the elastic response of the discrete beam; these parameters should be linked to the usual constitutive parameters of the material, for instance the Young and the tangential stiffness moduli, and to the geometric parameters of the beam, for instance the transversal cross-section area, the inertia and the shear correction factor; in addition, the stiffness parameters of the discrete beam might be considered as variables along the beam (functionally graded materials); an extended campaign of numerical simulations might be discover new and exotic mechanical behaviors (see, e.g., Alibert et al, 2003; Sepecher et al, 2011; Misra et al, 2018; De Angelo et al, 2019; Turco et al, 2019; Scerrato and Giorgio, 2019); *ii*) it is intriguing the development of continuum models⁴, such as reported, e.g., in Boutin et al (2017); Giorgio et al (2018, 2019); Barchiesi et al (2019b); Placidi et al (2020); Barchiesi et al (2019a); Abdoul-Anziz and Sepecher (2018); Abdoul-Anziz et al (2019); Andreaus et al (2018); Abali et al (2015); Spagnuolo and Andreaus (2019) based on the discrete model and on the results presented here; their use could help to identify the stiffness parameter of the discrete model besides to be useful for developing continuum models devoted to the analysis of plane or curved structures moulded as, e.g., shells and tubes (see Greco et al, 2018, 2019a,b; Greco and Cuomo, 2015; Greco, 2020; Abali et al, 2016; Yang et al, 2018); *iii*) it is promising the extension of elastic stability theory for micromorphic, strain-gradient media and granular materials, likewise the nonlinear elasticity theory (see, e.g. Ogden, 1997; Fu and Ogden, 1999), and to Cosserat media (see, e.g., Eremeev and Zubov, 1994; Sheydakov and Altenbach, 2016; Lakes, 2018; Solyaev et al, 2020; Balobanov and Niiranen, 2018; Misra and Poorsolhjoui, 2015; Pideri and Sepecher, 1997; dell'Isola et al, 2015; Niiranen et al, 2019); *iv*) it should be considered the extension to problems where dynamics effects have to necessarily be considered (see, e.g., Giorgio, 2020; Giorgio and Del Vescovo, 2019, 2018; Giorgio et al, 2017; Laudato and Barchiesi, 2019) or technical problems which consider the active control of vibrations (see Chróścielewski et al, 2019) and therein references.

Acknowledgements For this work I am indebted to many people of the M&MOCS International Research Center. I wish to thank all of them for their invaluable suggestions and fruitful discussions.

References

Abali BE, Müller WH, Eremeyev VA (2015) Strain gradient elasticity with geometric nonlinearities and its computational evaluation. *Mechanics of Advanced Materials and Modern Processes*

⁴ See the exegesis of the work *Fundamentals of the mechanics of continua* by E. Hellinger reported in Eugster and dell'Isola (2017, 2018a,b) for an insightful analysis on the continuum idea.

- 1(1):1–11
- Abali BE, Wu CC, Müller WH (2016) An energy-based method to determine material constants in nonlinear rheology with applications. *Continuum Mechanics and Thermodynamics* 28(5):1221–1246
- Abdoul-Anziz H, Seppecher P (2018) Strain gradient and generalized continua obtained by homogenizing frame lattices. *Mathematics and mechanics of complex systems* 6(3):213–250
- Abdoul-Anziz H, Seppecher P, Bellis C (2019) Homogenization of frame lattices leading to second gradient models coupling classical strain and strain-gradient terms. *Mathematics and Mechanics of Solids* 24(12):3976–3999
- Alibert JJ, Seppecher P, dell’Isola F (2003) Truss modular beams with deformation energy depending on higher displacement gradients. *Mathematics and Mechanics of Solids* 8(1):51–73
- Andreas U, Spagnuolo M, Lekszycki T, Eugster SR (2018) A Ritz approach for the static analysis of planar pantographic structures modeled with nonlinear Euler–Bernoulli beams. *Continuum Mechanics and Thermodynamics* 30(5):1103–1123
- Balobanov V, Niiranen J (2018) Locking-free variational formulations and isogeometric analysis for the Timoshenko beam models of strain gradient and classical elasticity. *Computer Methods in Applied Mechanics and Engineering* 339:137–159
- Barchiesi E, Eugster SR, Placidi L, dell’Isola F (2019a) Pantographic beam: a complete second gradient 1d-continuum in plane. *Zeitschrift für angewandte Mathematik und Physik* 70(5):135
- Barchiesi E, Ganzosch G, Liebold C, Placidi L, Grygoruk R, Müller WH (2019b) Out-of-plane buckling of pantographic fabrics in displacement-controlled shear tests: experimental results and model validation. *Continuum Mechanics and Thermodynamics* 31(1):33–45
- Boutin C, dell’Isola F, Giorgio I, Placidi L (2017) Linear pantographic sheets: asymptotic micro-macro models identification. *Mathematics and Mechanics of Complex Systems* 5(2):127–162
- Cazzani A, Stochino F, Turco E (2016a) An analytical assessment of finite element and isogeometric analyses of the whole spectrum of Timoshenko beams. *ZAMM-Zeitschrift für Angewandte Mathematik und Mechanik* 96(10):1220–1244
- Cazzani A, Stochino F, Turco E (2016b) On the whole spectrum of Timoshenko beams. Part I: a theoretical revisit. *Zeitschrift für angewandte Mathematik und Physik* 67(2):24
- Cazzani A, Stochino F, Turco E (2016c) On the whole spectrum of Timoshenko beams. Part II: further applications. *Zeitschrift für angewandte Mathematik und Physik* 67(2):25
- Chróścielewski J, Schmidt R, Eremeyev VA (2019) Nonlinear finite element modeling of vibration control of plane rod-type structural members with integrated piezoelectric patches. *Continuum Mechanics and Thermodynamics* 31(1):147–188
- Clarke MJ, Hancock GJ (1990) A study of incremental-iterative strategies for non-linear analyses. *International Journal for Numerical Methods in Engineering* 29(7):1365–1391
- De Angelo M, Barchiesi E, Giorgio I, Abali BE (2019) Numerical identification of constitutive parameters in reduced-order bi-dimensional models for pantographic structures: application to out-of-plane buckling. *Archive of Applied Mechanics* 89(7):1333–1358
- Della Corte A, Battista A, dell’Isola F, Seppecher P (2019) Large deformations of Timoshenko and Euler beams under distributed load. *Zeitschrift für angewandte Mathematik und Physik* 70(2):52
- dell’Isola F, Andreas U, Placidi L (2015) At the origins and in the vanguard of peridynamics, non-local and higher-gradient continuum mechanics: an underestimated and still topical contribution of Gabrio Piola. *Mathematics and Mechanics of Solids* 20(8):887–928
- dell’Isola F, Seppecher P, Alibert JJ, et al (2019a) Pantographic metamaterials: an example of mathematically driven design and of its technological challenges. *Continuum Mechanics and Thermodynamics* 31(4):851–884
- dell’Isola F, Seppecher P, Spagnuolo M, et al (2019b) Advances in pantographic structures: design, manufacturing, models, experiments and image analyses. *Continuum Mechanics and Thermodynamics* 31(4):1231–1282
- Elishakoff I (2020) Who developed the so-called Timoshenko beam theory? *Mathematics and Mechanics of Solids* 25(1):97–116

- Eremeev VA, Zubov LM (1994) On the stability of elastic of elastic bodies with couple stresses. *Mechanics of Solids* 29(3):172–181
- Eremeyev V, Altenbach H (2017) Basics of mechanics of micropolar shells. In: *Shell-like Structures*, vol 572, Springer, pp 63–111
- Eremeyev VA (2019) Two-and three-dimensional elastic networks with rigid junctions: modeling within the theory of micropolar shells and solids. *Acta Mechanica* 230(11):3875–3887
- Eugster SR, dell’Isola F (2017) Exegesis of the introduction and Sect. I from “Fundamentals of the mechanics of continua”** by E. Hellinger. *ZAMM-Zeitschrift für Angewandte Mathematik und Mechanik* 97(4):477–506
- Eugster SR, dell’Isola F (2018a) Exegesis of Sect. II and III. A from “Fundamentals of the mechanics of continua” by E. Hellinger. *ZAMM-Zeitschrift für Angewandte Mathematik und Mechanik* 98(1):31–68
- Eugster SR, dell’Isola F (2018b) Exegesis of Sect. III. B from “Fundamentals of the mechanics of continua” by E. Hellinger. *ZAMM-Zeitschrift für Angewandte Mathematik und Mechanik* 98(1):69–105
- Fu YB, Ogden RW (1999) Nonlinear stability analysis of pre-stressed elastic bodies. *Continuum Mechanics and Thermodynamics* 11(3):141–172
- Giorgio I (2020) A discrete formulation of Kirchhoff rods in large-motion dynamics. *Mathematics and Mechanics of Solids* 25(5):1081–1100
- Giorgio I, Del Vescovo D (2018) Non-linear lumped-parameter modeling of planar multi-link manipulators with highly flexible arms. *Robotics* 7(4):60
- Giorgio I, Del Vescovo D (2019) Energy-based trajectory tracking and vibration control for multilink highly flexible manipulators. *Mathematics and Mechanics of Complex Systems* 7(2):159–174
- Giorgio I, Della Corte A, dell’Isola F (2017) Dynamics of 1D nonlinear pantographic continua. *Nonlinear Dynamics* 88(1):21–31
- Giorgio I, dell’Isola F, Steigmann DJ (2018) Axisymmetric deformations of a 2nd grade elastic cylinder. *Mechanics Research Communications* 94:45–48
- Giorgio I, dell’Isola F, Steigmann DJ (2019) Edge effects in hyper nets. *Comptes Rendus Mécanique* 347(2):114–123
- Greco L (2020) An iso-parametric G^1 -conforming finite element for the nonlinear analysis of Kirchhoff rod. Part I: the 2D case. *Continuum Mechanics and Thermodynamics* pp 1–24
- Greco L, Cuomo M (2015) Consistent tangent operator for an exact Kirchhoff rod model. *Continuum Mechanics and Thermodynamics* 27(4-5):861–877
- Greco L, Cuomo M, Contrafatto L (2018) A reconstructed local B formulation for isogeometric Kirchhoff–Love shells. *Computer method in applied mechanics and engineering* 332:462–487
- Greco L, Cuomo M, Contrafatto L (2019a) A quadrilateral G^1 -conforming finite element for the Kirchhoff plate model. *Computer Methods in Applied Mechanics and Engineering* 346:913–951
- Greco L, Cuomo M, Contrafatto L (2019b) Two new triangular G^1 -conforming finite elements with cubic edge rotation for the analysis of Kirchhoff plates. *Computer Methods in Applied Mechanics and Engineering* 356:354–386
- Gross A, Pantidis P, Bertoldi K, Gerasimidis S (2019) Correlation between topology and elastic properties of imperfect truss-lattice materials. *Journal of the Mechanics and Physics of Solids* 124:577–598
- Hencky H (1921) Über die angenäherte lösung von stabilitätsproblemen im raum mittels der elastischen gelenkkette. PhD thesis, Engelmann
- Kiendl J, Auricchio F, Hughes TJ, Reali A (2015) Single-variable formulations and isogeometric discretizations for shear deformable beams. *Computer Methods in Applied Mechanics and Engineering* 284:988–1004
- Lakes RS (2018) Stability of Cosserat solids: size effects, ellipticity and waves. *Journal of Mechanics of Materials and Structures* 13(1):83–91
- Laudato M, Barchiesi E (2019) Non-linear dynamics of pantographic fabrics: modelling and numerical study. In: *Wave Dynamics, Mechanics and Physics of Microstructured Metamaterials*, Springer, pp 241–254

- Luu AT, Kim NI, Lee J (2015) Isogeometric vibration analysis of free-form Timoshenko curved beams. *Meccanica* 50(1):169–187
- Meza LR, Das S, Greer JR (2014) Strong, lightweight, and recoverable three-dimensional ceramic nanolattices. *Science* 345(6202):1322–1326
- Meza LR, Phlipot GP, Portela CM, et al (2017) Reexamining the mechanical property space of three-dimensional lattice architectures. *Acta Materialia* 140:424–432
- Misra A, Poursolhjouy P (2015) Identification of higher-order elastic constants for grain assemblies based upon granular micromechanics. *Mathematics and Mechanics of Complex Systems* 3(3):285–308
- Misra A, Lekszycki T, Giorgio I, Ganzosch G, Müller WH, dell’Isola F (2018) Pantographic metamaterials show atypical poynting effect reversal. *Mechanics Research Communications* 89:6–10
- Niiranen J, Balobanov V, Kiendl J, Hosseini SB (2019) Variational formulations, model comparisons and numerical methods for Euler–Bernoulli micro- and nano-beam models. *Mathematics and Mechanics of Solids* 24(1):312–335
- Ogden RW (1997) *Non-linear elastic deformations*. Courier Corporation, Dover, Mineola
- Pideri C, Seppecher P (1997) A second gradient material resulting from the homogenization of an heterogeneous linear elastic medium. *Continuum Mechanics and Thermodynamics* 9(5):241–257
- Placidi L, dell’Isola F, Barchiesi E (2020) Heuristic homogenization of Euler and pantographic beams. In: *Mechanics of Fibrous Materials and Applications*, Springer, pp 123–155
- Riks E (1972) The application of Newton’s method to the problem of elastic stability. *Journal of Applied Mechanics, Transactions ASME E*(4):1060–1065
- Rodrigues O (1840) Des lois géométriques qui régissent les déplacements d’un système solide dans l’espace, et de la variation des coordonnées provenant de ces déplacements considérés indépendamment des causes qui peuvent les produire. *Journal de mathématiques pure et appliquées* 1(5):380–440
- Scerrato D, Giorgio I (2019) Equilibrium of two-dimensional cycloidal pantographic metamaterials in three-dimensional deformations. *Symmetry* 11(12):1523
- Seppecher P, Alibert JJ, dell’Isola F (2011) Linear elastic trusses leading to continua with exotic mechanical interactions. In: *Journal of Physics: Conference Series*, IOP Publishing, vol 319, p 012018
- Sheydaikov DN, Altenbach H (2016) Stability of inhomogeneous micropolar cylindrical tube subject to combined loads. *Mathematics and Mechanics of Solids* 21(9):1082–1094
- Solyaev Y, Lurie S, Barchiesi E, Placidi L (2020) On the dependence of standard and gradient elastic material constants on a field of defects. *Mathematics and Mechanics of Solids* 25(1):35–45
- Spagnuolo M, Andreaus U (2019) A targeted review on large deformations of planar elastic beams: extensibility, distributed loads, buckling and post-buckling. *Mathematics and Mechanics of Solids* 24(1):258–280
- Turco E (2018) Discrete is it enough? The revival of Piola–Hencky keynotes to analyze three-dimensional *Elastica*. *Continuum Mechanics and Thermodynamics* 30(5):1039–1057
- Turco E, dell’Isola F, Cazzani A, Rizzi NL (2016) Hencky-type discrete model for pantographic structures: numerical comparison with second gradient continuum models. *Zeitschrift für angewandte Mathematik und Physik* 67(4):85
- Turco E, Misra A, Sarikaya R, Lekszycki T (2019) Quantitative analysis of deformation mechanisms in pantographic substructures: experiments and modeling. *Continuum Mechanics and Thermodynamics* 31(1):209–223
- Turco E, Barchiesi E, Giorgio I, dell’Isola F (2020) A Lagrangian Hencky-type non-linear model suitable for metamaterials design of shearable and extensible slender deformable bodies alternative to Timoshenko theory. *International Journal of Non-Linear Mechanics* 123:103481
- Vangelatos Z, Komvopoulos K, Grigoropoulos C (2019a) Vacancies for controlling the behavior of microstructured three-dimensional mechanical metamaterials. *Mathematics and Mechanics of Solids* 24(2):511–524

- Vangelatos Z, Melissinaki V, Farsari M, Komvopoulos K, Grigoropoulos C (2019b) Intertwined microlattices greatly enhance the performance of mechanical metamaterials. *Mathematics and Mechanics of Solids* 24(8):2636–2648
- Wriggers P (2008) *Nonlinear finite element methods*. Springer Science & Business Media
- Yang H, Ganzosch G, Giorgio I, Abali BE (2018) Material characterization and computations of a polymeric metamaterial with a pantographic substructure. *Zeitschrift für angewandte Mathematik und Physik* 69(4):105



Chapter 12

Nonlinear Phenomena in Granular Solids: Modeling and Experiments

Marco Laudato

Abstract The International Conference on Nonlinear Solid Mechanics (ICoNSoM) 2019, held in Rome from 16th to 19th of June 2019, had as main goal to gather together researchers in the field of nonlinear Solid Mechanics in a stimulating research environment. This work is a rational report of activities of one of the several mini-symposia held during the conference titled “Nonlinear Phenomena in Granular Solids: Modeling and Experiments”. The main aim is to provide the interesting reader with the main topics treated during the discussions and to furnish all the relevant bibliography. Additional information, such as the abstracts of all the talks, can be found at the official web-site of the conference: <http://www.memocsevents.eu/iconsom2019/>.

Keywords: Granular solids · Continuum mechanics

12.1 Introduction

The study of granular materials is one of the key topics in the current landscape of Solid Mechanics. It is possible to find applications of results and methods of granular mechanics in several areas of fast and recent development such as biomechanics, geophysics, and material development (dell’Isola et al, 2015, 2017; Alibert et al, 2003; Barchiesi et al, 2019; Abali et al, 2017; Giorgio et al, 2016, 2017; dell’Isola et al, 2019a,b; Yang et al, 2018; Giorgio et al, 2009; Lossouarn et al, 2015; Alessandrini et al, 2004). One of the main reasons of this vast applicability is that several kinds of materials can be considered under the umbrella of granular materials. They span from soft membranes made of aggregations of cells to highly packed and dense solids made of particulate. From both the mathematical and experimental point of view, in

M. Laudato

Dipartimento di Ingegneria e Scienze dell’Informazione e Matematica, Università degli Studi dell’Aquila. Via Vetoio, Coppito, 67100 L’Aquila, Italy.

e-mail: marco.laudato@graduate.univaq.it

all the forms that they have been studied, granular material represents a formidable challenge due to fundamental role played by the properties of the grains themselves and their interaction. This has been the main motivation to dedicate a symposium on modeling and experimental challenges in nonlinear granular mechanics within the International Conference of Nonlinear Solid Mechanics 2019 (ICoNSoM 2019), held in Rome from 16th to 19th of June 2019. The International Research Center on Mathematics and Mechanics of Complex Systems (M&MoCS) of L'Aquila University together with the McGill University of Montreal, the Roma Tre University, and the Laboratoire International Associé Coss&Vita have conceived the ICoNSoM 2019 international conference to allow the interaction and exchange of new ideas and points of view between scientists and engineers from all the areas of Solid Mechanics.

Due to the number of topics treated, the conference has been divided into thematic symposia. The main goal of this paper is to report the activities and the discussions of the *Nonlinear Phenomena in Granular Solids: Modeling and Experiments* symposium. In the next section, we will describe the content of the topics treated during the symposium and we will indicate all the relevant references. We aim for providing a comprehensive snapshot of the current state of the art of the research in this fundamental framework.

12.2 Nonlinear Phenomena in Granular Solids: Modeling and Experiments

The symposium *Nonlinear phenomena in granular solids: modeling and experiments* has been the stage of ten contributions. In this section, we will review the content of the talks and provide the relevant bibliography.

The contributions have been presented according to their more applicative or theoretical nature. In the first group we have seen the talks by Tatiana Yuzhina on deformation and deconstruction of hardwood trees, Mikhail Gonov on the dynamic properties of concrete under compression, Ioan Ionescu on damage probing in cemented granular materials, and Nakase Hitoshi on the study of risk assessment of nuclear facilities under severe scenarios. In the second group we have gathered the contributions by Niel Kruyt on the role of fabric in the behavior of granular material, Takashi Matsushima on grain-scale description of higher-order continuum model for granular solid, Luca Placidi on damage and plastic evolution of second gradient effective elastic moduli of heterogeneous granular materials, Payam Poorsolhjoui on micro-macro identification from grain properties, Maurizio Romeo on electromagnetic microcontinuum approaches to granular media, and Antoine Wautier on strain localization from a mesoscale point of view.

12.2.1 Deformation and Destruction at Deformation Rate of Order $10^3 s^{-1}$ Wood of Hardwood Trees - Tatiana Yuzhina

Tatiana Yuzhina, in her talk “*Deformation and destruction at deformation rate of order $10^3 s^{-1}$ wood of hardwood trees*” presented the results of tests on birch and aspen with different directions, with respect to the fibers location, of cutting samples. The steepness of the load branches and the destructive stresses have been analyzed with respect to different cutting angles and the resulting behavior, including also plasticity, have been represented in terms of stress-strain diagrams. In particular, the greatest destructive stress as well as the greatest steepness of the load branches has been observed at cutting angle of 0° . On the other hand, the minimum values for such parameters have been observed for 90° cut corners. A remarkable behavior of these kinds of wood is that, after exhaustion, they show a relaxation behavior which passes into the area of ideal plasticity until the end of the load. Once the reasons of this behavior have been discussed (Bragov et al, 2018), the results of the analysis of the behavior of the wood batches with respect to the room temperature have been shown. The reader is invited to see the papers by Bragov and Lomunov (1997); Zhao et al (2016); Sciarra et al (2007); dell’Isola et al (2009); Madeo et al (2013); Turco (2018); Turco et al (2019); Bilotta and Turco (2017); Igumnov et al (2019) to gain a deeper insight into the subject, especially from a theoretical viewpoint.

12.2.2 Experimental Study of the Dynamic Properties of Concrete under Compressive Load - Mikhail Gonov

Mikhail Gonov presented a talk titled “*Experimental study of the dynamic properties of concrete under compressive load*”. The talk discussed the study of the deformation and fracture of concrete under dynamic loads within the framework of Kolsky method. The main goal of such tests were to characterize the high-speed deformation and destruction of fine concrete. In particular, the role played by copper pulse shapers in the dynamic tests has been discussed. The tests consisted of 35 test shots carried out with copper pulse shapers at 7 different speed. In this kind of tests, the role of the pulse shaper is to enhance the quality of the basic premise of the Kolsky method on the homogeneity of the highly deformed state of the samples. To check on the quality of this assumption, an accurate comparison of the results obtained in dynamic tests with the pulse formers and in absence of them has been performed and the results (Bragov et al, 2013) have been presented. Many efforts are expended to understand the complicated behavior of a very complex material as the concrete do is. In addition to the presentation summarized here, some relevant articles can be provided by Konstantinov et al (2018); Giorgio et al (2019); Giorgio and Scerrato (2017); Scerrato et al (2014, 2016); Chiaia et al (2015); Kezmane et al (2017); Contrafatto and Cuomo (2006); Contrafatto et al (2012, 2017, 2016); Stochino et al (2016).

12.2.3 Damage Probing in Cemented Granular Materials with Ultrasound - Ioan Ionescu

The analysis of fault core sliding or earthquakes in different states of materials has been discussed in the talk “*Damage probing in cemented granular materials with ultrasound*” by Ioan Ionescu. In particular, the results of the experimental and numerical investigation of the transition from cohesive to granular states of synthetic rock under different loadings have been discussed (Langlois and Jia, 2014; Gomez et al, 2020). The rock model used during the investigation is cemented granular material in which it is possible to tune both the nature and amount of cements and the packing density. Damage has been modeled in geometric configuration by considering an elasto-plastic deformation due to a quasi-static load. In this way the contact stiffness between the grains has been minimized during the damage evolution. The comparison of the results on wave velocity in damaged samples have been, finally, presented and discussed (Khidas and Jia, 2012).

12.2.4 The Role of Fabric in the Behavior of Granular Material - Niels Kruyt

During the talk “*The role of fabric in the behavior of granular material*” by Niels Kruyt, the interplay between the behavior of particles at micro-scale and the continuum model at macro-scale have been discussed. In particular, the speaker went through an overview on the role of fabric in characteristic behavior of granular materials such as shear strength, dilatancy, and elasto-plasticity (Pouragha et al, 2019). The evolution of the fabric of a initially isotropic granular assemblies undergoing small strain has been analyzed by means of a systematic approach in which the fabric changes during the evolution were modeled in terms of two-dimensional isotropic functions by means of a representation theorem. The results on this analysis on the evolution of the fabric has been presented and the crucial role played by contact gains and losses during the evolution has been elucidated (Kruyt, 2012, 2010; Fortin et al, 2005; Bonelli et al, 2012).

12.2.5 Grain-Scale Description of Higher-Order Continuum Model for Granular Solid - Takashi Matsushima

In the talk by Takashi Matsushima, “*Grain-scale description of higher-order continuum model for granular solid*”, the results of a series of distinct element method based simulations aimed at exploring the shear band width as a function of packing density and of the grain properties have been presented. In particular, it has been presented the results on the analysis of the relation between the shear band width and

maximum dilation rate within the framework of strain gradient theory (Matsushima and Chang, 2011; Matsushima et al, 2002). Although it is well known that such finite width localization zone cannot be forecasted by classical first order elasticity theories, all the higher-order continuum theories are still phenomenological and the physical nature of the needed higher-order terms has not been clarified. The results of this analysis have been discussed, highlighting the relation between the maximum dilation rate, which is well described by strain-gradient theory, and the shear band width.

12.2.6 Validation of a Simple Model Using the Distinct Element Method for Numerical Simulations of Slope Collapse - Nakase Hitoshi

The contribution “*Validation of a simple model using the distinct element method for numerical simulations of slope collapse*” by Nakase Hitoshi was focusing on the study of risk assessment of nuclear facilities under severe scenarios, like earthquakes. In particular, the results of the investigation, based on the development of a model based on distinct element method simulations, on the reaching distance of fallen rocks and the impacts on nuclear facilities, as well as the risk of slope failure have been presented and deeply discussed (Nakase et al, 2017). In order to reduce the computational cost of distinct element method simulations based on clump elements to model the complex shape of sand or rocks, a new approach focusing on the geo-technical behavior of such complex shaped particles has been proposed. In this method, although the rock mass geometry is simplified, the probabilistic behavior of a single collision is carefully modeled in terms of the roughness of slope. The results of this method and the comparison with the standard approaches have been discussed in the final part of the talk.

12.2.7 Damage and Plastic Evolution of Second Gradient Effective Elastic Moduli of Heterogeneous Granular Materials - Luca Placidi

Luca Placidi, in his talk “*Damage and plastic evolution of second gradient effective elastic moduli of heterogeneous granular materials*”, discussed a damage elasto-plastic model aimed at describing the evolution of anisotropy of a heterogeneous granular solid. In particular, the micro-mechanical model has been defined by considering a collection of particles interacting via inter-particle contacts, while to facilitate the derivation of the overall stiffness tensors, the interactions have been considered as continuous in the orientation space (Solyaev et al, 2019; Placidi et al, 2019). In the final part of the talk, some examples involving anisotropy have been discussed.

In particular, in order to entail the anisotropy of the heterogeneous granular solid, a model for elasto-plastic damage, based on spring interaction between the grains, has been outlined. The effectiveness of this model has been analyzed on some relevant examples and compared with standard numerical approaches (see, e.g., Placidi et al, 2018a; Placidi and Barchiesi, 2018; Abali et al, 2015; Placidi et al, 2018b, 2020; Nguyen and Niiranen, 2020).

12.2.8 Micro-Macro Identification: Continuum Parameters from Grain Properties - Payam Poorsolhjoui

In the contribution “*Micro-macro identification: continuum parameters from grain properties*” by Payam Poorsolhjoui a numerical approach to derive average grain-scale properties used in the Granular Micromechanics Approach has been presented. In particular, the results of the analysis under both small and large deformations and the evidences of non-affine movements in the assembly and their relations with higher gradient theories have been precisely discussed (Poorsolhjoui and Misra, 2019). The main advantage in the use of the Granular Micromechanics Approach with respect to other coarse-grained based models is that it is based on a statistical analysis of the directional distribution of both stiffness and geometric properties of the grain pair interactions. Starting with such knowledge of the microstructure, in the final part of the talk it has been discussed a numerical approach to derive the macroscopic properties of the materials. Finally, some considerations on the application of this approach on large deformations problems have been discussed. The literature on micro-macro identification of granular materials is absolutely vast, so it is quite difficult to recall all papers about that subject. However, a selection of papers considered of the utmost esteem by the writer is as follows (Misra and Poorsolhjoui, 2015a; Chang and Misra, 1990; Yang and Misra, 2012; Misra and Poorsolhjoui, 2015b; Misra and Singh, 2015; Misra and Poorsolhjoui, 2017; NejadSadeghi et al, 2019; Misra et al, 2020; De Angelo et al, 2020; Abali et al, 2019; De Angelo et al, 2019).

12.2.9 Electromagnetic Microcontinuum Approach to Granular Media - Maurizio Romeo

Maurizio Romeo, in his talk “*Electromagnetic microcontinuum approach to granular media*”, discussed an approach to the analysis of electro-magneto-elastic interactions in continuum mechanics. In particular, by exploiting the microcontinuum theory framework (Misra and Poorsolhjoui, 2016), an extension has been presented in Romeo (2011) regarding the classical constitutive approach to electromagnetic interactions (Abali and Queiruga, 2019). In this approach, micro-deformations are directly related to electric multipoles and, consequently, the expressions for electric

polarization and magnetization can be explicitly derived. The equations resulting from a variational method have been discussed, highlighting the effects of external electromagnetic dipole and quadrupole fields on granular materials (Romeo, 2016, 2018). The balance equations obtained in this way include Ampère law and Gauss law in the usual formalization in terms of scalar and vector potentials.

12.2.10 Strain Localization from a Mesoscale Point of View - Antoine Wautier

Antoine Wautier, in his contribution “*Strain localization from a mesoscale point of view*”, presented the results of his investigation on the micro-mechanical mechanism responsible for the strain localization pattern in granular materials. This response is a peculiar characteristic of granular materials: on loose granular material only a pure hardening behavior happens and it is not possible to observe any strain localization. In particular, by performing an analysis of the mechanical and geometrical characteristic of force chains inside and outside the shear band area, it has been shown that the hardening regime is linked to the concentration of the load on less and less force chains and to the degradation of the contact network. Finally, an explanation of the softening regime in terms of force chain rotations within the shear band domain has been discussed (Wautier et al, 2018a). It is also worth noting the works by Wautier and Guzina (2015); Wautier et al (2017); Nicot et al (2017); Wautier et al (2018b); Eremeyev et al (2019); Eremeyev (2019); Eremeyev and Sharma (2019)

12.3 Conclusions

The centrality of Granular Mechanics in modern Solid Mechanics clearly emerges from the several topics touched during the *Nonlinear Phenomena in Granular Solids: Modeling and Experiments* symposium. Starting from very applicative investigations (such as wood and concrete characterizations, as discussed in the first two contributions) to theoretical discussions on generalized theory of elasticity and electromagnetism (e.g. the talks by Luca Placidi and Maurizio Romeo), Granular Mechanics appears to be an eclectic tool which, if properly understood, will bring promising developments in Solid Mechanics. Of course during the interesting discussions, moderated by the excellent work made by the chairmen, several open problems and questions, such as the role of the grains at different scales of description or the need of generalized theories of elasticity to properly describe the granular behavior, have been highlighted. The role of conferences like International Conference of Nonlinear Solid Mechanics 2019 (and of papers like the present one) is exactly to push this kind of discussions which are catalyst for the advancement of science. To this regard, the symposium *Nonlinear Phenomena in Granular Solids: Modeling and Experiments* can be considered a successful experience. We expect similar reports from other

symposia with the hope of spreading the ideas and creating new collaborations, which are the main and ultimate goals of events like ICOnSoM 2019.

References

- Abali BE, Queiruga AF (2019) Theory and computation of electromagnetic fields and thermomechanical structure interaction for systems undergoing large deformations. *Journal of Computational Physics* 394:200–231
- Abali BE, Müller WH, Eremeyev VA (2015) Strain gradient elasticity with geometric nonlinearities and its computational evaluation. *Mechanics of Advanced Materials and Modern Processes* 1(1):4
- Abali BE, Müller WH, dell'Isola F (2017) Theory and computation of higher gradient elasticity theories based on action principles. *Archive of Applied Mechanics* 87(9):1495–1510
- Abali BE, Yang H, Papadopoulos P (2019) A computational approach for determination of parameters in generalized mechanics. In: Altenbach H, Müller WH, Abali BE (eds) *Higher Gradient Materials and Related Generalized Continua*, *Advanced Structured Materials*, vol. 120, Springer, Cham, chap 1, pp 1–18
- Alessandrini S, Andreus U, dell'Isola F, et al (2004) Piezo-electromechanical (PEM) Kirchhoff–Love plates. *European Journal of Mechanics-A/Solids* 23(4):689–702
- Alibert JJ, Seppecher P, dell'Isola F (2003) Truss modular beams with deformation energy depending on higher displacement gradients. *Mathematics and Mechanics of Solids* 8(1):51–73
- Barchiesi E, Spagnuolo M, Placidi L (2019) Mechanical metamaterials: a state of the art. *Mathematics and Mechanics of Solids* 24(1):212–234
- Bilotta A, Turco E (2017) Elastoplastic analysis of pressure-sensitive materials by an effective three-dimensional mixed finite element. *ZAMM-Zeitschrift für Angewandte Mathematik und Mechanik* 97(4):382–396
- Bonelli S, Millet O, Nicot F, Rahmoun J, De Saxcé G (2012) On the definition of an average strain tensor for two-dimensional granular material assemblies. *International Journal of Solids and Structures* 49(7-8):947–958
- Bragov A, Lomunov A (1997) Dynamic properties of some wood species. *Le Journal de Physique IV* 7(C3):C3–487
- Bragov A, Petrov YV, Karihaloo BL, Konstantinov AY, Lamzin D, Lomunov A, Smirnov I (2013) Dynamic strengths and toughness of an ultra high performance fibre reinforced concrete. *Engineering Fracture Mechanics* 110:477–488
- Bragov AM, Konstantinov AY, Lomunov AK, Yuzhina TN, Filippov AR (2018) Experimental complexes for investigation of behavior of materials at a strain rate of $5 \cdot 10^2 \div 10^5 \text{ s}^{-1}$. In: *MATEC Web of Conferences*, EDP Sciences, vol 226, p 03024
- Chang CS, Misra A (1990) Application of uniform strain theory to heterogeneous granular solids. *Journal of engineering mechanics* 116(10):2310–2328
- Chiaia B, Kumpyak O, Placidi L, Maksimov V (2015) Experimental analysis and modeling of two-way reinforced concrete slabs over different kinds of yielding supports under short-term dynamic loading. *Engineering Structures* 96:88–99
- Contrafatto L, Cuomo M (2006) A framework of elastic–plastic damaging model for concrete under multiaxial stress states. *International Journal of Plasticity* 22(12):2272–2300
- Contrafatto L, Cuomo M, Fazio F (2012) An enriched finite element for crack opening and rebar slip in reinforced concrete members. *International journal of fracture* 178(1-2):33–50
- Contrafatto L, Cuomo M, Gazzo S (2016) A concrete homogenisation technique at meso-scale level accounting for damaging behaviour of cement paste and aggregates. *Computers & Structures* 173:1–18
- Contrafatto L, Cuomo M, Greco L (2017) Meso-scale simulation of concrete multiaxial behaviour. *European Journal of Environmental and Civil Engineering* 21(7-8):896–911

- De Angelo M, Barchiesi E, Giorgio I, Abali BE (2019) Numerical identification of constitutive parameters in reduced-order bi-dimensional models for pantographic structures: application to out-of-plane buckling. *Archive of Applied Mechanics* 89(7):1333–1358
- De Angelo M, Placidi L, NejadSadeghi N, Misra A (2020) Non-standard timoshenko beam model for chiral metamaterial: Identification of stiffness parameters. *Mechanics Research Communications* 103:103,462
- dell'Isola F, Madeo A, Seppecher P (2009) Boundary conditions at fluid-permeable interfaces in porous media: A variational approach. *International Journal of Solids and Structures* 46(17):3150–3164
- dell'Isola F, Andraus U, Placidi L (2015) At the origins and in the vanguard of peridynamics, non-local and higher-gradient continuum mechanics: An underestimated and still topical contribution of Gabrio Piola. *Mathematics and Mechanics of Solids* 20(8):887–928
- dell'Isola F, Della Corte A, Giorgio I (2017) Higher-gradient continua: The legacy of Piola, Mindlin, Sedov and Toupin and some future research perspectives. *Mathematics and Mechanics of Solids* 22(4):852–872
- dell'Isola F, Seppecher P, Alibert JJ, et al (2019a) Pantographic metamaterials: an example of mathematically driven design and of its technological challenges. *Continuum Mechanics and Thermodynamics* 31(4):851–884
- dell'Isola F, Seppecher P, Spagnuolo M, et al (2019b) Advances in pantographic structures: design, manufacturing, models, experiments and image analyses. *Continuum Mechanics and Thermodynamics* 31(4):1231–1282
- Eremeyev VA (2019) On anti-plane surface waves considering highly anisotropic surface elasticity constitutive relations. In: *Wave Dynamics, Mechanics and Physics of Microstructured Metamaterials*, Springer, pp 1–9
- Eremeyev VA, Sharma BL (2019) Anti-plane surface waves in media with surface structure: Discrete vs. continuum model. *International Journal of Engineering Science* 143:33–38
- Eremeyev VA, Rosi G, Naili S (2019) Comparison of anti-plane surface waves in strain-gradient materials and materials with surface stresses. *Mathematics and mechanics of solids* 24(8):2526–2535
- Fortin J, Millet O, de Saxcé G (2005) Numerical simulation of granular materials by an improved discrete element method. *International Journal for Numerical Methods in Engineering* 62(5):639–663
- Giorgio I, Scerrato D (2017) Multi-scale concrete model with rate-dependent internal friction. *European Journal of Environmental and Civil Engineering* 21(7-8):821–839
- Giorgio I, Culla A, Del Vescovo D (2009) Multimode vibration control using several piezoelectric transducers shunted with a multiterminal network. *Archive of Applied Mechanics* 79(9):859
- Giorgio I, Andraus U, Scerrato D, dell'Isola F (2016) A visco-poroelastic model of functional adaptation in bones reconstructed with bio-resorbable materials. *Biomechanics and modeling in mechanobiology* 15(5):1325–1343
- Giorgio I, Andraus U, dell'Isola F, Lekszycki T (2017) Viscous second gradient porous materials for bones reconstructed with bio-resorbable grafts. *Extreme Mechanics Letters* 13:141–147
- Giorgio I, De Angelo M, Turco E, Misra A (2019) A Biot–Cosserrat two-dimensional elastic nonlinear model for a micromorphic medium. *Continuum Mechanics and Thermodynamics* pp 1–13
- Gomez Q, Uenishi K, Ionescu IR (2020) Quasi-static versus dynamic stability associated with local damage models. *Engineering Failure Analysis* p 104476
- Igumnov L, Litvinchuk S, Ipatov A, Iuzhina T (2019) The boundary-element approach to modeling the dynamics of poroelastic bodies. In: *International Conference on Theoretical, Applied and Experimental Mechanics*, Springer, pp 311–315
- Kezmane A, Chiaia B, Kumpyak O, Maksimov V, Placidi L (2017) 3d modelling of reinforced concrete slab with yielding supports subject to impact load. *European Journal of Environmental and Civil Engineering* 21(7-8):988–1025
- Khidas Y, Jia X (2012) Probing the shear-band formation in granular media with sound waves. *Physical Review E* 85(5):051,302

- Konstantinov AY, Basalin AV, Gonov ME, Filippov AR (2018) Numerical analysis of influence of length of the working part of specimen on dynamic diagrams of constructional materials obtained by the kolsky method. In: MATEC Web of Conferences, EDP Sciences, vol 226, p 03023
- Kruyt N (2012) Micromechanical study of dispersion and damping characteristics of granular materials. *Journal of mechanics of materials and structures* 7(4):347–361
- Kruyt NP (2010) Micromechanical study of plasticity of granular materials. *Comptes rendus mécanique* 338(10-11):596–603
- Langlois V, Jia X (2014) Acoustic probing of elastic behavior and damage in weakly cemented granular media. *Physical Review E* 89(2):023,206
- Lossouarn B, Deü JF, Aucejo M (2015) Multimodal vibration damping of a beam with a periodic array of piezoelectric patches connected to a passive electrical network. *Smart Materials and Structures* 24(11):115,037
- Madeo A, dell'Isola F, Darve F (2013) A continuum model for deformable, second gradient porous media partially saturated with compressible fluids. *Journal of the Mechanics and Physics of Solids* 61(11):2196–2211
- Matsushima T, Chang CS (2011) Quantitative evaluation of the effect of irregularly shaped particles in sheared granular assemblies. *Granular matter* 13(3):269–276
- Matsushima T, Chambon R, Caillerie D (2002) Large strain finite element analysis of a local second gradient model: application to localization. *International journal for numerical methods in engineering* 54(4):499–521
- Misra A, Poursolhjouy P (2015a) Identification of higher-order elastic constants for grain assemblies based upon granular micromechanics. *Mathematics and Mechanics of Complex Systems* 3(3):285–308
- Misra A, Poursolhjouy P (2015b) Micro-macro scale instability in 2d regular granular assemblies. *Continuum Mechanics and Thermodynamics* 27(1-2):63–82
- Misra A, Poursolhjouy P (2016) Granular micromechanics based micromorphic model predicts frequency band gaps. *Continuum Mechanics and Thermodynamics* 28(1-2):215–234
- Misra A, Poursolhjouy P (2017) Elastic behavior of 2d grain packing modeled as micromorphic media based on granular micromechanics. *Journal of Engineering Mechanics* 143(1):C4016,005
- Misra A, Singh V (2015) Thermomechanics-based nonlinear rate-dependent coupled damage-plasticity granular micromechanics model. *Continuum Mechanics and Thermodynamics* 27(4-5):787–817
- Misra A, NejadSadeghi N, De Angelo M, Placidi L (2020) Chiral metamaterial predicted by granular micromechanics: verified with 1d example synthesized using additive manufacturing. *Continuum Mechanics and Thermodynamics* pp 1–17
- Nakase H, Iwamoto T, Cao G, Tabei K, Sakaguchi H, Matsushima T (2017) Reproduction analysis of actual slope collapse and parametric study for evacuation of the deposit volume by a simple model of distinct element method. *Doboku Gakkai Ronbunshu A1 Kozo, Jishin Kogaku (Online)* 73(4):1–694
- NejadSadeghi N, Placidi L, Romeo M, Misra A (2019) Frequency band gaps in dielectric granular metamaterials modulated by electric field. *Mechanics Research Communications* 95:96–103
- Nguyen THA, Niiranen J (2020) A second strain gradient research model with a numerical implementation for quasi-brittle materials with micro-architectures. *Mathematics and Mechanics of Solids* 25(3):515–546
- Nicot F, Xiong H, Wautier A, Lerbet J, Darve F (2017) Force chain collapse as grain column buckling in granular materials. *Granular Matter* 19(2):18
- Placidi L, Barchiesi E (2018) Energy approach to brittle fracture in strain-gradient modelling. *Proceedings of the Royal Society A: Mathematical, Physical and Engineering Sciences* 474(2210):20170,878
- Placidi L, Barchiesi E, Misra A (2018a) A strain gradient variational approach to damage: a comparison with damage gradient models and numerical results. *Mathematics and Mechanics of Complex Systems* 6(2):77–100

- Placidi L, Misra A, Barchiesi E (2018b) Two-dimensional strain gradient damage modeling: a variational approach. *Zeitschrift für angewandte Mathematik und Physik* 69(3):56
- Placidi L, Misra A, Barchiesi E (2019) Simulation results for damage with evolving microstructure and growing strain gradient moduli. *Continuum Mechanics and Thermodynamics* 31(4):1143–1163
- Placidi L, Barchiesi E, Misra A, Andreaus U (2020) Variational methods in continuum damage and fracture mechanics. *Encyclopedia of continuum mechanics* Berlin: Springer-Verlag
- Poorsolhjoui P, Misra A (2019) Granular micromechanics based continuum model for grain rotations and grain rotation waves. *Journal of the Mechanics and Physics of Solids* 129:244–260
- Pouragha M, Kruyt NP, Wan R (2019) Fabric evolution in granular materials under strain probing. In: *Desiderata Geotechnica*, Springer, pp 151–161
- Romeo M (2011) Micromorphic continuum model for electromagnetoelastic solids. *Zeitschrift für angewandte Mathematik und Physik* 62(3):513–527
- Romeo M (2016) A microstructure continuum approach to electromagneto-elastic conductors. *Continuum Mechanics and Thermodynamics* 28(6):1807–1820
- Romeo M (2018) Microcontinuum approach to electromagneto-elasticity in granular materials. *Mechanics Research Communications* 91:33–38
- Scerrato D, Giorgio I, Madeo A, Limam A, Darve F (2014) A simple non-linear model for internal friction in modified concrete. *International Journal of Engineering Science* 80:136–152
- Scerrato D, Giorgio I, Della Corte A, Madeo A, Dowling N, Darve F (2016) Towards the design of an enriched concrete with enhanced dissipation performances. *Cement and Concrete Research* 84:48–61
- Sciara G, dell’Isola F, Coussy O (2007) Second gradient poromechanics. *International Journal of Solids and Structures* 44(20):6607–6629
- Solyaev Y, Lurie S, Barchiesi E, Placidi L (2019) On the dependence of standard and gradient elastic material constants on a field of defects. *Mathematics and Mechanics of Solids* p 1081286519861827
- Stochino F, Cazzani A, Giaccu GF, Turco E (2016) Dynamics of strongly curved concrete beams by isogeometric finite elements. In: *Conference on Italian Concrete Days*, Springer, pp 231–247
- Turco E (2018) In-plane shear loading of granular membranes modeled as a Lagrangian assembly of rotating elastic particles. *Mechanics Research Communications* 92:61–66
- Turco E, dell’Isola F, Misra A (2019) A nonlinear Lagrangian particle model for grains assemblies including grain relative rotations. *International Journal for Numerical and Analytical Methods in Geomechanics* 43(5):1051–1079
- Wautier A, Guzina BB (2015) On the second-order homogenization of wave motion in periodic media and the sound of a chessboard. *Journal of the Mechanics and Physics of Solids* 78:382–414
- Wautier A, Bonelli S, Nicot F (2017) Scale separation between grain detachment and grain transport in granular media subjected to an internal flow. *Granular Matter* 19(2):22
- Wautier A, Bonelli S, Nicot F (2018a) Flow impact on granular force chains and induced instability. *Physical Review E* 98(4):042,909
- Wautier A, Bonelli S, Nicot F (2018b) Micro-inertia origin of instabilities in granular materials. *International Journal for Numerical and Analytical Methods in Geomechanics* 42(9):1037–1056
- Yang H, Ganzosch G, Giorgio I, Abali BE (2018) Material characterization and computations of a polymeric metamaterial with a pantographic substructure. *Zeitschrift für angewandte Mathematik und Physik* 69(4):105
- Yang Y, Misra A (2012) Micromechanics based second gradient continuum theory for shear band modeling in cohesive granular materials following damage elasticity. *International Journal of Solids and Structures* 49(18):2500–2514
- Zhao S, Zhao J, Han G (2016) Advances in the study of mechanical properties and constitutive law in the field of wood research. In: *IOP Conference Series: Materials Science and Engineering*, IOP Publishing, vol 137, p 012036



Chapter 13

A Tool to Describe Particle System Evolution from Swarm Robotics Behavior

Ramiro dell'Erba

Abstract A technique, known as position based dynamics, can be used to provide a visual description of the evolution of a two-dimensional particle system without solving the differential equations of dynamics. To this aim we applied an algorithm generally employed in submarine robot swarm control; the position of a particle in a lattice, like a robot element of a swarm, is determined by the position of its neighbors. By this way we generated an interaction's law based on the reciprocal position of particles without the definition of forces. We have therefore created software able to reproduce some behavior of deformable bodies according to Cauchy's standard model and second gradient theory. It gives a plausible simulation of continuum deformation and fracture and can be useful to describe final and sometime intermediate, configuration of a continuum material under assigned strain of some of its points; the advantages are in saving computational time, with respect to solving classical differential equation. Many aspects have to be still investigated, like the relationships describing the interaction rules between particles and its physical meaning and some results does not sound very good. In this paper we try to focus the job done and what is coming over.

Keywords: Position based dynamics · Robot swarm

13.1 Introduction

Position based dynamics (PBD) (Bender et al, 2015) is a technique used in computer animation since some years; its efficiency, simplicity and robustness gain it successful. PBD is not dedicate to compute real physical phenomena but its aim is to generate plausible, to the eye of the spectator, simulation saving computational cost

R. dell'Erba
ENEA Technical Unit technologies for energy and industry - Robotics Laboratory
e-mail: ramiro.dellerba@enea.it

(Umetani et al, 2014); the obtained results sacrifice some accuracy compared with finite element methods (FEM). The PBD method does not compute forces and solve heavy differential equations but it employs a different approach, based on position, where the new position of a lattice's particle is computed starting from its neighbor's positions. One of the advantages is the easy description of complex objects and can take profit of the increase of the GPU power, that led the method to popularity. In our Laboratory, we are working on the control system of a robotic swarm (see Fig. 13.1); the control system is inspired from fish school behavior and we have applied the same principle (dell'Erba, 2015; Moriconi and dell'Erba, 2012); in our laboratory we are working on this topic since many years. To reach a geometric configuration the single element of a robotic swarm is subject to flocking rule quite similar to PBD algorithm (Battista et al, 2016; dell'Erba, 2018a,b). Basically the displacement of a particle (discretized continuum equivalent to a swarm element) is computed using neighbors position. Indeed the compute of new position for a particle group is equivalent to a constrained geometrical problem where we use a transformation operator. Matrices representing the particles configurations, C_t , for a discrete set of time steps t_1, t_2, \dots, t_n and the transformation operator led from a configuration to another. One of the differences, between our methods and PBD, lies in the use of the velocity of the particles often used in PBD; this, in our opinion, hides the dynamic inside so, up to now we avoid using them. Complex micro-structures are not easily analyzed by Cauchy Continuum theory and poor software can be applied to enlighten some deformation aspects. Moreover these structures are able to generate large set of experimental data that are difficult to manage. Another argument is that classical Cauchy continua sometimes are not able to give required accuracy prediction in highly non-homogeneous microstructure; to overcome this problem generalizations have to be introduced, considering additional degrees of freedom to take in account for the kinematics at the level of the microstructure, (Seddik et al, 2008; Placidi et al, 2009; Pietraszkiewicz and Eremeyev, 2009; Altenbach et al, 2009b; Eremeyev et al, 2012; Altenbach et al, 2009a; Altenbach and Eremeyev, 2013; Barchiesi et al, 2018a; Placidi et al, 2019; Rosi et al, 2017; Turco, 2019; Turco et al, 2017b; Franciosi and Lebail, 2004), or including in the deformation energy density higher gradients of the displacement than the first one (Abali et al, 2017; Cuomo et al, 2017; Turco et al, 2016b; dell'Isola et al, 2015b; Javili et al, 2013; Seppacher et al, 2011; Forest et al, 2011; Placidi, 2014; Andreaus et al, 2016; Abali et al, 2015; Placidi et al, 2016; dell'Isola et al, 2015a; Alibert et al, 2003) in the deformation energy. The last is an important topic if we consider the actual technological interest towards exotic mechanical metamaterials able to perform targeted tasks (Bückmann et al, 2012; dell'Isola et al, 2019b; Barchiesi et al, 2018b; Carcaterra et al, 2015; Turco et al, 2017a; dell'Isola et al, 2016a; Milton and Seppacher, 2012), for these reasons the availability new and more efficient algorithms is at the centre of attention on this time. The software we have proposed can show a large range of behaviors just modifying its parameters and/or lattice type. In this paper we recall the work just done but focussing our attention on what still must be investigated and something that still does not fit. Particularly attention has been posed about a beam subject to

a shear load, to underline the influence of the parameter's choices. We also outline the differences with the solution of the ordinary differential equations.

13.2 Method

Extended description of the algorithm is reported in Battista et al (2016); dell'Erba (2018a,b). A two-dimensional body is represented in a discrete form using particles that, at the initial time, are posed in the nodes of a lattice. We can choice (Choice 1) the lattice to describe the body between the plane Bravais lattices (five) but we have used also honey comb lattice. This is the first of the choices we have to do in our model and every of them determine different behaviors, starting from the same initial conditions. To describe the body deformation, we are considering four kinds of different particles with different behaviors; it is easily possible to increase this number, to describe other behaviors owing the modular structure of the algorithm. We underline that the role of the particles can be changed at any time step during body's deformation. The kinds of particles are the following:

1. The leaders; the motion is assigned and their displacement generate the motion of the other particles.
2. The followers; their motion is computed using the rules of interaction between them and with other particles, typically neighbors.
3. The frame; these particles are introduced because any particle must have the same number of neighbors, to avoid collapsing and edge effects. A frame rule motion is assigned to compute their motion (see Figure 13.2 and 13.3).
4. The ghost; these not existing particles are an escamotage used to describe fracture mechanism (see Figure 13.4).

Now we shall see how the particle's motion is computed. The leader's motion is given so we just have it. Concerning the follower's motion we have to do some other choices. As first (Choice 2) we have to choose the neighbors of any of them. It is usual to employ the first n_c particles, where n_c is the lattice coordination number. This choice is the case of first gradient theory; it is possible to use a larger set of neighbors, i.e. the neighbors of the neighbors. In this last case, we obtain the second gradient case. To this aim we extend the interaction points using a supplementary external shell. This technique can be iterated to nth order interaction (see Figures 13.2 and 13.3). The Choice 3 is concerning how the particles interact between them. Practically we have to define as the position of a particle is computed with respect of the other particle's position. We can decide, as example, to use a rule where the new x coordinate of the particle j is in the centre of gravity of the neighbors

$$x_j(t) = \frac{\sum_{k=2}^{\text{all neighbors of } j} x_k(t)}{N} \quad (13.1)$$

N is the total number of neighbors and an equation like (13.1) can be used for the y coordinate. So far, the coordinate of a follower point is computed as the

average value of its neighbors; increasing the shell's number we determine the order of interaction. It is possible to use different rules to achieve different constitutive equations behavior. Possible generalizations of Eq. (13.1) are geometric, power and weighted mean. Possible weight is the particles Euclidean distances $dis(k, j)$ between the particles k and j . Our aim is to imitate Hooke's law, where force is increased with increasing displacement. By Eq. (13.1) we note as x and y coordinate are independent so Poisson effect cannot be obtained. A possibility to obtain it is to use

$$y_j(t) = K * (x_j(t) - x_j(t_0)) * da + \frac{\sum_{k=2}^{\text{all neighbors of } j} y_k(t)}{N} \quad (13.2)$$

Where da is a function of the distance from the central axis, K a parameter determining the recall force and $x(t_0)$ the x coordinate at time t_0 . So far modification on x coordinate has effect on the y coordinate. The Euclidean distance, $dis(k, j)$, can be used as weight.

$$x_j(t) = \frac{\sum_{k=2}^{\text{all neighbors of } j} dis(k, j) x_k(t)}{\sum_{k=2}^{\text{all neighbors of } j} dis(k, j)} \quad (13.3)$$

It is interesting to force the follower's displacement to overcome equilibrium position, computed from barycentre. This leads the lattice to oscillate.

$$x_j(t) = \frac{\sum_{k=2}^{\text{all neighbors of } j} w(k, j) x_k(t)}{\sum_{k=2}^{\text{all neighbors of } j} w(k, j)} + fd \left(\frac{\sum_{k=2}^{\text{all neighbors of } j} w(k, j) x_k(t)}{\sum_{k=2}^{\text{all neighbors of } j} w(k, j)} - MT(j, t_0) \right) \quad (13.4)$$

Where $w(k, j)$ is the weight, fd is a feedback factor and $MT(i, t_0)$ is the x coordinate of j point at t_0 to have memory of the initial configuration.

Using an algebraically point of view we can affirm as the compute of new set of position for all the follower particles can be considered as a constrained geometrical problem. The set of particle position, at a certain time, can be represented by a bi-dimensional matrix; each elements of the matrix contains the coordinates of one particle. Therefore, we use transformation operator leading from the matrix describing particles configuration, C_t , to the matrix relative to other time steps t_1, t_2, \dots, t_n . It must be underlined that the neighbors can be dynamically changed at every time step. We have chosen, in this paper, to keep fix the neighbors of every particle as they are at the initial time t_0 ; therefore we are considering crystalline lattice and are dealing with materials in solid phase. This means that the concept of neighbors is Lagrangian, and neighborhood is preserved in time evolution; exception to this assumption is considered in fracture case. Changing metric can be used to customize neighbor's definition in other way; as example it is possible to consider the points whose Euclidean distance (weighted or not to take into account anisotropies of the lattice) is less than a prefixed threshold, instead to consider the coordination number. Therefore at each time step the displacement of one shell propagates, starting from

the leaders, up to involve all the other particles of the lattice. Note as, at the beginning, only a limited number of points are involved. To avoid edge effects any follower has to interact with the same number of elements; therefore we have to build an external shell of point, a frame, surrounding the body. Frame motion has its rule: it follows the motion of an assigned follower of its competence; could be the case where the assigned followers are more (i.e. in a corner). In this case an average displacement, or (Choice 4), a more generic complex rule could be considered. To describe fracture phenomena, we have used ghost points. We decide a threshold, df , called as fracture distance (Choice 5) to be overcome to declare fracture. Therefore if distance between points is larger than fracture distances we say that the points stop to influence each other so are no longer considered in computing follower position. We have introduced ghost points with the aim to balance point's displacements calculation, preserving symmetry. Where we can put the ghost points? A usual choice (Choice 6), is the one so the original shape of the lattice is recovered (see Figure 13.4). Anyway, other choices are possible and lead to different results (Battista et al, 2016; dell'Erba, 2018a,b).



Fig. 13.1 VENUS, element of the swarm realized in our laboratory.

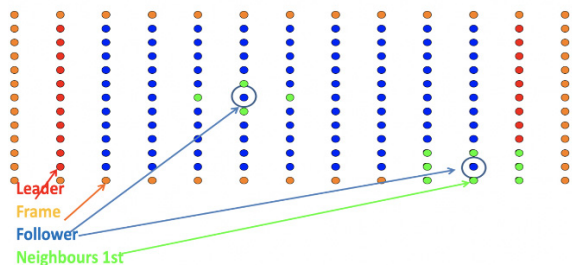


Fig. 13.2 Kind of particles.

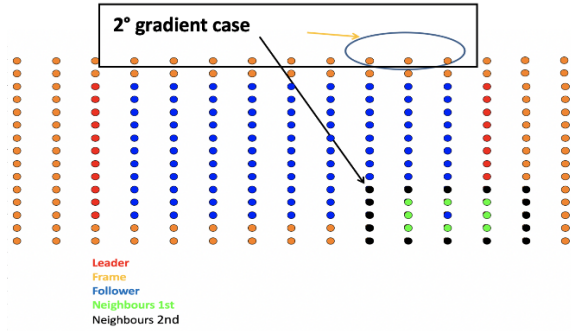


Fig. 13.3 Kind of particles (2nd gradient case).

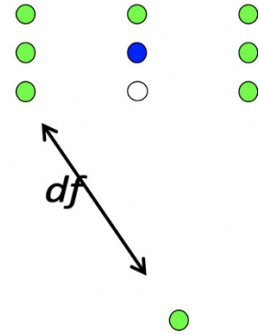


Fig. 13.4 Fracture mechanism: ghost.

In a next future we would like to consider the proposed model in a fully variational setting, that provide clear methodological advantages (see (Lanczos, 2012) for an introduction and (Placidi et al, 2008; dell’Isola and Placidi, 2011; dell’Isola et al, 2016b; dell’Isola and Gavriljuk, 2012; dell’Isola et al, 2014) for cases regarding continua with non-classical properties); we also try to introduce pseudo energetic parameters using two formulas $PE1$ and $PE2$. $PE1$ can be considered as a measure of how much we are far from the initial configuration, i.e.

$$PE1(t, j) = \sum_{k=1}^{\text{all neighbors of } j} (dis(t, k, j) - dis(t_0, k, j))^2 \tag{13.5}$$

Where $dis(t, k, j)$ is the Euclidean distance between points k and j at time t . It is clear as, by this formula, we try to emulate potential energy of material point subject to Hooke’s law. Temporal contiguous configuration C_t and C_{t-1} are compared by $PE2$:

$$PE2(t, j) = \|C_t - C_{t-1}\| \tag{13.6}$$

Where $\|\cdot\|$ is the Norm of the vector defined by the point j at time t and $t - 1$. Remember as these two formula are artifices; they have no direct connection with the usual energy definition, so we call it pseudo-energy. Anyway, they have shown

to be useful in understanding deformation behavior. In this paper we use them just a little; extensive use of these formulas can be finding in Battista et al (2016); dell'Erba (2018a,b).

13.3 Results

In this section we briefly show some of the more significant results obtained applying this software, in previous works (Battista et al, 2016; dell'Erba, 2018a,b) where different strain of the leaders, with different choices, have been investigated. Some more complex samples behavior, like ASTM, the respect of Saint Venant principle have also been described; moreover, we are looking for the limits of the tool, so we searched and found some not satisfactory results that will be discussed in this paper.

13.3.1 Case a) Tensile Test

Consider a square shape specimen subjected to pull and release in tensile test. The sample is subject to strain from right side (left side is clamped) with constant velocity in x direction (speed is 0.6 unit length each step time); the specimen is represented by a square lattice 10×10 unit. After a while the pull is stopped and the leaders allow to return to the original configuration (this has the meaning that we have changed category of the leaders and now they are followers) by attraction from the other points. The rule, driving follower's motion is barycentre. Therefore each point try to reach the barycentre of its neighbors (Eq. (13.1)); coordination number of the lattice determine the neighbors; so far after the first time step the leader's motion determine a movement of the first layer of neighbors that propagates during time steps to the other particles. Each time step a larger shell of points is involved in the whole displacement, up to regards all the lattice points. To describe second gradient (Battista et al, 2016; dell'Erba, 2018a,b) we have to consider also the neighbors of the first neighbors. In Figure 13.5, we show the lattice configuration in different time; $PE1$ contour plot is on the right of the picture. The leaders are presented as red points while the followers are in blue color. The frame is in orange color. From the plot of Fig. 13.5, we could outline as the x displacement of the points is not depending on the y coordinate as first impression; however, the $PE1$ picture advises as of a light convexity of the contours (second picture of Fig. 13.5) showing as this is not true.

In fact, a better examination of the point's movements shows as, close to the frame, the displacements, have a lower value with respect to what happen in the central points of the lattice. This can be understood as an edge effect. If we consider points on a vertical line those that are closer to the frame experiment the neighbors influence with a little delay. This because the frame and of the followers have different rule to determine their displacement. Therefore, they see a different situation with

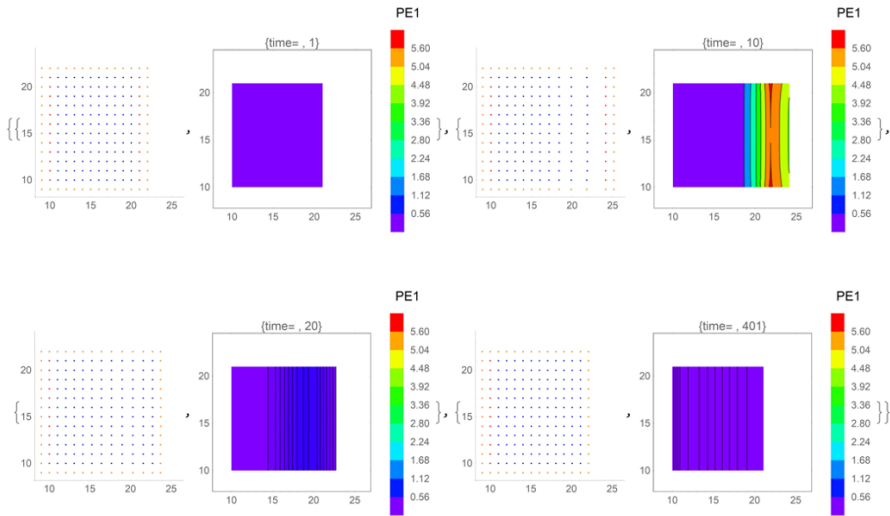


Fig. 13.5 Configuration of the lattice over different time (1,10, 20 and 401) and $PE1$ contour plot.

respect to a point close to the centre of the line. We can also note that the maximum values of $PE1$ (red area): it is one line on its left because, in this example, some neighbors of the leaders belong to the frame and are always close to them, owing to the frame rule. The tool is modular and very adaptable. So if we are intentioned to avoid this convexity effect we can use a different frame or mirroring the followers with the effect to simulate an infinite sample. Moreover, noted as at $t = 401$ the lattice is still not completely back to the initial configuration because asymptotic nature of the relaxation process. If we consider a central point of the lattice (i.e. sixth column, seventh row, points are numbered from left to right and from bottom to up) that we can numbered as point $j = 67$ we note as the value of the $PE1$ increases when points are pulled; there is a time delay because of the need of a propagation time of the shell, as can be noted from Figure 13.6; the $PE1$ decrease when the leaders change category and become followers. Now they are only subjected to the rules toward an equilibrium position obtained by barycentre. Changing point the shape of the curve is not changed but can be more or less flared. In Figure 13.7 and Figure 13.8 the time evolution of the x coordinates of the point $j = 67$ (centre of the lattice) and of another point, close to the leaders, ($j = 115$) are shown. Also, in this picture we can recognize the coordinate x increases linearly (velocity is constant), after a delay (but less for $j = 115$), because of the need of a propagation time; later it decrease to back to the original position.

A light modification of the barycentre rule can easily generate instabilities and oscillations in the lattice; for example, if we add to Eq. (13.1) a little feedback term, proportional to the difference between actual and initial position, we can overshoot the old equilibrium position. The obtained result is showed in Figure 13.9 and Figure

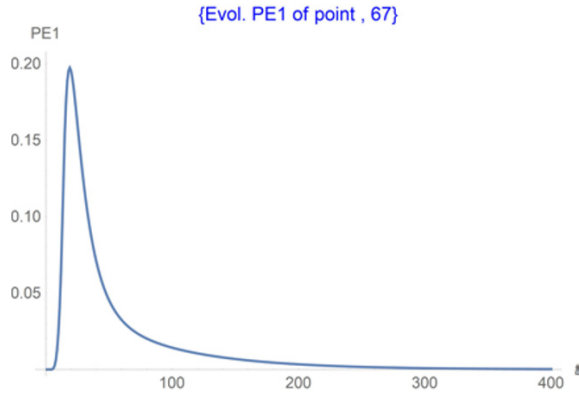


Fig. 13.6 $PE1$ of the central point's $j = 67$ versus time.

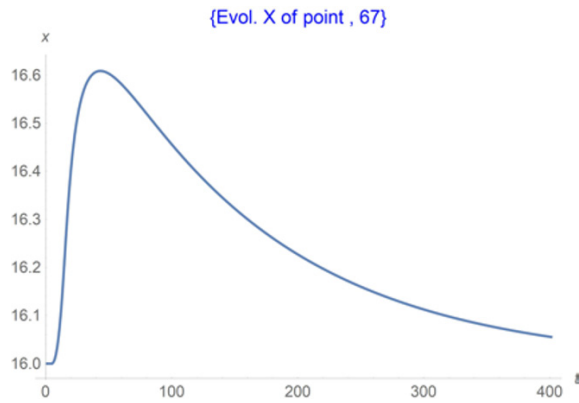


Fig. 13.7 X Evolution of the point $j = 67$ versus time.

13.10 (we used different feedback); note as also the reaction time is changed. Using higher feedback instabilities can be generated (see Figure 13.11).

13.3.2 Case b) Shear Test with Poisson Effect

An interesting case, always using a square lattice, can be seen in Figure 13.12 where the final configuration is shown after a shear test. Here we have used a rule for the follower making use of “mixed coordinate”, which means the y coordinate is dependent on the evolution of the x coordinate. This allows us to obtain lateral contraction, i.e. Poisson effect. The result of the shear test is a strange “window” flag. We have used a first and a second gradient model, changing the shell of neighbors. Differences are in a stiffer reaction in the second gradient case, owing to the larger numbers of neighbors involved in calculating the follower's positions. Because of the lateral contraction, the y coordinate of points above this axis decrease, with shear,

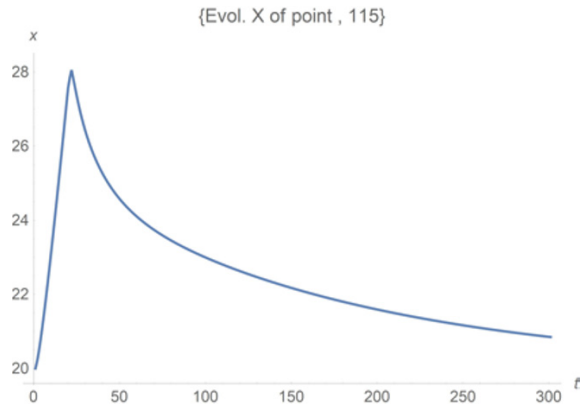


Fig. 13.8 X Evolution of the point $j = 115$ versus time.

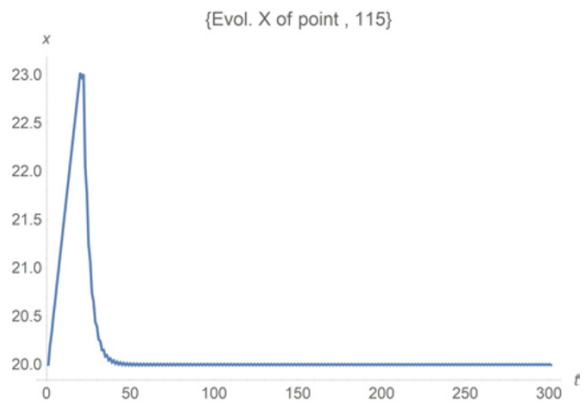


Fig. 13.9 X Evolution $j = 115$ versus time (modified rule with feedback).

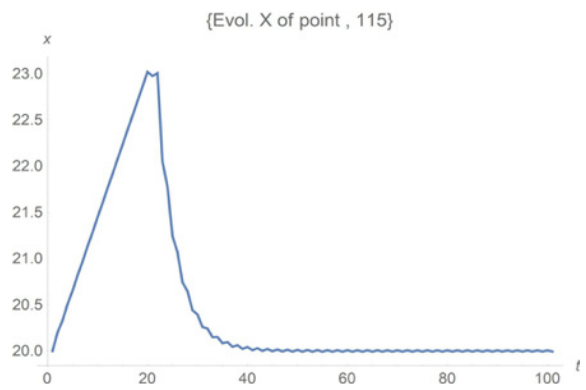


Fig. 13.10 X Evolution $j = 115$ versus time (modified rule with feedback).

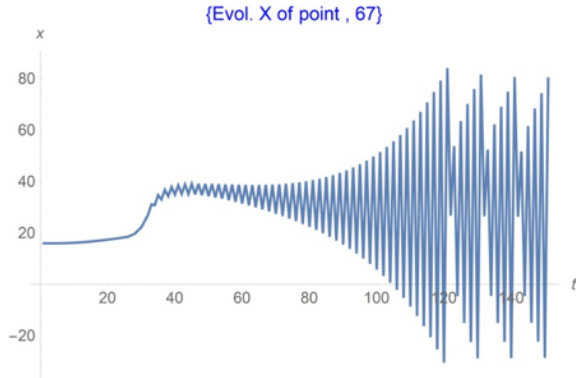


Fig. 13.11 X Evolution of point $j = 67$ versus time (modified rule with feedback).

while below they are increased. Note the delay reaction time, because the involved points have to be informed about the displacement of the leaders.

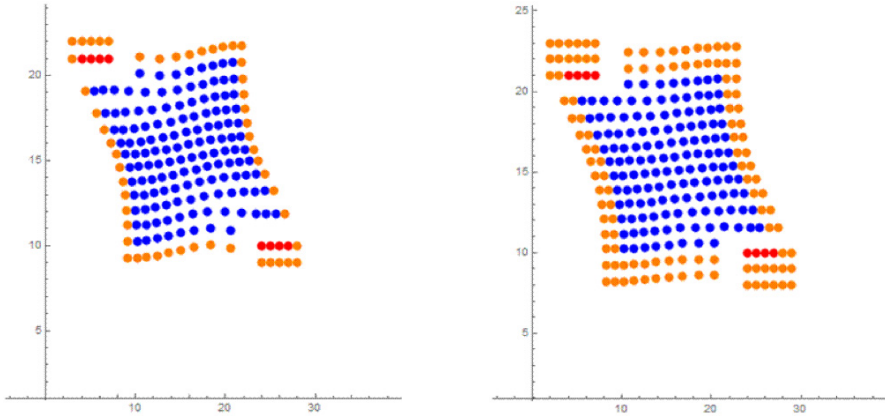


Fig. 13.12 Final configuration of the lattice with Poisson effect in shear test square lattice, first and second gradient case.

13.3.3 Case c) Fracture Test

For the next example we shall consider a square sample undergone a tensile test with fracture (Figure 13.13 just before fracture). Fracture distances are 6 units and speed is 0.5 units/step, for 150 steps long. When a distance between the points is larger than fracture distances the sample is broken and the followers go to equilibrium position; if no followers remain attached to the leaders (it depends on the distances, we shall see later in other cases) they return to their initial position. As explained

in a preceding work (Battista et al, 2016; dell'Erba, 2018a,b) the convexity, in the fracture mechanism, is related to the presence of the frame. Analysis of $PE1$ plot show as, before fracture, there are areas of strain, and consequently stress for ordinary materials, concentration. Higher strain areas are close to the leaders. The trend of the follower points is quite linear during traction but it becomes non linear when the followers remain alone and return back. This because the traction is imposed with constant speed while the reassembly of the points is driven by the follower's rule. Once again involving a larger number of neighbors lead to a stiffer behavior as can be seen in Figure 13.14 (second gradient case).

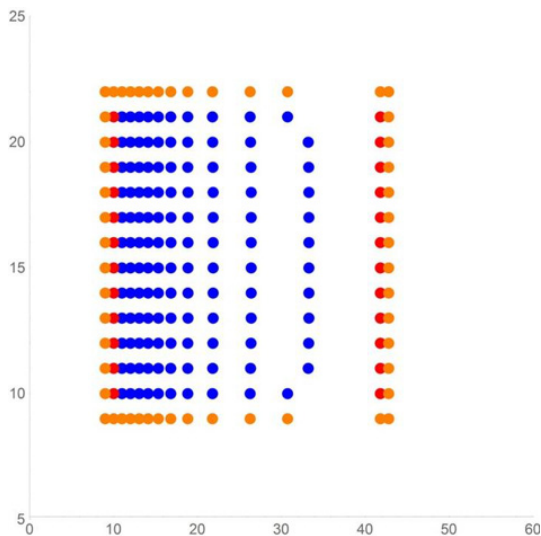


Fig. 13.13 Fracture test of square specimen square lattice.

13.3.4 Case d) The Importance of the Frame Rules

In the case of hexagonal lattice, we can choose two different rules for the frame, as can be seen from Figure 13.15. In the first case a frame point displacement is just the same of the corresponding follower. But in some case, like hexagonal lattice, we can decide there are more than one corresponding follower and choose the point frame displacement as the average value of them; in the case of Fig. 13.15 they are two.

This led to different final deformed configuration as can be outlined in Figure 13.16 and 13.17. The presence of a frame point in the middle leads the final configuration to a concavity. The absence of followers on the right side, once again is depending on the leader's speed.

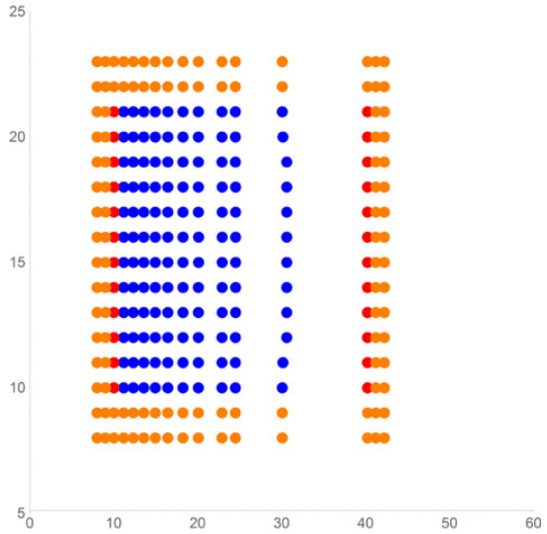


Fig. 13.14 Same as Figure 13.13 but second gradient

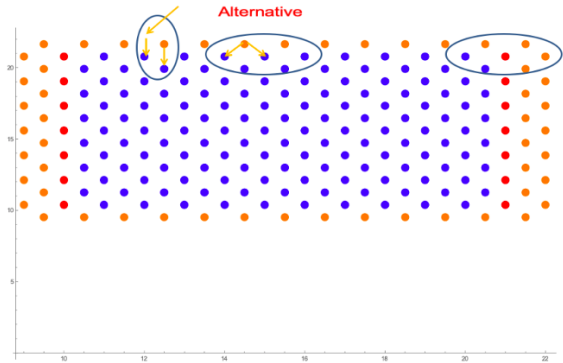


Fig. 13.15 Alternative choice for the frame rule displacement. In the first case each frame point is moving as a corresponding follower. In the second case as the average value of more followers assigned.

13.3.5 Case e) The Importance of the Lattice

Consider now an oblique lattice (Figure 13.18). Owing to the asymmetry (see look at the five red leaders on the right) of the leaders with respect to the frame a particular breakage fracture can be observed. In fact if we consider a symmetry axes in x direction we can note two leaders close to the frame in the upper level and only one close to the bottom. This leads to a fracture starting from the bottom where the attraction of the leaders is lower. It seems to rip a piece of paper. The fracture distance is 10 units and the speed is 0.4 unit/time step.

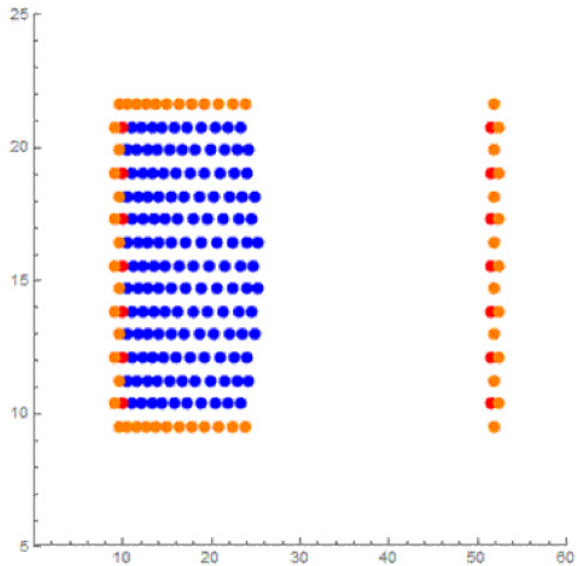


Fig. 13.16 Final configuration in fracture test hexagonal lattice.

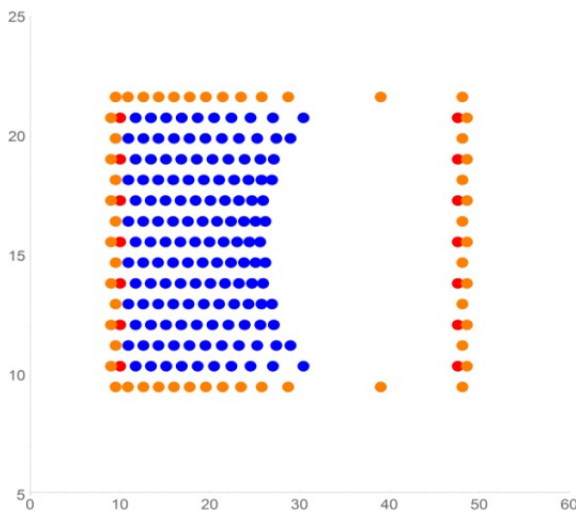


Fig. 13.17 Same as Figure 13.16 but with different frame rule.

13.3.6 Case f) Fracture the Importance of the Lattice and of the Neighbors

In this case, we use a rectangular centered lattice for tensile test but we reduce the neighbors' number, n_c , to five. This gives more mobility to the model leading to a more plastic behavior and increasing the number of the detached points; The fracture mechanism is quite different together as well as the final configuration (see Figure 13.19). This example shows, once again, that change in model parameters lead to

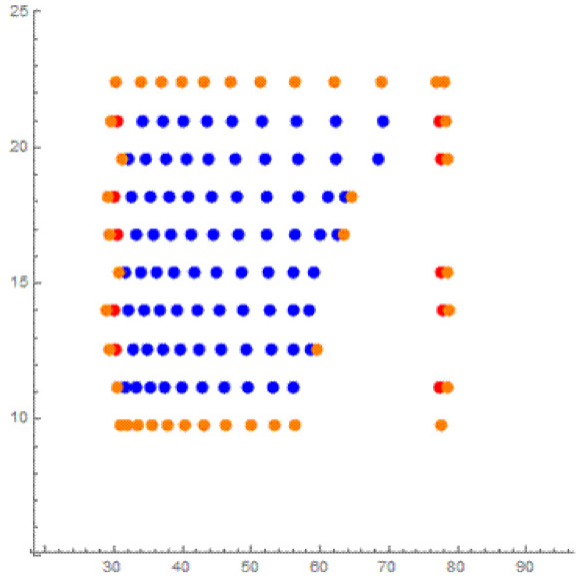


Fig. 13.18 Fracture in tensile test with oblique lattice.

different behaviors. The lower numbers of particles involved render the sample much more fluid, allowing detachment of a larger number of particles, as we can see on the right side of the pictures (see Figure 13.20).

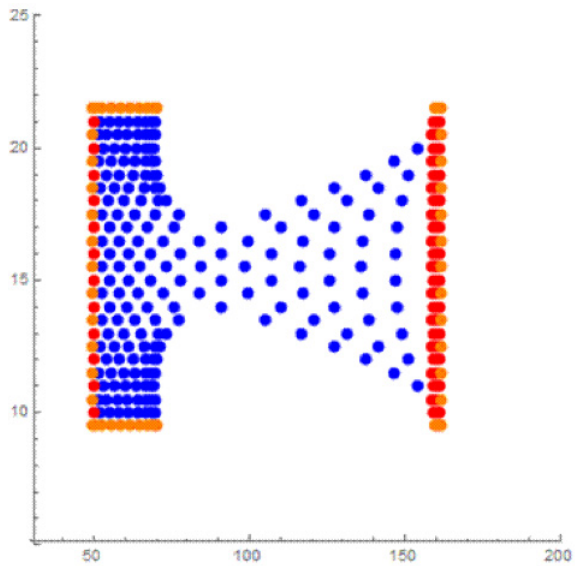


Fig. 13.19 Fracture on tensile test rectangular centered lattice $n_c=5$.

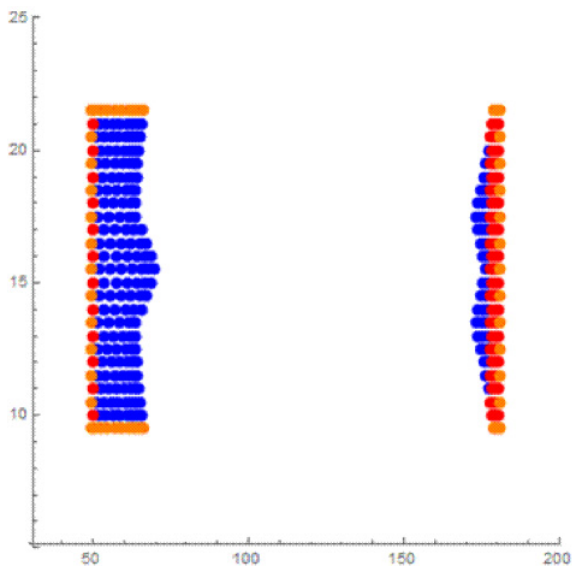


Fig. 13.20 Final configuration of Figure 13.19.

13.3.7 Case g) ASTM Test

In order to investigate sample behavior of more complex shape we consider specimen ASTM D638 standards for tensile tests. The specimen is clamped at both ends on a surface and pulled on one side, so, in this case, the leaders are many; the test speed is of 2.5 unit/step, in x positive direction, for 150 traction step e 2500 relaxation step. We shall consider tensile test with Poisson effect, change of the lattice and fracture; many other cases can be found in the references. In Figure 13.21 the sample before the test is shown; note the double set of frame points because we are considering 2° gradient case. A larger number of time steps is required for relaxation, owing to the larger number of points used to describe the specimen; this does not mean a longer relaxation time, because unit time is arbitrary, only because the influence of the displacement propagates at two shell (second gradient case) each time step we need many steps to involve the whole sample. In Figure 13.22 the elongated sample (first gradient case) while in Figure 13.23 the second gradient case. Once again the second gradient case seems to be stiffer with respect of the first gradient. It should be noted that the sample does not reach a symmetric final configuration as we can expect (see last figure); we have also wait for 10000 time relaxation steps without modification. On the contrary if we use a rectangular shape sample it does (the points are equally spaced). There is no physical reason for this, our opinion is that this effect is linked to the particular equilibrium condition generate by the geometry. We are working on this and on higher gradient computations. In the two cases we are considering the Poisson effect it is possible to see lateral contraction. It seems the points cluster to create islands but this effect must be investigated better. In case of second gradient interaction this does not occur, as can be seen in Figure 13.23. The

fracture test (see Figures 13.24, 13.25, and 13.26) is considered for the rectangular centered lattice. Distance fracture is 11 units and the speed was 0.6step/unit time. As can be seen, the fracture occurs close to the top of the profile and not in the central area. Studies, in progress, show as the fracture zone can be moved by varying working conditions. We can render the fracture more or less brittle changing the model parameters like neighbors' number, type of lattice, speed etc. As example in second gradient the same sample has a more brittle behavior; or if I use a speed of 2.5 step/unit time in the same condition I will get no followers on the right side of the fractured sample. We can observe differences in the internal distribution on the points and in the convexity of the propagation front of the deformation i.e. see the convexity of the points owing to the different lattice used compared to the preceding case. It must be underlined as, changing the model parameters, the deformation and fracture behavior can be expressed also by results like Figures 13.25 and 13.26 that does not sound very familiar for simple elastic materials. Once again, we have the need to connect the constitutive parameters of the material with the parameters of our model to obtain significative behavior in according with the material characteristic.

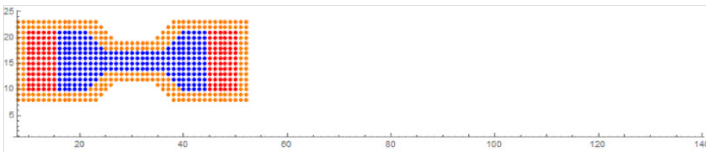


Fig. 13.21 ASTM sample 2nd gradient before tensile tests.

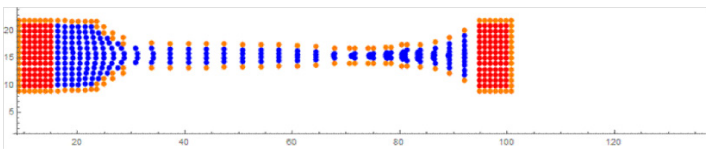


Fig. 13.22 ASTM sample Poisson effect square lattice.

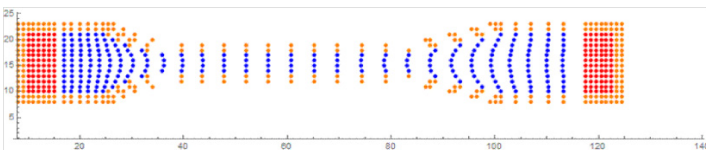


Fig. 13.23 ASTM sample Poisson effect square lattice 2nd gradient.

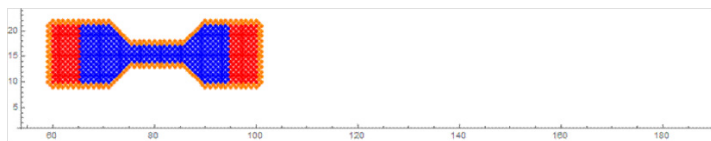


Fig. 13.24 ASTM rectangular centered lattice before tensile test.

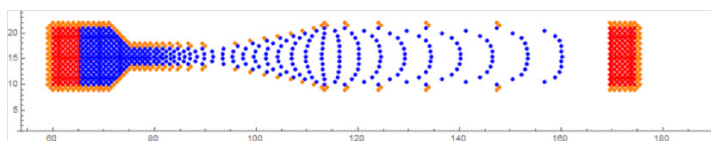


Fig. 13.25 AASTM rectangular centered lattice after tensile test.

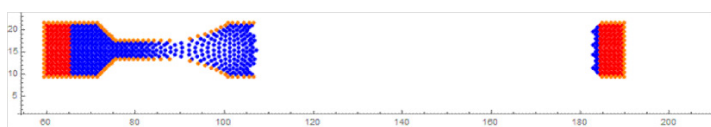


Fig. 13.26 ASTM square lattice fracture.

13.3.8 The Beam

13.3.8.1 Case h) Short Beam

In this paragraph we want to investigate the behavior of our tool applied to a bi dimensional bending beam loaded at one end and compare the results with that obtained solving, numerically, ordinary differential equations. We consider a bi-dimensional elastic short square beam (X and Y coordinate range is from 10 to 21 in the not deformed configuration) with materials parameters $Y = 1000 \text{ N/m}^2$ and $\nu = 0.33$, where Y is the Young modulus, ν the Poisson coefficient; this value is close to that of a medium molecular weight polypropylene (Avella et al, 1996, 1995, 1993). The load is on the right boundary (Neumann condition) and on the left there are no displacements (Dirichlet conditions).

$$\frac{Y}{2(1 + \nu)} \nabla^2 \mathbf{u} + \frac{Y}{2(1 - \nu)} \left(\frac{\partial}{\partial x} \mathbf{u} + \frac{\partial}{\partial y} \mathbf{v} \right) = 0 \tag{13.7}$$

$$\frac{Y}{2(1 + \nu)} \nabla^2 \mathbf{v} + \frac{Y}{2(1 - \nu)} \left(\frac{\partial}{\partial x} \mathbf{u} + \frac{\partial}{\partial y} \mathbf{v} \right) = 0 \tag{13.8}$$

$\mathbf{u}(x, y)$ and $\mathbf{v}(x, y)$ are the displacements function. We choice as boundary conditions 50 Pa load as shear stress on the beam (Neumann condition for $x = 21$) and $\mathbf{u}(10, y) = \mathbf{v}(10, y) = 0$ as Dirichlet condition. The equations can be solved numerically discretizing the beam using a 10×10 square lattice; the found solution is shown in Figure 13.27 together with the Von Mises plot in Figure 13.28; in red color

is plotted the obtained deformed mesh. The equations have been solved by Mathematica software carefully, owing the presence of Neumann boundary conditions, to prevent early evaluation. Mesh is regular.

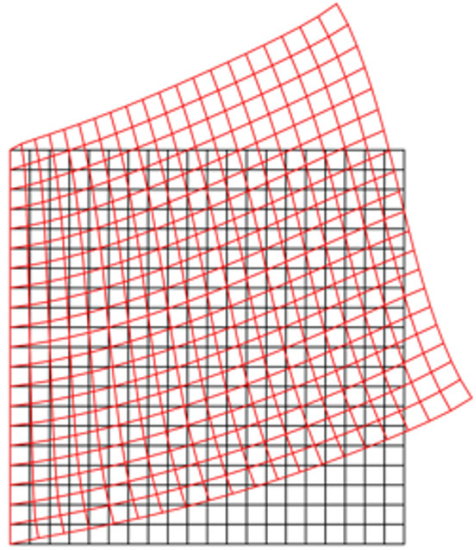


Fig. 13.27 FEM solutions of bi-dimensional square beam, under shear stress.

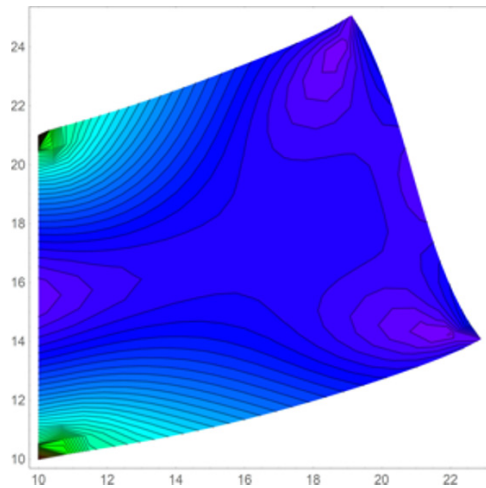


Fig. 13.28 Von Mises plot of FEM solutions.

To apply our tool, we have to give the leaders movements, choice the algorithm (i.e. the lattice, the interaction rules of the followers etc.) and to compute the strain once the followers have readjusted in the equilibrium position, when a sufficiently

long time. The leaders we have chosen are the right and left points of the beam, therefore we assign the displacements of them as the solution obtained from the FEM equations. Later we look at the arrangement of the other points to see the final shape of the beam. The important thing to point out is that we still have no criteria on the choice of the tool, like lattice, interaction law between the followers etc... As first attempt we use a square lattice with no weight in computing the coordinates of the followers. In Figure 13.29 the resulting configuration is shown, together with the FEM solution represented by red points; in Figure 13.30 is plotted the corresponding Von Mises plot. Left and right points of the beam are overlapped because they are the leaders and we have just imposed their displacement as the FEM solution of the deformed beam. It should be noted as external configuration of the beam is similar but the internal displacement of the points, i.e. the strain, is quite different; this can be seen better comparing the Von Mises plot of Figure 13.28 and Figure 13.30. Changing the tool's parameters can lead to different configuration, and of course to different strain of the beam, as shown in a paper in press; almost none of them are satisfactory.

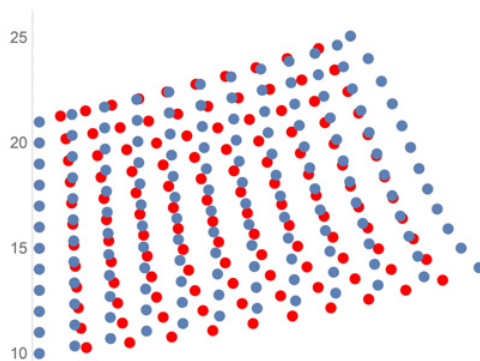


Fig. 13.29 Beam deformation.

Second gradient case has showed no appreciable differences; we have tried to give quantitative measurements of the discrepancies with the FEM solutions, using the average value of the sum of the square differences between coordinates, in many cases. Nobody emerges as the best match so we can conclude that the beam deformation can be sometimes very similar to the FEM solution but the Von Mises stress plot is quite always unsatisfactory. This point needs to be study again to a better understanding of the physic behind the tool and what should be drive our choices in the tool to describe material continuum. We have to remember that the materials parameters Y and ν does not appear explicitly in our algorithm but they are hidden into the interaction relationship between the followers, the neighbors and the choice of the lattice. We do not know how to select our choices to match the well-known problem and we hope to do this in a next paper. Changing the parameters of our tool we obtain different results nobody of them perfectly coincident with classical solution but, owing to the flexibility of the tool, we believe it exist a parameters combination to fit the deformed beam; but this is meaningless until we do not understand how to

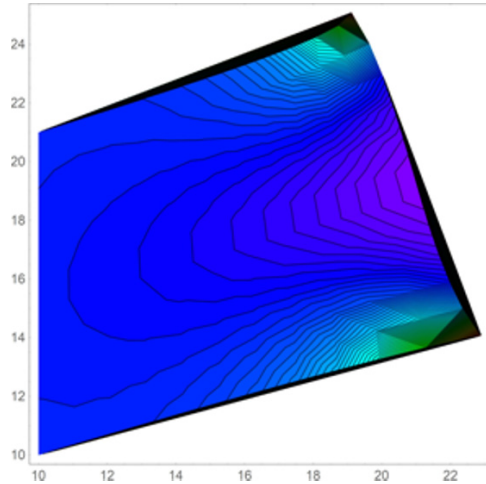


Fig. 13.30 Corresponding Von Mises Plot.

choose the parameters.. The reason of this lie in the fact that, up to now, we do not start from the constitutive equations of the materials leading to the rules governing points displacement. We have to work on how to connect the rules of our model with classical physical proprieties of the material.

13.3.8.2 Case i) Long Beam

Also in the case of longer beam we can try many combination of the parameters tool to fit the deflection of our beam but it is useless: we need to connect the constitutive parameters with the tool. If we increase the ratio length/width of our beam from 1 to 5 the results are still different (see Figure 13.31, 13.32, 13.33, and 13.34). As can be seen the results do not behave as we expected and show a wide range of possibilities in which we could choose. Similar results were obtained if we increase the ratio length/width up to 10 or more. In spite of the fact that external shape of the beam can sometimes be acceptable, once again we can note as the displacement of the internal particles is quite different from the FEM solutions; it is clear that the differences are sometimes noticeable, as outlined by the Von Mises' graphs. So far we stop trial and errors to think about how to reach a better understanding of the physical process behind the tool. So far we have a theory to drive the numerous choices we have to do using the tool to describe material continuum deformation but we need further studies on this differences that are left to future works.

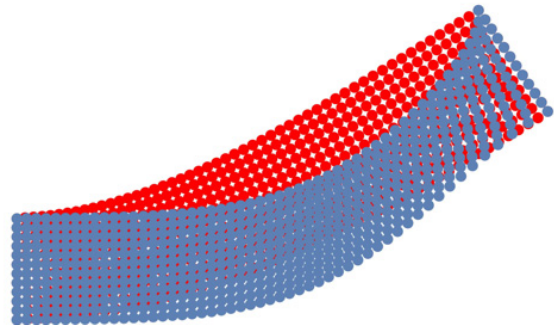


Fig. 13.31 Square lattice.

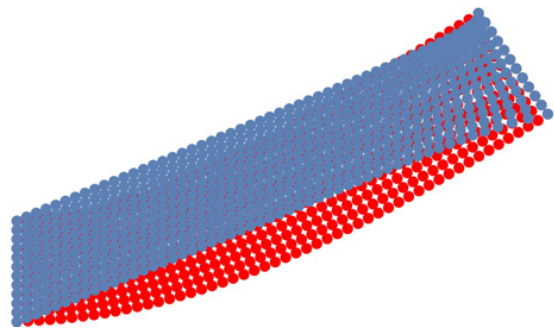


Fig. 13.32 Square lattice reduced neighbors numbers.

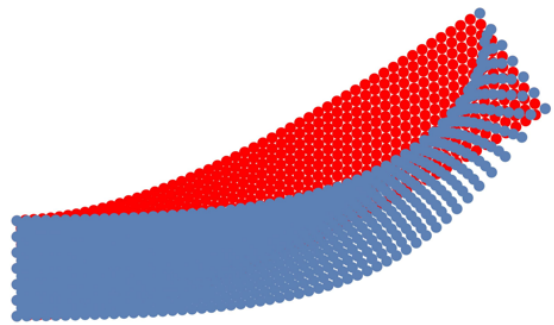


Fig. 13.33 Hexagonal lattice.

13.4 Future Work and Conclusion

How to relate materials parameters with the choices we do in our tool is one of the most important topics to be developed, to make a connection with the methods we normally use in Continuum Mechanics. At this point we do not know how direct our tool's choices to describe a particular material continuum, characterized by a certain set of constitutive equations; In the beam deformation we have used Young's modulus

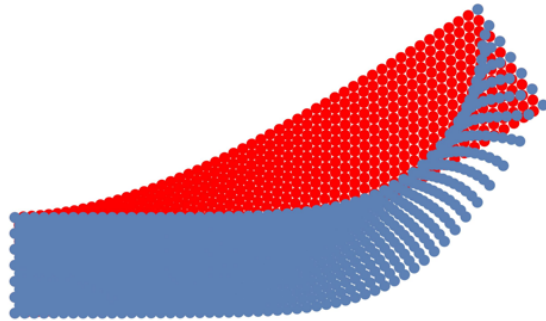


Fig. 13.34 Hexagonal lattice reduced neighbors numbers.

and Poisson's coefficient assigned but there is no relationship to connect them with the parameters of our model. This is the reason of the discrepancy in the resulting deformation compared to FEM solution. To generalize in 3D the tool is quite easy but optimization of the code, to keep low the computation time (order of seconds by using a normal PC Desktop), must be still investigated. We are also relaxing the hypothesis that the neighbors are always the same; this allows as describing liquid and gas. This approach leads one calculation step more because it needs to compute the neighbors, which in this case are defined as the particles belong to a certain volume, at each time step. We are also introducing an interesting feature: constrained on the particle's motion. This could be useful describing structured object like pantograph (Misra et al, 2018; Boutin et al, 2017; Giorgio et al, 2018; Spagnuolo et al, 2017; De Angelo et al, 2019; Andreaus et al, 2018; Turco et al, 2016a; Turco and Rizzi, 2016; dell'Isola et al, 2019a). It can be described as a set of beams with constrained point in the pivot; in the Hencky vision can be conceived as a set of point interconnected by springs. Some more developments, concerning different fracture mechanism, different frame to avoid edge effects, other interactions rules and adaptive lattice are in progress. A cellular automaton seems have good chance to enhance our work. A cellular automata is a simple computational mechanism; as example, it changes the colour of each cell of a lattice based on a transformation rule look at the color of neighbors's cells. Some trials to use them in Mechanics have been done (Dong et al, 2013; Konovalenko et al, 2010). One of the principal limits of Cellular automata system is regarding as they do not evolve sufficiently; therefore they reach, often quickly, a limited asymptote in their order of complexity. We are working on how to apply to our tool because the principles are very similar. Working on flocking rules that are governing how underwater robots swarm reach and maintain an assigned geometric configuration, we found a profitably use in describing deformation of bi-dimensional continuum medium. We have discussed a software tool, just presented in previous works, able to describe strain deformation of a continuum medium in a plausible way taking in account complex physical effects. The tool is based on Position Based Dynamic. Differently from the PBD methods used in computer graphics, we still do not ask for the knowledge of the velocity and do not introduce any kind of forces to take in account mechanical effects. The strain is imposed by assigning the motion of some

particles called leaders; the other particles called followers are moving according to some rules, derived from our experience in robots swarm. Like in a bird swarm the motion of the followers is determined using the position of their neighbors. So far the deformed configuration is computed not using Newton law but only by the relative positions between the particles of the lattice describing medium and by the rules describing how a particle must be positioned with respect to its neighbors. One of the principal advantages is in the saving machine time for computing. Practically we are computing the action of a transformation operator between two matrices representing the two configurations; the job can be easily parallelized between the video card GPU cores, to save computational cost with respect to solve FEMs. The results still are at a preliminary stage, though they are interesting. We have used a frame to take in account edge effects; fracture mechanism has been described using a threshold effect. We showed that changing in parameters like, lattice, numbers of neighbors, fracture distance, interaction rules, allows us to describe very different behavior. Considerations on pseudo energy have been introduced to describe different deformation regimes like elastic and plastic. This led to a better understanding of the process, preliminary to introduce a potential interactions, depending on the distance between the particles, which could be able to give back the well known physical behavior. Therefore, we are proposing a tool that can be considered just a graphic representation of plausible deformation behavior. This because, actually, we just imitate a known behavior adjusting the algorithm parameters until we reach something we know. Results of previous works have showed they have good similarity according with the predictions of standard FEM simulations; this is true also in fracture case. In this paper we have outlined some discrepancies with respect to FEM solution like for a beam under shear stress. We have collected some success showing plausible deformation in different conditions but when we consider a beam under loading the need to connect constitutive equations with the parameters of our tool emerges powerfully. However the tool has demonstrated enough flexibility to give chances that, if we will be able to connect it with the constitutive parameters, it can be useful to describe the large number of behavior we find in different materials, inclusive of interesting complex biological tissues.

Acknowledgements The author is grateful to Prof. Victor A. Eremeyev, Prof. Pierre Seppecher and Prof. Francesco dell'Isola for the fruitful discussion on this topic we had in MEMOCS Workshop on Models of Complex Materials and Systems in Arpino.

References

- Abali BE, Müller WH, Eremeyev VA (2015) Strain gradient elasticity with geometric nonlinearities and its computational evaluation. *Mechanics of Advanced Materials and Modern Processes* 1(1)
- Abali BE, Müller WH, dell'Isola F (2017) Theory and computation of higher gradient elasticity theories based on action principles. *Archive of Applied Mechanics* 87(9):1495–1510
- Alibert JJ, Seppecher P, dell'Isola F (2003) Truss modular beams with deformation energy depending on higher displacement gradients. *Mathematics and Mechanics of Solids* 8(1):51–73

- Altenbach H, Eremeyev VA (2013) Generalized continua from the theory to engineering applications. CISM International Centre for Mechanical Sciences 541
- Altenbach H, Eremeyev VA, Lebedev LP, Rendón LA (2009a) Acceleration waves and ellipticity in thermoelastic micropolar media. *Archive of Applied Mechanics* 80(3):217–227
- Altenbach J, Altenbach H, Eremeyev VA (2009b) On generalized cosserat-type theories of plates and shells: a short review and bibliography. *Archive of Applied Mechanics* 80(1):73–92
- Andreas U, dell'Isola F, Giorgio I, Placidi L, Lekszycki T, Rizzi NL (2016) Numerical simulations of classical problems in two-dimensional (non) linear second gradient elasticity. *International Journal of Engineering Science* 108:34 – 50
- Andreas U, Spagnuolo M, Lekszycki T, Eugster SR (2018) A Ritz approach for the static analysis of planar pantographic structures modeled with nonlinear Euler–Bernoulli beams. *Continuum Mechanics and Thermodynamics* 30(5):1103–1123
- Avella M, dell'Erba R, Martuscelli E, Ragosta G (1993) Influence of molecular mass, thermal treatment and nucleating agent on structure and fracture toughness of isotactic polypropylene. *Polymer* 34(14):2951 – 2960
- Avella M, Dorazio L, Martuscelli E (1995) Influence of molecular-weight and molecular-weight distribution on crystallization and thermal-behavior of isotactic polypropylene. *POLYMER NETWORKS & BLENDS* 5(1):47–54
- Avella M, Dell'Erba R, Martuscelli E (1996) Fiber reinforced polypropylene: Influence of ipp molecular weight on morphology, crystallization, and thermal and mechanical properties. *Polymer Composites* 17(2):288–299
- Barchiesi E, dell'Isola F, Laudato M, Placidi L, Seppecher P (2018a) A 1D continuum model for beams with pantographic microstructure: Asymptotic micro-macro identification and numerical results. *Advances in Mechanics of Microstructured Media and Structures* pp 43–74
- Barchiesi E, Spagnuolo M, Placidi L (2018b) Mechanical metamaterials: a state of the art. *Mathematics and Mechanics of Solids* 24(1):212–234
- Battista A, Rosa L, dell'Erba R, Greco L (2016) Numerical investigation of a particle system compared with first and second gradient continua: Deformation and fracture phenomena*. *Mathematics and Mechanics of Solids* 22(11):2120–2134
- Bender J, Müller M, Macklin M (2015) Position-based simulation methods in computer graphics. In: *Eurographics (tutorials)*
- Boutin C, dell'Isola F, Giorgio I, Placidi L (2017) Linear pantographic sheets: Asymptotic micro-macro models identification. *Mathematics and Mechanics of Complex Systems* 5(2):127–162
- Bückmann T, Stenger N, Kadic M, Kaschke J, Frölich A, Kennerknecht T, Eberl C, Thiel M, Wegener M (2012) Tailored 3D mechanical metamaterials made by dip-in direct-laser-writing optical lithography. *Advanced Materials* 24(20):2710–2714
- Carcattera A, dell'Isola F, Esposito R, Pulvirenti M (2015) Macroscopic description of microscopically strongly inhomogenous systems: A mathematical basis for the synthesis of higher gradients metamaterials. *Archive for Rational Mechanics and Analysis* 218(3):1239–1262
- Cuomo M, dell'Isola F, Greco L, Rizzi N (2017) First versus second gradient energies for planar sheets with two families of inextensible fibres: Investigation on deformation boundary layers, discontinuities and geometrical instabilities. *Composites Part B: Engineering* 115:423 – 448
- De Angelo M, Spagnuolo M, D'Annibale F, Pfaff A, Hoschke K, Misra A, Dupuy C, Peyre P, Dirrenberger J, Pawlikowski M (2019) The macroscopic behavior of pantographic sheets depends mainly on their microstructure: experimental evidence and qualitative analysis of damage in metallic specimens. *Continuum Mechanics and Thermodynamics* 31(4):1181–1203
- dell'Erba R (2015) Determination of spatial configuration of an underwater swarm with minimum data. *International Journal of Advanced Robotic Systems* 12(7):97
- dell'Erba R (2018a) Position-based dynamic of a particle system: a configurable algorithm to describe complex behaviour of continuum material starting from swarm robotics. *Continuum Mechanics and Thermodynamics* 30(5):1069–1090
- dell'Erba R (2018b) Swarm robotics and complex behaviour of continuum material. *Continuum Mechanics and Thermodynamics* 31(4):989–1014

- dell'Isola F, Gavriluyk S (2012) Variational models and methods in solid and fluid mechanics, vol 535. Springer Science & Business Media
- dell'Isola F, Placidi L (2011) Variational principles are a powerful tool also for formulating field theories. CISM International Centre for Mechanical Sciences pp 1–15
- dell'Isola F, Auffray N, Eremeyev VA, Madeo A, Placidi L, Rosi G (2014) Least action principle for second gradient continua and capillary fluids: A Lagrangian approach following Piola's point of view. *The complete works of Gabrio Piola: Volume I* pp 606–694
- dell'Isola F, Andreus U, Placidi L (2015a) At the origins and in the vanguard of peridynamics, non-local and higher-gradient continuum mechanics: an underestimated and still topical contribution of Gabrio Piola. *Mathematics and Mechanics of Solids* 20(8):887–928
- dell'Isola F, Madeo A, Seppecher P (2015b) Cauchy tetrahedron argument applied to higher contact interactions. *Archive for Rational Mechanics and Analysis* 219(3):1305–1341
- dell'Isola F, Bucci S, Battista A (2016a) Against the fragmentation of knowledge: The power of multidisciplinary research for the design of metamaterials. *Advanced Methods of Continuum Mechanics for Materials and Structures* pp 523–545
- dell'Isola F, Della Corte A, Greco L, Luongo A (2016b) Plane bias extension test for a continuum with two inextensible families of fibers: A variational treatment with lagrange multipliers and a perturbation solution. *International Journal of Solids and Structures* 81:1 – 12
- dell'Isola F, Seppecher P, et al (2019a) Advances in pantographic structures: design, manufacturing, models, experiments and image analyses. *Continuum Mechanics and Thermodynamics* 31(4):1231–1282
- dell'Isola F, Seppecher P, et al (2019b) Pantographic metamaterials: an example of mathematically driven design and of its technological challenges. *Continuum Mechanics and Thermodynamics* 31(4):851–884
- Dong YF, Zhang GC, Xu AG, Gan YB (2013) Cellular automata model for elastic solid material. *Communications in Theoretical Physics* 59(1):59–67
- Eremeyev VA, Lebedev LP, Altenbach H (2012) *Foundations of micropolar mechanics*. Springer Science & Business Media
- Forest S, Cordero N, Busso E (2011) First vs. second gradient of strain theory for capillarity effects in an elastic fluid at small length scales. *Computational Materials Science* 50(4):1299 – 1304
- Franciosi P, Lebail H (2004) Anisotropy features of phase and particle spatial pair distributions in various matrix/inclusions structures. *Acta Materialia* 52(10):3161 – 3172
- Giorgio I, Harrison P, dell'Isola F, Alsayednoor J, Turco E (2018) Wrinkling in engineering fabrics: a comparison between two different comprehensive modelling approaches. *Proceedings of the Royal Society A: Mathematical, Physical and Engineering Sciences* 474(2216):20180.063
- Javili A, dell'Isola F, Steinmann P (2013) Geometrically nonlinear higher-gradient elasticity with energetic boundaries. *Journal of the Mechanics and Physics of Solids* 61(12):2381 – 2401
- Konovalenko I, Smolin A, Psakhie S (2010) Multilevel simulation of deformation and fracture of brittle porous materials in the method of movable cellular automata. *Physical Mesomechanics* 13(1):47 – 53
- Lanczos C (2012) *The variational principles of mechanics*. Courier Corporation
- Milton G, Seppecher P (2012) A metamaterial having a frequency dependent elasticity tensor and a zero effective mass density. *physica status solidi (b)* 249(7):1412–1414
- Misra A, Lekszycki T, Giorgio I, Ganzosch G, Müller WH, Dell'Isola F (2018) Pantographic metamaterials show atypical Poynnting effect reversal. *Mechanics Research Communications* 89:6–10
- Moriconi C, dell'Erba R (2012) The localization problem for HARNESS: a multipurpose robotic swarm. In: *SENSORCOMM 2012, The Sixth International Conference on Sensor Technologies and Applications*, pp 327–333
- Pietraszkiewicz W, Eremeyev V (2009) On natural strain measures of the non-linear micropolar continuum. *International Journal of Solids and Structures* 46(3):774 – 787
- Placidi L (2014) A variational approach for a nonlinear 1-dimensional second gradient continuum damage model. *Continuum Mechanics and Thermodynamics* 27(4-5):623–638

- Placidi L, dell'Isola F, Ianiro N, Sciarra G (2008) Variational formulation of pre-stressed solid–fluid mixture theory, with an application to wave phenomena. *European Journal of Mechanics - A/Solids* 27(4):582 – 606
- Placidi L, Greve R, Seddik H, Faria SH (2009) Continuum-mechanical, anisotropic flow model for polar ice masses, based on an anisotropic flow enhancement factor. *Continuum Mechanics and Thermodynamics* 22(3):221–237
- Placidi L, Greco L, Bucci S, Turco E, Rizzi NL (2016) A second gradient formulation for a 2d fabric sheet with inextensible fibres. *Zeitschrift für angewandte Mathematik und Physik* 67(5)
- Placidi L, Rosi G, Barchiesi E (2019) Analytical solutions of 2-dimensional second gradient linear elasticity for continua with cubic-d4 microstructure. *New Achievements in Continuum Mechanics and Thermodynamics* pp 383–401
- Rosi G, Placidi L, dell'Isola F (2017) “fast” and “slow” pressure waves electrically induced by nonlinear coupling in biot-type porous medium saturated by a nematic liquid crystal. *Zeitschrift für angewandte Mathematik und Physik* 68(2)
- Seddik H, Greve R, Placidi L, Hamann I, Gagliardini O (2008) Application of a continuum-mechanical model for the flow of anisotropic polar ice to the edml core, antarctica. *Journal of Glaciology* 54(187):631–642
- Sepecher P, Alibert JJ, dell'Isola F (2011) Linear elastic trusses leading to continua with exotic mechanical interactions. *Journal of Physics: Conference Series* 319:012,018
- Spagnuolo M, Barcz K, Pfaff A, dell'Isola F, Franciosi P (2017) Qualitative pivot damage analysis in aluminum printed pantographic sheets: Numerics and experiments. *Mechanics Research Communications* 83:47 – 52
- Turco E (2019) How the properties of pantographic elementary lattices determine the properties of pantographic metamaterials. *New Achievements in Continuum Mechanics and Thermodynamics* pp 489–506
- Turco E, Rizzi NL (2016) Pantographic structures presenting statistically distributed defects: Numerical investigations of the effects on deformation fields. *Mechanics Research Communications* 77:65 – 69
- Turco E, Barcz K, Pawlikowski M, Rizzi NL (2016a) Non-standard coupled extensional and bending bias tests for planar pantographic lattices. part i: numerical simulations. *Zeitschrift für angewandte Mathematik und Physik* 67(5)
- Turco E, dell'Isola F, Cazzani A, Rizzi NL (2016b) Hencky-type discrete model for pantographic structures: numerical comparison with second gradient continuum models. *Zeitschrift für angewandte Mathematik und Physik* 67(4)
- Turco E, Giorgio I, Misra A, dell'Isola F (2017a) King post truss as a motif for internal structure of (meta)material with controlled elastic properties. *Royal Society Open Science* 4(10):171,153
- Turco E, Golaszewski M, Giorgio I, Placidi L (2017b) Can a Hencky-type model predict the mechanical behaviour of pantographic lattices? *Mathematical Modelling in Solid Mechanics* pp 285–311
- Umetani N, Schmidt R, Stam J (2014) Position-based elastic rods. In: *ACM SIGGRAPH 2014 Talks*, pp 1–1



Chapter 14

Characterization of Polystyrene under Shear Deformation Using Molecular Dynamics

Maximilian Ries, Paul Steinmann, and Sebastian Pfaller

Abstract Nano-filled polymers are becoming more and more important to meet the continuously growing requirements of modern engineering problems. The investigation of these composite materials at the molecular level, however, is either prohibitively expensive or just impossible. Multiscale approaches offer an elegant way to analyze such nanocomposites by significantly reducing computational costs compared to fully molecular simulations. When coupling different time and length scales, however, it is in particular important to ensure that the same material description is applied at each level of resolution. The Capriccio method (Pfaller et al, 2012, 2013), for instance, couples a particle domain modeled with molecular dynamics (MD) with a finite element based continuum description and has been used i.a. to investigate the effects of nano-sized silica additives embedded in atactic polystyrene (PS), cf. Pfaller et al (2016); Liu et al (2017). However, a simple hyperelastic constitutive law is used so far for the continuum description which is not capable to fully match the behavior of the particle domain. To overcome this issue and to enable further optimization of the coupling scheme, the material model used for the continuum should be derived directly from pure MD simulations under thermodynamic conditions identical to those used by the Capriccio method. To this end, we analyze the material response of pure PS under uniaxial deformation using strain-controlled MD simulations (Ries et al, 2019). Analogously, we perform simulations under pure shear deformation to obtain a comprehensive understanding of the material behavior. As a result, the present PS shows viscoelastic characteristics for small strains, whereas viscoplasticity is observed for larger deformations. The insights gained and data generated are used to select a suitable material model whose parameters have to be identified in a subsequent parameter optimization.

Keywords: Molecular dynamics · Simulation of polymers · Mechanical properties of polymers · Material characterization

M. Ries, P. Steinmann, S. Pfaller
Chair of Applied Mechanics, Friedrich-Alexander-Universität Erlangen-Nürnberg
e-mail: maximilian.ries@fau.de, paul.steinmann@fau.de, sebastian.pfaller@fau.de

14.1 Introduction and Methodology

In contrast to continuum mechanical approaches, particle-based simulation methods like molecular dynamics (MD) enable the investigation of mechanisms taking place at the molecular level. However, due to the high computational costs of such methods, only small systems can be examined. To overcome this, partitioned-domain multi-scale techniques were developed, which allow to simulate regions of high interest at a fine resolution while treating the remaining regions on a coarse scale to reduce the overall computational effort. One example is the Capriccio method (Pfaller et al, 2012, 2013) that couples a particle domain modeled with MD with a finite element based continuum. This approach was already successfully employed to investigate the effects of nano-sized silica additives embedded in atactic polystyrene by Pfaller et al (2016); Liu et al (2017).

When a material is treated at different resolutions, it is necessary that the individual material descriptions fully match. The material behavior on the fine scale is predefined by the interactions between the particles usually given by force fields. Consequently, the constitutive law used for the continuum has to be identified and parameterized accordingly. To this end, we introduce a methodology to characterize the mechanical behavior of a material directly from MD simulations (Ries et al, 2019) based on a classification scheme by Haupt (1993) depicted in Tab. 14.1. Similar ideas of analyzing constitutive behavior via numerical pseudo-experiments have been applied for other classes of materials as well, e.g., Turco et al (2019).

Table 14.1 Classification scheme to characterize material behavior introduced by (Haupt, 1993) (visualization: (Ries et al, 2019))

| | | rate dependence | |
|-------------------------|-----|------------------|------------|
| | | yes | no |
| quasi-static hysteresis | yes | visco-plasticity | plasticity |
| | no | visco-elasticity | elasticity |

We have derived four load cases from this, visualized in Fig. 14.1: time proportional loading with different strain rates to evaluate the rate dependence, time periodic tests either with varying strain amplitude or varying strain rate to quantify the inelastic effects, and relaxation tests with preceding time periodic loading to identify whether a quasi-static hysteresis exists.

Up to now, we applied this scheme to investigate atactic polystyrene as a model system under uniaxial deformation and identified purely elastic behavior for small strains, followed by a viscoplastic regime for larger deformations (Ries et al, 2019).

In this contribution, we supplement our work with examining the same material under pure shear deformation: First, we show how this deformation can be applied

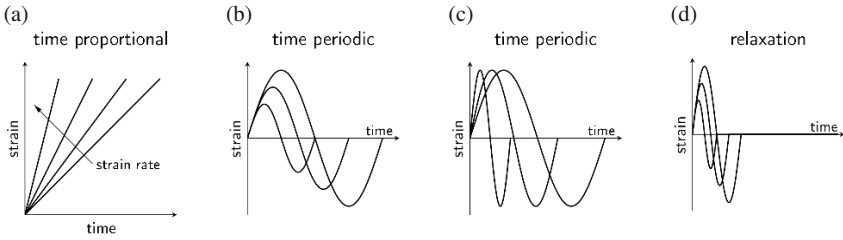


Fig. 14.1 Applied deformation: (a) time proportional with varying strain rate, (b) time periodic with different strain amplitude, (c) time periodic with different maximum strain rate, (d) relaxation tests with different preceding strain amplitudes

within the MD framework, then we present and discuss the results obtained from the individual load cases.

The acquired insights and the generated data are used by Zhao et al (2020) for the identification and calibration of a suitable constitutive law. Fig. 14.2 illustrates the procedure needed to use multiscale modeling techniques to gain deeper insights into polymer nanocomposites or fracture of polymers and puts the scope of this contribution into context.

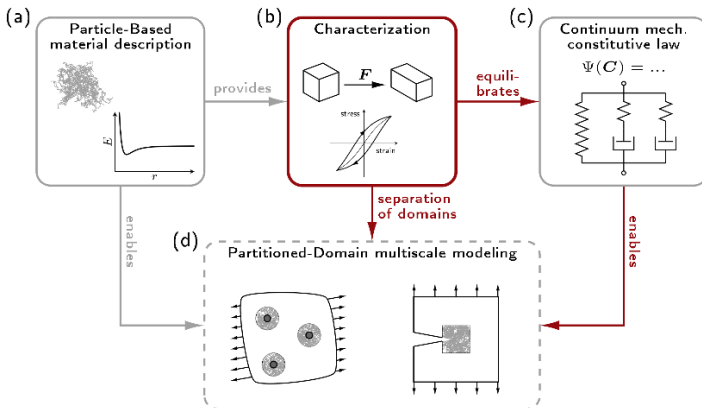


Fig. 14.2 Schematic overview: Particle-based material description (a), characterization procedure (b), continuum mechanical constitutive law (c) and partitioned-domain multiscale investigations (d), (Ries et al, 2019)

14.2 Preparation of MD Systems

As a model system, atactic PS is investigated in coarse-grained resolution in which each monomer is substituted by a so-called superatom. As a result, the number of particles and thus the computational effort is reduced by a factor of 16 compared to the fully atomistic model. This enables us to examine samples consisting of a sufficiently large number of polymer chains at reasonable computation times. On the contrary, the reduced number of particles leads to an implicit speed-up of the dynamics at the coarse-grained model and thus all subsequently derived quantities evaluated on the coarse-grained level do not match their atomistic counterparts. However, this does not affect the significance of our results, as our aim is to reproduce the behavior of the coarse-grained particle model by a continuum description.

The coarse-grained force fields describing the interactions between the superatoms were derived by Ghanbari et al (2011), who applied an iterative Boltzmann inversion approach (Reith et al, 2003) presented in Qian et al (2008).

The PS chains are placed in the simulation box via a self-avoiding random-walks algorithm implemented by Ghanbari et al (2011). In our case, these MD systems consist of 300 PS chains with 200 superatoms each, resulting in 60 000 particles, such that 180 000 degrees of freedom have to be considered.

Subsequently, the MD samples are equilibrated with a constant number of particles in three steps: Firstly, the molecules are given 5 ns to disentangle at constant volume and a temperature of 590 K (NVT ensemble) followed by an equilibration of 20 ns under constant temperature and atmospheric pressure of 101.3 kPa (NPT ensemble). Secondly, the samples are cooled down to 100 K at a constant cooling rate of 5 K ns^{-1} . This is significantly below the glass transition temperature of 170 K of coarse-grained PS (Rahimi et al, 2012). Lastly, the systems are kept at constant temperature and pressure for another 2 ns to ensure sufficient equilibration at low temperature.

These steps are carried out under periodic boundary conditions with the MD solver IBIsCO developed by Karimi-Varzaneh et al (2011). In order to obtain statistically reliable results, 10 slightly different samples are generated in this way.

A more detailed description of the initialization and equilibration of the MD samples can be found in Ries et al (2019).

14.3 Pure Shear Deformation within MD

In order to analyze the behavior of the MD simulation box by means of continuum mechanics, we need to link the deformation of the MD system to the continuum deformation. To this end, we consider the undeformed continuum body to be a cube and the deformed configuration to be a cuboid, both coinciding with the outlines of the initial and deformed MD system, as depicted in Fig. 14.3. This allows us to track the location of each particle before and after the deformation with position vectors \mathbf{X} and $\mathbf{x}(t)$, respectively.

Furthermore, the overall deformation of the sample can be captured, e.g., with the Green–Lagrange strain

$$\mathbf{E} = 0.5 \cdot [\mathbf{F}^t \cdot \mathbf{F} - \mathbf{1}] \quad (14.1)$$

derived from the deformation gradient

$$\mathbf{F} = \frac{\partial \mathbf{y}(\mathbf{X}, t)}{\partial \mathbf{X}} \quad (14.2)$$

with the deformation map $\mathbf{y}(\mathbf{X}, t)$.

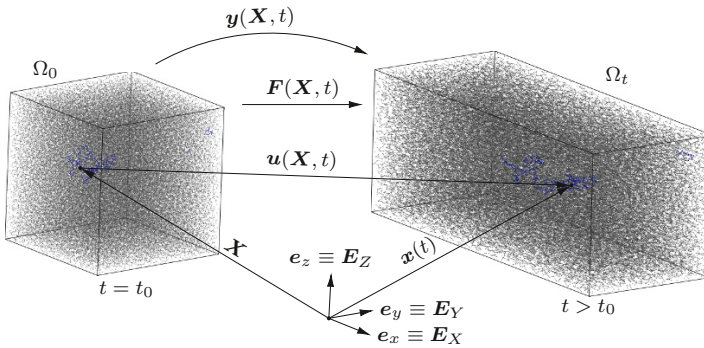


Fig. 14.3 Continuum mechanical setting: Initial (Ω_0) and current configuration (Ω_t) of the MD simulation box, position vectors \mathbf{X} and $\mathbf{x}(t)$, deformation map $\mathbf{y}(\mathbf{X}, t)$, displacement $\mathbf{u}(\mathbf{X}, t)$ and deformation gradient $\mathbf{F}(\mathbf{X}, t)$, (Ries et al, 2019)

The MD code used only supports deforming the sample normal to the coordinate axes and thus a shear deformation cannot be applied directly. However, we can exploit the transformation rules of tensors and apply stretch in \tilde{e}_x -direction, compression in \tilde{e}_z -direction while leaving the \tilde{e}_y -direction unchanged as shown in Fig. 14.4 (a). A rotation of 45° around the $\tilde{e}_y \equiv e_y$ -axis results in the desired pure shear deformation cf. Eq. 14.3 and Fig. 14.4 (b).

$$[\tilde{\mathbf{E}}] = \frac{1}{2} \begin{bmatrix} [\lambda^2 - 1] & 0 & 0 \\ 0 & 0 & 0 \\ 0 & 0 & -[\lambda^2 - 1] \end{bmatrix} \xleftrightarrow{\text{rot } y \ 45^\circ} [\mathbf{E}] = \frac{1}{2} \begin{bmatrix} 0 & 0 & [\lambda^2 - 1] \\ 0 & 0 & 0 \\ [\lambda^2 - 1] & 0 & 0 \end{bmatrix} \quad (14.3)$$

In the MD simulation, this deformation is applied stepwise via adjusting the box lengths in the different directions accordingly which requires an NVT ensemble. Controlling the length of the MD simulation box in each direction, and thus the overall deformation, can be understood as Dirichlet boundary condition in terms of continuum mechanics. In each of these loadsteps the Cauchy stress tensor is

computed as

$$\tilde{\sigma}(t) = -[\mathbf{p}(t) - p_{\text{atm}}\mathbf{1}] \quad (14.4)$$

from the pressure tensor \mathbf{p} and atmospheric pressure p_{atm} . Moreover, the stress is filtered loadstep-wise to exclude numerical noise and the equilibration at the beginning of each loadstep (Ries et al, 2019). Rotating the stress tensor by 45° to the e_i coordinate system enables an investigation of the relation between the applied shear strain $E_{xz}(t)$ and the resulting stress state $\sigma(t)$ which will be discussed in the following.

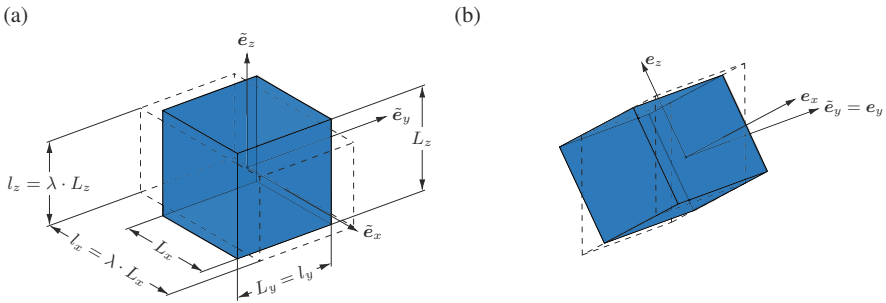


Fig. 14.4 Pure shear deformation: (a) in \tilde{e}_i coordinate system with stretch λ_i , undeformed and deformed box dimensions L_i and ℓ_i , respectively and (b) in e_i coordinate system obtained by 45° -rotation around $\tilde{e}_y \equiv e_y$ illustrating the actual shear deformation

14.4 Simulation Results

The components of the Cauchy stress tensor σ due to time periodic loading with strain amplitude of $E_{xz}^a = 4\%$ and maximum strain rate of $\dot{E}_{xz}^{\text{max}} = 1\% \text{ ns}^{-1}$ are shown over time in Fig. 14.5. Note that the stresses are expressed in σ to keep comparability to our previous contributions Pfaller et al (2019); Ries et al (2019), while \mathbf{E} is chosen to account for large deformations, despite the fact that they are not work conjugate. The stress state is clearly dominated by σ_{xz} , which follows the applied sinusoidal deformation, while the other two shear stresses vanish. On the contrary, the normal stress components σ_{xx} , σ_{yy} , σ_{zz} coincide and fluctuate around zero with twice the deformation frequency. Since the other stress components are considerably small compared to the stress in xz -direction, only σ_{xz} is evaluated in the following.

The shear stress σ_{xz} obtained from time-proportional simulations with different strain rates is depicted in Fig. 14.6. Overall, the faster the load is applied the stiffer the material responds, which indicates a clear dependence on the load rate which is characteristic for viscous material behavior. For each individual curve, the stress

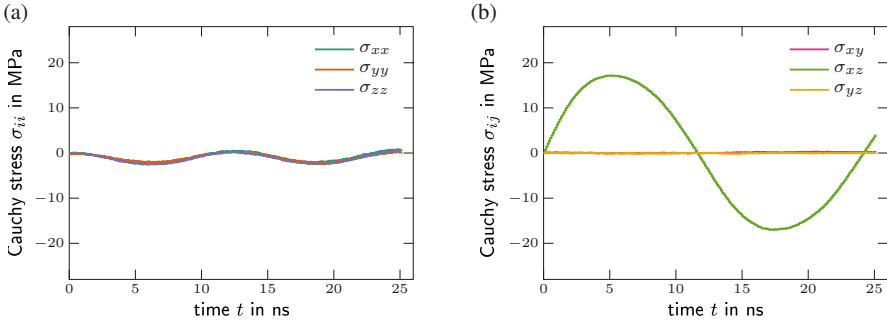


Fig. 14.5 Comparison of the components of the Cauchy stress tensor σ over time t for time periodic pure shear test, strain amplitude $E_{xz}^a = 4\%$ and maximum strain rate $\dot{E}_{xz}^{\max} = 1\% \text{ ns}^{-1}$: (a) normal stress components σ_{xx} , σ_{yy} , σ_{zz} and (b) shear stress components σ_{xy} , σ_{xz} , σ_{yz}

increases linearly up to 1% strain and then flattens noticeably. Once the maximum stress is reached, σ approximately remains constant.

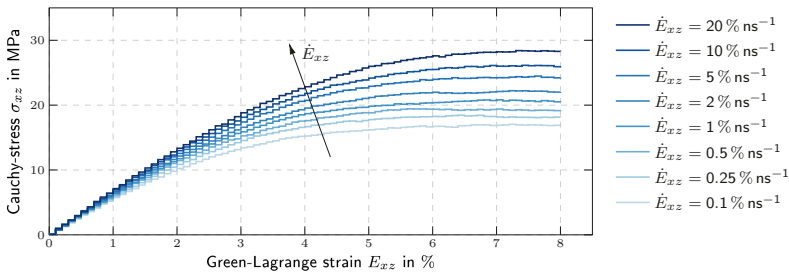


Fig. 14.6 Influence of strain rate: Cauchy stress in shear direction σ_{xz} over Green-Lagrange strain in shear direction e_{xz} for time proportional pure shear tests with maximum strain $E_{xz}^{\max} = 8\%$ and strain rates from $\dot{E}_{xz} = 0.1\% \text{ ns}^{-1}$ to $20\% \text{ ns}^{-1}$

Time periodic loading leads to a stress- strain hysteresis as depicted in Fig. 14.7 for a strain amplitude $E_{xz}^a = 8\%$ and an initial strain rate $\dot{E}_{xz}^{\max} = 1\% \text{ ns}^{-1}$. In the first loading cycle, a stress maximum of 20.1 MPa and a minimum of -17.6 MPa are obtained while in the subsequently cyclic softening leads to a stabilization of the hysteresis reaching $\sigma_{xz}^{\max} = 16.2$ MPa and $\sigma_{xz}^{\min} = -16.0$ MPa. This behavior is qualitatively observed for the other strain amplitudes investigated, too.

Since a stress-strain hysteresis is obtained, inelastic effects, i.e. viscosity and/or plasticity, have to be present. In contrast to other materials, polymers dissipate energy usually by chain slippage and disentanglement, while e.g. for concrete dissipation is induced by internal friction (Giorgio and Scerrato, 2017). These can be quantified by computing the dissipated energy density per cycle as

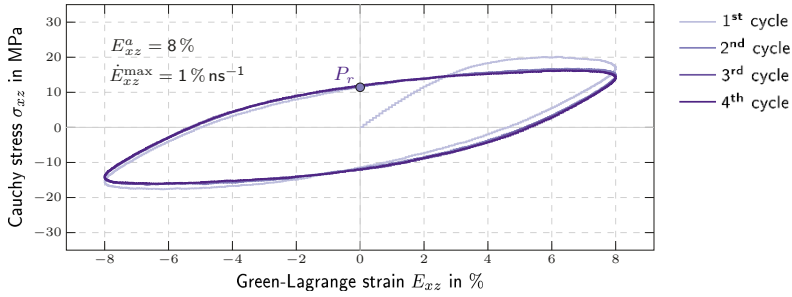


Fig. 14.7 Time periodic pure shear: Cauchy stress σ_{xz} over Green-Lagrange strain E_{xz} in shear direction for strain amplitude $E_{xz}^a = 8\%$ and maximum strain rate $\dot{E}_{xz}^{\max} = 1\% \text{ ns}^{-1}$, starting points P_r for relaxation test

$$d_0^{\text{cyc}} = \int_{\text{cyc}} \mathbf{S} : d\mathbf{E} = \int_{\text{cyc}} 2S_{xz} \cdot dE_{xz} \tag{14.5}$$

with the Piola–Kirchhoff stress $\mathbf{S} = J\mathbf{F}^{-1} \cdot \boldsymbol{\sigma} \cdot \mathbf{F}^{-t}$ and \int_{cyc} denoting the integral over one deformation cycle. Fig. 14.8 (a) indicates that for strain amplitudes up to 2% there is almost no dissipation and thus the samples behave purely elastic. For larger deformations, however, d_0^{cyc} and therewith the inelasticity increases quadratically. Next to this dependence on the strain amplitude, there is also a correlation with the strain rate as depicted in Fig. 14.8 (b). For small \dot{E}_{xz} , the largest dissipation occurs approaching an asymptote at $0\% \text{ ns}^{-1}$. For increasing strain rates, however, d_0^{cyc} decreases rapidly before flattening and reaching its minimal value. A likely explanation is that for small deformation rates, the polymer chains have more time to rearrange and thus to dissipate more energy compared to high strain rates.

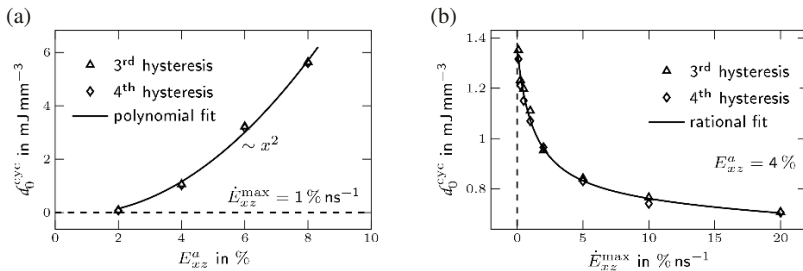


Fig. 14.8 Dissipated energy density d_0^{cyc} derived from cyclic pure shear tests for (a) different strain amplitudes with E_{xz}^a with \dot{E}_{xz}^{\max} and (b) different maximum strain rates \dot{E}_{xz}^{\max} with $E_{xz}^a = 4\%$

14.5 Relaxation Tests

So far, we identified the presence of inelasticity for large deformations, but we could not distinguish between viscous and plastic effects. In order to do so, we apply zero strain to the MD samples after having been subjected to one deformation cycle. Thus the starting point of the relaxation tests coincides with the end point of the first stress-strain hysteresis, labeled P_r , cf. Fig.14.7. Since at this point the sample is not subjected to a deformation, the elastic part of the stress has to vanish and thus elastic effects are eliminated. On the contrary, the viscous part of the stress degrades over time due to relaxation effects such as rearrangement of polymer chains, while the plastic part of the stress remains unchanged.

This evolution of the shear stress σ_{xz} over the relaxation time is depicted in Fig.14.9 for preceding strain amplitudes E_{xz}^a from 2 % to 8 %. First, we observe an initial increase of σ_{xz} which is more pronounced for larger preceding deformation. At P_r the samples are experiencing zero strain, but maximum deformation rate \dot{E}_{xz}^{\max} which is now instantly reduced to zero. Since the present material exhibits partly viscous behavior, as displayed in Fig. 14.6, this discontinuity has to lead to a temporary increase of the stress since the deformation is completely prescribed.

Afterwards, the stress degrades over time with decreasing slope and eventually approaches a constant level. This relaxation effect is more distinct for larger E_{xz}^a , which implies a correlation between viscosity and applied load. The remaining σ_{xz} indicates that the samples experience also plastic effects even for the smallest preceding deformation.

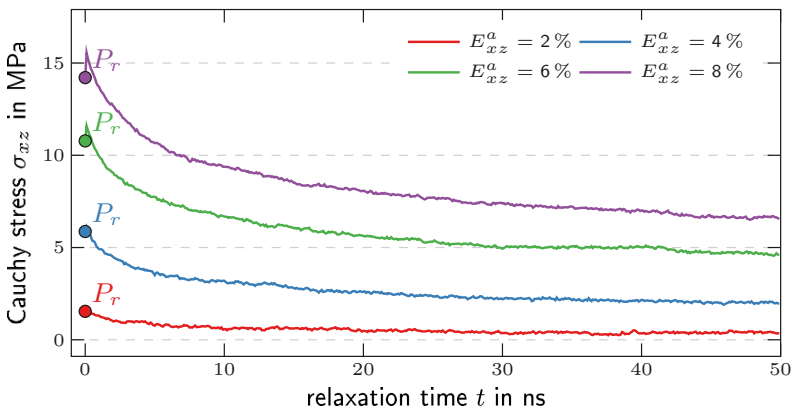


Fig. 14.9 Identification of plasticity on the basis of relaxation tests with $E_{xz} = 0\% = \text{const}$ with preceding cyclic loading with different strain amplitudes E_{xz}^a

14.6 Summary and Outlook

In this contribution, we thoroughly discuss the application of a pure shear deformation within the MD framework from a continuum mechanical point of view. We investigate atactic polystyrene as a model system and successfully employ a characterization scheme for the material behavior of polymers (Ries et al, 2019). From time proportional tests, we observe a rate dependent material behavior and time periodic simulations reveal an elastic regime for small deformations. However, inelastic effects are present, which could be decomposed into viscous and plastic parts by relaxation tests.

On the one hand, these findings underline the applicability of the used characterization scheme. On the other hand, the obtained data and the gained insights can be utilized to further validate the constitutive law calibrated for this model material in Zhao et al (2020). Embedding this constitutive law into multiscale techniques like the Capriccio method will enable us to investigate complex polymer phenomena such as fracture or the behavior of nanocomposites.

Acknowledgements We thank for the very fruitful discussions with Michael C. Böhm (†) from the Theoretical Physical Chemistry Group at Technical University Darmstadt and with Christian Wick from the PULS Group at Friedrich-Alexander Universität Erlangen-Nürnberg. Furthermore, we would like to thank Lukas Laubert for performing the MD simulations.

References

- Ghanbari A, Ndoro TV, Leroy F, Rahimi M, Böhm MC, Müller-Plathe F (2011) Interphase structure in silica–polystyrene nanocomposites: a coarse-grained molecular dynamics study. *Macromolecules* 45(1):572–584
- Giorgio I, Scerrato D (2017) Multi-scale concrete model with rate-dependent internal friction. *European Journal of Environmental and Civil Engineering* 21(7-8):821–839
- Haupt P (1993) On the mathematical modelling of material behavior in continuum mechanics. *Acta Mechanica* 100(3):129–154
- Karimi-Varzaneh HA, Qian HJ, Chen X, Carbone P, Müller-Plathe F (2011) Ibisco: A molecular dynamics simulation package for coarse-grained simulation. *Journal of computational chemistry* 32(7):1475–1487
- Liu S, Pfaller S, Rahimi M, Possart G, Steinmann P, Böhm MC, Müller-Plathe F (2017) Uniaxial deformation of polystyrene–silica nanocomposites studied by hybrid molecular dynamics–finite element simulations. *Computational Materials Science* 129:1–12
- Pfaller S, Possart G, Steinmann P, Rahimi M, Müller-Plathe F, Böhm MC (2012) A comparison of staggered solution schemes for coupled particle–continuum systems modeled with the Arlequin method. *Computational Mechanics* 49(5):565–579
- Pfaller S, Rahimi M, Possart G, Steinmann P, Müller-Plathe F, Böhm M (2013) An arlequin-based method to couple molecular dynamics and finite element simulations of amorphous polymers and nanocomposites. *Computer Methods in Applied Mechanics and Engineering* 260:109–129
- Pfaller S, Possart G, Steinmann P, Rahimi M, Müller-Plathe F, Böhm M (2016) Investigation of interphase effects in silica–polystyrene nanocomposites based on a hybrid molecular-dynamics–finite-element simulation framework. *Physical Review E* 93(5):052,505

- Pfaller S, Kergañner A, Steinmann P (2019) Optimisation of the capriccio method to couple particle-and continuum-based simulations of polymers. *Multiscale Science and Engineering* 1(4):318–333
- Qian HJ, Carbone P, Chen X, Karimi-Varzaneh HA, Liew CC, Müller-Plathe F (2008) Temperature-transferable coarse-grained potentials for ethylbenzene, polystyrene, and their mixtures. *Macromolecules* 41(24):9919–9929
- Rahimi M, Iriarte-Carretero I, Ghanbari A, Böhm MC, Müller-Plathe F (2012) Mechanical behavior and interphase structure in a silica-polystyrene nanocomposite under uniaxial deformation. *Nanotechnology* 23:305,702
- Reith D, Pütz M, Müller-Plathe F (2003) Deriving effective mesoscale potentials from atomistic simulations. *Journal of computational chemistry* 24(13):1624–1636
- Ries M, Possart G, Steinmann P, Pfaller S (2019) Extensive cgmd simulations of atactic ps providing pseudo experimental data to calibrate nonlinear inelastic continuum mechanical constitutive laws. *Polymers* 11(11):1824
- Turco E, Dell’Isola F, Misra A (2019) A nonlinear lagrangian particle model for grains assemblies including grain relative rotations. *International Journal for Numerical and Analytical Methods in Geomechanics* 43(5):1051–1079
- Zhao W, Ries M, Steinmann P, Pfaller S (2020) A viscoelastic constitutive model for polymers based on molecular dynamics simulation under finite uniaxial deformation. manuscript in preparation



Chapter 15

Manufacturing and Morphing Behavior of High-Amplitude Corrugated Laminates

Gerald Rolf Kress & Daniel Thomas Filipovic

Abstract Unidirectionally fiber-reinforced materials are highly orthotropic with respect to stiffness, strength, or thermal expansion. Flat and unsymmetric laminates made of such materials will become curved when temperature changes. As fiber-reinforced plastics (FRP) are typically processed at elevated temperatures, i.e. curing of thermoset and melting of thermoplastic materials, the temperature-induced curvature will appear at service temperatures. This chapter explains in Sections 15.2 through 15.8 how the effect can be used to create corrugated laminates where the corrugation shape consists of circular sections with or without undercuts. The deformations occurring after releasing the cured laminates from the flat lamination surface, as well as the morphing behavior, imply large deformations which we address with an analytic nonlinear morphing model explained in Sections 15.9 through 15.11.

All modeling relies on periodicity of the corrugation pattern and large extension along the direction transverse to the corrugations. The nonlinear deformations within one representative unit cell are found by integration of curvature and strain that depend on internal line reactions, and these in turn must be in equilibrium with external morphing force. The equilibrium residual is removed by using the Newton minimization method. The verified model is used to simulate morphing deformation and to study the influence of laminate thickness and corrugation amplitude on line-force-stretch diagrams.

Keywords: Composite materials · Corrugated laminates · Flexible skin · Moldless manufacturing · Large deformation

G.R. Kress, D.T. Filipovic
ETH Zürich, Tannenstr. 3, Zurich, Switzerland
e-mail: gkress@ethz.ch, fidaniel@ethz.ch

15.1 Introduction

A long plate with a corrugated center section is shown in Fig. 15.1, which could

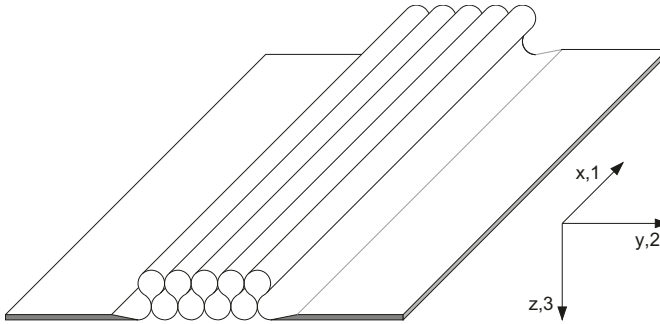


Fig. 15.1 Long plate with thin-walled corrugated section. Source (Kress and Filipovic, 2019)

be part of a morphing-wing design. This application for corrugated laminates is so obvious because of the extreme orthotropy along the directions along and transverse to the corrugations. The low in-plane extensional stiffness along the corrugated direction provides for the desired compliance along the wing chord direction whereas the in-plane extensional stiffness transverse to the corrugations contributes via the parallel-axis theorem to the wing bending stiffness along the span direction. Moreover, if the corrugation amplitude is very high, its extreme bending stiffness about the chord direction assigns the function of stringer to the corrugated laminate.

15.1.1 Research on Morphing-Wing Applications

Starting with the work of Yokozeki et al (2006), corrugated laminates made from fiber-reinforced materials are considered as candidate solutions for the flexible skins needed in morphing wing design, and receive much research attention (Dayyani et al, 2015; Airoidi et al, 2018; Chillara and Dapino, 2020). Six of the ten papers on manufacturing methods mentioned in the literature review by Airoidi et al (2018) allude in their titles to the application of corrugated laminates as flexible skins for morphing wings.

There are problems with the aerodynamic properties of corrugated laminates. One of those is that external pressure can lead to large deformations because of the high in-plane compliance along the chord and the bending compliance about the span directions. The structural response to uniform pressure of high-amplitude corrugated laminates with corrugation patterns consisting of circular sections has been studied by Thurnherr et al (2016a) with the result that structural deflection is

controlled by the extremely high bending stiffness about the chord direction and that the deflections can be kept very small if the corrugated laminate is supported by sliding rails at some sufficiently small spacing along the span direction. Airoidi et al (2018) report that the other aerodynamic problem is represented by the direct effects of corrugation on aerodynamic performance, and refer to the studies by Thill et al (2010c) and Xia et al (2014). The former authors state that the studies elaborated a rule-of-thumb that the ratio of the height of corrugation to the chord length of the aerodynamic profiles must be kept at very low levels ($< 1\%$) to prevent a degradation of the performance.

15.1.2 Manufacturing Methods for Corrugated Laminates

The patents by Chavannas (1962) and Lemelson (1970) relate to the manufacture of corrugated materials for packaging purposes; these materials are not reinforced with fibers. Johnson and Welsh (1978) patented a sine wave beam web and method of manufacture. The patent includes fiber-reinforced plastics and the manufacturing method requires molds. Donnecker et al (1999) disclose a method for making a corrugated fiber-reinforced preform for a corrugated channel. Their method requires shaping tools. Ashraf (2009) describes a method for producing a corrugated stretch laminate. His method requires forming machinery.

Apart from applications as sandwich-core structures, the open literature considers corrugated laminates mostly in context of flexible skins for the application of morphing wings. Airoidi et al (2018) provide a most recent literature review including manufacturing of corrugated laminates (Yokozeki et al, 2006; Thill et al, 2007; Ghabezi and Golzar, 2013; Airoidi et al, 2013; Fournier et al, 2013; Thill et al, 2010b; Panichelli et al, 2015; Schmitz and Horst, 2014), where only Schmitz and Horst (2014) consider corrugation shapes consisting of circular sections. Quality insurance in the production of thermoplastic sine wave beam production is addressed by Fischer et al (2017). The circular-sections corrugation shape offers advantages regarding modeling ease (Kress and Winkler, 2010, 2011; Filipovic and Kress, 2018; Kress and Filipovic, 2019) and distributions of interlaminar stresses (Thurnherr et al, 2016c).

Because of the undercuts appearing in high-amplitude circular-sections corrugation shapes, see Fig. 15.1, it is doubtful whether mold-based manufacturing methods can be used for economic manufacturing processes of corrugated laminates. Forming with cylinders leaves the questions of how to obtain good laminate quality and how to arrive at reasonable manufacturing costs. The present authors believe that the only cost-effective method for creating such corrugated laminates are mold-less manufacturing methods such as suggested in the review paper by Khoo et al (2015) and more recently also addressed by Hoa (2017). The investigation of a manufacturing method for high-amplitude corrugated thin-walled laminates (Filipovic and Kress, 2019) is used for the presentations in this chapter.

15.1.3 Substitute-Plate Modeling

Under the premise that the layers within a laminate are perfectly bonded with each other and that the total thickness is much larger than the distances away from free edges and load-introduction points, a laminate behaves like a thin plate albeit with more complex stiffness-couplings than ordinary plates made from homogeneous materials. The relation between plate deformations and internal line reactions is then described with the ABD matrix, see (15.7) and further explanations in Section 15.2.2. Globally, i.e. with sufficiently large in-plane extension, if compared to the distances to free edges, load-introduction points, and to the length of one periodic unit cell of the corrugation pattern, the static behavior of a corrugated laminate can also be described with a substitute flat-plate model, where a tilde symbol $\tilde{A}\tilde{B}\tilde{D}$ indicates corrugated laminate. Finding correct expressions for the entries of the matrices \tilde{A} , \tilde{B} , and \tilde{D} is the subject of the research field called substitute-plate modeling.

As early as 1986, Briassoulis (1986) reviews analytical expressions for equivalent stiffnesses of orthotropic thin shells given in the literature to analyze corrugated shells based on the assumption that these can be analyzed as thin, equivalent orthotropic shells of uniform thickness. He also derives new expressions with improved mapping of equivalent properties. Yokozeki et al (2006) base a simple analytical model on beam theory to predict stiffness along the corrugated direction of laminates made from woven composite which is considered a homogeneous material. Kress and Winkler (2010) use thin-shell theory together with a unit-cell approach and the generalized plane-strain assumption with respect to the direction transverse to the corrugations to derive exact solutions for deformations and state variables valid for symmetric cross-ply laminates, where the corrugation shape is composed of circular sections. Kress and Winkler (2011) derive a finite-element formulation based on the same assumption of generalized plane strain that reduces the number of independent spatial variables from three down to two. The finite-element mesh is subject to the periodicity conditions of the unit-cell approach. The model can simulate the behavior of any corrugation shape, maps any laminate design correctly, and captures all through-thickness effects which is in contrast to the limitations of thin-shell theory. Both of their models produce a substitute-plate $\tilde{A}\tilde{B}\tilde{D}$ matrix. Xia and Friswell (2011) and Xia et al (2012) suggest an homogenization-based analytical model, which can be used for any corrugation shape. The base-sheet laminate ABD matrix must be free of couplings between extension and bending, extension and shear, as well as bending and torsion. Park et al (2016) present an analytical homogenization model for corrugated composite laminates that can be applied to any corrugation geometry. They give explicit expressions to calculate not only the effective extensional and bending stiffness but also the effective transverse shear stiffness for a composite corrugated panel. Nguyen-Minh et al. perform static (Nguyen-Minh et al, 2019) and vibration (Nguyen-Minh et al, 2018) analyses for which they develop homogenization models and cell-based smoothed Mindlin plate elements. They use their new methods to analyze trapezoidal and sinusoidally corrugated panels. Most recently, Moro et al (2019), have extended the exact model by Kress and Winkler (2010), which is limited to symmetric cross-ply laminates, to be valid for arbitrary laminate stack-up. The

various models have in common that they can calculate substitute-plate properties of corrugated laminates only under the assumption of small deformations, i.e. predicted stiffnesses are initial values.

15.1.4 Stresses in Corrugated Laminates

Using the reduced finite-element approach by Kress and Winkler (2011), Thurnherr et al (2016b) present a parameter study on the influence of corrugation amplitude and different lay-ups on interlaminar stresses where they consider two geometries, one consists of circular sections and the other is a sinusoidal shape. They derive favorable configurations to minimize normalized interlaminar stresses. Soltani et al (2019) used a layer-wise finite-element formulation to predict deformations and interlaminar stresses of corrugated laminates with circular-sections corrugation shape under large extension along the corrugations, and validated their results with experiments.

15.1.5 Deformation Limits of Corrugated Laminates

Winkler and Kress (2010) determine the maximal possible deformations of a corrugated sheet where the corrugation pattern consists of two circular segments. The influence of the lay-up of cross-ply laminates and the influence of the geometry is investigated. The calculations are based on considerations of layer-wise strains that are calculated with the help of an analytical singly-curved shell model. For the evaluation of the influence of geometric nonlinearities, finite element simulations are performed and compared to the linear strain limit calculations. The influence of scalable geometry parameters is also investigated. Schmitz and Horst (2014) investigate deformation limits of circular corrugated unidirectional reinforced composites for bending-dominated applications. They use a two-dimensional analytical stress-function approach that takes through-thickness normal stresses into account. Possible failure modes, namely fiber fracture and layer delamination, of unidirectional laminated corrugated sheets are predicted. Soltani et al (2019) used a layer-wise finite-element formulation to predict all stress components in corrugated laminates with circular-sections corrugation shape under large extension along the corrugations. They found that interlaminar failure is the dominant initiating failure mode in thicker unidirectional laminates and validated their results with experiments.

15.1.6 Large Deformation of Corrugated Laminates

It is the direction along the corrugations where large deformations can appear if the corrugation amplitude is high enough. Thurnherr et al (2016c) perform struc-

tural simulations with experimental validation to better understand the non-linear structural response. They also develop a simplistic non-linear model based on rods and rotational springs to efficiently simulate the highly non-linear load-displacement curves of corrugated laminates with high accuracy. However, the highly abstracted rod model maps neither the actual geometry nor the stresses within the laminate. Ren and Zhu (2016) present a nonlinear planar beam formulation with stretch and shear deformations to study equilibria of a beam under arbitrary end forces and moments. The slope angle and stretch of the centroid line, and shear strain of cross-sections, are chosen as dependent variables in this formulation, and end forces and moments can be either prescribed or result from essential boundary conditions. For thin beams, where shear-strain influence on deformation is negligible, Kress and Winkler (2009) use the same modeling idea some years earlier in context of finding realistic honeycomb-wall shapes resulting from the expansion process. This approach is used to develop the model for describing highly non-linear morphing deformations in the present work.

Recent contributions to the understanding of the behavior and modeling of planar beams include the extensive review of modeling techniques for mapping large deformations of planar elastic beams by Spagnuolo and Andreus (2019) as well as the evidence of motion around curled stable equilibrium configurations in the nonlinear dynamics of beams, found by Baroudi et al (2019). Soltani et al (2019) used a layer-wise finite-element formulation to predict deformations and interlaminar stresses of corrugated laminates with circular-sections corrugation shape under large extension along the corrugations.

15.1.7 Structure of the Paper

In view of the morphing-wing application, manufacturing of high-amplitude corrugated laminates harboring shape undercuts and prediction of nonlinear deformation behavior are interrelated. The manufacturing modeling and simulation aspects are treated in Sections 15.2 through 15.8 and a nonlinear morphing model is developed in Sections 15.9 through 15.11. Discussion and conclusion are placed in Sections 15.12 and 15.13, respectively.

15.2 Geometry and Classical Theory of Laminated Plates Recall

In order to be able to predict the flat-laminate design for creating a corrugated laminate by the thermal curvature effect, where corrugation amplitude and periodic length must meet specified values, it is necessary to consider the classical theory of laminated plates (CTLTP) and some geometric relations for describing the geometry of corrugation shapes consisting of circular sections.

15.2.1 Circular-Sections Corrugation Shape Geometry

Fig. 15.2 indicates the reference coordinates in which the corrugated laminate is described and the curvilinear coordinates along the laminated sheet mid-plane. The

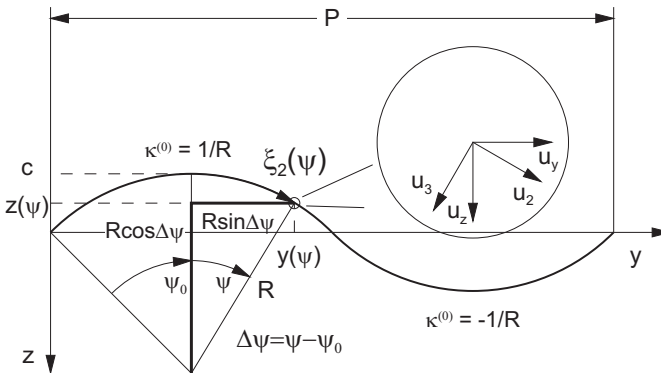


Fig. 15.2 Corrugated laminate reference coordinates. Source: Kress and Filipovic (2019)

relation between circular-segments radius R , corrugation amplitude c , and periodic length of the corrugation pattern P is given with (Kress and Winkler, 2010):

$$R = \frac{16c^2 + P^2}{32c} . \tag{15.1}$$

This equation is rearranged to calculate the periodic length of one corrugation-pattern unit cell for given reference-shape curvature R and the ratio \bar{c} that is the corrugation amplitude c normalized with respect to the periodic length P :

$$P = R \frac{32\bar{c}}{16\bar{c}^2 + 1} ; \quad \bar{c} = \frac{c}{P} , \tag{15.2}$$

where Fig. 15.3 illustrates that the normalized amplitude \bar{c} is a shape characteristic. It appears in Figure 15.3, and Fig. 15.4(a) illustrates it more systematically, that the highest normalized shape curvature $\bar{\kappa} = P/R$ appears at intermediate corrugation amplitude, specifically at the semi-circular shape. Note that extreme morphing stretches, where the corrugated laminate tends to become flat, will create less bending curvatures for high-amplitude corrugations than for corrugation shapes composed of semi-circles ($\bar{c} = 0.25$). The condition, that the laminate with sheet thickness t must not penetrate itself, gives the upper bound of the corrugation amplitude c (Filipovic and Kress, 2018):

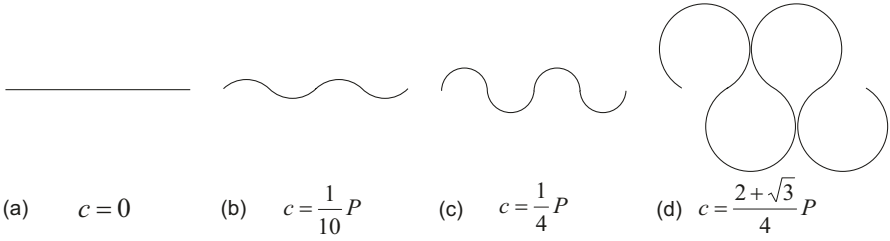


Fig. 15.3 Shapes and amplitude-periodic-length ratios. The simplified relation for the maximum-amplitude shape (d) ignores sheet thickness t

$$0 \leq c \leq \frac{P - t + \sqrt{(P - t)^2 - \frac{P^2}{4}}}{2}. \tag{15.3}$$

The curved-sheet length L_s , covering one period of corrugation, is given with (Kress and Winkler, 2010):

$$L_s = 4\psi_0 R, \tag{15.4}$$

where the opening angle ψ_0 is defined in Fig. 15.2 and is calculated with (Kress and Filipovic, 2019):

$$\psi_0 = \arccos \left(1 - \frac{c}{R} \right). \tag{15.5}$$

If the corrugated-shape unit cell with undeformed length P is stretched to flatness, its length will increase from P to L_s . This thought allows the estimate of maximum morphing capacity in terms of stretch λ (Kress and Filipovic, 2019):

$$\lambda_{lim} = \frac{L_s}{P}, \tag{15.6}$$

where Fig. 15.4(b) illustrates that the morphing stretch limit increases progressively

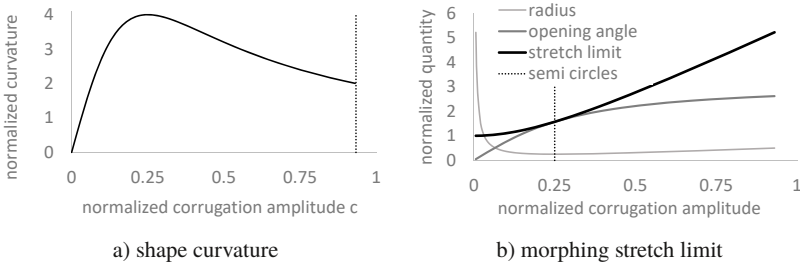


Fig. 15.4 Shape curvature $\bar{\kappa}^{(0)}$ (a) and morphing-stretch limit λ_{lim} (b) versus shape parameter \bar{c}

with normalized corrugation amplitude \bar{c} . For a maximum-corrugation amplitude shown in Fig. 15.3 (d) where $\bar{c} \approx 0.933$, the stretch limit reaches a value of more than five. Note that the stretch limit in (15.6) is based on a pure geometric consideration and that material strength may dictate lower values, depending on material strain limits and the ratio of laminate thickness to reference-shape curvature.

15.2.2 Excerpts of the Classical Theory of Laminated Plates

The proposed manufacturing method relies on temperature-induced curvature where the ratio of laminate thickness t to bending radius R remains rather small so that the classical theory of laminated plates (CTLP), see for instance in Jones (1975), is applicable. The circular-section radius R is estimated by the bending curvature, suffered by an unsymmetric laminate due to a temperature difference ΔT between processing and service temperatures. The deformations of an infinitesimally small plate element under mechanical and thermal loads are calculated with

$$\begin{Bmatrix} \mathbf{N} \\ \mathbf{M} \end{Bmatrix}^{equ} + \begin{Bmatrix} \mathbf{N} \\ \mathbf{M} \end{Bmatrix}^{mec} = \begin{bmatrix} \mathbf{A} & \mathbf{B} \\ \mathbf{B} & \mathbf{D} \end{bmatrix} \begin{Bmatrix} \boldsymbol{\varepsilon}^0 \\ \boldsymbol{\kappa} \end{Bmatrix}, \quad (15.7)$$

where the superscripts equ and mec indicate internal line reactions to thermal and to mechanical loading, respectively. The line forces \mathbf{N} and the line moments \mathbf{M} in (15.7) contain the components:

$$\mathbf{N}^T = \{ N_x \ N_y \ N_{xy} \} \quad \mathbf{M}^T = \{ M_x \ M_y \ M_{xy} \}. \quad (15.8)$$

The mid-plane strains $\boldsymbol{\varepsilon}^0$ and the plate curvatures $\boldsymbol{\kappa}$ contain the components:

$$\boldsymbol{\varepsilon}^{0T} = \{ \varepsilon_x^0 \ \varepsilon_y^0 \ \varepsilon_{xy}^0 \} \quad \boldsymbol{\kappa}^T = \{ \kappa_x \ \kappa_y \ \kappa_{xy} \}. \quad (15.9)$$

The membrane-, coupling-, and bending-stiffness matrices contain the components:

$$\mathbf{A} = \begin{bmatrix} A_{11} & A_{12} & A_{16} \\ A_{12} & A_{22} & A_{26} \\ A_{16} & A_{26} & A_{66} \end{bmatrix} \quad \mathbf{B} = \begin{bmatrix} B_{11} & B_{12} & B_{16} \\ B_{12} & B_{22} & B_{26} \\ B_{16} & B_{26} & B_{66} \end{bmatrix} \quad \mathbf{D} = \begin{bmatrix} D_{11} & D_{12} & D_{16} \\ D_{12} & D_{22} & D_{26} \\ D_{16} & D_{26} & D_{66} \end{bmatrix} \quad (15.10)$$

The equivalent line loads are calculated by

$$\begin{Bmatrix} \mathbf{N} \\ \mathbf{M} \end{Bmatrix}^{equ} = \sum_{k=1}^N \bar{\mathbf{Q}}_k \bar{\boldsymbol{\alpha}}_k \begin{Bmatrix} (z_k - z_{k-1}) \\ \frac{1}{2} (z_k^2 - z_{k-1}^2) \end{Bmatrix} \Delta T, \quad (15.11)$$

where N is the number of layers in the laminate and where $\bar{\mathbf{Q}}_k$ and $\bar{\boldsymbol{\alpha}}_k$ denote the reduced stiffness matrix (for plane-stress situations) and the coefficients of thermal expansions of the k^{th} layer; respectively, transformed to the reference system:

$$\bar{\mathbf{Q}}_k = \begin{bmatrix} \bar{Q}_{11} & \bar{Q}_{12} & \bar{Q}_{16} \\ \bar{Q}_{12} & \bar{Q}_{22} & \bar{Q}_{26} \\ \bar{Q}_{16} & \bar{Q}_{26} & \bar{Q}_{66} \end{bmatrix}_k \quad \bar{\boldsymbol{\alpha}} = \begin{Bmatrix} \bar{\alpha}_1 \\ \bar{\alpha}_2 \\ \bar{\alpha}_6 \end{Bmatrix}. \quad (15.12)$$

These equations calculate double curvatures corresponding with saddle shapes of unsymmetric bi-stable plates of moderate extension (Hyer, 1982). Corrugated laminates, on the other hand, approximately undergo cylindrical bending,

$$\kappa_{xx} \approx 0, \quad (15.13)$$

where the direction x is indicated in Fig. 15.1, if the corrugation amplitudes c are sufficiently large if compared to the periodic length P but much smaller than the extension transverse to the corrugations. For cross-ply laminates, and if no shear deformation or twist are applied, the following internal reactions vanish in linear theory:

$$N_x = N_{xy} = M_{xy} = 0. \quad (15.14)$$

Obeying these constraints gives a more accurate estimate of the temperature deformations under cylindrical bending with the following equations to be resolved for the mid-plane strains and the curvature, where the equivalent and the mechanical line loads in (15.7) superimpose each other to give the fictitious line reactions indicated with the superscript $()^{\text{fict}}$:

$$\begin{Bmatrix} N_x \\ N_y \\ M_y \end{Bmatrix}^{\text{equ}} + \begin{Bmatrix} N_x \\ N_y \\ M_y \end{Bmatrix}^{\text{mec}} = \begin{Bmatrix} N_x \\ N_y \\ M_y \end{Bmatrix}^{\text{fict}} = \begin{bmatrix} A_{11} & A_{12} & B_{12} \\ A_{12} & A_{22} & B_{22} \\ B_{12} & B_{22} & D_{22} \end{bmatrix} \begin{Bmatrix} \varepsilon_x^0 \\ \varepsilon_y^0 \\ \kappa_y \end{Bmatrix}. \quad (15.15)$$

The total-strain distributions are linear through the laminate's thickness:

$$\boldsymbol{\varepsilon}(z) = \boldsymbol{\varepsilon}^0 + z\boldsymbol{\kappa} = \begin{Bmatrix} \varepsilon_x^0 \\ \varepsilon_y^0 \\ 0 \end{Bmatrix} + z \begin{Bmatrix} 0 \\ \kappa_y \\ 0 \end{Bmatrix}. \quad (15.16)$$

Stresses in laminate layer k are calculated with

$$\boldsymbol{\sigma} = \bar{\mathbf{Q}}_k [\boldsymbol{\varepsilon}(z) - \boldsymbol{\alpha}_k \Delta T] \quad z_{k-1} \leq z \leq z_k \quad (15.17)$$

In the absence of mechanical loads, the local stresses in (15.17) are referred to as residual stresses. They arise with a change of temperature away from a stress-free reference, or processing, temperature. For strength prediction the local stresses have to be transformed into material coordinates.

15.3 Feasibility Study

The feasibility study addresses the questions:

1. Can thermal curvature with realistic laminate thickness be high enough?
2. Will the residual stresses remain small enough to guarantee strength?
3. Will the margins of strength allow for sufficient morphing stretches?

15.3.1 Materials

The feasibility study considers three typical carbon-fiber reinforced epoxies where Table 15.1 shows the relevant material properties of prepregs with layer thickness $h = 0.125$ mm.

Table 15.1 Relevant material properties of unidirectional composites with fiber-volume fraction $v_f = 0.6$: Elastic constants, coefficients of thermal expansion (CTE), and values of strength transverse to the fibers under tensile and compressive stress. Source: DORNIER SYSTEM GmbH

| fiber | E_1 | E_2 | ν_{12} | α_1 | α_2 | Y_T | Y_C |
|-------|--------|-------|------------|----------------------|------------|-------|-------|
| | [MPa] | | [-] | $[10^{-6}/\text{K}]$ | | [MPa] | |
| T 300 | 135000 | 10000 | 0.27 | -0.6 | 30 | 55 | 170 |
| M 40 | 220000 | 7000 | 0.35 | -0.8 | 30 | 50 | 150 |
| GY 70 | 290000 | 5000 | 0.41 | -1.0 | 30 | 40 | 130 |

15.3.2 Laminate Thermal Deformation Coefficients

Table 15.2 shows bending curvatures of various laminate stack-ups made from the

Table 15.2 Laminate temperature-curvature coefficients $\kappa_y^T [10^{-4}/\text{mm K}]$. Layer thickness $h = 0.125$ mm.

| fiber | [90/0] | | [90/0 ₂] | | [90/0 ₃] | | [90/0 ₄] | |
|-------|--------|--------|----------------------|--------|----------------------|--------|----------------------|--------|
| | cyl | saddle | cyl | saddle | cyl | saddle | cyl | saddle |
| T300 | 1.023 | 1.063 | 1.086 | 1.107 | 0.886 | 0.897 | 0.715 | 0.722 |
| M40 | 0.635 | 0.640 | 0.908 | 0.915 | 0.840 | 0.844 | 0.715 | 0.718 |
| GY70 | 0.407 | 0.412 | 0.721 | 0.725 | 0.757 | 0.764 | 0.685 | 0.687 |

materials whose properties are listed in Table 15.1 and visualized in Fig. 15.5. The curvatures per unit temperature change $\Delta T = 1^\circ\text{C}$ relate to cylindrical bending (cyl) and deformation without kinematic constraint (saddle). It can be seen that the constraint of cylindrical bending has a relatively small influence on the coefficients of thermal curvature (CTC). All materials find higher CTC values for numbers n_0 , of span-wise oriented layers, larger than one. *T300* and *M40* find the highest values for $n_0 = 2$ and *GY70* for $n_0 = 3$. The highest CTC values are obtained by *T300*, which we ascribe to the relatively small Young’s modulus in fiber direction that allows higher bending. We conclude that, out of the present selection, laminates $[90/0]$ or $[90/0_2]$ made from *T300* epoxy prepreg are best candidates for making corrugated laminates with the help of thermal deformation. We assume that $\Delta T = -150^\circ\text{C}$ is a realistic temperature difference available for creating curvature for thermoset resin types with curing temperature of $T_{cur} = 180^\circ\text{C}$. It will create a bent-shape radius of

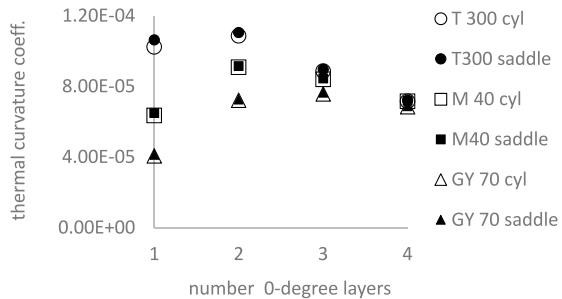
$$R = \frac{1}{\kappa_y^T \Delta T} \tag{15.18}$$

For the laminates $[90/0]$ and $[90/0_2]$ we find $R = 65.1\text{ mm}$ and $R = 61.4\text{ mm}$, respectively. Laminate symmetry prevents thermal curvatures to appear, see the left column in Table 15.3. A typical laminate-analysis program assumes no deformation

Table 15.3 Laminate thermal-deformation coefficients (T300). Layer thickness $h = 0.125\text{ mm}$.

| | $[90/0_2]_s$ | $[90/0_2]$ saddle | $[90/0_2]$ cylinder |
|-----------------------------------|--------------|----------------------|------------------------|
| $\epsilon_x^0 [10^{-6}/\text{K}]$ | 3.800 | 2.47 | -0.638 |
| $\epsilon_y^0 [10^{-6}/\text{K}]$ | 0.956 | 14.90 | 14.767 |
| $\kappa_x [10^{-6}/\text{mm/K}]$ | 0.000 | -32.80 | 0.000 |
| $\kappa_y [10^{-6}/\text{mm/K}]$ | 0.000 | 110.00 | 108.630 |

Fig. 15.5 Thermal curvature coefficients for cylindrical bending (open markers) and for unconstrained infinitesimal small plates (solid markers)



constraints under line loads so that for an unsymmetric laminate both curvature components appear, see the center column in the table. Cylindrical bending implies that one of the two bending curvatures must be zero. This constraint changes the midplane strain ϵ_y^0 and the non-vanishing curvature κ_y only slightly away from those of the unconstrained laminate seen in the right column. However, the relatively large change of ϵ_x^0 might affect residual stresses significantly.

15.3.3 Residual Stresses

Residual stresses in fiber direction, σ_1 , are always so much less than the respective stress limits that fiber failure is not an issue. Under the present loading conditions of the considered cross-ply laminates shear stresses τ_{12} do not appear. Therefore, Tables 15.4 and 15.5 only list direct residual stresses transverse to the fiber direction, σ_2 , for the symmetric and the unsymmetric laminates [90/0] and [90/0₂]; respectively. The symmetric versions are free of bending and the unsymmetric versions are subject to temperature load without any kinematic constraint (saddle) and the cylindrical-bending constraint (cylinder). The material strength is assessed with the margin of safety

$$M_S = \frac{Y_t - \sigma_2}{\sigma_2} \tag{15.19}$$

For the symmetric [90/0]_s laminate, the transverse stresses are tensile and the same in

Table 15.4 Stresses σ_2 [MPa] with margins of safety [%] at ply interfaces (IF) in symmetric and unsymmetric laminates [90/0] made from T300. Layer thickness $h = 0.125$ mm.

| ply | deg | IF | [90/0] _s | [90/0] saddle | [90/0] cylinder |
|-----|-----|-----|---------------------|------------------|--------------------|
| 1 | 90 | bot | 41.2 (33) | 16.0 (244) | 44.5 (24) |
| 1 | 90 | top | 41.2 (33) | 30.6 (78) | 39.3 (40) |
| 2 | 0 | bot | 41.2 (33) | 30.6 (78) | 33.0 (67) |
| 2 | 0 | top | 41.2 (33) | 16.0 (244) | 13.7 (301) |

all layers. Much smaller stress values are found in the unsymmetric laminate [90/0]. For the symmetric [90/0₂]_s laminate the transverse stresses shown in Table 15.5 are tensile but slightly higher in the 90° than in the 0° layers. The constraint of cylindrical bending about the x direction reduces the stress in the 0° layer significantly but the maximum stress in the 90° direction is increased, reducing the margin of safety down to $M_S = 19\%$. Transverse stresses at the surface $z = 0.1875$ become negative but do not challenge the compressive strength of $Y_c = 170$ MPa.

The plots in Fig. 15.6 give a visual impression of the stress distributions based on the data provided in the tables. Stresses within the 90° and 0° layers are plotted with solid and dashed lines, respectively. The vertical lines marked with open squares give

Table 15.5 Stresses σ_2 [MPa] with margins of safety [%] at ply interfaces (IF) in symmetric and unsymmetric laminates $[90/0_2]$ made from T300. Layer thickness $h = 0.125$ mm.

| ply | deg | IF | $[90/0_2]_s$ | $[90/0_2]$ saddle | $[90/0_2]$ cylinder |
|-----|-----|-----|--------------|----------------------|------------------------|
| 1 | 90 | bot | 42.0 (31) | 34.4 (60) | 46.3 (19) |
| 1 | 90 | top | 42.0 (31) | 34.9 (60) | 40.8 (35) |
| 2 | 0 | bot | 38.9 (41) | 31.2 (76) | 32.7 (68) |
| 2 | 0 | top | 38.9 (41) | 12.0 (358) | 12.2 (351) |
| 3 | 0 | bot | 38.9 (41) | 12.0 (358) | 12.2 (351) |
| 3 | 0 | top | 38.9 (41) | -7.1 (2294) | -8.2 (1973) |

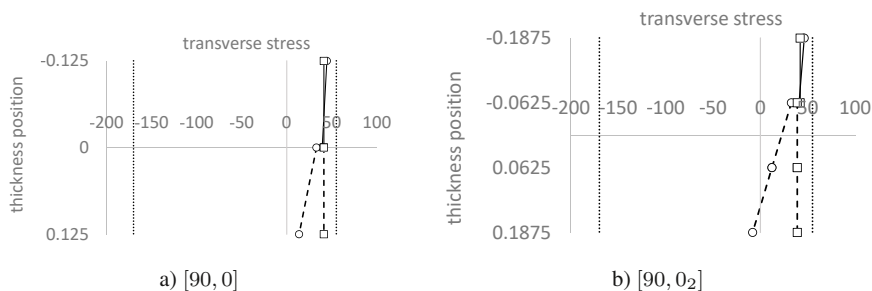


Fig. 15.6 σ_2 in laminates $[90, 0]$ (a) and $[90, 0_2]$ (b), Solid lines in 90° layer, dashed lines in 0° layers, vertical lines correspond with total bending constraint, dotted lines indicate material strength

the stress distributions without bending deformation as they occur in symmetric laminates. The slanted lines marked with open circles correspond to cylindrical bending. Dotted lines indicate the tensile-stress and compressive-stress limits, respectively. Morphing action applied to maximum-amplitude corrugated laminates will tend to reduce the thermally induced bending curvature so that the stress distributions will move closer to those of the symmetric laminates, thereby reducing the highest tensile stresses. The analysis of residual stresses indicates feasibility of the proposed manufacturing method.

15.4 Design Procedure

The structural requirement of a given application may lead to other laminate designs than suggested in the feasibility study. The here described design procedure focuses on finding the information for making the lay-up in terms of prepreg patches for a desired corrugated shape.

1. obtain material data and curing process data

2. specify unsymmetric laminate design
3. calculate temperature curvature κ_y^T from (15.8) and (15.11) \rightarrow radius R
4. choose c/P ratio for desired shape
5. calculate periodic length P from (15.2)
6. perform stress analysis
7. calculate curved length L_s from (15.5) and (15.4) for prepreg cutting

Step 3 requires application of the classical theory of laminated plates. Steps 4 through 6 may be iterated for maximizing the margin of safety against inter-fiber failure (matrix failure or debonding).

15.5 Mold-Less Manufacturing

Fig. 15.7 indicates a schematic of the design principle for integrating flat and corrugated sections in the same manufacturing process. The section, that will assume a corrugated shape evolving with cooling after curing, is within the dashed vertical lines. Outside of this section, the laminate increases gradually in thickness where the figure suggests simple tapering. Interlaminar shearing or peeling stresses in the tapering will be very small as only small line loads can be transmitted along the corrugated direction. A 90-degree layer runs throughout the corrugated part in order to avoid lap jointing. The lay-up ensues from bottom to



Fig. 15.7 Stacking sequence for one complete corrugation period. Dashed lines indicate transition to non-morphing parts of the design. For better visualization, the ratio between length and thickness is not to scale.

top on a flat substrate (or a gently curved substrate for the aerodynamic shape of a wing). After lay-up, the standard steps of vacuum bagging and curing in an autoclave must be performed to obtain the formed design shown in Fig. 15.8. The advantages of the suggested manufacturing method include:

1. no tooling other than for flat laminates required
2. same high quality as of flat laminates
3. additional manufacturing effort marginal
4. fully integrated design of corrugated parts in skin
5. automation potential: automated tape laying

Consequently, realizing flexible skin integrated in morphing-wing designs implies lower costs if compared with other manufacturing methods.

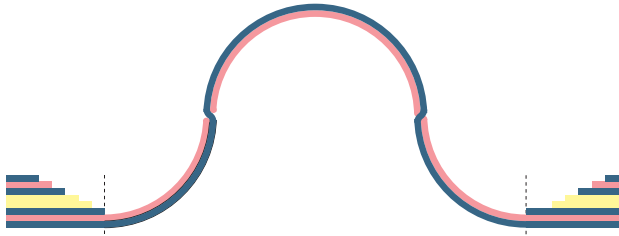


Fig. 15.8 Laminate shown in Fig. 15.7 after manufacturing process.

15.6 Process Simulations

The geometrically nonlinear structural analysis with the finite-element method (FEM) first simulates the creation of a corrugation shape by thermal deformation due to cooling after the processing step, and it secondly simulates the large deformations under morphing action. The results of the the FEM simulations in terms of deformed shapes and stress distributions are used to verify the predictions by the classical theory of laminated plates (CTLP). The same FEM procedure is also used to verify the nonlinear morphing model explained in Sections 15.9 through 15.11.

15.6.1 Simulation Tools and Verification

A proprietary data generator reads the data from the text file shown in Fig. 15.9 and generates a text file containing *ANSYS-Parametric-Design-Language* (APDL) commands for controlling the structural-analysis steps. The bending-radius $R(\Delta T)$ must be obtained by CTLP. Areas are created for each circular section according to the scheme indicated in Fig. 15.7 and attributed the respective material laws for 90° and 0° layers. Mesh density is determined by using one row of rectangular finite elements per layer, with lateral size between one and ten times the layer thickness. A convergence study showed that, within this range, element size has negligible effect on final results. The unsymmetric laminate $[0/90]$ has been used for comparison of CTLP predictions and FEM simulation results. The considered result is the axial displacement that occurs when the flat laminate takes on the corrugated shape upon cooling down by $\Delta T = -150^\circ C$, see *estimated thermal displacement* in Fig. 15.9. The error measure,

```

LAYER THICKNESS                H :          0.1250
NUMBER OF ZERO-DEGREE LAYERS   N_0 :          1
AMPLITUDE TO PERIODIC LENGTH   C_TO_P :        0.933
BENDING RADIUS ESTIMATE        R :          65.1
NUMBER OF PERIODS               N_P :          1
TEMPERATURE CHANGE              DELTA_T :       -150.0
# TEMPERATURE LOAD STEPS       N_STEPS_TEMP :    11
APPLIED GLOBAL STRAIN [%]      EPS_Y :          0.0000
# STRAIN LOAD STEPS            N_STEPS_EPS :      0
-----
CURVED LENGTH                    S_L :          681.7
PERIODIC LENGTH AFTER THERMAL LOAD p :          130.2
ESTIMATED THERMAL DISPLACEMENT U_DT :       -551.5
SPECIFIED DISPLACEMENT        U_TOT :          0.0
    
```

Fig. 15.9 Data generator text input file. Quantities below the dashed line are derived.

$$\Delta_{ux} = \frac{u_y^{FEM} - u_y^{CTLP}}{u_y^{CTLP}} [\%], \tag{15.20}$$

obtains agreement better than 0.2%.

15.6.2 FEM Residual Stress Evaluations

The color coding in Fig. 15.10 depicts the distribution of the stress σ_x within a small section of the 0° layer at the apex of the corrugation pattern. It can be taken from the false-color scaling shown in Fig. 15.10 that minimum and maximum stress

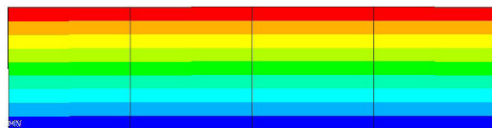


Fig. 15.10 FEM evaluation of σ_x within 0° layer at corrugation apex



values (13.5/33) agree closely with those values obtained by the classical theory of laminates plates listed in Table 15.4 (13.7/33).

15.7 Aerodynamic Sliding Overlaps Design

The suggested fabrication method mitigates the aerodynamic penalty of corrugated flexible skins: Fig. 15.11 shows that parts of the laminate can be designed so that they serve as sliding overlaps covering the corrugations and creating a closed aerodynamically smooth surface with tolerable deviations from smoothness. The sliding

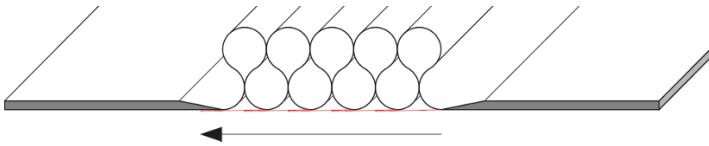


Fig. 15.11 Aerodynamic scales design; arrow indicates air flow direction

overlaps are laminated together with the other layers along the curved sections as indicated in Fig. 15.11. This implies high stiffness and strength of the sliding overlaps along the chord direction. As the overlaps, or scales, contribute to 90° layer thickness, the lamination plan shown in Fig. 15.12 foresees double numbers of the respective

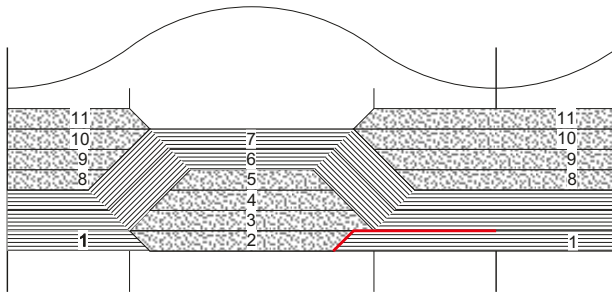


Fig. 15.12 Scales design lamination scheme. Length-to-thickness ratios not realistic. Red line indicates separation of scale from the rest of the laminate by Teflon foil.

layers. To maintain similar thermal curvature coefficients as listed in Table 15.2, and with them similar geometric corrugation parameters, individual layers must have half of the thickness considered in previously considered laminate designs, namely 0.125 mm → 0.0625 mm, where the smaller thickness is realistic as such prepregs are commercially available.

15.8 Corrugated Laminate Demonstrator

15.8.1 Autoclave-Table Size

Of the table area of 800 mm \times 2000 mm some width along the edges must be reserved for applying the sealing material for the vacuum bagging. We choose a net lay-up area of 700 mm \times 1900 mm. Because of the large curved length per corrugation period the corrugations are placed parallel to the larger plate extension.

15.8.2 Material

A prepreg made by *North Thin-Ply Technologies*, namely NTPT THINPREGTM 513, was used to make a demonstrator. Table 15.6 lists values issued in the data sheets for fiber and matrix whereas the composite properties have been estimated with the simplified equations by Chamis (1983).

Table 15.6 Material properties. Young's moduli [MPa], CTE [10^{-6} K^{-1}]

| | | E | | α | | ν | |
|-----------|--------------|----------|----------|---------------|---------------|------------|------------|
| matrix | 513 | 4100 | | 55.0 | | 0.3 | |
| | | E_{fL} | E_{fT} | α_{fL} | α_{fT} | ν_{fL} | ν_{fT} |
| fiber | T800 | 29400 | 1600 | -0.3 | 28.1 | 0.2 | 0.01 |
| composite | $v_f = 55\%$ | 163545 | 9143 | 0.002 | 39.3 | 0.24 | - |
| composite | $v_f = 60\%$ | 178040 | 9672 | -0.004 | 37.9 | 0.24 | - |
| composite | $v_f = 65\%$ | 192535 | 10241 | -0.009 | 36.5 | 0.24 | - |

15.8.3 Prototype for Measuring Thermal Curvature

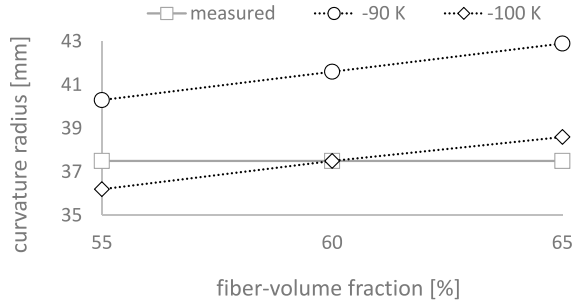
The first prototype-laminate consists of three regions,

$$[90/0_2] - [0_2/90] - [90/0_2],$$

where the outer regions measure 50 mm along the 90° direction and the inner one 100 mm. The dimension of the laminated plate along the other direction is 400 mm. The outer regions with reversed stack-up sequence help to suppress saddle shapes. We used a processing temperature of $T_{\text{proc}} = 120^\circ\text{C}$. Fig. 15.13a) shows the resulting part after applying the autoclave process. The thickness of a 3-layer laminate was measured at 0.18 mm so that cured layer thickness is 0.06 mm. At a room temperature



a) prototype



b) shape curvature versus volume fraction

Fig. 15.13 First prototype for measuring thermal curvature (a) and measured and predicted shape curvatures (b).

of about 20°C, its radius of curvature has been measured as $R = 37.5$ mm. Using the material properties listed in Table 15.6, we predicted the curvature radii shown in the plot to the right in Fig. 15.13b), which are in good agreement with the measurement, particularly for the higher temperature difference $\Delta T = -100$ K.

15.8.4 Corrugated-Laminate Sample with Three Unit Cells

The thermal curvature measured on the prototype indicate that the curved length of one maximum-amplitude circular section is about 210 mm. Fig. 15.14 illustrates that the demonstrator laminate consists of nine regions,

$$[90/0]_s - [0_2/90] - [90/0_2] - [0_2/90] - [90/0_2] - [0_2/90] - [90/0_2] - [0_2/90] - [90/0]_s,$$

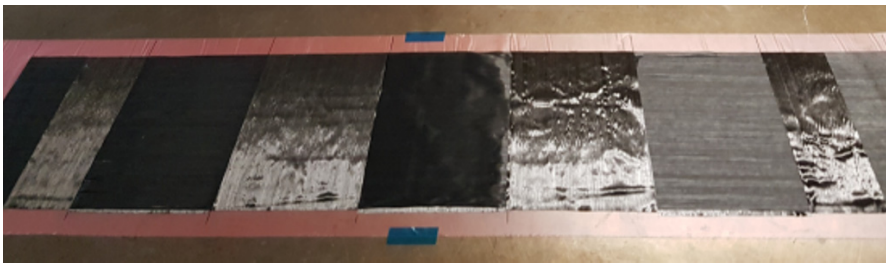


Fig. 15.14 Demonstrator laminate after laying process

where the two outer regions on each side of the laminate have a width of 105 mm whereas the other regions have a width of 210 mm. Upon the curing process within the autoclave and removal of the auxiliary materials, the laminate takes on the shape of a corrugated laminate shown in Fig. 15.15.

15.9 Morphing Model

The development of an analytic morphing model (Kress and Filipovic, 2019) has been motivated by the analysis of the manufacturing process and the FEM morphing simulations presented so far. The theory holds for corrugated laminates where the reference configuration is a periodic corrugation pattern consisting of circular sections and where the laminates are much thinner than the circular-sections radii. Thus, the deformations are nonlinear whereas the material strains remain small (Kress and Winkler, 2009; Ren and Zhu, 2016).

15.9.1 Geometric and Mechanical Unit Cells

The sketch to the left in Fig. 15.16 shows one periodic unit cell of the corrugation pattern and indicates the natural and essential boundary conditions. At all points marked with open circles the bending moment M_y vanishes. The left-most point is fixed in space but allowed to rotate. The point at the right of the geometric unit cell does not move along z , $u_z = 0$, and a specified displacement $u_y = \hat{u}$ imposes morphing strain. The geometric-unit-cell is point symmetric with respect to its center point, and the two circular segments are in themselves symmetric with respect to vertical lines. Therefore, the point marked with a solid circle cannot rotate. Because of these circumstances, and even though the stacking sequence of the first circular section, say $[0_n/90_m]$, is reversed in the second one, the structural behavior of the geometric unit cell is fully de-

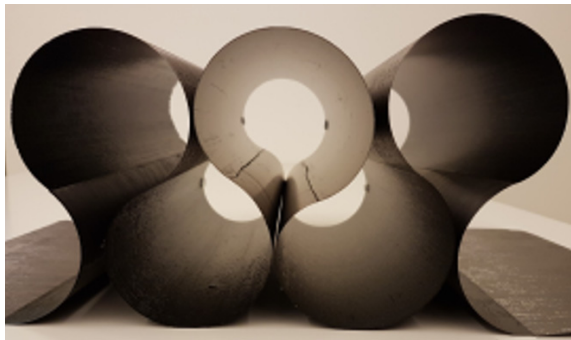


Fig. 15.15 Cured demonstrator laminate after cool-down

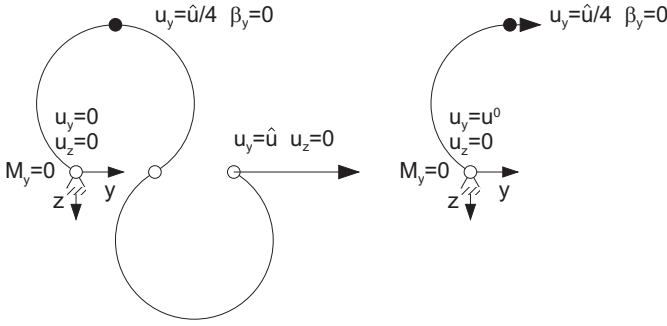


Fig. 15.16 Geometric and mechanical unit cells

scribed by the mechanical unit cell shown in the sketch to the right of the figure. The relation between stress resultants and deformations is described in the local system shown in Fig. 15.2, where the coordinate mapping between the moving trihedral $x \xi_2 \xi_3$ and the reference system xyz is given with

$$\begin{Bmatrix} x \\ \xi_2 \\ \xi_3 \end{Bmatrix} = \begin{bmatrix} 1 & 0 & 0 \\ 0 & \cos \theta & \sin \theta \\ 0 & -\sin \theta & \cos \theta \end{bmatrix} \begin{Bmatrix} x \\ y \\ z \end{Bmatrix}. \tag{15.21}$$

For writing convenience of subscripts, we prefer to replace the symbol ξ_2 with s .

15.9.2 Reference Configuration

Fig. 15.2 indicates points in the reference configuration,

$$y^{(0)}(\xi_2) = R \sin \Delta \psi; \quad z^{(0)}(\xi_2) = R [1 - \cos \Delta \psi] - c, \tag{15.22}$$

where

$$\Delta \psi = \psi - \psi_0 = \frac{\xi_2}{R} - \psi_0 = \kappa^0 \xi_2 - \psi_0, \tag{15.23}$$

Point B in the reference configuration shown in Fig. 15.17 is given with:

$$y_B^{(0)} = \frac{P}{4}; \quad z_B^{(0)} = -c. \tag{15.24}$$

15.9.3 Cylindrical Bending and Constitutive Equations

Cylindrical bending implies that curvature deformations vanish, $\varepsilon_x^1 = \varepsilon_{xs}^1 = 0$. We also assume that the midplane strain transverse to the corrugations and the shearing

strain vanish, $\varepsilon_x^0 = \varepsilon_{xs}^0 = 0$. As the laminate is free of couplings between in-plane shear and normal line forces as well as between twist and bending moments, $\varepsilon_{xs}^0 = 0$. The remaining relations between line loads and laminate deformations are:

$$\begin{aligned} N_x &= A_{12}\varepsilon_s^0 & M_x &= D_{12}\varepsilon_s^1 \\ N_s &= A_{22}\varepsilon_s^0 + B_{22}\varepsilon_s^1 & M_s &= B_{22}\varepsilon_s^0 + D_{22}\varepsilon_s^1 \end{aligned} \tag{15.25}$$

15.9.4 Mechanical Unit-Cell Equilibrium

Fig. 15.17 redraws the mechanical unit cell identified in Fig. 15.16, where θ coincides

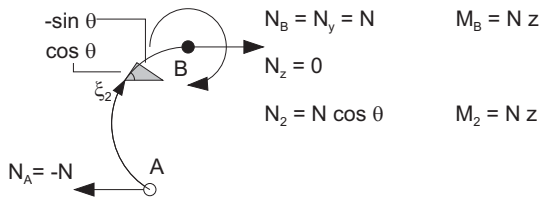


Fig. 15.17 Equilibrium at unit cell and internal stress resultants

with $\Delta\varphi$ if no deformation is applied, and indicates stress resultants reacting to the essential boundary conditions. A specified line force $N_B = N_y = N$ causes the reaction line force $N_A = -N$ at point A. The internal moment at B is obtained from the cross product of the reaction N_A and distance between the line along which N_A acts and point B:

$$\begin{Bmatrix} 0 \\ 0 \\ z_B \end{Bmatrix} \times \begin{Bmatrix} 0 \\ -N \\ 0 \end{Bmatrix} = \begin{Bmatrix} z_B N \\ 0 \\ 0 \end{Bmatrix} = \begin{Bmatrix} M_B \\ 0 \\ 0 \end{Bmatrix} \tag{15.26}$$

The local mid-surface in-plane line force $N_2(\xi_2)$ along ξ_2 is a component of N obtained from the transformation rule (15.21),

$$N_2(\xi_2) = N \cos(\theta) , \tag{15.27}$$

whereas the local transverse force $Q_3(\xi_2)$ is not considered as the laminate thickness is assumed much smaller than the corrugation-shape curvature. We connect the local line loads with the second and the fourth of the laminate constitutive equations in (15.22) to obtain:

$$\begin{Bmatrix} N \cos(\theta) \\ Nz \end{Bmatrix} = \begin{bmatrix} A_{22} & B_{22} \\ B_{22} & D_{22} \end{bmatrix} \begin{Bmatrix} \varepsilon_2^0 \\ \varepsilon_2^1 \end{Bmatrix} . \tag{15.28}$$

Resolving (15.28) for the laminate deformations gives:

$$\begin{Bmatrix} \varepsilon_2^0 \\ \varepsilon_2^1 \end{Bmatrix} = \frac{1}{D} \begin{bmatrix} D_{22} & -B_{22} \\ -B_{22} & A_{22} \end{bmatrix} \begin{Bmatrix} N \cos(\theta) \\ Nz \end{Bmatrix}, \quad (15.29)$$

where D is the determinant:

$$D = A_{22}D_{22} - B_{22}^2. \quad (15.30)$$

15.9.5 Curvature and Rotation

The curvature $\kappa^{(t)}(\xi_2)$ of the deformed configuration is the sum of shape curvature of the reference configuration $\kappa^{(0)} = 1/R$ and of the bending curvature $\varepsilon_2^1(\xi_2)$ due to deformation caused by mechanical load N in (15.29):

$$\kappa^{(t)}(\xi_2) = \kappa^{(0)} + \varepsilon_2^1(\xi_2), \quad (15.31)$$

where the linear distributions of the bending moment M_2 and of the bending strain $\varepsilon_2^1(\xi_2)$ along z is considered. The total slope follows from integrating the curvature along the curvilinear coordinate ξ_2 (Kress and Winkler, 2009; Ren and Zhu, 2016):

$$\theta^{(t)}(\xi_2) = \int_0^{\xi_2} \kappa^{(t)}(\sigma) d\sigma + C_1 \quad (15.32)$$

where the integration constant C_1 must be adjusted to maintain the symmetry condition at B , namely $\theta_B^{(t)} = 0$. The total slope equals the angle of rotation in the directional transformation (15.21).

15.9.6 Deformed Configuration

The deformed configuration is calculated from integrating mid-plane strain ε_2^0 and rotation θ over the curved length ξ_2 .

15.9.6.1 Stretch of Line Elements

A reference-configuration line element of the mid-surface $d\xi_2^{(0)}$ changes length by the stretch λ :

$$d\xi_2^{(t)} = \lambda d\xi_2^{(0)} = (1 + \varepsilon_2^0) d\xi_2^{(0)}. \quad (15.33)$$

At position ξ_2 the stretching of the line element gives the incremental displacements (Ren and Zhu, 2016):

$$du_y^0 = \cos(\theta) \varepsilon_2^0 d\xi_2^{(0)} ; \quad du_z^0 = -\sin(\theta) \varepsilon_2^0 d\xi_2^{(0)} . \quad (15.34)$$

Note that the stretch of the line elements becomes significant at the end of morphing action when the corrugated laminate has become almost flat.

15.9.6.2 Integration of the Rotation

Positions of points in the deformed configuration are found by integrating the slope (Kress and Winkler, 2009) and thereby considering the stretch (Ren and Zhu, 2016) of line elements:

$$du_y = du_y^0 + du_y^1 ; \quad du_z = du_z^0 + du_z^1 . \quad (15.35)$$

At position ξ_2 the stretching of the line element gives the incremental displacements:

$$y^{(t)}(\xi_2) = \int_0^{\xi_2} \cos(\theta) \lambda d\sigma ; \quad z^{(t)}(\xi_2) = - \int_0^{\xi_2} \sin(\theta) \lambda d\sigma . \quad (15.36)$$

At the reference configuration the point B indicated in Fig. 15.17 has the position $y_B^{(0)} = P/4, z_B^{(0)} = -c$. Deformation changes that position to:

$$y_B^{(t)} = \int_0^{L_s} \cos(\theta) \lambda d\sigma ; \quad z_B^{(t)} = - \int_0^{L_s} \sin(\theta) \lambda d\sigma . \quad (15.37)$$

15.9.6.3 Displacements in Reference Coordinates

Displacements follow from the difference between current and reference configurations:

$$u_y = y^{(t)} - y^{(0)} ; \quad u_z = z^{(t)} - z^{(0)} , \quad (15.38)$$

which yields:

$$u_y = \int_0^{\xi_2} \cos(\theta) \lambda d\sigma - y^{(0)} ; \quad u_z = - \int_0^{\xi_2} \sin(\theta) \lambda d\sigma - z^{(0)} . \quad (15.39)$$

15.10 Morphing Solution Algorithm

Deformed configurations of the problem at hand depend most directly on an applied line force N . On the other hand, it is desired to specify morphing stretch $\hat{\lambda}_{\text{morph}}$. Fig. 15.18 illustrates that the solution algorithm is therefore partitioned into outer and inner iterative processes, where the outer process finds the line force effectuating that the actual stretch λ_{morph} is equal to the specified stretch $\hat{\lambda}_{\text{morph}}$, and where the

inner loop finds a deformed configuration where the stress resultants agree with the distributions of the internal line force and line moment that equilibrate the external line force N . For creating force-displacement diagrams from zero up to the specified

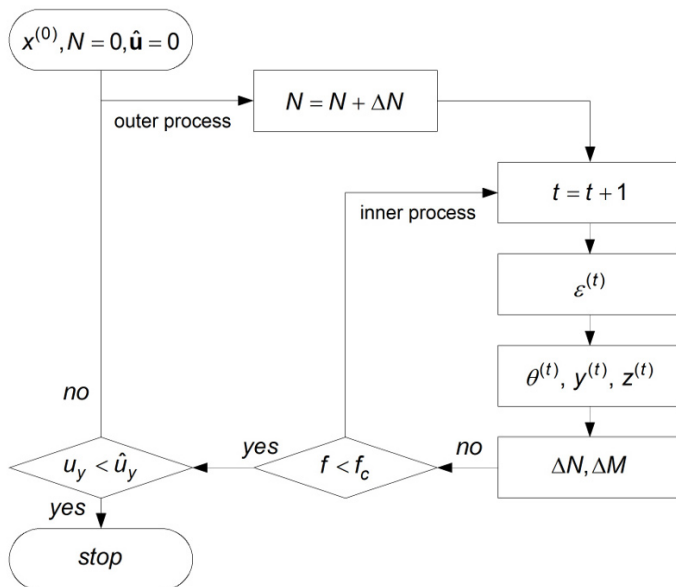


Fig. 15.18 Solution scheme. All symbols are defined in the following Section 15.10.1.

displacement \hat{u}_y , N is increased in steps and the respective deformed configurations are calculated by the inner process. As soon as the current displacement $u_y(\lambda_{\text{morph}})$ comes close to or exceeds the specified value $u_y(\hat{\lambda}_{\text{morph}})$, the outer process starts to minimize the difference between current and specified displacements.

15.10.1 Inner Process

A loop on load steps creates the data points for line-force-displacement diagrams, as Fig. 15.18 shows. The procedure starts with applying the line force N to the reference configuration $y^{(0)}(\xi_2)$ and $z^{(0)}(\xi_2)$ to calculate curvature and mid-plane strain after (15.29), angles θ after (15.32), and the deformed configuration after (15.36). At this point, the deformed configuration's stress resultants cannot be in equilibrium with the external line force N . A scalar error measure is provided with:

$$f = \int_0^{L_s} \begin{Bmatrix} \Delta N_2 \\ \Delta M_2 \end{Bmatrix}^T \begin{Bmatrix} \Delta N_2 \\ \Delta M_2 \end{Bmatrix} ds, \quad (15.40)$$

where

$$\begin{Bmatrix} \Delta N_2 \\ \Delta M_2 \end{Bmatrix} = \begin{Bmatrix} N_2^{int} \\ M_2^{int} \end{Bmatrix} - \begin{Bmatrix} N_2^{ext} \\ M_2^{ext} \end{Bmatrix}, \quad (15.41)$$

where the first term in the parentheses presents stress resultants corresponding with the laminate deformations,

$$\begin{Bmatrix} N_2^{int} \\ M_2^{int} \end{Bmatrix} = \begin{bmatrix} A_{22} & B_{22} \\ B_{22} & D_{22} \end{bmatrix} \begin{Bmatrix} \varepsilon_2^0 \\ \varepsilon_2^1 \end{Bmatrix}, \quad (15.42)$$

and the second term contains the line reactions dictated by global equilibrium. In a numerical presentation of the problem, the integral becomes a sum over all entries of the data-point arrays:

$$f = \sum_{k=1}^{n+1} f_k = \sum_{k=1}^{n+1} \begin{Bmatrix} \Delta N_2 \\ \Delta M_2 \end{Bmatrix}_k^T \begin{Bmatrix} \Delta N_2 \\ \Delta M_2 \end{Bmatrix}_k \Delta s, \quad (15.43)$$

where the curved mid-plane length L_s is subdivided into n sections of equal length Δs and the state variables are assigned to the $n + 1$ interface and end points. The plate deformations $\varepsilon_{2_k}^0$ and $\varepsilon_{2_k}^1$ completely control the deformed configuration and are therefore solution parameters of the quadratic error function, or objective, f . The Newton method minimizes the objective,

$$\varepsilon_k^{(t+1)} = \varepsilon_k^{(t)} + \Delta \varepsilon_k^{(t)}, \quad (15.44)$$

where the array ε_k contains midplane strain and bending curvature and where the improvement $\Delta \varepsilon^{(t)}$ is:

$$\varepsilon_k^{(t)} = \begin{Bmatrix} \varepsilon_2^0 \\ \varepsilon_2^1 \end{Bmatrix}_k^{(t)}, \quad \Delta \varepsilon_k^{(t)} = -(\nabla \nabla f)^{-1} \nabla f_k^{(t)}. \quad (15.45)$$

The derivatives, namely the gradient $\nabla f_k^{(t)}$,

$$\nabla f_k^{(t)} = 2 \begin{Bmatrix} \Delta N_2 \\ \Delta M_2 \end{Bmatrix}_k^{(t)T} \begin{bmatrix} A_{22} & B_{22} \\ B_{22} & D_{22} \end{bmatrix} ds, \quad (15.46)$$

and the Hesse matrix $\nabla \nabla f^{(t)}$,

$$\nabla \nabla f_k = 2 \begin{bmatrix} A_{22} & B_{22} \\ B_{22} & D_{22} \end{bmatrix}^T \begin{bmatrix} A_{22} & B_{22} \\ B_{22} & D_{22} \end{bmatrix} ds, \quad (15.47)$$

can be calculated analytically. The increments $\Delta\varepsilon_k^{(t)}$ of mid-plane strain and curvature are:

$$\Delta\varepsilon_k^{(t)} = -\varepsilon_k^{(t)} - \frac{1}{D} \begin{bmatrix} D_{22} & -B_{22} \\ -B_{22} & A_{22} \end{bmatrix} \begin{Bmatrix} N_2^{ext} \\ M_2^{ext} \end{Bmatrix}_k^{(t)}, \quad (15.48)$$

so that the Newton Method gives the up-date rule:

$$\varepsilon_k^{(t+1)} = -\frac{1}{D} \begin{bmatrix} D_{22} & -B_{22} \\ -B_{22} & A_{22} \end{bmatrix} \begin{Bmatrix} N_2^{ext} \\ M_2^{ext} \end{Bmatrix}_k^{(t)}. \quad (15.49)$$

As the line loads equilibrating external loading depend on deformations, the up-date must be improved in iterations. We find rapid convergence of this procedure up to intermediate stretch values, or deformations, above which the procedure tends to diverge. This phenomenon is generally caused by the objective function deviating too far away from a quadratic polynomial so that the minimum-point estimates of the Newton method become erroneous. The problem is mitigated by the modified Newton method employing line searches:

$$\varepsilon_k^{(t+1)} = \varepsilon_k^{(t)} + \alpha \Delta\varepsilon_k^{(t)} \quad (15.50)$$

where α is the step length minimizing f along the search direction $\Delta\varepsilon_k^{(t)}$.

15.10.2 Outer Process

In order to let the actual deformed length $y_B^{(k)}$ converge against the specified value \hat{y}_B , we use the interval section method which is based on the rule of proportion:

$$N^{(k+1)} = N^{(k-1)} + \left(N^{(k)} - N^{(k-1)} \right) \frac{\left(\hat{y}_B - y_B^{(k-1)} \right)}{\left(y_B^{(k)} - y_B^{(k-1)} \right)} \quad (15.51)$$

The updated length $y_B^{(k+1)}$ should be closer to the specified stretch than the previous values:

$$\left| \Delta y_B(N^{(k+1)}) \right| < \min \left(\left| \Delta y_B^{(k-1)} \right|, \left| \Delta y_B^{(k)} \right| \right), \quad (15.52)$$

where

$$\Delta y_B(N^{(k+1)}) = y_B(N^{(k+1)}) - \hat{y}_B; \quad \Delta y_B^{(k)} = y_B^{(k)} - \hat{y}_B. \quad (15.53)$$

If condition (15.52) applies, the line force N^{k+1} replaces either N^k or N^{k-1} depending on which of the two leads to greater deviation of the actual stretch away from its specified value.

$$\Delta y_B^{(k-1)} > \Delta y_B^{(k)} \begin{cases} \text{true} \rightarrow N^{(k-1)} = N^{(k+1)} \\ \text{false} \rightarrow N^{(k)} = N^{(k+1)} \end{cases} \quad (15.54)$$

15.11 Morphing Simulations

15.11.1 Material, Laminates, and Reference Shape

The sample problem uses a unidirectional laminate of thickness $t = 1$ mm made from prepregs T300/epoxy where Table 15.1 shows relevant material properties. The samples include a symmetric laminate $[90]$ and an unsymmetric one $[90, 0_2]$, both of thickness $t = 1$ mm. The laminates are formed into corrugations with periodic length $P = 100$ mm and amplitude $c = 93.3$ mm.

15.11.2 Deformed Configurations

Fig. 15.19 shows plots of the deformed shapes under the specified displacements

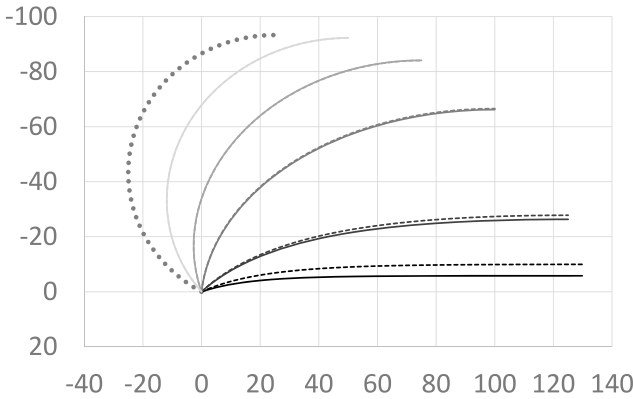


Fig. 15.19 Reference and morphed shapes of corrugated laminates $[90, 0_2]$ (solid lines) and $[90_3]$ (dashed lines) with maximum corrugation amplitude; stretches: 2, 3, 4, 5, and 5.2.

mentioned in the figure caption. It appears that the influence of laminate design increases at higher stretches where the line force gains significance over the line moment. The strain-bending coupling of the unsymmetric laminate then causes higher deflections. For verifying the results of the analytical model, the deformations of the corrugated laminate with symmetric layup, as shown in Fig. 15.19 have also

been simulated by using a commercial FEM program (ANSYS, 2017), see Fig. 15.20. The curved length of the quarter-unit-cell model is meshed with 100 two-

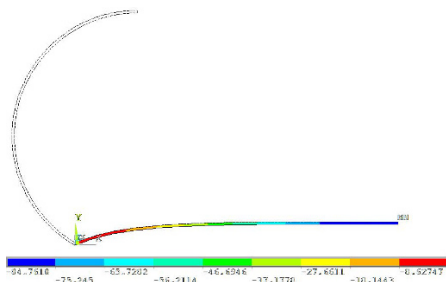


Fig. 15.20 Deformed configuration for the symmetric laminate obtained with a commercial FEM program

dimensional finite elements with quadratic shape functions for mapping plain strain problems. Under a specified displacement at point B of \hat{u}_y the FEM simulation yields a position $z_B = -8.54$ mm whereas the present analytical model evaluates $z_B = -8.48$ mm. The relative deviation between the two displacements, where the FEM result is used as reference, is -0.7% . If the vertical displacement is considered rather than the position, the relative deviation is one order of magnitude smaller.

15.11.3 Stretch-Line-Force Diagrams

The observation, that at higher stretches the line force gains a more significant role on the deformations, is corroborated with the knee-shape characteristic of global line-force-stretch diagrams shown in Fig. 15.21(a) where the knee-shape becomes more pronounced for thinner wall thickness. Fig. 15.21(b) shows the influence of corrugation amplitude c at the same thickness $t = 1$ mm. The diagrams indicate that not only the stretch limits reduce quickly but also that the average force required to approach the respective stretch limits increase significantly with decreasing corrugation amplitude.

15.12 Discussion

It can be seen from Fig. 15.19 that, for the relatively moderate stretch value $\lambda = 2$ of a high-amplitude corrugated laminate, the displacement of material points towards the neutral plane of the corrugated laminate is small, so that the reduction of the cross-sectional bending moment of inertia remains small as well. Considering the

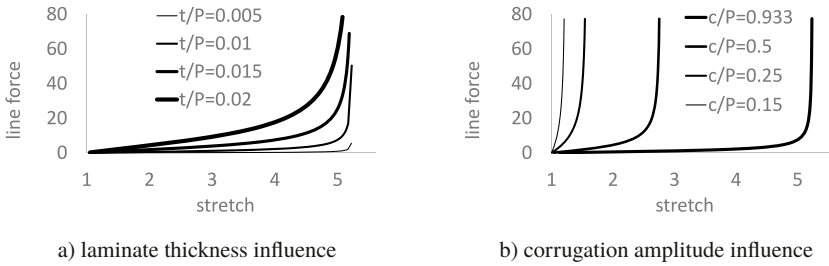


Fig. 15.21 Influence of laminate thickness (a) and corrugation amplitude (b) on force-stretch diagrams

potential application as a flexible part embedded in wing skin, the high-amplitude corrugated laminate could also play the role of a local wing-skin stiffener where the bending stiffness contribution remains unaffected within moderate morphing stretches. In addition to its mechanical advantages, the high-amplitude corrugation shape, where the laminate almost touches itself, causes less aerodynamic roughness than lower amplitudes (Thill et al, 2010a), where the sketch of a wing skin with integrated flexible-skin section shown in Fig. 15.1 gives a visual impression.

Other advantages of the high-amplitude corrugated laminate consisting of circular segments is that bending curvature is smaller than for lower amplitudes or other corrugation shapes (Thurnherr et al, 2016c) and, by choosing thickness-to-shape-curvature ratios small enough, bending stresses can be kept below values critical for fatigue strength. Moreover, there is no need to fully utilize maximum morphing stretches of high-amplitude corrugated laminates: at stretch $\lambda = 2$ (corresponds with 100% structural strain of the flexible-skin section) the deformed shape retains much of the bending moment of inertia of the reference shape and actuation force as well as material strains remain small.

15.13 Conclusion

This study has shown that mold-less forming of unsymmetric laminates solves the problem of manufacturing high-amplitude corrugated laminates where the corrugation shape consist of piece-wise circular sections. Predictions of the mathematical manufacturing model agree very well with FEM simulations. The manufacturing process can be used to make corrugated laminates with integrated flat scales to produce an aerodynamically sufficiently smooth surface for application as flexible skin in morphing-wing design. Preliminary prototype and corrugated-laminate demonstrator validate the thermal-curvature predictions of the mathematical modeling. As tooling, other than necessary for making flat laminates, is not needed, the manu-

facturing method relying on thermal forming is more economic than other methods requiring molds or machinery.

A nonlinear morphing model has been developed. The model allows to instantaneously create diagrams of structural response to applied stretch or force. The deformed configuration at specified stretch shows excellent agreement with the results of commercial FEM software modeling.

Utilizing only a small part of the high stretchability of large-amplitude corrugated laminates does not change their shape characteristics significantly, so that the cross-sectional bending stiffness is maintained. All results indicate practical advantages of the high-amplitude corrugation shape consisting of circular sections over other corrugation shapes.

Acknowledgements The authors gratefully acknowledge the support of the Swiss National Science Foundation (Project No. 169468 and Grant No. 200021-169468/1). They also thank Dr. Shelly Arreguin for proof reading.

References

- Airoldi A, Fournier S, Borlandelli E, Bettini P, Sala G (2013) Design and manufacturing of skins based on composite corrugated laminates for morphing aerodynamic surfaces. *Smart Materials and Structures* 26(4):045,024
- Airoldi A, Sala G, Di Landro LA, Bettini P, Gilardelli A (2018) Composite Corrugated Laminates for Morphing Applications. In: Concilio, A, L Lecce, I Dimino, R Pecora (ed) *Morphing Wing Technologies - Large Commercial Aircraft and Civil Helicopters*, Elsevier Ltd, Politecnico di Milano, Milano, Italy, chap 9, pp 247–276
- ANSYS (2017) ANSYS® Academic Research, Release 18.2. ANSYS Inc.
- Ashraf A (2009) Method for producing a corrugated stretch laminate. US-7,501,034 B2
- Baroudi D, Giorgio I, Battista A, Turco E, Igunnov L (2019) Nonlinear dynamics of uniformly loaded elastica: Experimental and numerical evidence of motion around curled stable equilibrium configurations. *ZAMM - Zeitschrift für Angewandte Mathematik und Mechanik* 99(7):e201900,121–1–20
- Brissoulis D (1986) Equivalent Orthotropic Properties of Corrugated Sheets. *Computers & Structures* 23:129–138
- Chamis C (1983) Simplified composite micromechanics equations for hygral, thermal, and mechanical properties. In: 38th Ann. Conf. of the Society of the Plastics Industry (SPI), 7-11-Feb. 1983, Reinforced Plastics/Composites Inst., Houston, TX; U.S.A.
- Chavannas M (1962) Method of making an embossed laminated structure. US-3,026,231
- Chillara V, Dapino M (2020) Review of morphing laminated composites. *Applied Mechanics Reviews* 72(1):010,801
- Dayyani I, Shaw A, Saavedra Flores E, Friswell M (2015) The Mechanics of Composite Corrugated Structures: A Review with Applications in Morphing Aircraft. *Composite Structures* 133:358–380
- Donnecker P, Varholak Jr N, Schmitz M, Goodridge H, Lauder J, Skaggs K (1999) Method for fabricating a corrugated composite channel. US-5,882,462
- Filipovic D, Kress G (2018) A planar finite element formulation for corrugated laminates transverse shear force. *Composite Structures* 201:958–967
- Filipovic D, Kress G (2019) Manufacturing method for high-amplitude corrugated thin-walled laminates. *Composite Structures*

- Fischer F, Beyrle M, Thellmann AH, Endrass M, Stefani T, T G, Kupke M (2017) Corrugated composites: Production-integrated quality assurance in carbon fiber reinforced thermoplastic sine wave beam production. *Advanced Manufacturing: Polymer & Composites Science* 3(1):10–20
- Fournier S, Airoidi A, Borlandelli E, Sala G (2013) Flexible composite supports for morphing skins. In: AIDAA Napoli XXII, Napoli, XXII Conference of Italian Association of Aeronautics and Astronautics, Naples, Italy
- Ghabezi P, Golzar M (2013) Mechanical analysis of trapezoidal corrugated composite skins. *Applied Composite Materials* 20(4):341–353
- Hoang S (2017) Factors affecting the properties of composites made by 4d printing (moldless composite manufacturing). *Advanced Manufacturing: Polymer & Composites Science* 3(3):101–109
- Hyer M (1982) The room-temperature shapes of four-layer unsymmetric cross-ply laminates. *J Composite Materials* 16:318
- Johnson W, Welsh R (1978) Sine wave beam web and method of manufacture. US-4,084,029
- Jones R (1975) *Mechanics of Composite Materials*. Hemisphere Publishing Corporation
- Khoo Z, Teoh J, Liu Y, Chua C, Yang S, An J, Leong K, Yeong W (2015) 3d printing of smart materials: A review on recent progresses in 4d printing. *Virtual and Physical Prototyping* 10(3):103–122
- Kress G, Filipovic D (2019) An analytical nonlinear morphing model for corrugated laminates. *Curved and Layered Structures* 6:56–66
- Kress G, Winkler M (2009) Honeycomb sandwich residual stress deformation pattern. *Composite Structures* 89:294–302
- Kress G, Winkler M (2010) Corrugated laminate homogenization model. *Composite Structures* 92(3):795–810
- Kress G, Winkler M (2011) Corrugated laminate analysis: A generalized plane strain problem. *Composite Structures* 93(5):1493–1504
- Lemelson J (1970) Composite material, apparatus and methods for producing same. US-3,523,055
- Moro A, Filipovic D, Kress G, Winkler M (2020) Thin-shell-theory solutions for the static structural response of circular-sections shaped corrugated laminates. *Composite Structures* 236: 111739
- Nguyen-Minh N, Tran-Van N, Bui-Xuan T, Nguyen-Thoi T (2018) Free vibration analysis of corrugated panels using homogenization methods and a cell-based smoothed mindlin plate element (cs-min3). *Thin-Walled Structures* 124:184–201
- Nguyen-Minh N, Tran-Van N, Bui-Xuan T, Nguyen-Thoi T (2019) Static analysis of corrugated panels using homogenization models and a cell-based smoothed mindlin plate element (cs-min3). *Frontiers of Structural Civil Engineering* 13(2):251–272
- Panichelli P, Airoidi A, Quaranta G, Sala G (2015) Morphing composite structures for adaptive high lift devices. In: *Proceedings of the 6th International Conference on Mechanics and Materials in Design*, Ponta Delgada, Portugal, pp 26–30
- Park KJ, Jung K, Kim YW (2016) Evaluation of homogenized effective properties for corrugated composite panels. *Composite Structures* 140:644–654
- Ren H, Zhu W, Wang D, Fan (2016) A nonlinear planar beam formulation with stretch and shear deformations under end forces and moments. *International Journal of Non-Linear Mechanics* 85:126–142
- Schmitz A, Horst P (2014) Bending deformation limits of corrugated unidirectionally reinforced composites. *Composite Structures* 107:103–111
- Soltani Z, Kordkheili S, Kress G (2019) Experimental and numerical study of geometrically nonlinear behavior of corrugated laminated composite shells using a nonlinear layer-wise shell formulation. *Engineering Structures* 184:61–73
- Spagnuolo M, Andreus U (2019) A targeted review on large deformations of planar elastic beams: Extensibility, distributed loads, buckling and post-buckling. *Mathematics and Mechanics of Solids* 24:258–280
- Thill C, Etches J, Bond I, Potter K, Weaver P (2007) Corrugated composite structures for aircraft morphing skin applications. In: *18th International Conference of Adaptive Structures and Technologies*, Ottawa, Ontario, Canada

- Thill C, Downsborough J, Lai S, Bond I, Jones D (2010a) Aerodynamic study of corrugated skins for morphing wing applications. *Aeronautical Journal* 3407:237–244
- Thill C, Etches JA, Bond IP, Potter KD, Weaver PM (2010b) Composite corrugated structures for morphing wing skin applications. *Smart Materials and Structures* 19(12):124,009
- Thill C, Etches JA, Bond IP, Potter KD, Weaver PM, Wisnom MR (2010c) Investigation of trapezoidal corrugated aramid/epoxy laminates under large tensile displacements transverse to the corrugation direction. *Composites Part A: Applied Science and Manufacturing* 41(1):168–176
- Thurnherr C, Mirabito Y, Kress G, Ermanni P (2016a) Highly corrugated laminates deflection under uniform pressure. *Composite Structures* 154:31–38
- Thurnherr C, Ruppen L, Kress G, Ermanni P (2016b) Interlaminar stresses in corrugated laminates. *Composite Structures* 140:296–308
- Thurnherr C, Ruppen L, Kress P, Ermanni P (2016c) Non-linear stiffness response of corrugated laminates in tensile loading. *Composite Structures* 157:31–38
- Winkler M, Kress G (2010) Deformations limits for corrugated cross-ply laminates. *Composite Structures* 92(6):1458–68
- Xia Y, Friswell M (2011) Equivalent models of corrugated laminates for morphing skins. *Active Passive Smart Struct Integr Syst* 7977(797711-79711-0)
- Xia Y, Flores E, Friswell M (2012) Equivalent models of corrugated panels. *Int J Solids Struct* 49(13):1453–62
- Xia Y, Bilgen O, Friswell M (2014) The effects of corrugated skins on aerodynamic performances. *J Intell Mater Syst and Struct* 25(7):786–794
- Yokozeki T, Takeda SI, Ogasawara T, Ishikawa T (2006) Mechanical properties of corrugated composites for candidate materials of flexible wing structures. *Composites Part A: Applied Science and Manufacturing* 37(10):1578–1586

Part III
Applications of Nonlinear Dynamics



Chapter 16

An FE-BE Method for the Hydroelastic Vibration Analysis of Plates and Shells Partially in Contact with Fluid

I. Tugrul Ardic, M. Erden Yildizdag, and Ahmet Ergin

Abstract In this study, a combined finite element (FE)–boundary element (BE) method is presented to investigate the dynamic characteristics of shell and plate structures in contact with fluid. The numerical procedure consists of two parts. In the first part, the dynamic characteristics of structures are obtained under in-vacuo condition by using the finite element method. Then, in the second part, fluid-structure interaction effects are computed in terms of generalized added mass coefficients by using the boundary element method. In analyses, surrounding fluid is assumed ideal, i.e. inviscid, incompressible and irrotational, in the context of linear hydroelasticity theory. In order to show the applicability of the proposed method, the dynamic characteristics of two different structures —a vertical rectangular plate in contact with fluid on one side and a horizontal cylindrical shell partially filled with fluid— are investigated and compared with the results obtained with a commercial software, ANSYS.

16.1 Introduction

Vibration is one of the most important phenomena in engineering, and a broad range of studies investigating different aspects of vibrating structures can be found in literature (see, e.g., Alessandrini et al, 2005; Giorgio and Del Vescovo, 2019, 2018; Baroudi et al, 2019; Giorgio et al, 2017; Barchiesi et al, 2018; Abd-alla et al,

I. T. Ardic, M. E. Yildizdag, A. Ergin

Department of Naval Architecture and Ocean Engineering, Istanbul Technical University, Maslak, 34469, Istanbul, Turkey

e-mail: ardic@itu.edu.tr, yildizdag@itu.edu.tr, ergina@itu.edu.tr

M. E. Yildizdag

International Research Center for the Mathematics and Mechanics of Complex Systems, University of L'Aquila, Italy

e-mail: yildizdag@itu.edu.tr

2017; Cazzani et al, 2018; Bersani et al, 2016). Particularly, dynamic interaction between structures and their surrounding fluid media is of great concern in numerous engineering problems, e.g. vibration of water retaining structures (i.e. dam, storage tank, etc.) under earthquake loading, design of internal structures of nuclear reactors, structural designs in aerospace and shipbuilding industries. For a structure in contact with a fluid of comparable density, the presence of the fluid strongly affects the dynamic response behavior of the structure. This is one of the complex engineering problems, involving the determination of reactive forces due to induced pressure at fluid-structure interface as a result of transferring structural vibrations into fluid. As a special engineering discipline, hydroelasticity is known as a branch of science which is, as expressed in Bishop and Price (1979), concerned with the motion of deformable bodies through liquids.

Shells and plates have a wide range of applications as structural components in shipbuilding, aerospace and petrochemical industries. Therefore, accurate estimation of induced fluid loading on vibrating plates and shells is of practical importance to assess the reliability of these structural components under different circumstances. For a freely vibrating plate or shell, effect of interaction forces on the dynamic characteristics of the structure is relatively weak when the density of surrounding fluid is low, such as air. However, when the vibrating structure is in contact with a fluid of comparable density, such as water, fluid loading significantly alters the dynamic characteristics of the structure from those in vacuo. Therefore, motion of both the structure and fluid is strongly coupled.

Hydroelastic vibration of plates and shells has been extensively studied by many researchers. One of the pioneering studies in this field was presented by Warburton (1961). In his study, dynamic analysis of an infinitely long cylindrical shell submerged into infinitely deep fluid medium and/or filled with liquid was carried out analytically under the assumption that the mode shapes do not change both in air and when in contact with water. A fundamental work on fluid-coupled thin plates was performed experimentally by Lindholm et al (1965), with the aim of obtaining the wet dynamic characteristics (wet natural frequencies and corresponding wet mode shapes) of clamped rectangular plates submerged into fluid. In the study, the experiments were conducted to determine the wet dynamic characteristics of rectangular plates for different aspect ratios and submergence depths. Meyerhoff (1970) obtained the dynamic characteristics of a thin rectangular plate submerged in an incompressible and inviscid fluid by using dipole singularities to model fluid effects.

A number of analytical and semi-analytical methods have been conducted to predict elastic response of cylindrical shells in contact with fluid. For example, Chiba et al (1984a,b) and Goncalves and Ramos (1996) investigated the dynamic characteristics of partially liquid-filled, and clamped vertical cylindrical shells by using the Galerkin method. In both studies, cylindrical shells are clamped at the rigid bottom surface. Askari and Jeong (2010) studied a slightly different problem that a vertical cylindrical shell is clamped at the upper end and free at the bottom edge, and the dynamic characteristics of the fluid-coupled system was extracted by using the Rayleigh-Ritz method. Jeong and Lee (1996) carried out an analytical study based on Fourier series expansion to obtain natural frequencies of both partially liquid-

filled and partially submerged circular cylindrical shells. Jeong (1999) applied the same methodology to investigate the dynamic characteristics of cylindrical shells concentrically or eccentrically submerged in a rigid fluid container. Implementation of the wave propagation approach to solve acoustic wave equation was first applied by Zhang (2002) to study the dynamic behavior of submerged cylindrical shells. In this context, displacement fields of cylindrical shells are defined as traveling waves. Recently, the same approach was adopted by Zhang et al (2017) to analyze the free and forced vibration characteristics of fully-submerged elliptical cylindrical shells. In these studies, fluid medium is assumed to be compressible, inviscid and irrotational, and thus, the motion is governed by the Helmholtz equation, and shells are assumed to be infinitely submerged into fluid to neglect the free surface effects. When cylindrical shells are horizontally in contact with fluid, which is a typical configuration in many engineering problems, mathematical model become rather complex due to the lack of axial symmetry. This type of problem was first studied by Amabili and Dalpiaz (1995) and Amabili et al (1996), using experimental and semi-analytical methods, respectively. In the semi-analytical study, the solution of fluid problem was obtained analytically by the method of separation of variables, applying the infinite frequency limit boundary condition on the free surface. As done in the work of Jeong and Lee (1996), the radial displacements of the shell was defined by Fourier series expansion.

On the other hand, a lot of attempts have been made to investigate the dynamic characteristics of plates in contact with fluid using analytical approaches. In earlier studies, substantial simplifications have been made for analyzing rectangular and circular plates (see, e.g., De Espinosa and Gallego-Juarez, 1984; Kwak, 1991). Robinson and Palmer (1990) performed the modal analysis of a rectangular plate floating on the free surface of a stationary fluid under the assumptions of potential theory. Amabili et al (1996) investigated the free vibration of both circular and annular plates submerged into fluid, bounded with rigid walls and the free surface, including sloshing effects. Kwak (1997) calculated NAVMI (Non-dimensional Added Virtual Mass Incremental) factors for circular plates placed in an opening on the infinite rigid wall and in contact with fluid on one side. Cho et al (2014) investigated the free vibration characteristics of both bare and stiffened panels vertically in contact with stationary fluid. In this study, the kinetic and potential energy functionals of the system were obtained by superposing the energy components of the plate and stiffener, and the displacements of the plates were represented by orthogonal polynomials with Timoshenko beam function properties. The Rayleigh-Ritz method is often used to solve plate vibration problems due to its inherent advantage of being based on very general assumptions for obtaining optimal solutions with approximation properties of the trial spaces (see Amabili et al, 1996; Meylan, 1997; Jeong, 2003; Jeong and Kim, 2009; Liao and Ma, 2016; Datta and Jindal, 2019). For example, Kwak and Yang (2013) obtained the virtual added mass matrix of a partially immersed vertical rectangular plate in elliptical coordinates by using orthogonal Mathieu functions together with the Rayleigh-Ritz method. A theoretical model was developed by Askari et al (2013) to investigate the hydroelastic vibration of circular plates immersed in fluid by using the Rayleigh-Ritz method including the free surface effects. In the study, the compatibility conditions were satisfied both at the plate-liquid interface

and between the upper and lower liquid subdomains divided by plate. Then, the total velocity potential was defined as superposition of velocity potentials induced by the free surface and deformation of the plate, and the wet mode shapes were obtained by superposition of a finite number of admissible functions selected as dry mode shapes of the plate.

For structures with complex geometries such as mono- or multi-hull vessels, aircrafts, multi-purpose offshore structures and space vehicles, it is not possible to deal with the problem by using analytical approaches. Thus, alternative computational methods have been developed for the dynamic response analysis of such complex structures under the effect of fluid environment. In earlier studies, the finite element method (FEM) was recognized as a powerful numerical tool for the solution of fluid-structure interaction problems. In this direction, Zienkiewicz and Newton (1969) developed a method to solve fluid-structure interaction problems in which fluid and structure domains are both modeled with finite elements. In their method, fluid environment is governed by the acoustic wave equation, and fluid pressure acts as fundamental unknown in the matrix equations. The main drawback in this formulation is that the matrices are not symmetric. An alternative FEM formulation, in which the fluid displacement is main unknown instead of pressure, is developed by Kalinowski (1974) to take the advantage of symmetric matrices. Following these two seminal papers, FEM has been successfully applied in hydroelastic vibration problems, dealing with various structures such as rectangular plates (Marcus, 1978; Motley et al, 2013), spherical shells (Liang et al, 2001), steelworks in fluid-carrying vessels (Volcy et al, 1980) and stiffened cylindrical shells (Hsu and Jen, 2010). One of the major drawbacks in FEM approaches is that, when the structure vibrates in an unbounded fluid environment, the entire geometry including surrounding fluid region must be discretized with finite elements. Clearly, this situation leads to a considerable increase in the number of elements and computation time. In order to overcome this difficulty, Fu and Price (1987) developed a hybrid model in which the structural problem is handled by FEM and the fluid problem by the boundary element method (BEM). Dealing with the fluid problem by using BEM, as discretization is only performed over the wetted surface of the structure, instead of the entire surrounding fluid, the method provides a substantial advantage in terms of computation time. In order to take the advantage of this approach, several researchers investigated hydroelastic vibration problems of different geometries (see Junge et al, 2011; Zheng et al, 2017). For example, Ergin and Temarel (2002) used a combined FE-BE method to calculate the free vibration characteristics of thin circular cylindrical shells in contact with internal and external liquid. In this study, it was pointed out that the mode shapes of the cylindrical shell partially in contact with fluid differed significantly from those obtained under in-vacuo condition. The same methodology adopted by Ergin and Uğurlu (2003) to calculate natural frequencies and corresponding mode shapes of clamped rectangular plates both in-vacuo and in contact with fluid. Recently, Yildizdag et al (2019) examined the hydroelastic vibration characteristics of the same plate immersed in fluid in vertical and horizontal positions, respectively, by using an isogeometric FE-BE approach.

The central theme of this study is to present a general numerical strategy for investigating natural frequencies and corresponding mode shapes of plate and shell structures partially in contact with fluid. The fluid environment is considered within the context of potential theory, i.e., fluid is inviscid, incompressible, and its motion is irrotational. By assuming that the structure vibrates with a relatively high frequency and the corresponding fluid pressure is in phase with the structural acceleration, the linearized fluid-structure interaction system is established, and generalized fluid-structure interaction forces are derived from the linear form of the Bernoulli equation. By using this linearized hydroelasticity theory, the fluid-structure interaction problem may be divided into in-vacuo (dry) and wet parts, and each problem can be analyzed separately. In the absence of any external force and structural damping, the in-vacuo part of the analysis is performed by solving the equation of motion with FEM. The surface normal velocity components of the fluid on the wetted part of the structure are obtained by applying continuity condition, in other words, the normal velocities on the wetted surface are expressed in terms of in-vacuo modal displacements. In the wet part of the analysis, BEM is applied to obtain hydrodynamic forces associated with each principle mode. The wetted surface is discretized with boundary elements (hydrodynamic panels), with a point source of constant strength placed at the geometric center of each panel. In the absence of axial flow, free surface waves and viscous effects, the interaction between the structure and fluid takes place only through the inertial effect of fluid (added mass coefficients). Therefore, the total generalized mass matrix, which is formed by merging the generalized structural mass and hydrodynamic added mass matrices, is used to solve the eigenvalue problem for the fluid-structure system. The numerical framework presented here is applied to two specific geometries: a rectangular plate and a horizontal cylindrical shell, partially in contact with fluid. In order to assess the validity and accuracy of the method, wet natural frequencies and corresponding mode shapes are compared with those obtained by commercially available finite element program, ANSYS (2013).

16.2 Mathematical Model

16.2.1 *In-Vacuo (Dry) Structural Analysis*

In the absence of structural damping and external forces, motion of the structure can be defined by

$$\mathbf{M}\ddot{\mathbf{x}}(t) + \mathbf{K}\mathbf{x}(t) = \mathbf{0} \quad (16.1)$$

where \mathbf{M} is the structural mass matrix and \mathbf{K} is the structural stiffness matrix. Here, $\ddot{\mathbf{x}}$ and \mathbf{x} are the acceleration and displacement vectors of the structure, respectively. By assuming the structure oscillates harmonically in time, a trial solution can be express as follows

$$\mathbf{x} = \mathbf{u}e^{i\omega t} \quad (16.2)$$

where \mathbf{u} represents the amplitude vector of the displacements, and ω is the frequency of oscillation. By using this expression, Eq. (16.1) takes the following form

$$(-\omega^2\mathbf{M} + \mathbf{K})\mathbf{u} = \mathbf{0}. \quad (16.3)$$

Eq. (16.3) defines an eigenvalue problem, and the non-trivial solutions of this system can only be obtained when the following condition is satisfied,

$$\det[-\omega^2\mathbf{M} + \mathbf{K}] = 0. \quad (16.4)$$

Here, Eq. (16.4) is called characteristic equation, or frequency equation. For a structure having N degrees of freedom, the characteristic equation possesses N distinct roots, $\omega_1^2, \omega_2^2, \dots, \omega_n^2$, and the square roots of these quantities represent the natural frequencies of the structure. For every frequency, ω_r , there is a corresponding vector of amplitudes, \mathbf{u}_r . The eigenvector \mathbf{u}_r corresponding to the natural frequency ω_r denotes the r -th principal modal vector.

Based on orthogonality of modal vectors, a vector space consisting of modal vectors can be formed and the response of the system can be defined by superposition of the displacements in the principal modes

$$\mathbf{U} = \sum_{r=1}^N D_r p_r(t) = \mathbf{D}\mathbf{p}(t) \quad (16.5)$$

where \mathbf{D} and \mathbf{p} are $N \times N$ modal matrix consisting of modal vectors and $N \times 1$ column vector representing the principal modes, respectively. Substituting Eq. (16.5) into Eq. (16.3) and multiplying by \mathbf{D}^T , the equation of motion is obtained in terms of the principal coordinates of the structure

$$(-\omega^2\mathbf{a} + \mathbf{c})\mathbf{p} = \mathbf{0}. \quad (16.6)$$

Here, \mathbf{a} and \mathbf{c} denote the generalized mass and stiffness matrices, respectively, and they are $\mathbf{a} = \mathbf{D}^T\mathbf{M}\mathbf{D}$ and $\mathbf{c} = \mathbf{D}^T\mathbf{K}\mathbf{D}$, respectively.

One of the useful and important features of modal vectors is that they are orthogonal. This is to say that:

$$\begin{aligned} \mathbf{u}_s^T \mathbf{K} \mathbf{u}_r &= 0 && \text{if } r \neq s, \\ \mathbf{u}_s^T \mathbf{K} \mathbf{u}_r &= \omega_r^2 a_{rr} && \text{if } r = s, \end{aligned}$$

and

$$\begin{aligned} \mathbf{u}_s^T \mathbf{M} \mathbf{u}_r &= 0 && \text{if } r \neq s, \\ \mathbf{u}_s^T \mathbf{M} \mathbf{u}_r &= a_{rr} && \text{if } r = s. \end{aligned}$$

16.2.2 Wet Analysis

16.2.2.1 Formulation of the Fluid Problem

By assuming the fluid is ideal, i.e. inviscid and incompressible, and its motion is irrotational, there exists a fluid velocity vector, $\mathbf{v}(x, y, z)$, defined as the gradient of the velocity potential function, $\phi(x, y, z)$, satisfies the Laplace's equation,

$$\nabla^2 \phi(x, y, z) = 0. \quad (16.7)$$

For a system under fluid-structure interaction effects, the Laplace equation defines a boundary value problem. Therefore, boundary conditions must be defined over the entire wetted surface of the elastic body and also on the free surface. There is no fluid transfer in the direction perpendicular to the wetted surface of the elastic structure. As a result, the normal fluid velocity must be equal to the normal velocity on the structure and this condition for the r -th modal vibration of the elastic structure in contact with a quiescent fluid can be expressed as

$$\frac{\partial \phi_r}{\partial \mathbf{n}} = \mathbf{u}_r \cdot \mathbf{n} \quad \text{on } S_w. \quad (16.8)$$

Here, \mathbf{n} is the unit normal vector on the wetted surface, S_w , and \mathbf{u}_r is the r -th modal displacement vector of the median surface of the structure. Furthermore, it is assumed that the structure vibrates at relatively high frequencies; thus, the effect of free surface waves due to the modal distortions of the structure is neglected in the mathematical model. Thus, the free surface boundary condition is simplified and expressed as follows

$$\phi_r = 0, \quad \text{on the free surface.} \quad (16.9)$$

In this study, the free surface boundary condition given in Eq. (16.9) is satisfied by using the image method (Kito, 1970). For this purpose, an imaginary surface is introduced by mirroring the wetted part of the structure by taking the free surface as mirror plane, and the modal displacements over the wetted surface are also mirrored, as described in Fig. 16.1. Hence, by utilizing the image method, the fluid-structure interaction problem is reduced to classical Neumann problem.

16.2.2.2 Numerical Evaluation of Perturbation Potential

The boundary integral equation formulation for a three-dimensional inviscid flow, due to time-harmonic oscillating structure, can be expressed by unknown source strength, ϕ^* , over the wetted and image surfaces.

$$c\phi(P) = \iint_{S_w+S_i} q(Q)\phi^*(P, Q) ds - \iint_{S_w+S_i} \phi(Q)q^*(P, Q) ds \quad (16.10)$$

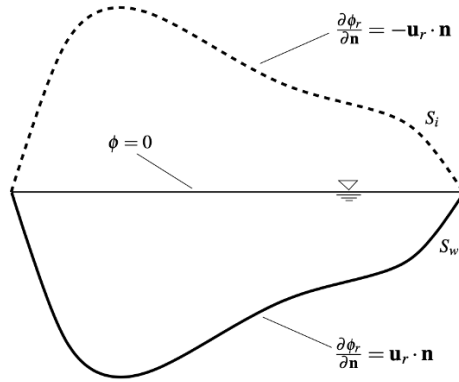


Fig. 16.1 Wetted surface and its image.

where ϕ^* is the fundamental solution for the velocity potential. Here, c is a space-angle constant and it is 0.5 for constant-strength source panels. The integral equation, Eq. (16.10), allows us to calculate unknown velocity potential $\phi(Q)$ both over the wetted boundary and inside the fluid domain when the flux $q(Q)$ is known. In this equation, Q and P represent the field and load points on the wetted and imaginary surfaces, respectively, and $S_w + S_i$ denotes the total wetted and imaginary surfaces. The fundamental solution of the Laplace operator, ϕ^* , and the cartesian components of its gradient, q^* , are given for 3-D case, respectively, as

$$\phi^*(P, Q) = \frac{1}{4\pi r}, \tag{16.11}$$

$$q_x^* = -\frac{r_{,x}}{4\pi r^2}, \quad q_y^* = -\frac{r_{,y}}{4\pi r^2}, \quad q_z^* = -\frac{r_{,z}}{4\pi r^2} \tag{16.12}$$

where r is the Euclidean distance,

$$r = \sqrt{(x_Q - x_P)^2 + (y_Q - y_P)^2 + (z_Q - z_P)^2}, \tag{16.13}$$

between the source and field points. Here, $r_{,x}$, $r_{,y}$ and $r_{,z}$ are the projections of the Euclidean distance, r , on the x , y and z axes, respectively, and expressed as follows

$$r_{,x} = \frac{x_Q - x_P}{r}, \quad r_{,y} = \frac{y_Q - y_P}{r}, \quad r_{,z} = \frac{z_Q - z_P}{r}. \tag{16.14}$$

The integral equation in Eq. (16.10) is a Fredholm equation of the second kind, and it must be satisfied over the wetted and imaginary surfaces of the elastic body. This equation can be numerically solved by dividing the wetted and imaginary surfaces of the structure into hydrodynamic panels, and the flux and unknown velocity potential are taken as constant over each panel. In this framework, the numerical solution of Eq. (16.10) is satisfied only at the geometric center of each panel. Therefore,

the surface integrals in Eq. (16.10) may be written as the sum of integrals over N constant-strength quadrilateral panels

$$\frac{1}{2}\phi_i = - \sum_{j=1}^N q^* \phi_j + \sum_{j=1}^N \phi^* q_j. \quad (16.15)$$

In Eq. (16.15), it is assumed that all q_j values are obtained from the in-vacuo (dry) analysis (each column of the matrix \mathbf{D} is defined in Eq. (16.5)), and therefore, the corresponding unknown source strengths at each panel, ϕ_j , are calculated from the solution of Eq. (16.15) for each principal mode shape.

16.2.2.3 Generalized Fluid-Structure Interaction Forces

Generalized fluid-structure interaction forces are calculated by using the pressure distribution on the wetted surface, obtained by solving the potential flow problem. The r -th component of the generalized fluid-structure interaction force due to k -th modal vibration can be obtained by using the following equation

$$Z_{rk} = \iint_{S_w} P_k \mathbf{u}_r \cdot \mathbf{n} ds. \quad (16.16)$$

The fluid pressure acting on the wetted surface of the structure due to the k -th modal vibration can be calculated using the linearized form of the Bernoulli equation,

$$P_k = \omega^2 \rho \phi_k. \quad (16.17)$$

Thus, the r -th component of the generalized fluid-structure interaction force amplitude due to the k -th modal vibration takes the following form

$$Z_{rk} = \iint_{S_w} (\omega^2 \rho \phi_k) \mathbf{u}_r \cdot \mathbf{n} ds, \quad (16.18)$$

and then the generalized added mass term, A_{rk} , can be expressed as follows

$$A_{rk} = \frac{\rho}{\omega^2} \iint_{S_w} \omega^2 \phi_k \mathbf{u}_r \cdot \mathbf{n} ds. \quad (16.19)$$

If the k -th principal coordinate is in the form of $p_k(t) = p_k e^{i\omega t}$, then the r -th component of the generalized fluid-structure interaction force can be written as

$$Z_{rk} = A_{rk} \omega^2 p_k e^{i\omega t} = -A_{rk} \ddot{p}_k. \quad (16.20)$$

16.2.2.4 Calculation of Wet Frequencies and Mode Shapes

Fluid-structure interaction forces acting on a freely vibrating structure in the vicinity of a free surface vary with frequency. In this study, it is assumed that the structure vibrates with a relatively high frequency, thus the generalized added mass is constant and independent of vibration frequency. The generalized equation of motion may therefore be written as

$$[-\omega^2(\mathbf{a} + \mathbf{A}) + \mathbf{c}] \mathbf{p}_0 = \mathbf{0} \quad (16.21)$$

where \mathbf{c} and \mathbf{a} denote the generalized structural stiffness and generalized mass matrices, respectively. The $M \times M$ matrix \mathbf{A} represents the frequency-independent generalized added mass matrix. By solving the eigenvalue problem expressed in Eq. (16.21), one can obtain each wet natural frequency, ω_k , and corresponding eigenvector $\mathbf{p}_{0k} = \{p_{k1}, p_{k2}, \dots, p_{kM}\}$. The wet mode shapes of the structure can be defined as superposition of the dry modes, where the contribution of the j -th mode is represented by p_{kj} ,

$$\mathbf{q}_k(x, y, z) = \sum_{j=1}^M \mathbf{u}_j(x, y, z) p_{kj} \quad (16.22)$$

where M denotes the number of modes considered in the analysis. It should be noted that the fluid-structure interaction forces associated with the inertial effect of the fluid do not have the same spatial distribution as those of the in-vacuo modal forms. As a consequence, this produces hydrodynamic coupling between in-vacuo modes.

16.3 Numerical Examples

In this section, the presented FE-BE procedure is applied to two different structures (rectangular plate and cylindrical shell) in contact with fluid, in order to demonstrate the applicability of the method. In the numerical examples, flat shell elements are adopted to conduct the in-vacuo analyses. The FEM formulation of flat shell elements used in this study can be found in Appendix.

16.3.1 Vertical Rectangular Plate in Contact with Fluid on One Side

The proposed mathematical model is first applied to a rectangular plate partially in contact with fluid on one side and clamped along its all edges (see Fig. 16.2). The rectangular plate has the length $\ell = 2.0$ m, height $h = 1.4$ m and thickness $t = 10$

mm. The plate is made of steel with the following material properties: Young's Modulus, $E = 206 \text{ GPa}$, Poisson's Ratio, $\nu = 0.3$, and density, $\rho_s = 7850 \text{ kg/m}^3$. The density of surrounding fluid is $\rho_f = 1025 \text{ kg/m}^3$, and d denotes the submerging depth.

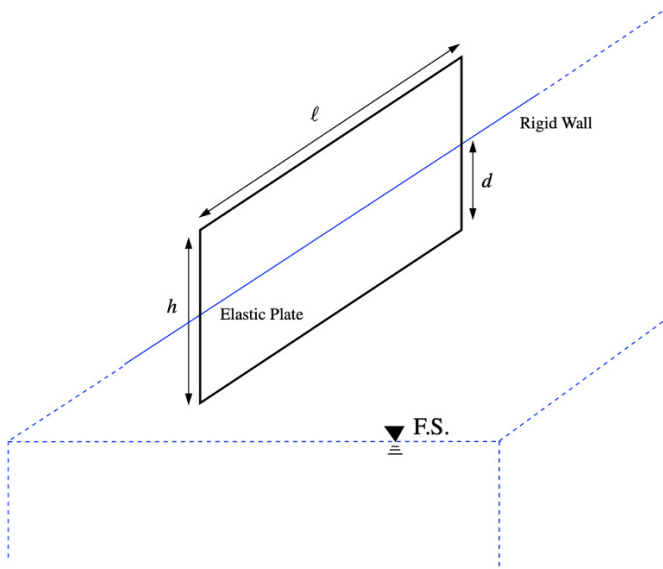


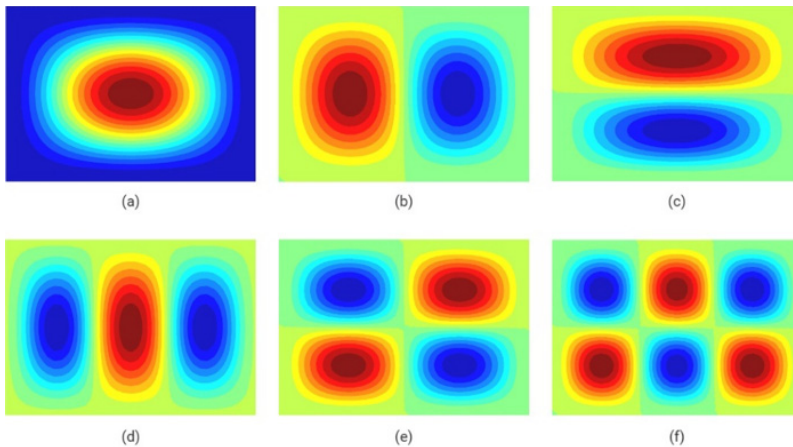
Fig. 16.2 Vertical cantilever plate in contact with fluid on one side.

In the first part of the analysis (i.e. dry analysis), natural frequencies and corresponding mode shapes under in-vacuo condition are obtained by solving the equation of motion. The results obtained by the present method are compared with those calculated using a commercial finite element software, ANSYS. In order to show the convergence of the first six natural frequency values, the structure was discretized by 300, 588, and 972 elements, respectively. The calculated frequency values are shown in Table 16.1 for the first six dry modes. The presented results clearly show that the differences between the calculated values in the 2nd and 3rd idealizations are negligible.

Moreover, the first six in-vacuo mode shapes of the rectangular plate are shown in Fig. 16.3. As expected, the complexity of the modal configurations increases with increasing frequency. These mode shapes may be classified into two groups, as symmetric and antisymmetric with respect to the axis passing through the longitudinal center of the plate. With this respect, the 1st, 3rd, 4th and 6th modes are symmetric, and the 2nd and 5th modes are antisymmetric. In Table 16.2, S and A stand for symmetry and antisymmetry, respectively.

Table 16.1 Convergence of dry natural frequencies (Hz).

| Mode | This study | | | ANSYS 7500 El. |
|-------|------------|---------|---------|-------------------|
| | 300 El. | 588 El. | 972 El. | |
| 1 (S) | 34.69 | 34.74 | 34.76 | 34.78 |
| 2 (S) | 55.27 | 55.43 | 55.49 | 55.56 |
| 3 (A) | 83.65 | 83.77 | 83.83 | 83.83 |
| 4 (S) | 89.77 | 90.04 | 90.16 | 90.25 |
| 5 (A) | 102.21 | 102.68 | 102.87 | 103.06 |
| 6 (S) | 133.96 | 124.01 | 135.72 | 135.72 |

**Fig. 16.3** In-vacuo mode shapes of rectangular plate: (a) 1st mode (34.76 Hz); (b) 2nd mode (55.49 Hz); (c) 3rd mode (83.83 Hz); (d) 4th mode (90.16 Hz); (e) 5th mode (102.87 Hz); (f) 6th mode (135.29 Hz).

In the second part of the analysis (i.e. wet analysis), wet natural frequencies and corresponding mode shapes of the rectangular plate are obtained for four different submerging ratios, namely $d/h = 0.25, 0.50, 0.75, 1.00$. The results obtained by the proposed FE-BE procedure are compared with those obtained by ANSYS. In ANSYS, the rectangular plate is discretized with four-node quadrilateral SHELL181 elements, and the surrounding fluid domain is modeled by FLUID30 elements. The density and sonic velocity are 1025 kg/m^3 and 1507 m/s , respectively. As the structure vibrates in high-frequency region, the infinite frequency limit condition is imposed on the free surface of fluid ($\phi = 0$).

In Table 16.2, a convergence study is presented for the wet frequencies obtained by using the proposed FE-BE procedure. In this study, for each submerging depth ratio (d/h), three different panel idealizations are adopted, and the results are compared with those obtained using ANSYS. The number of hydrodynamic panels adopted over the wetted surface, respectively, is 145, 344 and 580 for $d/h = 0.25$; 290,

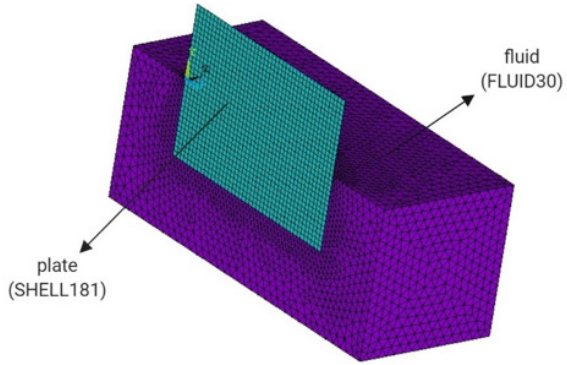


Fig. 16.4 ANSYS model of vertical plate in contact with fluid ($d/h = 0.5$).

645 and 1160 for $d/h = 0.50$; 435, 990 and 1740 for $d/h = 0.75$; 580, 1290 and 2320 for $d/h = 1.00$. As expected, the wet natural frequencies are lower than the corresponding in-vacuo frequencies. Difference between in-vacuo and wet natural frequencies is significant for the submerging depth ratio $d/h = 1.00$. As it is observed from Table 16.2, differences between the 2nd and 3rd idealizations for all submerging depth ratios are negligible. In addition, the converged values compare perfectly well with those of ANSYS. The maximum differences between the 3rd idealization and ANSYS which correspond to the first modes are 2.4%, 1.6% and 3.7% for submerging depth ratios $d/h = 0.25, 0.50$ and 1.00 , respectively, while,

Table 16.2 Convergence of wet natural frequencies (Hz) for submerging depth ratios $d/h = 0.25, 0.50, 0.75$ and 1.00 .

| Mode | This study | | | ANSYS 881000 El. |
|-------|------------|---------|---------|---------------------|
| | 145 El. | 344 El. | 580 El. | |
| 1 (S) | 33.17 | 33.19 | 33.19 | 33.99 |
| 2 (S) | 54.19 | 54.21 | 54.22 | 54.18 |
| 3 (A) | 76.23 | 76.29 | 76.30 | 76.33 |
| 4 (S) | 87.70 | 87.71 | 87.71 | 87.71 |
| 5 (A) | 94.05 | 94.06 | 94.06 | 93.94 |
| 6 (S) | 124.09 | 124.01 | 123.96 | 123.67 |

(a) $d/h = 0.25$

| Mode | This study | | | ANSYS 938000 El. |
|-------|------------|---------|----------|---------------------|
| | 290 El. | 645 El. | 1160 El. | |
| 1 (S) | 22.66 | 22.65 | 22.63 | 22.99 |
| 2 (S) | 37.98 | 37.91 | 37.87 | 37.79 |
| 3 (A) | 61.07 | 60.92 | 60.86 | 60.51 |
| 4 (S) | 63.91 | 63.73 | 63.65 | 63.66 |
| 5 (A) | 80.37 | 80.22 | 80.16 | 80.09 |
| 6 (S) | 97.75 | 97.22 | 96.99 | 96.80 |

(b) $d/h = 0.50$

| Mode | This study | | | ANSYS 968000 El. |
|-------|------------|---------|----------|---------------------|
| | 435 El. | 990 El. | 1740 El. | |
| 1 (S) | 15.46 | 15.43 | 15.41 | 15.39 |
| 2 (S) | 28.46 | 28.37 | 28.33 | 28.21 |
| 3 (A) | 49.18 | 49.01 | 48.93 | 48.11 |
| 4 (S) | 64.64 | 64.38 | 64.26 | 64.14 |
| 5 (A) | 0.000 | 0.000 | 0.516 | 0.000 |
| 6 (S) | 83.20 | 82.69 | 82.48 | 82.38 |

(c) $d/h = 0.75$

| Mode | This study | | | ANSYS 1616500 El. |
|-------|------------|----------|----------|----------------------|
| | 580 El. | 1290 El. | 2320 El. | |
| 1 (S) | 13.28 | 13.24 | 13.22 | 12.73 |
| 2 (S) | 26.02 | 25.88 | 25.82 | 25.52 |
| 3 (A) | 42.86 | 42.53 | 42.40 | 41.56 |
| 4 (S) | 47.73 | 47.32 | 47.15 | 46.59 |
| 5 (A) | 56.56 | 56.02 | 55.80 | 55.41 |
| 6 (S) | 79.71 | 78.73 | 78.33 | 77.61 |

(d) $d/h = 1.00$

for submerging depth ratio $d/h = 0.75$, the maximum difference (1.7%) is obtained for the 3rd mode.

In Table 16.3, the generalized added mass coefficients, for submerging depth ratios $d/h = 0.25, 0.50, 0.75$ and 1.00 , are presented for the first 8 distortional mode shapes (five symmetric and three antisymmetric). The generalized added mass coefficients are scaled to a generalized mass of 1 kg m^2 . The off-diagonal terms given in the table represent the hydrodynamic coupling between in-vacuo modes. It is clear that all the coefficients increase with increasing submerging depth ratio, due to increase in wetted surface area. It can also be observed that the hydrodynamic coupling is strong between symmetric modes themselves as well as antisymmetric modes. However, the coupling between these two mode groups are negligible. In particular, strong coupling can be observed between 1st and 3rd symmetric as well as 2nd and 5th antisymmetric modes for submerging depth ratio $d/h = 0.50$. The diagonal terms are dominant compared to the off-diagonal terms, especially for submerging depth ratios 0.75 and 1.00 .

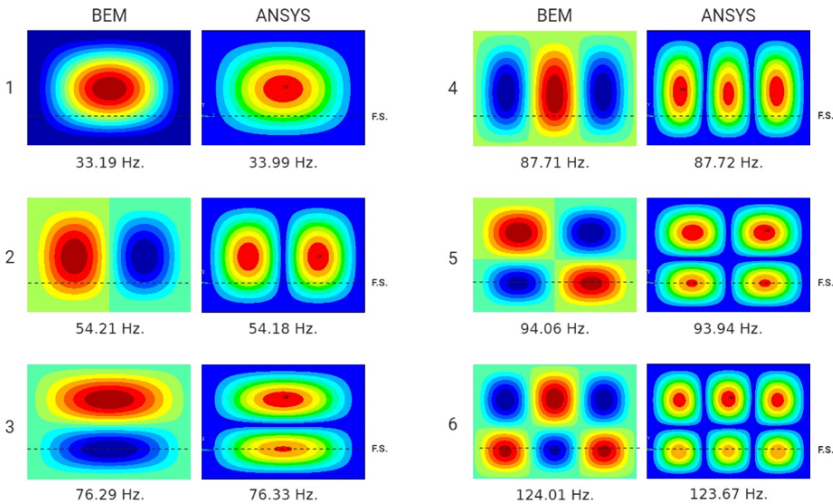


Fig. 16.5 Natural frequencies and associated modes of rectangular plate for submerging depth ratio $d/h = 0.25$.

Figs. 16.5-16.8 show the calculated wet mode shapes and wet frequencies for $d/h = 0.25, 0.50, 0.75$ and 1.00 , respectively. In order to obtain the wet mode shapes, the generalized added mass matrix is first formed by solving Eq. (16.19). Then, the eigenvalue problem expressed in Eq. (16.21) is solved for obtaining wet natural frequencies and corresponding mode shapes. A maximum number of $M = 24$ in-vacuo modes was adopted in computations.

It is clear that the differences between in-vacuo and wet mode shapes are noticeable, especially for higher submerging depth ratios (0.5 and higher). It can also be

Table 16.3 Generalized added mass coefficients (kg m^2) for rectangular plate partially submerged in fluid.

| Mode | 1 (S) | 2 (A) | 3 (S) | 4 (S) | 5 (A) | 6 (S) | 7 (A) | 8 (S) |
|-------|-------|-------|-------|-------|-------|-------|-------|-------|
| 1 (S) | 0.05 | 0.00 | 0.09 | 0.00 | 0.00 | 0.00 | 0.00 | -0.13 |
| 2 (A) | 0.00 | 0.05 | 0.00 | 0.00 | 0.09 | 0.00 | 0.00 | 0.00 |
| 3 (S) | 0.09 | 0.00 | 0.19 | 0.00 | 0.00 | 0.00 | 0.00 | -0.26 |
| 4 (S) | 0.00 | 0.00 | 0.00 | 0.05 | 0.00 | -0.09 | 0.00 | 0.01 |
| 5 (A) | 0.00 | 0.09 | 0.00 | 0.00 | 0.18 | 0.00 | 0.00 | 0.00 |
| 6 (S) | 0.00 | 0.00 | 0.00 | -0.09 | 0.00 | 0.18 | 0.00 | -0.01 |
| 7 (A) | 0.00 | 0.00 | 0.00 | 0.00 | 0.00 | 0.00 | 0.05 | 0.00 |
| 8 (S) | -0.13 | 0.00 | -0.26 | 0.01 | 0.00 | -0.01 | 0.00 | 0.36 |

(a) $d/h = 0.25$

| Mode | 1 (S) | 2 (A) | 3 (S) | 4 (S) | 5 (A) | 6 (S) | 7 (A) | 8 (S) |
|-------|-------|-------|-------|-------|-------|-------|-------|-------|
| 1 (S) | 1.11 | 0.00 | 1.24 | -0.06 | 0.00 | 0.03 | 0.00 | 0.56 |
| 2 (A) | 0.00 | 0.94 | 0.00 | 0.00 | 1.02 | 0.00 | 0.06 | 0.00 |
| 3 (S) | 1.24 | 0.00 | 1.58 | -0.11 | 0.00 | 0.09 | 0.00 | 1.02 |
| 4 (S) | -0.06 | 0.00 | -0.11 | 0.81 | 0.00 | -0.85 | 0.00 | -0.08 |
| 5 (A) | 0.00 | 1.02 | 0.00 | 0.00 | 1.27 | 0.00 | 0.10 | 0.00 |
| 6 (S) | 0.03 | 0.00 | 0.09 | -0.85 | 0.00 | 1.04 | 0.00 | 0.09 |
| 7 (A) | 0.00 | 0.06 | 0.00 | 0.00 | 0.10 | 0.00 | 0.70 | 0.00 |
| 8 (S) | 0.56 | 0.00 | 1.02 | -0.08 | 0.00 | 0.09 | 0.00 | 1.09 |

(b) $d/h = 0.50$

| Mode | 1 (S) | 2 (A) | 3 (S) | 4 (S) | 5 (A) | 6 (S) | 7 (A) | 8 (S) |
|-------|-------|-------|-------|-------|-------|-------|-------|-------|
| 1 (S) | 3.78 | 0.00 | -1.39 | 0.35 | 0.00 | -0.15 | 0.00 | 0.02 |
| 2 (A) | 0.00 | 2.77 | 0.00 | 0.00 | 0.85 | 0.00 | 0.29 | 0.00 |
| 3 (S) | -1.39 | 0.00 | 2.18 | -0.22 | 0.00 | 0.14 | 0.00 | 0.97 |
| 4 (S) | 0.35 | 0.00 | -0.22 | 2.20 | 0.00 | -0.60 | 0.00 | -0.05 |
| 5 (A) | 0.00 | 0.85 | 0.00 | 0.00 | 1.70 | 0.00 | 0.15 | 0.00 |
| 6 (S) | -0.15 | 0.00 | 0.14 | -0.60 | 0.00 | 1.41 | 0.00 | 0.09 |
| 7 (A) | 0.00 | 0.29 | 0.00 | 0.00 | 0.15 | 0.00 | 1.76 | 0.00 |
| 8 (S) | 0.02 | 0.00 | 0.97 | -0.05 | 0.00 | 0.09 | 0.00 | 1.43 |

(c) $d/h = 0.75$

| Mode | 1 (S) | 2 (A) | 3 (S) | 4 (S) | 5 (A) | 6 (S) | 7 (A) | 8 (S) |
|-------|-------|-------|-------|-------|-------|-------|-------|-------|
| 1 (S) | 5.59 | 0.00 | 0.47 | 0.70 | 0.00 | 0.12 | 0.00 | 0.86 |
| 2 (A) | 0.00 | 3.63 | 0.00 | 0.00 | 0.13 | 0.00 | 0.49 | 0.00 |
| 3 (S) | 0.47 | 0.00 | 2.94 | 0.13 | 0.00 | 0.15 | 0.00 | 0.28 |
| 4 (S) | 0.70 | 0.00 | 0.13 | 2.76 | 0.00 | 0.08 | 0.00 | 0.19 |
| 5 (A) | 0.00 | 0.13 | 0.00 | 0.00 | 2.42 | 0.00 | 0.05 | 0.00 |
| 6 (S) | 0.12 | 0.00 | 0.15 | 0.08 | 0.00 | 2.02 | 0.00 | 0.06 |
| 7 (A) | 0.00 | 0.49 | 0.00 | 0.00 | 0.05 | 0.00 | 2.12 | 0.00 |
| 8 (S) | 0.86 | 0.00 | 0.28 | 0.19 | 0.00 | 0.06 | 0.00 | 2.11 |

(d) $d/h = 1.00$

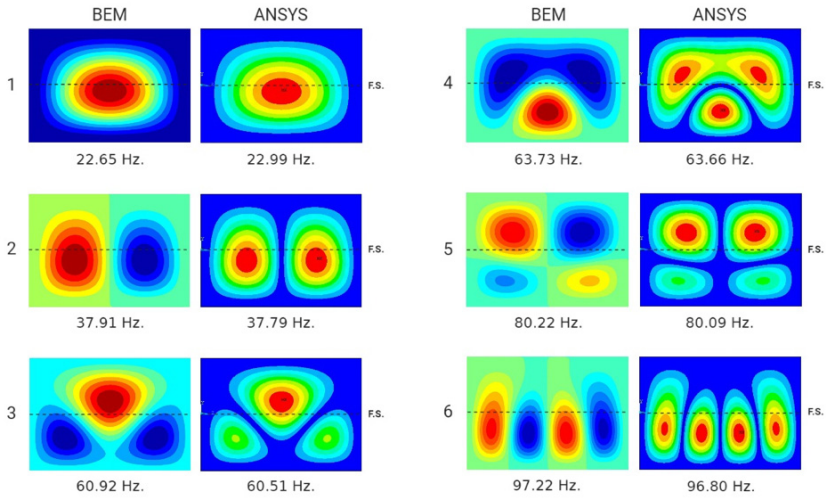


Fig. 16.6 Natural frequencies and associated modes of rectangular plate for submerging depth ratio $d/h = 0.50$.

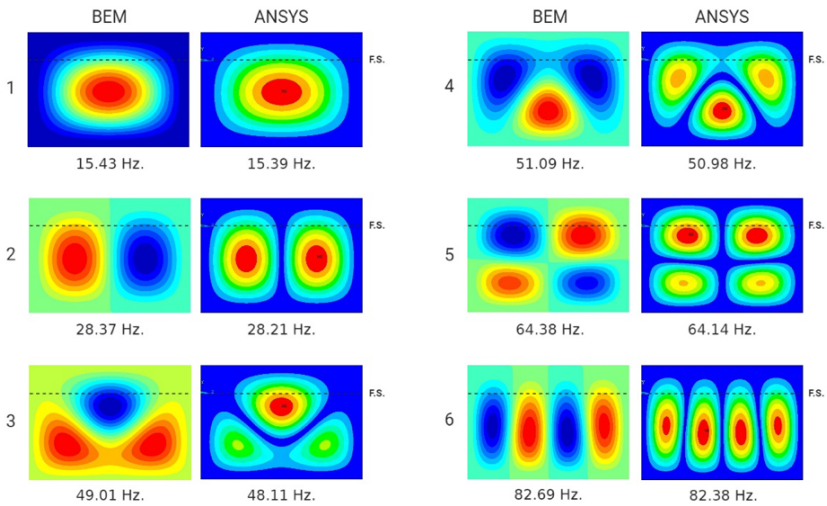


Fig. 16.7 Natural frequencies and associated modes of rectangular plate for submerging depth ratio $d/h = 0.75$.

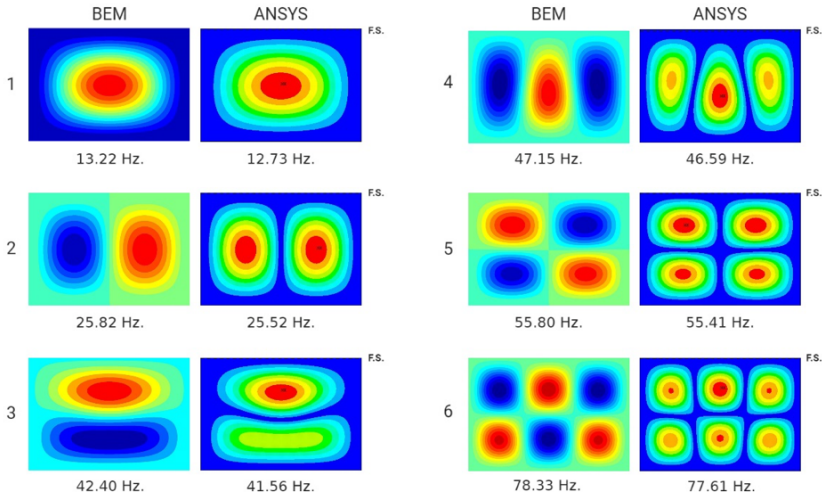


Fig. 16.8 Natural frequencies and associated modes of rectangular plate for submerging depth ratio $d/h = 1.00$.

said that the maximum difference, compared to those in vacuo, occurs for submerging depth ratios $d/h = 0.5$ and 0.75 . For all the depth ratios, changes in the first and second wet modes are insignificant, compared to the higher ones. In general these two fundamental mode shapes do not show a significant difference, compared to the corresponding dry ones, but the location of maximum displacement shift slightly in the vertical direction. It must also be realized that for all the depth ratios, the wet mode shapes preserve their symmetry or antisymmetry with respect to the vertical axis passing through the longitudinal center of the plate.

16.3.2 Horizontal Cylindrical Shell Partially Filled with Fluid

In the second numerical example, the hydroelastic vibration analysis of a horizontal cylindrical shell partially filled with fluid is considered (see Fig. 16.9). The mechanical and geometrical properties of the cylindrical shell are: Young’s modulus, $E = 206$ GPa, Poisson’s ratio, $\nu = 0.3$, mass density, $\rho_s = 7680$ kg/m³, thickness, $t = 1$ mm, length, $l = 0.664$ m, radius, $r = 0.175$ m. d denotes the filling depth of fluid, which has a density of $\rho_f = 1025$ kg/m³.

The cylindrical shell is sealed with thin circular caps at both ends. These caps are resistant to radial loads, allowing for forces acting on their normal planes. Zhang et al (2001) has emphasized that the effect of these end caps on the hydroelastic vibration of circular shells is negligible. Therefore, in the numerical analysis, it is

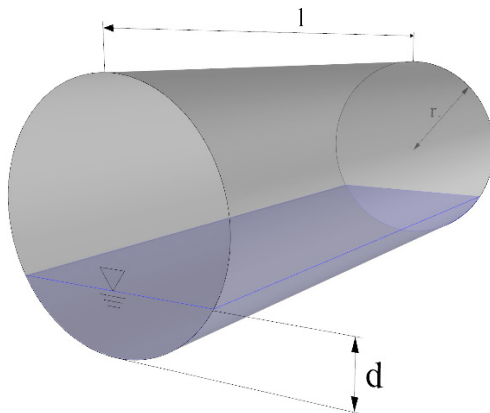


Fig. 16.9 Horizontal cylindrical shell partially filled with fluid.

assumed that the cylindrical shell is simply supported at both ends, instead of having caps at the ends.

Firstly, the in-vacuo dynamic response analysis of the cylindrical shell is carried out to obtain the in-vacuo natural frequencies and corresponding mode shapes, using the FEM formulation given in Appendix. To assess the accuracy of the obtained natural frequencies, a convergence study is carried out, and the results are compared with those obtained by ANSYS. In Table 16.4, the convergence of the first eight dry natural frequencies are presented for three different idealizations; 1900, 3470 and 7500 elements, respectively. As the number of elements increases, a monotonic convergence is observed, and the differences between the 3rd discretization and ANSYS become negligibly small. In Table 16.4, m denotes the number of half waves in the axial direction while n denotes the number of waves around the circumference.

Table 16.4 Convergence of dry natural frequencies (Hz).

| Mode (m - n) | This study | | | ANSYS |
|-----------------------|------------|----------|----------|----------|
| | 1900 El. | 3470 El. | 7500 El. | 7500 El. |
| 1-4 | 228.37 | 226.39 | 225.30 | 224.42 |
| 1-4 | 228.37 | 226.39 | 225.30 | 224.42 |
| 1-5 | 240.12 | 236.45 | 234.06 | 232.15 |
| 1-5 | 240.12 | 236.45 | 234.06 | 232.15 |
| 1-6 | 316.93 | 308.52 | 303.78 | 299.25 |
| 1-6 | 316.93 | 308.52 | 303.78 | 299.25 |
| 1-3 | 323.71 | 322.91 | 322.31 | 321.86 |
| 1-3 | 323.71 | 322.91 | 322.31 | 321.86 |

The calculated mode shapes for the first eight dry natural frequencies are shown in Fig. 16.10. As in Table 16.4 and Fig. 16.10, for each dry natural frequency, the mode shapes are obtained in pairs, satisfying the orthogonality condition. It must also be realized that the fundamental in-vacuo natural frequency does not correspond to the mode shape with the lowest number of waves around the circumference ($n = 2$). The order of modes depends on the internal strain energy and geometrical characteristics of the cylindrical shell under study.

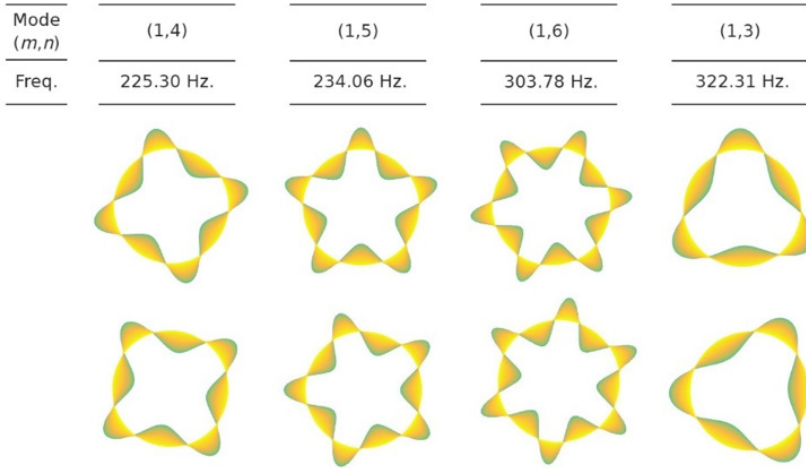


Fig. 16.10 First eight dry mode shapes of cylindrical shell.

In the second part of the analysis, the hydroelastic vibration characteristics of the cylindrical shell are investigated for three different filling depth-to-diameter ratios, $d/2r = 0.2, 0.5$ and 0.8 . In ANSYS, the cylindrical shell is discretized with four-node quadrilateral SHELL181 elements, and fluid is modeled with FLUID30 elements (see Fig. 16.11).

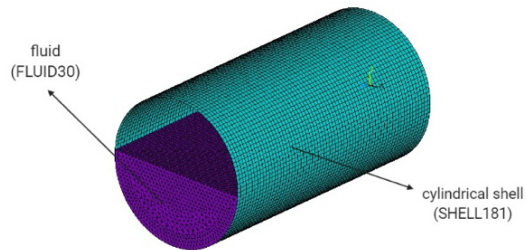


Fig. 16.11 ANSYS model of horizontal cylindrical shell partially filled with fluid ($d/2r = 0.50$).

Table 16.5 Convergence of wet natural frequencies (Hz) for filling ratios $d/2r = 0.20, 0.50$ and 0.80 .

| Mode | This study | | | ANSYS 536400 El. | Mode | This study | | | ANSYS 673400 El. |
|------|------------|----------|----------|---------------------|------|------------|----------|----------|---------------------|
| | 1350 El. | 2195 El. | 3190 El. | | | 952 El. | 1710 El. | 3752 El. | |
| 1 | 112.23 | 111.05 | 110.68 | 114.23 | 1 | 101.04 | 99.33 | 98.80 | 97.85 |
| 2 | 113.41 | 111.98 | 111.54 | 114.59 | 2 | 101.76 | 100.07 | 99.45 | 98.99 |
| 3 | 175.87 | 173.43 | 172.77 | 180.85 | 3 | 134.73 | 132.32 | 131.65 | 127.89 |
| 4 | 185.55 | 183.95 | 182.94 | 191.19 | 4 | 135.23 | 133.03 | 131.78 | 130.92 |
| 5 | 241.21 | 241.13 | 241.05 | 239.42 | 5 | 185.41 | 181.39 | 180.53 | 180.08 |
| 6 | 242.65 | 242.31 | 242.07 | 240.18 | 6 | 187.12 | 184.18 | 183.64 | 181.68 |

(a) $d/2r = 0.20$

(b) $d/2r = 0.50$

| Mode | This study | | | ANSYS 968000 El. |
|------|------------|----------|----------|---------------------|
| | 1360 El. | 2430 El. | 1740 El. | |
| 1 | 97.47 | 96.01 | 95.58 | 94.02 |
| 2 | 97.96 | 96.45 | 96.02 | 94.92 |
| 3 | 115.21 | 113.13 | 112.47 | 110.04 |
| 4 | 116.96 | 115.09 | 114.34 | 113.08 |
| 5 | 141.30 | 139.21 | 138.46 | 136.38 |
| 6 | 148.16 | 145.20 | 144.77 | 143.53 |

(c) $d/2r = 0.80$

In order to check the convergence of the wet natural frequencies of cylindrical shell, for each filling ratio, three different idealizations are adopted, and the results are compared with those obtained by ANSYS. The number of hydrodynamic panels (boundary elements) over the wetted surface is 1350, 2195 and 3190 for $d/2r = 0.20$; 952, 1710 and 3752 for $d/2r = 0.50$; and 1360, 2430 and 5360 for $d/2r = 0.80$, respectively. As can be seen from Table 16.5, for all the filling ratios, results exhibit monotonic convergence, and the differences between the results of the 2nd and 3rd idealizations are negligibly small. Moreover, the predicted natural frequencies for the 3rd idealization compare very well with those obtained by ANSYS, and differences are in the range of 0.1% and 4.7%. As expected, the wet natural frequencies are lower than their in-vacuo counterparts, due to increasing inertia of the system, and the differences become significant with increasing filling ratio.

In Table 16.6, the generalized added mass coefficients for the first twelve distortional mode shapes are presented for filling ratios $d/2r = 0.20, 0.50$ and 0.80 , respectively. These values are normalized to a generalized structural mass of 1 kgm^2 . It is observed that the diagonal terms of the added mass matrices are considerably larger than the off-diagonal terms, which represent the hydrodynamic coupling between in-vacuo modes. Furthermore, the generalized added mass coefficients become larger for higher filling ratios due to increasing wetted surface area of the structure.

Table 16.6 Generalized added mass coefficients (kg m²) for the horizontal cylindrical shell partially in contact with fluid.

| m-n | 1-4 | 4-4 | 1-5 | 5-5 | 1-6 | 6-6 | 1-3 | 3-3 | 1-7 | 7-7 | 1-8 | 8-8 |
|-----|-------|-------|-------|-------|-------|-------|-------|-------|-------|-------|-------|-------|
| 1-4 | 1.40 | 0.03 | -0.32 | 1.11 | 0.13 | -0.70 | -1.33 | 0.10 | -0.21 | 0.02 | -0.12 | -0.01 |
| 4-4 | 0.03 | 1.46 | -1.03 | -0.32 | 0.61 | 0.13 | 0.10 | 1.38 | 0.02 | -0.20 | 0.01 | -0.12 |
| 1-5 | -0.32 | -1.03 | 1.20 | 0.01 | -0.90 | -0.01 | 0.03 | -0.82 | 0.03 | 0.53 | -0.01 | -0.21 |
| 5-5 | 1.11 | -0.32 | 0.01 | 1.26 | 0.01 | -0.94 | -0.79 | -0.03 | -0.51 | 0.02 | 0.20 | -0.01 |
| 1-6 | 0.13 | 0.61 | -0.90 | 0.01 | 0.97 | 0.00 | -0.01 | 0.28 | -0.02 | -0.90 | 0.02 | 0.49 |
| 6-6 | -0.70 | 0.13 | -0.01 | -0.94 | 0.00 | 0.96 | 0.31 | 0.01 | 0.87 | -0.03 | -0.45 | 0.02 |
| 1-3 | -1.33 | 0.10 | 0.03 | -0.79 | -0.01 | 0.31 | 1.84 | -0.02 | -0.11 | -0.03 | 0.24 | 0.00 |
| 3-3 | 0.10 | 1.38 | -0.82 | -0.03 | 0.28 | 0.01 | -0.02 | 1.93 | 0.03 | 0.20 | 0.00 | -0.30 |
| 1-7 | -0.21 | 0.02 | 0.03 | -0.51 | -0.02 | 0.87 | -0.11 | 0.03 | 0.81 | 0.01 | -0.65 | -0.03 |
| 7-7 | 0.02 | -0.20 | 0.53 | 0.02 | -0.90 | -0.03 | -0.03 | 0.20 | 0.01 | 0.85 | 0.03 | -0.67 |
| 1-8 | -0.12 | 0.01 | -0.01 | 0.20 | 0.02 | -0.45 | 0.24 | 0.00 | -0.65 | 0.03 | 0.72 | -0.01 |
| 8-8 | -0.01 | -0.12 | -0.21 | -0.01 | 0.49 | 0.02 | 0.00 | -0.30 | -0.03 | -0.67 | -0.01 | 0.69 |

(a) $d/2r = 0.20$

| m-n | 1-4 | 4-4 | 1-5 | 5-5 | 1-6 | 6-6 | 1-3 | 3-3 | 1-7 | 7-7 | 1-8 | 8-8 |
|-----|-------|-------|-------|-------|-------|-------|-------|-------|-------|-------|-------|-------|
| 1-4 | 2.36 | -0.05 | -1.57 | 0.41 | -0.20 | 0.01 | -0.11 | 1.73 | 0.39 | 0.03 | 0.05 | 0.00 |
| 4-4 | -0.05 | 2.50 | -0.43 | -1.55 | -0.01 | 0.17 | 1.66 | 0.11 | -0.03 | 0.36 | 0.00 | -0.04 |
| 1-5 | -1.57 | -0.43 | 2.04 | -0.03 | -0.99 | -0.33 | -0.03 | -0.23 | 0.08 | 0.01 | -0.24 | 0.15 |
| 5-5 | 0.41 | -1.55 | -0.03 | 1.95 | -0.35 | -0.93 | -0.25 | 0.03 | -0.01 | 0.09 | -0.17 | -0.23 |
| 1-6 | -0.20 | -0.01 | 0.99 | -0.35 | 1.64 | 0.04 | -0.12 | -0.36 | 1.06 | -0.04 | 0.03 | -0.09 |
| 6-6 | 0.01 | 0.17 | -0.33 | -0.93 | 0.04 | 1.68 | -0.45 | -0.09 | -0.04 | -0.99 | -0.08 | 0.03 |
| 1-3 | -0.11 | 1.66 | -0.03 | -0.25 | -0.12 | -0.45 | 2.85 | 0.03 | -0.03 | 0.14 | -0.28 | -0.12 |
| 3-3 | 1.73 | 0.11 | -0.23 | 0.03 | 0.36 | -0.09 | 0.03 | 2.93 | -0.09 | 0.03 | -0.11 | 0.32 |
| 1-7 | 0.39 | -0.03 | 0.08 | -0.01 | 1.06 | -0.04 | -0.03 | -0.09 | 1.41 | 0.03 | 0.17 | -0.86 |
| 7-7 | 0.03 | 0.36 | 0.01 | 0.09 | -0.04 | -0.99 | 0.14 | 0.03 | 0.03 | 1.36 | 0.84 | 0.19 |
| 1-8 | 0.05 | 0.00 | -0.24 | -0.17 | 0.03 | -0.08 | -0.28 | -0.11 | 0.17 | 0.84 | 1.20 | 0.03 |
| 8-8 | 0.00 | -0.04 | 0.15 | -0.23 | -0.09 | 0.03 | -0.12 | 0.32 | -0.86 | 0.19 | 0.03 | 1.18 |

(b) $d/2r = 0.50$

| m-n | 1-4 | 4-4 | 1-5 | 5-5 | 1-6 | 6-6 | 1-3 | 3-3 | 1-7 | 7-7 | 1-8 | 8-8 |
|-----|-------|-------|-------|-------|-------|-------|-------|-------|-------|-------|-------|-------|
| 1-4 | 3.55 | 0.00 | -1.23 | -0.03 | -0.02 | -0.70 | -1.51 | -0.03 | 0.00 | -0.14 | -0.23 | -0.01 |
| 4-4 | 0.00 | 3.40 | 0.03 | -1.22 | -0.67 | 0.02 | 0.03 | -1.60 | -0.14 | 0.00 | -0.01 | 0.24 |
| 1-5 | -1.23 | 0.03 | 2.75 | 0.00 | -0.02 | -1.01 | -0.71 | -0.01 | -0.01 | -0.51 | 0.09 | 0.01 |
| 5-5 | -0.03 | -1.22 | 0.00 | 2.90 | -0.96 | 0.02 | 0.01 | -0.74 | -0.51 | 0.01 | 0.01 | -0.11 |
| 1-6 | -0.02 | -0.58 | -0.02 | -0.96 | 2.37 | 0.00 | 0.00 | -0.09 | -0.83 | 0.00 | 0.02 | -0.47 |
| 6-6 | -0.70 | 0.02 | -1.01 | 0.02 | 0.00 | 2.37 | -0.11 | 0.00 | 0.00 | -0.78 | 0.44 | 0.02 |
| 1-3 | -1.51 | 0.07 | -0.71 | 0.01 | 0.00 | -0.11 | 4.50 | 0.01 | 0.00 | 0.22 | -0.28 | -0.01 |
| 3-3 | -0.03 | -1.61 | -0.01 | -0.74 | -0.09 | 0.00 | 0.01 | 4.25 | 0.26 | 0.00 | -0.01 | 0.31 |
| 1-7 | 0.00 | -0.04 | -0.01 | -0.51 | -0.83 | 0.00 | 0.00 | 0.26 | 1.96 | 0.00 | 0.03 | -0.70 |
| 7-7 | -0.14 | 0.00 | -0.51 | 0.01 | 0.00 | -0.78 | 0.22 | 0.00 | 0.00 | 2.03 | 0.67 | 0.03 |
| 1-8 | -0.23 | -0.02 | 0.09 | 0.01 | 0.02 | 0.44 | -0.28 | -0.01 | 0.03 | 0.67 | 1.69 | 0.00 |
| 8-8 | -0.01 | 0.24 | 0.01 | -0.11 | -0.47 | 0.02 | -0.01 | 0.31 | -0.70 | 0.03 | 0.00 | 1.72 |

(c) $d/2r = 0.80$

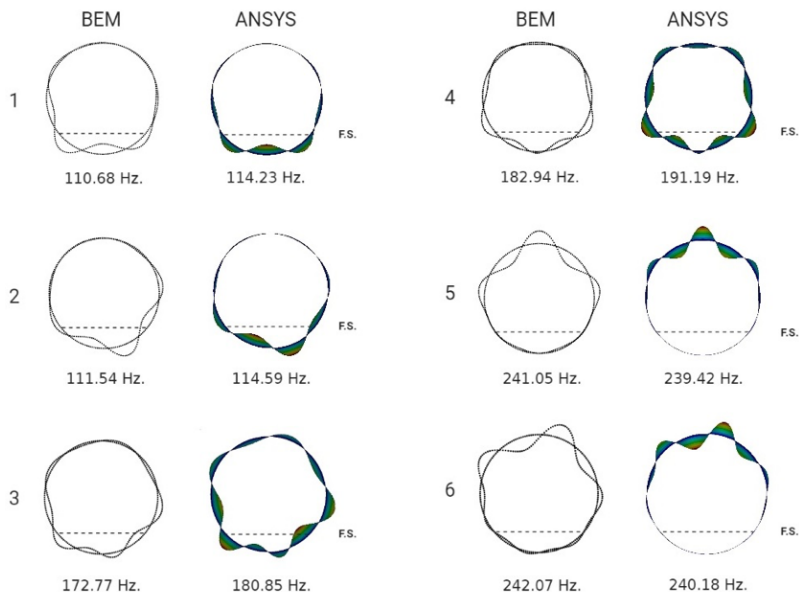


Fig. 16.12 Natural frequencies and associated mode shapes of cylindrical shell for $d/2r = 0.20$.

The first six wet natural frequencies and associated mode shapes are shown in Figs. 16.12, 16.13 and 16.14, for $d/2r = 0.20, 0.50$ and 0.80 , respectively. All the wet modes shown have one longitudinal half wave ($m = 1$) along the longitudinal axis, and only the circumferential mode shapes are presented. In contrast to mode shapes under in-vacuo condition, the wet mode shapes do not occur in pairs, and they are simply numbered with increasing frequency. For all the filling ratios, mode shapes are either symmetric or antisymmetric, with respect to the axis passing through the center of the cylinder and perpendicular to the free surface. In general, the predicted mode shapes compare very well with those obtained by ANSYS.

16.4 Conclusions

In this study, a FE-BE method is presented for the hydroelastic vibration analysis of plates and shells partially contact with fluid. In order to show the applicability of the method, two different numerical examples—a vertical rectangular plate in contact with fluid on one side and a horizontal cylindrical shell partially filled with fluid—are studied. The predicted results by the present method are also compared with those obtained by ANSYS—a commercial software. It can be concluded that the presented numerical procedure is suitable to investigate relatively high-frequency vibrations of elastic structures partially in contact with fluid.

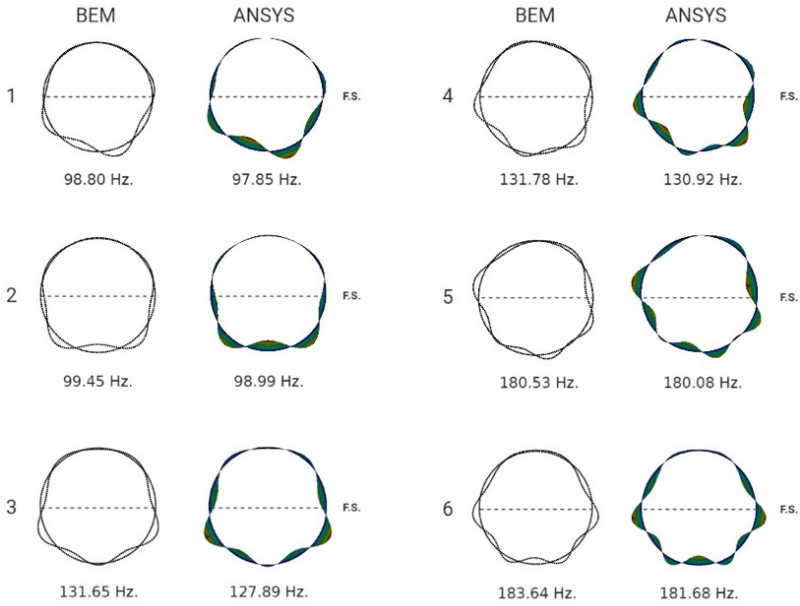


Fig. 16.13 Natural frequencies and associated mode shapes of cylindrical shell for $d/2r = 0.50$.

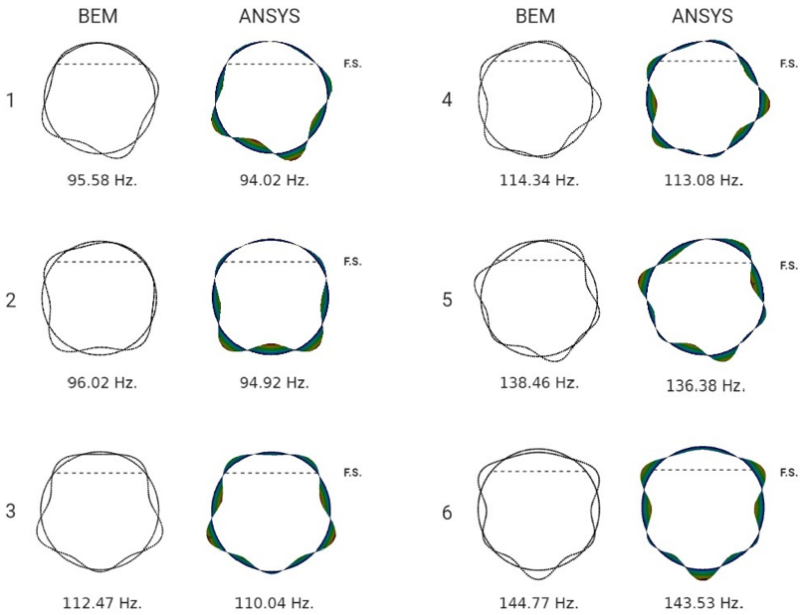


Fig. 16.14 Natural frequencies and associated mode shapes of cylindrical shell for $d/2r = 0.80$.

In the numerical examples, idealizations in both in-vacuo and wet analyses are independent from each other, and both depend on the complexity of the structure and the convergence. For both the rectangular plate and the horizontal cylindrical shell, the convergence studies (see Tables 16.1, 16.2, 16.4 and 16.5) show that differences are in an acceptable range. Also, the predicted frequencies compare very well with the results obtained by ANSYS.

The present work demonstrates the versatility of the proposed method by studying two different structures partially in contact with fluid. Moreover, the numerical framework can be adopted to analyze more complex structures such as materials exhibiting higher-gradient effects (for example, see those presented in dell'Isola and Seppecher, 1995; Alibert et al, 2003; dell'Isola et al, 2012; Cuomo et al, 2016; Abali et al, 2017; Barchiesi et al, 2019; Vangelatos et al, 2019c,b,a; dell'Isola et al, 2019a,b; Eremeyev et al, 2018; Rahali et al, 2020; Eremeyev and Turco, 2020; Chróścielewski et al, 2020). Application of the presented framework for such complex materials is currently under investigation by the authors. Also, the free surface effects should be taken into account to have a better understanding of the phenomenon.

Appendix

In this study, flat shell elements are used to conduct the in-vacuo analyses. In the formulation of this shell element, it is assumed that bending and in-plane force resultants are independent from each other. Therefore, the problem is considered as a combination of 2-D plane stress and plate bending problems. Then, element stiffness and mass matrices of each problem are combined in a suitable manner to define total element stiffness and mass matrices. In this study, the plane stress problem is formulated with bilinear displacement rectangular elements, and the plate bending problem is modeled with MZC (Melosh-Zienkiewicz-Cheung) rectangular element formulation (see Fig. 16.15).

Plane Stress Formulation

There is a wide number of elements developed based upon the assumptions of two-dimensional elasticity. Among the formulations available, the bilinear displacement rectangle element, developed by Melosh (1963) is preferred in this study to model plane stress field of flat shell elements. A geometric configuration of this type of element with a thickness t is given in Fig. 16.15. The dimensionless centroidal coordinates are defined as follows

$$\xi = \frac{x}{a}, \quad \eta = \frac{y}{b} \quad (16.23)$$

where $2a$ and $2b$ are width and height, respectively. For plane stress elements, the displacement field is defined with translations in the plane, formed by local x and y

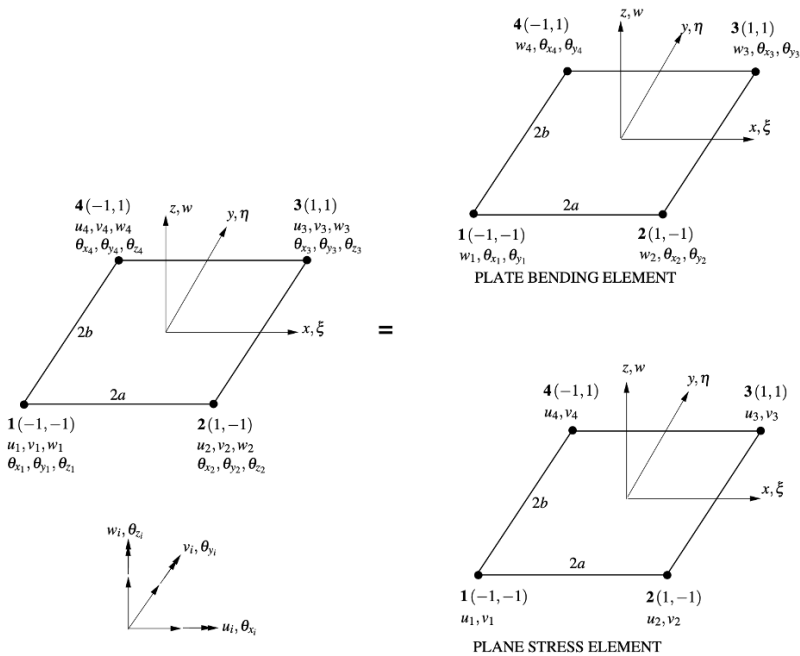


Fig. 16.15 Flat shell element.

coordinates. The first node is placed lower left corner, and the consecutive nodes are designated in counterclockwise direction. The nodal displacement vector is written as

$$\mathbf{q} = \{q_1, q_2, \dots, q_7, q_8\} = \{u_1, v_1, \dots, u_4, v_4\}. \tag{16.24}$$

For the displacement field, which is bilinear in ξ and η , the displacements are defined as

$$u = c_1 + c_2\xi + c_3\eta + c_4\xi\eta, \tag{16.25}$$

$$v = c_5 + c_6\xi + c_7\eta + c_8\xi\eta. \tag{16.26}$$

By using these displacement functions, the geometric matrix, \mathbf{G} , is introduced as follows:

$$\mathbf{G} = \begin{bmatrix} 1 & \xi & \eta & \xi\eta & 0 & 0 & 0 & 0 \\ 0 & 0 & 0 & 0 & 1 & \xi & \eta & \xi\eta \end{bmatrix} \tag{16.27}$$

The geometric matrix is evaluated at each node to obtain the following matrix:

$$\mathbf{H} = \begin{bmatrix} \mathbf{g}_1 \\ \mathbf{g}_2 \\ \mathbf{g}_3 \\ \mathbf{g}_4 \end{bmatrix} = \begin{bmatrix} 1 & -1 & -1 & 1 & 0 & 0 & 0 & 0 \\ 0 & 0 & 0 & 0 & 1 & -1 & -1 & 1 \\ 1 & 1 & -1 & -1 & 0 & 0 & 0 & 0 \\ 0 & 0 & 0 & 0 & 1 & 1 & -1 & -1 \\ 1 & 1 & 1 & 1 & 0 & 0 & 0 & 0 \\ 0 & 0 & 0 & 0 & 1 & 1 & 1 & 1 \\ 1 & -1 & 1 & -1 & 0 & 0 & 0 & 0 \\ 0 & 0 & 0 & 0 & 1 & -1 & 1 & -1 \end{bmatrix} \quad (16.28)$$

where \mathbf{g}_i is a 2×8 matrix evaluated at i th node ($i = 1, 2, 3, 4$). Then, the matrix formed by displacement shape functions, $\mathbf{N} = \mathbf{G}\mathbf{H}^{-1}$, is written as:

$$\mathbf{N} = \begin{bmatrix} N_1 & 0 & N_2 & 0 & N_3 & 0 & N_4 & 0 \\ 0 & N_1 & 0 & N_2 & 0 & N_3 & 0 & N_4 \end{bmatrix} \quad (16.29)$$

where

$$\begin{aligned} N_1 &= \frac{1}{4}(1 - \xi)(1 - \eta), & N_2 &= \frac{1}{4}(1 + \xi)(1 - \eta), \\ N_3 &= \frac{1}{4}(1 + \xi)(1 + \eta), & N_4 &= \frac{1}{4}(1 - \xi)(1 + \eta). \end{aligned}$$

Next, in order to define the linear differential operator formed by the derivatives with respect to cartesian coordinates, chain rule is applied as follows:

$$\begin{aligned} \frac{\partial}{\partial x} &= \frac{\partial}{\partial \xi} \frac{\partial \xi}{\partial x} + \frac{\partial}{\partial \eta} \frac{\partial \eta}{\partial x} = \frac{1}{a} \frac{\partial}{\partial \xi}, \\ \frac{\partial}{\partial y} &= \frac{\partial}{\partial \xi} \frac{\partial \xi}{\partial y} + \frac{\partial}{\partial \eta} \frac{\partial \eta}{\partial y} = \frac{1}{b} \frac{\partial}{\partial \eta}. \end{aligned}$$

Then, the differential operator, \mathbf{D}^p , is written as:

$$\mathbf{D}^p = \begin{bmatrix} \frac{\partial}{\partial x} & 0 \\ 0 & \frac{\partial}{\partial y} \\ \frac{\partial}{\partial y} & \frac{\partial}{\partial x} \end{bmatrix} = \begin{bmatrix} \frac{1}{a} \frac{\partial}{\partial \xi} & 0 \\ 0 & \frac{1}{b} \frac{\partial}{\partial \eta} \\ \frac{1}{b} \frac{\partial}{\partial \eta} & \frac{1}{a} \frac{\partial}{\partial \xi} \end{bmatrix}. \quad (16.30)$$

For isotropic materials, the stress-strain operator is defined as follows:

$$\mathbf{E} = \frac{E}{(1 - \nu^2)} \begin{bmatrix} 1 & \nu & 0 \\ \nu & 1 & 0 \\ 0 & 0 & \frac{1-\nu}{2} \end{bmatrix} \quad (16.31)$$

where E and ν represent Young's modulus and Poisson's ratio, respectively. Finally, element stiffness matrix, \mathbf{K} , and mass matrix, \mathbf{M} , are calculated as follows:

$$\mathbf{K}^p = abt \int_{-1}^{+1} \int_{-1}^{+1} \mathbf{B}^T \mathbf{E} \mathbf{B} \, d\xi d\eta \quad (16.32)$$

$$\mathbf{M}^p = \rho abt \int_{-1}^{+1} \int_{-1}^{+1} \mathbf{G}^T \mathbf{G} \, d\xi d\eta \quad (16.33)$$

In the expressions given in Eqs. 16.32 and 16.33, the matrix \mathbf{B} is defined as

$$\mathbf{B} = \mathbf{D} \mathbf{G} = \frac{1}{ab} \begin{bmatrix} 0 & b & 0 & b\eta & 0 & 0 & 0 & 0 \\ 0 & 0 & 0 & 0 & 0 & 0 & a & a\xi \\ 0 & 0 & a & a\xi & 0 & b & 0 & b\eta \end{bmatrix}. \quad (16.34)$$

The element stiffness and mass matrices given in Eqs. 16.32 and 16.33 have a dimension of 8×8 . To combine these matrices with those of the plate bending problem, it is convenient to divide these matrices as follows:

$$\mathbf{K}^p = \begin{bmatrix} \left[\mathbf{K}_{11}^p \right] & & & & & & & \\ \left[\mathbf{K}_{21}^p \right] & \left[\mathbf{K}_{22}^p \right] & & & & & \text{Sym.} & \\ \left[\mathbf{K}_{31}^p \right] & \left[\mathbf{K}_{32}^p \right] & \left[\mathbf{K}_{33}^p \right] & & & & & \\ \left[\mathbf{K}_{41}^p \right] & \left[\mathbf{K}_{42}^p \right] & \left[\mathbf{K}_{43}^p \right] & \left[\mathbf{K}_{44}^p \right] & & & & \end{bmatrix}_{8 \times 8}, \quad (16.35)$$

$$\mathbf{M}^p = \begin{bmatrix} \left[\mathbf{M}_{11}^p \right] & & & & & & & \\ \left[\mathbf{M}_{21}^p \right] & \left[\mathbf{M}_{22}^p \right] & & & & & \text{Sym.} & \\ \left[\mathbf{M}_{31}^p \right] & \left[\mathbf{M}_{32}^p \right] & \left[\mathbf{M}_{33}^p \right] & & & & & \\ \left[\mathbf{M}_{41}^p \right] & \left[\mathbf{M}_{42}^p \right] & \left[\mathbf{M}_{43}^p \right] & \left[\mathbf{M}_{44}^p \right] & & & & \end{bmatrix}_{8 \times 8}, \quad (16.36)$$

where $\left[\mathbf{K}_{ij}^p \right]$ and $\left[\mathbf{M}_{ij}^p \right]$ are 2×2 sub-matrices of the element stiffness and mass matrices, respectively ($i, j = 1, 2, 3, 4$). The superscript p denotes the in-plane effects.

Plate Bending Formulation

In this study, MZC rectangular element, originally developed by Melosh Melosh (1963), is used to model plate bending contributions of flat shell elements. As seen from Fig. 16.15, this element has only one generic displacement, w , and rotations,

θ_{x_i} and θ_{y_i} , with respect to the local axes x and y . For this type of plate element, the following nodal displacement vector is introduced

$$\mathbf{q} = \{q_1, q_2, \dots, q_{12}\} = \{w_1, \theta_{x_1}, \theta_{y_1}, \dots, w_4, \theta_{x_4}, \theta_{y_4}\} \quad (16.37)$$

and the displacement function is expressed as

$$w = c_1 + c_2\xi + c_3\eta + c_4\xi^2 + c_5\xi\eta + c_6\eta^2 + c_7\xi^3 + c_8\xi^2\eta + c_9\xi\eta^2 + c_{10}\eta^3 + c_{11}\xi^3\eta + c_{12}\xi\eta^3. \quad (16.38)$$

The matrix formed by displacement shape functions is derived as

$$\mathbf{N}_i = [N_{i_1} N_{i_2} N_{i_3}]$$

where

$$\begin{aligned} N_{i_1} &= \frac{1}{8}(1 + \xi_0)(1 + \eta_0)(2 + \xi_0 + \eta_0 - \xi^2 - \eta^2) \\ N_{i_2} &= \frac{-1}{8}\eta_i(1 + \xi_0)(1 - \eta_0)(1 + \eta_0)^2 \\ N_{i_3} &= \frac{1}{8}\xi_i(1 - \xi_0)(1 + \eta_0)(1 + \xi_0)^2 \end{aligned}$$

and

$$\xi_0 = \xi_i\xi, \quad \eta_0 = \eta_i\eta, \quad (i = 1, 2, 3, 4)$$

The differential operator (curvature matrix) for the plate bending problem is defined as follows:

$$\mathbf{D}^b = \left\{ \frac{\partial^2}{\partial x^2}, \frac{\partial^2}{\partial y^2}, \frac{2\partial^2}{\partial x\partial y} \right\}. \quad (16.39)$$

By utilizing the curvature matrix and shape functions, one can obtain strain-displacement matrix as follows

$$\mathbf{B}_i^b = \mathbf{D}^b \mathbf{N}_i = \begin{bmatrix} N_{i_1,xx} & N_{i_2,xx} & N_{i_3,xx} \\ N_{i_1,yy} & N_{i_2,yy} & N_{i_3,yy} \\ 2N_{i_1,xy} & 2N_{i_2,xy} & 2N_{i_3,xy} \end{bmatrix} \quad (i = 1, 2, 3, 4), \quad (16.40)$$

The local strain-displacement matrix is a 3×12 matrix, and it is formed as

$$\mathbf{B}^b = [\mathbf{B}_1^b \quad \mathbf{B}_2^b \quad \mathbf{B}_3^b \quad \mathbf{B}_4^b]_{3 \times 12} \quad (16.41)$$

In particular, \mathbf{B}_1^b is calculated as

$$\mathbf{B}_1^b = \frac{1}{4a^2b^2} \begin{bmatrix} 3\xi(1-\eta)b^2 & 0 & (1-3\xi)(1-\eta)ab^2 \\ 3(1-\xi)\eta a^2 & -(1-\xi)(1-3\eta)a^2b & 0 \\ (4-3\xi^2-3\eta^2)ab & (1-\eta)(1+3\eta)ab^2 & -(1-\xi)(1+3\xi)a^2b \end{bmatrix} \quad (16.42)$$

For an isotropic and homogeneous material, the generalized bending constitutive matrix is given as

$$\mathbf{E}^b = \frac{Et^3}{12(1-\nu^2)} \begin{bmatrix} 1 & \nu & 0 \\ \nu & 1 & 0 \\ 0 & 0 & \frac{1}{2}(1-\nu) \end{bmatrix}. \quad (16.43)$$

Finally, the element stiffness matrix, \mathbf{K}^b , and the mass matrix, \mathbf{M}^b , for plate bending elements are calculated as follows

$$\mathbf{K}^b = ab \int_{-1}^1 \int_{-1}^1 \mathbf{B}^{bT} \mathbf{E}^b \mathbf{B}^b d\xi d\eta, \quad (16.44)$$

$$\mathbf{M}^b = \rho tab \int_{-1}^1 \int_{-1}^1 \mathbf{N}^T \mathbf{N} d\xi d\eta. \quad (16.45)$$

The element stiffness and mass matrices of bending element given in Eqs. 16.44 and 16.45 have dimensions of 12×12 . Again, for convenience, these matrices are divided into sub-matrices to show the contributions to each degree of freedom as follows

$$\mathbf{K}^b = \begin{bmatrix} \left[\mathbf{K}_{11}^b \right] & & & \\ \left[\mathbf{K}_{21}^b \right] & \left[\mathbf{K}_{22}^b \right] & & \text{Sym.} \\ \left[\mathbf{K}_{31}^b \right] & \left[\mathbf{K}_{32}^b \right] & \left[\mathbf{K}_{33}^b \right] & \\ \left[\mathbf{K}_{41}^b \right] & \left[\mathbf{K}_{42}^b \right] & \left[\mathbf{K}_{43}^b \right] & \left[\mathbf{K}_{44}^b \right] \end{bmatrix}_{12 \times 12} \quad (16.46)$$

$$\mathbf{M}^b = \begin{bmatrix} \left[\mathbf{M}_{11}^b \right] & & & \\ \left[\mathbf{M}_{21}^b \right] & \left[\mathbf{M}_{22}^b \right] & & \text{Sym.} \\ \left[\mathbf{M}_{31}^b \right] & \left[\mathbf{M}_{32}^b \right] & \left[\mathbf{M}_{33}^b \right] & \\ \left[\mathbf{M}_{41}^b \right] & \left[\mathbf{M}_{42}^b \right] & \left[\mathbf{M}_{43}^b \right] & \left[\mathbf{M}_{44}^b \right] \end{bmatrix}_{12 \times 12} \quad (16.47)$$

The derived mass and stiffness matrices in the local coordinates must be transformed into an identified reference coordinate system. All the transformations are accomplished by a simple process. The displacements of a node are transformed from global to local coordinates by the following transformation matrix

$$\mathbf{T} = \begin{bmatrix} \Lambda & 0 & 0 & 0 & 0 & 0 \\ 0 & \Lambda & 0 & 0 & 0 & 0 \\ 0 & 0 & \Lambda & 0 & 0 & 0 \\ 0 & 0 & 0 & \Lambda & 0 & 0 \\ 0 & 0 & 0 & 0 & \Lambda & 0 \\ 0 & 0 & 0 & 0 & 0 & \Lambda \end{bmatrix} \quad (16.49)$$

with Λ being a 3×3 matrix of direction cosines between the two sets of axes given by

$$\Lambda = \begin{bmatrix} \cos(\xi, x) & \cos(\xi, \eta) & \cos(\xi, z) \\ \cos(\eta, x) & \cos(\eta, \eta) & \cos(\eta, z) \\ \cos(\zeta, x) & \cos(\zeta, \eta) & \cos(\zeta, z) \end{bmatrix} \quad (16.50)$$

where $\cos(\xi, x)$ is the cosine of the angle between ξ and x axes. Thus, the stiffness and mass matrices of an element in global coordinates are computed with the following transformation

$$\bar{\mathbf{K}} = \mathbf{T}^T \mathbf{K} \mathbf{T}, \quad (16.51)$$

$$\bar{\mathbf{M}} = \mathbf{T}^T \mathbf{M} \mathbf{T} \quad (16.52)$$

where $\bar{\mathbf{K}}$ and $\bar{\mathbf{M}}$ are the global stiffness and mass matrices. Once the stiffness matrices of all the elements have been determined in a common global coordinate system, the assembly of the elements follow the standard solution pattern.

References

- ANSYS (2013) Mechanical APDL Command Reference, ANSYS, Inc., Release 15.0
- Abali BE, Müller WH, dell'Isola F (2017) Theory and computation of higher gradient elasticity theories based on action principles. *Archive of Applied Mechanics* 87(9):1495–1510
- Abd-alla AN, Alshaiikh F, Del Vescovo D, Spagnuolo M (2017) Plane waves and eigenfrequency study in a transversely isotropic magneto-thermoelastic medium under the effect of a constant angular velocity. *Journal of Thermal Stresses* 40(9):1079–1092
- Alessandroni S, Andreus U, dell'Isola F, Porfiri M (2005) A passive electric controller for multi-modal vibrations of thin plates. *Computers & structures* 83(15-16):1236–1250
- Alibert JJ, Seppecher P, dell'Isola F (2003) Truss modular beams with deformation energy depending on higher displacement gradients. *Mathematics and Mechanics of Solids* 8(1):51–73

- Amabili M, Dalpiaz G (1995) Breathing vibrations of a horizontal circular cylindrical tank shell, partially filled with liquid. *Journal of vibration and acoustics* 117(2):187–191
- Amabili M, Frosali G, Kwak MK (1996) Free vibrations of annular plates coupled with fluids. *Journal of sound and vibration* 191(5):825–846
- Askari E, Jeong KH (2010) Hydroelastic vibration of a cantilever cylindrical shell partially submerged in a liquid. *Ocean Engineering* 37(11-12):1027–1035
- Askari E, Jeong KH, Amabili M (2013) Hydroelastic vibration of circular plates immersed in a liquid-filled container with free surface. *Journal of sound and vibration* 332(12):3064–3085
- Barchiesi E, Laudato M, Di Cosmo F (2018) Wave dispersion in non-linear pantographic beams. *Mechanics Research Communications* 94:128–132
- Barchiesi E, Spagnuolo M, Placidi L (2019) Mechanical metamaterials: a state of the art. *Mathematics and Mechanics of Solids* 24(1):212–234
- Baroudi D, Giorgio I, Battista A, Turco E, Igumnov LA (2019) Nonlinear dynamics of uniformly loaded elastica: Experimental and numerical evidence of motion around curled stable equilibrium configurations. *ZAMM-Journal of Applied Mathematics and Mechanics/Zeitschrift für Angewandte Mathematik und Mechanik* p e201800121
- Bersani AM, Della Corte A, Piccardo G, Rizzi NL (2016) An explicit solution for the dynamics of a taut string of finite length carrying a traveling mass: the subsonic case. *Zeitschrift für angewandte Mathematik und Physik* 67(4):108
- Bishop RED, Price W (1979) *Hydroelasticity of Ships*. Cambridge University Press
- Cazzani A, Rizzi NL, Stochino F, Turco E (2018) Modal analysis of laminates by a mixed assumed-strain finite element model. *Mathematics and Mechanics of Solids* 23(1):99–119
- Chiba M, Yamaki N, Tani J (1984a) Free vibration of a clamped-free circular cylindrical shell partially filled with liquid—Part I: Theoretical analysis. *Thin-walled structures* 2(3):265–284
- Chiba M, Yamaki N, Tani J (1984b) Free vibration of a clamped-free circular cylindrical shell partially filled with liquid—Part II: Numerical results. *Thin-Walled Structures* 2(4):307–324
- Cho DS, Kim BH, Vladimir N, Choi TM (2014) Natural vibration analysis of vertical rectangular plates and stiffened panels in contact with fluid on one side. *Proceedings of the Institution of Mechanical Engineers, Part M: Journal of Engineering for the Maritime Environment* 230(1):114–125
- Chróścielewski J, dell’Isola F, Eremeyev VA, Agnieszka S (2020) On rotational instability within the nonlinear six-parameter shell theory. *International Journal of Solids and Structures*, doi: 10.1016/j.ijsolstr.2020.04.030
- Cuomo M, dell’Isola F, Greco L (2016) Simplified analysis of a generalized bias test for fabrics with two families of inextensible fibres. *Zeitschrift für angewandte Mathematik und Physik* 67(3):61
- Datta N, Jindal R (2019) Modelling a spade rudder as a hollow two-way tapered kirchhoff’s plate: free dry and wet vibration study with numerical verification. *Applied Ocean Research* 82:385–396
- De Espinosa FM, Gallego-Juarez JA (1984) On the resonance frequencies of water-loaded circular plates. *Journal of sound and vibration* 94(2):217–222
- dell’Isola F, Seppecher P (1995) The relationship between edge contact forces, double forces and interstitial working allowed by the principle of virtual power. *Comptes rendus de l’Académie des sciences Série IIb, Mécanique, physique, astronomie* p 7
- dell’Isola F, Seppecher P, Madeo A (2012) How contact interactions may depend on the shape of Cauchy cuts in Nth gradient continua: approach “à la D’Alembert”. *Zeitschrift für angewandte Mathematik und Physik* 63(6):1119–1141
- dell’Isola F, Seppecher P, Alibert JJ, et al (2019a) Pantographic metamaterials: an example of mathematically driven design and of its technological challenges. *Continuum Mechanics and Thermodynamics* 31(4):851–884
- dell’Isola F, Seppecher P, Spagnuolo M, et al (2019b) Advances in pantographic structures: design, manufacturing, models, experiments and image analyses. *Continuum Mechanics and Thermodynamics* 31(4):1231–1282
- Eremeyev VA, Turco E (2020) Enriched buckling for beam-lattice metamaterials. *Mechanics Research Communications* 103:103,458

- Eremeyev VA, dell'Isola F, Boutin C, Steigmann D (2018) Linear pantographic sheets: existence and uniqueness of weak solutions. *Journal of Elasticity* 132(2):175–196
- Ergin A, Temarel P (2002) Free vibration of a partially liquid-filled and submerged, horizontal cylindrical shell. *Journal of Sound and vibration* 254(5):951–965
- Ergin A, Uğurlu B (2003) Linear vibration analysis of cantilever plates partially submerged in fluid. *Journal of Fluids and Structures* 17(7):927–939
- Fu Y, Price WG (1987) Interactions between a partially or totally immersed vibrating cantilever plate and the surrounding fluid. *Journal of Sound and Vibration* 118(3):495–513
- Giorgio I, Del Vescovo D (2018) Non-linear lumped-parameter modeling of planar multi-link manipulators with highly flexible arms. *Robotics* 7(4):60
- Giorgio I, Del Vescovo D (2019) Energy-based trajectory tracking and vibration control for multilink highly flexible manipulators. *Mathematics and Mechanics of Complex Systems* 7(2):159–174
- Giorgio I, Rizzi NL, Turco E (2017) Continuum modelling of pantographic sheets for out-of-plane bifurcation and vibrational analysis. *Proceedings of the Royal Society A: Mathematical, Physical and Engineering Sciences* 473(2207):20170,636
- Goncalves PB, Ramos NRSS (1996) Free vibration analysis of cylindrical tanks partially filled with liquid. *Journal of Sound and Vibration* 195(3):429–444
- Hsu CY, Jen CY (2010) The transient response of imperfect thin-walled stiffened cylindrical shell exposed to side-on underwater explosion. In: *ASME 2009 28th International Conference on Ocean, Offshore and Arctic Engineering*, American Society of Mechanical Engineers Digital Collection, pp 11–21
- Jeong KH (1999) Dynamics of a concentrically or eccentrically submerged circular cylindrical shell in a fluid-filled container. *Journal of Sound and vibration* 224(4):709–732
- Jeong KH (2003) Free vibration of two identical circular plates coupled with bounded fluid. *Journal of Sound and Vibration* 260(4):653–670
- Jeong KH, Kim JW (2009) Hydroelastic vibration analysis of two flexible rectangular plates partially coupled with a liquid. *Nuclear Engineering and Technology* 41(3):335–346
- Jeong KH, Lee SC (1996) Fourier series expansion method for free vibration analysis of either a partially liquid-filled or a partially liquid-surrounded circular cylindrical shell. *Computers & structures* 58(5):937–946
- Junge M, Brunner D, Gaul L (2011) Solution of fe-be coupled eigenvalue problems for the prediction of the vibro-acoustic behavior of ship-like structures. *International Journal for Numerical Methods in Engineering* 87(7):664–676
- Kalinowski AJ (1974) Fluid-structure interaction problems using finite elements. In: *Fifth Navy-NASTRAN Colloquium*, Naval Ship Research and Development Center, Bethesda, Maryland, pp 71–86
- Kito F (1970) *Principles of Hydro-elasticity*. Keio University
- Kwak MK (1991) Vibration of circular plates in contact with water. *Journal of Applied Mechanics* 58(2):480–483
- Kwak MK (1997) Hydroelastic vibration of circular plates. *Journal of Sound and Vibration* 201(3):293–303
- Kwak MK, Yang DH (2013) Free vibration analysis of cantilever plate partially submerged into a fluid. *Journal of Fluids and Structures* 40:25–41
- Liang CC, Hsu CY, Lai WH (2001) A study of transient responses of a submerged spherical shell under shock waves. *Ocean engineering* 28(1):71–94
- Liao CY, Ma CC (2016) Vibration characteristics of rectangular plate in compressible inviscid fluid. *Journal of Sound and Vibration* 362:228–251
- Lindholm US, Kana DD, Chu WH, Abramson HN (1965) Elastic vibration characteristics of cantilever plates in water. *Journal of Ship Research* 9:11–22
- Marcus MS (1978) A finite-element method applied to the vibration of submerged plates. *Journal of Ship Research* 22(2)
- Melosh RJ (1963) Basis for derivation of matrices for the direct stiffness method. *AIAA Journal* 1(7):1631–1637

- Meyerhoff WK (1970) Added masses of thin rectangular plates calculated from potential theory. *J Ship Res* 14:100–111
- Meylan MH (1997) The forced vibration of a thin plate floating on an infinite liquid. *Journal of sound and vibration* 205(5):581–591
- Motley MR, Kramer MR, Young YL (2013) Free surface and solid boundary effects on the free vibration of cantilevered composite plates. *Composite structures* 96:365–375
- Rahali Y, Eremeyev VA, Ganghoffer JF (2020) Surface effects of network materials based on strain gradient homogenized media. *Mathematics and Mechanics of Solids* 25(2):389–406
- Robinson NJ, Palmer SC (1990) A modal analysis of a rectangular plate floating on an incompressible liquid. *Journal of sound and vibration* 142(3):453–460
- Vangelatos Z, Gu GX, Grigoropoulos CP (2019a) Architected metamaterials with tailored 3d buckling mechanisms at the microscale. *Extreme Mechanics Letters* 33:100,580
- Vangelatos Z, Komvopoulos K, Grigoropoulos C (2019b) Vacancies for controlling the behavior of microstructured three-dimensional mechanical metamaterials. *Mathematics and Mechanics of Solids* 24(2):511–524
- Vangelatos Z, Melissinaki V, Farsari M, Komvopoulos K, Grigoropoulos C (2019c) Intertwined microlattices greatly enhance the performance of mechanical metamaterials. *Mathematics and Mechanics of Solids* 24(8):2636–2648
- Volcy GC, Baudin MM, Bereau MD (1980) Hydroelasticity and vibrations of internal steelwork of tanks. Tech. rep.
- Warburton GB (1961) Vibration of a cylindrical shell in an acoustic medium. *Journal of Mechanical Engineering Science* 3(1):69–79
- Yildizdag ME, Ardic IT, Demirtas M, Ergin A (2019) Hydroelastic vibration analysis of plates partially submerged in fluid with an isogeometric fe-be approach. *Ocean Engineering* 172:316–329
- Zhang GJ, Li TY, Zhu X, Yang J, Miao YY (2017) Free and forced vibration characteristics of submerged finite elliptical cylindrical shell. *Ocean Engineering* 129:92–106
- Zhang XM (2002) Frequency analysis of submerged cylindrical shells with the wave propagation approach. *International Journal of Mechanical Sciences* 44(7):1259–1273
- Zhang XM, Liu GR, Lam KY (2001) The effects of baffles and end-caps on coupled vibration and sound radiation of finite cylindrical shells. *Int J Eng Simulation* 2:19–25
- Zheng CJ, Zhang C, Bi CX, Gao HF, Du L, Chen HB (2017) Coupled fe-be method for eigenvalue analysis of elastic structures submerged in an infinite fluid domain. *International Journal for Numerical Methods in Engineering* 110(2):163–185
- Zienkiewicz OC, Newton RE (1969) Coupled vibrations of a structure submerged in a compressible fluid. In: *Symposium on Finite Element Techniques*. Germany: Univ. of Stuttgart



Chapter 17

A Multimodal Approach for Automation of Mechanical Design

Klaus Hoschke, Konstantin Kappe, Werner Riedel, and Stefan Hiermaier

Abstract A multimodal approach for the automation of mechanical design is proposed. It is based on nonlinear programming incorporating topology optimization (TO) and multiple modes of mechanical analysis of the structure. The material plastication, large strain and transient failure behavior of interim optimized designs are evaluated in a nonlinear analysis. As a result, early stage validation of results from topology optimization (TO) and automatic design iteration are achieved.

A design approach is implemented, which is based on generative design and aims for safety and lightweight construction under the aspects of structural ductility and fail-safe behaviour in overstraining. The scheme is developed with a high degree of automation, such that effective weighting of technical design criteria can be achieved and design optimization results can be directly manufactured. The application is demonstrated in simulation analysis as well as through experimental testing of 3D printed structures.

17.1 Introduction

The mechanical design of functional components is a multidisciplinary task. For efficient virtual product development, the intelligent handling of engineering knowledge in multidisciplinary tools and automated design iteration is crucial. To achieve this aim, mathematical programming is for example incorporated in design optimization procedures. Specifically, topology optimization (TO) has proven to be a powerful tool for finding layouts of lightweight parts that efficiently withstand mechanical loads. Nevertheless, the modeling and the optimization procedure must be applicable to the individual design problem, and validation in high fidelity procedures as

K. Hoschke, K. Kappe, W. Riedel, S. Hiermaier
Fraunhofer Institute for High-Speed Dynamics, Ernst-Zermelo-Straße 4, 79104 Freiburg, Germany
e-mail: Klaus.Hoschke@emi.fraunhofer.de, Konstantin.Kappe@emi.fraunhofer.de,
Werner.Riedel@emi.fraunhofer.de, Stefan.Hiermaier@emi.fraunhofer.de

well as costly iterations are often necessary.

Most mechanical design steps are undertaken today in a virtual environment. The interconnection and management of data and knowledge in procedures have been elaborated on ever since. Currently, various guidelines and processes have been established in different industries or product classes. Specific technologies for distributed work and design automation have been proposed (Sandberg et al, 2016). Master models are a kind of basis concept for parallel and distributed design work. Approaches for reusing of design solutions can be product configurations or platforms that use concepts of modularization, building blocks and derived product designs. Automated design iterations and the implementation of knowledge into models by implementation of mathematical programming and parametrization strategies for multidisciplinary design optimization (MDO) have been discussed (see, e.g., Herskovits, 2012). Knowledge-based engineering (KBE) is a broader technological approach to the intelligent capture and reuse of knowledge in product development by trying to establish a language-based framework for all before-mentioned approaches (see, e.g., La Rocca, 2012).

Regardless, several different expertise and laborious coordination are still necessary for the mechanical design of a functional part. Although managed intelligently and virtually, results need to be regularly harmonized, collectively validated and changes are iterated several times. In this work, a multimodal approach related to the frameworks of KBE and MDO is proposed for mechanical part design. It aims to automate the procedures as far as possible by integrating different domains, particularly modes of mechanical description and analysis, in an intelligent design scheme, which is based on topology optimization.

A common approach to lightweight mechanical design is the following, as interpreted from Dubbel and Davies (2013): 1) The construction material as well as the manufacturing technology are predetermined according to technical specifications. 2) The loading conditions (operational loads and event loads) are modeled based on an approximated number of load cycles during the service life and mapped on to the admissible stress state of the material. 3) A first design is drafted based on topology optimization (TO) or experience and conservative assumptions on the structural sizing 4) High fidelity simulation analysis and mockup testing are applied for validation and the design is iterated until it meets the technical specification.

The aspect of this scheme limiting effectiveness and automation, is the significant discrepancy between first design drafts and validated, engineered results in steps 3) and 4). The latter most often require many costly iterations. In a TO based approach, one major drawback is the insufficient capability of modeling and efficiently solving complex nonlinear mechanical design problems, as will be further discussed. The resulting lack of dependability of topology-optimized results will require manual interpretation and elaborate revision.

The most common objective for lightweight design is the optimization of the stiffness-to-weight ratio. This approach can be modeled as a TO problem of minimizing the mean compliance of the structure subject to a mass constraint and is elaborated further in this monograph. The solid isotropic material with penalization (SIMP) is the most common approach to the parametrization of this optimization problem, as

discussed in Bendsoe and Sigmund (2013) and an extensive overview of TO methods is given in Sigmund and Maute (2013). SIMP is widely implemented in commercial software and already applied to large scale problems, although largely restricted to static and linear-elastic tasks. It is a very effective method to optimize for stiffness of a structure. In the classical approach, it disregards local stress concentrations and material plastification. However, singular loading events that might be the result of misuse or an impact and which lead to overstraining and material failure are very important for the sizing of components for a safe service life (Dubbel and Davies, 2013).

For the purpose of more reliable topology results, new single mode methods in the field of topology optimization have been described recently, namely the fail-safe topology optimization (FSO) and the redundant topology optimization (RTO) (Jansen et al, 2014; Zhou and Fleury, 2016; Mohr, 2011). FSO is based on a local damage model in a multiple-model topology optimization (MMO) aiming for more resilient designs in case of material failure with random location. Some of its aspects will be adapted in this work and a new MMO formulation is developed. Nonlinear material behavior as well as transient loading are disregarded so far in FSO and RTO, as well as in the well-developed robust- (RTO) and reliability-based (RBTO) TO methods for robustness against uncertainties. The implementation of material and geometrical non-linearities in topology optimization methods has been addressed in the past (see, e.g., Abdi et al, 2018; Schwarz et al, 2001; Li et al, 2018) but has not yet been applied to large scale problems or found their way into commercial software. This is mainly due to the path-dependent property of the sensitivity analysis, which makes the latter elaborate and computationally unduly costly. Desmorat and Desmorat (2008) avoids this in a TO aiming for fatigue resistance by using a damage law for cyclic elasto-plasticity on an energetic basis. In doing so, the otherwise necessary evolution relations are circumvented in this specific application. Nonlinear and transient response was addressed by methods like the equivalent static loads method (ESLM) or by hybrid cellular automata (HCA), and applied particularly in crashworthiness design or multi-body dynamics (see Ahmad et al, 2017; Duddeck et al, 2016). Still, material failure and graceful degradation related design constraints like fail-safe behavior and redundancy have not been considered with those methods. Of the aforementioned, ESLM and HCA are the only multimodal and most well-known approaches for applications with nonlinear problems. The multimodal design scheme proposed in this work can be described as more general and differences as well as possible integration of the latter methods will be discussed later on.

Apart from the multitude of methods and approaches to the robustness and safety of optimized structures, efficient solving of associated design problems still remains an underdeveloped issue in the field of TO, especially in the regime of industrial applications. In this monograph, a multimodal design scheme for safe, lightweight design is proposed, that can be applied with commercially available software, takes nonlinear material behavior and failure into account, and is suitable for transient mechanics. It will be formulated as a generative design model in the KBE framework. The approach combines and advances available methods of TO, namely SIMP, FSO and MMO and aims at providing design engineers with an automated design

tool to generate lightweight and also safe design solutions. The approach is so far implemented in 2D and highly automated incorporating commercial software. The potential of the approach is shown in an example problem and validated in 3D printing of optimized structures and mechanical testing.

17.2 Theoretical Framework

In the following, the description of the mechanical analysis modes and numerical approach as well as the theoretical background of the applied TO model are presented.

17.2.1 Linear, Elastic, and Static Problem Description

For the design of a mechanical part, it is initially assumed that the loading condition is static and resulting deformations are sufficiently small and reversible. The constitutive relation is assumed to be well approximated by a Cauchy-elastic material. The governing equations for this case are the relations of static elasticity, described e.g. in Hughes (2012), which can be derived from the conservation laws in the equilibrium condition. The strain measure being the kinematic relation of displacements \mathbf{u} and strains ϵ can be derived from an infinitesimal element in the geometrically linearized form.

$$\vec{\epsilon} = \frac{1}{2} ((\nabla \vec{u})^T + \nabla \vec{u}) \quad \text{or} \quad \vec{\epsilon} = \vec{L} \vec{u} \quad (17.1)$$

\mathbf{L} is a differential operator that will be used for shortness in the description later on. The compatibility condition of Saint-Venant of a linear elastic continuum domain that deforms without gaps or overlaps reduces the number of differential equations of (17.1) to six. The constitutive relation associating strains with stresses for a linear-elastic, homogeneous and isotropic material, which is a reasonable assumption for most metals, is described by Hooke's law. The elasticity tensor \mathbf{E} is then a function of only two independent scalars, for example Young's modulus Y and Poisson's ratio ν .

$$\vec{\sigma} = \vec{E} : \vec{\epsilon}, \quad \vec{E} = f(Y, \nu) \quad (17.2)$$

To find approximated solutions for the displacements, strains and stresses due to loading conditions, the finite element method is used. For the derivation of the specific relations, the principle of the minimum of the potential energy is utilized in the weak form, which states: The best solution as well as the approximated solution of the displacement field \mathbf{u} that fulfills the conservation laws results in the minimum of potential energy. Consequently, for the variation of the potential energy Π one can write

$$\delta \Pi(\vec{u}, \vec{L}u) = 0 \quad (17.3)$$

Using the weak form and implementing the relations of linear elasticity yields

$$\delta \Pi = \int_{\Omega} \left(\delta \vec{u}^T \vec{L}^T \right) \vec{E} \left(\vec{L} \vec{u} \right) d\Omega - \int_{\Omega} \vec{u}^T \vec{f} d\Omega - \int_{\Gamma_{\sigma}} \vec{u}^T \vec{t} d\Gamma = 0 \quad (17.4)$$

(17.4) formulates the variation of the potential energy as a functional of \mathbf{u} eliminating the stress and strain relations. \mathbf{f} are the volume forces and \hat{t} the traction vector of prescribed stresses. To solve a discrete set of node displacements in a finite element discretization, the elastic potential in the weak form is discretized spatially with ansatz functions and differentiated in the discrete node displacements \hat{u} , see Hughes (2012) for more details. The discrete form can be written in the well-known form

$$\frac{d\Pi}{d\vec{u}} = \vec{K}\vec{u} - \vec{r} = 0 \quad (17.5)$$

The global stiffness matrix \mathbf{K} is composed of the element stiffness matrices and depends on the quantities of material, geometry and discretization. The vector of node values \mathbf{r} contains the prescribed boundary conditions. In this linear, elastic and static design problem, the nodal displacements can be directly received by solving the linear set of equations of (17.5).

17.2.2 Nonlinear, Plastic, and Transient Problem Description

Secondly, assume a design problem, where the loading leads to the material responding with irreversible plastic deformation and eventually to total failure due to rupture. The stress-strain relation then becomes nonlinear and the assumptions of linear elasticity and Hooke's law cannot be applied. In addition, other forms of non-linearity as well as the time dependence should be considered depending on the particular problem. The here presented description is based on references Hiermaier (2007); Hughes (2012); Sanchez (2018).

Nonlinear Geometry

For large displacements, the geometric relations in the governing equations need to be described with a nonlinear theory that is not based on the linearized deformation of an infinite element. In addition, other strain measures might be more suitable to the modeling of observed deformations. Large displacements might occur in problems with linear-elastic materials, small deformations and small strains, e.g. for ropes or shell structures, but often appear for large strains in plastic deformation. In general terms, the deformation gradient \mathbf{F} describes the transformation of a deformed \vec{X} and

an undeformed line segment \vec{x} of the material, as in (17.6). From this geometrical description, suitable measures for stress and strain can be derived for the constitutive relations.

Nonlinear Material

For nonlinear material behavior, the stress and strain measure as well as the stress-strain constitutive relation need to be modeled according to the material observations. The common approach for technical materials like metals is to describe the kinematics of plasticity by decomposition of the elastic and plastic contributions to the deformation. It is illustrated here using the deformation gradient tensor

$$\vec{F} = \frac{d\vec{x}}{d\vec{X}}, \quad \vec{F} = \vec{F}^e \cdot \vec{F}^p \quad (17.6)$$

The selection of a constitutive model is based on practical aspects. A popular example used in this work for metals and often utilized in transient engineering applications with strain-rate dependency is the Johnson-Cook constitutive and damage model. It uses a logarithmic strain measure (true strain) and assumes that plastification is initiated when the material stress state exceeds the elastic limit, also referred to as the yield stress. A yield criterion is specified in dependence of the von Mises stress state σ_M in the form of an isotropic yield function F . It additionally depends on a set of history variables γ that are evolved in time.

$$F = F(\sigma_M, \gamma) \quad (17.7)$$

In a similar way, the Johnson-Cook damage model introduces a damage history variable to the yield function to indicate material that has lost its load carrying capability. The requirement $F = 0$ is the consistency condition for the plasticity model. When $F < 0$, the material is assumed to behave elastic, otherwise the plastic strain increments are solved from the plastic model. For a more detailed description of plastic material modeling and the Johnson-cook models, the reader is referred to Hiermaier (2007); Sanchez (2018).

Nonlinear Boundary Conditions

The set of conditions on the boundary nodes of the spatially discretized domain are clustered into Neumann boundary conditions purporting stress states, or Dirichlet boundary conditions purporting displacements, respectively. Those relations can vary in time or become nonlinear, when they depend on the displacement of the boundary of the body. Additionally, new nonlinear boundary conditions can appear, e.g., by material rupture or contact events.

Nonlinear, Transient Solution Method

To solve a nonlinear, transient problem, the finite element system of equations needs to be extended to the conservation laws of transient dynamics and the dependence of the relations from the displacement field as well as its derivatives in time. The momentum balance in discrete form reads

$$\vec{M}\ddot{\vec{u}} + \vec{C}\dot{\vec{u}} + \vec{K}\vec{u} - \vec{r} = 0 \quad (17.8)$$

In (17.8) \vec{M} and \vec{C} are the mass and damping matrix of the system. All relations in (17.8) potentially evolve in time and depend on the displacement field. There are generally two solution strategies that use a time integration process in a discretized time domain. The time is typically discretized by a finite difference method and the increments are calculated on the basis of stability criteria of the numerical approach. An implicit time integration scheme will approximate the progression of the state variables in time and solve a transformed system of nonlinear but time-independent equations that is a function of known and unknown state variables. Instead, an explicit time integration scheme will solve the unknown state variables directly from the extrapolation of the known state variables in time. The time integration scheme is chosen based on the dynamic character of the analysis problem. Usually, the explicit method is more suitable when small time steps need to be utilized for the description of the system response, e.g. in high-speed impact scenarios or strong non-linearities, e.g. in rupturing events. It has the drawback that the numerical stability of the time stepping scheme depends on the information transport of wave propagation through the discretized spatial domain. The step-size can only be increased up to a limited extent by non-physical manipulations, e.g. by manipulating the nodal material density. The stability of an implicit scheme depends on the invertibility of matrices in (17.8) and the extent of nonlinearity in the solution that needs to be well-approximated and can potentially allow much larger time steps.

In the solution strategy of the multimodal approach, both time integration schemes can generally be utilized, depending on the particular problem, and the reason for the method of choice in the implemented design problem will be explained later on.

17.2.3 Topology Optimization

For the implementation of intelligent design iterations with the TO method, the design problem needs to be transferred into a mathematical description of a structural optimization problem. For this purpose, an objective function as a relation of design criteria (e.g. stiffness, weight, cost) is specified in dependence of design variables. The objective function is then gradually minimized with respect to the set of feasible design solutions and typically, a set of constraint functions. The latter can be natural bounds or consistency constraints. For topology optimization, the design variables are a modeling approach of the material distribution, respectively the topology of

the structure. The TO problem becomes the search for the best material distribution in a material domain Ω_{mat} as part of a bigger design space Ω , for which the boundary conditions are specified. For the common parametrization of this distribution problem, the stiffness tensor is utilized as being non-homogeneous

$$\vec{E} = \vec{E}(\vec{x}) = \rho(\vec{x})\vec{E}^0, \quad \rho(\vec{x}) = \begin{cases} 1 & \text{if } x \in \Omega_{mat} \\ 0 & \text{if } x \in \Omega \setminus \Omega_{mat} \end{cases} \quad (17.9)$$

This problem is also named the discrete TO problem of finding the discrete distribution of the stiffness tensor $\vec{E}(\vec{x})$ respectively its indicator function $\rho(\vec{x})$, being the design variable. A very effective TO objective for lightweight is the minimization of the structure's mean compliance subject to a mass constraint. This description can be directly related to the common criteria of maximizing the stiffness to weight ratio of a lightweight construction. It is the optimization problem that is utilized in this work and described further on in more detail.

The mean compliance C , according to Schumacher (2005), is understood as the work performed by the applied external stresses and volume forces on the displacements, minus the internal energy increment necessary for the prescribed displacements in the equilibrium state

$$C = \int_{\Gamma_t} \vec{u}^T \vec{t} d\Gamma + \int_{\Omega} \vec{u}^T \vec{f} d\Omega - \int_{\Gamma_a} \hat{\vec{u}}^T \vec{t} d\Gamma \quad (17.10)$$

And the approximated mean compliance \tilde{c} can be solved by

$$\tilde{c} = \vec{u}^T \vec{r} \quad (17.11)$$

In the case of exclusively prescribed loads, the mean compliance of the static problem can also be derived from the variation of the total potential energy as twice the strain energy or twice the work of the external loads against the corresponding displacements at equilibrium

$$C_{\hat{\sigma}} = \int_{\Omega} \vec{\sigma} : \vec{\epsilon} d\Omega \quad (17.12)$$

One can conclude from (17.12) that a minimization of $C_{\hat{\sigma}}$ for prescribed external forces minimizes the domain integral of the strain energy density. Consequently, the minimization of the compliance also minimizes the mean stress level in the structure. The difficulty of minimizing the maximum stress in the structure as part of the objective function, which would be beneficial from an engineering standpoint, was mentioned in the introduction. It is generally preferred to use an objective functional of non-localized variables that are integrated over the domain (Schumacher, 2005). This is due to the potential delocalization or degeneration of the objective phenomenon from one optimization iteration to the next. A highly nonlinear and localized objective such as the local stress can generally lead to non-convergence of the optimization or ill-posedness of the optimization problem (Bendsoe and Sigmund, 2013).

In the discrete form, the optimization problem of the mean compliance can be written as follows

$$\min_{\vec{E}_e, \vec{u}} \vec{u}^T \vec{r} \quad (17.13)$$

$$\text{subject to : } \vec{K}(\vec{E}_e)\vec{u} = \vec{r}, \quad \vec{E}_e \in \vec{E}_{ad} \quad (17.14)$$

(17.14) is the discrete equality condition of the linear-elastic and static problem that needs to be fulfilled in every iteration of the optimization and \vec{E}_{ad} is the set of admissible stiffness tensors. In the iteration process, the compliance should be minimized in respect to the design variable fields \vec{E}_e and \vec{u} , which represent the material distribution and the solution of the displacement field by a finite element analysis. For completeness, a mass or volume constraint is necessary, which is depicted in (17.16). Otherwise, the full design domain would be utilized with material for minimum compliance, contradicting the material distribution objective.

The optimization problem of (17.13)-(17.14) can be identified as a distributed, integer valued problem in the element stiffness tensors. Consequently, it has a high number of design variables, which is not beneficial to the solution process (Bendsoe and Sigmund, 2013). For this reason, a very common approach, most popular within the SIMP method, is the representation of the material distribution through a continuous artificial density field function as the material indicator function. The formulation is as follows

$$\vec{E}_e(\vec{x}) = \rho(\vec{x})^p \vec{E}^0, \quad p > 1 \quad (17.15)$$

$$\int_{\Omega} \rho(\vec{x}) d\Omega \leq V; \quad 0 \leq \rho(\vec{x}) \leq 1, \quad x \in \Omega \quad (17.16)$$

$$E_{e,ijkl}(\rho = 0) = 0; \quad E_{e,ijkl}(\rho = 1) = E_{e,ijkl}^0 \quad (17.17)$$

The SIMP approach is therefore solving a continuous topology problem, where the domain is discretized by finite elements and the density field, which becomes the design variable, is a continuous field function in the bounds of 0 and 1. This non-physical density can be related to the volume occupied by material as can be seen in (17.16) and used for the definition of the before mentioned volume or mass constraint. The density field interpolates between the material properties represented by the stiffness tensor. For density values of 0 and 1, the performance can be evaluated by the correct physics of the material. To circumvent non-physical intermediate densities in the design domain, the SIMP method utilizes a punishment strategy by using the penalty factor of $p > 1$ to steer the design to a 0 and 1 solution. As stated in Bendsoe and Sigmund (2013), the SIMP method generally leads to differentiable and good-behaved descriptions that can be efficiently solved by gradient-based optimization algorithms.

17.3 Multimodal Approach for the Mechanical Design

The multimodal approach to mechanical design proposed in this work can be described in the context of the known concepts of knowledge based engineering (KBE) and multidisciplinary design optimization (MDO). Following the KBE description of La Rocca (2012), the MDO formulation of the multimodal design scheme can be viewed as a generative model of the mechanical design, which automatically generates an engineered solution from the input data derived from technical specifications. For the topology design of mechanical parts, an MDO description can become very complex. This is due to the geometric complexity and number of possible design solutions that makes the simultaneous evaluation and optimization of multiple physical quantities challenging. Also, the automatic generation of high fidelity CAD models for design iteration and validation becomes important (see, e.g., Amadori et al, 2012). The particular involvement of topology optimization and interconnection with the direct validation of results in a high fidelity analysis mode is therefore novel in the multimodal approach. In Fig. 17.1, the overview of the design scheme is illustrated.

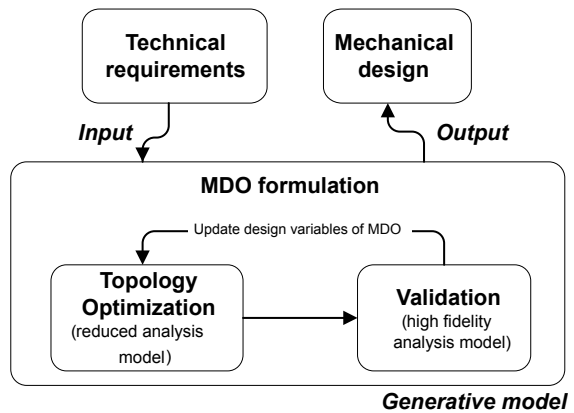


Fig. 17.1 Overview of the multimodal mechanical design scheme as a generative model in the KBE framework

In the mode conversion from the TO mechanical description to the validation, an automated CAD generation is clearly preferred to enable a higher accuracy of the computation e.g. with mesh refinement. The MDO formulation of the multimodal scheme then describes the problem of finding the optimized mechanical design, which should be a comparatively mature solution, when the validation result matches the design requirements and constraints, and additionally the optimization of performance criteria is converged. Until then, the design variables and optimization parameters are updated by a nonlinear programming scheme. In the next section, it can be seen that such a generative model can be assembled for specific applications, respectively design problems.

Due to some similarities, here follows a discussion of other known multimodal approaches to nonlinear design problems in relation to the proposed design scheme. Reviewed representatives are the ESLM and HCA nonlinear topology optimization

approaches. Both are multimodal approaches and HCA has been specifically designed for crashworthiness applications (see, e.g., Duddeck et al, 2016). In both methods, initially a high fidelity model, e.g. a nonlinear and transient analysis, is run on the design to solve the displacement field and design criteria in an outer loop. In ESLM for the design iteration, equivalent static loads (ESL) are calculated globally or for a selection of time steps using the linear finite element stiffness matrix of a reduced model. The ESLs are then applied to a multiple load TO formulation on that reduced model in an inner loop. In contrast, a common HCA approach is the use of an empiric local update rule in the inner loop that tries to homogenize the strain energy for the nonlinear loading.

Both of the methods are tailored to specific applications. As noted in Duddeck et al (2016) they have both difficulties of handling strong non-linearities like material rupture or buckling. In addition, the spatial discretization of the high fidelity model is not independent from the reduced model in those approaches due to the nodal character of the ESL calculation and the local update rule in HCA. This can be a drawback in the validation quality of the high fidelity model. Anyway, both methods could be potentially integrated in a generative model of the presented general multimodal scheme of Fig. 17.1 by addition of an additional high fidelity validation of the converged nonlinear topology optimization result. The latter then becomes an interim result and the design can be automatically iterated according to an MDO strategy.

17.4 Safe, Lightweight Design Scheme

The multimodal approach is discussed hereafter by means of its application to a safe, lightweight design (SLD) scheme. The safety of lightweight optimized structures is ensured by enhancing the capabilities of graceful degradation in overstraining by worst-case events and simultaneously optimizing for stiffness. Matters of uncertainty e.g. leading to spatially random material failure are not discussed here but could be included in the future.

Worst-case events usually have a much lower cycle number than operating loads and thus are allowed a higher stress state or even plastic deformation. They are typically approximated by worst-case assumptions of static loads only allowed for linear-elastic deformations, which is also the common approach of implementing them in a SIMP topology optimization formulation. In the SIMP approach, they are possibly the loads that lead to the highest compliance of the structure. Thereby, they can overreachingly steer the design solution and lead to unnecessary high safety margins for the topology result. The multimodal approach applied in this safe, lightweight design scheme aims for more efficient but reliable design solutions for such worst-case scenarios.

In Fig. 17.2, an overview of the design scheme, including procedures and interactions, is given with illustrations of a cantilever beam under a bending load.

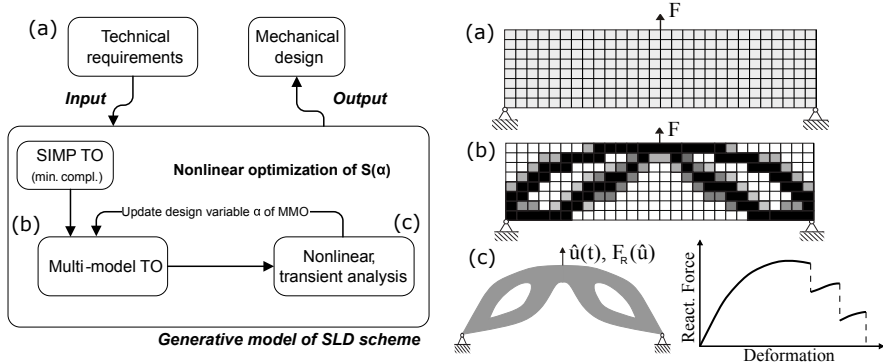


Fig. 17.2 Overview of the save, lightweight design scheme and procedures (left) and illustration of a cantilever design problem (right).

The scheme consists of a standard min. compliance SIMP topology optimization and a subsequent nonlinear optimization, with the goal of enhancing the structural ductility by elastic-plastic energy absorption and fail-safe behavior of the stiffness-optimized topology for a worst-case scenario. For this purpose, a local damage model is used in a multiple-model topology optimization (MMO) approach for generating redundant load paths. In contrast to the FSO approach discussed in Jansen et al (2014); Zhou and Fleury (2016), no random local damage model is used, but instead, the damage model for the MMO is generated from a SIMP topology result and density distribution. In that way, potentially a much smaller number of models (here only two) needs to be evaluated in the MMO. Also, knowledge about potentially critical sections in the worst-case can be applied. The MMO has then the goal to find alternative load paths with a structural redundancy in the resulting topology. The MMO models are weighted with a characteristic parameter, which is the design variable for the nonlinear programming scheme.

The MMO based TO is solely based on the linear, elastic and static analysis mode of the structure. Additionally, the nonlinear, plastic and transient analysis mode is introduced in the nonlinear optimization strategy. The latter is automatically generated from the MMO boundary conditions and density distribution result, as will be described in 17.5.2 and 17.5.3. In the optimization, a safety measure is evaluated, which is parametrically optimized based on characteristic values of the deformation energy and fail-safe behavior in the validation by the nonlinear analysis.

The complete generative design model is automated to a high degree. So far, the critical manual and empirical steps are the derivation of the models for the MMO, as described in the next section, as well as the initial definition of conversion aspects of boundary conditions between the low and high fidelity analysis modes.

17.5 Implementation and Demonstration

The implementation of the SLD scheme is described in the following example of a tension cantilever beam supported on one side and loaded by a unidirectional and uniformly distributed tension force. This example is chosen because the numerical results can be easily tested in a tension test experiment. The material is a 3D printing aluminum alloy (AlMgSc). The material properties are assumed homogeneous and isotropic and the following characteristic mechanical values are taken. They have been derived from tensile test measurements on 3D printed specimen without heat and surface treatment are Young's modulus $Y = 59$ GPa, yield stress $R_{p0.2} = 210$ MPa, ultimate tensile strength $R_m = 319$ MPa and density $\rho = 2,7$ g/cm³. The design problem and SIMP topology result solved in a commercial code are illustrated in the upper model (0) of Fig. 17.3.

17.5.1 Multiple-Model Topology Optimization

The MMO approach to fail-safe behavior proposed here is a new concept but based on the basic idea of a local damage model in FSO of Jansen et al (2014); Zhou and Fleury (2016). From the density result (0) in Fig. 17.3, where black regions represent fully dense material, multiple domains are derived for the MMO model definition. The areas are filtered empirically for the description of the local damage model by a weakening of the local element stiffness through the Young's modulus. This procedure will most probably lead to the assignment of a low density value to the weakened elements, due to the low mechanical effectiveness. The derived two models for the MMO are illustrated in the bottom of Fig. 17.3. Model (1) is weakened in the areas where the topology result of (0) has dense material. For this reason, alternative load paths are to be found in optimizing the compliance of this model. The distribution of weakened elements for Model (2) is similar to the inverse of the density of the topology result of (0) and thus will lead to a similar result. The support (I) and load application areas (III) are equally defined as non-design space with a Young's modulus of Y^0 for both derived models (1) and (2). Areas (II) are filtered empirically by a search algorithm to allow for intersections of the not weakened domains in the individual model.

The min. compliance objective for the MMO is defined as the weighted compliance of the two models suspect to a volume constraint, as in (17.18) and (17.19).

$$\min_{\rho, \vec{u}} \tilde{c}(\rho) = \alpha \tilde{c}_1(\rho) + \tilde{c}_2(\rho) \quad (17.18)$$

$$\int_{\Omega} \rho(x) d\Omega \leq V; \quad 0 \leq \rho(x) \leq 1, \quad x \in \Omega \quad (17.19)$$

In (17.18) \tilde{c} is a combined weighted compliance value, whereas \tilde{c}_1 corresponds to model (1) and \tilde{c}_2 to (2). For the individual model, the equilibrium condition of

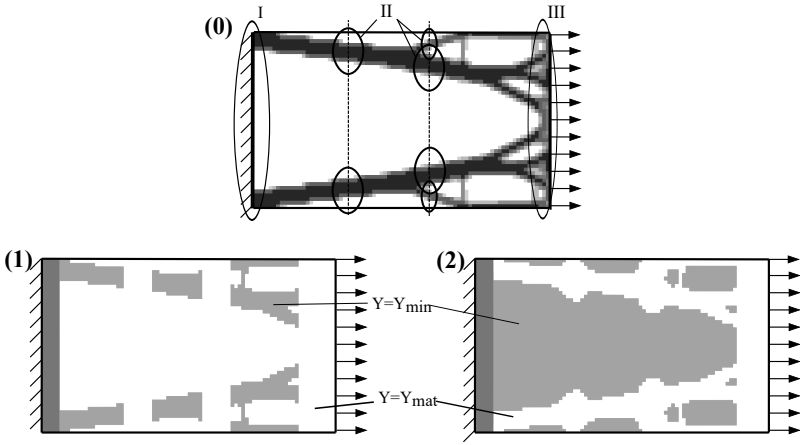


Fig. 17.3 Generation of models for MMO from the density result of the min. compliance optimization.

(17.14) holds as well as the SIMP parametrization of (17.15) and (17.17) for the areas $Y = Y_{mat}$. For the areas where $Y = Y_{min}$ holds $Y_{min}(x) = \rho(x)^p Y_{min}^0$ with an arbitrary weakened Young's modulus Y_{min}^0 .

The models are weighted with the characteristic parameter α , which is to be determined in the nonlinear optimization. The simultaneous minimization of the compliance in both models with local damage areas, when suitably determined, is supposed to lead to the formation of redundant load paths in the resulting design.

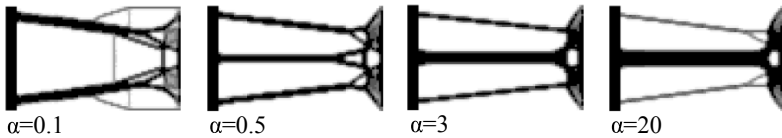


Fig. 17.4 Topology results of the MMO depending on the characteristic parameter α .

In Fig. 17.4, the MMO results for the described configuration from Fig. 17.3 are illustrated. For values of α below 0.5 and more significantly below 0.1 the second model has higher weighting and the density result converges to a result similar to the stiffness optimized SIMP topology of the initial design problem. For increasing values of α , the alternative model (1) has a higher impact on the MMO result.

17.5.2 Conversion of Analysis Modes

In the multimodal SLD scheme, both the linear-elastic and static analysis mode as well as the nonlinear, plastic and transient analysis mode are used. The first one is utilized for fast iterations in the topology optimization. The nonlinear, plastic and transient analysis is used as a validation of the topology design and iteration of the nonlinear optimization by evaluating the safety measure objective function. For a graceful degradation in overstraining design goal, both should be modeling approaches of the same mechanical design problem. The conversion as well as the information value are to be discussed for the particular problem, as will be done for the implementation of the worst-case validation hereafter. The following mechanical mode conversions are composed for the SLD scheme:

Constitutive relation:

linear-elastic, Hooke's law \Rightarrow nonlinear, plastic model of Johnson-Cook

Loading boundary condition (LBC):

Neumann LBC of prescribed static load \Rightarrow Dirichlet LBC of prescribed linear increasing displacement

Time dependency:

static problem \Rightarrow time-dependent material state variables and boundary conditions

In the SLD scheme implementation, both modes are designed to have preferably concordant information value when no or insignificant plastic deformation occurs. For this purpose, the nonlinear, time-dependent problem is designed to be quasi-static, also matching the experimental setup, as will be seen later. From Hooke's law it can be derived that in the static problem, the displacement increases linearly with the prescribed force or likewise the reaction force increases linearly with a prescribed displacement. The external work in the static problem can be denoted as follows

$$W_{ext,stat} = \frac{1}{2} \vec{u}^T \vec{F} = -\frac{1}{2} \vec{u}^T \vec{F}_R; \quad (17.20)$$

For a single point load or point displacement, the external energy as well as the stress and strain fields of both analysis modes would match for concordant prescribed loads and displacements in the linear elastic regime. It is to be noted that the distribution of local stresses and strains can be significantly different between the modes for distributed loads or displacements, due to the differences in local stiffness of the structure, as is illustrated in Fig. 17.5.

The nonlinear analysis should validate the performance of the structure by overstraining in a disproportionate worst-case scenario. For this purpose, a preferably equivalent LBC is applied to both analysis modes but with an overloading characteristic in the nonlinear analysis. Initially, a time-dependent LBC is chosen such that the energy from external forces, and the strain energy of both analysis modes match in the linear elastic deformation regime. For this purpose, a prescribed displacement is applied to increase linearly with time (with a constant, but sufficiently small velocity to match the quasi-static condition). It will result in a linearly increasing reaction force of the structure, as long as no plastification occurs and the material relation

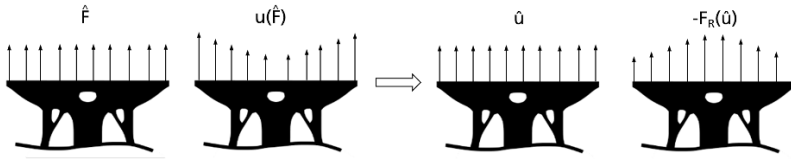


Fig. 17.5 Comparison of prescribed distributed loads (left half) respectively displacements (right half) and consecutive structural response

can be assumed as being linear-elastic. While the latter holds true, the work done by the external loading condition then matches for both analysis modes. This is a simplification as local plastic strains can appear also for small loads or displacements depending on the local stress state. The overloading scenario emerges, when the further increasing displacement leads to a significant plastic deformation and subsequently to rupture of structural members.

The same accordance could be achieved for a prescribed force matching the static Neumann LBC but linearly increases in time. This condition would have benefits in matching local stress distributions of the two modes in the linear elastic regime. Still, this prescribed overstraining force condition is not preferred here for the nonlinear analysis, as the transition from elastic to plastic behavior and ultimately failure of the material would happen in a very short time interval, making it improper for evaluation of the plastic deformation and graceful degradation capabilities of the structure. However, for a prescribed linearly increasing displacement, the deformation energy also in the plastic and failure regime can be suitably evaluated by the analysis of the structure and by measuring of the reaction forces, as will be seen in the numerical and experimental results.

17.5.3 Conversion of the Analysis Domain and Spatial Discretization

The topology result of the MMO is a continuous density field. Therefore, filtering with a density threshold and a geometrical smoothing operation are applied to obtain a discrete geometry.

$$M_{e,nl} = \{M_e \in \Omega | \rho_e > \rho_l\} \tag{17.21}$$

$M_{e,nl}$ in (17.21) is the set of elements considered for the geometry reconstruction for the high fidelity model. All elements are considered with a density ρ_e greater than a defined threshold ρ_l , which should be in accordance with the volume constraint but should also lead to a consistent geometry with smooth transitions of structural members.

Fig. 17.6 illustrates the automated geometry reconstruction and remeshing of the design domain. This process enhances the flexibility of the proposed scheme as

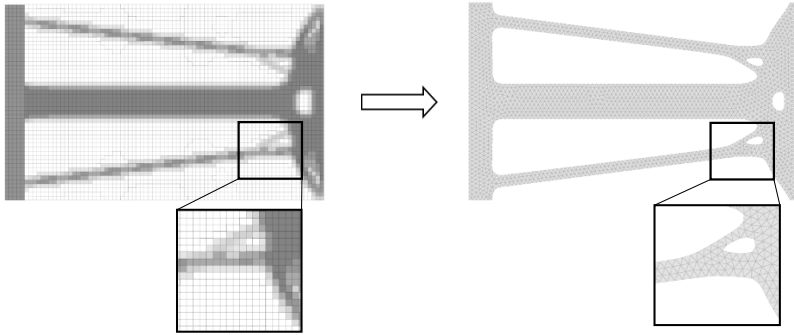


Fig. 17.6 Spatial transformation and discretization conversion between the analysis modes

the descriptions of both analysis modes become as independent as intended for the particular problem. Moreover, the accuracy as well as computational efficiency of the validation step can potentially be increased significantly. Thus, when the nonlinear optimization converges and the validation meets the acceptance criteria, the design is expected to be comparatively mature.

17.5.4 Nonlinear Analysis and Nonlinear Optimization

The objective of the nonlinear optimization is to find the best value of α , for which the design has an optimized performance in the worst-case scenario. Here it is assumed that the safety of the structure in overloading can be enhanced by increasing the load carrying capacity, structural ductility and energy absorption capabilities before and after material rupture or collapse of the structure. More complex or conflicting safety objectives, which are known e.g. from crashworthiness design problems, are not considered here. A safety measure for energy absorption and fail-safe behavior in the worst-case scenario is defined as follows

$$S(\alpha) = E_{nl,tot}^V(\alpha) + \beta E_{nl,rup}^V(\alpha) \quad (17.22)$$

The safety measure $S(\alpha)$ is defined as a relation of the deformation energy in the nonlinear analysis. The latter is a function of α , as the geometry for the nonlinear analysis depends on the weighting parameter in the MMO. While $E_{nl,tot}^V$ denotes in (17.22) the total volume specific deformation energy, $E_{nl,rup}^V$ corresponds to the portion between first rupture of one structural member until global failure. The scalar parameter β is a weighting factor that can be used to put emphasis on the fail-safe behavior of the structure and will be neglected for the example problem.

As the failure behavior is potentially highly nonlinear and multiple ruptures should be resolved accurately, a nonlinear analysis with explicit time-integration is preferred in the shown example and has shown more stable results than the implicit approach.

The LBC in the nonlinear analysis of a constant tension velocity was described in the last section and its value in the simulation was chosen to match the traverse speed of 1.0 mm/s of the experimental tension testing setup. In Fig. 17.7, the stress distribution in the nonlinear, transient analysis directly before the first rupture is compared between the standard topology result of the SIMP method and the Design b), which was optimized with the SLD scheme. Both designs fail at different times and prescribed displacements, as will be seen in the summary graphs of Fig. 17.10. The markers and numbering indicate the position and sequence of the ruptures. The star marks a simultaneous rupture of members in design a), which can be seen as a cascading behaving leading to a total collapse and is clearly not fail-safe.

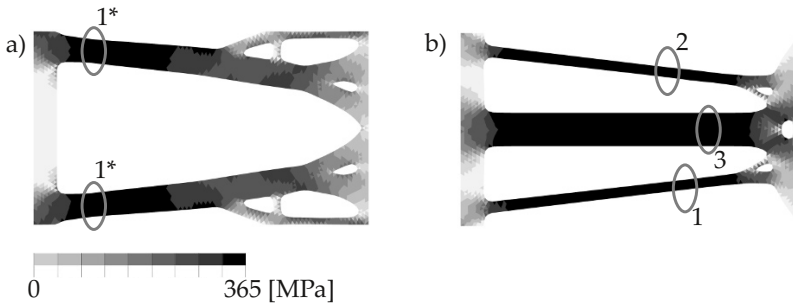


Fig. 17.7 Stress distribution before first rupture (at a different time and prescribed displacement) of the standard SIMP topology of design a) and the design b); the latter optimized with the SLD scheme

The nonlinear optimization is performed with a golden-section search and the optimized value of α that has been found after 7 iterations in the nonlinear optimization for the described design problem is $\alpha_{opt} = 17.23$.

17.6 Experimental Validation by Testing of 3D Printed Structures

For experimental validation, the two configurations of Fig. 17.7 are designed for 3D printing with equal mass and tested in tension.

An AlMgSc aluminum alloy is used with approximated mechanical values described in the last section. At the current stage, the analysis does not consider that the mechanical properties for the 3D printed material can be inhomogeneous with possibly included material defects, and can depend on the cross sectional dimension. Each specimen is fixed on the left side of Fig. 17.8 and loaded axially with a uniform traverse speed of 1.0 mm/s on the other side. The applied force raised by the machine for impinging the uniform speed on the specimen is measured in the experiment. In Fig. 17.9 and the graphs of Fig. 17.10, the tensile test results are illustrated. The

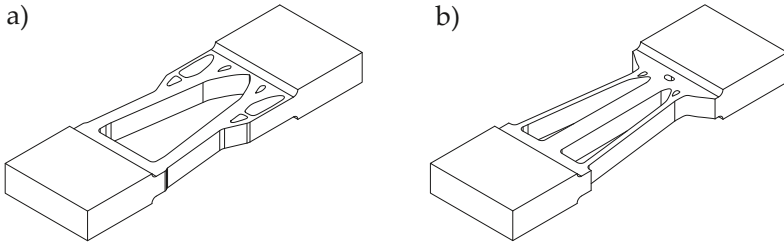


Fig. 17.8 CAD models for 3D printing of designs a) and b) with equal mass, thickness and clamping area

rupture areas and sequence of rupture are marked in white and by numeration. The SIMP design a) shows a collapsing failure directly when the first rupture occurs, due to the simultaneous breaking of the two marked beams. On the contrary, the configuration b) optimized by the proposed design scheme shows the intended structural ductility and fail-safe behavior. First, the beams with smaller cross section rupture, followed by the larger beam. The whole structure collapses at a higher level of tensile displacement, as shown in Fig. 17.10.

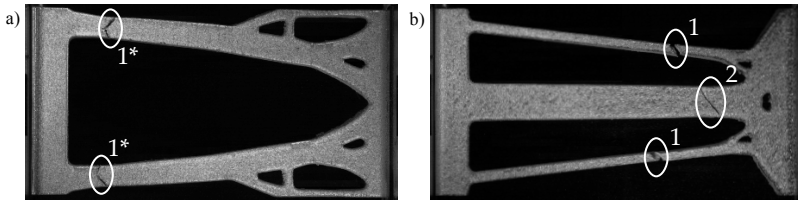


Fig. 17.9 3D printed specimen after tensile testing; left: design a) with indication of simultaneous rupture locations; right: design b) optimized with the SLD scheme with indication of fail-safe rupture sequence.

Table 17.1 Summary of simulation and experimental data of the compared designs a) and b); F_{max} indicates the maximum force applied by the test machine, respectively the maximum reaction force in the nonlinear analysis. The experimental data are mean values of three experiments, respectively, in which the standard deviation has been small.

| Design | F_{max} kN | E_{tot} J | E_{rup} J |
|-----------------|--------------|-------------|-------------|
| Design (a) Sim. | 42.6 | 122.9 | 0 |
| Design (b) Sim. | 46.8 | 307.3 | 40.3 |
| Design (a) Exp. | 42.97 | 191.87 | 0 |
| Design (b) Exp. | 47.87 | 312.17 | 52.33 |

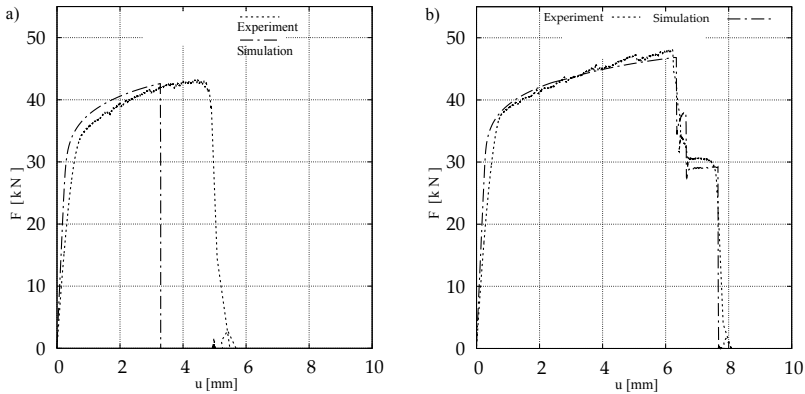


Fig. 17.10 Nonlinear analysis and experimental testing of 3D printed specimen; left: design a) from standard SIMP topology optimization; right: design b), result with $\alpha_{opt} = 17.23$ from the SLD scheme.

Fig. 17.10 and Tab. 17.1 compare the results of the measured and simulated applied force for the impinging displacement during the tensile test. The stiffness in the elastic regime differs between experiment and simulation. This is typically observed due to the settling of the clamped system and the stiffnesses of machine and mounting system and should not be of greater concern for the significance of the measurement. The simulation and experimental results are in good agreement and the same characteristic behavior can be observed. However, the data for the SIMP topology in a) differs slightly in the plastic regime. The latter could be due to the geometrical assumptions for the CAD models, complexity of the local shapes, the topology and notch effects, as well as modeling discrepancies of the plastic behavior of the material. Future, more detailed observation of the local damage behavior should be supported by extended digital image correlation, as described in Réthoré et al (2008). Nevertheless, the overall characteristic of the simulation and the successful optimization is validated with the experiments. The energy absorption as well as the maximum load carrying capacity before breakage are significantly improved for the overstraining scenario. Also, fail-safe behavior was successfully implemented for the SLD optimized design.

17.7 Conclusion

A multimodal scheme was proposed, described as a generative model in a KBE framework for automation of mechanical part design. By utilizing multiple modes of mechanical modeling and automated conversion, the potential shortcomings of the singular description should be circumvented. A specific scheme was presented for the application of safe, lightweight design (SLD), improving the structural ductility, energy absorption and fail-safe behavior of topology-optimized structures in

a worst-case overloading scenario. The common singular model approach to TO is based on the linear, elastic and static mechanical description of the design problem and cannot deal with the potential nonlinear, plastic and transient response of the structure due to substantial loading. The multimodal SLD scheme presented here was successfully implemented to overcome this deficiency. It was demonstrated on the numerical example of a cantilever beam under tensile loading. The design solution was 3D printed and validated in comparison to the result of the standard method in a tensile test experiment.

Embedded in the SLD scheme, a new MMO approach to fail-safe design was developed. It differs from the known FSO approach for random location of failure by using SIMP stiffness-optimized topology result for derivation of the MMO models. Thereby, a much smaller number of models is necessary. In the demonstrated example, only two models were used because the local damage model is applied to the optimized material domain instead of many localized areas of the complete design domain. This significantly enhances computational effectiveness of the MMO. It could be demonstrated for the example problem that redundancy of load paths is added to the structure and the energy absorption capabilities were improved substantially. The design optimized with the SLD scheme and new MMO approach was furthermore able to withstand significant loads after the first rupture and thus failed in a safe manner. This particular result has the potential of enhancing safety margin and safety factor assumptions in mechanical design.

The findings demonstrate the high potential of the multimodal scheme in improving the topology of the mechanical designs and design maturity, due to high fidelity validation. It was demonstrated in the SLD scheme, putting an additional focus on the nonlinear, plastic structural response as opposed to solely optimizing for linear, elastic stiffness. The SLD scheme is implemented in an automated way on the basis of commercial software tools. Still, there are manual and empirical design steps in the conception that need further improvement and automation. The derivation of models for the MMO is especially critical for the success of the optimization approach. Also, the correlation of boundary conditions in the linear analysis and the nonlinear analysis needs further investigation. For now, the SLD scheme is conceived for two-dimensional design problems with unidirectional loads. The extension to three dimensions and more complex boundary conditions in commercial applications will be the topic of future research.

Another prospect is the interconnection of the presented approach with the design of mechanical metamaterials. The latter can have exotic and compelling mechanical properties (Barchiesi et al, 2019). From the perspective of enhancing energy absorption and structural ductility pantographic lattices have shown very interesting qualities in withstanding large deformations before breaking (dell'Isola et al, 2016; Barchiesi et al, 2020). In addition, such metamaterials have many redundant load paths and can thus be expected to show an intrinsic fail-safe behavior. As the design with metamaterials is a very complicated task, it could on the other hand benefit of the automated high fidelity validation in a multimodal scheme. The latter could also be the case for other complex design problems that depend on elaborate analysis, e.g., in multi-discipline or impact engineering.

References

- Abdi M, Ashcroft I, Wildman R (2018) Topology optimization of geometrically nonlinear structures using an evolutionary optimization method. *Engineering Optimization* 50(11):1850–1870
- Ahmad Z, Sultan T, Zoppi M, Abid M, Jin Park G (2017) Nonlinear response topology optimization using equivalent static loads—case studies. *Engineering Optimization* 49(2):252–268
- Amadori K, Tarkian M, Ölvander J, Krus P (2012) Flexible and robust CAD models for design automation. *Advanced Engineering Informatics* 26(2):180–195
- Barchiesi E, Spagnuolo M, Placidi L (2019) Mechanical metamaterials: a state of the art. *Mathematics and Mechanics of Solids* 24(1):212–234
- Barchiesi E, Eugster SR, dell’Isola F, Hild F (2020) Large in-plane elastic deformations of bi-pantographic fabrics: asymptotic homogenization and experimental validation. *Mathematics and Mechanics of Solids* 25(3):739–767
- Bendsoe MP, Sigmund O (2013) *Topology optimization: theory, methods, and applications*. Springer Science & Business Media
- dell’Isola F, Giorgio I, Pawlikowski M, Rizzi NL (2016) Large deformations of planar extensible beams and pantographic lattices: heuristic homogenization, experimental and numerical examples of equilibrium. *Proceedings of the Royal Society A: Mathematical, Physical and Engineering Sciences* 472(2185):20150,790
- Desmorat B, Desmorat R (2008) Topology optimization in damage governed low cycle fatigue. *Comptes Rendus Mecanique* 336(5):448–453
- Dubbel H, Davies B (2013) *Dubbel-Handbook of mechanical engineering*. Springer Science & Business Media
- Duddeck F, Hunkeler S, Lozano P, Wehrle E, Zeng D (2016) Topology optimization for crashworthiness of thin-walled structures under axial impact using hybrid cellular automata. *Structural and Multidisciplinary Optimization* 54(3):415–428
- Herskovits J (2012) *Advances in structural optimization*, vol 25. Springer Science & Business Media
- Hiermaier S (2007) *Structures under crash and impact: continuum mechanics, discretization and experimental characterization*. Springer Science & Business Media
- Hughes TJ (2012) *The finite element method: linear static and dynamic finite element analysis*. Courier Corporation
- Jansen M, Lombaert G, Schevenels M, Sigmund O (2014) Topology optimization of fail-safe structures using a simplified local damage model. *Structural and Multidisciplinary Optimization* 49(4):657–666
- La Rocca G (2012) Knowledge based engineering: Between AI and CAD. Review of a language based technology to support engineering design. *Advanced engineering informatics* 26(2):159–179
- Li L, Zhang G, Khandelwal K (2018) Failure resistant topology optimization of structures using non-local elastoplastic-damage model. *Structural and Multidisciplinary Optimization* 58(4):1589–1618
- Mohr DP (2011) *Redundante topologieoptimierung*. PhD thesis, Universität der Bundeswehr München, Fakultät für Luft-und Raumfahrttechnik, Neubiberg
- Réthoré J, Hild F, Roux S (2008) Extended digital image correlation with crack shape optimization. *International Journal for Numerical Methods in Engineering* 73(2):248–272
- Sanchez JJ (2018) *The finite strain Johnson Cook plasticity and damage constitutive model in ALEGRA*. Tech. rep., Sandia National Lab.(SNL-NM), Albuquerque, NM (United States)
- Sandberg M, Gerth R, Lu W, Jansson G, Mikkavaara J, Olofsson T (2016) Design automation in construction: An overview. In: 33rd CIB W78 Conference 2016, Oct. 31st–Nov. 2nd 2016, Brisbane, Australia
- Schumacher A (2005) *Optimierung mechanischer strukturen*. Springer
- Schwarz S, Maute K, Ramm E (2001) Topology and shape optimization for elastoplastic structural response. *Computer Methods in Applied Mechanics and Engineering* 190(15-17):2135–2155

- Sigmund O, Maute K (2013) Topology optimization approaches. *Structural and Multidisciplinary Optimization* 48(6):1031–1055
- Zhou M, Fleury R (2016) Fail-safe topology optimization. *Structural and Multidisciplinary Optimization* 54(5):1225–1243



Chapter 18

Forced Longitudinal Fractional Type Vibrations of a Rod with Variable Cross Section

Katica R. (Stevanović) Hedrih

Abstract Forced longitudinal creep vibrations of a fractional type rheological rod with variable cross section are investigated. Partial fractional order differential equation and particular solutions for the case of forced creep longitudinal fractional type vibrations of the rod of creep material of a fractional type are determined. Corresponding eigen amplitude functions, from author's earlier published reference, containing expressions for different boundary conditions (rod with free ends, cantilever rod with weight on the free end, rod with weights at the both free ends) and different forms of variable cross sections (conical-shape rod, exponential-shape rod, catenary shape rod) as well as series of corresponding eigen values and natural circular frequencies of longitudinal creep fractional type vibrations are used for composing new determined general and particular solutions for describing forced longitudinal fractional type vibrations of the rod with variable cross section and presented in this paper.

Also, in this paper, the series of the eigen time-functions, for corresponding eigen amplitude functions, for forced longitudinal fractional type oscillations of a rod with variable cross section are determined. For solving ordinary fractional order differential equations and determination of the particular integral, Laplace transform and properties of three functions in convolution are used.

Energy analysis of the system of longitudinal fractional type oscillations in the rod with fractional type dissipation of mechanical energy is presented. The rate of the fractional type dissipation of mechanical energy of the rod's longitudinal vibrations as well as for its free and its forced fractional type modes is determined. On the basis of previously produced energy analysis, two theorems of change total mechanical energy of the rod's oscillations and of the free and also of forced modes of longitudinal fractional type vibrations of rod are defined. Normalized values of the kinetic and potential energies and normalized generalized function of fractional type dissipation of mechanical energy of free and also forced modes of longitudinal vibrations of

K. R. (Stevanović) Hedrih

Mathematical Institute of Serbian Academy of Sciences and Arts, Belgrade, Serbia.

e-mail: khedrih@sbb.rs; katicah@mi.sanu.ac.rs

a fractional type rod with variable cross section are expressed and introduced for energy analyses.

Keywords: Forced vibrations · Fractional order derivative · Variable cross section · Series of eigen time functions · Energy analysis

18.1 Introduction

Mechanics of hereditary material is being intensively developed and filled up with new research monographs (Rabotnov, 1977; Goroshko and Hedrih (Stevanović), 2001). This field of mechanics of hereditary medium is previously presented in scientific literature by monographs and papers as in Goroshko and Puchko (1997); Slonimsky (1961); Stojanovic (1965); Savin and Ruschisky (1976); Abali (2017) and is widely used in engineering analyses of strength and deformability of constructions made of new construction materials.

Actuality of that direction of development of mechanics is conditioned by engineering practice with utilizing the new construction materials on synthetic base, the mechanical properties of which often have pointed creep rheological character (Slonimsky, 1961; Abali, 2017).

The university books by Rašković (1965) obtain the classical theory of longitudinal oscillations of homogeneous rods and beams, and in Bishop (1952) we can find mathematical theory of corresponding partial differential equations. Bishop (1952) demonstrates some results on longitudinal waves in beams and Cohen and Whitman (1977) present research concerning waves in elastic rods. The effect of an arbitrarily mass on the longitudinal vibrations of a bar is investigated by Cutchins (1980).

As presented by Hedrih (Stevanović) and Filipovski (1995, 1999, 2002a,b), studies in nonlinear oscillations of longitudinal vibrations of an elastic and rheological rod with variable cross section are of interest in engineering systems applications such as ultrasonic transducers and ultrasonic concentrator as in Abramov et al (1984).

In Hedrih (Stevanović) and Filipovski (2002a), longitudinal creep vibrations are examined in a fractional type rheological rod with a variable cross section. Partial differential equation and particular solutions for the case of natural free longitudinal fractional type vibrations of the rod are derived. For the case of natural free fractional type vibrations, eigen amplitude function and eigen time-functions are determined for different examples of boundary conditions. Different boundary conditions are analyzed and series of natural circular frequencies and eigen values of fractional rod properties of longitudinal creep fractional type vibrations are obtained, their values are compiled in tables. By using MathCad software tools a series of graphical presentation of the time-function particular modes is presented. Among others, Bačlić and Atanacković (2000) is one of first published in the Serbian scientific literature in the field of fractional order derivative applied in vibrations of rod with constant cross sections. Also, we refer to Atanacković et al (2014) as a scientific

reference containing mathematical foundation of fractional calculus for applications in mechanics of continuum media with fractional type properties of materials.

In Hedrih (Stevanović) (2005, 2014b,c) and also Hedrih (Stevanović) (2014a, 2018); Hedrih (Stevanović) and Machado (2015), the generalized function of fractional type dissipation of the system energy and extended Lagrange differential equations in matrix form and for discrete fractional type system as well as dynamics of hybrid fractional type discrete continuum system dynamics are investigated and new results are presented. In a review reference (Rossikhin and Shitikova, 2010) series of applications of fractional calculus for dynamic problems of solid mechanics: novel trends and recent results are presented.

18.2 Fundamentals of Mechanics of Hereditary and Fractional Type Materials and Systems

The notions hereditary elasticity and viscoelasticity are equivalent in the material scientific literature. Rabotnov (1977), also in papers of V. Volter, claims that the notion hereditary elasticity is more adequate such that we give a better description on the essence of this phenomenon. This term expresses the ability of rheological body to specifically “remember” the history of loading (stretching). Viscoelastic body possesses the particularity of deforming:

- for the short-time-loading, fast form (shape) reconstruction of the body form after unloading occurs;
- for the long-time-loading, establishing of the form (shape) needs necessarily a long-time period after unloading, i.e. viscous-elastic bodies “remember” or “memorize”, which is reflexed in term “hereditary elasticity”

18.3 Constitutive Relation of the Fractional Type Material of the Rod

We assume that the rod is made of creep rheological material with fractional type properties. Taking into account that material of the rod is with fractional type dissipation of energy, the constitutive normal stress-strain relation of rod’s material is defined by fractional order derivative in the form:

$$\sigma(z, t) = -\{E_0\varepsilon(z, t) + E_\alpha \mathfrak{D}_t^\alpha[\varepsilon(z, t)]\}, \quad \alpha \in (0, 1), \quad t \in (0, b), \quad (18.1)$$

where $\mathfrak{D}_t^\alpha[\cdot]$ is the differential fractional order operator of α^{th} fractional order derivative, in the following form:

$$\mathfrak{D}_t^\alpha [\varepsilon(z, t)] = \frac{1}{\Gamma(1 - \alpha)} \frac{d}{dt} \int_0^t \frac{\varepsilon(z, \tau)}{(t - \tau)^\alpha} d\tau, \quad \alpha \in (0, 1), \quad t \in (0, b), \quad (18.2)$$

and $\sigma(z, t)$ normal stress for the plane cross section $A(z)$, and $\varepsilon_z(z, t) = \frac{\partial w(z, t)}{\partial z}$ is dilatation of the line element in direction orthogonal to the rod's cross section and in direction of rod's axis z .

Taking that strain, $\varepsilon_z(z, t)$, of an elementary linear element in rod's axial direction is in the form: $\varepsilon_z(z, t) = \frac{\partial w(z, t)}{\partial z}$, previous constitutive fractional type stress-strain relation in axial direction (18.1) is in the following form:

$$\sigma(z, t) = - \left\{ E_0 \frac{\partial w(z, t)}{\partial z} + E_\alpha \mathfrak{D}_t^\alpha \left[\frac{\partial w(z, t)}{\partial z} \right] \right\}, \quad \alpha \in (0, 1), \quad t \in (0, b). \quad (18.3)$$

18.4 Partial Fractional Order Differential Equation of Longitudinal Fractional Type Vibrations of a Rod with Variable Cross Section

Let us consider a deformable rod of a fractional type material properties, presented in Figure 18.1 (left), and with variable cross section $A(z)$, whose axis is straight and in the direction z . Figure 18.1 (right) shows an infinitesimal element of length

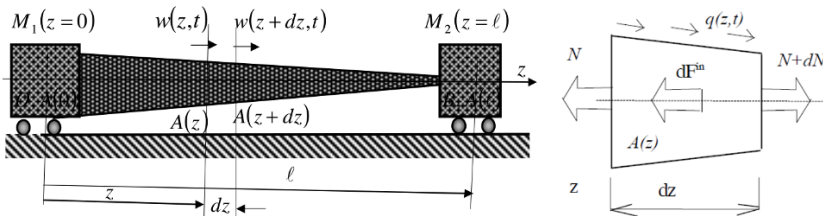


Fig. 18.1 Drawing of the system to be analyzed. *Left:* Rod with variable cross section and two weights on both ends; *Right:* An elementary part of length dz .

dz with variable cross section $A(z)$, where z denotes coordinates along rod's axis starting on the left end of the rod.

Normal axial surface force acting on the left cross sections $A(z)$ at the distance z measured from left end of the rod, directed in negative direction of the axis z reads

$$N(z, t) = -A(z)\sigma(z, t), \quad (18.4)$$

while its value in cross section on distance $z + dz$ is

$$N(z + dz, t) = A(z)\sigma(z, t) + \frac{\partial}{\partial z} \langle A(z)\sigma(z, t) \rangle dz, \quad (18.5)$$

where t is time, and $\sigma(z, t)$ is normal stress in the points of cross section at the distance z that is constant on the cross-section according to introduced assumption. Moreover deplaning of cross section is neglected considering that all points have the same axial displacement determined by coordinate $w(z, t)$ of axial displacements.

According to the D’Alambert’s principle of dynamical equilibrium of all forces, following equation could be written for dynamical equilibrium of forces acting on rod’s element:

$$\begin{aligned} \rho A(z) dz \frac{\partial^2 w(z, t)}{\partial t^2} &= -N(z, t) + N(z + dz, t) + q(z, t)A(z) dz \\ &= \frac{\partial N(z, t)}{\partial z} dz + q(z, t)A(z) dz, \end{aligned} \quad (18.6)$$

where ρ is rod material’s mass density, and $q(z, t)$ is a distributed volume force in axial direction. Substituting expressions (18.4) and (18.5) into equation (18.6) leads to

$$\frac{\partial^2 w(z, t)}{\partial t^2} - \frac{1}{\rho A(z)} \frac{\partial}{\partial z} [A(z)\sigma(z, t)] = \frac{1}{\rho} q(z, t). \quad (18.7)$$

Introducing previous fractional type constitutive stress-strain relation (18.3) into dynamic equation (18.7) of forced longitudinal fractional type vibrations, following partial fractional order differential equation can be written

$$\begin{aligned} \frac{\partial^2 w(z, t)}{\partial t^2} - \frac{E_0}{\rho A(z)} \frac{\partial}{\partial z} [A(z)\sigma(z, t)] &= \\ = \frac{E_\alpha}{\rho A(z)} \frac{\partial}{\partial z} \left[A(z) \mathfrak{D}_t^\alpha \left[\frac{\partial w(z, t)}{\partial z} \right] \right] + \frac{1}{\rho} q(z, t). \end{aligned} \quad (18.8)$$

If we introduce $c_0^2 = E_0/\rho$ and $c_\alpha^2 = E_\alpha/\rho$, then the partial fractional order differential equation (18.8) gets the following form:

$$\begin{aligned} \frac{1}{c_0^2} \frac{\partial^2 w(z, t)}{\partial t^2} - \frac{1}{A(z)} \frac{\partial}{\partial z} [A(z)\sigma(z, t)] &= \\ = \frac{c_\alpha^2}{c_0^2 A(z)} \frac{\partial}{\partial z} \left[A(z) \mathfrak{D}_t^\alpha \left[\frac{\partial w(z, t)}{\partial z} \right] \right] + \frac{1}{E_0} q(z, t). \end{aligned} \quad (18.9)$$

18.5 Solution of Partial Fractional Order Differential Equation

18.5.1 Free Longitudinal Fractional Type Oscillation

For free longitudinal fractional type vibrations proposing solution in the form $w(z, t) = Z(z)T(t)$, as in Hedrih (Stevanović) and Filipovski (2002a), partial fractional order differential equation is separated in system of two independent equations: first is ordinary differential equation along eigen amplitude function $Z(z)$ of the coordinate z as an argument and second is one ordinary fractional order differential equation along eigen time function $T(t)$ of the time t as argument, in the following forms:

$$\begin{aligned} Z''(z) + \frac{A'(z)}{A(z)}Z'(z) + k^2Z(z) &= 0, \\ \ddot{T}(t) + \omega_0^2T(t) + \omega_\alpha^2\mathfrak{D}_t^\alpha[T(t)] &= 0, \end{aligned} \quad (18.10)$$

where $\omega_0^2 = k^2c_0^2$ is introduced.

In Hedrih (Stevanović) and Filipovski (2002a) eigen amplitude functions $Z_s(z)$, $s = 1, 2, 3, \dots, \infty$ are determined for different variable cross sections (conical-shape rod, exponential-shape rod, catenary shape rod) of the rod and for different boundary conditions (rod with free ends, cantilever rod with weight on the free end, rod with weights at the both free ends), (for details see Hedrih (Stevanović) and Filipovski, 2002a)) with their corresponding characteristic numbers. Also, eigen time functions $T_s(t)$, $s = 1, 2, 3, \dots, \infty$ for each of infinite number of eigen amplitude functions $Z_s(z)$, $s = 1, 2, 3, \dots, \infty$ are determined as solution of ordinary fractional order differential equation (18.10)₂.

Eigen amplitude functions $Z_s(z)$, $s = 1, 2, 3, \dots, \infty$ satisfy orthogonality conditions. Characteristic numbers are: $\omega_{0s}^2 = k_s^2c_0^2$, $\omega_{\alpha s}^2 = k_s^2c_\alpha^2$, $s = 1, 2, 3, \dots, \infty$. Generalized family solutions, which satisfies the boundary conditions is in the form for free fractional type longitudinal vibrations

$$w(z, t) = \sum_{s=1}^{\infty} Z_s(z)T_s(t). \quad (18.11)$$

In previous solution (18.11) of the partial fractional order differential equation (18.9) for free longitudinal fractional type vibrations for $q(z, t) \equiv 0$, it is possible in each of the time functions from set $T_s(t)$, $s = 1, 2, 3, \dots, \infty$ to separate two particular approximate solutions, as fractional type modes, which look like cosine and look like sine, for details see Atanacković et al (2014); Hedrih (Stevanović) (2014a, 2018); Hedrih (Stevanović) and Machado (2015), as follows:

$$T_s(t, \alpha, \omega_{0s}, \omega_{(\alpha)s}) = T_s(0)\xi_{\cos,s}(t, \alpha, \omega_{0s}, \omega_{(\alpha)s}) + \dot{T}_s(0)\xi_{\sin,s}(t, \alpha, \omega_{0s}, \omega_{(\alpha)s}) \quad (18.12)$$

where $T_s(0)$ and $\dot{T}_s(0)$ are integration constants determined by the initial conditions.

The first particular integral in the solution (18.12) is a cosine like, fractional order particular solution (particular mode) for free cosine fractional type vibration mode

$$\xi_{\cos,s}(t, \alpha, \omega_{0s}, \omega_{(\alpha)s}) = \sum_{k=0}^{\infty} (-1)^k \omega_{(\alpha)s}^{2k} t^{2k} \sum_{m=0}^k \binom{k}{m} \frac{\omega_{(\alpha)s}^{-2m} t^{-\alpha m}}{\omega_{0s}^{2m} \Gamma(2k+1-\alpha m)}, \quad (18.13)$$

where $\alpha \in (0, 1)$ and $t \in (0, b)$. For $\alpha = 0$ is the particular solution—particular mode is pure linear and periodic—in the form

$$\xi_{\cos,s}(t, \alpha, \omega_{0s}, \omega_{(\alpha)s})|_{\alpha=0} = \cos\left(t\sqrt{\omega_{0s}^2 + \omega_{(\alpha=0)s}^2}\right). \quad (18.14)$$

For $\alpha = 1$ is the particular solution linear and dissipative in the form

$$\xi_{\cos,s}(t, \alpha, \omega_{0s}, \omega_{(\alpha)s})|_{\alpha=1} = \exp\left(-\frac{1}{2}\omega_{(\alpha=1)s}^2 t\right) \cos\left(t\sqrt{\omega_{0s}^2 + \frac{1}{4}\omega_{(\alpha=1)s}^4}\right). \quad (18.15)$$

The second particular integral in the solution (18.12) is a sinus like, fractional order as follows:

$$\xi_{\sin,s}(t, \alpha, \omega_{0s}, \omega_{(\alpha)s}) = \sum_{k=0}^{\infty} (-1)^k \omega_{(\alpha)s}^{2k} t^{2k+1} \sum_{m=0}^k \binom{k}{m} \frac{\omega_{(\alpha)s}^{-2m} t^{-\alpha m}}{\omega_{0s}^{2m} \Gamma(2k+2-\alpha m)}, \quad (18.16)$$

where $\alpha \in (0, 1)$ and $t \in (0, b)$. For $\alpha = 0$ is the particular solution once more linear and periodic

$$\xi_{\sin,s}(t, \alpha, \omega_{0s}, \omega_{(\alpha)s})|_{\alpha=0} = \sin\left(t\sqrt{\omega_{0s}^2 + \omega_{(\alpha=0)s}^2}\right). \quad (18.17)$$

For $\alpha = 1$, the particular solution reads

$$\xi_{\sin,s}(t, \alpha, \omega_{0s}, \omega_{(\alpha)s})|_{\alpha=1} = \exp\left(-\frac{1}{2}\omega_{(\alpha=1)s}^2 t\right) \sin\left(t\sqrt{\omega_{0s}^2 + \frac{1}{4}\omega_{(\alpha=1)s}^4}\right). \quad (18.18)$$

18.5.2 Forced Longitudinal Fractional Type Oscillation

For forced longitudinal fractional type vibrations of a rod with variable cross sections, described by partial fractional order differential equation (18.9), we propose previous form of a general solution as in (18.11) using eigen amplitude functions $Z_s(z)$, $s = 1, 2, 3, \dots, \infty$ as being the same as in the case of the corresponding linear longitudinal oscillations of rod satisfying corresponding form of variable cross section $A(z)$ (conical-shape rod, exponential-shape rod, catenary shape rod) and corresponding boundary conditions (rod with free ends, cantilever rod with weight on the free end, rod with weights at the both free ends), we refer to Hedrih (Stevanović) and Filipovski (2002a). We propose that eigen time functions $T_s(t)$ are considered as unknowns to be determined by condition that the general solution (18.11) satisfies partial fractional order differential equation (18.9).

Then, for that reason, after introducing the proposed previous general solution (18.11), into partial fractional order differential equation (18.9), and taking into account that eigen amplitude functions $Z_s(z)$ satisfy ordinary differential equations (18.10) such that it can be written

$$\begin{aligned} & \frac{1}{c_0^2} \frac{\partial^2 \sum_{s=1}^{\infty} Z_s(z) T_s(t)}{\partial t^2} - \frac{1}{A(z)} \frac{\partial}{\partial z} \left[A(z) \frac{\partial \sum_{s=1}^{\infty} Z_s(z) T_s(t)}{\partial z} \right] = \\ & = \frac{c_\alpha^2}{c_0^2 A(z)} \frac{\partial}{\partial z} \left[A(z) \mathfrak{D}_t^\alpha \left[\frac{\partial \sum_{s=1}^{\infty} Z_s(z) T_s(t)}{\partial z} \right] \right] + \frac{1}{E_0} q(z, t) \end{aligned} \tag{18.19}$$

or in the form

$$\begin{aligned} \sum_{s=1}^{\infty} \left\langle \frac{1}{c_0^2} Z_s(z) \ddot{T}_s(t) + k_s^2 Z_s(z) T_s(t) \right\rangle = & - \left[\frac{c_\alpha^2}{c_0^2} \sum_{s=1}^{\infty} \mathfrak{D}_t^\alpha [T_s(t)] k_s^2 Z_s(z) \right] + \\ & + \frac{1}{E_0} q(z, t) \end{aligned} \tag{18.20}$$

or in the form

$$\sum_{s=1}^{\infty} Z_s(z) \left\langle \ddot{T}_s(t) + k_s^2 c_0^2 T_s(t) + k_s^2 c_\alpha^2 \mathfrak{D}_t^\alpha [T_s(t)] \right\rangle = \frac{c_0^2}{E_0} q(z, t) . \tag{18.21}$$

Next, let us multiply the previous equation (18.21) by $Z_r(z) dz$ leading to

$$\begin{aligned} \sum_{s=1}^{\infty} A(z) Z_s(z) Z_r(z) dz \left\langle \ddot{T}_s(t) + k_s^2 c_0^2 T_s(t) + k_s^2 c_\alpha^2 \mathfrak{D}_t^\alpha [T_s(t)] \right\rangle = \\ = \frac{c_0^2}{E_0} q(z, t) A(z) Z_r(z) dz . \end{aligned} \tag{18.22}$$

By integrating previously obtained equation (18.22) along length of rod in interval $z \in (0, \ell)$ between left and right end of rod it can be written following:

$$\begin{aligned} \sum_{s=1}^{\infty} \int_0^\ell A(z) Z_s(z) Z_r(z) dz \left\langle \ddot{T}_s(t) + k_s^2 c_0^2 T_s(t) + k_s^2 c_\alpha^2 \mathfrak{D}_t^\alpha [T_s(t)] \right\rangle = \\ = \frac{c_0^2}{E_0} \int_0^\ell q(z, t) A(z) Z_r(z) dz , \end{aligned} \tag{18.23}$$

and taking into account that eigenamplitude functions $Z_s(z)$, $s = 1, 2, 3, \dots \infty$ satisfied ordinary differential equation (18.10) and orthogonality conditions, it follows:

$$\int_0^\ell A(z) Z_s(z) Z_r(z) dz = \begin{cases} 0 & \text{for } s \neq r \\ m_s & \text{for } s = r \end{cases} \tag{18.24}$$

follows system of the ordinary fractional order differential equations in the form:

$$\ddot{T}_s(t) + \omega_{0s}^2 T_s(t) + \omega_{(\alpha)s}^2 \mathfrak{D}_t^\alpha [T_s(t)] = \frac{c_0^2}{m_s E_0} \int_0^\ell q(z, t) A(z) Z_s(z) dz, \quad (18.25)$$

with $s = 1, 2, 3, \dots \infty$. After using

$$h_s(t) = h_{0s} f_s(t) = \frac{c_0^2}{m_s E_0} \int_0^\ell q(z, t) A(z) Z_s(z) dz \quad (18.26)$$

the following system of the ordinary fractional order differential equations follows:

$$\ddot{T}_s(t) + \omega_{0s}^2 T_s(t) + \omega_{(\alpha)s}^2 \mathfrak{D}_t^\alpha [T_s(t)] = h_s(t) = h_{0s} f_s(t), \quad s = 1, 2, 3, \dots \infty \quad (18.27)$$

describing eigen time functions $T_s(t)$, $s = 1, 2, 3, \dots \infty$ for each from the set of eigen amplitude function $Z_s(z)$, $s = 1, 2, 3, \dots \infty$ for forced longitudinal fractional type vibrations of rod with variable cross sections satisfying corresponding form of variable cross section $A(z)$ (conical-shape rod, exponential-shape rod, catenary shape rod) and corresponding case of the boundary conditions (rod with free ends, cantilever rod with weight on the free end, rod with weights at the both free ends).

Let us consider the special case of external excitation force, and in reduced form $h_s(t) = h_{0s} f_s(t) = h_{0s} \sin(\Omega_0 t)$

$$\ddot{T}_s(t) + \omega_{0s}^2 T_s(t) + \omega_{(\alpha)s}^2 \mathfrak{D}_t^\alpha [T_s(t)] = h_{0s} \sin(\Omega_0 t), \quad s = 1, 2, 3, \dots \infty \quad (18.28)$$

and after applying a Laplace transformation $\mathfrak{L}\{\cdot\}$ to the previous ordinary fractional order differential equation, we obtain

$$\mathfrak{L}\{\ddot{T}(t)\} + \omega_{(\alpha)s}^2 \mathfrak{L}\{\mathfrak{D}_t^\alpha [T_s(t)]\} + \omega_{0s}^2 \mathfrak{L}\{T_s(t)\} = h_0 \mathfrak{L}\{\sin(\Omega_0 t)\}, \quad (18.29)$$

with $s = 1, 2, 3, \dots \infty$. By using the following Laplace transformations:

$$\begin{aligned} \mathfrak{L}\{\ddot{T}_s(t)\} &= p^2 \mathfrak{L}\{T_s(t)\} - [pT_s(0) + \dot{T}_s(0)], \\ \mathfrak{L}\{\mathfrak{D}_t^\alpha [T_s(t)]\} &= p^\alpha \mathfrak{L}\{T_s(t)\} - \frac{d^{\alpha-1}}{dt^{\alpha-1}} T_s(0), \end{aligned} \quad (18.30)$$

for

$$\frac{d^{\alpha-1}}{dt^{\alpha-1}} T_s(0) = 0, \quad (18.31)$$

we acquire

$$\mathfrak{L}\{\mathfrak{D}_t^\alpha [T_s(t)]\} = p^\alpha \mathfrak{L}\{T_s(t)\}, \quad \mathfrak{L}\{\sin(\Omega_0 t)\} = \frac{\Omega_0}{p^2 + \Omega_0^2}, \quad (18.32)$$

where p is a complex variable, with real and imaginary parts, the solution $\mathfrak{L}\{T_s(t)\}$ of the equation (18.29) is in the following form:

$$\mathfrak{L}\{T_s(t)\} = \frac{[pT_s(0) + \dot{T}_s(0)]}{\langle p^2 + \omega_{(\alpha)s}^2 p^\alpha + \omega_{0s}^2 \rangle} + \frac{\Omega_0 h_{0s}}{(p^2 + \Omega_0^2) \langle p^2 + \omega_{(\alpha)s}^2 p^\alpha + \omega_{0s}^2 \rangle}. \quad (18.33)$$

Then, it is necessary to determine the general solution of eigen time function $T_s(t) = \mathfrak{L}^{-1}\mathfrak{L}\{T_s(t)\}\{\xi\}$ of the ordinary fractional order differential equation (18.28).

The solution along $\mathfrak{L}\{T_s(t)\}$ in the form (18.33) is possible to separate in two terms:

- The first term in solution (18.33) corresponds to the solution $T_{s,\text{free}}(t, \alpha, \omega_{0s}, \omega_{(\alpha)s})$, $s = 1, 2, 3, \dots \infty$ of ordinary fractional order differential equation (18.29) for $h_{0s} = 0$, and describes free fractional type vibrations and analytical approximate solution $T_{s,\text{free}}(t, \alpha, \omega_0, \omega_{(\alpha)})$, $s = 1, 2, 3, \dots \infty$ is in the form (18.11) in which modes (18.12) and (18.16) are included (see Hedrih (Stevanović) and Filipovski, 2002a, 1995), where $T_s(0)$ and $\dot{T}_s(0)$ are integral constants.
- The second term in solution (18.33) corresponds to a particular solution

$$T_{s,\text{part}}(t, \alpha, \omega_{0s}, \omega_{(\alpha)s}, \Omega_0), \quad s = 1, 2, 3, \dots \infty$$

of the ordinary fractional order differential equation (18.28) and describes one forced mode of a longitudinal fractional type forced vibrations.

Let us take into account that Laplace transformation of two functions, $f_{1,s}(t)$ and $f_{2,s}(t)$ are

$$\begin{aligned} \mathfrak{L}\{f_{1,s}(t)\} &= \frac{\Omega_0 h_{0s}}{(p^2 + \Omega_0^2)} = h_{0s} \mathfrak{L}\{\sin(\Omega_0 t)\}, \quad s = 1, 2, 3, \dots \infty \\ \mathfrak{L}\{f_{2,s}(t)\} &= \frac{1}{\langle p^2 + \omega_{(\alpha)s}^2 p^\alpha + \omega_{0s}^2 \rangle} = \mathfrak{L}\{T_{\text{sin},s}(t)\} \\ \mathfrak{L}\{T_{\text{sin},s}(t)\} &\approx \mathfrak{L}\left\{ \sum_{k=0}^{\infty} (-1)^k \omega_{(\alpha)s}^{2k} t^{2k+1} \sum_{m=0}^k \binom{k}{m} \frac{\omega_{(\alpha)s}^{-2m} t^{-\alpha m}}{\omega_{0s}^{2m} \Gamma(2k + 2 - \alpha m)} \right\} \end{aligned} \quad (18.34)$$

furthermore, Laplace transform of product of the two functions, $\mathfrak{L}\{f_{1,s}(t)f_{2,s}(t)\} = \mathfrak{L}\{f_{1,s}(t)\}\mathfrak{L}\{f_{2,s}(t)\}$, is equal to product of their Laplace transforms determined by expressions (18.34)_{1,2} such that it equals the second term in the solution (18.33).

Particular solution, corresponding to one of the modes of forced longitudinal fractional type vibrations, and it is in the form of the function $f_{3,s}(t)$ with its Laplace transform $\mathfrak{L}\{f_{3,s}(t)\}$ given by $\mathfrak{L}\{f_{1,s}(t)\}$, $\mathfrak{L}\{f_{2,s}(t)\}$, and $\mathfrak{L}\{f_{1,s}(t)f_{2,s}(t)\} = \mathfrak{L}\{f_{1,s}(t)\}\mathfrak{L}\{f_{2,s}(t)\}$. These functions $f_{1,s}(t)$, $f_{2,s}(t)$, $f_{3,s}(t)$ are in convolution (denoted by $*$), if they satisfy,

$$f_{3,s}(t) = \int_0^t f_{1,s}(t - \tau)f_{2,s}(\tau)d\tau = \int_0^t f_{1,s}(\tau)f_{2,s}(t - \tau)d\tau, \quad s = 1, 2, 3, \dots \infty \quad (18.35)$$

Then, the particular solution $T_{s,\text{part}}(t, \alpha, \omega_{0s}, \omega_{(\alpha)s}, \Omega_0)$, $s = 1, 2, 3, \dots \infty$ of the ordinary fractional order differential equation (18.28) corresponds to one forced

mode of fractional type vibrations under the external volume sinusoidal excitation $h_0 \sin(\Omega_0 t)$ in the form:

$$T_{s,\text{part},\sin}(t, \alpha, \omega_{0s}, \omega_{(\alpha)s}, \Omega_0) = \langle h_{0s} \sin(\Omega_0 t) \rangle * \xi_{\sin,s}(t, \alpha, \omega_{0s}, \omega_{(\alpha)s}), \tag{18.36}$$

or in the expanded form:

$$T_{s,\text{part},\sin}(t, \alpha, \omega_{0s}, \omega_{(\alpha)s}, \Omega_0) = \langle h_{0s} \sin(\Omega_0 t) \rangle * \left\langle \sum_{k=0}^{\infty} (-1)^k \omega_{(\alpha)s}^{2k} t^{2k+1} \sum_{m=0}^k \binom{k}{m} \frac{\omega_{(\alpha)}^{-2m} s t^{-\alpha m}}{\omega_{0s}^{2m} \Gamma(2k + 2 - \alpha m)} \right\rangle, \tag{18.37}$$

$s = 1, 2, 3, \dots \infty$

or in the form

$$T_{s,\text{part},\sin}(t, \alpha, \omega_{0s}, \omega_{(\alpha)s}, \Omega_0) = \int_0^t \langle h_{0s} \sin(\Omega_0(t - \tau)) \rangle \times \left\langle \sum_{k=0}^{\infty} (-1)^k \omega_{(\alpha)s}^{2k} \tau^{2k+1} \sum_{m=0}^k \binom{k}{m} \frac{\omega_{(\alpha)s}^{-2m} \tau^{-\alpha m}}{\omega_{0s}^{2m} \Gamma(2k + 2 - \alpha m)} \right\rangle d\tau. \tag{18.38}$$

Taking into account previous analysis general approximate solutions for eigen time functions $T_s(t)$, $s = 1, 2, 3, \dots \infty$, which corresponds to the eigen amplitude functions $Z_s(z)$, $s = 1, 2, 3, \dots \infty$, we obtain

$$T_s(t, \alpha, \omega_{0s}, \omega_{(\alpha)s}, \Omega_0) = T_{s,\text{free}}(t, \alpha, \omega_{0s}, \omega_{(\alpha)s}) + T_{s,\text{part}}(t, \alpha, \omega_{0s}, \omega_{(\alpha)s}, \Omega_0), \tag{18.39}$$

or in the expanded form

$$T_s(t, \alpha, \omega_{0s}, \omega_{(\alpha)s}, \Omega_0) = T_s(0) \sum_{k=0}^{\infty} (-1)^k \omega_{(\alpha)s}^{2k} t^{2k} \times \sum_{j=0}^k \binom{k}{j} \frac{(\mp 1)^j \omega_{(\alpha)s}^{-2j} t^{-\alpha j}}{\omega_{0s}^{2j} \Gamma(2k + 1 - \alpha j)} + \dot{T}_s(0) \sum_{k=0}^{\infty} (-1)^k \omega_{(\alpha)s}^{2k} t^{2k+1} \times \sum_{j=0}^k \binom{k}{j} \frac{(\mp 1)^j \omega_{(\alpha)s}^{-2j} t^{-\alpha j}}{\omega_{0s}^{2j} \Gamma(2k + 2 - \alpha j)} + \int_0^t \langle h_{0s} \sin(\Omega_0(t - \tau)) \rangle \times \left\langle \sum_{k=0}^{\infty} (-1)^k \omega_{(\alpha)s}^{2k} \tau^{2k+1} \sum_{m=0}^k \binom{k}{m} \frac{\omega_{(\alpha)s}^{-2m} \tau^{-\alpha m}}{\omega_{0s}^{2m} \Gamma(2k + 2 - \alpha m)} \right\rangle d\tau, \tag{18.40}$$

with $\alpha \in (0, 1)$, $t \in (0, b)$, $s = 1, 2, 3, \dots \infty$.

18.6 Energy Analysis

Taking into account that material of the rod is with fractional type dissipation of the mechanical energy, constitutive normal stress-state relation of rod's material is defined by fractional order derivative in the form (18.3) and that dilatation is in the form $\varepsilon_z(z, t) = \frac{\partial w(z, t)}{\partial z}$, elementary work of a rod's element with volume $dA(z)dz$ is in the form: $d\mathbf{A} = \frac{1}{2}\sigma(z, t)\varepsilon_z(z, t)dA(z)dz$ or in the form:

$$d\mathbf{A} = -\frac{1}{2}\left\{E_0\frac{\partial w(z, t)}{\partial z} + E_\alpha\mathfrak{D}_t^\alpha\left[\frac{\partial w(z, t)}{\partial z}\right]\right\}\frac{\partial w(z, t)}{\partial z}dA(z)dz \quad (18.41)$$

and in order to obtain the total work of the rod during the longitudinal vibrations, we must integrate on the cross section and along rod's axis

$$\mathbf{A} = -\int_0^\ell \int_A \frac{1}{2}\left\{E_0\frac{\partial w(z, t)}{\partial z} + E_\alpha\mathfrak{D}_t^\alpha\left[\frac{\partial w(z, t)}{\partial z}\right]\right\}\frac{\partial w(z, t)}{\partial z}dA(z)dz \quad (18.42)$$

and the following expression reads

$$\begin{aligned} \mathbf{A} = & -\frac{1}{2}E_0\langle T(t)\rangle^2 \int_0^\ell \left(\frac{\partial Z(z)}{\partial z}\right)^2 A(z)dz - \\ & -\frac{1}{2}E_\alpha T(t)\mathfrak{D}_t^\alpha[T(t)] \int_0^\ell \left(\frac{\partial Z(z)}{\partial z}\right)^2 A(z)dz, \end{aligned} \quad (18.43)$$

or in the transformed form along one mode as follows:

$$\mathbf{A} = -\frac{1}{2}\left\langle E_0\langle T(t)\rangle^2 + E_\alpha T(t)\mathfrak{D}_t^\alpha[T(t)]\right\rangle \int_0^\ell \left(\frac{\partial Z(z)}{\partial z}\right)^2 A(z)dz. \quad (18.44)$$

Previously obtained expression depends of eigen amplitude functions $Z_s(z)$, $s = 1, 2, 3, \dots, \infty$ for free and forced longitudinal fractional type vibrations of rod with variable cross sections satisfying corresponding form of variable cross section $A(z)$ (conical-shape rod, exponential-shape rod, catenary shape rod) and corresponding case of the boundary conditions (rod with free ends, cantilever rod with weight on the free end, rod with weights at the both free ends).

In expression (18.43) and (18.44), the first term presents deformation work in area of elastic deformation and is the potential energy stored in deformed rod, and second term presents work because of fractional type dissipative forces during rod's deformation and corresponds to fractional type dissipation rod's energy during longitudinal vibrations.

Elementary kinetic energy of rod's element with the volume $dA(z)dz$ is in the form:

$$d\mathbf{E}_k = \frac{1}{2}\rho A(z)dz \left[\frac{\partial w(z, t)}{\partial t}\right]^2, \quad (18.45)$$

and in order to obtain the total kinetic energy of the rod during the longitudinal vibrations must be integrated on the cross section and along the rod resulting in the

following form:

$$E_k = \frac{1}{2} \rho \left[\frac{\partial T(t)}{\partial t} \right]^2 \int_0^\ell A(z) [Z(z)]^2 dz . \tag{18.46}$$

Work of the external volume force applied to the rod in axial direction is

$$A = \int_0^\ell \int_A \frac{1}{2} q(z, t) \frac{\partial w(z, t)}{\partial z} dAdz = \frac{1}{2} \int_0^\ell q(z, t) \frac{\partial w(z, t)}{\partial z} A(z) dz . \tag{18.47}$$

Relation between total mechanical energy (sum of kinetic and potential energies) of the system and generalized function of fractional type energy dissipation carried on a eigen time function in one eigen amplitude function

Let us consider an ordinary fractional order differential equation from the system (18.28) along eigen time functions $T_s(t)$, $s = 1, 2, 3, \dots \infty$. Each of these ordinary fractional order differential equations presents an independent forced fractional type mode of longitudinal fractional type oscillations of rod with a variable cross section. Also, each of these ordinary fractional order differential equations presents a partial fractional type oscillator with one degree of freedom and with generalized coordinate $T_s(t)$, $s = 1, 2, 3, \dots \infty$, see Figure 18.2. Expressions of the normalized kinetic

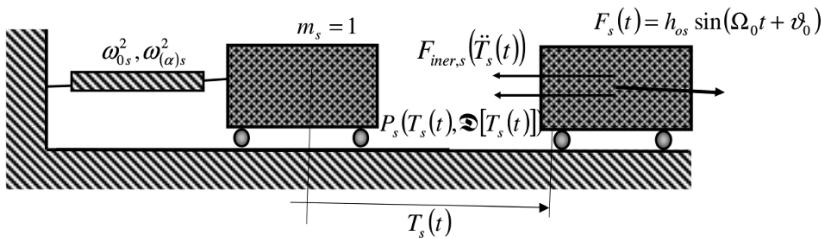


Fig. 18.2 Mechanical fractional type oscillator with one degree of freedom corresponding to one eigen time function $T_s(t)$ fractional type mode

$\tilde{E}_{k,s}$ and normalized potential $\tilde{E}_{p,s}$ energies and normalized generalized function $\tilde{\Phi}_{\alpha,s,0 < \alpha < 1}$ of fractional type dissipation of system energy of the mechanical fractional type oscillator with one degree of freedom, as presented in Figure 18.2, are as follows:

$$\tilde{E}_{k,s} = \frac{1}{2} \langle \dot{T}_s(t) \rangle^2 , \quad \tilde{E}_{p,s} = \frac{1}{2} \omega_{0s}^2 \langle T_s(t) \rangle^2 \tag{18.48}$$

and

$$\tilde{P}_{\alpha,s,0 < \alpha < 1} = \frac{1}{2} \omega_{(\alpha)s}^2 \left\{ \mathfrak{D}_t^\alpha [T_s(t)] \right\}^2 , \quad s = 1, 2, 3, \dots \infty \tag{18.49}$$

Unit mass particle is considered as a fractional type oscillator loaded by the following normalized active and fictitious forces: $F_s(T_s(t), \mathfrak{D}[T_s(t)])$ —a restitutive force in the form: $F_{\text{rest},s}(T_s(t), \mathfrak{D}[T_s(t)]) = -\langle \omega_{0s}^2 T_s(t) + \omega_{(\alpha)s}^2 \mathfrak{D}_t^\alpha [T_s(t)] \rangle$, $F_s(t) = h_{os} \sin(\Omega_0 t + \vartheta_0)$ —external active force with an amplitude h_{os} and circular frequency Ω_0 , phase ϑ_0 , and a normalized fictitious force of inertia $F_{\text{iner},s}(\ddot{T}_s(t)) = -\ddot{T}_s(t)$. Based on the principle of dynamical equilibrium of mass particle, one can write the ordinary fractional order differential equation in the form (18.28).

Let us start from the matrix fractional order differential equation (18.28)

$$\frac{d}{dt} \frac{\partial \tilde{\mathbf{E}}_k}{\partial \{\dot{T}_s(t)\}} - \frac{\partial \tilde{\mathbf{E}}_k}{\partial \{T_s(t)\}} + \frac{\partial \tilde{\mathbf{E}}_p}{\partial \{T_s(t)\}} + \frac{\partial \tilde{\mathbf{P}}_\alpha}{\partial (\mathfrak{D}_t^\alpha \{T_s(t)\})} + \frac{\partial \tilde{\Phi}}{\partial \{\dot{T}_s(t)\}} = \{h_{0s}\} \sin(\Omega_0 t + \vartheta_0), \tag{18.50}$$

with an explicit notation for matrix columns $\{T_s\} = \begin{pmatrix} T_1 \\ T_2 \\ \vdots \end{pmatrix}$ as well as matrix rows

$(T_s) = (T_1, T_2, \dots)$ and by using

$$\begin{aligned} \tilde{\mathbf{E}}_k &= \sum_{s=1}^{s=n} \tilde{\mathbf{E}}_{k,s} = \frac{1}{2} \sum_{s=1}^{s=n} \langle \dot{T}_s(t) \rangle^2, \quad \tilde{\mathbf{E}}_p = \sum_{s=1}^{s=n} \tilde{\mathbf{E}}_{p,s} = \frac{1}{2} \sum_{s=1}^{s=n} \omega_{0s}^2 \langle T_s(t) \rangle^2, \\ \tilde{\mathbf{P}}_\alpha &= \sum_{s=1}^{s=n} \tilde{\mathbf{P}}_{\alpha,s,0 < \alpha < 1} = \frac{1}{2} \sum_{s=1}^{s=n} \omega_{(\alpha)s}^2 \left\{ \mathfrak{D}_t^\alpha [T_s(t)] \right\}^2, \end{aligned} \tag{18.51}$$

and

$$\tilde{\Phi} = \sum_{s=1}^{s=n} \tilde{\Phi}_s = \frac{1}{2} \sum_{s=1}^{s=n} b_s \langle \dot{T}_s(t) \rangle^2, \tag{18.52}$$

with $s = 1, 2, 3, \dots \infty$. Coefficient of the normalization is in the form:

$$M_s = \int_0^\ell A(z) [Z_s(z)]^2 dz, \quad s = 1, 2, 3, \dots \infty. \tag{18.53}$$

Next, let us multiply by the matrix $(\dot{T}_s(t))$, at the left side, each term of the matrix equation (18.50) such that

$$\begin{aligned} (\dot{T}_s(t)) \frac{d}{dt} \frac{\partial \tilde{\mathbf{E}}_k}{\partial \{\dot{T}_s(t)\}} - (\dot{T}_s(t)) \frac{\partial \tilde{\mathbf{E}}_k}{\partial \{\dot{T}_s(t)\}} + (\dot{T}_s(t)) \frac{\partial \tilde{\mathbf{E}}_p}{\partial \{\dot{T}_s(t)\}} + \\ + (\dot{T}_s(t)) \frac{\partial \tilde{\mathbf{P}}_\alpha}{\partial (\mathfrak{D}_t^\alpha \{T_s(t)\})} + (\dot{T}_s(t)) \frac{\partial \tilde{\Phi}}{\partial \{\dot{T}_s(t)\}} = (\dot{T}_s(t)) \{h_{0s}\} \sin(\Omega_0 t + \vartheta_0), \end{aligned} \tag{18.54}$$

Taking into account the latter products, we obtain the following relations:

$$\begin{aligned} (\dot{T}_s(t)) \frac{d}{dt} \left\langle \frac{\partial \tilde{\mathbf{E}}_k}{\partial \{\dot{T}_s(t)\}} \right\rangle &= \frac{d}{dt} \left\langle (\dot{T}_s(t)) \frac{\partial \tilde{\mathbf{E}}_k}{\partial \{\dot{T}_s(t)\}} \right\rangle - (\ddot{T}_s(t)) \frac{\partial \tilde{\mathbf{E}}_k}{\partial \{\dot{T}_s(t)\}}, \\ (\dot{T}_s(t)) \frac{\partial \tilde{\mathbf{E}}_k}{\partial \{\dot{T}_s(t)\}} &= 2\tilde{\mathbf{E}}_k, \end{aligned} \quad (18.55)$$

as well as

$$\begin{aligned} \left\langle (\ddot{T}_s(t)) \frac{\partial \tilde{\mathbf{E}}_k}{\partial \{\dot{T}_s(t)\}} + (\dot{T}_s(t)) \frac{\partial \tilde{\mathbf{E}}_k}{\partial \{\dot{T}_s(t)\}} \right\rangle &= \frac{d\tilde{\mathbf{E}}_k}{dt}, \quad (\dot{T}_s(t)) \frac{\partial \tilde{\mathbf{E}}_p}{\partial \{T_s(t)\}} = \frac{d\tilde{\mathbf{E}}_p}{dt}, \\ (\dot{T}_s(t)) \frac{\partial \tilde{\Phi}_s}{\partial \{\dot{T}_s(t)\}} &= 2\tilde{\Phi}_s, \quad (\dot{T}_s(t)) \frac{\partial \tilde{\mathbf{P}}_\alpha}{\partial (\mathcal{D}_t^\alpha \{T_s(t)\})} = (\dot{T}_s(t)) \tilde{C}_\alpha \{\mathcal{D}_t^\alpha \{T_s(t)\}\}, \end{aligned} \quad (18.56)$$

for $\alpha \neq 0$ and $0 < \alpha \leq 1$. Finally by using the last relations in equation (18.54), we obtain the following relation between rate of decreasing of the normalized sum $\tilde{\mathbf{E}}_k + \tilde{\mathbf{E}}_p$ of kinetic and potential energies and normalized generalized function $\tilde{\mathbf{P}}_\alpha$ of fractional type system energy dissipation and normalized Rayleigh function $\tilde{\Phi}$ and external excitation, as follows:

$$\frac{d\langle \tilde{\mathbf{E}}_k + \tilde{\mathbf{E}}_p \rangle}{dt} = -2\tilde{\Phi} - (\dot{T}_s(t)) \frac{\partial \tilde{\mathbf{P}}_\alpha}{\partial (\mathcal{D}_t^\alpha \{T_s(t)\})} + (\dot{T}_s(t)) \{h_{0s}\} \sin(\Omega_0 t + \vartheta_0), \quad (18.57)$$

for $\alpha \neq 0$ and $0 < \alpha \leq 1$. By taking into account that system's normalized total mechanical energy, $\tilde{\mathbf{E}} = \tilde{\mathbf{E}}_k + \tilde{\mathbf{E}}_p$, the last relation is rewritten

$$\frac{d\tilde{\mathbf{E}}}{dt} = -2\tilde{\Phi} - (\dot{T}_s(t)) \frac{\partial \tilde{\mathbf{P}}_\alpha}{\partial (\mathcal{D}_t^\alpha \{T_s(t)\})} + (\dot{T}_s(t)) \{h_{0s}\} \sin(\Omega_0 t + \vartheta_0). \quad (18.58)$$

For the case of generalized function of fractional order system with the total energy dissipation in the form (18.8), previous relations (18.11) and (18.12) are obtained as follows:

$$\frac{d\langle \tilde{\mathbf{E}}_k + \tilde{\mathbf{E}}_p \rangle}{dt} = -2\tilde{\Phi} - (\dot{T}_s(t)) \tilde{C}_\alpha \{\mathcal{D}_t^\alpha \{T_s(t)\}\} + (\dot{T}_s(t)) \{h_{0s}\} \sin(\Omega_0 t + \vartheta_0), \quad (18.59)$$

and

$$\frac{d\tilde{\mathbf{E}}}{dt} = -2\tilde{\Phi} - (\dot{T}_s(t)) \tilde{C}_\alpha \{\mathcal{D}_t^\alpha \{T_s(t)\}\} + (\dot{T}_s(t)) \{h_{0s}\} \sin(\Omega_0 t + \vartheta_0). \quad (18.60)$$

On the basis of previously obtained relation (18.60) between systems of normalized total mechanical energy and normalized Rayleigh function and normalized generalized function of fractional type system energy dissipation for considered forced independent modes of the fractional type longitudinal vibrations of rod with variable cross section system dynamics, it is possible to formulate a theorem of system total mechanical energy degradation in the following form:

Theorem 18.1. For a class of fractional order no conservative free and forced modes of longitudinal fractional type vibrations of a rod with variable cross section system dynamics, with infinite degrees of freedom, and defined by: matrix of inertia properties, $\tilde{\mathbf{A}} = (\tilde{a}_{kj})_{\substack{\downarrow k=1,2,\dots,\infty \\ \rightarrow j=1,2,\dots,\infty}}$; $\tilde{a}_{kk} = 1$, matrix of rigidity properties, $\tilde{\mathbf{C}} = (\tilde{c}_{kj})_{\substack{\downarrow k=1,2,\dots,\infty \\ \rightarrow j=1,2,\dots,\infty}}$, $\tilde{c}_{kj} = 0$, $\tilde{c}_{kk} = \omega_{0k}^2$, matrix of viscoelastic creep fractional type properties, $\tilde{\mathbf{C}}_\varepsilon = (\tilde{c}_{(\alpha)kj})_{\substack{\downarrow k=1,2,\dots,\infty \\ \rightarrow j=1,2,\dots,\infty}}$, $\tilde{c}_{(\alpha)kj} = 0$, $\tilde{c}_{(\alpha)kk} = \omega_{(\alpha)k}^2$, and matrix of viscous linear material with properties $\tilde{\mathbf{B}} = (\tilde{b}_{kj})_{\substack{\downarrow k=1,2,\dots,\infty \\ \rightarrow j=1,2,\dots,\infty}}$, $\tilde{b}_{kj} = 0$, $\tilde{b}_{kk} = \tilde{b}_k$, rate of fractional type system normalized total mechanical energy, $\tilde{\mathbf{E}} = \tilde{\mathbf{E}}_k + \tilde{\mathbf{E}}_p$, degradation, in the system of eigen time functions, $T_s(t)$, $s = 1, 2, 3, \dots, \infty$, which corresponds to the system of eigen amplitude functions, $Z_s(z)$, is equal to sum of negative double Rayleigh function, $2\tilde{\Phi}$, and matrix product between velocity, $(\dot{T}_s(t))$, and first partial derivative, $\frac{\partial \tilde{\mathbf{P}}_\alpha}{\partial (\mathfrak{D}_t^\alpha \{T_s(t)\})}$, of normalized generalized function of fractional type dissipation of energy of longitudinal fractional type vibrations of a rod with variable cross section with respect to the fractional order derivative $\mathfrak{D}_t^\alpha \{x\}$ for free vibrations and for forced vibrations plus power of the work of external excitation along time functions derivative $(\dot{T}_s(t))$, $s = 1, 2, 3, \dots, \infty$, mathematically described by relation (18.58).

Also, it can be written in the following form:

$$\frac{d\tilde{\mathbf{E}}}{dt} = -2\tilde{\Phi} - \sum_{s=1}^{s=n} \sum_{r=1}^{r=n} \dot{T}_s(t) \frac{\partial \tilde{\mathbf{P}}_\alpha}{\partial (\mathfrak{D}_t^\alpha [\dot{T}_r(t)])} + \sum_{s=1}^{s=n} \sum_{r=1}^{r=n} \dot{T}_s(t) \{h_{0r}\} \sin(\Omega_0 t + \vartheta_0), \tag{18.61}$$

for $\alpha \neq 0$ and $0 < \alpha \leq 1$. From previously obtained results, we conclude that energy relation expressed by eigen time functions, $T_s(t)$, as system's longitudinal vibration main coordinates, which correspond to eigen amplitude functions, $Z_s(z)$, is possible to be applied for determining analogous energy relations for each of the free or forced fractional type mode along eigen time functions. Next, for that reason, taking into account expressions (18.29)-(18.34), and introducing energy relations (18.51), (18.52), we obtain the following relation:

$$\sum_{s=1}^{s=n} \left\langle \frac{d}{dt} \langle \tilde{\mathbf{E}}_{kin,s} + \tilde{\mathbf{E}}_{pot,s} \rangle + 2\tilde{\Phi}_s + \dot{T}_s(t) \frac{\partial \tilde{\mathbf{P}}_\alpha}{\partial (\mathfrak{D}_t^\alpha [T_s(t)])} \right\rangle = 0, \quad 0 < \alpha \leq 1, \tag{18.62}$$

and in final form of relation between normalized kinetic, $\tilde{\mathbf{E}}_{kin,s}$, and potential, $\tilde{\mathbf{E}}_{pot,s}$, with $s = 1, 2, \dots, n$, energies carried at one of s^{th} independent eigen main fractional type free and forced mode of longitudinal fractional type vibrations of a rod, and $\tilde{\Phi}_s$ and $\tilde{\mathbf{P}}_{\alpha \neq 0,s}$, $s = 1, 2, \dots, n$, respectively. These are functions of a linear and fraction type rod with longitudinal vibrations at one s^{th} eigen main fractional type mode is possible to write in the following form:

$$\begin{aligned} \frac{d}{dt} \langle \tilde{\mathbf{E}}_{kin,s} + \tilde{\mathbf{E}}_{pot,s} \rangle = & -2\tilde{\Phi}_s - \dot{T}_s(t) \frac{\partial \tilde{\mathbf{P}}_\alpha}{\partial (\mathfrak{D}_t^\alpha [T_s(t)])} + \\ & + \dot{T}_s(t) h_{0s} \sin(\Omega_0 t + \vartheta_0), \end{aligned} \quad (18.63)$$

with $0 < \alpha \leq 1$, $s = 1, 2, \dots, n$.

On the basis of previously obtained relation (18.63) between eigen main fractional type mode total mechanical energy, $\tilde{\mathbf{E}}_s = \tilde{\mathbf{E}}_{k,s} + \tilde{\mathbf{E}}_{p,s}$, $s = 1, 2, \dots, n$, and corresponding Rayleigh function $\tilde{\Phi}_s$ and generalized function $\tilde{\mathbf{P}}_\alpha$ of fractional type energy dissipation, for the considered class of the fractional type longitudinal vibrations of a rod with variable cross section, it is possible to formulate the following theorem of rod eigen main fractional type mode total mechanical energy degradation.

Theorem 18.2. *A class of fractional type no conservative free and forced modes of longitudinal fractional type vibrations of a rod with variable cross section described by ordinary fractional order differential equations with infinite degrees of freedom*

$$\ddot{T}_s(t) + \omega_{0s}^2 T_s(t) + \omega_{(\alpha)s}^2 \mathfrak{D}_t^\alpha [T_s(t)] = h_{0s} \sin(\Omega_0 t), \quad s = 1, 2, 3, \dots, \infty \quad (18.64)$$

is defined by following matrices: matrix of inertia properties $\tilde{\mathbf{A}} = (\tilde{a}_{kj})_{\substack{\downarrow k=1,2,\dots,\infty \\ \rightarrow j=1,2,\dots,\infty}}$; $\tilde{a}_{kj} = 0$, $\tilde{a}_{kk} = 1$, matrix of rigidity properties $\tilde{\mathbf{C}} = (\tilde{c}_{kj})_{\substack{\downarrow k=1,2,\dots,\infty \\ \rightarrow j=1,2,\dots,\infty}}$, $\tilde{c}_{kj} = 0$, $\tilde{c}_{kk} = \omega_{0k}^2$, matrix of viscoelastic creep fractional type properties, $\tilde{\mathbf{C}}_\varepsilon = (\tilde{c}_{(\alpha)kj})_{\substack{\downarrow k=1,2,\dots,\infty \\ \rightarrow j=1,2,\dots,\infty}}$, $\tilde{c}_{(\alpha)kj} = 0$, $\tilde{c}_{(\alpha)kk} = \omega_{(\alpha)k}^2$, and matrix of viscous linear material with properties $\tilde{\mathbf{B}} = (\tilde{b}_{kj})_{\substack{\downarrow k=1,2,\dots,\infty \\ \rightarrow j=1,2,\dots,\infty}}$, $\tilde{b}_{kj} = 0$, $\tilde{b}_{kk} = \tilde{b}_k$, rate of fractional type system normalized total mechanical energy, $\tilde{\mathbf{E}}_s = \tilde{\mathbf{E}}_{k,s} + \tilde{\mathbf{E}}_{p,s}$, degradation, in the system of eigen time functions, $T_s(t)$, $s = 1, 2, 3, \dots, \infty$, which corresponds to the system of eigen amplitude functions, $Z_s(z)$, being equal to the sum of negative double Rayleigh function, $2\tilde{\Phi}$, and product between velocity, $(\dot{T}_s(t))$, and first partial derivative, $\frac{\partial \tilde{\mathbf{P}}_\alpha}{\partial (\mathfrak{D}_t^\alpha [T_s(t)])}$, of normalized generalized function of fractional type dissipation of energy of corresponding mode of longitudinal fractional type vibrations of a rod with variable cross section with respect to the fractional order derivative $\mathfrak{D}_t^\alpha [T_s(t)]$ for free vibrations and for forced vibrations plus power of the work of external excitation along time functions $T_s(t)$, $s = 1, 2, 3, \dots, \infty$, mathematically described by relation (18.63).

Also, it can be written in the following form:

$$\frac{d\tilde{\mathbf{E}}_s}{dt} = -2\tilde{\Phi}_s - \dot{T}_s(t) \frac{\partial \tilde{\mathbf{P}}_\alpha}{\partial (\mathfrak{D}_t^\alpha [T_s(t)])} + h_{0s} \dot{T}_s(t) \sin(\Omega_0 t + \vartheta_0), \quad (18.65)$$

for $\alpha \neq 0$, $0 < \alpha < 1$, $s = 1, 2, 3, \dots, \infty$ or in the form:

$$\frac{d\tilde{\mathbf{E}}_s}{dt} = -2\tilde{\Phi}_s - \tilde{c}_{\alpha,ss} \dot{T}_s(t) \mathfrak{D}_t^\alpha [T_s(t)] + h_{0s} \dot{T}_s(t) \sin(\Omega_0 t + \vartheta_0), \quad (18.66)$$

for $\alpha \neq 0$, $0 < \alpha < 1$, $s = 1, 2, 3 \dots \infty$. Based on previously derived relations, we conclude that no interactions appear between energy carried on the independent eigen time fractional type modes.

18.7 Concluding Remarks

In this work, in the first part, main original results of theory of forced longitudinal fractional type vibrations of a rod, with variable cross section, and graded material with fractional type properties are presented. This theory about independent forced fractional type eigen main modes described by corresponding independent ordinary, fractional order differential equations along eigen time functions in corresponding eigen amplitude forms must consider coupling with results related to determined forms of eigen amplitude function of longitudinal vibrations of a rod with different variable cross sections and different boundary conditions, presented by Hedrih (Stevanović) and Filipovski (1999, 2002a).

In the second part, forced longitudinal creep vibrations of a fractional type rheological rod with variable cross section are investigated. Partial fractional order differential equation and particular solutions for the case of forced creep longitudinal fractional type vibrations of the rod of creep material of a fractional type are determined.

Acknowledgements This research is partly supported by the Ministry of Sciences of Republic Serbia through Mathematical Institute SANU Belgrade Grants OI 174001 “Dynamics of hybrid systems with complex structures.”

References

- Abali BE (2017) Computational Reality, Solving Nonlinear and Coupled Problems in Continuum Mechanics, Advanced Structured Materials, vol 55. Springer Nature, Singapore
- Abramov O, Horbenko I, Shveгла S (1984) Ultrasonic Processing of Materials (in Russian). Mašinstroenie, Moscow
- Atanacković TM, Pilipović S, Stanković B, Zorica D (2014) Fractional calculus with applications in mechanics. Wiley Online Library
- Bačlić BS, Atanacković TM (2000) Stability and creep of a fractional derivative order viscoelastic rod. Bulletin (Académie serbe des sciences et des arts Classe des sciences mathématiques et naturelles Sciences mathématiques) pp 115–131
- Bishop R (1952) Longitudinal waves in beams. The Aeronautical Quarterly 3(4):280–293
- Cohen H, Whitman AB (1977) Waves in elastic rods. Journal of Sound and Vibration 51(2):283–302
- Cutchins MA (1980) The effect of an arbitrarily located mass on the longitudinal vibrations of a bar. Journal of Sound and Vibration 73(2):185–193
- Goroshko OA, Hedrih (Stevanović) KR (2001) Analytical Dynamics (Mechanics) of Discrete Hereditary Systems (in Serbian), vol 426. University of Niš
- Goroshko OA, Puchko NP (1997) Lagrangian equations for the multibodies hereditary systems. Facta Universitatis, Series Mechanics, Automatic Control and Robotics 2(7):209–222

- Hedrih (Stevanović) KR (2005) Partial fractional differential equations of creeping and vibrations of plate and their solutions (first part). *Journal of the Mechanical Behavior of Materials* 16(4/5):305
- Hedrih (Stevanović) KR (2014a) Elements of mathematical phenomenology in dynamics of multi-body system with fractional order discrete continuum layers. *International Journal of Mechanics* 8:345–352
- Hedrih (Stevanović) KR (2014b) Generalized function of fractional order dissipation of system energy and extended lagrange differential equations in matrix form. Dedicated to 86th Anniversary of Radu Miron, *Tensor* 75(1):35–51
- Hedrih (Stevanović) KR (2014c) Multi membrane fractional order system vibrations. *Journal of Theoretical and Applied Mechanics* 41(S1):43–60
- Hedrih (Stevanović) KR (2018) Analytical dynamics of fractional type discrete system. *Advances in Theoretical and Applied Mechanics* 11(1):15–47
- Hedrih (Stevanović) KR, Filipovski A (1995) Models analogy of the longitudinal and torsional vibrations of rods with variable cross section (in serbian). *Naučno-tehnički pregled* 45(8):13–20
- Hedrih (Stevanović) KR, Filipovski A (1999) Longitudinal vibrations of rheological rod with variable cross section. *Communications in Nonlinear Science and Numerical Simulation* 4(3):193–199
- Hedrih (Stevanović) KR, Filipovski A (2002a) Longitudinal creep vibrations of a fractional derivative order rheological rod with variable cross section. *Facta universitatis-series: Mechanics, Automatic Control and Robotics* 3(12):327–349
- Hedrih (Stevanović) KR, Independent Fractional Type Modes of Free and Forced Vibrations of Discrete Continuum Hybrid Systems of Fractional Type with Multi-Deformable Bodies. *New Trends in Nonlinear Dynamics Proceedings of the First International Nonlinear Dynamics Conference (NODYCON 2019)*, Editors: Lacarbonara, W., Balachandran, B., Ma, J., Tenreiro Machado, J.A., Stepan, G., 2020. Volume III. Pages 315–324.
- Hedrih (Stevanović) KR, Machado JAT (2015) Discrete fractional order system vibrations. *International Journal of Non-Linear Mechanics* 73:2–11
- Rabotnov YN (1977) *Elements of Hereditary Mechanics of Solid Bodies* (in Russian). Moscow, Nauka
- Rašković D (1965) *Theory of Oscillations* (in Serbian). Naučna knjiga, Belgrad
- Rossikhin YA, Shitikova MV (2010) Application of fractional calculus for dynamic problems of solid mechanics: novel trends and recent results. *Applied Mechanics Reviews* 63(1):010,801
- Savin GN, Ruschisky Y (1976) *Elements of Hereditary Media Mechanics* (in Ukrainian). Vyscha Shkola, Kyiv
- Slonimsky GL (1961) On the law of deforming of high polymer bodies. *Rep Acad Sci USSR* 140(2)
- Stojanovic R (1965) *Introduction to Nonlinear Mechanics of Continuum* (in Serbian). Zavod za izdavanje udžbenika, Belgrad



Chapter 19

Comparative Numerical Analysis of Composites in the Aspect of Contact Algorithm

Agnieszka Derewonko

Abstract Node-to-segment and segment-to-segment contact algorithms are the most popular methods implemented in FEM-based engineering software. The article presents the differences in formulation of these algorithms and a comparative assessment of the numerical analysis results for a compressed composite specimen. A contact problem is employed to determine a contact area. The results of the numerical analyses are presented in the form of three-dimensional graphs obtained in the Matlab environment for selected external load values. Percentage errors of strain and stress are calculated in order to compare the results of numerical analysis and experimental tests.

Keywords: Contact problem · Composite · Finite element method

19.1 Introduction

Contact problem is a highly non-linear phenomenon involving enormous computational effort. The correct choice of the appropriate calculation algorithm enables reduction of this inconvenience, while maintaining reliable analysis results. Modern simulation techniques for contact problems, using the finite element method, are based on a theory of nonlinear continuum mechanics. The most important of these methods include those concerning the discretization of the contact region (Zavarise and De Lorenzis, 2009; Gonzalez et al, 2014; Paggi and Wriggers, 2016) and the schemes for formulating and solving the incremental equilibrium equations

A. Derewonko
Department of Mechanics and Applied Computer Science
Faculty of Mechanical Engineering
Military University of Technology
Sylwestra Kaliskiego Street 2, 00-908 Warsaw, Poland
e-mail: agnieszka.derewonko@wat.edu.pl

(Oliver et al, 2009; Hartmann et al, 2009; Zavarise and Wriggers, 2011; Zavarise and De Lorenzis, 2012; Cavaliere, 2012; Sauer and De Lorenzis, 2013; Panagiotopoulos et al, 2018) for them. The foundations of contact algorithms, presented in Chapter 2, are based on works (Wriggers, 2006, 1995; Laursen and Simo, 1993a; Simo and Laursen, 1992; Simo et al, 1985; Zavarise et al, 1995, 1998).

The effect of the applied contact algorithm on the size of the contact area calculated by the program for a single node is presented. Two sets of nodes form two contact surfaces. The comparison was carried out with the use of numerical analysis of the compression test of a multi-layer composite. It is a fragment of the sensitivity analysis of the model carried out as a preliminary stage of work aiming at developing the numerical method for predicting the adhesive joint failure initiation. Assumptions and genesis of the method are presented in paper (Derewonko, 2018).

Aspects, such as a more comprehensive orthotropic model as the one proposed in (Giorgio et al, 2018; Spagnuolo et al, 2020), dissipation is not considered due to friction of the fibers (Nadler and Steigmann, 2003; Giorgio and Scerrato, 2017) and damage model as in (Placidi et al, 2018; Placidi and Barchiesi, 2018).

19.2 The Contact Problems

The basic condition of contact algorithms is non-penetration of the contacting surfaces. In the case of large deformations, the Lagrange description is used to formulate this criterion. In the current configuration, the distance between two points with the same initial coordinates belonging to two separated contact surfaces is verified. In the mathematical aspect, non-penetration of those points is a limiting condition based on a micro mechanical approach. It is implemented as the distance function minimization of both surfaces in the natural coordinate system and the current configuration. The distance function, g_N , fulfilling the orthogonality condition is defined as the distance between the point belonging to one surface and its projection into the reference surface. The basic condition of non-penetration is described by the general formula

$$g_N = [x^1 - \hat{x}_t^2(\hat{\xi}^1, \hat{\xi}^2)] \cdot \bar{\mathbf{n}}^2 \geq 0, \quad (19.1)$$

where $(\hat{\xi}^1, \hat{\xi}^2)$ is the minimizer of the distance function for point belonging to one contact surface x^1 , $\hat{x}_t^2(\hat{\xi}^1, \hat{\xi}^2)$ is the tangent vector and $\bar{\mathbf{n}}^2$ denotes the normal vector to the reference surface.

The relative movement of two contacting bodies in the tangential direction is considered as a relative slip (velocity) and is related to the change of the solution point $(\hat{\xi}^1, \hat{\xi}^2)$ of the minimal distance problem.

Normal contact stresses follow either from constraint equations or from constitutive interface equations. In the first case, the contact problem is treated as constraint optimization. The Kuhn-Tucker condition is formulated for frictionless contact problems in the following forms

$$g_N \geq 0, p_N \leq 0, p_N g_N = 0, \quad (19.2)$$

where p_N is the normal component of the stress vector.

In the second case, the micromechanical behavior of the contact area is checked taking into account, e.g., the roughness of both contact surfaces. Local constitutive equations for pressure and tangential stress on the surface at point x^1 relative to the reference surface are formulated. The general form of the constitutive law can be written in one of the following forms

$$p_N = f(d) \text{ or } d = h(p_N), \quad (19.3)$$

where d is the current mean plane distance, p_N is the contact pressure and f and h are non-linear functions.

In the case of non-existence of relative movement of both contact surfaces, the relative distance between the corresponding points of both surfaces in the tangential direction, g_T , is equal to zero. This is a stick condition. The stick condition is implemented by introducing a non-linear equation of constraint on tangent motion in the contact interface. This limitation is usually associated with the Lagrange multiplier, λ_T , which corresponds to the reaction force.

Constitutive equations for contact with friction are mostly formulated within elastoplasticity. Two states, slick and slip, are described.

It is assumed that the surface deformations generated in the stick state vanish after removing the external load, and the resulting shear stresses, t_T , are described by the following formula

$$t_T = c_T g_T^e, \quad (19.4)$$

where c_T is a material parameter and g_T^e is a sticking part of the movement.

This type of algorithm is called adhesive contact.

The slip criterion function depends on contact pressure p_N and material parameter μ

$$\hat{f}_s(t_T) = \|t_T\| - \mu p_N \leq 0, \quad (19.5)$$

where $\hat{f}_s(t_T)$ is the tangent component of the contact force.

In general, the contact problem is treated as a boundary value problem. For mathematical description of this type of problem, a weak form of the local momentum equation for the solid, boundary conditions for deformation and stress field, constraint equations in the form of $g_N \geq 0$ and nonlinear constitutive equations are used.

A general form of the obtained variational inequality is a function of variables such as virtual displacement, η , body forces, \bar{f}^γ , Kirchhoff stress, τ^γ . Another variables are boundary conditions for deformations, φ^γ , and stress fields, \hat{t}^γ .

The integration of such formulated inequality is performed in the reference configuration. However, the stress tensor and the gradient operator are evaluated in relation to the current coordinates.

The algorithms for solving variational inequalities, based on the finite element method, use methods well-known from the optimization theory. These include active set strategies, commonly implemented in existing computer aided design programs.

The advantage of this method is the formulation of variational inequality as the equation for a single increment of the external load

$$\sum_{\gamma=1}^2 \left\{ \int_{\Omega^\gamma} \boldsymbol{\tau}^\gamma \cdot \text{grad } \boldsymbol{\eta}^\gamma dV - \int_{\Omega^\gamma} \bar{\boldsymbol{f}}^\gamma \cdot \boldsymbol{\eta}^\gamma dV - \int_{\Gamma_c^\gamma} \bar{\boldsymbol{t}}^\gamma \cdot \boldsymbol{\eta}^\gamma dA \right\} + \text{“contact contribution”} = 0. \quad (19.6)$$

Virtual displacement is also a test function, the value of which is zero at the boundary of the contact surface. Formulation of a weak form of the interface for two bodies in contact with surface Γ_c is dependent on the applied method.

In the Lagrange multipliers method, the weak form of the interface has the form of

$$\int_{\Gamma_c} (\lambda_N \cdot \delta g_N + \boldsymbol{\lambda}_T \cdot \delta \boldsymbol{g}_T) dA \quad (19.7)$$

where λ_N is the Lagrange multiplier, which corresponds to the contact pressure p_N .

When relative tangential slip g_T is zero in the stick state, a constraint equation, in which λ_T corresponds to the reaction force, is formulated. In the slip state, expression $\lambda_T \cdot \delta g_T$ takes the form of $t_T \cdot \delta g_T$ where t_T is the tangential stress vector.

Also, in the penalty function method, two states, stick and slip, are distinguished. In the first case, the weak form of the interface takes the form of

$$\int_{\Gamma_c} (\epsilon_N \cdot g_N \cdot \delta g_N + \epsilon_T \cdot \boldsymbol{g}_T \cdot \delta \boldsymbol{g}_T) dA \quad (19.8)$$

with limitations on the value of the penalty function in the normal and the tangent direction $\epsilon_N > 0$, $\epsilon_T > 0$.

However, in the case of a slip state, a tangential stress vector t_T is implanted instead of quotient $\epsilon_T \cdot g_T$ in equation (19.8),

$$\int_{\Gamma_c} (\epsilon_N \cdot g_N \cdot \delta g_N + \boldsymbol{t}_T \cdot \delta \boldsymbol{g}_T) dA \quad (19.9)$$

In both methods, the weak form of the interface equilibrium equation is a function of increments of the distance between the contact nodes, in the both normal and tangent direction to its surface. The tangential stress vector is usually determined by friction laws.

A serious problem with application of the Lagrange multipliers method and the penalty function is ill-conditioning of the system of equations. Therefore, both methods were combined with the augmented Lagrangian formulation (Oden, 1981; Simo and Taylor, 1985), in which the variation of the total energy of two bodies Π is described by the following formula

$$\delta \Pi_p = \delta \Pi + \int_{\Gamma_c} \left[\lambda_N \delta g_N + \delta \lambda_N \left(g_N - \frac{1}{\epsilon_N} \lambda_N \right) \right] d\Gamma \rightarrow \text{STAT} \quad (19.10)$$

STAT is an abbreviation for stationary value (maximum or minimum) at the actual displacement, since solution for displacement is obtained by finding a stationary value of the total potential energy.

The second part of equation (19.10) leads to the constitutive law, evaluated locally, in the form of $\lambda_N = \epsilon_N g_N$ that links the penalty function with the Lagrange multiplier.

In this approach, Lagrange multiplier $\bar{\lambda}_N$ is introduced and remained constant during the iteration loop to solve equation (19.6), which is non-linear with respect to φ_γ deformation.

The description of variables in FEM is a shape function, N_I , of the finite elements used. In the Lagrange approach (19.7), both a change in the distance between nodes δg_N and the Lagrange multiplier λ_N are discretized in the local coordinate system.

$$\lambda_N^h = \sum_K M_K(\xi) \lambda_{NK} \quad \text{and} \quad \delta g_N^h = \sum_I N_I(\xi) \delta g_{NI} \quad (19.11)$$

Interpolations are selected to satisfy the Ladyshenskaya–Babuska–Brezzi condition (Kikuchi and Oden, 1988).

In the case of the penalty function, only displacements are discretized, also in the local system

$$g_N^h = \sum_I N_I(\xi) g_{NI} \quad \text{and} \quad g_N^h = \sum_I N_I(\xi) \delta g_{NI} \quad (19.12)$$

The most commonly implemented discretization procedures in CAE programs are node-to-segment (NTS) and the segment-to-segment (STS). In the NTS procedure, the distance between the contact surfaces is defined as the distance between the center node of one surface and its projection into the reference surface. In the STS procedure, the corner nodes of the segment of one contact surface are projected onto the segment of the other contact surface. However, there are different variants of both procedures implemented in CAE programs. For example, in the MarcTM program, for finite elements with a linear shape function, in the NTS procedure, the normal vector and projection are calculated based on the piecewise linear representation of the element. However, in the STS procedure, a number of auxiliary points are determined. Then, the auxiliary points are projected onto the segment of the second contact surface instead of corner nodes. This approach allows definition of a larger number of normal vectors at the adjacent contact segments and more accurate determination of the actual contact surface (MSC Software Corporation, 2013). Details for both procedures of discretization, both for small and large deformations, can be found, among others, in (Simo et al, 1985; Wriggers and Simo, 1985; Wriggers et al, 1990; Papadopoulos and Taylor, 1992). Matrix formulation of equation (19.6) based on FEM is dependent on a shape function of the finite element, N_I , and labeled as G .

In the case of the penalty function method, the general matrix formulation of weak equation (19.6) in the form of a discrete system of equations, has the form of

$$\mathbf{G}_c^p(\mathbf{v}) = \mathbf{G}(\mathbf{v}) + \bigcup_{s=1}^{n_c} \mathbf{G}_s^c(\mathbf{v}) = \mathbf{0} \quad (19.13)$$

where $\mathbf{G}(\mathbf{v})$ is the contribution of the contacting bodies depending on the shape function.

$\mathbf{G}_s^c(\mathbf{v})$ depends on the discretization procedure for s associated with an active contact element, i.e., a node or a segment.

The system of equations in the case of the Lagrange multipliers is defined for both surfaces (1, 2) and takes the form of

$$\mathbf{G}_c^1(\mathbf{v}, \boldsymbol{\lambda}) = \mathbf{G}(\mathbf{v}) + \cup_{s=1}^{n_c} \mathbf{C}_s^l(\mathbf{v})^T \boldsymbol{\lambda}_s = \mathbf{0} \quad (19.14a)$$

$$\mathbf{G}_c^2(\mathbf{v}, \boldsymbol{\lambda}) = \cup_{s=1}^{n_c} \mathbf{C}_s^g(\mathbf{v}) = \mathbf{0} \quad (19.14b)$$

where matrix $\mathbf{C}_s^l(\mathbf{v})$ is a function of change δg_s and $\mathbf{C}_s^g(\mathbf{v})$ is a matrix dependent on the distance g_s . Both matrices also depend on the chosen discretization procedure.

The solutions of both systems of equations using Newton-Raphson method requires taking into account a change of the normal vector to the contact surface (Laursen and Simo, 1993a; Curnier and Alart, 1988; Laursen and Simo, 1993b).

Algorithms for solving the contact problem are divided into global algorithms, necessary to define an appropriate number of active constraint equations, and into local algorithms for determining the contact stresses. For solving systems of equations (19.13) and (19.14a) in global algorithms, the Newton-Raphson method is usually used. Since it is difficult to estimate the parameters of the equations, additionally, the augmented Lagrangian technique is usually applied together with Uzawa type algorithms, i.e., algorithms for solving problems with saddle points. This leads to an inner loop for the contact and outer loop for the update the Lagrangian parameters (Bertsekas, 1984; Glowinski and Le Tallec, 1984; Laursen and Simo, 1991). In the local algorithm, stress is updated using a return algorithm based on objective (Euler's backward) integration.

19.3 Research Object

The analyses concerned a fourteen-layer composite made of the prepreg CE 8201-245-45/120, i.e. the KDK8042 carbon fabric saturated with E201 epoxy resin. Material of each layer (lamina) is characterized by the same volume fraction and mechanical properties of fibers in the warp and the weft directions.

The object of considerations is the compression test carried out as a step in experimental determination of properties of the composite defined above. The specimens were loaded linearly with increasing force, with a maximum value of 25,000 N. In order to limit the number of variables in numerical analyses, the maximum value of compressive force is lower than the average failure force determined in laboratory tests.

The specimen size, was adopted in accordance with ASTM D 3410 Method A (ASTM Committee D-30, 1990), however, to avoid buckling phenomena, short specimens were used (Fig. 19.1).

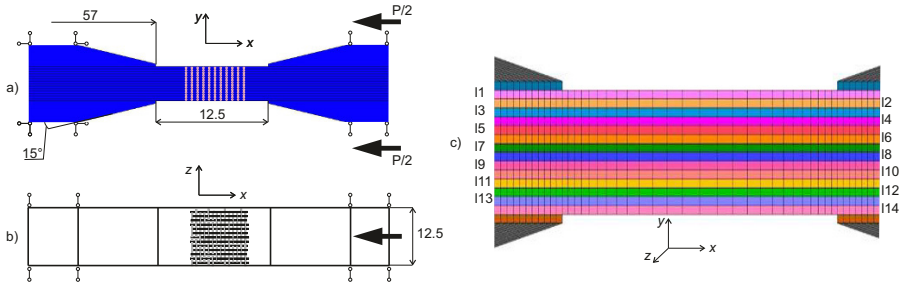


Fig. 19.1 Boundary conditions and loads: (a) in xy plane, (b) in xz plane, (c) part of a specimen model created from elements of the Hex type.

The boundary conditions in experimental tests and numerical simulation are the same.

All translational degrees of freedom are removed from the nodes forming the upper and the lower surfaces of the left grip. For the right grip, displacement along the direction of the applied load (x -axis) is possible (Fig. 19.1a). In the other two directions, translational degrees of freedom are removed also from the nodes forming the upper and the lower surfaces of the grip (Fig. 19.1b). Displacement along x -axis is caused by the shear load applied to both surfaces of the right grip (Fig. 19.1a). The value of the maximum force (24,938 N) is divided into a double value of the area of the upper surface of the grip (Fig. 19.1a) to determine the shear load. A linear function of the shear load with a maximum value of 17.5 N/mm² is formulated. The body forces, due to gravity, are also modeled.

Hex type three-dimensional eight-node finite elements with linear shape functions, with eight integral points, are used to represent the geometry of the specimen (Fig. 19.1c). Model of a single lamina with thickness of 0.27 mm is created from one layer of finite elements.

Material constants are summarized in Table 19.1.

Table 19.1 Mechanical properties of composite material

| E_1 MPa | E_2 MPa | E_3 MPa | G_{12} MPa | G_{31} MPa | G_{23} MPa | ν_{12} | ν_{31} | ν_{23} |
|-----------|-----------|-----------|--------------|--------------|--------------|------------|------------|------------|
| 53258 | 53258 | 9759 | 3494 | 2581 | 2581 | 0.0237 | 0.5356 | 0.5356 |

The elastic model of isotropic material, with Young modulus of 6800 MPa and Poisson’s ratio of 0.27, is used to describe the material constitutive model for grips.

In order to determine the interface stress between individual laminates, an adhesive type contact algorithm is used. The same type of a contact algorithm is introduced between the grips and the specimen.

The augmented Lagrange method is used to formulate the contact conditions (contact constraints and constitutive equations) as part of the incremental step (Simo and Laursen, 1992; Alart and Curnier, 1991; Pietrzak and Curnier, 1999). To prevent

the nodes penetration of one surface in other one, the Iterative Penetration Checking Procedure is applied, which allows for simultaneous fulfilment of the contact constraints and global equilibrium in iteration. The Newton–Raphson procedure is used. To solve contact problems, the Additive Decomposition Updated Lagrange procedure is introduced. This formulation uses Cauchy stress and true strain and is suitable for analyses with large elastic and plastic strain. True strain is energetically conjugated with a strain measure. A geometric stiffness matrix and an initial stiffness matrix, based on the current deformed configuration, are calculated when Updated Lagrange formulation is chosen. The Additive Decomposition procedure divides the deformation increment into elastic and plastic parts. This results in a constant value of volumetric strain for von Mises plasticity in lower-order solid elements (e.g. Hex type), which prevents locking this type of a finite element. The Coulomb bilinear friction model is introduced in the NTS procedure. In the STS procedure, the Augmentation options based on a bilinear penetration field is used.

19.4 Validation of Numerical Models

Shear tests are carried out for a composite specimen of the shape and dimensions shown in Fig. 19.1. The specimens for testing are cut from a sheet of prepreg and E201 epoxy resin in accordance with the pre-impregnation manufacturer's recommendations. The basic purpose of the tests is to determine the elastic modulus of compression E_{is} , compression strength (failure) R_{is} and failure deformations ε_{is} in the plane perpendicular to the force direction. The load of the specimens is carried out at a constant speed of the traverse (10 mm/min). The mean value of the failure force obtained in the laboratory tests is approximately 26,885 N. The models are validated by comparison values from experimental tests and numerical analyses of strain and stress in the load direction. For this purpose, the strain and stress percentage errors of the numerical analyses are determined according to the following dependencies

$$e_{\varepsilon} = \frac{\varepsilon_{ex} - \varepsilon_{nu}}{\varepsilon_{ex}} \cdot 100\% \quad (19.15a)$$

$$e_{\sigma} = \frac{\sigma_{ex} - \sigma_{nu}}{\sigma_{ex}} \cdot 100\% \quad (19.15b)$$

where ε_{ex} and σ_{ex} are reference strain and stress measured in experimental tests, ε_{nu} and σ_{nu} are component of strain and stress in the x -axis direction from numerical analyses.

The values of x component of strain and stress obtained in the analyses are read in the node whose coordinates correspond to the location where the strain gauge is attached.

The percentage errors of strain (Fig. 19.2) and stress (Fig. 19.3) in a function of the external load are presented in the form of column graphs. To distinguish the results of the subsequent analyses, the following rules were applied. The letters ns

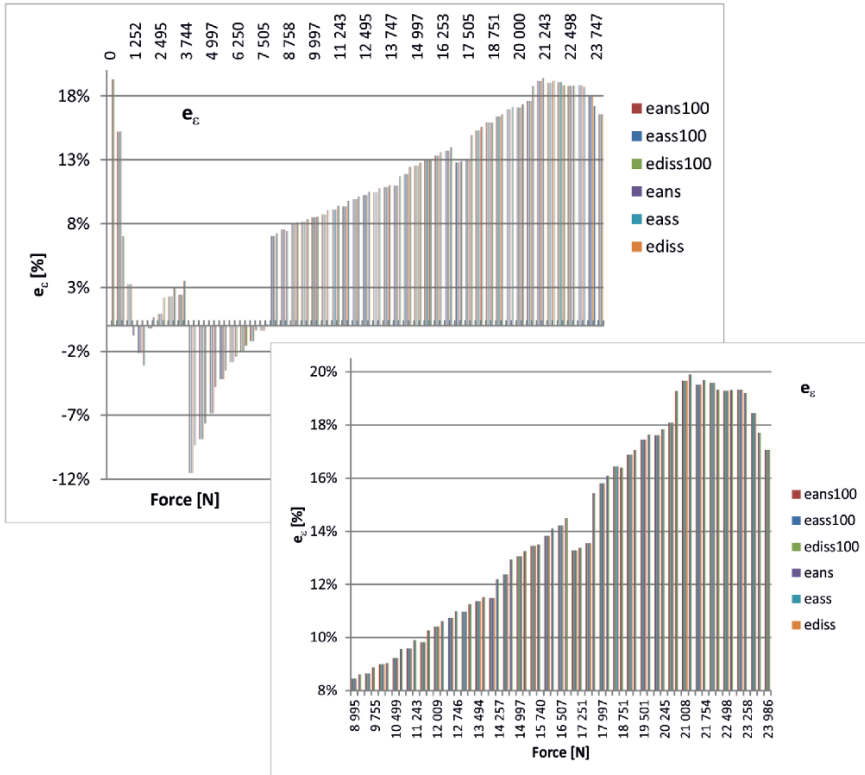


Fig. 19.2 Percentage errors of strain.

and *ss* refer to the NTS and STS discretization procedures, *a* and *di* refer to the analytical and discrete description of the contact geometry, while numbers 50 and 100 indicate the number of the external load increments.

The maximum percentage error is less than 18% for strain and less than 5.3% for stress, which means a slight influence of the contact problem solving method on the results of analyses. Local tips on both graphs are noticed for the initial phase of calculation.

19.5 Results of Numerical Simulations

The consequence of the specimen compression is large deformation of its middle part (Fig. 19.4a).

During numerical analysis, the contact forces are obtained directly from the finite element solution, whereas the contact stress is derived from the contact force divided by the area around the node. A contact area is calculated with the use of a shape

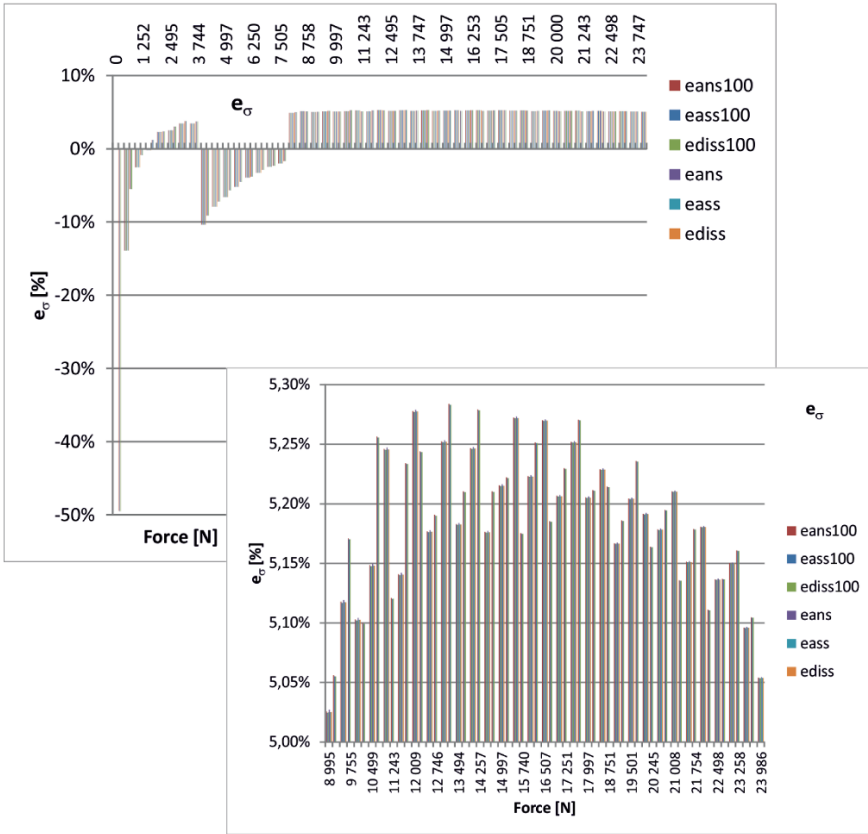


Fig. 19.3 Percentage errors of stress.

function. Therefore, a contact area for a linear finite element is found by dividing the contact force by contact stress.

This option was used to assess the size of the contact area depending on the number of iterations, description of the contact surface geometry (analytic and discrete) and a type of discretization (NTS and STS). For each node belonging to both contact surfaces of the first (l_1) and the second (l_2) lamina, the contact surface area was determined.

The percentage value of the relative contact area, rd_{cat} for the node, is specified as the relative contact area for the results of one type of analysis with respect to another analysis

$$rd_{cat} = \frac{A_{cat} - A_{cr}}{A_{cr}} \cdot 100\% \tag{19.16}$$

The lower indices cat are the designations of the compared analyses, where cr is the reference analysis.

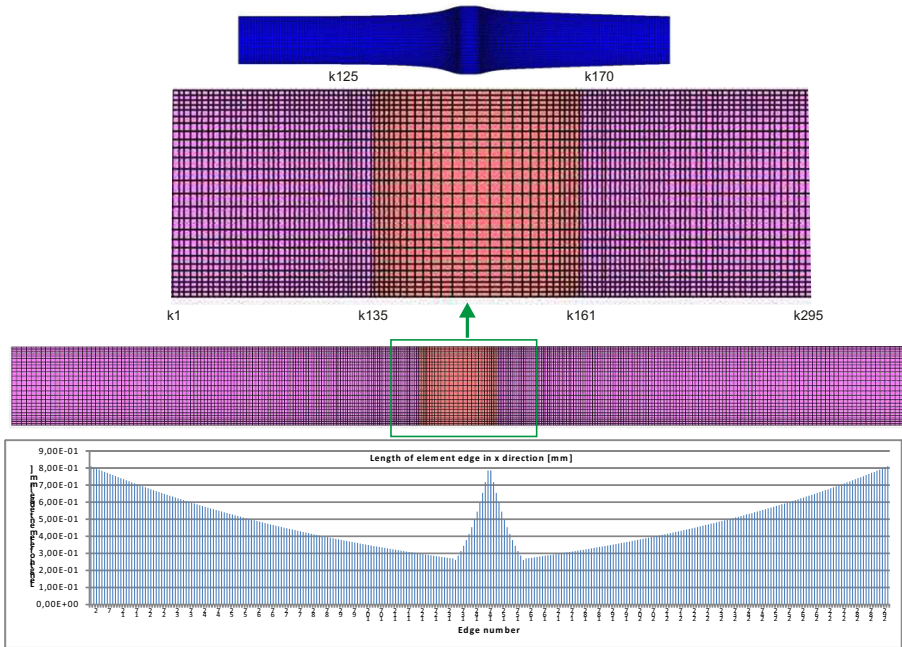


Fig. 19.4 (a) Specimen deformation for the maximum compressive force, (b) edge numbering, (c) specimen model, (d) distribution of edge lengths of finite elements along x axis.

The results of the analyses as a function of the external load are presented in spatial diagrams created for nodes lying across the subsequent edges from this area (Fig. 19.4c). The specimen measurement area, along with the numbers of the selected edges, are shown in Fig. 19.4b. Figure 19.4d also shows the distribution of edge lengths of the finite elements along the x -axis. The numbers on the horizontal axis correspond to the edge number. The horizontal plane of the graphs forms the external load axis (F) perpendicular to the coordinate axis of the nodes in the direction of the specimen (z) width. The percentage value of the relative contact area is on the axis normal to this plane.

The first comparisons are related to an influence of the number of external load increments on the percentage values of the relative contact area, rd_{assi} and rd_{dissi} , which are determined in accordance with dependence (19.16). The values are calculated for the corresponding levels of the external load on the basis of the results obtained in the analyses assuming its division into fifty and into a hundred increments. The reference values are the contact areas obtained in the analyses with fifty external load increments.

In the case of the STS procedure, both for the analytical (*ass*) and discrete (*diss*) description of the contact geometry, the percentage value of the relative contact area does not depend on its contact surface, i.e. $l1$ or $l2$. However, there are differences in the nature and the maximum of the percentage value of the relative contact area.

The results are presented for the edges lying in the area of the left grip (k130 and k131), for edges at the beginning of the measurement region (k135 to k138) and for the edge where a rapid change in the nature of the distribution occurs. Edge k148 is in the middle of the specimen measurement area, whereas k161 is last edge in this region. In Fig. 19.5 there are presented distributions of the percentage value of the relative contact area for analytical analysis (*ass*) and for discrete analysis (*diss*) for the selected edges.

The influence of the number of external load increments and the discretization procedure on distributions of the percentage value of the relative contact area (*dansi*) in the case of analyses using the analytical NTS (*ans*) procedure is shown in Fig. 19.6. The graphs present the results for the upper (*l1*) and lower (*l2*) lamina of the analyzed contact surface. The results are presented for the same edges as in Fig. 19.5.

The influence of the contact geometry description is important mainly for nodes belonging to the boundaries of the contact area. Application of the analytical description of the contact surface geometry in the case of the STS procedure reduces the local “jumps” caused by inaccuracies of the coordinates corresponding to nodes. In the discrete description of geometry, the object deformation causes local standard discontinuities to the contact area.

To compare the impact of the NTS (*ns*) and STS (*ss*) discretization procedure, the percentage value of the relative contact area is calculated according to the expression

$$rd_{anss} = \frac{A_{ass} - A_{ans}}{A_{ans}} \cdot 100\% \quad (19.17)$$

The area for the NTS (*ns*) procedure was assumed as the reference value. Graphs for analyses with fifty load increments for both contact surfaces and for edges inside the measurement region are presented in Fig. 19.7.

19.6 Summary and Conclusions

The mapping of the adhesive contact between two bonded layers enables determination of their local delamination, especially in the case of compression of a multi-layer composite. However, the correct selection of the contact problem algorithm is important.

The calculation of the percentage value of the relative contact area allows determining the influence of three parameters of contact algorithms, discretization procedure, description of the contact surface geometry and the number of load increments on the results of calculations. An influence of other parameters of the model, such as the type and size of finite elements, have not been considered.

The presented results of numerical analyses of six model variants showed that the effect of the segment-to-segment discretization procedure (STS) is a lack of dependence of the contact area size on the node belonging to the contacting surface. However, the analytical description of the contact surface geometry for this procedure is vital in the initial phase of the load and for the nodes forming the outer edges along

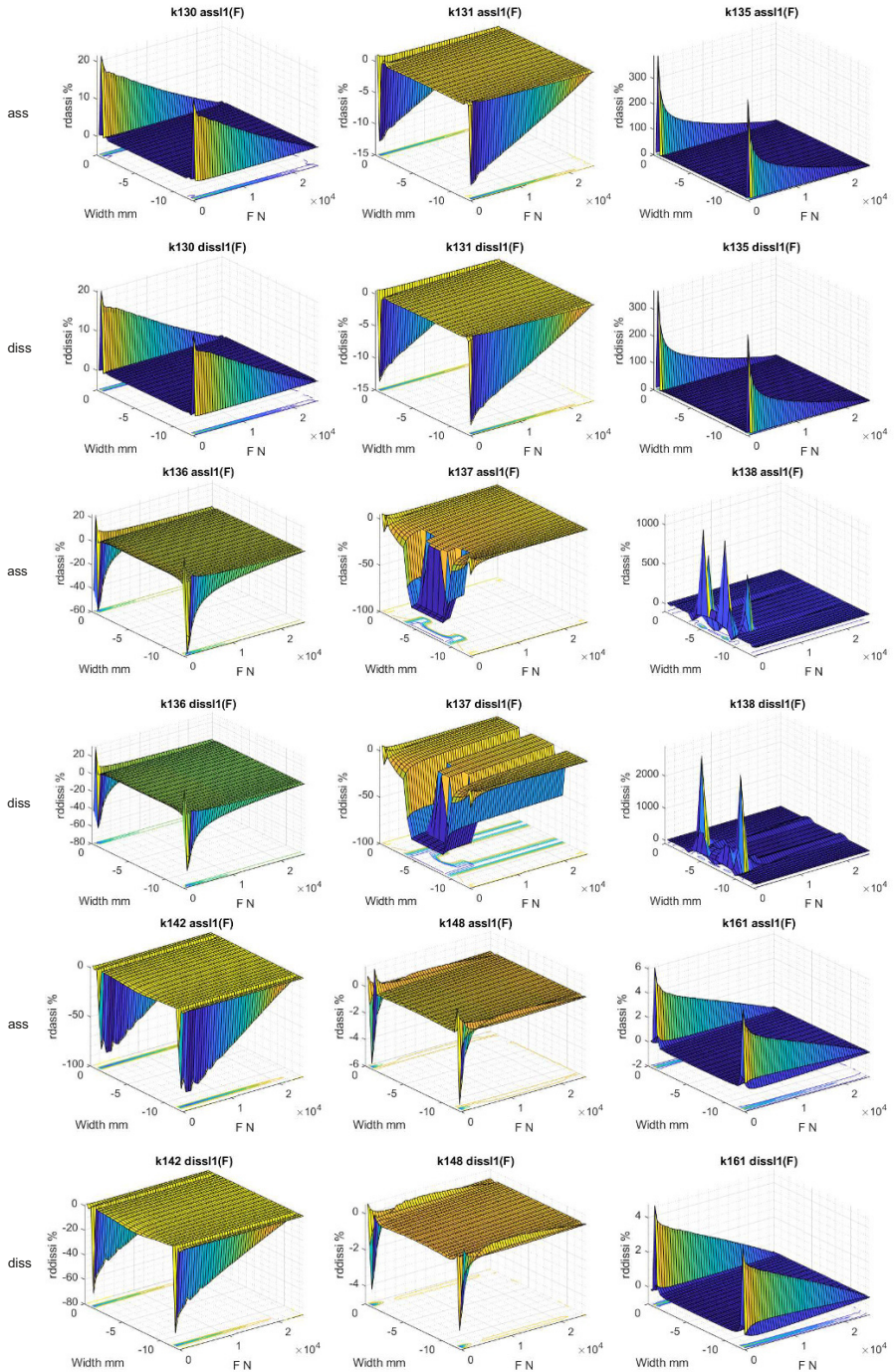


Fig. 19.5 Distributions of percentage value of the relative contact area for analytical analysis and for discrete analysis for selected edges.

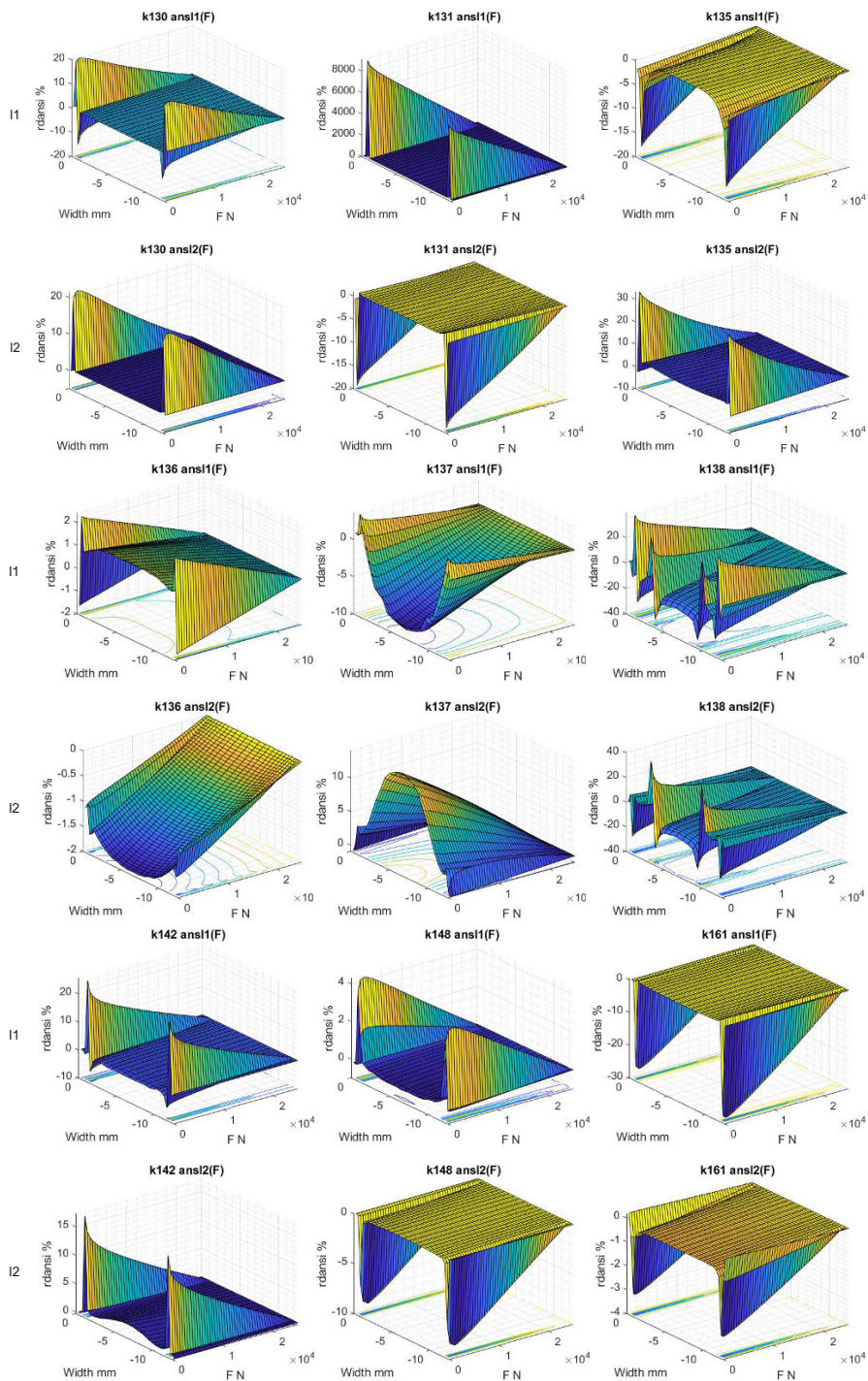


Fig. 19.6 Distributions of percentage value of the relative contact area for analytical NTS procedure analyses for selected edges.

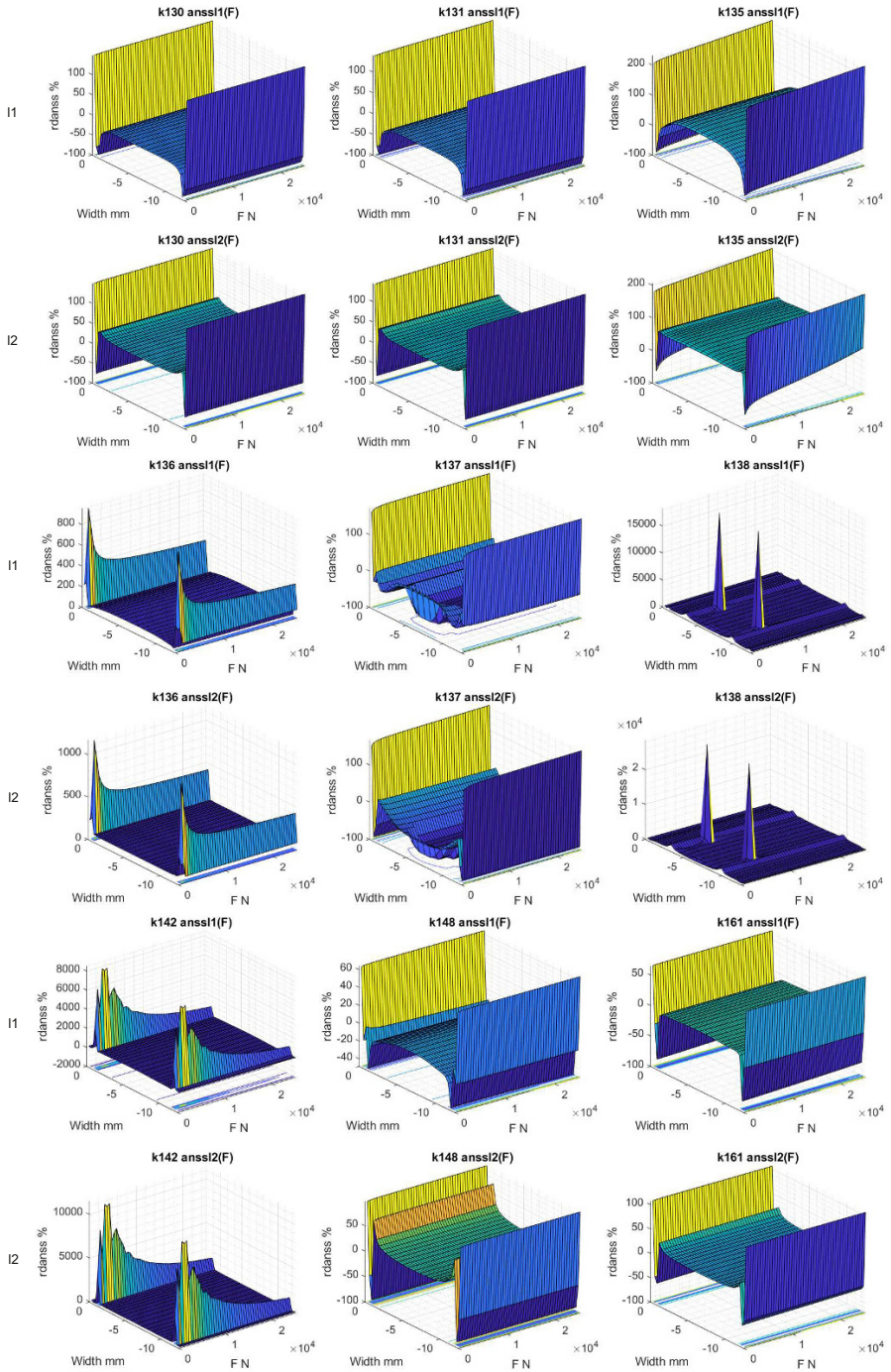


Fig. 19.7 Distributions of percentage value of the relative contact area of analytical STS and analytical NTS procedure for fifty increments, for both contact surfaces.

the length of the bonding interface, especially in the case of the load acting in this direction. The use of the node-to-segment discretization procedure (NTS) results in differentiation of the size of the contact areas, depending on the node belonging.

The number of load increments is mainly relevant for contact areas around the nodes belonging to the specimen outer edges lying along the length of the specimen. This is the result of using the Simpson's method to numerically integrate the surface area. The use of finite elements with linear shape functions, such as Hex elements, makes the accuracy of the results independent of the length of the integration step, i.e. the number of load increments. Local jumps of the percentage value of the relative difference in the contact area may result, for example, from a lack of correspondence of pairs of nodes in the contact area.

The paper proves that the optimal method for solving numerical analysis of a static problem with the contact problem is the algorithm with the segment-to-segment procedure, the discrete geometry description (smoothing the contact surfaces) and with the bilinear Coulomb's friction model. To solve the contact equations, a large strain method in the updated Lagrange description should be used.

This is the preliminary stage of work towards development of a numerical method for predicting failure initiation of the adhesive joint and the load causing it.

Acknowledgements The research has been funded from Ministry of Science and Higher Education within statutory activities 2019.

References

- Alart P, Curnier A (1991) A mixed formulation for frictional contact problems prone to newton like solution methods. *Computer Methods in Applied Mechanics and Engineering* 92(3):353–375, DOI 10.1016/0045-7825(91)90022-X
- ASTM Committee D-30 (1990) ASTM standards and literature references for composite materials. <https://www.astm.org/Standards/D3410.htm>, [accessed 22.05.2018]
- Bertsekas D (1984) *Constrained Optimization and Lagrange Multiplier Methods*. Academic Press, New York
- Cavaliere CA FJ (2012) An augmented Lagrangian method to solve three-dimensional nonlinear contact problems. *Latin American Applied Research* 42(8):281–289, DOI 10.1002/nme.4391
- Curnier A, Alart P (1988) A generalized newton method for contact problems with friction. *Journal de Mécanique Théorique et Appliquée* 7(suppl. 1):67–82, URL <http://infoscience.epfl.ch/record/54198>, special issue entitled "Numerical Methods in Mechanics of Contact Involving Friction"
- Derewonko A (2018) Observations on fem modelling of adhesive joint debonding. *International Journal of Adhesion and Adhesives* 81:65–73, DOI 10.1016/j.ijadhadh.2017.11.010
- Giorgio I, Scerrato D (2017) Multi-scale concrete model with rate-dependent internal friction. *European Journal of Environmental and Civil Engineering* 21(7–8):821–839, DOI 10.1080/19648189.2016.1144539
- Giorgio I, Harrison P, dell'Isola F, Alsayednoor J, Turco E (2018) Wrinkling in engineering fabrics: a comparison between two different comprehensive modelling approaches. *Proceedings of the Royal Society A: Mathematical, Physical and Engineering Sciences* 474(2216):65–73, DOI 10.1098/rspa.2018.0063

- Glowinski R, Le Tallec P (1984) Finite elements in nonlinear incompressible elasticity. In: JT Oden J, Carey G (eds) *Finite Elements: Special problems in solid mechanics*, Prentice-Hall
- Gonzalez A, Lauber J, Guerra T, Massa F, Tison T (2014) Large Time Simulation Reduction for Solving the Mechanical Contact Problem: A Fuzzy Control Approach. In: *IFAC Proceedings Volumes*, Elsevier, vol 79, pp 2558–2563, DOI 10.3182/20140824-6-ZA-1003.01175
- Hartmann S, Oliver J, Weyler R, Cante J, , Hernández J (2009) A contact domain method for large deformation frictional contact problems. part 2: Numerical aspects. *Computer Methods in Applied Mechanics and Engineering* 198(33–36):2607–2631, DOI 10.1016/j.cma.2009.03.009
- Kikuchi N, Oden J (1988) *Contact Problems in Elasticity: A Study of Variational Inequalities and Finite element Methods*. Society for Industrial and Applied Mathematics (SIAM), Philadelphia, DOI 10.1137/1.9781611970845
- Laursen T, Simo J (1991) On the formulation and numerical treatment of finite deformation frictional contact problems. In: Wriggers P, Wagner W (eds) *Computational Methods in Nonlinear Mechanics*, Springer, Berlin
- Laursen T, Simo J (1993a) Algorithmic symmetrization of coulomb frictional problems using augmented Lagrangians. *Computer Methods in Applied Mechanics and Engineering* 108:133–146, DOI 10.1016/0045-7825(93)90157-S
- Laursen T, Simo J (1993b) A continuum-based finite element formulation for the implicit solution of multibody. *International Journal for Numerical Methods in Engineering* 36(20):3451–3485, DOI 10.1002/nme.1620362005
- MSC Software Corporation (2013) *Marc 2013 Volume A: Theory and User Information*. <https://simcompanion.mscsoftware.com/>
- Nadler B, Steigmann D (2003) A model for frictional slip in woven fabrics. *Comptes Rendus Mecanique* 331(12):797–804, DOI 10.1016/j.crme.2003.09.004
- Oden J (1981) Exterior penalty methods for contact problems in elasticity. In: W Wunderlich W, Stein E, Bathe K (eds) *Nonlinear Finite Element Analysis in Structural Mechanics*, Springer, pp 655–665
- Oliver J, Hartmann S, Cante J, Weyler R, Hernández J (2009) A contact domain method for large deformation frictional contact problems. part 1: Theoretical basis. *Computer Methods in Applied Mechanics and Engineering* 198(33–36):2591–2606, DOI 10.1016/j.cma.2009.03.006
- Paggi M, Wriggers P (2016) Node-to-segment and node-to-surface interface finite elements for fracture mechanics. *Computer Methods in Applied Mechanics and Engineering* 300:540–560, DOI 10.1016/j.cma.2015.11.023, URL <https://www.sciencedirect.com/science/article/pii/S0045782515003837>, accessed 05.06.2018
- Panagiotopoulos C, Mantic V, Roubicek T (2018) Two adhesive-contact models for quasistatic mixed-mode delamination problems. *Mathematics and Computers in Simulation* 145(8):18–33, DOI 10.1016/j.matcom.2016.10.004
- Papadopoulos P, Taylor R (1992) A mixed formulation for the finite element solution of contact problems. *Computer Methods in Applied Mechanics and Engineering* 94(3):373–389, DOI 10.1016/0045-7825(92)90061-N
- Pietrzak G, Curnier A (1999) Large deformation frictional contact mechanics: continuum formulation and augmented Lagrangean treatment. *Computer Methods in Applied Mechanics and Engineering* 92(3–4):353–375, DOI 10.1016/S0045-7825(98)00388-0
- Placidi L, Barchiesi E (2018) Energy approach to brittle fracture in strain-gradient modelling. *Proceedings of the Royal Society A: Mathematical, Physical and Engineering Sciences* 474(2210):77–100, DOI 10.1098/rspa.2017.0878
- Placidi L, Barchiesi E, Misra A (2018) A strain gradient variational approach to damage: a comparison with damage gradient models and numerical results. *Mathematics and Mechanics of Complex Systems* 6(2):77–100, DOI 10.2140/memocs.2018.6.77
- Sauer R, De Lorenzis L (2013) An augmented Lagrangian method to solve three-dimensional nonlinear contact problems. *Latin American Applied Research* 42(8):281–289, DOI 10.1002/nme.4391
- Simo J, Laursen T (1992) An augmented Lagrangian treatment of contact problems involving friction. *Computers & Structures* 42:97–116, DOI 10.1016/0045-7949(92)90540-G

- Simo J, Taylor R (1985) Consistent tangent operators for rate-independent elastoplasticity. *Computer Methods in Applied Mechanics and Engineering* 48(3):101–118, DOI 10.1016/S0045-7825(85)90054-4
- Simo J, Wriggers P, Taylor R (1985) A perturbed Lagrangian formulation for the finite element solution of contact problems. *Computer Methods in Applied Mechanics and Engineering* 50(2):163–180, DOI 10.1016/0045-7825(85)90088-X
- Spagnuolo M, Franciosi P, Dell’Isola F (2020) A Green operator-based elastic modeling for two-phase pantographic-inspired bi-continuous materials. *International Journal of Solids and Structures* 188:282–308, DOI 10.1016/j.ijsolstr.2019.10.018
- Wriggers P (1995) Finite element algorithms for contact problems. *Archives of Computational Methods in Engineering* 2(4):1–49, DOI 10.1016/0045-7825(93)90157-S
- Wriggers P (2006) *Computational Contact Mechanics*, 2nd edn. Springer, DOI 10.1007/978-3-540-32609-0
- Wriggers P, Simo J (1985) A note on tangent stiffness for fully nonlinear contact problems. *Computer Methods in Applied Mechanics and Engineering* 1(5):199–203, DOI 10.1002/cnm.1630010503
- Wriggers P, Vu Van T, Stein E (1990) Finite element formulation of large deformation impact-contact problems with friction. *Computers and Structures* 37(3):319–331, DOI 10.1016/0045-7949(90)90324-U
- Zavarise G, De Lorenzis L (2009) A modified node-to-segment algorithm passing the contact patch test. *International Journal for Numerical Methods in Engineering* 79(4):379–416, DOI 10.1002/nme.2559
- Zavarise G, De Lorenzis L (2012) An augmented Lagrangian algorithm for contact mechanics based on linear regression. *International Journal for Numerical Methods in Engineering* 91(8):825–842, DOI 10.1002/nme.4294
- Zavarise G, Wriggers P (eds) (2011) *Trends in Computational Contact Mechanics*, LNCS, vol 58. Springer-Verlag, Berlin Heidelberg
- Zavarise G, Wriggers P, Schrefler B (1995) On augmented Lagrangian algorithms for thermo-mechanical contact problems with friction. *International Journal for Numerical Methods in Engineering* 38(17):2929–2949, DOI 10.1002/nme.1620381706
- Zavarise G, Wriggers P, Schrefler B (1998) A method for solving contact problems. *International Journal for Numerical Methods in Engineering* 42(3):473–498, DOI 10.1002/(SICI)1097-0207(19980615)42:3<473:AID-NME367>3.0.CO;2-A



Chapter 20

Vibration Analysis Based Spalling Defect Severity Assessment of Spur Gearbox Using a Dynamic Model

Vishwadeep C. Handikherkar & Vikas M. Phalle

Abstract Gears are toothed mechanical elements used in the industries for changing speed, increasing/decreasing torque and transmitting power between two shafts. Due to variable loads harsh operating conditions faults develop in the gears such as pitting, spalling, crack and broken tooth. Spalling is the most common fault observed on the gear tooth, these are the deeper cavities developed from subsurface defects. Over a period of time these faults grow, and the health of the system continues to degrade causing system breakdown and economic loss. Therefore, early detection of fault is of utmost importance. Vibration analysis is the most widely used fault diagnosis technique in the rotating machinery. When fault develops on the gears its gear mesh stiffness reduces and resulting into the change in the vibration response of the gearbox. In this paper, the time varying mesh stiffness for healthy (gear tooth without fault) and tooth having spall fault of varying severity is evaluated using the potential energy method. Further, a dynamic model of one stage spur gearbox is presented to obtain the vibration response of the healthy and faulty gearbox to study the influence of fault and fault severity by using time domain and frequency domain features.

Keywords: Spur Gear · Dynamic Model · Spall defect · Severity Assessment

20.1 Introduction

Gears are the subsystems of the rotating machineries, these are used in many industrial machines, wind turbine, automotive applications, locomotives, ships and airplanes etc. for changing speed, torque and transmitting power. These gears operate with different load and speed conditions, bad lubrication, and manufacturing

V. C. Handikherkar, V. M. Phalle
Veermata Jijabai Technological Institute, Mumbai.
e-mail: vishwadeepch@gmail.com, vmphalle@me.vjti.ac.in

or installation problem. Due to variable loads and harsh operating conditions faults such as pitting, spalling, crack and broken tooth develop in the gears. Spalling is formation of deeper cavities that are mainly developed from subsurface defects and is one of the common defects on the gear tooth (Saxena et al, 2016). Al-Meshari et al (2012) found in his gearbox failure investigation that spalling of gear tooth is one of the major causes of gearbox failure. Therefore, early indication of spalling is an important task to avoid system shutdown and economic loss. The various methods for fault diagnosis are oil debris analysis, acoustic analysis; vibration signal analysis etc. out of this vibration analysis is the most widely used fault diagnosis technique for the fault detection in rotating machinery. Kankar et al (2012) used a vibration data collected from the rotor bearing system for the rotor and bearing fault classification. Engine fault classification using the multi sensor vibration data was carried out by Jafarian et al (2018). Andreaus et al (2017) presented a beam crack detection method using the wavelet analysis based on the displacement data collected at various points.

Vibration in gears are caused due to external excitations such as fluctuation of applied load, input speed and internal excitations such as time varying mesh stiffness, transmission error etc. Therefore, calculation of time-varying gearmesh stiffness is important for obtaining a vibration response. There are different methods of evaluating the gearmesh stiffness such as Finite Element Analysis, Potential Energy Method, Square Waveform Method and Experimental Method (Liang et al, 2018). Yang and Lin (1987) developed a gearmesh stiffness calculation method based on the potential energy method. It includes energy stored in the tooth due to Hertzian Contact, Bending, and Axial compressive. Further, Tian et al (2004) extended this model by including shear energy for evaluation of the gearmesh stiffness. Numerous gear dynamic models have been proposed for the dynamic analysis of the gearbox. The different methods of gearbox dynamic modeling techniques were reviewed by Liang et al (2018). Bartelmus (2001) developed 8 DoF dynamic model having both torsional and lateral motions as well as considering the friction.

Liang et al (2016) have modelled a gear tooth pitting growth using circular pits and evaluated the influence of tooth pitting of the mesh stiffness of external gears. A single degree of freedom model for a low contact ratio spur gear was developed considering the time varying gear-mesh stiffness and viscous damping proportional to the TVMS by Amabili and Rivola (1997). The model helps in studying the stability characteristics and steady state response of the system. Abouel-seoud et al (2012) presented a dynamic response of wind turbine gearbox using a 12 degree of freedom dynamic model of gearbox. In this they have considered three tooth faults viz. cracking, spalling and breakage. Amabili and Fregolent (1998) proposed new method for the identification of the natural frequency, damping and tooth profile errors in the spur gear pair. Mohammed et al (2015) developed a 12 DOF dynamic model of one stage spur gearbox including the gyroscopic effect. The simulations were carried out for different crack sizes and the vibration response was obtained. Time domain features such as RMS, kurtosis and the crest factor were extracted from the vibration response for fault detection. Omar et al (2012) developed a 9 DoF dynamic model considering the gear size, transmission errors and gear crack, this model is then

validated with the experimental test rig. Tian et al (2012) investigated the sensitive indicators for crack propagation level assessment using statistical indicators and the discrete wavelet transform (DWT). Sharma and Parey (2016) have provided a different condition indicators used for the gear fault diagnosis.

In the present paper, gear-mesh stiffness for healthy and spalled gear have been calculated using the potential energy method. This gear-mesh stiffness values were utilized to obtain the dynamic response of the system using a 6-DoF dynamic model. Later time domain statistical features were calculated for the early indication of spall fault.

20.2 Evaluation of Gear-Mesh Stiffness

In this paper, gear-mesh stiffness is evaluated based on the potential energy method proposed by Yang and Lin (1987) and further refined by Tian et al (2004) for the calculation of the gear-mesh stiffness. Figure 20.1 shows the geometry of the single tooth used for the calculation of stiffness. The total mesh stiffness can be obtained by the equation (20.1) for single pair of teeth in contact and equation (20.2) for the two pairs of teeth in contact.

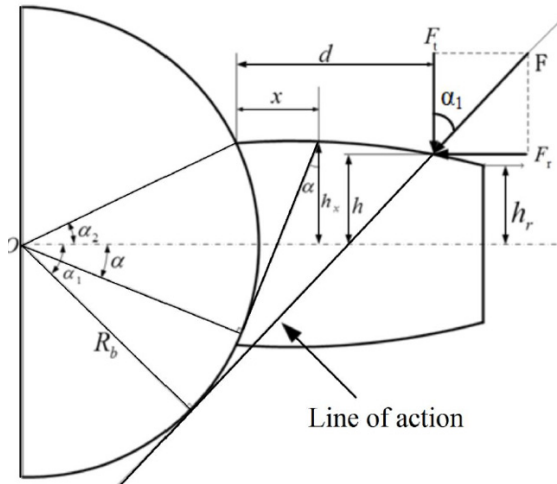


Fig. 20.1 Geometry of the tooth

$$K_t = \frac{1}{\frac{1}{K_{hp}} + \frac{1}{K_{ap}} + \frac{1}{K_{bp}} + \frac{1}{K_{sp}} + \frac{1}{K_{ag}} + \frac{1}{K_{bg}} + \frac{1}{K_{sg}}} \tag{20.1}$$

$$K_t = \sum_{i=1}^2 \frac{1}{\frac{1}{K_{hpi}} + \frac{1}{K_{api}} + \frac{1}{K_{bpi}} + \frac{1}{K_{spi}} + \frac{1}{K_{agi}} + \frac{1}{K_{bgi}} + \frac{1}{K_{sgi}}} \quad (20.2)$$

The expressions of Hertzian stiffness, axial compressive stiffness, shear stiffness and bending stiffness components are shown in equations (20.3) to (20.6) respectively Hertzian stiffness (K_h)

$$K_h = \frac{\Pi E L_s}{4(1 - \nu)} \quad (20.3)$$

Axial compressive stiffness K_a

$$\frac{1}{K_a} = \int_{-\alpha_1}^{\alpha_2} \frac{R_b \sin^2 \alpha_1 (\alpha_2 - \alpha) \cos \alpha}{2EA_s} d\alpha \quad (20.4)$$

Shear stiffness K_s

$$\frac{1}{K_s} = \int_{-\alpha_1}^{\alpha_2} \frac{1.2R_b(1 + \nu) \cos^2 \alpha_1 (\alpha_2 - \alpha) \cos \alpha}{2EA_s} d\alpha \quad (20.5)$$

Bending stiffness K_b

$$\frac{1}{K_b} = \int_{-\alpha_1}^{\alpha_2} \frac{R_b^3 [(1 + \cos \alpha_1) ((\alpha_2 - \alpha) \sin \alpha - \cos \alpha)]^2 (\alpha_2 - \alpha) \cos \alpha}{2EA_s} d\alpha \quad (20.6)$$

Spall fault is considered as the rectangle as shown in Figure 20.2. In equation (20.3) and (20.6) the values of L_s , A_s and I_s will vary according to the equations (20.7) and (20.9)

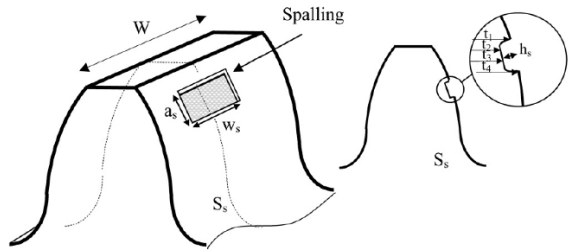


Fig. 20.2 Geometry of spalled tooth

$$L_s = \begin{cases} L_s & \text{For healthy region.} \\ L_s - l_s & \text{For spalled region.} \end{cases} \quad (20.7)$$

$$A_s = \begin{cases} 2h_x L & \text{For healthy region.} \\ 2h_x L - h_s l_s & \text{For spalled region.} \end{cases} \quad (20.8)$$

$$I_s = \begin{cases} \frac{2}{3}h_x^3L & \text{For healthy region.} \\ \frac{1}{12}[8h_x^3L] - \frac{1}{12}[h_s^3l_s] & \text{For spalled region.} \end{cases} \quad (20.9)$$

The gear-mesh stiffness of spur gear having gear parameters as given in Table 20.1 is evaluated for different spalling fault sizes as given in Table 20.2.

Table 20.1 Gear parameters

| Gear Parameter | Value |
|--------------------------------------|---|
| Number of teeth on Pinion/Gear | $N_p=19, N_g=48$ |
| Pressure angle | 20 deg |
| Diametrical pitch | $P=0.2032 \text{ m}^{-1}$ |
| Width of teeth | $L=0.16 \text{ m}$ |
| Contact ratio | $C_r = 1.6456$ |
| Young's modulus | $E = 2.068 \times 10^{11} \text{ Pa}$ |
| Poisson's ratio | $\nu=0.3$ |
| Mass of the Pinion/Gear | $m_p = 0.96 \text{ kg}, m_g = 2.88 \text{ kg}$ |
| Mass moment of inertia of the Pinion | $I_p = 4.3659 \times 10^{-4} \text{ kg m}^2$ |
| Mass moment of inertia of the Gear | $I_g = 8.3602 \times 10^{-4} \text{ kg m}^2$ |
| Mass moment of inertia of the motor | $I_m = 0.0021 \text{ kg m}^2$ |
| Mass moment of inertia of the load | $I_b = 0.0105 \text{ kg m}^2$ |
| Input shaft frequency | $f_1 = 30 \text{ Hz}$ |
| Mesh frequency | $f_m = 570 \text{ Hz}$ |
| Input motor torque | $M_1 = 11.9 \text{ Nm}$ |
| Output load torque | $M_2 = 48.8 \text{ Nm}$ |
| Torsional stiffness of the coupling | $k_p = k_g = 4.4 \times 10^4 \text{ Nm/rad}$ |
| Damping coefficient of the coupling | $c_p = c_g = 5.0 \times 10^5 \text{ Nm/rad}$ |
| Radial stiffness of the bearing | $k_1 = k_2 = 6.56 \times 10^7 \text{ Nm/rad}$ |
| Damping coefficient of the bearing | $c_1 = c_2 = 1.8 \times 10^5 \text{ Nm/rad}$ |
| Base circle radius of Pinion/Gear | $R_{b1} = 0.02834 \text{ m}, R_{b2} = 0.0716 \text{ m}$ |

The gear-mesh stiffness was evaluated for healthy and tooth having spall faults for the gear parameters tabulated in Table 20.1 and for different spalling size as given in Table 20.2. The gearmesh stiffness for the one revolution of pinion is represented for healthy and faulty gear are represented in Figure 20.3 and 20.4 respectively.

20.3 Dynamical Model and Simulation

For obtaining a vibration response a dynamic model developed by Bartelmus (2001) having both torsional and lateral motions have been utilized (Figure 20.5). It is a 8 degree of freedom mass-spring-damper dynamic model with M1 input torque by

Table 20.2 Different sizes of spall fault

| No. | As (m) | Ws (m) | Hs (m) |
|-----|---------|--------|--------|
| 1 | 0 | 0 | 0 |
| 2 | 0.00071 | 0.016 | 0.001 |
| 3 | 0.0014 | 0.032 | 0.001 |
| 4 | 0.0021 | 0.048 | 0.001 |
| 5 | 0.0029 | 0.064 | 0.001 |
| 6 | 0.0036 | 0.080 | 0.001 |
| 7 | 0.0043 | 0.096 | 0.001 |
| 8 | 0.0050 | 0.112 | 0.001 |
| 9 | 0.0057 | 0.128 | 0.001 |

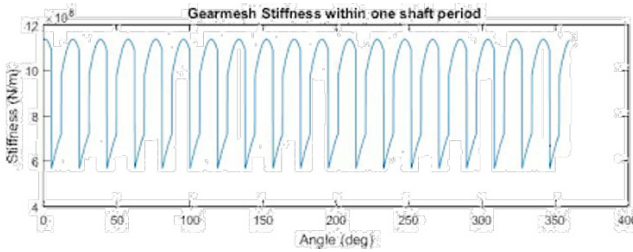


Fig. 20.3 Gearmesh stiffness of healthy gearbox

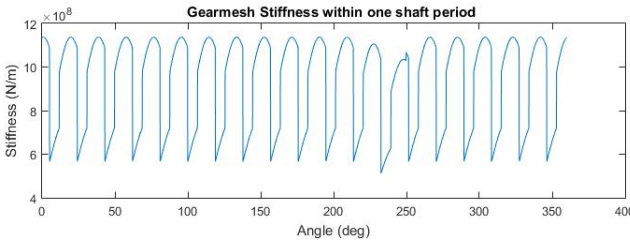


Fig. 20.4 Gearmesh stiffness of gear with spalled tooth

motor and M2 output torque. Two flexible coupling is used one to connect the motor with the input shaft carrying pinion and second to connect shaft carrying gear and load. The pinion and gear shafts are mounted on the rolling element bearings and these bearings are then mounted on the gearbox casing. The equations of motion are given as follows (Equations (20.10)–(20.17)):

$$m_1 \ddot{y}_1 + c_1 \dot{y}_1 + k_1 y_1 = -F_k - F_c \tag{20.10}$$

$$m_2 \ddot{y}_2 + c_2 \dot{y}_2 + k_2 y_2 = F_k + F_c \tag{20.11}$$

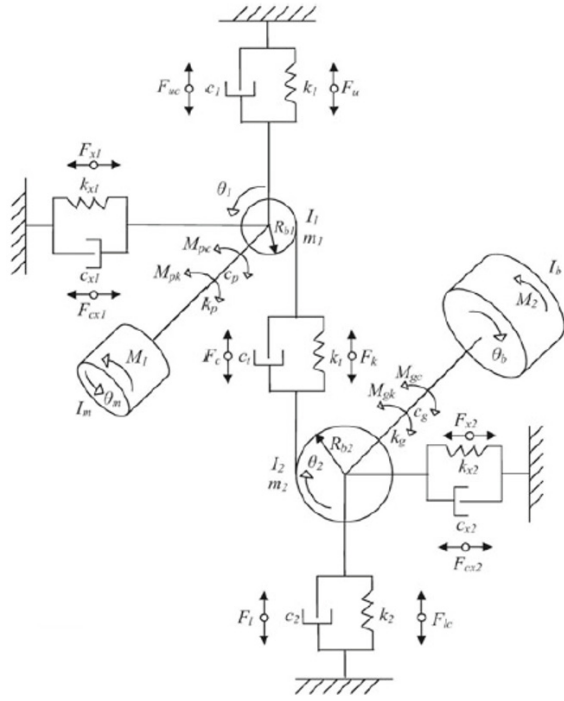


Fig. 20.5 8 Degree of freedom dynamic model

$$I_1 \ddot{\theta}_1 = k_p(\theta_m - \theta_1) + c_p(\dot{\theta}_m - \dot{\theta}_1) - R_{b1}(F_k + F_c) \quad (20.12)$$

$$I_2 \ddot{\theta}_2 = k_g(\theta_b - \theta_2) + c_g(\dot{\theta}_b - \dot{\theta}_2) + R_{b2}(F_k + F_c) \quad (20.13)$$

$$I_m \ddot{\theta}_m = M_1 - k_p(\theta_m - \theta_1) - c_p(\dot{\theta}_m - \dot{\theta}_1) \quad (20.14)$$

$$I_b \ddot{\theta}_b = -M_2 + k_g(\theta_2 - \theta_b) + c_g(\dot{\theta}_2 - \dot{\theta}_b) \quad (20.15)$$

$$F_k = k_t(R_{b1}\theta_1 - R_{b2}\theta_2 + y_1 - y_2) \quad (20.16)$$

$$F_c = c_t(R_{b1}\dot{\theta}_1 - R_{b2}\dot{\theta}_2 + \dot{y}_1 - \dot{y}_2) \quad (20.17)$$

where,

- I_m/I_b = Mass moment of inertia of rotor/load
- I_1/I_2 = Mass moment of inertia of pinion/gear
- M_1 = Input Motor Torque
- M_2 = Output torque from load
- m_1/m_2 = Mass of pinion/gear

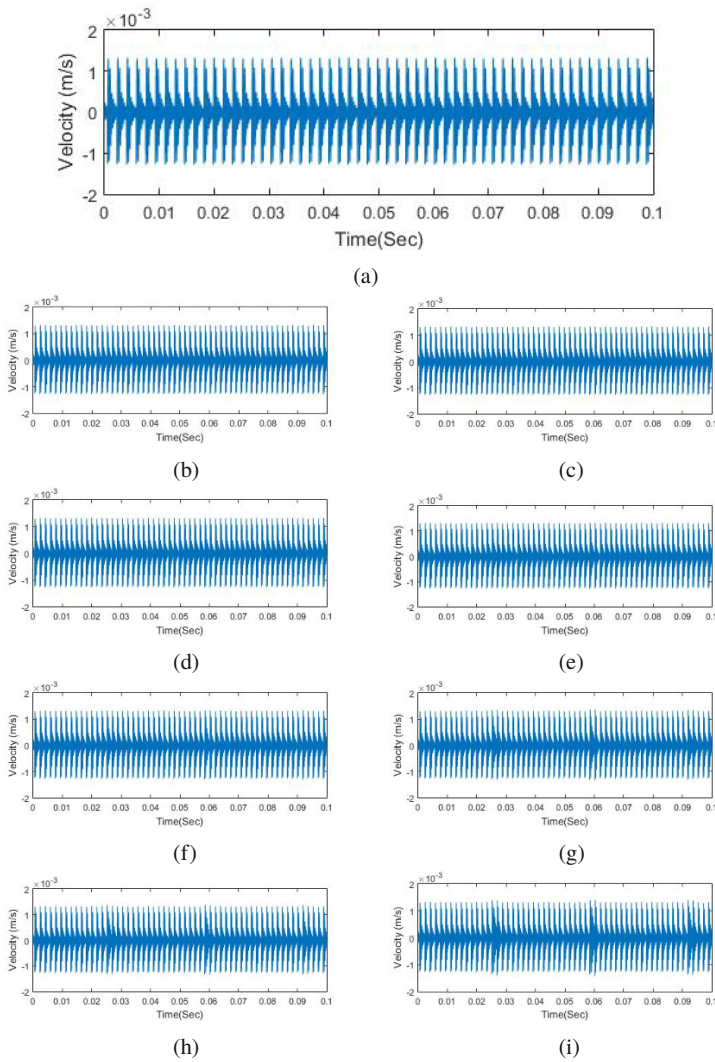
R_{b1}/R_{b2} = Base circle of pinion/gear
 k_p/k_g = Torsional stiffness of flexible coupling Input/Output
 c_p/c_g = Torsional damping of flexible coupling Input/Output
 k_1/k_2 = Vertical Radial stiffness of bearing Input/Output
 c_1/c_2 = Vertical Radial viscous damping coefficient of bearing Input/Output
 y_1/y_2 = Linear displacement of Pinion/Gear in the y -direction
 θ_m = Angular displacement of Motor
 θ_b = Angular displacement of Load
 θ_1/θ_2 = Angular displacement of pinion/gear
 and,
 F_k – stiffness inter-tooth force,
 F_c – damping inter-tooth force,
 F_u – internal stiffness force of input bearing,
 F_{uc} – internal damping force of input bearing,
 F_l – internal stiffness force of output bearing,
 F_{lc} – internal damping force of output bearing,
 M_{pk} – stiffness moment of input couplings,
 M_{pc} – damping moment of input couplings,
 M_{gk} – stiffness moment of output couplings,
 M_{gc} – damping moment of output couplings,
 k_t – total mesh stiffness,
 c_t – mesh damping coefficient

We pay our attention to the y -direction vibration since this direction is along the direction of gear dynamic force. As the equations (20.10)–(20.15) are combination of torsional and lateral vibration the analytical solution is not possible therefore, these equations are solved simultaneously in the MATLAB using ODE15s solver with sampling frequency of 100000. The vibration response was obtained for various conditions given in Table 20.2. Table 20.3 shows the figures for result of vibration response for different conditions given in Table 20.2 for 0.1 s.

20.4 Results and Discussion

The potential energy method has been utilized for calculating the time varying gear-mesh stiffness for various conditions presented in Table 20.2. The gear parameters used in this study are given in table 20.1. Figure 20.3 shows the TVMS for the no fault or healthy condition and Figure 20.4 depicts the TVMS for the higher severity condition of spall fault. The figure clearly shows that there is a decrease in the TVMS when the spalled tooth pair is coming in contact. As the spall severity increases the value of TVMS decreases for contacting gear tooth pair. Variation in the TVMS causes the change in vibration response of gearbox for healthy and faulty case. 6-DoF dynamic model was utilized to obtain the vibration response for each condition. These equations of motion are solved in MATLAB using ODE15s

Table 20.3 Vibration response



solver. Table 20.3 figures (a-i) shows the vibration response of the gearbox for various conditions given in Table 20.2 for the duration of 0.1 s. For different spall severity level there is an increase in the vibration and different vibration response is obtained as shown in the table 20.3 figures (a-i). Further these time domain signals are converted in to the frequency domain using the FFT, these results are presented in figures (a-i) in table 20.4 . Figures clearly show that as the severity increases the amplitude of 6th harmonic of gear-mesh frequency increases also the side bands associated this increases. Also, 12 time domain features (Clearance Factor, Crest

Table 20.4 FFT

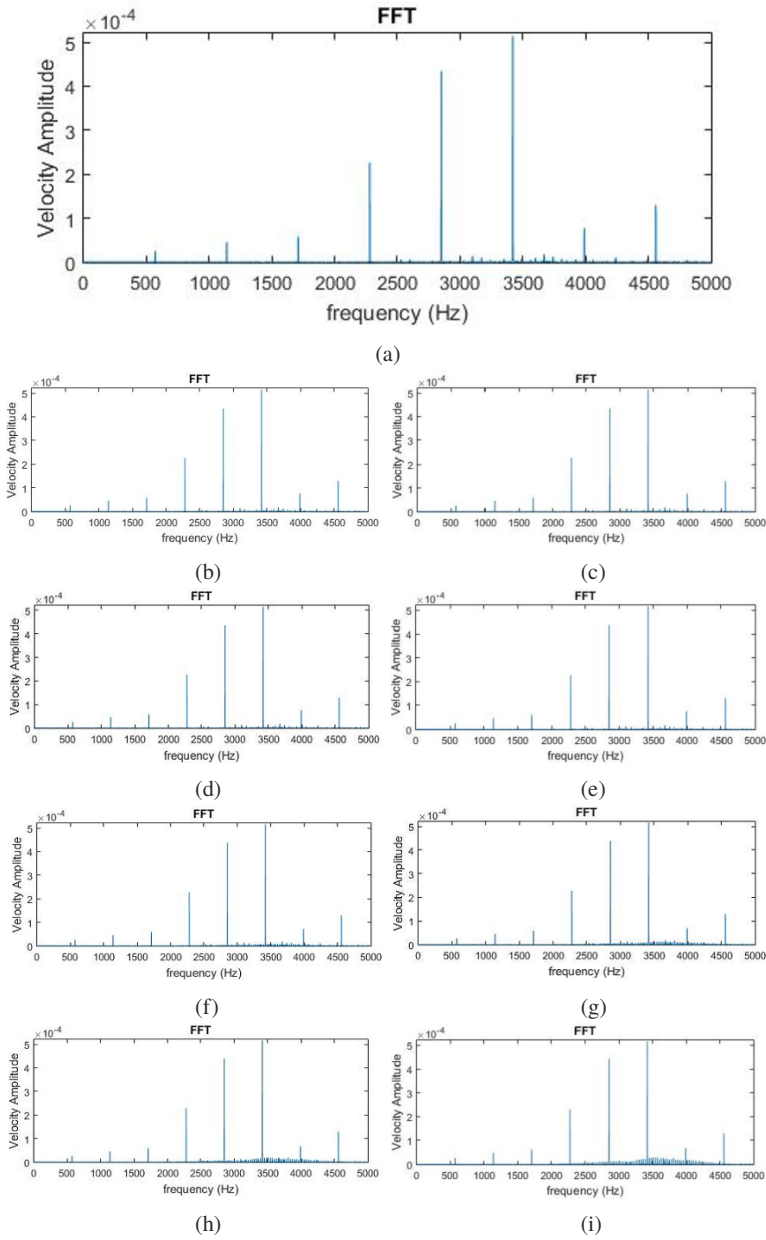
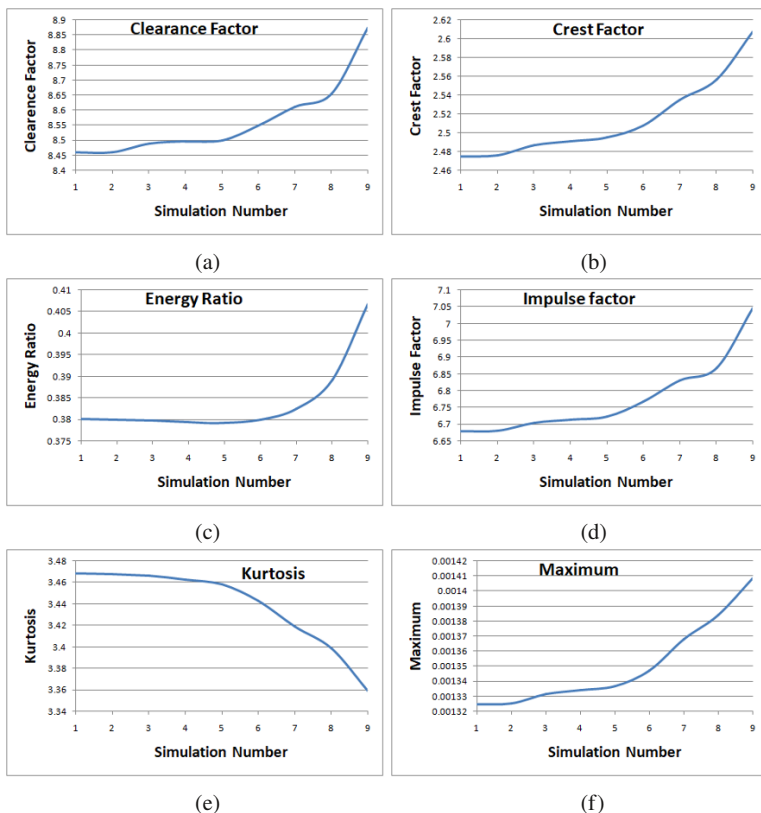


Table 20.5 Variation of time domain features

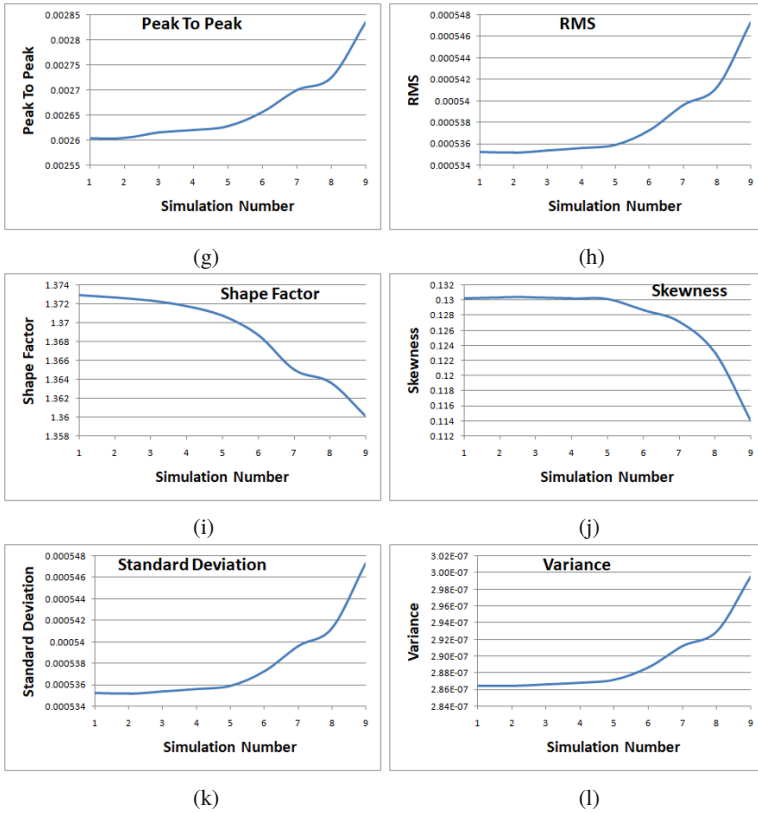


Factor, Energy Ratio, Impulse Factor, Kurtosis, Maximum, Peak to Peak, Root Mean Square (RMS), Shape factor, Skewness, Standard Deviation and Variance) were obtained for the early indication of the fault severity. The variation of these features for different severity conditions is depicted in Tables 20.5, 20.6. Except Kurtosis, Shape Factor and Skewness all other features are showing increase in the value as the spall severity increases. Out of these features Energy ratio, Standard Deviation, RMS and Variance shows the small change up to 50% severity and then shows the considerable increase. Remaining features Clearance Factor, Crest Factor, Impulse Factor, Maximum show considerable increase in the value as the severity increases.

20.5 Conclusion

This paper deals with the spall fault severity assessment of gearbox using simulated vibration signals. TVMS for healthy as well as spalling defects of different severity

Table 20.6 Variation of time domain features



was calculated using the potential energy method and a 6-DoF dynamic model has been employed to obtain the simulated time domain vibration signals. FFT results show that the 6th harmonics of gear-mesh frequency and its side bands show considerable change for different spall size. Time domain features Clearance Factor, Crest Factor, Impulse Factor, Maximum shows the variation in the values for different spall severity hence they are good indicators of spall fault severity.

References

Abouel-seoud SA, Dyab ES, Elmorsy MS (2012) Influence of tooth pitting and cracking on gear meshing stiffness and dynamic response of wind turbine gearbox. *Int J Sci Adv Technol* 2(3):151–165

Al-Meshari A, Al-Zahrani E, Diab M (2012) Failure analysis of cooling fan gearbox. *Engineering Failure Analysis* 20:166–172

- Amabili M, Fregolent A (1998) A method to identify modal parameters and gear errors by vibrations of a spur gear pair. *Journal of sound and vibration* 214(2):339–357
- Amabili M, Rivola A (1997) Dynamic analysis of spur gear pairs: steady-state response and stability of the sdof model with time-varying meshing damping. *Mechanical systems and signal processing* 11(3):375–390
- Andreaus U, Baragatti P, Casini P, Iacoviello D (2017) Experimental damage evaluation of open and fatigue cracks of multi-cracked beams by using wavelet transform of static response via image analysis. *Structural Control and Health Monitoring* 24(4):e1902
- Bartelmus W (2001) Mathematical modelling and computer simulations as an aid to gearbox diagnostics. *Mechanical Systems and Signal Processing* 15(5):855–871
- Jafarian K, Mobin M, Jafari-Marandi R, Rabiei E (2018) Misfire and valve clearance faults detection in the combustion engines based on a multi-sensor vibration signal monitoring. *Measurement* 128:527–536
- Kankar PK, Sharma SC, Harsha SP (2012) Vibration-based fault diagnosis of a rotor bearing system using artificial neural network and support vector machine. *International Journal of Modelling, Identification and Control* 15(3):185–198
- Liang X, Zuo MJ, Feng Z, Liu L (2016) A mesh stiffness evaluation model to reflect tooth pitting growth of a pair of external spur gears. In: 2016 Prognostics and System Health Management Conference (PHM-Chengdu), IEEE, pp 1–6
- Liang X, Zuo MJ, Feng Z (2018) Dynamic modeling of gearbox faults: A review. *Mechanical Systems and Signal Processing* 98:852–876
- Mohammed OD, Rantatalo M, Aidanpää JO (2015) Dynamic modelling of a one-stage spur gear system and vibration-based tooth crack detection analysis. *Mechanical Systems and Signal Processing* 54:293–305
- Omar FK, Moustafa KA, Emam S (2012) Mathematical modeling of gearbox including defects with experimental verification. *Journal of Vibration and Control* 18(9):1310–1321
- Saxena A, Parey A, Chouksey M (2016) Time varying mesh stiffness calculation of spur gear pair considering sliding friction and spalling defects. *Engineering Failure Analysis* 70:200–211
- Sharma V, Parey A (2016) A review of gear fault diagnosis using various condition indicators. *Procedia Engineering* 144:253–263
- Tian X, Zuo MJ, Fyfe KR (2004) Analysis of the vibration response of a gearbox with gear tooth faults. In: ASME 2004 International Mechanical Engineering Congress and Exposition, American Society of Mechanical Engineers Digital Collection, pp 785–793
- Tian Z, Zuo MJ, Wu S (2012) Crack propagation assessment for spur gears using model-based analysis and simulation. *Journal of Intelligent Manufacturing* 23(2):239–253
- Yang D, Lin J (1987) Hertzian damping, tooth friction and bending elasticity in gear impact dynamics. *Journal of mechanisms, transmissions, and automation in design* 109(2):189–196



Chapter 21

Simulation of Self Compensating Hydrostatic Bearing Using Finite Element Analysis

Sumit J. Patil, Abhishek N. Khairnar, Vikas M. Phalle, and Praveen K. Limaye

Abstract Self-compensating hydrostatic bearings provide higher stiffness and straightening characteristics than ordinary journal bearings. The high end as well as precision applications, such characteristics are desirable. The design we discuss (Patil et al, 2018) is such a self-compensating hydrostatic bearing used in actuators. The self-compensation principle is used by connecting opposite pockets of hydrostatic journals in a specific way to achieve greater stiffness. Extending our work (Patil et al, 2018) to model the flow of lubricant in one dimension, in this paper we use finite element method to numerically solve a 2-D Reynolds Equation that models the lubricant flow in bearing under study. Use of Finite Element Method over Finite Difference Method is also defended in this study based on the non-linear nature of governing equation and ease of computation. We have modified the generalized 2-D Reynolds Equation to represent the flow in bearings for actuators. Then we have used Galerkin Approach to formalize the FEA for Reynolds Equation. Appropriate boundary conditions are set for the problem according to necessary assumptions and design. The pressure over bearing surface is set as an independent variable and the solution thus obtained is the pressure distribution over bearing surface. This is further used to calculate the weight carrying capacity of bearing. The results obtained from numerical simulation helped design the geometry of bearing for desired stiffness and weight carrying capacity. The future scope for refining the assumptions and eventually, the numerical simulation is also discussed in this paper.

Keywords: Hydrostatic bearings · Finite element method · Self compensating journal bearings

S. J. Patil, A. N. Khairnar, V. M. Phalle
Veermata Jijabai Technological Institute, Mumbai.
e-mail: sjpatil_b15@me.vjti.ac.in, ankhairnar_b15@me.vjti.ac.in, vmphalle@me.vjti.ac.in

P. K. Limaye
Bhabha Atomic Research Centre (BARC), Mumbai
e-mail: pklimaye@barc.gov.in

21.1 Introduction

This paper emphasizes the extension of one of the approaches taken in our work (Patil et al. 2018) in which we have briefly discussed solutions of Reynolds equation using FEM. For the particular case emphasized in the work, its boundary conditions have also been discussed depending upon steady or transient situations. Our idea is to use the grooves over the bearing surface to connect opposite lands on pockets that create self-compensating action, thus saving the space required for piping and leakage prevention on holes.

We mainly focused on designing a mathematical model which precisely replicates the fluid domain inside self-compensating hydro-static bearing and its effect. In this paper, we have worked on the finite element method applied to model the flow of fluid lubricant in the bearing we have designed. Previously, the results of using analytical methods to optimize the design have been published. This work aims at refining assumptions and using FEM for better modeling.

FEM is a powerful numerical technique having advantages in terms of computational efficiency over other numerical techniques. Though memory requirements are more for FEM than other numerical techniques such as FVM (due to more degrees of freedom per node). It is useful in fluid problems too because of the ease in the modelling of complex geometries, the consistent treatment of differential-type boundary conditions and the possibility to be programmed in a flexible and general-purpose format (Donea and Huerta, 2003). We will see how it can be formulated for a fluid flow between two circular surfaces (Modeled as Reynolds Equation) in a hydrostatic bearing application with actuating motion. The problem has been solved in 2 dimensions.

Prior to solving this problem in 2-dimensions, it has been formulated and coded in 1-dimension for convenience in computer implementation and understanding. The 2-D case presented in this paper has been implemented by doing appropriate changes in the code for 1-D implementation. The 1-D formulation is left out of the paper as the 2-D case is presented in detail. For computer implementation, MATLAB is used and the functions written are explained in detail in the paper.

The Finite Element Method has been used in literature by Nagaraju et al (2002); Sharma et al (2011, 2012) in very similar kinds of problems. Zuo et al (2013) have used the second approach by deriving Reynolds Equation for the flow between shaft and bearing, solving that PDE using Finite Element Method (FEM), and getting the pressures and other parameter values at each pocket. The finite element method and its application in fluid flow problems (especially in fluid lubrication) have been covered extensively by Thornton et al (1982) in Chapter 7 of 'Finite Element Methods for Engineers'.

For computer implementation, Finite Element Analysis in Thermofluids by Sert (2014), his online lecture notes have been referred. A readily available mesh generator written in MATLAB called 'mesh2d' has been used for mesh generation. It can freely be downloaded at <http://github.com/dengwirda/mesh2d> (Engwirda, 2014). It can be used to generate meshes of triangular elements over 2D domains. Even Thornton

et al (1982) has separate sections as guidance for computer implementation of the Finite Element Method in fluid lubrication problems.

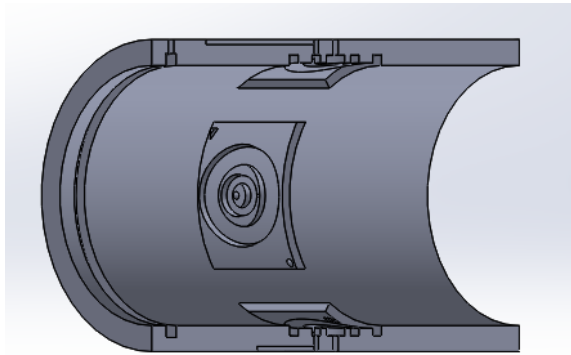


Fig. 21.1 Bearing cross-section and geometry over which flow is modelled.

21.2 Methodology

1. Begins with writing down the Reynolds equation for one's case and formulate FEM for the differential equation.
2. Discretize the problem according to geometry.
3. Apply proper boundary conditions.
4. Apply Galerkin criteria or Variational principle to get an integral functional that has to be minimized.
5. Minimize the functional or residual in local coordinate system.
6. Get local matrix equations using fluidity matrices for individual elements.
7. Write a global equation that can be solved by an iterative procedure.

21.3 Steps in Implementation of FEM

Following subsections cover steps listed in methodology.

21.3.1 Step 1 - Setting up the Governing Equation

Reynolds equation has a very generalized form for application to hydrodynamic and hydrostatic bearings (Rowe, 2012). Derived from Navier-Stokes equations, it is a PDE which governs the phenomena of fluid lubrication. It is given as-

$$\frac{\partial}{\partial x} \left[\frac{-h^3}{12\eta} \frac{\partial P}{\partial x} + \left(\frac{U_1 + U_2}{2} \right) h \right] + \frac{\partial}{\partial y} \left[\frac{-h^3}{12\eta} \frac{\partial P}{\partial y} + \left(\frac{V_1 + V_2}{2} \right) h \right] + \frac{\partial h}{\partial t} = 0 \tag{21.1}$$

where, h is the clearance between shaft and bearing. $U_1, U_2,$ and V_1, V_2 are fluid velocities in x and y direction at the shaft surface and at the bearing surface respectively.

Making suitable assumptions by keeping in mind our design, we can derive the specific PDE that governs fluid flow in this bearing. To reduce this general Reynolds equation to obtain governing equation, following are the assumptions:

1. Division of the fluid supplied is only in the axial direction
2. No fluid crosses pocket lands in the circumferential direction
3. Squeezing effect is negligible
4. Viscosity is constant
5. The shaft has zero rotational speed and is in a strictly actuating motion

Above assumptions let us neglect last time-dependent term in generalized Reynolds equation and also $U_1 = U_2 = 0$ and $V_1 = 0$ (no-slip boundary condition). We keep only the V_2 term because the bearing is to be used in actuator application where the shaft will have this one velocity in axial direction.

Considering these assumptions, the Reynolds equation for the design becomes-

$$\frac{\partial}{\partial x} \left[\frac{-h^3}{12\eta} \frac{\partial P}{\partial x} \right] + \frac{\partial}{\partial y} \left[\frac{-h^3}{12\eta} \frac{\partial P}{\partial y} + \left(\frac{V_2}{2} \right) h \right] = 0 \tag{21.2}$$

For implementing FEM, it has been assumed that the pressure inside the pocket remains constant. Also, for the analysis purpose, only two pockets have been assumed on the bearing. The domain is as given in fig. 21.2

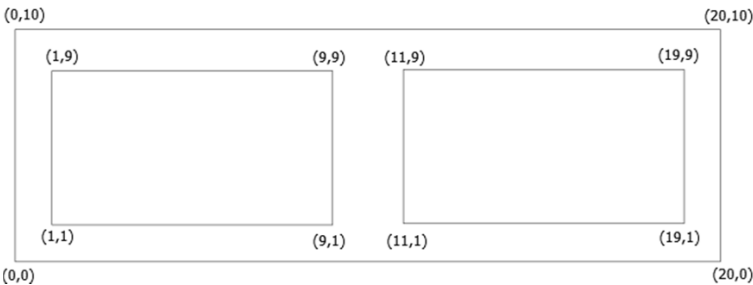


Fig. 21.2 Domain of the solution after neglecting inner lands in pockets

Also, the domain has been shown as spread out rectangle that is originally a cylindrical bearing. The co-ordinates show dimensions of the bearing used in the calculations.

21.3.2 Step 2 - Mathematical Formulation of FEM

The foremost requirement for the formulation of finite element method is a governing equation, which we has been derived in the previous section. For any general governing equation of the form-

$$\Phi(a) - f = 0 \quad (21.3)$$

where Φ is any operator (a differential or combination of several operators) acting on an independent variable a which one wishes to find (pressure or velocity in fluid problems) and f being any function, FEM formulation is about identifying the solution domain and discretizing it into smaller elements and obtaining values of 'a' at nodes of each element using numerical techniques and then approximating them using interpolation shape functions inside the element.

Comparing Eq. (21.2) and Eq. (21.3), the independent variable is P whereas the operator Φ and f are:

$$\Phi = \frac{\partial}{\partial x} \left[\frac{-h^3}{12\eta} \frac{\partial}{\partial x} \right] + \frac{\partial}{\partial y} \left[\frac{-h^3}{12\eta} \frac{\partial}{\partial y} \right] \quad (21.4)$$

$$f = -\frac{\partial}{\partial y} \left[\left(\frac{V_2}{2} \right) h \right] \quad (21.5)$$

For simplicity of notation, the formulation and integrals are shown on the representative Eq. (21.3) instead of lengthy original Eq. (21.2).

Starting with a single element fig. 21.2, the value of pressure inside the element is given in terms of values of pressure at nodes P_1 , P_2 , P_3 , and P_4 using shape functions as interpolators.

$$P(x, y) = \sum_{i=1}^4 N_i P_i = [N_i][P_i]' \quad (21.6)$$

here, N is a shape function whose choice depends on the judgement and nature of the problem one deals with. Now the solution $P(x, y)$ will be an approximate solution because we have just interpolated the node values to get the value inside the element. If we put that approximate value in governing equation, we get an error, which we call Residue (21.7).

$$\Phi(\hat{P}) - f = R \quad (21.7)$$

where \hat{P} is an approximate value of P .

Now the Galerkin's criteria will give

$$\int (\Phi(\hat{P}) - f) N_i dA = 0 \quad (21.8)$$

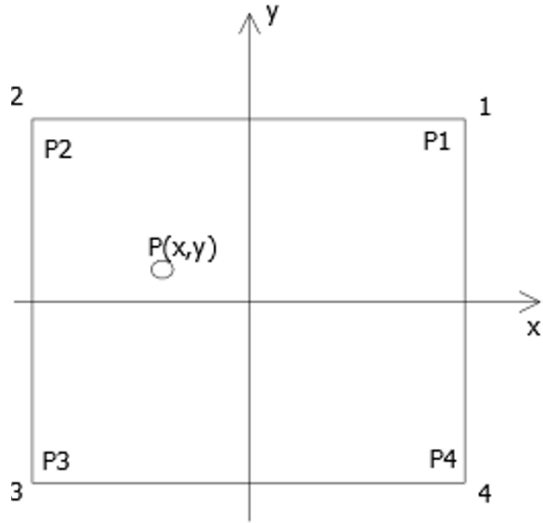


Fig. 21.3 Single 4-noded element in the local co-ordinate system.

We may write residual minimizing integrals at each node of an element considered separately– one by one. In this way we obtain 4 integral equations, they can be written as 4 linear algebraic equations in 4 node variables $P_1, P_2, P_3,$ and P_4 . To make the system of these equations solvable, boundary conditions of flow have to be incorporated at each node on the boundary. Then these equations can be represented in matrix form, a 4×4 matrix equation for the element in fig. 21.3.

$$[K_P]_{4 \times 4} [P]_{4 \times 1} + [K_v]_{4 \times 4} [V_2]_{4 \times 1} = [Q]_{4 \times 1} \tag{21.9}$$

where K_P and K_v are called fluidity matrices and 4×1 matrices P and V_2 are matrices with variable P and V_2 values at nodes 1, 2, 3 and 4. Matrix $[Q]$ is a flow matrix.

The elements of fluidity matrices and flow matrix are as follows

$$K_{P_{i,j}} = - \int \frac{h^3}{12\eta} \left(\frac{\partial N_i}{\partial x} \frac{\partial N_j}{\partial x} + \frac{\partial N_i}{\partial y} \frac{\partial N_j}{\partial y} \right) dA \tag{21.10}$$

$$K_{v_{i,j}} = \int \frac{h}{2} \left(\frac{\partial N_i}{\partial y} N_j \right) dA \tag{21.11}$$

$$Q_i = \int q N_i ds \tag{21.12}$$

Every single element in the domain will have such a 4×4 matrix equation in its local co-ordinate system. All such single elemental matrix equations can be assembled in a global co-ordinate system to obtain one Global Matrix equation for the entire domain under study.

The right way to club the elemental matrix equations in global co-ordinates can be found in any text on finite element method such as (Chandrupatla et al, 2002). The size of the global matrix equation depends on the number of nodes in the mesh imposed on the discretized solution domain. Hence finer the mesh, smaller will be the elements and more will be the number of equations. Global matrix equation of the following form (with n nodes in total)

$$[K_P]_{n \times n} [P]_{n \times 1} + [K_v]_{n \times n} [V_2]_{n \times 1} = [Q]_{n \times 1} \quad (21.13)$$

can be solved using direct methods like Gauss Elimination. Code for the same can be written for computer implementation. The solution obtained is pressure distribution over the solution domain at each node.

21.3.3 Step 3 - Meshing of the Solution Domain

The meshing is an important factor in FEM to get good quality solutions that converge. In the code for computer implementation, the domain shown in previous subsections fig. 21.2 has been used for meshing. There is a room for controlling the meshing density in the code.

For meshing, a MATLAB package called MESH2D has been used. It is readily available on the GitHub. The package has been used effectively in the main code. Different shapes of elements can be set using this package but we have proceeded with triangular elements for their effectiveness in capturing fluid behaviour better than other elements.

Following is a sample mesh generated using the code

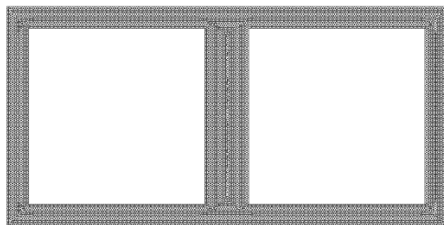


Fig. 21.4 Computer generated mesh on the solution domain.

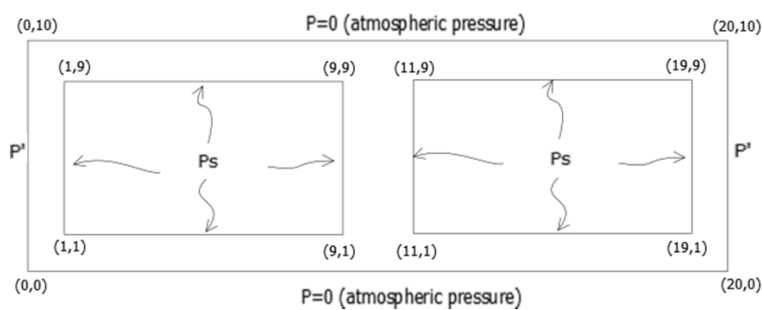


Fig. 21.5 Boundary conditions over the domain.

21.3.4 Step 4 - Boundary Conditions on the Solution Domain

Over the domain shown in the previous subsection, fig. 21.5 shows the boundary conditions at each boundary.

1. The inner pockets have uniform pressure equal to supply pressure P_s at all the boundaries.
2. The axial ends of the bearing are open to atmosphere, hence these two edges have $P = 0$.
3. The edges formed by splitting cylinder to form this rectangular domain will have the same pressure P' .

These boundary conditions are very important in computer implementation and while writing code. These will be specified explicitly at each edge and/or boundary.

21.3.5 Step 5 - Computer Implementation

The coding for computer implementation is done in MATLAB and it consists of two main sets of code. One is an input file generator code and second is the main code that implements FEM.

Following functions are coded and called as per their functionality in the order that algorithm 1 depicts.

21.4 Results

Using the above steps to implement FEM and using the computer code to execute it, results are obtained in terms of pressure distribution over the domain for which we have solved the Reynold's equation.

Algorithm 1: Computer implementation of FEM

```

FUNCTION Steady 2D
{Main function that calls all other functions}
function setupProblem
{User provides necessary input values here}
function generateMesh
{Generate 2D mesh}
function setup
{Generate variables for GQ - Gauss Quadrature points and weights}
function calcShape
{Evaluate shape functions and their derivatives at GQ points}
function calcGlobalSys
{Calculate global K and F (Fluidity Matrices)}
function calcElemSys
{Calculate elemental Ke and Fe (Fluidity Matrices)}
function assemble
{Assemble elemental systems into a global system}
function applyBC
{Apply BCs to the global system of equations}
function solve
{Solve the global system of equations}
function postProcess
{Plot the approximate solution}

```

We can control number of nodes in the code to control fineness and coarseness of mesh. Following are two results fig. 21.6 and fig. 21.7– one with coarse mesh and one with fine mesh–

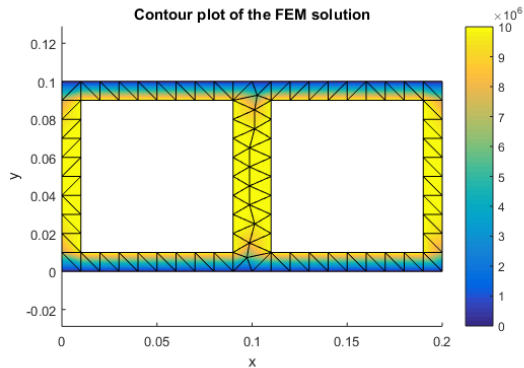


Fig. 21.6 Result with coarse mesh (185 Nodes)

But we need to see if the solution converges for the increasing fineness of mesh and hence if the solution is valid or not. Fig. 21.8 shows how the average pressure

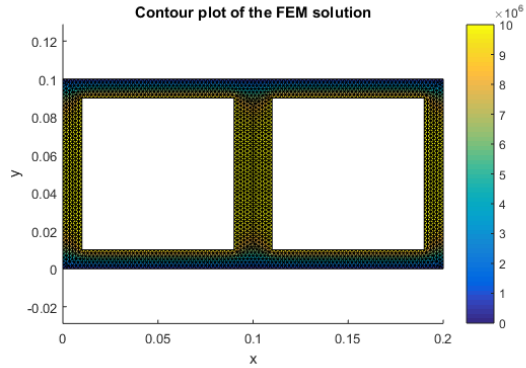


Fig. 21.7 Result with coarse mesh (2465 Nodes)

value converges to a single value with increasing mesh fineness, thus indicating convergence.

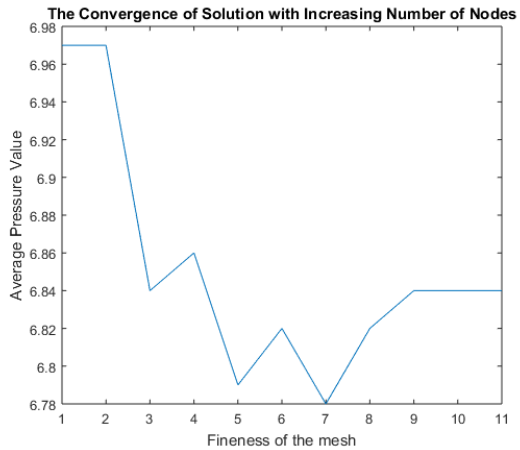


Fig. 21.8 Average pressure value converging with fineness of mesh

The misalignment of the bearing shaft due to loading and its effect on clearance and the varying gap is taken into account too. With the general code to implement FEM on the Reynolds Equation for hydrostatic bearing, only a model of clearance variation is needed to carry out the entire calculations. Hence we consider different functions ' $h(x, y)$ ' in the equation.

Some of the common misalignments and the clearance distributions they cause have been modelled as follows

1. Radial misalignment of the shaft by eccentricity ' e '

$$h = h_0 - e \cos\left(\frac{x}{r}\right) \quad (21.14)$$

2. Shaft inclination due to loading (function of y only)

$$h = 2h_0 \left(1 - \frac{y}{L}\right) \quad (21.15)$$

3. Combined Misalignment, $h(x, y)$

$$h(x, y) = h_0 - 2h_0 \left(1 - \frac{y}{L}\right) \cos\left(\frac{x}{r}\right) \quad (21.16)$$

where r and L are bearing inner radius and length respectively. These functions of h can be directly given as input to the FEM code. The computer code is general enough to handle these (fig. 21.9).

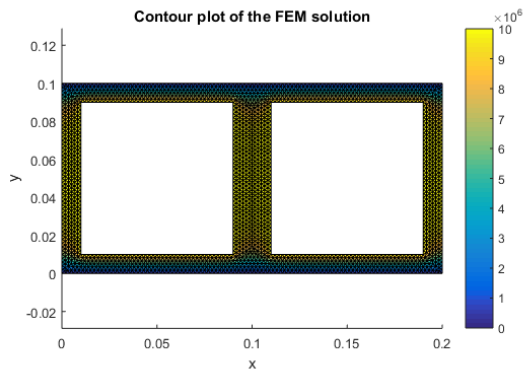


Fig. 21.9 Solution for pressure distribution in combined type misaligned of the bearing shaft.

21.5 Conclusion

Finite element method has been successfully applied to this fluid flow problem. The bearing performance can be easily predicted with this model and FEM solution by directly evaluating load carrying capacity using pressure distribution we get over the area. Effect of various misalignments can also be modelled into the problem as illustrated in the previous section.

Still there is following future scope for this work:

- The full might of this program has not yet been utilized, as more generalized functions (even non-linear) can be incorporated in modeling.
- Assumptions like neglecting the inner lands have been made, which when incorporated in FEM, can better model the self-compensation action.

- Authors aim at modeling the fluid flow in the time-dependent domain and also at incorporating the turbulence and other effects.

References

- Chandrupatla TR, Belegundu AD, Ramesh T, Ray C (2002) Introduction to finite elements in engineering, vol 10. Prentice Hall Upper Saddle River, NJ
- Donea J, Huerta A (2003) Finite element methods for flow problems. John Wiley & Sons
- Engwirida D (2014) Locally optimal delaunay-refinement and optimisation-based mesh generation. PhD thesis, University of Sydney
- Nagaraju T, Sharma SC, Jain S (2002) Influence of surface roughness effects on the performance of non-recessed hybrid journal bearings. *Tribology international* 35(7):467–487
- Patil S, Khairnar A, Phalle VM, Limaye P (2018) Design of self-compensating hydrostatic bearing for actuators. Available at SSRN 3347114
- Sert C (2014) Finite element analysis in thermofluids
- Sharma SC, Phalle VM, Jain S (2011) Performance analysis of a multirecess capillary compensated conical hydrostatic journal bearing. *Tribology International* 44(5):617–626
- Sharma SC, Phalle VM, Jain S (2012) Performance of a noncircular 2-lobe multirecess hydrostatic journal bearing with wear. *Industrial lubrication and Tribology* 64(3):171–181
- Thornton EA, Byron T, Heubner K (1982) The finite element method for engineers. Wiley USA
- Zuo X, Li S, Yin Z, Wang J (2013) Design and parameter study of a self-compensating hydrostatic rotary bearing. *International Journal of Rotating Machinery* 2013:1–10

Part IV
Experimental and Numerical Techniques



Chapter 22

An Experimental-Numerical Procedure for the Determination of “True” Stress-Strain Tensile Curve in Ductile Materials

Anatoliy M. Bragov, Aleksander Y. Konstantinov, and Andrey K. Lomunov

Abstract The present work describes experimental-numerical procedure, which allows constructing the full true stress-strain curve considering plastic strain localization or stress inhomogeneity due to the specimen shape feature. The input data are the force $F(t)$ acting on the specimen and the rate of change of specimen gauge length $V(t)$ over time. The true deformation diagram is constructed using iterative process, which is sequential correction of material’s stress-strain curve to get matching between experimental and obtained from numerical simulation integral forces. Some examples based on data obtained using Split Hopkinson Tension Bar are given.

Keywords: True stress · Deformation curve · Necking · Strain localization · Inverse analysis

22.1 Introduction

Tension experiments (including high strain rate tests) hold a special place in the system of basic experiments, used for identification of material behavior. This kind of tests allows determining deformation diagrams as well as ultimate fracture characteristics, which are necessary for prediction of strength of the structures. However, tensile tests have a number of features, which have to be taken into account while planning an experiment and interpreting its results. A specially shaped specimen is usually used. Specimens should have a gauge area and areas for their fixing in an experimental setup. Areas for fixing might affect stress and strain fields in gauge area (Fig. 22.1). These effects can be minimized by increasing the length of gauge area. This method is employed for static experiments. In case of dynamic loading there are

A. M. Bragov, A. Yu. Konstantinov, and A. K. Lomunov
Research Institute for Mechanics, National Research Lobachevsky State University of Nizhni Novgorod, av. Gagarin 23b6, Nizhny Novgorod, 603950, Russia
e-mail: bragov@mech.unn.ru, konstantinov.al@yandex.ru, lomunov@mech.unn.ru

some length limitations for gauge area due to the wave effects. Therefore, influence of fixing areas can be significant. Moreover, strain localization and necking process cause difficulties in obtaining true strength and strain characteristics of material. In this case, plastic deformation becomes inhomogeneous in the working part of the specimen. The stress state in the neck becomes volumetric, due to a change in the geometry of the sample (Shen and Jones, 1993). There are two main approaches to determining the true stress-strain curve in this case. The first is based on analytical (Malinin and Rzyso, 1981; Bridgman, 1955; Davidenkov and Spiridonova, 1946) or semi-empirical (Mirone, 2004; Gromada et al, 2011) models for estimating the components of the stress tensor in the neck. To do that, information on the geometry of the specimen in the localization zone (the radius of the minimum cross-section in the neck and the radius of curvature of the neck) is also used in addition to the integral force measured in the experiment. In recent years, many research efforts have been carried out to develop a more accurate and reliable method to extract the true stress-strain curve beyond necking by utilizing finite element method (FEM). Cabezas and Celentano (2004) produced an experimental and numerical analysis of the tensile test using sheet specimens and received correction factors for sheet specimens. Zhano and Li (1994) and Joun et al (2008) proposed an iterative approach to obtain the true stress-strain curve of a cylindrical sample up to fracture based on experimental F-dL curve and FEM simulations. Recently, a new experimental measurement tool of the high-resolution digital camera was employed by some researchers (Scheider et al, 2004; Dan et al, 2007) to overcome the difficulties in tracing the change in the geometry of the specimen. However, the problem in using this tool in dynamic testing is that the spatial resolution of the camera decreases sharply with increasing frequency of shooting. Therefore, it is difficult to obtain the necessary resolution both in space and in time at the same time. This paper describes an iterative procedure for constructing a true deformation curve based on the integral force history and the elongation law, which quickly converges and is easily integrated into the finite element program.

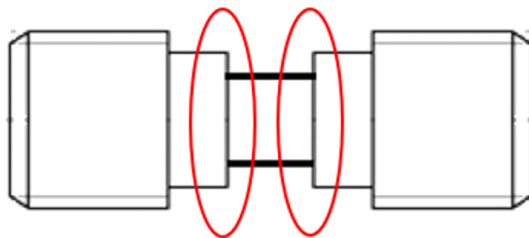


Fig. 22.1 Influence of fixing parts of specimen

22.2 Split Hopkinson Bar Technique

One of the most widely used loading techniques at high strain rates is the split Hopkinson pressure bar (SHPB) or the Kolsky method developed by Kolsky (1949). There are some review works (Field et al, 1994; Kolsky, 1949; Bacon and Lataillade, 2001; Gama et al, 2004) that describe a historical background of SHPB method. Classical compressive SHPB method has good theoretical justification and it is fairly well explored. But some practically important characteristics of materials cannot be determined from this type of experiment, namely ultimate strength and ultimate plastic strain. Moreover deformation diagram may be stress state dependent, that is the stress-strain curve obtained in tensile experiments may differ from compression one. Therefore, determination of deformation diagram in tension is an important independent problem. Some schemes of high rate tensile testing which use measuring bars technique can be found in works (Hauser, 1966; Eskandari and Nemes, 2000; Lindholm and Yeakley, 1968; Nicholas, 1981; Caverzan et al, 2012; Jiang and Zhang, 2006; Bragov et al, 2018). The main difference of these schemes is the way they generate tension pulse. The schemes with tube strikers used for impact tensile loading are very popular of late. This class of setups is known as the Split Hopkinson Tension Bar (SHTB) technique. In Harding (1992) such experimental device was used to investigate dynamic properties of composite materials. Similar loading schemes were employed in Arthington et al (2012); Chen et al (2002); Gerlach et al (2012); Hasenpouth (2010); Huh et al (2002); Noble and Harding (1994); Smerd et al (2005); Taniguchi et al (2007); Yokoyama (2003); Young (2015); Bragov et al (2018). In the present work, the Split Hopkinson Tension Bar method (Bragov et al, 2018) was used to register the processes in the samples during high-strain rate tension experiments.

22.3 True Stresses and Strains in the Tension Experiments

The determination of true stresses and true strains in static and dynamic tension experiments is complicated by localization of deformation (necking process) that violates uniformity and homogeneity of stress-strain state. Calculation of stresses and strains in a specimen on the basis of measured in the experiment integral force and elongation become challenging under these conditions. In addition, strain localization affects strain rate history, which increases dramatically in the neck zone. These interpretation features are considered in works (Mirone, 2013; Mirone et al, 2016). The appropriate correction of deformation diagram is required after the necking point (Bridgman, 1955). To evaluate effective true stresses a number of methods have been proposed by Alves and Jones (1999); Dietrich et al (1970); Gromada et al (2011); La Rosa et al (2003); Ling (1996); Malinin and Rzyzsko (1981); Mirone (2004); Zhang et al (1999); Bridgman (1955); Davidenkov and Spiridonova (1946). The strain threshold of the initiation of localization can be determined by the following conditions:

$$\frac{d\sigma_0}{d\varepsilon} = 0 \quad \text{or} \quad \frac{d\sigma}{d\varepsilon} = \frac{\sigma}{1 + \varepsilon} \quad \text{or} \quad \frac{d\sigma}{de} = \sigma \quad (22.1)$$

here σ and σ_0 are true and engineering stresses respectively, e and ε are true (logarithmic) and engineering strains, respectively.

The main complexity of Bridgmen's method (and similar approaches) is caused by the necessity of precise determination of minimum radius of the neck section and neck curvature. Another technique of deformation diagram correction, based on universal (material independent) polynomial was proposed by Mirone (2004). The coefficients of the polynomial are derived by generalization of a large amount of experimental data. Mirone (2004) has showed that the proposed procedure is material independent and allows the proper determination of effective stress with account for strain localization. The effective true stress after necking prediction by Mirone's procedure exhibits an error of about 5 % for quasistatic elasto-plasticity (Mirone, 2013). The high rate video registration was used in Gilat et al (2009); Kajberg and Wikman (2007); Li and Ramesh (2007) to obtain the specimen minimum radius history. In Bazhenov et al (2013); Ling (1996); Sasso et al (2008) numerical simulation was used to reconstruct the true deformation diagram based on tensile experimental data. The integral forces acting on the specimen and the specimen gauge elongation are determined during the test. In the traditional method an assumption of stress and strain fields uniformity is introduced to calculate stresses and strains based on forces and size changes. Therefore, it is only applicable till the moment of plastic strain localization (necking). This leads to losing a large part of stress-strain curve after the necking process. Time histories of neck radius and neck curvature during the whole tension process are to be used in the above analytical models, this being a challenging task for high rate experiments. The common approach for true stress-strain curve construction is an extension of the curve before necking using a fracture point. The plastic strain on fracture and effective true stress on fracture are determined using the minimum radius of the specimen in neck (a) and the radius of curvature of the neck profile (R), measured after testing the specimen. The main problem is the accurate determination of integral force acting on the specimen at the moment of its rupture. The shape of transmitted pulse, by which the force is measured, can be changed due to dispersion effect when using the Kolsky method (Bragov et al, 2019).

The sharp decrease in force occurs when specimen is fractured. Then propagating along measuring bar such a signal is blurred due to dispersion effect as shown in Fig. 22.2. In Fig. 22.2 the blue line corresponds to the initial signal (force in the specimen) and the orange one to the dispersed signal after the propagation in the measuring bar (force in the strain gauges position). The accurate determination of fracture force becomes essential. Moreover, it is necessary to know conditions (strain rate, stress state, temperature) under which the material characteristics are determined. The strain rate may increase significantly when deformation is localized. It is impossible to estimate the strain rate at fracture without the history of neck geometry.

The other method allowing true stress-strain curve construction including strain localization is the reverse identification method. It is based on numerical modeling

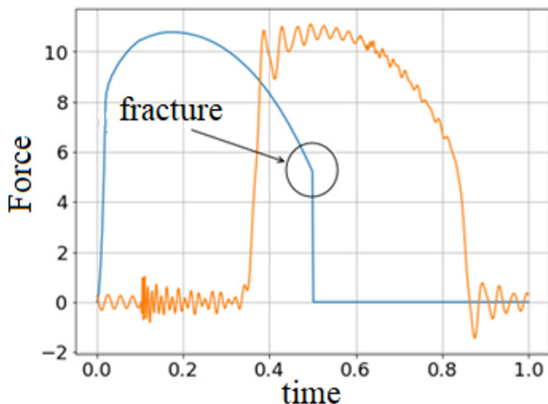


Fig. 22.2 Force blurring illustration

of tension process. The main advantages of this approach are: there is no need for registration of specimen geometry during experiment and the method takes into account all features of the process and specimen (non-uniformities of stress and strain fields, complexity of geometry, inertia effects and so on).

22.4 Experimental and Numerical Procedure of Construction a True Strain Curve According to Experiment on High-Speed Tension

In this paper, the restoration algorithm of a true material strain curve is realized on the basis of experimental results on dynamic tension of specimens. The algorithm is similar to the procedure described in (Bazhenov et al, 2013). An experimentally measured integral force acting on the specimen during tension $F_{exp}(t)$ as well as time dependence of a specimen’s gauge elongation $V(t)$ are used as input data. When using the Kolsky method for the high-speed tension these data can be calculated by formulas:

$$V(t) = c_I \cdot (\varepsilon^I(t) - \varepsilon^R(t)) - c_T \cdot \varepsilon^T(t) \tag{22.2}$$

$$F_{exp}(t) = E_T \cdot S_T \cdot \varepsilon^T(t) \tag{22.3}$$

where c_I, c_T are bar sound speeds of the incident (subscript I) and the transmission (subscript T) bars, E_T and S_T are Young modulus and cross section area of output bar, $\varepsilon^I, \varepsilon^R$ and ε^T are incident, reflected and transmitted pulses registered in measuring bars.

The following iterative procedure for determination of the true diagram is to be used:

1. The initial approximation of the material deformation diagram is selected (for example, it can be a diagram obtained by extrapolation of a logarithmic curve, or an ideal-plastic model) as a table.
2. Process of dynamic tension of a specimen is simulated according to the scheme provided in Fig. 22.3, where boundary conditions at the top are $V_y(t) = V(t)$, $V_x(t) = 0$. Axial speed of the upper boundary $V(t)$ is calculated by formula 22.2.
3. The integrated reaction force $F_{calc}(t)$ on the fixed side is to be obtained.
4. Values $(\varepsilon_p^i, \sigma_m^i)$ are determined for a discrete set of times t_i in a finite element in which the maximum effective plastic strain is realized (a finite element on a specimen's axis in a minimum section). Here ε_p^i is an effective plastic strain in the specified finite element, σ_m^i is von Mises stress in the specified finite element.
5. Tabular curve $(\varepsilon_p^i, \sigma_m^i \cdot \frac{F_{exp}(t_i)}{F_{calc}(t_i)})$ is accepted as an approximation of a true strain curve.
6. Steps 2-5 are repeated until the acceptable compliance of experimental and simulated forces is obtained or diagram at the next step stops changing significantly.

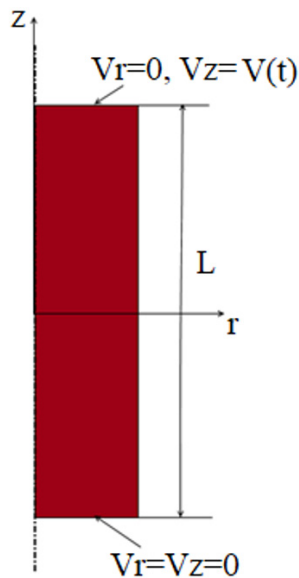


Fig. 22.3 Numerical simulation problem statement

This iterative procedure is illustrated in Fig. 22.4. The experimental force and forces obtained on various iterations are shown on the left of the figure, while on the right, the history of diagram changing during consecutive adjustments is presented.

It should be noted that the specified algorithm converges quickly enough, even with a not very successful choice of the initial approximation of the deformation curve (the model with a constant flow stress was used in the example).

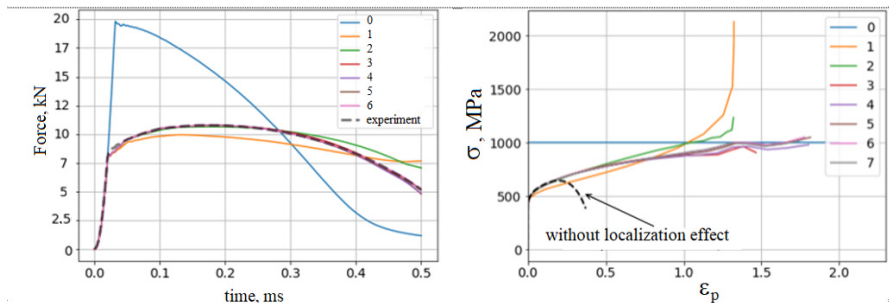


Fig. 22.4 Convergence of iterative procedure of definition of a true strain curve with the use of numerical modeling. On the left – comparison of forces, on the right – material diagrams for various iterations (number of iteration is shown in a legend)

Firstly, the procedure was tested on virtual experiments for materials with different strain hardening laws and gauge part geometries. Fig. 22.5 compares true curves (used in virtual experiments models-black dashed lines) with the curves constructed using the implemented procedure (markers). Figures 22.1 and 22.3 correspond to “hard” material with linear strain hardening. Figures 22.2 and 22.4 correspond to “soft” material with non-linear strain hardening. The gauge length of specimens in figures 22.1 and 22.2 was 10 mm, in figures 22.2 and 22.4 5 mm. The diameters of all specimens was 5 mm. The curves exhibit quite good agreement in a wide range of strains.

Secondly, the procedure was used to construct the true stress-strain curves for real materials. The data from SHTB experiments was used. Experiments with the following features were selected (Fig. 22.6):

1. High rate tension tests of short (gauge length 5 mm, diameter 6 mm) specimen made of copper M1 were performed. Non-uniformity of stresses and strains in working part occurs due to closure of fixing parts.
2. High rate tension of iron alloy. The deformation of working part is mainly uniform until fracture occurs.
3. High rate tension of aluminum alloy 1575 was carried out. Pronounced strain localization occurs.

The diagrams obtained for specimens described above (orange markers) are shown in Figs. 22.7-22.9. They are compared with curves constructed using the traditional procedure which does not account for strain localization (solid blue lines). Dashed lines in both cases (blue - traditional experiment processing, orange - experimental-numerical procedure) correspond to strain rate histories (left vertical axis). For short copper specimen (Fig. 22.7), the curves strongly differ even at small strains. The

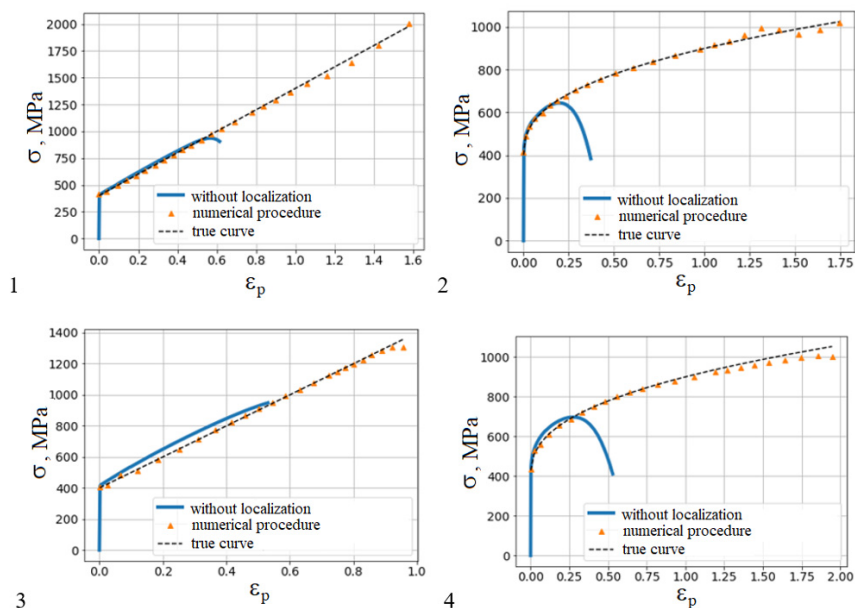


Fig. 22.5 Testing procedure on virtual experiments



Fig. 22.6 Tested specimens: from left to right – copper M1, EP-718 alloy, aluminum alloy 1575

local strain rate exceeds twice the averaged strain rate estimated without localization influence.

For iron alloy (Fig. 22.8), the stress-strain curves constructed with different methods coincide quite well. Taking localization into account allows to slightly extend the diagram to strains of about 35%. For aluminum alloy 1575 (Fig. 22.9) the curve constructed considering necking covers twice wider interval of strains.

Figure 22.10 demonstrates the shapes of specimens in real experiments and virtual tests. They are very similar.

22.5 Conclusions

The review of the current state of high rate tension experiment shows that the most popular technique for testing materials at strain rates, ranging from 10^2 to 10^4 s^{-1} is the Kolsky method or the Split Hopkinson Pressure Bar method and its numerous

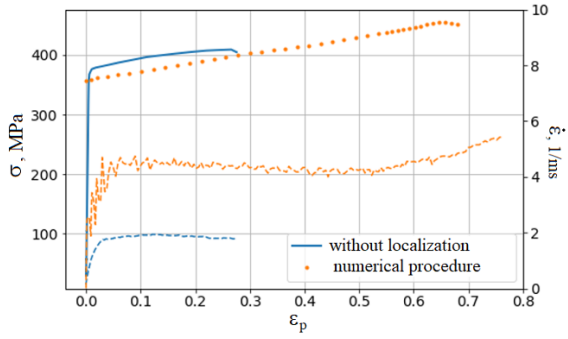


Fig. 22.7 High rate tension diagram of copper M1

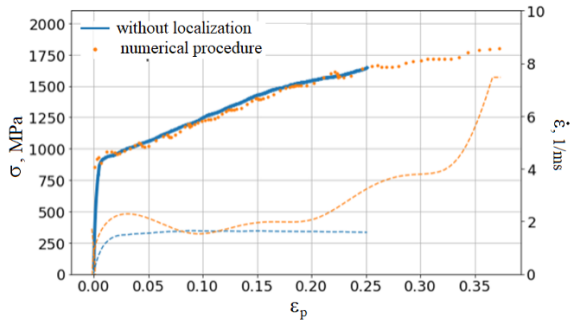


Fig. 22.8 High rate tension diagram of iron alloy

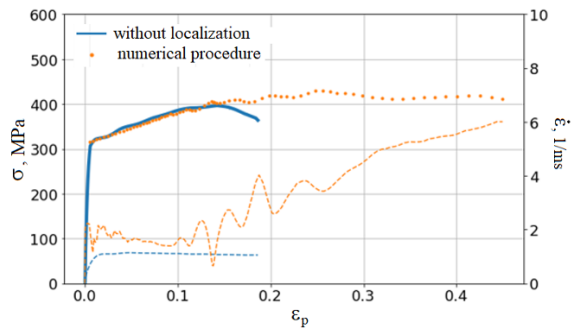


Fig. 22.9 High rate tension diagram of aluminum alloy 1575

modifications. However, there are a number of features intrinsic to high rate tension of visco-plastic specimens including stress and strain fields non-uniformity due to the closure of fixing parts of sample and strain localization (necking). Numerical analysis of high rate tension process proves that the true stress-strain curve can be accurately constructed on the basis of the history of neck geometry during tension. If the neck geometry data is unavailable, one can apply numerical simulation and reverse analysis technique to obtain true dynamic diagram. Such procedure has been implemented and tested in the present work.

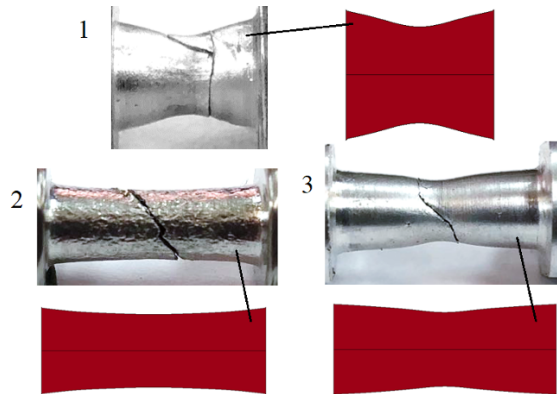


Fig. 22.10 Specimen shapes in real and virtual experiments: 1 - M1, 2 - Ep718, 3 - 1575

Acknowledgements The experimental study was supported by the grant of the Government of the Russian Federation (contract No.14.Y26.31.0031). The theoretical investigations were supported by the Grant of the President of the Russian Federation for young scientists (MD-1221.2019.8)

References

- Alves M, Jones N (1999) Influence of hydrostatic stress on failure of axisymmetric notched specimens. *Journal of the Mechanics and Physics of Solids* 47:643–667
- Arthington MR, Siviour CR, Petrinic N (2012) Improved materials characterisation through the application of geometry reconstruction to quasi-static and high-strain-rate tension tests. *Int J Imp Eng* 46(0):86–96
- Bacon C, Lataillade JL (2001) Development of the Kolsky-Hopkinson techniques and applications for non-conventional testing. *New Experimental Methods in Material Dynamics and Impact, Trends in Me-chanics of Materials*, eds WKNowacki, JRKlepaczko, Warsaw pp 1–58
- Bazhenov VG, Lomunov VK, Osetrov SL, Pavlenkova EV (2013) Experimental and computational method of studying large elastoplastic deformations of cylindrical shells in tension to rupture and constructing strain diagrams for an inhomogeneous stress-strain state. *Journal of Applied Mechanics and Technical Physics* 54(1):100–107
- Bragov A, Konstantinov A, Kruszka L, Lomunov A, Filippov A (2018) Dynamic properties of stainless steel under direct tension loading using a simple gas gun. *EPJ Web of Conferences*, V 183, N2035, DOI: 101051/epjconf/201818302035
- Bragov AM, Lomunov AK, Lamzin DA, Yu KA (2019) Dispersion correction in split-Hopkinson pressure bar: theoretical and experimental analysis. *Continuum Mech Thermodyn* pp 13, <https://doi.org/10.1007/s00161-019-00776-0>
- Bridgman PW (1955) *Studies in large plastic flow and fracture* [russian translation]. Izd Inostr Lit, Moscow
- Cabezas EE, Celentano DJ (2004) Experimental and numerical analysis of the tensile test using sheet specimens. *Finite Elements in Analysis and Design* 40(5-6):555–575
- Caverzan A, Cadoni E, di Prisco M (2012) Tensile behaviour of high performance fibre-reinforced cementitious composites at high strain rates. *International Journal of Impact Engineering* 45(0):28–38
- Chen W, Lu F, Cheng M (2002) Tension and compression tests of two polymers under quasistatic and dynamic loading. *Polymer Testing* 21(2):113–21

- Dan WJ, Zhang WG, Li SH, Lin ZQ (2007) An experimental investigation of large-strain tensile behavior of a metal sheet. *Materials and Design* 28(7):2190–2196
- Davidenkov NN, Spiridonova NI (1946) Analysis of the state of stress in the neck of a tensile test specimen. *Proc ASTM* 46:1147–1158
- Dietrich L, Miastkowski J, Szczepinski W (1970) Limiting capacity of the construction elements. PWN, Warsaw, (in Polish)
- Eslandari H, Nemes JA (2000) Dynamic testing of composite laminates with a tensile split Hopkinson bar. *Journal of Composite Materials* 34(4):260–273
- Field JE, Walley SM, Bourne NK, Huntley JM (1994) Experimental methods at high strain rate. *Journal de Physique IV, Colloque C3* pp 3–22
- Gama BA, Lopatnikov SL, Gillespie JWJ (2004) Hopkinson bar experimental technique: A critical review. *Appl Mech Rev* 57(4):223–250
- Gerlach R, Kettenbeil C, Petrinic N (2012) A new split hopkinson tensile bar design. *International Journal of Impact Engineering* 50:63–67
- Gilat A, Schmid TE, Walker AL (2009) Full field strain measurement in compression and tensile split Hopkinson bar experiments. *Experimental Mechanics* 49:291–302
- Gromada M, Mishuris G, Ochsner A (2011) Correction formulae for the stress distribution in round tensile specimens at neck presence. *SpringerBriefs in Applied Sciences and Technology Computational Mechanics* pp 1–89
- Harding J (1992) Mechanical behaviour of composite materials under impact loading. in: MA Meyers et al (Eds), *Shock-Wave and High Strain Rate Phenomena in Materials*, Dekker, New York pp 1–21
- Hasenpouth D (2010) Tensile high strain rate behavior of AZ31B magnesium alloy sheet. Master's Thesis: University of Waterloo
- Hauser FE (1966) Techniques for measuring stress-strain relations at high strain rates. *Experimental Mechanics* 6(8):395–402
- Huh H, Kang WJ, Han SS (2002) A tension split hopkinson bar for investigating the dynamic behavior of sheet metals. *Experimental Mechanics* 42(1):8–17
- Jiang B, Zhang R (2006) Tensile properties in the through-thickness direction for a carbon fiber woven reinforced composite at impact loading rate. *J Phys IV France* 134:1071–1075
- Joun M, Eom JG, Lee MC (2008) A new method for acquiring true stress-strain curves over a large range of strains using a tensile test and finite element method. *Mechanics of Materials* 40(7):586–593
- Kajberg J, Wikman B (2007) Viscoplastic parameter estimation by high strain-rate experiments and inverse modelling - speckle measurements and high-speed photography. *International Journal of Solids and Structures* 44:145–164
- Kolsky H (1949) An investigation of the mechanical properties of materials at very high rates of loading. *Proc Phys Soc London, Sect B* 62:676–700
- La Rosa G, Mirone G, Risitano A (2003) Post-necking elastoplastic characterization: degree of approximation in the bridgman method and properties of the flow-stress/true-stress ratio. *Metallurgical and Materials Transactions A* 34A (3):615–624
- Li Y, Ramesh KT (2007) An optical technique for measurement of material properties in the tension Kolsky bar. *International Journal of Impact Engineering* 34:784–798
- Lindholm US, Yeakley LM (1968) High strain-rate testing: Tension and compression. *Experimental Mechanics* 8(1):1–9
- Ling Y (1996) Uniaxial true stress-strain after necking. *AMP Journal of Technology* 5:37–48
- Malinin NN, Rzyzko J (1981) *Mechanics of materials*. PWN, Warsaw (in Polish)
- Mirone G (2004) A new model for the elastoplastic characterization and the stress-strain determination on the necking section of a tensile specimen. *International Journal of Solids and Structures* 41:3545–3564
- Mirone G (2013) The dynamic effect of necking in Hopkinson bar tension tests. *Mechanics of Materials* 58:84–96
- Mirone G, Corallo D, Barbagallo RI (2016) Interaction of strain rate and necking on the stress-strain response of uniaxial tension tests by Hopkinson bar. *Procedia Structural Integrity* 2:974–985

- Nicholas T (1981) Tensile testing of materials at high rates of strain. *Experimental Materials* 21(5):177–185
- Noble J, Harding J (1994) Temperature-measurement in the tensile Hopkinson bar test. *Measurement Science and Technology* 5(9):1163–1171
- Sasso M, Newaz G, Amodio D (2008) Material characterization at high strain rate by Hopkinson bar tests and finite element optimization. *Materials Science and Engineering A* 487:289–300
- Scheider I, Brocks W, Cornec A (2004) Procedure for the determination of true stress-strain curves from tensile tests with rectangular cross-section specimens. *Journal of Engineering Materials and Technology* 126(1):70–76
- Shen Q, Jones N (1993) Uniaxial true stress-strain curve for a ductile metal. *Nuclear Engineering and Design* 140(2):153–158
- Smerd R, Winkler S, Salisbury C, Worswick M, Lloyd D, Finn M (2005) High strain rate tensile testing of automotive aluminum alloy sheet. *International Journal of Impact Engineering* 32(1-4):541–60
- Taniguchi N, Nishiwaki T, Kawada H (2007) Tensile strength of unidirectional CFRP laminate under high strain rate. *Advanced Composite Materials* 16(2):167–180
- Yokoyama T (2003) Impact tensile stress-strain characteristics of wrought magnesium alloys. *Strain*, 39(4):167–175
- Young K (2015) Development of a tensile split Hopkinson pressure bar testing facility. PhD, University of Windsor, Ontario, Canada
- Zhang ZL, Hauge M, Odegard J, Thaulow C (1999) Determining material true stress-strain curve from tensile specimens with rectangular cross section. *International Journal of Solids and Structures* 36:2386–2405
- Zhao KS, Li ZH (1994) Numerical analysis of the stress-strain curve and fracture initiation for ductile material. *Engineering Fracture Mechanics* 49(2):235–241



Chapter 23

Experimental Study of the Dynamic Properties of Concrete under Compressive Load

Anatoliy M. Bragov, Mikhail E. Gonov, Andrey K. Lomunov,
and Vladimir Vl. Balandin

Abstract The report presents a study of the deformation and fracture of concrete under dynamic loads using the Kolsky method. Presented on the main technological method of manufacturing concrete samples for dynamic testing. The purpose of the test is to study the high-speed deformation and destruction of fine concrete. This article presents the results of tests of concrete for compression at deformation rates ranging from $4 \cdot 10^2 \text{ s}^{-1}$ to $2 \cdot 10^3 \text{ s}^{-1}$.

The conducted dynamic test of fine concrete for compression consisted of 35 test shots. Concrete was tested at 7 different speeds. Each test mode consisted of 5 test shots. 3 modes were carried out using copper pulse shapers.

Copper pulse shapers were used for research purposes. It is assumed that the pulse shaper improves the quality of the basic premise of the Kolsky method on the homogeneity of the intensely deformed state in a sample. The results of dynamic tests with pulse formers were compared with the results of tests without pulse formers.

The verification of the uniformity of the stress-strain state in the sample is performed using the formula $\varepsilon_I + \varepsilon_R = \varepsilon_T$, where ε_I - is the incident pulse, ε_R - is the reflected pulse, ε_T - is the transmitted pulse.

Keywords: Concrete · Dynamic test · Kolsky method · Compression · Dynamic strength

A. Bragov, M. Gonov, A. Lomunov, V. Vl. Balandin
Research Institute for Mechanics, National Research Lobachevsky State University of Nizhni Novgorod, av. Gagarin 23b6, Nizhny Novgorod, 603950, Russia
e-mail: bragov@mech.unn.ru, gonov_mikhail@mech.unn.ru, lomunov@mech.unn.ru, rustydog2007@yandex.ru

23.1 Introduction

Currently, the study of the properties of brittle materials such as concrete and its varieties is relevant. This is due to the fact that concrete is a heterogeneous material. This article presents a study of the deformation and fracture of concrete under compressive dynamic loads using the Kola method. Periodic dynamic tests of concrete complement and expand the overall picture of the deformation and fracture of concrete at high speed loads.

The relevance of the study of the dynamic properties of brittle materials is associated with impact and explosive effects. Impacts include natural disasters such as earthquakes, hurricanes, landslides, meteorite falls. This is largely due to climate change on our planet. Also shock and explosive impacts include civil and industrial disasters, man-made disasters. Today, there is also the threat of terrorist acts, the blasting of various explosive devices.

The studies were carried out using the Kolsky method using a Split-Hopkinson pressure bar and its modifications (Bragov A.M., 2015, 2017, 2018; Bragov and Lomunov, 1995; Lindholm, 1964; Davies and Hunter, 1963; Placidi et al, 2018; Placidi and Barchiesi, 2018; Scerrato et al, 2016; Giorgio and Scerrato, 2017; Scerrato et al, 2014).

In order to obtain dynamic characteristics and deformation diagrams during compression, fine-grained concrete of class B22.5 with a filler fraction of 1 – 5 mm was tested. Directly tested samples of circular cross section, with a diameter of 20 mm and a thickness of half less than 10 mm. Fine-grained concrete was tested to avoid large-scale effects due to the small diameter of the measuring rods equal to 20 mm.

23.2 The Method of Manufacturing Concrete Samples

At the beginning of the experiment, the test sample is installed between two precisely located and coaxial measuring rods (Figure 23.1). In this regard, a number of high requirements are imposed on the samples, such as: homogeneity of the material, accuracy and uniformity of the diameter and length of the sample; the parallelism of two faces of the sample and their smoothness (the presence of a plane), verticality, that is, the absence of eccentricity that causes bending.

Thus, the sample should be a geometrically accurate cylinder with a diameter to length ratio of 1 to 2. The optimal length of the sample should be half its diameter to reduce the effect of inertia and friction. In a compression test, the diameter of the sample shall not exceed the diameter of the measuring rods (Figure 23.2).

For self-production of samples, a technique was developed in our laboratory, which consists in drilling samples from pre-cut concrete plates of the required thickness. Rectangular or cubic samples of fine-grained concrete, in our case of class B22.5, are fixed with clamps on a stone-cutting machine Cedima *CTS – 57 G* and cut into plates of the required thickness (Figure 23.3). Next, the plates are

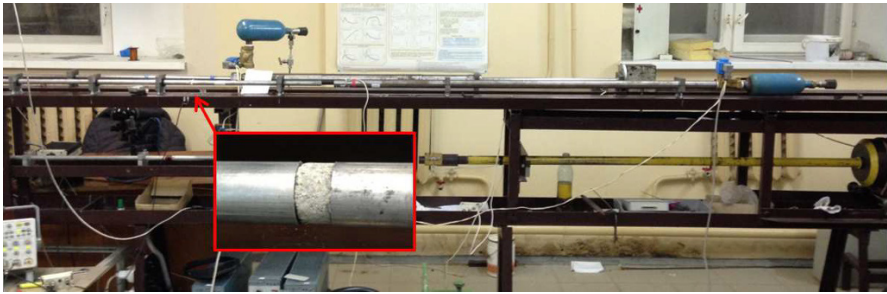


Fig. 23.1 Photo of experimental installation by the Kolsky method.



Fig. 23.2 Requirements for geometric parameters of samples

mounted on a *NS – 12M* drilling machine and a concrete sample is drilled using a diamond crown at low speeds (Figure 23.4)



Fig. 23.3 Stone cutting machine Cedima CTS-57 G



Fig. 23.4 Bench Drilling Machine

23.3 Test Results of Samples of Fine-Grained Concrete under Compressive Load

The performed dynamic compression test cycle consisted of 35 test shots. Before testing, the samples were sorted, measured and numbered (Figure 23.5).



Fig. 23.5 Sample preparation for testing

Concrete was tested at seven different speeds. Each mode consisted of five shots. Three modes were performed using copper pulse shapers. The strain rates ranged from 400 to 2000 s⁻¹ (inverse seconds). Copper pulse shapers were used to study and compare results. The reason for using copper formers is to check the higher quality fulfillment of the basic premise of the Kolsky method on the uniformity of the stress-strain state in the sample. Thus, it can be seen that the equality of forces at the ends of the bars is performed more qualitatively when a pulse shaper is used (Figure 23.6, 23.7).

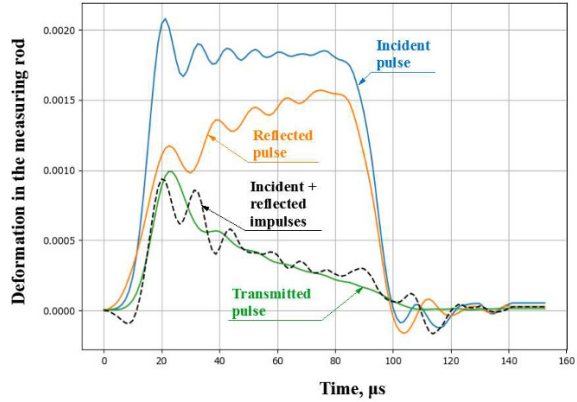


Fig. 23.6 Diagram pulses at a strain rate 1100 s⁻¹ without the use of a pulse shaper

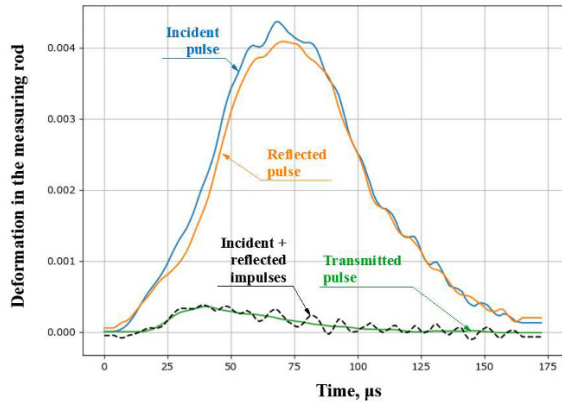


Fig. 23.7 Diagram pulses at a strain rate 1250 s⁻¹ using pulse shaper

The loading was performed using a cylindrical striker. The striker accelerated with a gas gun. The loading rate was regulated by various pressures in the gas gun chamber. Below are the test diagrams of concrete samples according to the Kolsky method. The diagrams show that the initial sections of the obtained diagrams are linear. The falling down branch of the deformation diagram and the inspection of the

sample indicate that the sample was destroyed during the experiment. In mode n.1 (Figure 23.8), the average speed of the striker corresponds to 14 m/s. The pressure in the chamber is 1.5 atmospheres. As the average strength, we can take the value of 75 MPa. The average strain rate is 700 s^{-1} .

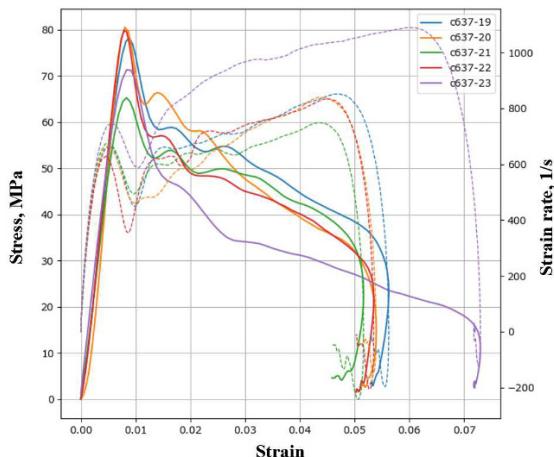


Fig. 23.8 Stress and strain curve for mode n.1

Stress and strain curve for mode No. 1
 $v_{\text{str.}}=14 \text{ m/s}$, $\dot{\epsilon}_{\text{av}}=700 \text{ s}^{-1}$, $\sigma_{\text{max,av}}=75 \text{ MPa}$

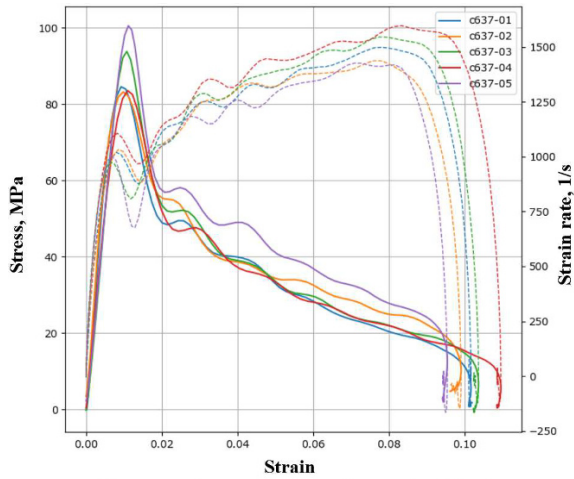
In mode n.2 (Figure 23.9), the average speed of the striker corresponds to 18m/s. The pressure in the chamber is 2.0 atm. As the average strength, we can take the value of 90 MPa. The average strain rate is 1000 s^{-1} . In mode n.3 (Figure 23.10), the average speed of the striker corresponds to 26 m/s. The pressure in the chamber is 3 atmospheres. As the average strength, we can take the value of 100 MPa. The average strain rate is 1700 s^{-1} .

In mode n.4 (Figure 23.11), the average speed of the striker corresponds to 31 m/s. The pressure in the chamber is 4 atmospheres. The average strength can be taken as 110 MPa. The average strain rate is 1900 s^{-1} .

In mode n.5 (Figure 23.12), a copper pulse former was used. The average speed of the striker corresponds to 19 m/s. The pressure in the chamber is 2 atmospheres. The average strength can be taken as 60 MPa. The average strain rate is 500 s^{-1} .

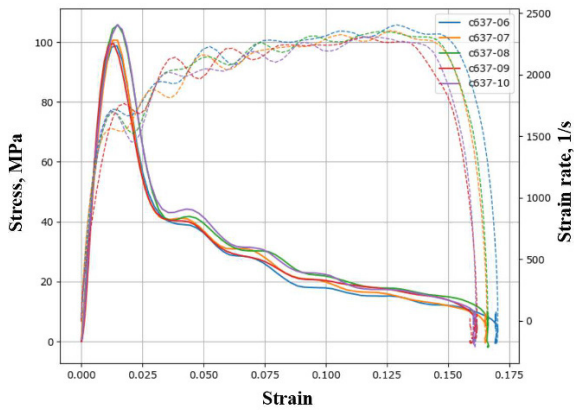
In mode n.6 (Figure 23.13), a copper pulse former was also used. The average speed of the striker corresponds to 36 m/s. The pressure in the chamber is 5 atmospheres. The average strength can be taken as 70 MPa. The average strain rate is 800 s^{-1} .

In mode n.7 (Figure 23.14), a copper pulse former was also used. The average speed of the striker corresponds to 61 m/s. The pressure in the chamber is 20 atmospheres. The average strength can be taken as 80 MPa. The average strain rate is 1200 s^{-1} .



Stress and strain curve for mode No. 2
 $v_{str.}=18 \text{ m/s}$, $\dot{\epsilon}_{av}=1000 \text{ s}^{-1}$, $\sigma_{max,av}=90 \text{ MPa}$

Fig. 23.9 Stress and strain curve for mode No 2



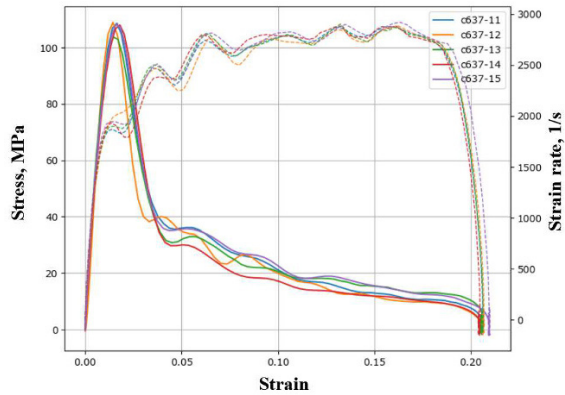
Stress and strain curve for mode No. 3
 $v_{str.}=26 \text{ m/s}$, $\dot{\epsilon}_{av}=1700 \text{ s}^{-1}$, $\sigma_{max,av}=100 \text{ MPa}$

Fig. 23.10 Stress and strain curve for mode No 3

The nature of the destruction of concrete samples after dynamic testing in accordance with the test mode can be seen in Figure 23.15.

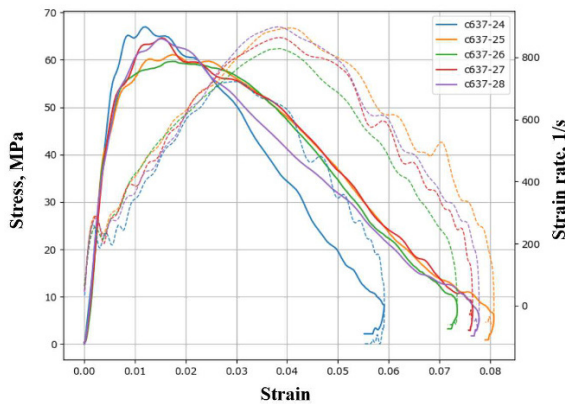
23.4 Conclusion

The report presents the main method of making concrete samples for dynamic tests according to the Kolsky method. Requirements for samples were considered. The used instrumental installations, such



Stress and strain curve for mode No. 4
 $v_{str.}=31 \text{ m/s}$, $\dot{\epsilon}_{av}=1900 \text{ s}^{-1}$, $\sigma_{max,av}=110 \text{ MPa}$

Fig. 23.11 Stress and strain curve for mode n.4



Stress and strain curve for mode No. 5
 $v_{str.}=19 \text{ m/s}$, $\dot{\epsilon}_{av}=500 \text{ s}^{-1}$, $\sigma_{max,av}=60 \text{ MPa}$

Fig. 23.12 Stress and strain curve for mode n.5

as a stone-cutting machine and a drilling machine, are considered.

The results of a series of experiments show that the samples obtained are useful for conducting dynamic tests using the Kolsky method.

This article presents the results of tests of concrete for compression at strain rates ranging from 400 to 2000 s⁻¹. Dynamic strength is in the range from 60 to 110 MPa. With increasing strain rate increases the dynamic strength of concrete.

The use of a copper pulse shaper, which improves the uniformity of the stress-strain state in the sample, is investigated. However, the pulse shaper reduces the strain rate.

Acknowledgements The method of manufacturing concrete samples for dynamic testing was developed with the financial support of the RFBR (grant 19-38-90225). The experimental investigations were supported by the grant of the Government of the Russian Federation (contract No.14.Y26.31.0031).

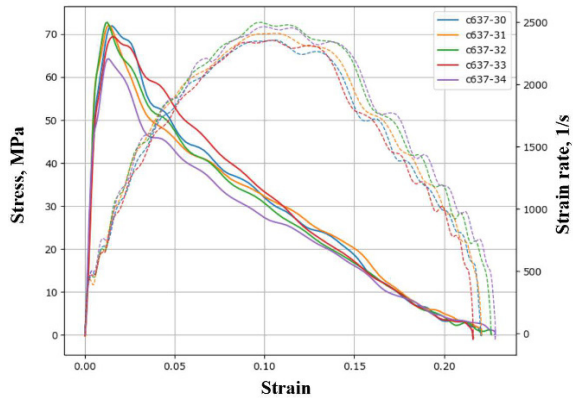


Fig. 23.13 Stress and strain curve for mode n.6

Stress and strain curve for mode No. 6
 $v_{str.}=36 \text{ m/s}$, $\dot{\epsilon}_{av}=800 \text{ s}^{-1}$, $\sigma_{max,av}=70 \text{ MPa}$

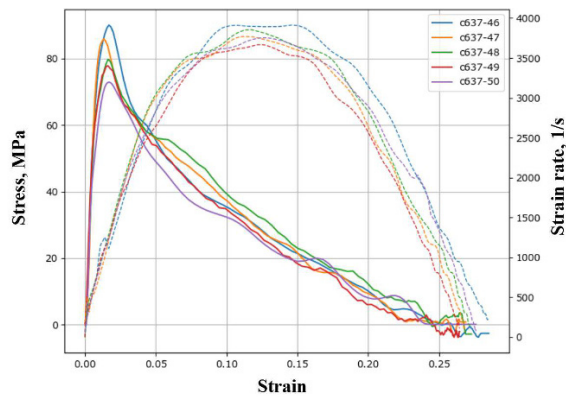


Fig. 23.14 Stress and strain curve for mode n.7

Stress and strain curve for mode No. 7
 $v_{str.}=61 \text{ m/s}$, $\dot{\epsilon}_{av}=1200 \text{ s}^{-1}$, $\sigma_{max,av}=80 \text{ MPa}$

References

- Bragov AM, Lomunov AK (1995) Methodological aspects of studying dynamic material properties using the Kolsky method. *International journal of impact engineering* 16(2):321–330
- Bragov AM, Lomunov AK (2017) Using the Kolsky method to study the processes of high-speed deformation of materials of various physical nature. Nizhny Novgorod State University Publishing House, Nizhny Novgorod
- Bragov AM, Lomunov AK, Igumnov LA (2015) High-speed deformation of fine-grained concrete and fiber-reinforced concrete. Publishing House of the UNN, Nizhny Novgorod
- Bragov AM, Lomunov AK, Konstantinov AYU (2018) An experimental and theoretical study of the processes of high-speed deformation and fracture of materials of various physical nature using the Kolsky method and its modifications. Publishing House of the Nizhny Novgorod State University, Nizhny Novgorod
- Davies EDH, Hunter SC (1963) The dynamic compression testing of solids by the method of the split Hopkinson pressure bar. *Journal of the Mechanics and Physics of Solids* 11(3):155–179

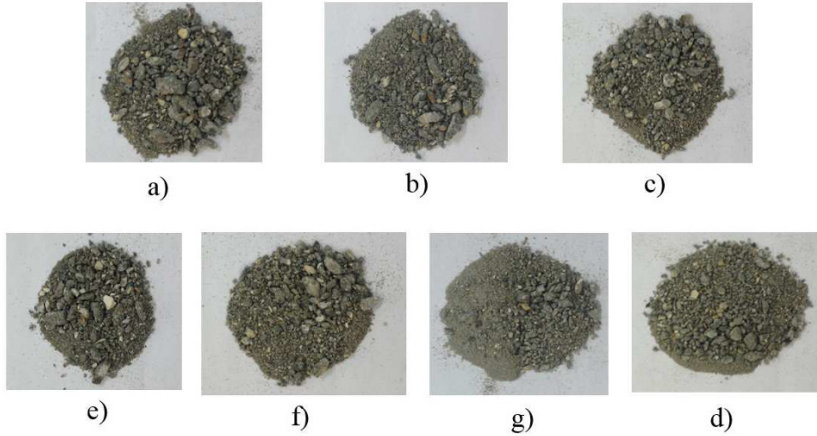


Fig. 23.15 The nature of the destruction of the samples a) mode n.1; b) mode n.2; c) mode n.3; d) mode n.4; e) mode n.5; f) mode n.6; g) mode n.7.

- Giorgio I, Scerrato D (2017) Multi-scale concrete model with rate-dependent internal friction. *European Journal of Environmental and Civil Engineering* 21(7-8):821–839
- Lindholm US (1964) Some experiments with the split Hopkinson pressure bar. *Journal of the Mechanics and Physics of Solids* 12(5):317–335
- Placidi L, Barchiesi E (2018) Energy approach to brittle fracture in strain-gradient modelling. *Proceedings of the Royal Society A: Mathematical, Physical and Engineering Sciences* 474(2210):20170,878
- Placidi L, Barchiesi E, Misra A (2018) A strain gradient variational approach to damage: a comparison with damage gradient models and numerical results. *Mathematics and Mechanics of Complex Systems* 6(2):77–100
- Scerrato D, Giorgio I, Madeo A, Limam A, Darve F (2014) A simple non-linear model for internal friction in modified concrete. *International Journal of Engineering Science* 80:136–152
- Scerrato D, Giorgio I, Della Corte A, Madeo A, Dowling NE, Darve F (2016) Towards the design of an enriched concrete with enhanced dissipation performances. *Cement and Concrete Research* 84:48–61



Chapter 24

FE-Analysis of Deformation and Failure of Structural Elements under Quasistatic Multifactor Effects

Vasilii Gorokhov, Dmitrii Zhegalov, Dmitrii Kazakov, Sergei Kapustin,
and Yuriy Churilov

Abstract Description of the numerical modeling technique within the framework of the damaged medium mechanics approaches to the processes of deformation and destruction of structures under quasi-static multifactor influences is presented. The results of finite element modeling of crack formation and development in structures under the following conditions: elastoplastic deformation, high-temperature creep, influence of aggressive corrosive medium are given.

Keywords: Plasticity · Creep · Crack · Corrosion · Finite element method · Mechanics of the damaged medium

24.1 Introduction

Operating conditions of modern structures are characterized by multiparametric effects of external fields of different nature. This leads to the degradation of the strength properties of the material and, ultimately, to the exhaustion of the design resource. Evolving damage strongly affects the mechanical characteristics of the material and, in particular, is the main reason for the loss of bearing capacity of materials with viscous types of fracture. This leads to the need to take into account the mutual influence of deformation and damage effects when formulating the equations of state of materials, which allow describing the influence of defects developing in the material on the mechanical behavior of the damaged material with the help of appropriate macroscopic parameters.

V. A. Gorokhov, D. V. Zhegalov, D. A. Kazakov, S. A. Kapustin, Yu. A. Churilov
Research Institute for Mechanics, National Research Lobachevsky State University of Nizhni Novgorod, av. Gagarin 23b6, Nizhny Novgorod, 603950, Russia
e-mail: vas-gor@rambler.ru, zhegalov@mech.unn.ru, kazakov@mech.unn.ru, sergei.kapustin@mail.ru, chyuan@rambler.ru

The introduction of such a macroscopic parameter was first proposed in Rabotnov (1966); Kachanov (1974) in the study of the processes of destruction of materials in the conditions of creep as a measure of damage ω , which is a measure of reducing the effective areas of action of stresses in relation to their initial undamaged value. Currently, in most practical applications, the damage measure ω is assumed to be a scalar value varying from $\omega = 0$ for undamaged material to $\omega = 1$ for completely destroyed material. Some theoretical and applied aspects of the development of approaches to the mechanics of the damaged medium (MDM) are presented in Bondar et al (1979); Murakami (1983); Lemaitre (1985); Shevchenko and Mazur (1986); Chaboche (1987); Beh and Korotkikh (1989); Kapustin (1989); Ju (1989); Bondar (1990); Kazakov et al (1999); Volkov and Korotkikh (2008); Kapustin et al (2015); Placidi et al (2018b,a); Placidi and Barchiesi (2018).

Modern theoretical and experimental studies of fracture phenomena make it possible to consider it as a multistage process of occurrence and development of irreversible defects in the material, determined by the entire kinetics of the stress-strain state of structures in the process of their loading (Kazakov et al, 1999; Fedorov, 1985; Mitenkov, 2007). According to this representation, three main stages of the material destruction process are successively developed. Within the limits of the first stage of development there is a need for more scattered on volume material of every kind in the form of micropores and microdefects which does not bring to appreciable influence of these on physical and mechanical characteristics of a material. The second stage is characterized by a further development and by the fact that the emerging issues are of critical importance, corresponding to the infringement of the continuity of the material at the point in question and its increasing influence on the physical and mechanical character of the material. With approach of this stage the intensive interaction of the damages defined by various mechanisms of destruction begins. The end of the stage corresponds to the appearance in the domain of macroscopic crack. In the limits of the third stage there is a merge of the formed macrodefects in one or several cracks leading to splitting into parts (fragmentation) of the considered element of a design.

Taking into account the above mentioned stages in the models used to describe the processes of damage accumulation in structural materials allows to expand the scope of application of the damaged medium mechanics relations, to explain the interaction of different damage mechanisms and the phenomenon of nonlinear damage summation.

24.2 Technique of Numerical Modeling of Deformation and Accumulation of Damages in Structural Elements under Quasi-Static Loading

In the proposed variant of the model of hierarchical model of the damaged material it is assumed that the additivity of the elastic Δe_{ij}^e and irreversible components of Δe_{ij}^{irr} changes in the deformation tensor (plasticity of Δe_{ij}^p and thermal creep of

Δe_{ij}^c) and incompressibility of the material under the conditions of plasticity and creep are valid.

It is also assumed that the influence of different types of damage on the deformation process is carried out by means of the scalar function introduced by Kachanov and Rabotnov.

The direct influence of damage on the deformation process is taken into account in the equations of equilibrium by introducing the dependence of the elastic characteristics of the material on the current value of the function ω . In this regard, when formulating a compound model of the damaged material, two stress characteristics were introduced into consideration: effective σ_{ij} acting on the damaged areas and reduced σ_{ij}^* statically equivalent to the first, but referred to intact areas. The former appear in all partial models that determine the state of the material at the point of the body, while the latter are used at the level of design description in the formulation of equilibrium equations and static boundary conditions.

Taking into account the comments made, specific equations of the compound model of the damaged material, which establish a link between the changes of the reduced stresses $\Delta\sigma_{ij}^*$ and deformations Δe_{ij} at the elementary step of the change of external influences, as well as the parameters characterizing the current state of the material, can be written in the form:

$$\begin{aligned} \Delta\sigma_{ij}^* &= 2G(\Delta e_{ij} - \Delta d_{ij}) + \delta_{ij}(K - \frac{2}{3}G)(\Delta e_{ii} - \Delta d_{ii}), \\ \Delta d_{ij} &= \Delta e_{ij}^* + \omega(\Delta e_{ij} - \Delta e_{ij}^*), \\ \Delta e_{ij}^* &= \Delta e_{ij}^p + \Delta e_{ij}^c - \frac{\Delta G^* \bar{\sigma}'_{ij}}{2G^* \bar{G}^*} + \delta_{ij} \left(\Delta(\alpha T) - \frac{\Delta K^* \bar{\sigma}}{3K^* \bar{K}^*} \right), \\ \Delta G^* &= G^* - \bar{G}^*, G^* = (1 - \omega)G, \bar{G}^* = (1 - \bar{\omega})\bar{G}, \\ \Delta K^* &= K^* - \bar{K}^*, K^* = (1 - \omega)K, \bar{K}^* = (1 - \bar{\omega})\bar{K}, \\ \Delta(\alpha T) &= \alpha T - \bar{\alpha} \bar{T}. \end{aligned} \quad (24.1)$$

where $\bar{K} = K(\bar{T})$, $K = K(T)$, $\bar{G} = G(\bar{T})$, $G = G(T)$ - modules of bulk and shear deformation of intact material, referred to the temperature level in the initial (at the beginning of the step) and current (at the end of the step) states; $\bar{\alpha} = \alpha(\bar{T})$, $\alpha = \alpha(T)$ - values of temperature expansion coefficients; $\bar{\sigma}'_{ij}$, $\bar{\sigma}$ - values of deviator and volumetric components of the stress tensor in the initial state. The values of change of plasticity Δe_{ij}^p and creep Δe_{ij}^c deformations appearing in (24.1) are described by the corresponding particular models.

Particular models of plasticity, creep, and damage accumulation, implemented as part of the considered model of damaged material, are based on variants of thermo-plasticity and thermal creep models, as well as various variants of kinetic equations describing damage accumulation for various fracture mechanisms. In particular, to describe the processes of elastoplastic deformation, a variant of the thermoplasticity model with combined hardening, proposed in Kazakov et al (1999); Volkov and Korkikh (2008) and a modified version of this model (Kazakov et al, 1999; Kapustin

et al, 2015) were employed. To describe the processes of thermal creep as a part of the general model of damaged material, a number of creep models based on the hypothesis of the existence of a creep surface and the gradient to it of the creep strain vector $\dot{\epsilon}_{ij}^c$ (Kazakov et al, 1999; Kapustin et al, 2015, 2008) have been implemented.

The processes of damage accumulation within the used model are described on the basis of the assumption that the damage at a point in the material occurs when the critical $W = W^R$ value is reached at this point by some energy W . The specific form of this energy is determined by the mechanism of the failure under consideration.

The ψ damage function is a normalized analogue of energy W (Kazakov et al, 1999; Kapustin et al, 2015). For undamaged material $\psi = 0$, the ψ value increases to a limit value of $\psi = 1$ during fracture. When several types of damage develop simultaneously in the material, the ψ_k function is used to describe each species. In the developed variant of the compound model the kinetic equations of damage accumulation are realized, which are conditioned by the development of plasticity deformations (on the basis of plastic loosening energy), creep deformations (on the basis of creep dissipation energy), and also on the basis of the criterion of brittle fracture (Kapustin et al, 2015; Gorokhov et al, 2010).

The change in the damage measure of each $\Delta\omega_k$ species is in turn related to the accumulated $\bar{\omega}$ value as well as the change in the damage function of the respective $\Delta\psi_k$ species.

The stage of damage accumulation is taken into account by introducing a variable that determines the completion of the first stage. This variable is the ψ_k^a value determined for each k -th damage type by the value of the above mentioned damage function by the end of the first stage. The dependence of the change in the $\Delta\omega_k$ damage measure on the change in the $\Delta\psi_k$ damage function is taken as (Kazakov et al, 1999; Kapustin et al, 2015):

$$\begin{aligned} \Delta\omega_k &= q\bar{\omega}^{\frac{q-1}{q}} \Delta\psi_k^0, \\ \Delta\psi_k^0 &= \frac{\Delta\psi_k}{1 - \psi_k^a} \text{ when } \psi_k > \psi_k^a, \\ \Delta\psi_k^0 &= 0 \text{ when } \psi_k \leq \psi_k^a. \end{aligned} \quad (24.2)$$

where $q = q(T)$ is a function of the material.

Research of behavior of designs on the basis of the considered physical relations is carried out by means of the combined step-by-step scheme in which steps of each level bear different functional loading, thus their sizes are defined for various reasons.

At the top level steps, called load steps, the task is linearized externally. The actual loading path is represented as a piecewise linear curve in the space of loading parameters and is approximated by a set of straight-line sections, the value of which is determined only from the conditions of satisfactory approximation of the real loading paths. The solution of nonlinear problems at the stages is carried out in the form of the method of initial stresses by iterative refinement of the equilibrium state for the current deformed configuration of the structure.

To calculate the changes in irreversible deformations and damage measures within a step, the latter is broken down into a series of lower level steps. On the internal steps all calculations are made independently for individual points of the structure without correction of equilibrium equations.

At each stage of loading, a non-linear boundary value problem is solved for the corresponding change of external influences, taking into account the entire previous history of irreversible deformation and accumulated damage to the material. The linearization of the problem at the loading stage is carried out in the form of the initial stress method. Numerical solution of linearized problems is carried out on the basis of FEM with the use of isoparametric square-law FE.

For the problems concerning estimation of durability of designs the analysis of performance of corresponding criterion conditions is made. The first one, associated with a local violation of strength, is determined by the condition that one or more adjacent physical nodes achieve an acceptable value of the damage measure ω_f

$$\omega \geq \omega_f . \quad (24.3)$$

The second criterion determines the condition of exhaustion by the design of its bearing capacity. Moreover, a small change in external influences of a given type leads to large changes in displacements and deformations, which increase rapidly with increasing load parameter, i.e. there is a loss of stability of irreversible deformation. Verification of this state of the structure is carried out by changing the determinant of the system of algebraic equations at the loading stages, as well as by analyzing changes in the vector of nodal displacements of the nonlinear part of the solution of the problem at the current stage in the process of successive approximations.

24.3 Technique of Modeling the Processes of Nucleation and Propagation of Cracks

In the majority of works devoted to application of MDM methods for analysis of structural failure, the study of the process ends with the moment of appearance of one or several macro-defects. However, the appearance of such macro-defects in individual points of the material cannot be a sign of structural failure, which usually occurs as a result of their subsequent merger into a crack and the propagation of this crack to a certain limit size. Therefore, the approaches that allow predicting the development of defects in the material from the moment of their origin to the maximum crack opening within the framework of MDM relations are of particular interest for the evaluation of structural strength.

In accordance with the above model ideas, in the process of step-by-step solution of the problem in separate zones of the structure material, the damage zones may appear and evolve, the intensity of which is characterized by the measure of damage ω . The increase in measure ω in the physical node of the construction leads to a decrease in the elasticity of the material (G and K modulus) in this node and thus

to a decrease in its resistance. At the same time in the area of such nodes there is a redistribution of stresses on the volume of material.

By the time the limit value $\omega = \omega_f$ is reached in the node (in calculations the limit value of the damage measure is taken equal to $\omega_f = 0.99$), the material in the area of such node ceases to resist further deformation, redistributing the perceived load on the nearest physical nodes. In the process of further evolution of the damage the following nodes are destroyed. At the same time, the interpolation of the damage functions between the neighboring destroyed nodes forms the line $\omega = \omega_f$, which corresponds to the trajectory of the studied crack propagation (Kapustin et al, 2015; Gorokhov et al, 2010). The implementation of this approach eliminates the need to rebuild the FE mesh of the partition of the studied area, and, therefore, change the topology and structure of information arrays for each case of local strength failure, without violating the conditions of the equilibrium state in the local damage zone and the structure as a whole. In this case, the process of successive destruction of neighboring nodes during loading can be considered as a process of crack propagation and continue calculations without changing the initial topology of the studied area.

To illustrate the possibility of using the proposed methodology in studying the nucleation and propagation of cracks, examples of numerical modeling of fracture processes of structural elements in various modes of quasistatic loading are considered below.

24.4 Numerical Modeling of Elastoplastic Fracture of a Flat Specimen with a Notch under Conditions of Plane Bending

The test sample is a rectangular prism with a length $l = 65$ mm, a width $b = 20$ mm and a height $h = 10$ mm, having in the middle section a transverse notch with a depth $\delta = 4$ mm constant over the entire width of the sample. The sample is made of AK-4 aluminum alloy and pivotally supported on two rigid supports. The loading of the sample was carried out by moving the grips of the testing machine through an indenter installed along the width of the sample in its central section.

Experimental studies related to the construction of the material functions of the material and to the study of the destruction process of such a sample were carried out by L.N. Kramarev. The material functions of the models of deformation and fracture of the AK-4 alloy, necessary for further calculations, are constructed from the results of tests of a series of standard samples under uniaxial tension. The verification of the obtained functions was carried out on the basis of numerical simulation of the process of destruction of a standard cylindrical sample of this material in an axisymmetric formulation.

In a numerical study, real loading was modeled by vertical displacements applied through a compensating spacer along a narrow strip on the upper face of the sample. Similar compensating gaskets were also installed in the area of supports to exclude the occurrence of undesirable plastic deformations during numerical studies.

Numerical modeling of the processes of deformation and fracture of the sample was carried out in a spatial setting for the symmetric 1/4 of its part, limited by the planes of symmetry in the longitudinal and transverse directions, using twenty-node isoparametric finite elements.

The load step size was selected on the basis of preliminary calculations from the condition of a satisfactory description of the $P - V$ curve (P is the force applied to the sample, V is the vertical displacement of the upper point of the central section of the sample), which characterizes the fracture of the sample.

Fig. 24.1 shows a picture of the crack propagation in the cross-section of the sample and a picture of the sample destroyed as a result of the experiment.

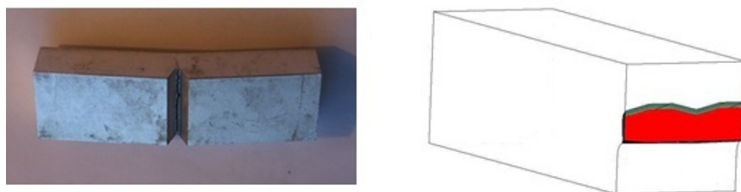


Fig. 24.1 Photograph of the sample destroyed in the experiment and a picture of the crack propagation based on the results of numerical modeling.

Fig. 24.2 shows a graph of the force P dependence on the displacement of the controlled point V , based on the results of numerical modeling, in the form of a dotted line and the results of the experiment indicated by a solid line.

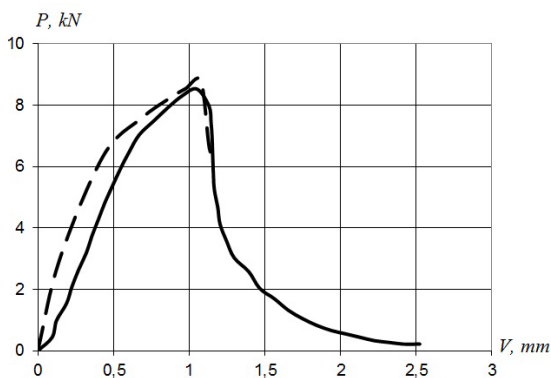


Fig. 24.2 Dependence of force P on the displacement of the controlled point V (solid line - experiment, dotted line - numerical modeling).

The given results allow us to judge that the results of numerical modeling of the fracture process on the basis of the above algorithm are in good agreement with the experimental data. The maximum force P , which differs from the experimental

value by 3%, is achieved in the calculation and experiment with displacements that differ by no more than 3.6%.

24.5 Numerical Modeling of the Crack Propagation Process in a Cylindrical Specimen with a Notch in the High-Temperature Creep

For the purpose of illustration of application of the technique considered above for modeling of processes of destruction of elements of designs in the conditions of creep below results of numerical research of laws of formation and propagation of cracks in the continuous cylindrical sample of circular cross-section, with the concentrator, at an axial tension, in the conditions of high-temperature creep are presented.

The shape of the concentrator in the sample is chosen in the form of a sharp incision without any rounding. According to the theory, the stress concentration coefficient (SCC) in such a cut should strive for infinity. However, according to Neiber (1947), the SCC in the acute incision is finite and corresponds to the value of such a coefficient in the rounded incision, the radius of which is determined by the structure of the material.

A numerical study was carried out in an axisymmetric formulation for the symmetric half of the fragment of the working part of the sample. The calculated region and the loading scheme of the symmetric fragment of the working part of the sample with the concentrator under consideration are shown in the form of an angular section shown in Fig. 24.3. The figure shows: x axis - axis of symmetry, y axis - plane of symmetry, sample length $ED = 7$ mm, sample radius $CD = 5$ mm, notch depth $BF = 1$ mm, notch width $AF = 0.5$ mm.

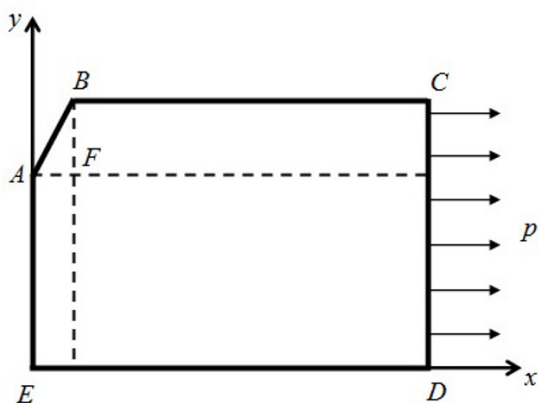


Fig. 24.3 The design scheme of the sample fragment.

The sample is made of a heat-resistant alloy, for which the material functions used to implement the above-mentioned models of ductility, creep, and damage accumulation were obtained and verified in Kapustin et al (2008). The process of loading the sample was carried out in three stages: stage 1 - warming up to temperature $T = 850^{\circ}\text{C}$; stage 2 - stretching by axial forces with intensity p , distributed over the ends of the sample; stage 3 - holding the loaded sample for 40 hours.

The destruction of the sample is considered as viscous due to the development of creep deformations, without taking into account the possible effects of brittle damage.

Numerical studies were carried out on a number of calculation options, differing in the value of tensile forces p , sampling FE parameters with constant sample sizes and shape, and the values of stress concentration factors in the region of the notch due to the sampling scheme used.

For the level of tensile stresses $p = 100$ MPa, several variants of problems have been calculated with various finite-element discretization schemes of the computational domain.

Fig. 24.4 shows the calculated curves of the dependence of the crack length l on the time of its steady propagation t for some of the considered options, indicated by numbers, characterizing the number of partitions n and the stress concentration coefficient value K_{σ} : 1) $n = 12, K_{\sigma} = 4.15$; 2) $n = 15, K_{\sigma} = 5.21$; 3) $n = 20, K_{\sigma} = 5.22$; 4) $n = 32, K_{\sigma} = 6.075$.

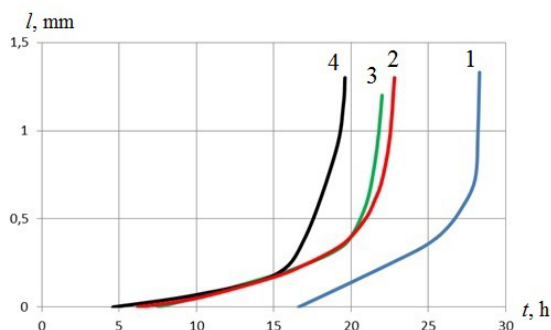


Fig. 24.4 The dependence of the crack length on the time of its propagation for different values of the stress concentration coefficient.

In all the considered variants, a uniform grid step was taken along the axis y . In addition, for all elements located along the AE line, the same aspect ratio of the mesh cells was assumed to be $h_x = h_y$.

The influence of the level of applied load p on the patterns of crack propagation in the specimen was also considered. Five variants of loads are considered: 1) $p = 140$ MPa; 2) $p = 120$ MPa; 3) $p = 100$ MPa; 4) $p = 90$ MPa; 5) $p = 80$ MPa. In all the considered variants, the $n = 20$ finite-element discretization scheme was used.

Fig. 24.5 presents the dependence of the crack length l on the exposure time. In the figure, the figure corresponds to the considered variant of the load level p .

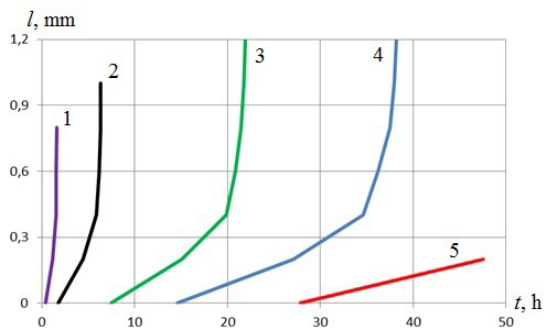


Fig. 24.5 The dependence of the crack length on time for different stress values.

The results show that an increase in tensile load leads to a decrease in time to the moment of crack formation, an increase in speed and a reduction in the time of its steady growth. For option load 1 ($p = 140$ MPa), the sample was destroyed almost immediately after the formation of a crack; for option 5 ($p = 80$ MPa), a crack was formed, but during the 40-hour holding period, the sample did not practically propagate into the sample.

Thus, as a result of the studies, the possibility of numerical modeling based on the FEM of the processes of the appearance and propagation of cracks in structural elements under high-temperature creep has been demonstrated. The regularities of crack initiation and development in a cylindrical sample with a concentrator subjected to axial tension under high-temperature creep conditions are established based on the assumption of viscosity of sample failure. The dependence of the calculation results on the FE parameters of the sample discretization in the region of the crack development path is shown. The dependences of the times of formation, steady growth, and the rate of crack propagation on the value of the stress concentration coefficient in the notch and the tensile stress intensity are established.

24.6 Numerical Modeling of Corrosion Failure of a Tubular Specimen under axial Tension

One of the important factors that significantly affect the physicomaterial characteristics of metals is the environment in which the structures under study or their individual elements are located.

The liquid or gas medium surrounding the metal can act on the surface layer of metals and, when it comes into physical or chemical interaction with it, harden or soften it. As a result of this interaction, the deformation and strength properties of metals change significantly. The long stay of loaded structures in an aggressive environment often leads to corrosion of the metal.

In Kapustin et al (2013), a modeling technique was developed on the basis of the ratios of the mechanics of the damaged medium of stress corrosion cracking (SCC) processes.

In order to check the efficiency of the proposed technique the numerical modeling of the process of corrosion destruction of a thin-walled tubular sample is performed. The results of experimental study of the destruction of such samples and the influence of various operational factors (stress level, temperature, composition of the environment) on the resistance against SCC steel X18H10T are given in Sandler and Kozin (1984).

Numerical modeling was carried out for a sample fragment (its working part) - a thin-walled cylindrical shell with a length of $L = 26$ mm, having an internal diameter of $D = 10$ mm, and a wall thickness of $h = 1.5$ mm.

The left part of the sample (along the length of the working part $L = 13$ mm) was immersed in a liquid chlorine-containing medium 0.5% NaCl solution), heated to a temperature of $T = 150^{\circ}\text{C}$. The temperature distribution was assumed constant over the thickness of the sample.

The temperature distribution graph along the generatrix of the sample fragment and the variant of its FE discretization are shown in Fig. 24.6.

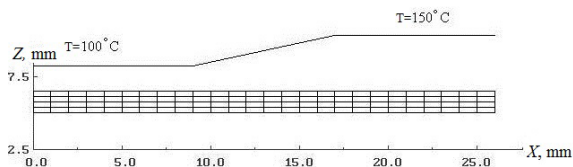


Fig. 24.6 Temperature distribution along the sample fragment.

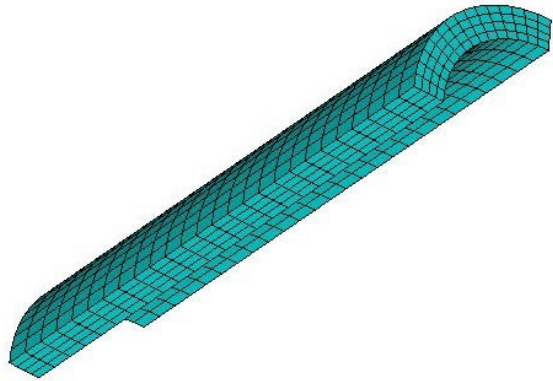
The specimen was tensioned by the axial force q , evenly distributed over its right end-face with subsequent holding under load until it is destroyed. In the simulation, the process of loading the sample was carried out in two stages. At the first stage, an instantaneous application of axial force was performed; at the second, exposure under load was performed. The calculations of the SCC of the sample were performed for a number of different axial force intensities: $q = 75, 100, 125, 150, 200$ MPa.

The numerical solution of the problems was carried out on the basis of the FEM in axisymmetric and spatial formulations using isoparametric finite elements with a quadratic law of variation of the displacement functions for two variants of sample fragmentation. The first discretization option in axisymmetric and spatial settings is shown in Fig. 24.6 and Fig. 24.7, respectively.

In the second variant, the number of FEs doubled both in thickness and in length of the fragment. Due to the good agreement between the results of numerical studies obtained for these options, more detailed discretization of the sample fragment was not required.

The material functions of the SCC models, the values of which were used to obtain the results presented below, were obtained on the basis of experimental data on the dependence of the fracture time on the stress level and a number of assumptions

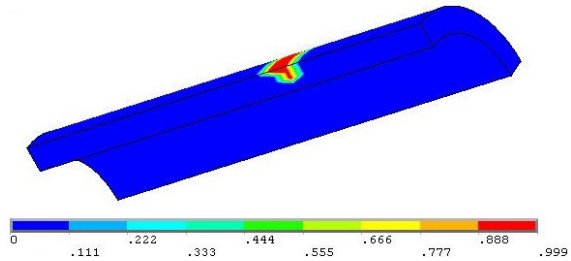
Fig. 24.7 Variant of FE discretization of a sample fragment in a spatial formulation.



about the duration of the various stages of the SCC process, which were further refined in the process of numerical simulation.

The distribution pattern of the ω damage measure over the sample volume for a moment of time close to the moment of failure for the load case $q = 100 \text{ MPa}$ is shown in Fig. 24.8

Fig. 24.8 Distribution of damage measure ω over the sample volume for load $q = 100 \text{ MPa}$.



A similar picture of the evolution of SCC processes was observed for other load cases. Based on the analysis of the results of numerical studies, it was found that the destruction of the sample for all the considered load cases occurs in the region of the interface between the corrosive medium and the air. The nature of the zones destroyed as a result of the SCC and the sequence of their development in time for all considered load cases qualitatively coincide. Moreover, the calculation results obtained on various types of grids within each load case are in good agreement with each other both qualitatively and quantitatively.

Fig. 24.9 shows the dependence of the fracture time of the sample on the level of the applied load obtained on the basis of experimental data (solid line) and the results of numerical simulation (points).

The given materials show that the results of numerical modeling are good quality (coincidence of the fracture zone along the length of the sample) and quantitatively

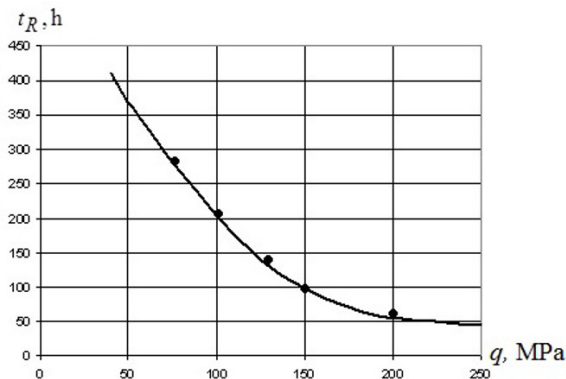


Fig. 24.9 Dependence of the failure time of the t_R sample on the applied load level q .

(the difference in the estimation of the time of complete fracture of the sample does not exceed 13%) are consistent with the experimental data.

24.7 Conclusion

The possibility of numerical modeling on the basis of FEM within the framework of the relations of mechanics of the damaged medium of the processes of occurrence and propagation of cracks in the elements of structures under the conditions of elasto-plastic deformation, high-temperature creep and influence of aggressive corrosive medium is demonstrated.

It is shown that the results of numerical modeling of the process of destruction of a sample with a concentrator, obtained on the basis of simultaneous consideration of plastic and brittle damages in the process of destruction, are in good agreement with the experimental data.

The regularities of occurrence and development of cracks in a cylindrical specimen with a concentrator under axial tension under conditions of high-temperature creep in the assumption of viscous fracture of the specimen are established. The dependence of the results of calculations on the parameters of FE-discretization of the sample in the area of the crack propagation trajectory is shown. The dependences of formation times, stable growth and crack propagation rate on the value of stress concentration coefficient in the notch and tensile stress intensity are determined.

It is shown that the results of numerical modeling of the SCC process of the sample under study are in good agreement with the experimental data. The predicted failure zone of the sample coincides with the actual one. The predicted failure times of the sample for all load variations are well consistent with the experimental values.

Acknowledgements The methodology and software have been developed with the financial support of a grant from the Government of the Russian Federation (14.Y26.31.0031), the results of solving

the problems of failure structural elements, obtained with the financial support of grant of the President of the Russian Federation (MD-2528.2019.1).

References

- Beh OI, Korotkikh YG (1989) Equations of mechanics of a damaged medium for cyclic nonisothermal processes of deformation of materials. *Applied problems of strength and plasticity Methods of solution* 51(1):28–37
- Bondar VS (1990) Mathematical modeling of inelastic behavior and accumulation of material damage. message 1. the joint model of inelasticity. *Applied problems of strength and plasticity Solution methods* 52(1):17–24
- Bondar VS, Gorokhov VB, Sannikov VI (1979) Investigation of low-cycle strength of the shells of rotation under complex heat-and-power loading. *Applied Problems of Strength and Plasticity Mechanics of Deformable Systems* 41(1):120–126
- Chaboche JL (1987) La mécanique de l'endommagement et son application aux prévisions de durée de vie des structures. *Rech depospat* 109(4):37–54
- Fedorov VV (1985) Kinetics of damage and destruction of solids. Fan, Tashkent
- Gorokhov VA, Kapustin SA, Churilov YA (2010) Numerical simulation of the failure process for an experimental sample with a concentrator under plane bending conditions. *Journal of Machinery Manufacture and Reliability* 49(6):549–553
- Ju JW (1989) On energy-based coupled elastoplastic damage theories: constitutive modeling and computational aspects. *Int J Solid and Struct* 25(7):803–833
- Kachanov LM (1974) Fundamentals of fracture mechanics. Science, Moscow
- Kapustin SA (1989) Numerical modeling of structural deformation processes taking into account the ratios of the mechanics of a damaged medium. *Applied problems of strength and plasticity Numerical modeling of physical and mechanical processes* 51(1):414
- Kapustin SA, Kazakov DA, Churilov YA, Galushchenko AI, Vakhterov AM (2008) Experimental and theoretical study of the behavior of heat-resistant alloy products under high-temperature creep. *Problems of strength and plasticity* 70(1):98–108
- Kapustin SA, Gorokhov VA, Churilov YA, Panov VA, Tryaev PV (2013) Modeling based on the ratios of the mechanics of a damaged medium of cracking processes under stress of stainless steels under aggressive corrosive environments. *Problems of strength and plasticity* 75(2):77–87
- Kapustin SA, Churilov YA, Gorokhov VA (2015) Modeling of nonlinear deformation and fracture of structures under conditions of multifactorial effects based on the FEM. Publishing House of Nizhny Novgorod State University, Nizhny Novgorod
- Kazakov DA, Kapustin SA, Korotkikh YG (1999) Modeling of the processes of deformation and fracture of materials and structures. Publishing House of Nizhny Novgorod State University, Nizhny Novgorod
- Lemaitre J (1985) Continuous damage model used to calculate fracture of plastic materials. *Theoretical Basis of Engineering Calculations Proceedings of the American Society of Mechanical Engineers* 107(1):90–98
- Mitenkov FM (2007) Methods of substantiation of the resource of nuclear power plants. Engineering, Moscow
- Murakami S (1983) The essence of the mechanics of environmental damage and its application to the theory of anisotropic damage at creep. *Theoretical Basis of Engineering Calculations Proceedings of the American Society of Mechanical Engineers* 5(2):28–36
- Neiber G (1947) Stress Concentration. OGIZ, Moscow
- Placidi L, Barchiesi E (2018) Energy approach to brittle fracture in strain-gradient modelling. *Proceedings of the Royal Society A: Mathematical, Physical and Engineering Sciences* 474(2210):20170.878

- Placidi L, Barchiesi E, Misra A (2018a) A strain gradient variational approach to damage: a comparison with damage gradient models and numerical results. *Mathematics and Mechanics of Complex Systems* 6(2):77–100
- Placidi L, Misra A, Barchiesi E (2018b) Two-dimensional strain gradient damage modeling: a variational approach. *Zeitschrift für angewandte Mathematik und Physik* 69(3):1–19
- Rabotnov YN (1966) *Creep of structural elements*. Science, Moscow
- Sandler NG, Kozin VA (1984) Corrosion cracking of steels of the KH18N10T type in steam-water chlorine-containing environments. *Protection of metals* 20(3):393–396
- Shevchenko YN, Mazur VN (1986) Solution of plane and axisymmetric boundary value problems of thermoviscous plasticity taking into account damage to the material during creep. *Applied Mechanics* 22(8):695–704
- Volkov IA, Korotkikh YG (2008) *Equations of state of viscoelastic plastic media with damage*. Fizmatlit, Moscow



Chapter 25

Numerical Analysis of Permeability Coefficient Influence on Dynamic Responses in Poroviscoelastic Solids Using BEM

Leonid A. Igumnov, Aleksander A. Ipatov, and Svetlana Yu. Litvinchuk

Abstract In the present paper wave propagation in poroviscoelastic solids is studied. Research is dedicated to modeling of a slow compressional wave in poroviscoelastic media by means of boundary-element method. Poroviscoelastic formulation is based on Biot's model of fully saturated poroelastic media with a correspondence principal usage. Standard linear solid model is employed in order to describe viscoelastic behavior of the skeleton in porous medium. The boundary-value problem of the three-dimensional dynamic poroviscoelasticity is written in terms of Laplace transforms. Modified Durbin's algorithm of numerical inversion of Laplace transform is used to perform solutions in time domain. The problem of the load acting on a poroelastic prismatic solid is solved by means of developed software based on boundary element approach.

25.1 Introduction

Wide range of natural and artificial materials can be treated as a porous media, for example rocks, soils, biological tissues, foams, ceramics, etc. Porous medium is a solid with pore system, filled with a liquid or gas. Wave propagation in saturated porous media is an important issue of engineering sciences, such as geophysics, geomechanics, seismic prospecting, bioengineering etc. Satisfactory accuracy of the results of such studies cannot be achieved using elastic or viscoelastic models of the material and requires the development of effective tools, methods and models. Thus, the problem of mathematical methods development and their application in wave propagation investigation in nonhomogeneous viscoelastic, poroelastic and poroviscoelastic solids appears. The poroelasticity theory was developed and nowadays

L. A. Igumnov, A. A. Ipatov, S. Yu. Litvinchuk
Research Institute for Mechanics, National Research Lobachevsky State University of Nizhny Novgorod, Nizhny Novgorod, Russia
e-mail: igumnov@mech.unn.ru, ipatov@mech.unn.ru, litvinchuk@mech.unn.ru

is important to engineering applications. However, in addition to the macroscopic effects, there exist many other time-dependent physical mechanisms. For example, the rock mass itself without fluid can exhibit creep behavior. These phenomena can be modeled as apparent viscoelastic mechanisms at the macroscopic level.

Studying of the dynamic processes in porous media began from the discovery of the experimental law of liquid filtration in a porous medium, made by Darcy (1956). In Frenkel (1944) developed full set of dynamic equations that describes acoustics of isotropic poroelastic media. The theory of two-phase porous material, which consists of elastic skeleton and fluid, was introduced by Biot (1956b,c). Biot theory is a generalization of classical theory of elasticity on saturated porous medium. The implementation of the solid viscoelastic effects in the theory of poroviscoelasticity was also first introduced by Biot (1956a). The dynamic interaction analysis involving poroelastic/poroviscoelastic media is extensively studied in literature (de Boer, 1996; Schanz, 2001; Detournay and Cheng, 1993; Giorgio et al, 2019). Some recent results regarding porous materials such as visco-poroelastic and partially saturated porous media can be found in Madeo et al (2013); Giorgio et al (2016). There are two major approaches to dynamic processes modeled by means of boundary element method (BEM): solving boundary integral equation (BIE) system directly in time domain or in Laplace or Fourier domain followed by the respective transform inversion (Goldshteyn, 1978; Bazhenov and Igumnov, 2008). Durbin developed an approach, namely fast Laplace inverse transform (FLIT) for numerical evaluation of the integrals (Durbin, 1974). Some modifications were recently proposed by Zhao (2004) in order to overcome a drawback of constant integration step in FLIT.

Biot's model correctly describes processes of deformation of an elastic porous medium and fluid flow in it. It is assumed that the space containing poroelastic medium is filled with a two-phase material, and one phase corresponds to the elastic skeleton, and the another one to the fluid in pores. Both phases are present at each point of the physical space, and the phase distribution in space is described by macroscopic quantities such as porosity. The fundamental property of a poroelastic saturated medium, following from Biot's theory, is the existence of two longitudinal waves in such media, fast and slow, and also a shear wave. The fast longitudinal wave and the transversal wave are similar in their nature to waves in an elastic medium, whereas the slow longitudinal wave is characteristic of a porous medium. The slow wave is more difficult to detect, as its amplitude is considerably smaller than that of the fast longitudinal wave. In present paper we demonstrate viscosity parameter influence on dynamic responses in poroviscoelastic solid and also in case of slow longitudinal wave modeling.

25.2 Mathematical Model

25.2.1 Poroelastic Formulation

Homogeneous body Ω in three-dimensional Euclidean space R^3 is considered, with the boundary Γ . It is assumed, that body Ω is isotropic poroviscoelastic. The set of differential equations of poroelasticity for displacements \bar{u}_i and pore pressure \bar{p} for Biot's model of fully saturated poroelastic continuum in Laplace domain take the following form Schanz (2001):

$$G\bar{u}_{i,jj} + \left(K + \frac{1}{3}G\right)\bar{u}_{j,ij} - (\psi - \beta)\bar{p}_{,i} - s^2(\varrho - \beta\varrho_f)\bar{u}_i = \bar{F}_i, \quad (25.1)$$

$$\frac{\beta}{s\varrho_f}\bar{p}_{,ii} - \frac{\phi^2 s}{R}\bar{p} - (\psi - \beta)s\bar{u}_{i,i} = \bar{a}_i, \quad (25.2)$$

where K and G are the elastic moduli of the porous material, p is the porous pressure of the filling material, \bar{F}_i is volume force density. Coefficient ψ is determined as

$$\psi = 1 - \frac{K}{K_s}, \quad (25.3)$$

where K_s is bulk modulus of the skeleton grains. In (25.2) R is parameter characterizing the relation between the solid body and the liquid:

$$R = \frac{\phi^2 K_f K_s^2}{K_f(K_s - K) + \phi K_s(K_s - K_f)} \quad (25.4)$$

$$\beta = \frac{\kappa\varrho_f\phi^2 s^2}{\phi^2 s + s^2\kappa(\varrho_a + \phi\varrho_f)}.$$

where $\varrho = \varrho_s(1 - \phi) + \phi\varrho_f$, ϱ_s is density of the skeleton grains, κ is permeability, ϱ_f is density of the filling material, K_f is the bulk modulus of the liquid.

A generalized unknown vector, which contains displacements and pore pressure and a generalized force vector are additionally introduced as

$$\bar{u}(\vec{x}, s) = (\bar{u}_1, \bar{u}_2, \bar{u}_3, \bar{p}) \quad \vec{x} \in \Omega, \quad \Omega \subset R^3, \quad (25.5)$$

$$\bar{t}(\vec{x}, s) = (\bar{t}_1, \bar{t}_2, \bar{t}_3, \bar{q}) \quad \vec{x} \in \Omega, \quad \Omega \subset R^3, \quad (25.6)$$

Equations (25.1) and (25.2), supplemented with boundary conditions:

$$u(\vec{x}, s) = \tilde{u}, \quad \vec{x} \in \Gamma^u, \quad (25.7)$$

$$t(\vec{x}, s) = \tilde{t}, \quad \vec{x} \in \Gamma^\sigma, \quad (25.8)$$

where Γ^u is the Dirichlet's boundary and Γ^σ is the Neumann's boundary, where corresponding generalized displacements and generalized tractions are prescribed.

25.2.2 Poroviscoelastic Formulation

Poroviscoelastic solution is obtained from poroelastic solution by means of the elastic-viscoelastic correspondence principle, applied to skeleton's constants K and G in Laplace domain. Forms of functions $\bar{K}(s)$ and $\bar{G}(s)$ are depends on chosen viscoelastic model. Material functions for Standard linear solid model are:

$$\bar{K}(s) = K^\infty \cdot \left[(\theta - 1) \frac{s}{s + \gamma} + 1 \right] \quad (25.9)$$

$$\bar{G}(s) = G^\infty \cdot \left[(\theta - 1) \frac{s}{s + \gamma} + 1 \right] \quad (25.10)$$

Parameter γ characterize viscosity. The equilibrium and instantaneous values of the relaxation function associated with material modules are connected as follows:

$$\theta = \frac{K^0}{K^\infty} = \frac{G^0}{G^\infty} \quad (25.11)$$

Equilibrium and instantaneous values are denoted by « ∞ » and «0» respectively.

25.3 Solution Method

25.3.1 Boundary-Element Approach

Boundary-value problem (25.1)–(25.8) is solved using the direct boundary element method (BEM), based on a combined use of integral Laplace transform and BIE's of the 3D isotropic theory of poroelasticity:

$$\vec{C}(\vec{y})\vec{u}(\vec{y}, s) + \int_{\Gamma} \vec{T}(\vec{x}, \vec{y}, s)\vec{u}(\vec{x}, s)d\Gamma = \int_{\Gamma} \vec{U}(\vec{x}, \vec{y}, s)\vec{t}(\vec{x}, s)d\Gamma$$

where $\vec{x}, \vec{y} \in \Gamma$, $\vec{U}(\vec{x}, \vec{y}, s)$ and $\vec{T}(\vec{x}, \vec{y}, s)$ are matrices of fundamental and singular solutions, respectively, \vec{x} is an integration point, \vec{y} is an observation point. The values of the coefficients of matrix \vec{C} are defined by the geometry of boundary Γ . A procedure for obtaining BIE's, based on the weighted residual method can be found in Schanz (2001). Some of the problems of the arising kernels of BIE's are discussed in Schanz (2009).

Equations (25.12) comprise singular integrals in the sense of Cauchy, which are quite difficult to compute. Use of the boundary properties of retarded potentials makes it possible, based on Ugodchikov and Hutoryanskii (1986), to write down a regular representation of equation (25.12):

$$\int_{\Gamma} \left(\vec{T}(\vec{x}, \vec{y}, s) \vec{u}(\vec{x}, s) - \vec{T}^0(\vec{x}, \vec{y}, s) \vec{u}(\vec{y}, s) - \vec{U}(\vec{x}, \vec{y}, s) \vec{t}(\vec{x}, s) \right) d\Gamma = 0 ,$$

where $\vec{T}^0(\vec{x}, \vec{y}, s)$ is singularity matrix and $\vec{x}, \vec{y} \in \Gamma$. Using Equation (25.12), it is possible to construct a boundary-element solution of the BIE.

In the result of spatial discretization, boundary Γ is represented with a set of K_E quadrangular eight-node boundary elements. The geometry of each element E_K is defined by biquadratic functions of form N_m and the global coordinates of nodes \vec{x}_m^k , related as (Bazhenov and Igumnov, 2008)

$$\vec{x}(\zeta) = \sum_{m=1}^8 N_m(\xi) \vec{x}_m^k , k = 1..K \tag{25.12}$$

where $\xi = (\xi_1, \xi_2) \in (-1, 1) \times (-1, 1)$ are local coordinates. According to correlated interpolation model Goldshteyn (1978), displacements are described using bilinear elements with the related bilinear functions of form $R_l(\xi)$, and surface generalized forces are described with constant boundary elements:

$$\vec{u}(\xi) = \sum_{l=1}^4 R_l(\xi) \vec{u}_l^k , \tag{25.13}$$

$$\vec{t}(\xi) = \vec{t}^k , \tag{25.14}$$

where \vec{u}_m^k and \vec{t}^k are nodal values of displacements and tractions, respectively, over element E_k .

A discrete representation of BIE's written at the nodes of the approximation of boundary functions \vec{y}^i , using the collocation method and accounting for (25.12)–(25.14), is of the following form:

$$\sum_{k=1}^{K_E} \sum_{m=1}^4 \Delta \vec{T}_{mi}^k \vec{u}_m^k = \sum_{k=1}^K \Delta \vec{U}_{mi}^k \vec{t}^k , \tag{25.15}$$

$$\Delta \vec{U}_{mi}^k = \int_{-1}^1 \vec{U}(\vec{x}^k(\xi), \vec{y}^i, s) J^k(\xi) d\xi , \tag{25.16}$$

$$\Delta \vec{T}_{mi}^k = \int_{-1}^1 \left(R_m(\xi) \vec{T}(\vec{x}^k(\xi), \vec{y}^i, s) - \vec{I} \cdot \vec{T}^0(\vec{x}^k(\xi), \vec{y}^i) \right) J^k(\xi) d\xi , \tag{25.17}$$

where \vec{I} is unit matrix, J^k is Jacobian of the local coordinates into global ones.

The elements of matrices $\Delta \vec{U}_{mi}^k, \Delta \vec{T}_{mi}^k$ are computed using numerical integration schemes depending on the kind of integral (nonsingular or singular). Nonsingular integrals arise, when the collocation point does not belong to the element. Here, standard Gaussian-type formula is used in combination with a hierarchical subdivision of the elements (Ugodchikov and Hutoryanskii, 1986). Singular integrals arise, when the collocation point is situated on the element being integrated over. In this

case, new local coordinates are introduced, making it possible to avoid a singularity in the integrand and to use Gaussian integration.

25.3.2 Laplace Transform Inversion

The inverse of Laplace transform is defined as the following contour integral:

$$L^{-1}\{\bar{f}(\vec{x}, s)\} = f(\vec{x}, t) = \frac{1}{2\pi i} \int_{\alpha-i\infty}^{\alpha+i\infty} \bar{f}(\vec{x}, s)e^{st} ds \tag{25.18}$$

where $\alpha > 0$ is the arbitrary real constant greater than the real parts of all singularities in $\bar{f}(\vec{x}, s)$. When values of $\bar{f}(\vec{x}, s)$ are available only at the sample points, analytical evaluation of integral in Eq. (25.18) is impossible. Supposing $s = \alpha + i\omega$ we have the following expressions (for convenience the spatial variable \vec{x} is omitted hereinafter):

$$f(0) = \frac{1}{\pi} \int_0^{\infty} \text{Re}[\bar{f}(\alpha + i\omega)] d\omega \tag{25.19}$$

$$f(0) = \frac{e^{\alpha t}}{\pi} \int_0^{\infty} \left[\text{Re}[\bar{f}(\alpha + i\omega)] \cos(\omega t) - \text{Im}[\bar{f}(\alpha + i\omega)] \sin(\omega t) \right] d\omega, t > 0. \tag{25.20}$$

Durbin (1974) developed an approach, namely fast Laplace inverse transform (FLIT) for numerical evaluation of the integrals in Eqs. (25.19) and (25.20). In this section, we briefly review a modifications recently proposed by Zhao (2004) in order to overcome a drawback of constant integration step in FLIT. Let R be large real number so we can rewrite Eqs. (25.19) and (25.20) as follows:

$$f(0) = \frac{1}{\pi} \lim_{R \rightarrow \infty} \int_0^R \text{Re}[\bar{f}(\alpha + i\omega)] d\omega \tag{25.21}$$

$$f(0) = \frac{e^{\alpha t}}{\pi} \lim_{R \rightarrow \infty} \int_0^R \left[\text{Re}[\bar{f}(\alpha + i\omega)] \cos(\omega t) - \text{Im}[\bar{f}(\alpha + i\omega)] \sin(\omega t) \right] d\omega, t > 0. \tag{25.22}$$

Defining the nodes as $0 = \omega_1 < \omega_2 < \dots < \omega_n < \omega_{n+1} = R$ we approximate Eqs. (25.21) and (25.22) as

$$f(0) \approx \frac{1}{\pi} \sum_{k=1}^n \int_{\omega_k}^{\omega_{k+1}} \operatorname{Re}[\bar{f}(\alpha + i\omega)] d\omega \tag{25.23}$$

$$f(t) \approx \frac{e^{\alpha t}}{\pi} \sum_{k=1}^n \int_{\omega_k}^{\omega_{k+1}} \left[\operatorname{Re}[\bar{f}(\alpha + i\omega)] \cos(\omega t) - \operatorname{Im}[\bar{f}(\alpha + i\omega)] \sin(\omega t) \right] d\omega, t > 0. \tag{25.24}$$

In each segment $[\omega_k, \omega_{k+1}]$, $k = \overline{1, n}$ the real and imaginary parts of $\bar{f}(s)$ are approximated with linear functions as follows

$$\operatorname{Re}[\bar{f}(\alpha + i\omega)] \approx F_k + \frac{F_{k+1} - F_k}{\omega_{k+1} - \omega_k} (\omega - \omega_k) \tag{25.25}$$

$$\operatorname{Im}[\bar{f}(\alpha + i\omega)] \approx G_k + \frac{G_{k+1} - G_k}{\omega_{k+1} - \omega_k} (\omega - \omega_k) \tag{25.26}$$

where $F_k = \operatorname{Re}[\bar{f}(\alpha + i\omega_k)]$, $G_k = \operatorname{Im}[\bar{f}(\alpha + i\omega_k)]$. Substituting Eq. (25.25) and (25.26) into Eqs. (25.23) and (25.24) and making direct integration we obtain

$$f(0) \approx \sum_{k=1}^n \left[\frac{(F_{k+1} - F_k) \Delta_k}{2\pi} \right] \tag{25.27}$$

$$f(t) \approx \frac{e^{\alpha t}}{\pi t^2} \sum_{k=1}^n \left[\frac{(F_{k+1} - F_k)}{\Delta_k} (\cos(\omega_{k+1}t) - \cos(\omega_k t)) + \frac{(G_{k+1} - G_k)}{\Delta_k} (\sin(\omega_{k+1}t) - \sin(\omega_k t)) \right] \tag{25.28}$$

where $t > 0$, $\Delta_k = \omega_{k+1} - \omega_k$.

25.4 Numerical Results

25.4.1 Test Example

Following problem is considered: three-dimensional poroelastic prismatic body is clamped at its left end, and subjected to uniaxial and uniform impact loading $t_2 =$

$t_2^*H(t)$, $t_2^* = -1\text{N/m}^2$ at the right end Fig. 25.1, $H(t)$ is a Heaviside step function. The remaining surfaces are traction free.

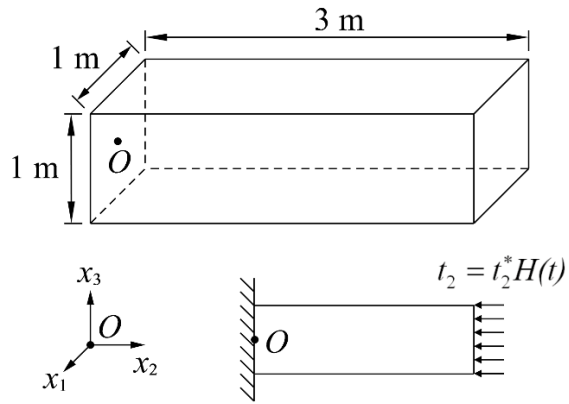


Fig. 25.1 Problem statement.

Poroelastic material parameters are (soil): $K = 2.1 \cdot 10^8 \text{ N/m}^2$, $G = 9.8 \cdot 10^7 \text{ N/m}^2$, $K_s = 1.1 \cdot 10^{10} \text{ N/m}^2$, $K_f = 3.3 \cdot 10^9 \text{ N/m}^2$, $\rho = 1884 \text{ kg/m}^3$, $\rho_f = 1000 \text{ kg/m}^3$, $\phi = 0.48$, $\kappa = 3.55 \cdot 10^{-9} \text{ m}^4/(\text{N} \cdot \text{s})$.

In this example, we consider Durbin’s method and its modification. A boundary-element mesh of 1152 quadrangular elements is employed in computations.

Algorithm 1. : Inverse Laplace transform of frequency domain Analytical solution of the problem with large number of sampling frequencies.

Algorithm 2. : Inverse Laplace transform of numerical boundary-element solution; constant step by ω , $\Delta_k = 0.5$, $k = 1, 2, \dots, 400$, $\omega_{\max} = 200$; integration time is 2093.3 seconds.

Algorithm 3. : Inverse Laplace transform of numerical boundary-element solution; variable integration step with following relation of its to produce $\Delta_k = \omega_{k+1} - \omega_k$ (Zhao’s algorithm): $\omega_k = e^{(kx)^m} - 1$, where $m = 0.8$, $k = 1, 2, \dots, 400$ and $x = \frac{1}{k}(\ln(\omega_{\max} + 1))^{1/m}$, with $\omega_{\max} = 200$, integration time is 2094 seconds.

Figures 25.2 and 25.3 shows the displacement $u_2(t)$ and pore pressure $p_2(t)$ at the point with coordinates (0.5, 1.5, 0.5).

Proposed approach is proved to be an accurate and efficient method. We may observe that modified algorithm gives more accurate results with the same time cost. Further computations are obtained with inverse Algorithm 3.

25.4.2 Poroviscoelastic Solutions

The 3D poroelastic column loaded by a Heaviside-type function is considered as example to study the behavior of transformation method. The width of the column is

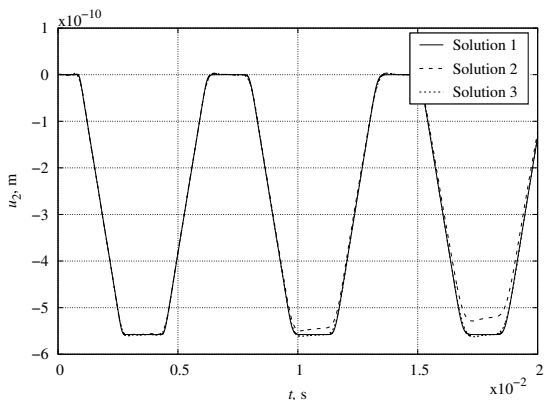


Fig. 25.2 Displacements $u_2(t)$ in case of different Laplace transform inversion algorithms.

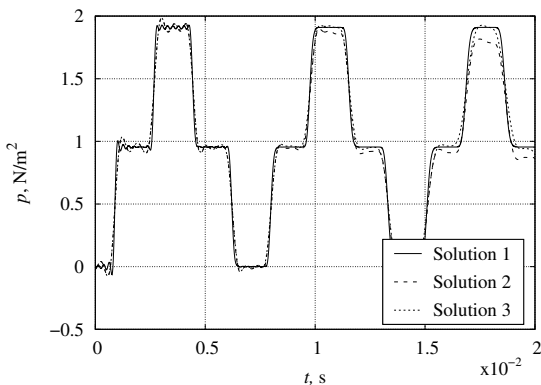


Fig. 25.3 Pore pressure $p(t)$ in case of different Laplace transform inversion algorithms.

1 m, the height 3 m. The column has zero displacements on one end and prescribed normal force on the other end. A boundary-element mesh of 1152 quadrangular elements is employed in computations. The problem statement is presented in Fig. 25.1. The parameters of the fully saturated porous material corresponds to the soil: $K = 2.1 \cdot 10^8 \text{ N/m}^2$, $G = 9.8 \cdot 10^7 \text{ N/m}^2$, $K_s = 1.1 \cdot 10^{10} \text{ N/m}^2$, $K_f = 3.3 \cdot 10^9 \text{ N/m}^2$, $\rho = 1884 \text{ kg/m}^3$, $\rho_f = 1000 \text{ kg/m}^3$, $\phi = 0.48$, $\kappa = 3.55 \cdot 10^{-9} \text{ m}^4/(\text{N} \cdot \text{s})$.

The principal differences may be observed when slow longitudinal wave is modeled. This wave has a large dispersion and is difficult to identify, so for its detection by numerical-analytical methods, it is necessary to artificially set a high values of permeability coefficient. On Fig. 25.4–25.5 calculation results with different permeability coefficients are presented.

On Fig. 25.4–25.5 calculation results with different permeability coefficients are presented.

For poroviscoelastic analysis standard linear solid model is employed. Standard linear solid model parameters are: $\theta = 10$, $\gamma = 10$, 1 and 0.1.

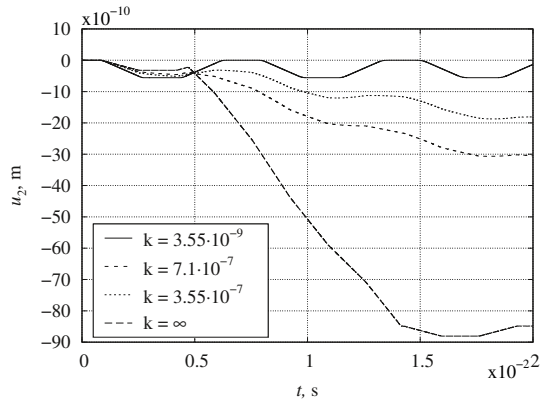


Fig. 25.4 Displacements $u_2(t)$ with different permeability coefficient value.

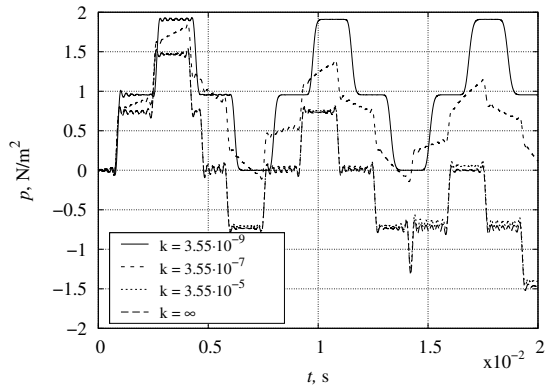


Fig. 25.5 Pore pressure $p(t)$ with different permeability coefficient value.

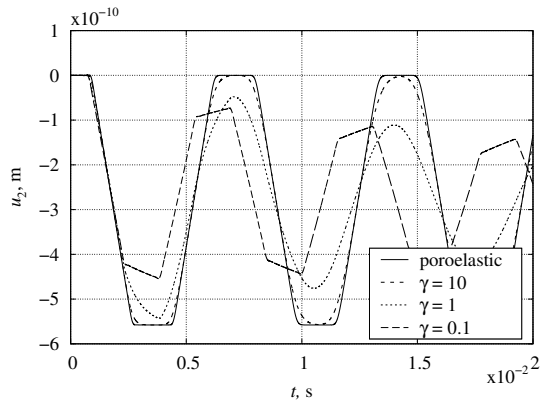


Fig. 25.6 Displacements $u_2(t)$ with different value of viscosity parameter.

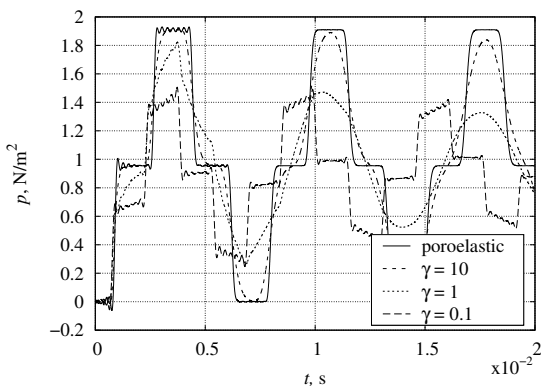


Fig. 25.7 Pore pressure $p(t)$ with different value of viscosity parameter.

An influence of material viscosity on transient responses of displacements and pore pressure is presented. On Fig. 25.6–25.7 the effect of the transition from instantaneous to equilibrium moduli in case of the standard linear solid model is presented.

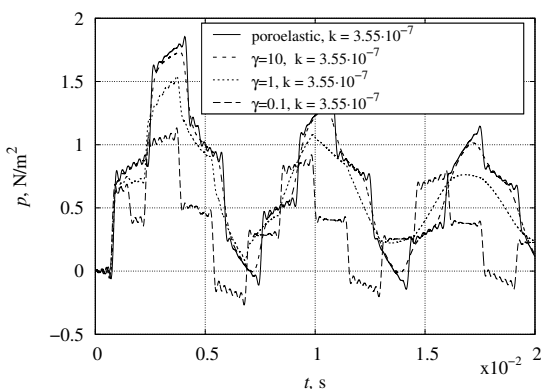


Fig. 25.8 Pore pressure $p(t)$ at the middle of the column for the increased permeability $\kappa = 3.55 \cdot 10^{-7}$ with different value of viscosity parameter.

On Fig. 25.8–25.9 presented poroviscoelastic solutions in case of increased of permeability coefficient and different values of viscosity parameter.

25.5 Conclusion

The results of numerical modeling of the poroviscoelastic medium are presented. The poroviscoelastic media modelling is based on Biot’s theory of porous material in combination with the elastic-viscoelastic corresponding principle. Boundary integral equations method and boundary element method are applied in order to

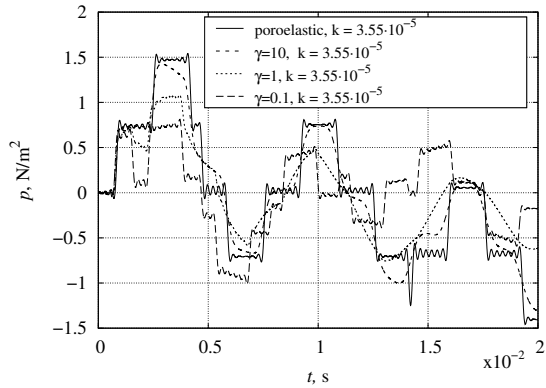


Fig. 25.9 Pore pressure $p(t)$ at the middle of the column for the increased permeability $\kappa = 3.55 \cdot 10^{-5}$ with different value of viscosity parameter.

solve three dimensional boundary-value problems. Viscous properties are described Standard linear solid models. A Laplace domain BEM formulation based on integral representations of the fundamental solutions has been presented for the analysis of three-dimensional poroviscoelastic problems. The boundary-element scheme is based on boundary integral equations for dynamic poroelasticity applied with time-step method of numerical Laplace transform inversion. The modified Durbin's methods were used to invert solution to the time domain. Numerical results comparison provided on the example of the problem about Heaviside-type load acting on the poroelastic column. Significant differences between numerical results are observed in case of slow longitudinal wave modeling. An influence of viscoelastic parameters on displacement responses is demonstrated on the example of a problem of the prismatic poroviscoelastic solid under Heaviside-type load. Proposed approach is proved to be an accurate and efficient method particularly well suited for the dynamic problems of the linear poroviscoelasticity.

Acknowledgements This work was supported by a grant from the Government of the Russian Federation (contract No. 14.Y26.31.0031) at the part problem formulation, numerical schemes modification and its verification, work was also supported by a grant of the Russian Science Foundation (16-19-10237-P) at the part of obtaining numerical results of permeability coefficient influence on poroviscoelastic responses.

References

- Bazhenov V, Igumnov L (2008) Boundary Integral Equations and Boundary Element Methods in Treating the Problems of 3D Elastodynamics with Coupled Fields. PhysMathLit
- Biot MA (1956a) General theory of deformation of a porous viscoelastic anisotropic solid. J Appl Phys 27:459–467
- Biot MA (1956b) Theory of propagation of elastic waves in a fluid-saturated porous solid. I. Low-frequency range. The Journal of the Acoustical Society of America 28(2):168–178

- Biot MA (1956c) Theory of propagation of elastic waves in a fluid-saturated porous solid. II. Higher frequency range. *The Journal of the Acoustical Society of America* 28(2):179–191
- de Boer R (1996) Highlights in the historical development of the porous media theory: Toward a consistent macroscopic theory. *Appl Mech Rev* 49(4):201–262
- Darcy H (1956) *Les Fontaines Publiques de la Ville de Dijon: Exposition et Application des Principes a Suivre et des Formules a Employer dans les Questions de Distribution Eau*. Dalmont
- Detournay E, Cheng AD (1993) Fundamentals of poroelasticity. *Analysis and Design Methods* pp 113–171
- Durbin F (1974) Numerical inversion of Laplace transforms: an efficient improvement to Dubner and Abate's method. *Computer Journal* 17(4):371–376
- Frenkel J (1944) On the theory of seismic and seismoelectric phenomena in a moist soil. *J Phys* 3(4):230–241
- Giorgio I, Andreas U, Scerrato D, dell'Isola F (2016) A visco-poroelastic model of functional adaptation in bones reconstructed with bio-resorbable materials. *Biomechanics and Modeling in Mechanobiology* 5(15):1325–1343
- Giorgio I, De Angelo M, Turco E, Misra A (2019) A Biot-Cosserat two-dimensional elastic non-linear model for a micromorphic medium. *Continuum Mechanics and Thermodynamics* doi: 10.1007/s00161-019-00848-1
- Goldshteyn R (1978) *Boundary Integral Equations Method: Numerical Aspects and Application in Mechanics*. Mir
- Madeo A, dell'Isola F, Darve F (2013) A continuum model for deformable, second gradient porous media partially saturated with compressible fluids. *Journal of the Mechanics and Physics of Solids* 11(61):2199–2211
- Schanz M (2001) *Wave Propagation in Viscoelastic and Poroelastic Continua: A Boundary Element Approach*. Springer-Verlag, Berlin
- Schanz M (2009) Poroelastodynamics: Linear models, analytical solutions, and numerical methods. *Applied Mechanics Reviews* 62(3):030,803
- Ugodchikov A, Hutoryanskii N (1986) *Boundary Integral Equations Method: Numerical Aspects and Application in Mechanics*. Kazan State University
- Zhao X (2004) An efficient approach for the numerical inversion of Laplace transform and its application in dynamic fracture analysis of a piezoelectric laminate. *Int J Solids Struct* 41:3653–3674



Chapter 26

Deformation and Destruction at Deformation Rate of Order 10^3 s^{-1} in Wood of Hardwood Trees

Anatoliy Bragov, Mikhail Gonov, Aleksander Konstantinov, Andrey Lomunov, and Tatiana Yuzhina

Abstract Tests on birch and aspen with different directions of cutting samples relative to the location of the fibers were performed. The tests were carried out on the installation with a Split Hopkinson Pressure Bar (SHPB) that implements the Kolsky method. The angles between the direction of application of the load and the direction of the location of the fibers were 0° , 30° , 45° , 60° and 90° . The experiments were carried out at temperatures of -40°C , $+20^\circ\text{C}$ and $+60^\circ\text{C}$. The strain rate was of the order of 10^3 s^{-1} . Dynamic stress-strain diagrams were obtained. The greatest steepness of the load branches and the greatest destructive stresses were observed for samples with a cutting angle of 0° . The smallest values of these parameters are noted at 90° cutting angle. It is noted that as the temperature of the test decreases, the magnitude of the stresses at which the specimens are destroyed increases for all the cutting angles of the specimens. There is a tendency to a decrease in the diagrams at a temperature of $+60^\circ\text{C}$ compared with the results at room temperature for almost all tested wood batches. At the same time, both the modules of the loading and unloading branches and the limiting (destructive) stresses decrease.

Keywords: Wood · Dynamic testing · Split-Hopkinson Pressure Bar · Cyclic compression · Shock loading

26.1 Introduction

In recent years, the number of shipments of nuclear waste, components of nuclear weapons, a wide range of toxic substances, etc. has increased, as well as grew up with

A. Bragov, M. Gonov, A. Konstantinov, A. Lomunov, T. Yuzhina
Research Institute for Mechanics, National Research Lobachevsky State University of Nizhni Novgorod, av. Gagarin 23b6, Nizhny Novgorod, 603950, Russia
e-mail: bragov@mech.unn.ru, gonov_mikhail@mech.unn.ru, konstantinov.al@yandex.ru, lomunov@mech.unn.ru, yuzhina_tatiana@mech.unn.ru

safety requirements during transportation. Calculations of the stress-strain state and strength of containers in which the above materials are transported are of particular importance. The problems of analyzing possible emergency situations are becoming more urgent. They are possible during transportation, may be accompanied by intense dynamic effects in the fall of containers, terrorist acts, man-made disasters, etc. Wood of different species can be used as one of the materials damping shock or explosive loading (Buchar et al, 2000; Adalian and Morlier, 1998; Eisenacher et al, 2013). It can mitigate the effects of such effects on containers and their contents. To reliably calculate the behavior of containers with similar damping materials under shock effects, data on the properties of wood are necessary. In particular, the dynamic stress-strain diagrams. Wood is a natural polymer composite material that has been used throughout history in wide technical applications (Johnson, 1986; Neumann, 2009). Timber has many advantages, including low weight, environmental friendliness and renewability. Knowledge of mechanical properties is the basis of theoretical models and engineering analysis. In wood, grain structure, density, moisture, annual rings and other natural factors are variable, but they must be taken into account when developing models of wood behavior, including dynamic effects. A composite model of wood has been studied over the years and has made significant progress. New models can consider the influence of temperature and strain rate, and in most cases can satisfy the requirements for wooden structures under impact loadings. However, the complexity of wood means that no model can be used for all purposes, and different models must be used to solve various specific problems. Simple theoretical models have been developed and continue to be developed to describe the consequences of phenomena that are caused by inertial effects active on the scale of the cellular structure of wood, i.e. microinertial effects. From the point of view of materials science, these models are based on the assumption that the tree is insensitive to speed, and the increase in destructive stresses is explained by the influence of inertial effects, and not the effects of viscoelasticity or viscoplasticity. In Reid et al (1993); Reid and Peng (1997); Harrigan et al (2005), a wood model was proposed that takes into account precisely the inertial effects. Misra suggested treating wood as a viscoelastic material that undergoes damage using the granular micromechanics approach (Misra and Singh, 2013; Misra and Poorsolhjoui, 2015, 2016; Giorgio et al, 2019). This approach assumes that the material has a granular mesostructure and is considered as a discrete or a particulate system. A micro-mechanical model devoted to study large deformations of cohesive granular media subjected to quasi-static external actions is presented and discussed (Turco, 2018). In recent years, scientists have focused on studying the effect on the mechanical properties of wood of its density, moisture, structure, cutting angle and type of stress-strain state (Widehammar, 2004; Allazadeh and Wosu, 2012; Zhao et al, 2016; Wouts et al, 2016). In these works, for a number of wood species, the most important characteristics were obtained, such as dynamic strain diagrams, ultimate strength and deformation characteristics, fracture energy, and the dependences of these characteristics on the strain rate were constructed.

26.2 Experimental Methods and Investigated Samples

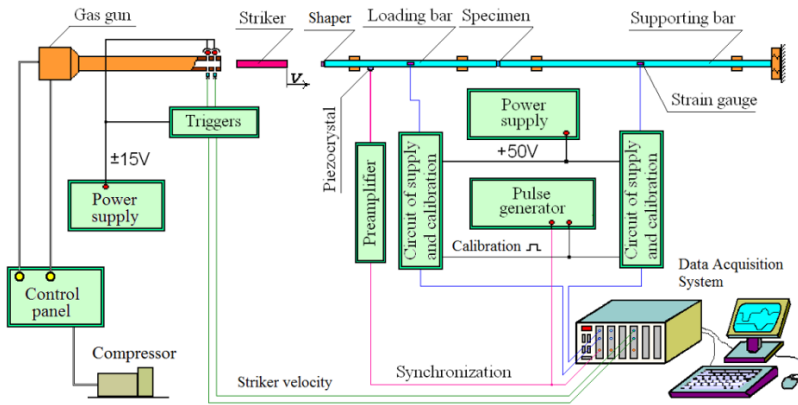


Fig. 26.1 Scheme of the set-up for compressive tests implements the Kolsky technique

The installation, which implements the Kolsky technique with a split Hopkinson pressure bar (figure 26.1) was used to study the dynamic properties of wood under compression (Bragov and Lomunov, 1995).

The Kolsky method (Kolsky, 1949) is based on the one-dimensional theory of the propagation of elastic waves in long thin bars. Traditionally, a system for testing under uniaxial compression consists of two long bars (loading and supporting) with sufficiently high yield strength as well as a thin sample in the form of a tablet located between their ends. Using a compact gas gun, an elastic compression pulse with amplitude proportional to the velocity of the impactor is excited in the loading bar. The measurement of elastic strain impulses in measuring bars is performed using low-base strain gauges glued on the lateral surface of measuring bars. During the test, the loading strain pulse $\epsilon_i(t)$ is recorded, the shape, amplitude and duration of which are determined by the choice of the length, material and speed of the striker accelerated in the barrel of the gas gun. The monitoring of this impulse allows one to evaluate the identity of the loading conditions of the test sample (in order to reveal the dispersion of properties), or to reveal the influence of any loading parameter on the dynamic behavior of the material under study. In addition, the reflected $\epsilon_r(t)$ from the sample and the transmitted $\epsilon_t(t)$ through it strain pulses are recorded, which are the “responses” of the material to the applied load and make it possible to construct a dynamic $\sigma(\epsilon)$ diagram of the test specimen under uniaxial stress condition (Kolsky, 1949).

The split-Hopkinson pressure bar had a diameter of 20 mm, made of aluminum alloy D16T. When testing wood, foam and loose soils there is a big difference in the acoustic impedances ρC (ρ and C are the material density and the sound velocity

in it, respectively) of the measuring bars and the specimen. The amplitude of the reflected pulse can reach 90% of the amplitude of the loading wave. In this case, the specimen is exposed to several loading cycles. To reliably record repeated loads during one experiment, it is necessary to exclude the effect on the loading process in the second and subsequent cycles of the pulse transmitted through the sample and then reflected from the back end of the supporting bar in the form of a tensile wave. For this to be achieved, the length of the supporting bar must be increased compared with the length of the loading bar (Bragov et al, 2001). The length of the supporting bar is increased by as many times as the loading cycles need to be registered. In this series of experiments, the loading bar had a length of 1.5 m, a supporting bar was 4.5 m, which made it possible to record one main and two additional loading cycles (figure 26.2).

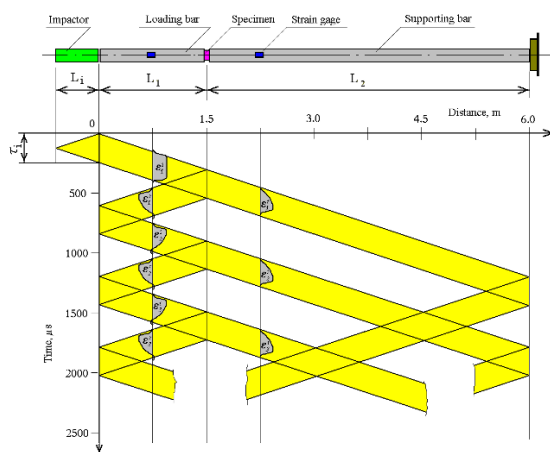


Fig. 26.2 Picture of wave propagation in the SHPB system during the registration of three sample loading cycles.

The mechanical properties of wood depend on the density, moisture, and even for one species are not the same, this is a consequence of different growing conditions of trees. In addition, the mechanical characteristics, such as elastic moduli, tensile strength and compression, can be significantly affected by the variability of properties in different parts of the trunk, different moisture, porosity, width of annual rings, etc. Some static characteristics of aspen and birch at a moisture of $\sim 15\%$ are presented in the table 26.1.

Specimens of air-dry birch and aspen (figure 26.3) for testing were fabricated in the form of tablets with a diameter of ~ 20 mm and a height of ~ 10 mm at different cutting directions relative to the axis of the tree trunk. The moisture content of the specimens was $\sim 10\%$. The moisture content of the samples was determined by the difference in mass of the sample in the initial state and after drying in an oven at a temperature of 100°C for 6 hours. To assess the degree of anisotropy, the angles between the direction of application of the load and the direction of the location of the fibers were 0° , 30° , 45° , 60° , and 90° for each material. The tests were carried out under uniaxial stress conditions. Since containers can be transported in different

Table 26.1 Static properties of the test woods

| Wood species | Density, g/cm^3 | Moisture, % | Compressive modulus | | Strength along | |
|--------------|--------------------------|-------------|-----------------------|------------------------|--------------------|------------------------|
| | | | along the fibers, MPa | across the fibers, MPa | at stretching, MPa | under compression, MPa |
| Birch | 0.62 | 15 | 16660 | 1124 | 120 | 45 |
| Aspen | 0.50 | 15 | - | - | 111 | 37 |

**Fig. 26.3** a) Aspen specimen, b) Birch specimen

climatic conditions, the tests were carried out at room temperature, as well as at temperatures of $+60^\circ\text{C}$ and -40°C .

For testing specimens at elevated temperatures ($+60^\circ\text{C}$) a miniature oven was used. It has a tubular structure. The tube oven is put on the ends of the measuring bars and the specimen located between them. For testing specimens at a temperature of -40°C , a detachable foam container was made. It contained a metal cuvette with liquid nitrogen. The test temperature was regulated by decreasing or increasing the gap between the lower and upper container halves. Samples before experiments were kept at the required temperature for several hours due to the very low thermal conductivity of the wood.

As an example, figure 26.4 shows diagrams $\sigma \sim \epsilon$ of birch specimens with different directions relative to the wood grain orientation at different temperatures. Each group is represented by two diagrams: one is characteristic of “elastic” deformation of samples at a low strain rate ($600 \dots 800 \text{ s}^{-1}$) and preserving their integrity. The other characterizes the behavior of materials in the event of their destruction (at strain rates of $1500 \dots 3000 \text{ s}^{-1}$). For each diagram, the dotted lines show the strain rates histories, the corresponding axis is on the right. The diagrams are located on the deformation axis conditionally with separation along the deformation axis. This allows you to more clearly assess the effect of strain rate. It is better to consider the initial sections of the diagrams, since they do not overlap each other.

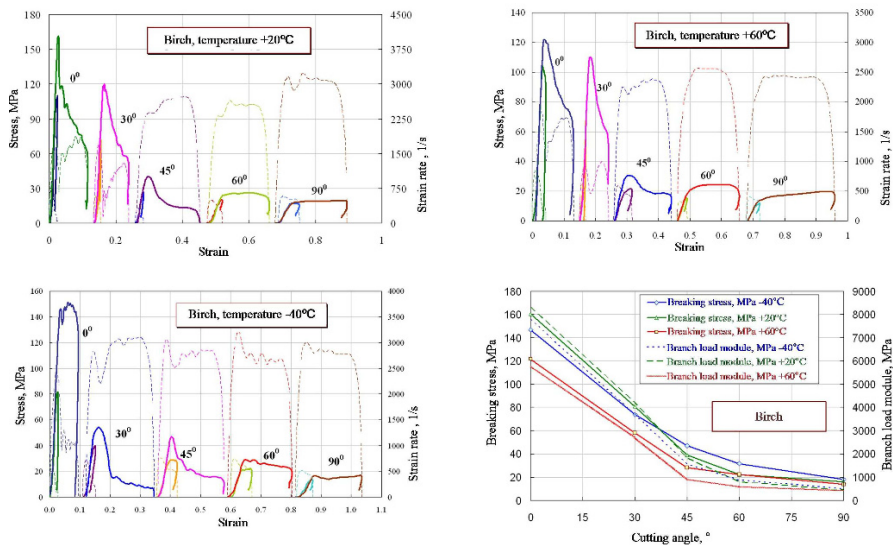


Fig. 26.4 Test results of birch specimens

The well-known tendency of a reduction in the strength properties of wood as a function of increasing sectioning angle to the wood grain is well demonstrated in the data presented (Bol’shakov et al, 2001; Bragov and Lomunov, 1997; Bragov et al, 2006). The largest values of the modules of the loading branches and failure stress are inherent in the specimens for all wood species with a cutting angle of 0° to the fiber orientation. The smallest values were for specimens with a cutting angle of 90°. Significant stress relaxation is seen for small cutting angles. A decrease in the bearing ability of the wood is seen for an increase in the degree of deformation. For the cutting angle 90°, the bearing capacity not only does not decrease, but, on the contrary, the material exhibits a certain hardening property.

A similar set of diagrams was obtained when testing aspen (figure 26.5).

It is interesting to compare the properties of different wood species under the same conditions. This is necessary to select the optimal breed for use in a protective structure. You need to choose the material that has the greatest strength and damping properties. As an example, Figure 26.6 shows a comparison of the properties of two wood species at room temperature. The energy absorption of the material was calculated as the area under the stress-strain curve. Sets of curves at different angles of cutting are also located on the strain axis conditionally for convenience of consideration. It is seen that birch has a higher strength properties and energy absorption, both along and across the fibers. The strength of both tested wood species along the fibers is an order of magnitude higher than across the fibers.

Quantitative assessment of the dynamic properties of wood will be used to equip the developed forecast models with parameters. Such models are necessary for

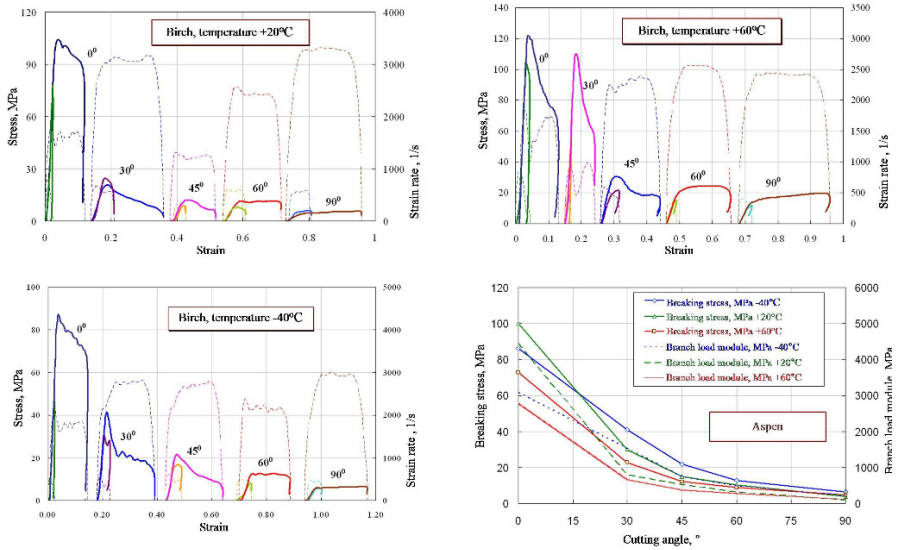


Fig. 26.5 Test results for aspen specimens

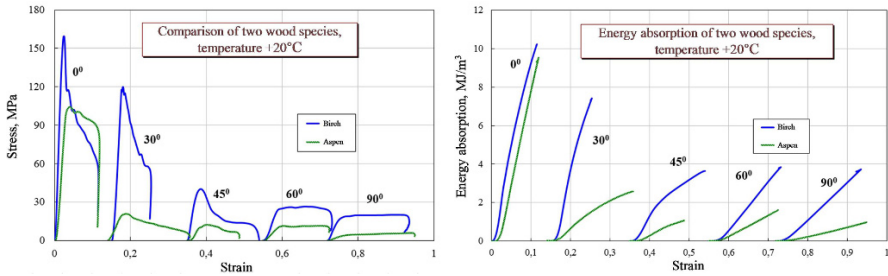


Fig. 26.6 Comparison of the strength properties and energy intensity of two wood specimens at room temperature

numerical modeling and optimization of structures using different species of wood as a damping material.

26.3 Conclusion

Dynamic testing of birch and aspen in a wide temperature range has been performed. The long duration of the specimen unloading process is noted. It exceeds the duration of the loading pulse several times. The entire unloading process of the specimen cannot be recorded due to insufficient length of the measuring bars.

There is a strong anisotropy of the properties of materials. Specimen with the direction of the fibers along the direction of the load had the greatest strength. The smallest across the direction of the load. The module of the load branch of the diagrams is nonlinear and, as a rule, smaller than the module of the discharge branch (while maintaining the integrity of the sample). The average value of the birch load branch with an angle of 0° has the largest value in the temperature range studied. The magnitude of the modules of the load branches of almost all batches of specimens at low temperature is higher than at normal temperature. The nature of the deformation and destruction of specimens strongly depends on the angle of cutting materials.

In this series of experiments with an angle of 30° , after exhaustion of the material the bearing ability, a section of relaxation was noted for both types of wood. This area smoothly passes into the area of ideal “plasticity” (or even a small “hardening”) until the end of the load. On the one hand, the reason for this behavior can be the destroying of relatively weak bonds between obliquely spaced annual cylindrical layers and the mutual displacement of these layers. On the other hand, the presence of friction on the ends of the sample and a sufficiently small angle of “reinforcement”, which limits this process and causes the fibers themselves to be included in the work.

With a decrease in the temperature of the test, the magnitude of the stresses at which the destruction of the specimens occurs increases for all the tested rocks for all the cutting angles of the specimen.

The obtained dynamic properties of wood will be used in the future to carry out numerical calculations of the behavior of protective containers under conditions of high-speed loading and the choice of their optimal design.

Acknowledgements Dynamic tests of birch were performed with partial financial support from the RFBR (grant 18-08-00808). Research of aspen behavior was supported by the grant from the Government of the Russian Federation (contract No. 14.Y26.31.0031)

References

- Adalian C, Morlier P (1998) Modeling the behavior of wood during the crash of a cask impact limiter. In: Packaging and transportation of radioactive materials, France: Societe Francaise d'Energie Nucleaire - SFEN
- Allazadeh MR, Wosu SN (2012) High strain rate compressive tests on wood. *Strain* 48(2):101–107
- Bol'shakov AP, Balakshina MA, Gerdyukov NN, Zotov EV, Muzyrya AK, Plotnikov AF, Novikov SA, Sinitsyn VA, Shestakov DI, Shcherbak YI (2001) Damping properties of sequoia, birch, pine, and aspen under shock loading. *Journal of Applied Mechanics and Technical Physics* 42(2):202–210
- Bragov A, Lomunov AK (1997) Dynamic properties of some wood species. *Le Journal de Physique IV* 7(C3):C3–487
- Bragov A, Lomunov A, Sergeichev I (2001) Modification of the Kolsky method for studying properties of low-density materials under high-velocity cyclic strain. *J App Mech Tech Phys* 42(6):1090–1094
- Bragov A, Lomunov A, Sergeichev IV, Gray III GT (2006) Dynamic behaviour of birch and sequoia at high strain rates. In: AIP Conference Proceedings, American Institute of Physics, vol 845, pp 1511–1514

- Bragov AM, Lomunov AK (1995) Methodological aspects of studying dynamic material properties using the Kolsky method. *Int J ImpEng* 16(2):321–330
- Buchar J, Severa L, Havlicek M, Rolic S (2000) Response of wood to the explosive loading. *Le Journal de Physique IV* 10(PR9):Pr9–529
- Eisenacher G, Scheidemann R, Neumann M, Wille F, Droste B (2013) Crushing characteristics of spruce wood used in impact limiters of type B packages. *PATRAM* 2013
- Giorgio I, De Angelo M, Turco E, Misra A (2019) A Biot–Cosserat two-dimensional elastic nonlinear model for a micromorphic medium. *Continuum Mechanics and Thermodynamics* doi: 10.1007/s00161-019-00848-1
- Harrigan JJ, Reid SR, Tan PJ, Reddy TY (2005) High rate crushing of wood along the grain. *International Journal of Mechanical Sciences* 47(4-5):521–544
- Johnson W (1986) Historical and present-day references concerning impact on wood. *International Journal of Impact Engineering* 4(3):161–174
- Kolsky H (1949) An investigation of the mechanical properties of materials at very high rates of loading. *Proceedings of the physical society Section B* 62(11):676
- Misra A, Pooorsolhjoui P (2015) Identification of higher-order elastic constants for grain assemblies based upon granular micromechanics. *Mathematics and Mechanics of Complex Systems* 3(3):285–308
- Misra A, Pooorsolhjoui P (2016) Granular micromechanics based micromorphic model predicts frequency band gaps. *Continuum Mechanics and Thermodynamics* 28(1-2):215–234
- Misra A, Singh V (2013) Micromechanical model for viscoelastic materials undergoing damage. *Continuum Mechanics and Thermodynamics* 25(2-4):343–358
- Neumann M (2009) Investigation of the behavior of shock-absorbing structural parts of transport casks holding radioactive substances in terms of design testing and risk analysis. *BAM dissertation series* 45
- Reid SR, Peng C (1997) Dynamic uniaxial crushing of wood. *International Journal of Impact Engineering* 19(5-6):531–570
- Reid SR, Reddy TY, Peng C (1993) Dynamic compression of cellular structures and materials. *Structural crashworthiness and failure* pp 257–294
- Turco E (2018) In-plane shear loading of granular membranes modeled as a lagrangian assembly of rotating elastic particles. *Mechanics Research Communications* 92:61–66
- Widehammar S (2004) Stress-strain relationships for spruce wood: Influence of strain rate, moisture content and loading direction. *Experimental mechanics* 44(1):44–48
- Wouts J, Haugou G, Oudjene M, Coutellier D, Morvan H (2016) Strain rate effects on the compressive response of wood and energy absorption capabilities—Part A: Experimental investigations. *Composite Structures* 149:315–328
- Zhao S, Zhao JX, Han GZ (2016) Advances in the study of mechanical properties and constitutive law in the field of wood research. In: *IOP Conference Series: Materials Science and Engineering*, IOP Publishing, vol 137, p 012036

Part V
Masonry Structures



Chapter 27

Effect of Shape Uncertainties on the Collapse Condition of the Circular Masonry Arch

Nicola Cavalagli, Vittorio Gusella, and Riccardo Liberotti

Abstract Heritage buildings, worldwide, are marked by the presence of masonry structural elements often affected by shape irregularities if compared with their initial condition. The trigger factors of such geometrical uncertainties can be ascribed to the over centuries deformation processes, to environmental factors or upstream to the constructive methods. The aim of the present paper is the evaluation of the influence of shape irregularities on the collapse condition of circular masonry arches in presence of horizontal seismic actions. In order to take into account a more reliable estimation of the arches bearing capacity a random generative model is developed considering shape uncertainties. A limit analysis based procedure, referring to Heyman's theory, is used in order to evaluate the horizontal loads multiplier. Then the collapse condition is studied through a probabilistic approach, by analysing the statistical moments up to second order of the results obtained by a Monte Carlo simulation.

Keywords: Unreinforced arch · Masonry structures · Shape uncertainties · Generative modelling · Limit analysis

27.1 Introduction

Masonry arch is one of the most diffused constructive system over architectural heritage buildings and infrastructures (Breccolotti et al, 2018; Galassi and Tempesta, 2015) and even now studied with several approaches (Andreus, 1990; Cazzani et al, 2016b,a; Stockdale et al, 2018; Grillanda et al, 2019; Tempesta and Galassi, 2019) not only to increase the knowledge about its behaviour in relation to the structural safety, including the use of new materials for strengthening (Autuori et al, 2017; Bertolesi

N. Cavalagli, V. Gusella, R. Liberotti

Department of Civil and Environmental Engineering, University of Perugia, Perugia, Italy
e-mail: nicola.cavalagli@unipg.it, vittorio.gusella@unipg.it, riccardo.liberotti@unipg.it

© Springer Nature Switzerland AG 2020

B. E. Abali and I. Giorgio (eds.), *Developments and Novel Approaches in Nonlinear Solid Body Mechanics*, Advanced Structured Materials 130,
https://doi.org/10.1007/978-3-030-50460-1_27

455



Fig. 27.1 Monastery Of Hosios Loukas in Greece. In dashed white lines the circular arc with nominal thickness and radius.

et al, 2018; Simoncello et al, 2019), but also for the purpose of conservation of its historical value. It is well known that the shape of historical structures is generally affected by irregularities (Ochsendorf, 2006; Cavalagli and Gusella, 2015; Aita et al, 2016; Pepi et al, 2017; Zampieri et al, 2018) due to several reasons: the weathering of materials, the action of long term deformation phenomena, local/global damages occurred over time, as well as the imperfections of the construction process, and more (Fig. 27.1).

In this framework, in addition, the scientific literature presents a lack of studies about the influence of such geometrical uncertainties on the bearing capacity of masonry structures, with the exceptions of specific contributions where the geometric features of the arches were deeply studied (De Arteaga and Morer, 2017), or where the damage pattern was described as deterministic or parametric variables (Zampieri et al, 2016, 2019). In previous papers (Cavalagli et al, 2016, 2017; Severini et al, 2018), the effects of geometrical uncertainties on the structural behaviour of masonry arches have been evaluated respectively with static and dynamic simulations. In those studies the uncertainties have been related to the voussoirs stereometry and size while deterministic characteristics were assumed for arch typology. Those first outcomes highlighted that for a certain magnitude of uncertainties the drop of strength cannot be neglected, as already pointed by several authors throughout the results of experimental tests (Ochsendorf, 2006; Romano and Ochsendorf, 2010; Zampieri et al, 2018).

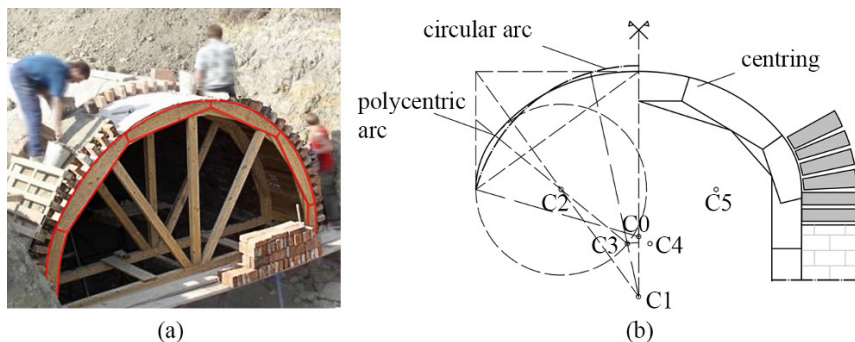


Fig. 27.2 (a) Construction of a masonry vault by means of centring; (b) Example of geometrical description of a centring as a polycentric arc.

Differently, the present contribution is aimed at proposing a probabilistic approach to assess the influence of the shape uncertainties described as the variation from a nominal geometry. That peculiarity is ascribed to the constructive methods related to the employment of the wooden frames, known as centring, designed according to ancient empirical rules. In order to take into account such features, a parametric model of a polycentric arch is developed, allowing to obtain random geometries starting from a deterministic nominal one, through the generation of different circular arcs modelled according to a family of input variables and connected together ensuring the tangent continuity.

By referring to Heyman's theory, a limit analysis based procedure was developed in order to evaluate the horizontal loads multiplier of the arches subject to horizontal seismic action. Then, by means of Monte Carlo simulation, the collapse condition was studied, whose statistical moments up to second order and probability density functions was rated for different levels of uncertainties. The comparison between the results for the nominal geometry and those obtained studying the reconfigured random arches outlined the influence of that shape uncertainties towards the bearing capacity of those masonry structures.

27.2 Generative Modelling of Masonry Arches with Uncertain Shape

27.2.1 Geometrical hypotheses

The arched structures are one of the most ancient load-bearing systems used already in the IV millennium b.C. This constructive technique foresees the use of a temporary shoring: the centring (Fig. 27.2(a)). Those elements are essential to prop up the voussoirs until they became a self-supporting masonry structure. The design of

such wooden frames envisages the union of different arc sectors with a view to outline the intrados corresponding with the designed arch (Veihelmann and Stefan, 2015). It is conceivable that such a construction process may result in geometrical imperfections affecting the final arch shape, so that, in this paper, this topic is ascribed as a-priori source of uncertainties and therefore investigated. A first attempt useful to describe the centring design, conceived by composition of several arc sectors, was the geometrical descriptive approach, i.e. the graphic construction of the polycentric arch, which is chosen as the reference shape for the following modelling implementation (Figure 27.2(b)).

27.2.2 The Random Defined Polycentric Arch

In literature Veihelmann and Stefan (2015) reported that the number of the arc sectors which constitute a centring is related to the vernacular constructive customs and to the project-size of the pursued arch. Without loss of generality in the method presentation, in this work polycentric arches composed by five arc sectors were studied, since it results a recurring circumstance for mildly sized arches. In order to achieve a simulation of the constructive method closer to the real one, the modelling procedure of the polycentric arches was addressed with a probabilistic approach by means of input random variables, which allow to obtain asymmetrical and irregular 2D random arches, starting from a nominal deterministic geometry. Five arcs are generated according to the values of the aforementioned parameters and assembled sequentially maintaining the tangent continuity all along the polycentric arch. The centre of every sector was forced to be on the line connecting the end point of the previous arc with its centre, ensuring the same tangent between adjacent arc sectors (Figure 27.3).

The circular arch has been selected as nominal geometry and it is defined by the following geometrical parameters

$$\begin{cases} \alpha = 180^\circ - 2\beta = 157.5^\circ \\ t/r_n = 0.15 \end{cases} \quad (27.1)$$

being α the angle of embrace, β the angle at the springer, r_n the radius and t the thickness. In the proposed model the angles, respectively of embrace ($\tilde{\alpha}_i$) and at the springer ($\tilde{\beta}_i$), and the radius of each single sector (\tilde{r}_i) are defined as random variables of whom the values are extracted starting by uniform probability density functions, referred to the nominal features for the mean values and to a priori tolerance values (ζ, χ, ε) for the lateral bounds delimiters (Figure 27.4)

$$\tilde{\beta}_i = E[\tilde{\beta}_i] + \zeta\beta\tilde{p}_{\beta_i} = \beta(1 + \zeta\tilde{p}_{\beta_i}) \quad (27.2)$$

$$\tilde{r}_i = E[\tilde{r}_i] + \chi r\tilde{p}_{r_i} = r(1 + \chi\tilde{p}_{r_i}) \quad (27.3)$$

$$\tilde{\alpha}_i = E[\tilde{\alpha}_i] + \varepsilon\alpha/n_s\tilde{p}_{\alpha_i} = \alpha/n_s\tilde{p}_{\alpha_i} = \alpha/n_s(1 + \varepsilon\tilde{p}_{\alpha_i}) \quad (27.4)$$

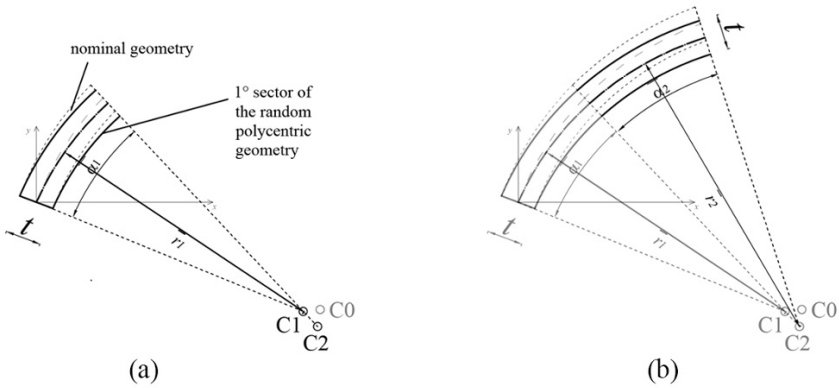


Fig. 27.3 Generation of the random polycentric arch: (a) location of C_2 on the line joining the previous sector’s end point and its C_1 ; (b) the new arc sector is created according to the random amplitude of its angle of embrace and to the length of its radius.

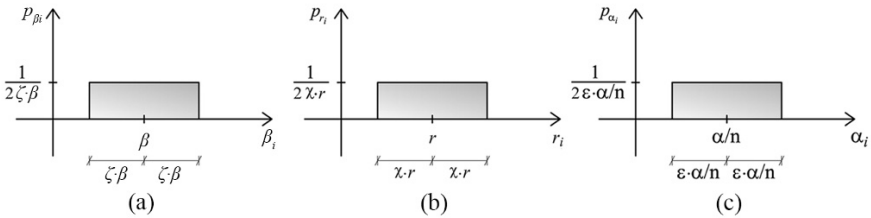


Fig. 27.4 Uniform probability density functions of the random angle at the springers $\tilde{\beta}_i$ (a), radius \tilde{r}_i (b) and angle of embrace $\tilde{\alpha}_i$ (c) of the arc sectors defining the irregular polycentric arch.

in which n_s indicates the number of arc sectors outlining the polycentric arch. The introduction of the parameter $\tilde{\beta}_i$ entails that the centre C_1 falls on a position not belonging to the line joining the C_0 and the first point of the polycentric arch. On the other hand, the thickness (t) and the span (l) are defined with their nominal values (Figure 27.5).

The deterministic value of the span represents a geometrical constraint necessary to make sets of arch samples comparable according to the ratio l/t . Moreover, this condition finds confirmation in the assumption that, usually, the span between the two piers is a predefined property, independently from the uncertainties related to the construction process. Considering the established geometrical rules, the probabilistic model generates the curved line passing through the centres of the joints. Since the thickness is a constant feature, its offsets outline the extrados and the intrados of the final arch profile. As mentioned, all the analyses have been conducted for a number of arc sectors (n_s) equal to five. The random parameter values were extracted from their own probability density functions (Figure 27.4) according to the equations (27.2), (27.3) and (27.4) producing 1000 samples of polycentric arches according

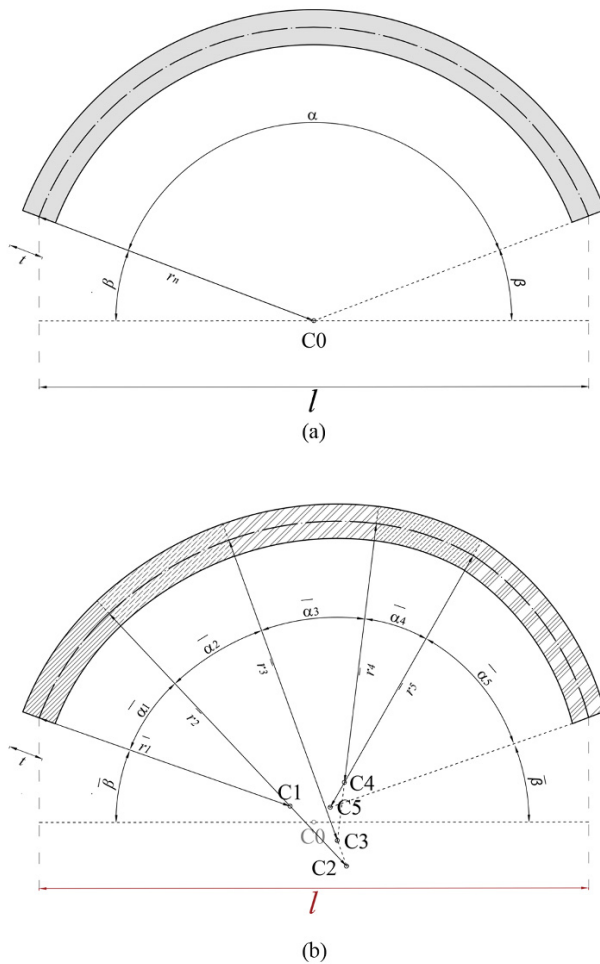


Fig. 27.5 (a) Nominal circular arch. (b) A generic sample of the random polycentric arch.

to the span constraint. The magnitudes of the uncertainties have been fixed at 0.10 for χ and ε , and 0.05 for ζ . This last range has been estimated following statistical evaluations deriving from a first attempt of modelling.

27.3 Limit Equilibrium Analysis

A limit analysis based procedure, referring to Heyman’s theory, finalized at the evaluation of the in-plane collapse condition of the masonry arch was developed.

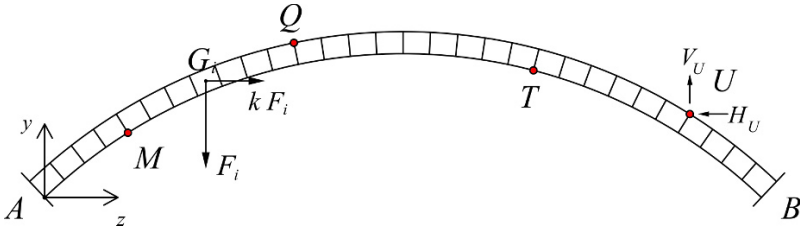


Fig. 27.6 Generic four-hinges collapse mechanism for an arch involved by vertical and horizontal loads.

The following hypotheses were considered: *i*) equilibrium condition (the line of thrust must be in equilibrium with the external loads), *ii*) resistance criterion (infinite compressive strength and no-tensile material, so that the thrust line fits everywhere within the thickness of the arch) and *iii*) mechanism condition (no slip can occur between the blocks). The arch is discretized in n voussoirs, resulting in $n + 1$ joints, not representing a specific stereotomy but only for the numerical resolution of the problem. A loads system considering the self-weight and the inertial horizontal actions, which were assumed to be directed from left to right, was applied. In the framework of such limit analysis, the horizontal actions were assumed as proportional to the dead loads through a multiplicative factor k . Being γ_m the masonry specific weight, it follows that the vertical (F_i) and horizontal (F_{S_i}) forces applied to the barycenter G_i of the area of the A_i of the i th voussoir (Figure 27.6) are defined as

$$F_i = \gamma_m A_i d \quad F_{S_i} = k F_i \tag{27.5}$$

It's well known as in presence of horizontal loads the collapse mechanism of a circular arch is characterized by four hinges, which occur alternatively at the intrados and at the extrados. According to this approach, once the arch's geometry has been generated, the position of the collapse hinges M , Q , T and U (Figure 27.6) and the corresponding horizontal load multiplier have been calculated by the iterative procedure which is articulated as follows. A first attempt configuration of the hinges is assumed; by denoting with V_U and H_U the vertical and horizontal internal forces at the hinge U , the momentum equilibrium around the remaining hinges gives

$$H_U(y_h - y_U) + V_U(z_h - z_U) - \sum_{i=1}^{n_{hU}} F_i(z_h - z_{G_i}) - k \sum_{i=1}^{n_{hU}} F_i(y_h - y_{G_i}) = 0 \tag{27.6}$$

where $h = T, M, Q$ qualifies the generic remaining hinge and n_{hU} represents the number of voussoirs comprised between the corresponding hinges. The resolution of the system of three equations deriving from the equation (27.6) leads to the three unknowns V_U , H_U and the k . By means of simple calculations, the internal forces involving each joint have been obtained

$$\begin{cases} N_j = H_j \cos \phi_j \pm V_j \sin \phi_j \\ M_j = V_U(z_U - z_{P_j}) + H_U(y_U - y_{P_j}) \mp \sum_{i=1}^{n_{jU}} F_i(z_{G_i} - z_{P_j}) \mp k \sum_{i=1}^{n_{jU}} F_i(y_{G_i} - y_{P_j}) \end{cases} \quad (27.7)$$

with ϕ_j the angle between the line perpendicular to the j th joint and the horizontal one and

$$\begin{aligned} H_j &= H_U \mp k \sum_{i=1}^{n_{jU}} F_i \\ V_j &= -V_U \pm \sum_{i=1}^{n_{jU}} F_i \end{aligned} \quad (27.8)$$

Finally, the line of thrust is obtained by linking the centres of pressure of the normal forces evaluated in each joint, defined by the eccentricity

$$e_j = \frac{M_j}{N_j} \quad (27.9)$$

where j denotes the generic joint. In addition the line of thrust must be contained between the intrados and extrados line order to satisfy the resistance criterion, i.e. the following condition must be satisfied at each joint

$$-\frac{t}{2} \leq e_j \leq \frac{t}{2} \quad (27.10)$$

It should be highlighted that the symbol of equality holds only for the hinges M , Q , T and U . Usually, the first trial hinges configuration is not the right one, so that the hinges have to be moved over to other positions and the equilibrium must be imposed again, until equation (27.10) is satisfied.

27.4 Analysis of the Results

Within this section the results obtained for the random polycentric arches, mainly in terms of the collapse load multiplier k , are reported and compared with the value corresponding to the nominal geometry. In Figure 27.7 the overlapping of 1000 samples of arches affected by shape uncertainties (black lines) and the arch having nominal geometry (red line) is shown. In particular, each curve represents the line of axis of the corresponding arch. The generic random arch is compared with the nominal geometry through a radial distance parameter ρ referred to the centre of the nominal arch (Figure 27.8), which has been introduced to obtain a measure of the shape uncertainty. In the application of the aforementioned numerical procedure, each arc sector was discretized into an equal number of voussoirs ($n_i = 30$), so that the total number of voussoirs allows to reach an almost exact solution (Figure 27.8).

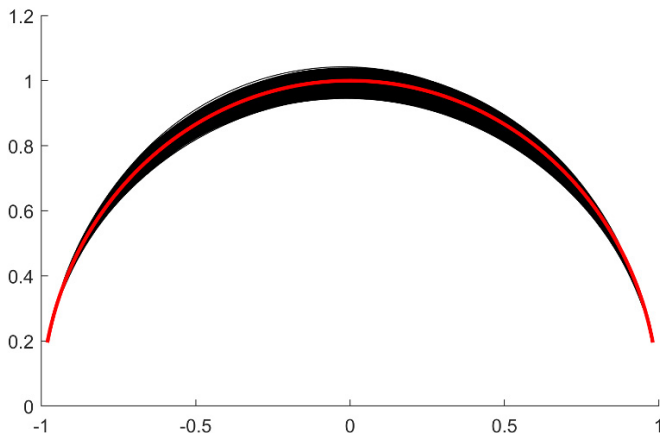


Fig. 27.7 Graphical comparison between 1000 samples of random arches (black line) and the nominal geometry (red line).

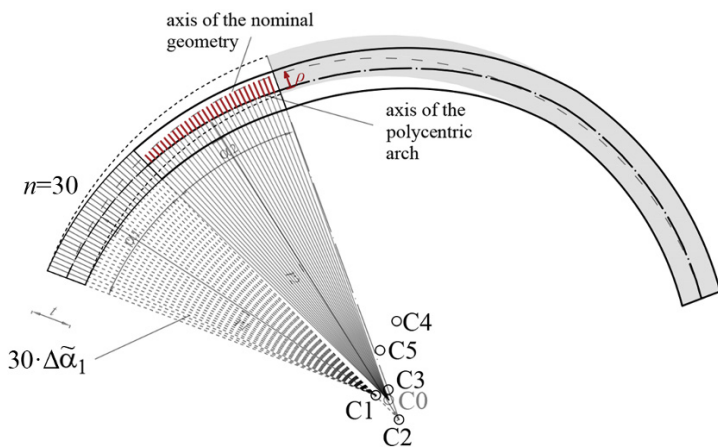


Fig. 27.8 Discretization detail of the random polycentric arch (e.g. resulting partitions of the first sector $\tilde{\alpha}_1$) and graphical definition of the distance parameter ρ on the second sector.

In Figure 27.9 the statistical analysis of the generated samples is represented. In particular, Figure 27.9(a) shows the $\tilde{\rho}$ random parameter distance from the nominal axis line in function of the dimensionless curvilinear abscissa ξ of the generic arch, with the overlapping of the mean values of them ($\bar{\rho}(\xi)$) evaluated in each joint (thick black line). At the same time, in Figure 27.9(b) the standard deviation of the random parameter $\sigma(\tilde{\rho})$ is plotted along the development of the arch. The results of the geometrical modelling highlight that the work hypotheses ($\varepsilon = \chi = 0.1$ and

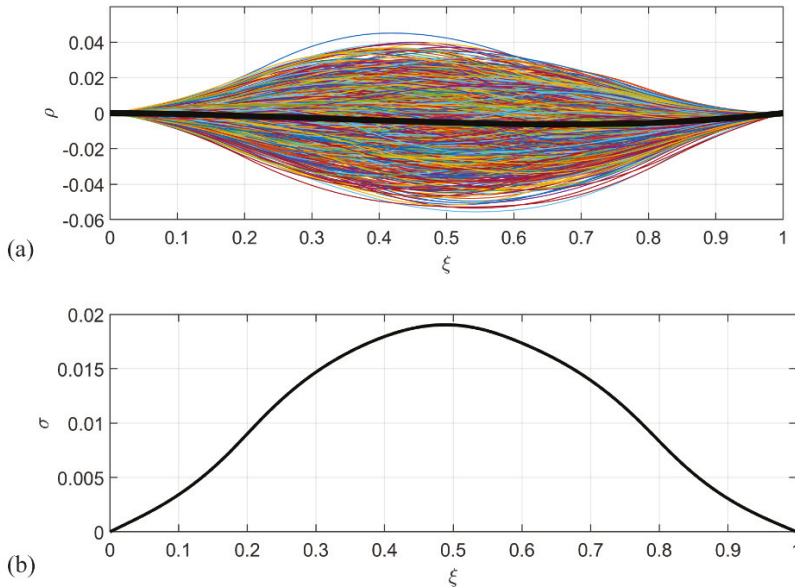


Fig. 27.9 Probabilistic modelling of the random polycentric arch: trend of $\tilde{\rho}$ parameter with mean values highlighted in black thick line (a) and standard deviation (b) in function of the dimensionless curvilinear abscissa ξ

$\beta = 0.05$) determine maximum values of the ρ parameter around 0.05, due to the particular construction procedure of the polycentric random arch.

In order to take into account the asymmetry of the random arch configuration, the collapse condition was evaluated in both the directions of the horizontal forces, i.e. from left to right (\tilde{k}_l) and from right to left (\tilde{k}_r). Then, the minimum value (\tilde{k}_{\min}) of the collapse load and the related mechanism were assumed as ultimate condition associated to the analysed sample. From the results obtained by the Monte Carlo simulation, the probability density functions of the random variables \tilde{k}_l , \tilde{k}_r and \tilde{k}_{\min} was estimated. These results are reported in Figure 27.10 and indicated through a dashed black line, a dot-dashed black line and a continuous red line respectively. In terms of mean values it should be noted as the introduction of uncertainties affects the bearing capacity of the arches, even if it depends by the level of irregularities and by their relation with the main nominal geometrical parameters, such as the radius, the angle of embrace and the thickness.

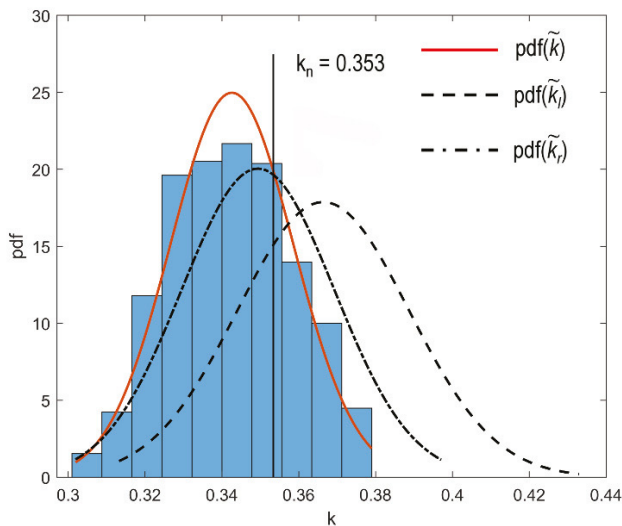


Fig. 27.10 Results of the probabilistic analysis and estimation of the probability density functions of k_l (dashed black line), k_r (dot-dashed black line) and k_{\min} (continuous red line).

27.5 Conclusion

In the present contribution, aiming at the assessment of the behaviour of masonry structures with irregular shapes, the limit conditions of a random polycentric arch affected by horizontal forces have been investigated. Among the plausible and multiple reasons of such deformed structural configurations, the consequences directly related to the uncertainties of construction work have been studied. By means of a probabilistic approach, based on a Monte Carlo simulation, the influence of those irregularities on the collapse load multiplier and the related mechanisms was evaluated. The results in terms of the reduction of the collapse load highlights a penalizing effect of such features regarding the seismic safety. Therefore the outcomes are promising encouraging further investigations on the items of this ongoing research indeed, given the versatility of the proposed procedure, the opportunity of applications with regard to the behaviour of different typology of arched structures is envisaged. Furthermore, the negative effects highlighted could take on a greater impact if combined with other classes of uncertainties considering, for example, the quality of the masonry texture and the stereometry of the voussoirs.

References

- Aita D, Barsotti R, Bennati S (2016) Influence of the wall shape on the collapse of arch-wall systems. *Structures and Architecture - Proceedings of the 3rd International Conference on Structures and Architecture, ICSA 2016* pp 760–766
- Andreus U (1990) Sliding-uplifting response of rigid blocks to base excitation. *Earthquake Engineering & Structural Dynamics* 19(8):1181–1196
- Autuori G, Cluni F, Gusella V, Pucci P (2017) Mathematical models for nonlocal elastic composite materials. *Advances in Nonlinear Analysis* 6(4):355–382
- Bertolesi E, Milani G, Fagone M, Rotunno T, Grande E (2018) Micro-mechanical fe numerical model for masonry curved pillars reinforced with frp strips subjected to single lap shear tests. *Composite Structures* 201:916–931
- Breccolotti M, Severini L, Cavalagli N, Bonfigli F, Gusella V (2018) Rapid evaluation of in-plane seismic capacity of masonry arch bridges through limit analysis. *Earthquake and Structures* 15(5):541–553
- Cavalagli N, Gusella V (2015) Structural investigation of 18th-century ogival masonry domes: From carlo fontana to bernardo vittone. *International Journal of Architectural Heritage* 9(3):265–276
- Cavalagli N, Gusella V, Severini L (2016) Lateral loads carrying capacity and minimum thickness of circular and pointed masonry arches. *International Journal of Mechanical Sciences* 115–116:645–656
- Cavalagli N, Gusella V, Severini L (2017) The safety of masonry arches with uncertain geometry. *Computers and Structures* 188:17–31
- Cazzani A, Malagù M, Turco E (2016a) Isogeometric analysis: a powerful numerical tool for the elastic analysis of historical masonry arches. *Continuum Mechanics and Thermodynamics* 28(1-2):139–156
- Cazzani A, Malagù M, Turco E (2016b) Isogeometric analysis of plane-curved beams. *Mathematics and Mechanics of Solids* 21(5):562–577
- De Arteaga I, Morer P (2017) The effect of geometry on the structural capacity of masonry arch bridges. *Computers and Structures* 188:17–31
- Galassi S, Tempesta G (2015) The matlab code of the method based on the full range factor for assessing the safety of masonry arches. *MethodsX* 6:1521–1542
- Grillanda N, Chiozzi A, Bondi F, Tralli A, Manconi F, Stochino F, Cazzani A (2019) Numerical insights on the structural assessment of historical masonry stellar vaults: the case of Santa Maria del Monte in Cagliari. *Continuum Mechanics and Thermodynamics* pp 1–24
- Ochsendorf J (2006) The masonry arch on spreading supports. *Structural Engineer* 84(2):29–35
- Pepi C, Gioffrè M, Comanducci G, Cavalagli N, Bonaca A, Ubertini F (2017) Dynamic characterization of a severely damaged historic masonry bridge. *Procedia Engineering* 199:3398–3403
- Romano A, Ochsendorf J (2010) The mechanics of gothic masonry arches. *International Journal of Architectural Heritage* 4(1):59–82
- Severini L, Cavalagli N, Gusella V (2018) Dynamic response of masonry arches with uncertain geometry under pulse-type motion. *Nonlinear Dynamics* 91(1):609–624
- Simoncello N, Zampieri P, Gonzalez-Libreros J, Pellegrino C (2019) Experimental behaviour of damaged masonry arches strengthened with steel fiber reinforced mortar (sfrm). *Composites Part B: Engineering* 177
- Stockdale G, Tiberti S, Camilletti D, Sferrazza Papa G, Basshofi Habieb A, Bertolesi E, Milani G, Casolo S (2018) Kinematic collapse load calculator: Circular arches. *SoftwareX* 7:174–179
- Tempesta G, Galassi S (2019) Safety evaluation of masonry arches. a numerical procedure based on the thrust line closest to the geometrical axis. *International Journal of Mechanical Sciences* 155:206–221
- Veihelmann K, Stefan H (2015) Hinges in historic concrete and masonry arches. *Proceedings of the ICE - Engineering History and Heritage* 168:54–63
- Zampieri P, Zanini M, Faleschini F (2016) Influence of damage on the seismic failure analysis of masonry arches. *Construction and Building Materials* 119:343–355

- Zampieri P, Cavalagli N, Gusella V, Pellegrino C (2018) Collapse displacements of masonry arch with geometrical uncertainties on spreading supports. *Computers and Structures* 208:118–129
- Zampieri P, Zanini M, Faleschini F (2019) Seismic capacity of masonry arches with irregular abutments and arch thickness. *Construction and Building Materials* 201:786–806



Chapter 28

Challenging Mathematical Insights into Masonry Domes over the Centuries

Raffaella Pavani

Abstract We focus on masonry domes which are considered architectural landmarks either in different historical periods and in different cultural contexts. From a mathematical point of view, an approximation of a dome is provided by a rotation solid whose cross-section gives the generating curve. Obviously, a frequent generating curve is the semicircumference, but here we want to highlight the role of parabola and catenary used as generating curves to make the structural load lighter. At the present they are well-studied different curves, but until the 17th century, they were considered the same curve, even though they significantly differ from the point of view of structural properties. Actually, catenary is the curve of a hanging chain, which exhibits a tension strength only. When it is “frozen” and inverted it exhibits a compression strength only, which means that it supports itself. Parabola does not exhibit such structural property, but catenary may differ from a convenient parabola very slightly so that building approximation makes a catenary appear as a parabola and this parabola is so close to a catenary that it approximately retains its structural properties, point by point. Here, we investigate the mathematical connection between catenary and parabola in masonry dome structure, referring in particular to Brunelleschi’s dome in Florence, Saint Peter’s dome in Rome and San Gaudenzio’s dome in Novara.

Keywords: Catenary · Funicular surface · Masonry domes · Renaissance domes

28.1 Introduction

Currently, we are accustomed to see buildings with curvilinear roofs of any material, of any curvature, of any regular or irregular shape. In the ancient centuries, instead,

R. Pavani
Department of Mathematics, Politecnico di Milano, Piazza L. da Vinci 32 - 20133 Milano, Italy
e-mail: raffaella.pavani@polimi.it

curvilinear coverings were provided by masonry domes only. They were ideally generated by the rotation of an arch around its vertical symmetry axis. In this way, cross-sections become curves, mainly parabolas and catenaries (aside from, obviously, semicircumferences).

The most ancient still standing example of the curve (we now call) catenary, used as a cross-section of a masonry vault, goes back to the so-called Ctesiphon arch (3rd century A.D., Taq Kasra – Iraq). Previously, corbelled domes appeared in Minoan civilization about 1500 B.C., but true masonry domes were found at ancient Ur (in the present Iraq) and are dated back to 2500 B.C. (Chant and Goodman, 1999). This would place knowledge of true masonry dome long before the rise of Roman Empire. Even though the true dome was not a Roman invention, Romans were the first civilization to overcome the challenges associated with the true dome and perfect the form, enlarging the span of dome they could build (e.g. Caracalla's Baths and Diocletian's Baths). It is worth mentioning the Pantheon dome which has been a landmark in Rome panorama since the 1st century B.C.; remarkably, it is not a true dome, but a corbelled dome.

Here we consider parabolas and catenaries as cross-sections of ancient domes and from a mathematical point of view we will discuss features of the two curves when used in architecture. We add that when a surface is generated by the rotation of a catenary around its symmetry axis, it is also called *funicular surface*.

We remind that the relevance of catenary in architecture and structural engineering was firstly introduced by Hooke's studies on inverted chain and its stability properties, which will be treated in the next Section. We notice that our analytical-numerical approach has to be inserted in the more general geometrical approach which, more recently, was strengthened by Heyman's "*safe theorem*" (Heyman, 1995). According to this theorem, if by an elastic analysis a thrust line can be found which lies within the wall thickness of an arch in equilibrium, then this is sufficient to guarantee that the structure is stable under the given loading. Since mathematically the equilibrium of an arch is given by a convenient catenary, it is clear that such analytical curve is really significant to architecture. Within this context, we suggest to refer to (Cazzani et al, 2016a,b; Grillanda et al, 2019) for different efficient numerical methods, detailed discussions and significant examples.

28.2 Parabola vs. Catenary

The parabola curve is the graphic of any analytical function which is a polynomial of degree two. From the point of view of classical geometry, any parabola can be built as a conic section, as it is known since the 4th century B.C. by the Greek mathematician Menecmus. From the point of view of architecture, parabola has no stability property.

Instead, catenary has excellent stability properties, but its equation is more complicated, involving a hyperbolic cosine. This curve represents the shape of a hanging chain (or inextensible cable) of uniform mass, fixed at the ends and subject to its

own weight only. This means that analytical expression of catenary is the solution of the differential equation providing the equilibrium of a hanging chain (or cable).

Suppose a cable with tension T . Let T_o be the tension in the cable at its lowest point. Let the origin be at this point. The horizontal force on the cable at that point is then T_o . Suppose we isolate a piece of the cable extending from the origin to the point (x, y) where the tension is T . Let ϑ be the tangent angle at (x, y) . Then for horizontal equilibrium we have $T_o = T \cos(\vartheta)$.

Let s be the arc length from the origin up to the point (x, y) . Let w be the weight of the cable per unit arc length. Then for the vertical equilibrium we have $ws = T \sin(\vartheta)$. Hence

$$\frac{dy}{dx} = \tan(\vartheta) = \frac{T \sin(\vartheta)}{T \cos(\vartheta)} = \frac{ws}{T_o} \quad (28.1)$$

Differentiating, we get

$$\frac{d^2y}{dx^2} = \frac{ws}{T_o} \frac{ds}{dx} = \frac{1}{a} \sqrt{1 + (dy/dx)^2} \quad (28.2)$$

Solution of this equation provides the equation of catenary

$$y(x) = a \cosh(x/a) , \quad (28.3)$$

where $a = T_o/ws$ is the *catenary constant*. For increasing values of a , catenary exhibits increasing span.

If the lowest point of the curve is in (x_0, y_0) then the catenary equation becomes

$$y(x) = a \cosh\left(\frac{x - x_0}{a}\right) + (y_0 - a) \quad (28.4)$$

If catenary is “frozen” and inverted, the chain (or cable) exhibits a compression strength only, which means that it supports itself. In 1671 Robert Hooke announced at the Royal Society in London he had found the shape of the optimal arch. In 1676 he published a book where he stated “*Ut continuum pendet flexible, sic stabit continuum rigidum inversum,*” i.e. as a flexible cable hangs, so, inverting it, a rigid body stands still. In Figure 28.1 we report a catenary and the corresponding inverted catenary. Then the inverted catenary, with the highest point in $(0, h)$, has the following equation

$$y(x) = -a (\cosh(x/a) - 1) + h \quad (28.5)$$

Given h and the intersection x with the axis of abscissas, we found the value of a by a numerical method which computes zeros of nonlinear functions.

Hooke did not provide any proof nor the analytical equation of the catenary. His assessment was based on experimental evidence only. However the topic was so interesting that the greatest contemporary mathematicians of that century (Leibniz, Huygens and Bernoulli brothers) studied the catenary curve in details, competing with each other, and succeeded in providing a complete mathematical description

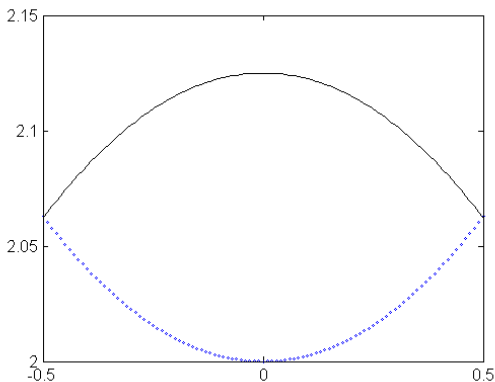


Fig. 28.1 Catenary and inverted catenary

of the properties of this curve related to its static equilibrium. It is worth noticing that it would be impossible to get such results by the previous classical approach of mathematics. The new analytical approach allowed mathematics to enlarge its field: analytical geometry was born. Later in (Gregory, 1697), it was investigated how the catenary form is the real shape of a stable arch, when it can be drawn within its section, since a catenary can sustain itself.

Even though the parabola fails to exhibit the structural properties of a catenary, the two curves are closely related from a mathematical point of view.

Firstly, from a geometrical point of view, the curve traced on the plane by the focus of a parabola rolling along a straight line, is exactly a catenary.

Then, from the analytical point of view, the equation of a catenary developed in power series provides a polynomial with even terms which provides a parabola, if the series is truncated at the second term. In more details, we have

$$a \cosh(x/a) = a + \frac{1}{2a}x^2 + \frac{1}{24a^3}x^4 + O(x^6) \tag{28.6}$$

Moreover, we notice that even the polynomial $p(x) = a + \frac{1}{2a}x^2 + \frac{1}{24a^3}x^4$ can be viewed as a parabola when the variable change $t = x^2$ is introduced. In order to enlighten this behavior, in Figure 28.2 the catenary through points $(0, 34)$, $(26, 0)$ is reported (in this case $a = 13.4496$) together with the approximating parabola $p(x)$ given above and plotted with respect to \sqrt{t} . In Figure 28.3 the same catenary is reported together with a parabola interpolating at the maximum point and endpoints. In the first case the maximum relative error between the two curves is 3% and in the second case is 7% (in infinity norm). This means that, in some circumstances, a parabola can be a very good approximation of a catenary. So, in practice, given a catenary it is always possible to find a parabola which, point by point, resembles such catenary and its structural properties.

This result supports the hypothesis that a particular parabola was used in any masonry dome built before the 17th century in such a way that the parabolic cross-

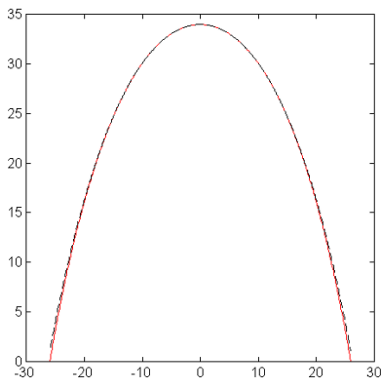


Fig. 28.2 Catenary and approximating parabola

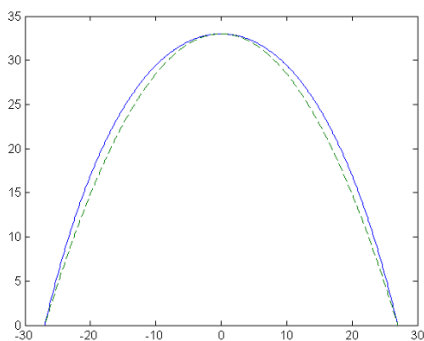


Fig. 28.3 Catenary and interpolating parabola

section of the rotation surface was actually resembling a catenary and its stability properties. Indeed, it is clear that the correct dimensioning of domes and arches was the result of empirical observations over a long period of time, when actually parabolas could be easily computed and built.

Moreover, there is experimental evidence that still in 19th century, catenaries as cross sections of rotation surfaces and vaults were not computed using the analytical approach (reported above) but using an analogical approach by oval curves, as pointed out in (Lluís-i Ginovart et al, 2017), referring to Spanish context.

Sometimes it may be hard to distinguish between a parabola and a catenary. In (Huylebrouck, 2007) a couple of significant examples are reported. In particular, here we present the example referring to Gaudi's Collegio Teresiano, reported in Figure 28.4.

In the cross-sections of those arches we can see either catenaries or parabolas. As it was reported in Huylebrouck (2007), data are taken so that the top becomes the minimum in $(0, 1)$, for increasing x and y : a least squares fitting provides the (weighted) catenary $y = -0.7468 + 1.75 \cosh(2.8x)$ with $R^2 = 99.988\%$.

Alternatively, the parabola $y = 0.985 + 7.63x^2$ fits with $R^2 = 99.985\%$. The method used in (Huylebrouck, 2007) was a pseudo-inverse algorithm; he concludes that "No naked eye can catch the difference" between catenary and parabola. Actually, the relative error between fitted parabola and catenary is 0.6%.

Here we used a "trust-region-reflective" method by the function `lqscurvefit` provided by MATLAB. We found as a fitting (weighted) catenary $y = -0.9462 + 1.95 \cosh(2.6684x)$ and as a fitting parabola $y = 1.0111 - 0.2771x + 8.2194x^2$. Figure 28.5 reports our fitting catenary in solid line, the experimental data by circles and our fitting parabola in dotted line. In both the cases the norm of the residual is equal to 0.4% , as well as the relative error between fitted catenary and parabola.

Again we can conclude that "No naked eye can catch the difference" between catenary and parabola. We remark that a fitting with a classical form of catenary does not provide good results.

Moreover, it is worth noticing that, in spite of appearance, our fitting parabola in practice overlaps the already published parabola in Huylebrouck (2007). This is due to the fact that both parabolas are close to the best approximation.

We remark that a parabola can be distinguished from a catenary by resorting also to geometric properties of parabola itself. In particular, one of these properties states:

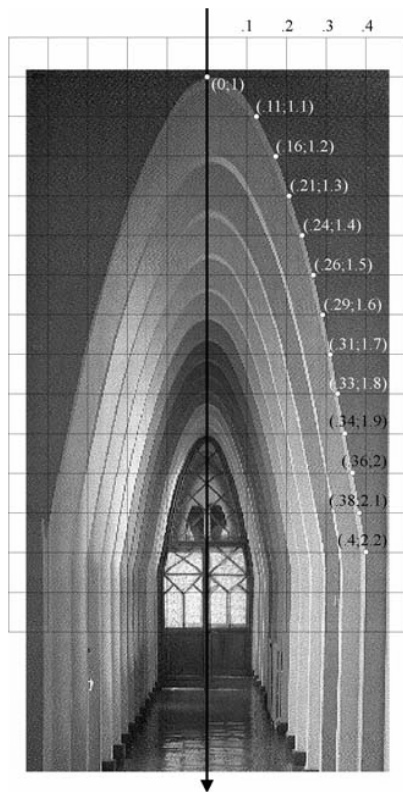


Fig. 28.4 Arches by Gaudi in Collegio Teresiano

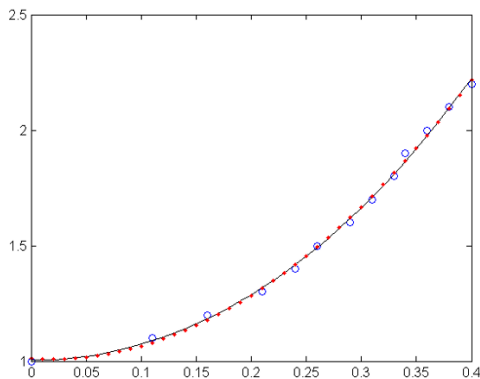


Fig. 28.5 Fitting experimental data by catenary and parabola

if a parabola has several parallel chords, their midpoints all lie on a line which is parallel to the axis of symmetry. Now, consider Gaudi's Paelle Guel as an example: the profile of the gate has to be considered as a catenary curve, since all the midpoints of parallel chords lie on a curve, which differs from a line parallel to the symmetry axis (e.g. see Ghione, 2009).

28.3 Case Study: Santa Maria del Fiore in Florence

The church of Santa Maria del Fiore was built according to a project by Arnolfo di Cambio, started in 1296 and grew up during a long period in the 14th century. The dome was built between 1420 and 1436 by Filippo Brunelleschi, who never described his method of building.

It is made up by eight membranes, based on an octagon at 55 m from the ground, so any horizontal section is octangular. However, within the thick octagonal dome, we can imagine a dome having circular section at every horizontal level; so safely the imaginary dome can be considered a possible thrust surface for the real structure (Heyman, 1995). The inner diameter of the dome is 45 m, the outer one is 54 m (e.g. see Como, 2017). Indeed the dome is built up by two shells with an inner space large about 1.2 m in between. The maximum height of intrados is 32.2 m and the maximum height of extrados is 35.75 m. The average height is 34 m over a 55 m high drum. These numbers remember the Fibonacci numbers: 1, 2, 3, 5, 8, 13, 21, 34, 55, 89, 144, 233, ... which are characterized by property that the ratio of two consecutive number tends to the golden ratio (that is about 1.618034) as they increase. But Brunelleschi did not refer to Fibonacci numbers, even though he certainly knew them, because, obviously, he did not use a meter as a unit of measure. Actually, he used the Florentine arm = 0.5836 m. So the inner diameter is 77 arms. The diameter was then divided into 5 parts (each of them 15.4 arms = 8.98 m long); so that centers

of the inner two curves of the intrados were found in order to have a "pointed fifth" arch as a cross-section. For the extrados, instead, it was used a "pointed fourth" arch. Figure 28.6, provided by (Conti, 2014), enlightens the building method of the cross-section of the dome.

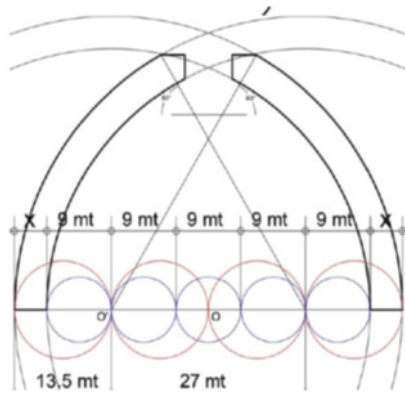


Fig. 28.6 Pointed arches

Here we propose that in the case of Brunelleschi’s dome, between the intrados, built by pointed fifth arch, and the extrados, built by pointed fourth arch, it is always possible to make a catenary run. Focusing on the masonry arch which represents the approximated cross-section of this dome, equilibrium can be visualized using a *thrust line*.

This theoretical line represents the path of the resultants of the compressive forces through the stone structure and has the shape of the inverted catenary discussed above. For a pure compression structure, equilibrium implies a thrust line that lies entirely within the masonry section. In Milankovitch (1907) it is provided an excellent mathematical treatment of this concept which was recently resumed and again studied in deep at MIT (Ma, USA), where new computational interactive equilibrium tools were produced (Block et al, 2006). In Figure 28.7 and Figure 28.8 we present our results about two possible catenaries running between intrados and extrados of Brunelleschi’s dome. Here we do not intend to study the optimal thrust line, but we aim just at presenting how thrust line (i.e. catenary) can be drawn by analytical formulas and approximated by convenient parabolas. Figure 28.7 reports catenary through (0, 35), (24, 0); Figure 28.8 reports catenary through (0, 33.5), (27, 0). In Figure 28.7 an Figure 28.8 catenary is given in solid line, the interpolating parabola through three points (the maximum and the ends points) is given in dashed line, whereas the approximating parabola from the series development is given in dotted line; its equation is

$$y(t) = a + \frac{1}{2a}t + \frac{1}{24a^3}t^2 \tag{28.7}$$

where $t = x^2$.

The maximum relative error between this second parabola and related catenary is 4% in Figure 28.7 and 2% in Figure 28.8. Again this means that we can find a parabola which completely overlaps related catenary. We remark that in Figure 28.7 the interpolating parabola through three points runs outside the wall thickness; instead the approximating parabola $y(t)$ always runs within the wall thickness and resembles the structural property of the catenary, point by point. From a numerical point of view, the approach by the approximating parabola is characterized mainly by two features: i) the computation of the catenary constant a solving numerically a nonlinear equation where a is the unknown; ii) the computation of $y(t)$ by a change of variable $t = x^2$ and then plot y vs \sqrt{t} .

Obviously, Brunelleschi did not follow this approach. However the Brunelleschi's choice was really effective even though he did not know catenary jet. He probably built and tested parabolas very close to a convenient unknown catenary and by intuition and experience he found very nice structural stability properties of his cross-section. Over the centuries Brunelleschi's dome substantially maintained a stable configuration (exhibiting a few minor structural problems only) and became a landmark of soundness and beauty.

28.4 Some More Ancient Masonry Domes

28.4.1 St. Peter's Dome in Rome

It was planned by Michelangelo, who worked on the construction of the renewed basilica beginning in 1547. The dome was concluded by Giacomo Della Porta, Michelangelo's disciple, in 1590. The dome has a double shell (following the example

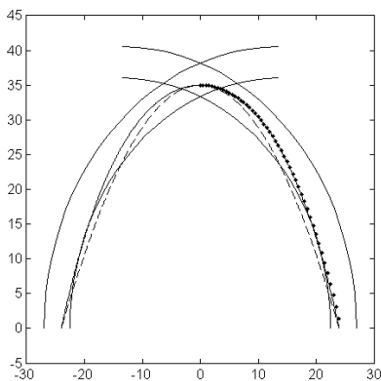


Fig. 28.7 Catenary through $(0, 35)$, $(24, 0)$

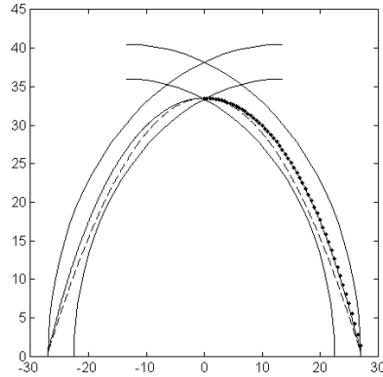


Fig. 28.8 Catenary through $(0, 33.5)$, $(27, 0)$

of more ancient Brunelleschi's dome) with an inner diameter of 42.56 m.; the height from the base to the top is 136.57 m.

As well as Brunelleschi, Michelangelo did not write anything about his project and this was a great disadvantage when by the end of the 17th century the dome started to show a serious chance of collapsing. In 1743 the Pope assigned to Giovanni Poleni the task of studying the structure and solving the problem. At that time Poleni was a famed engineer and mathematician and he knew very well the role of catenary in structure stability; he built small models in scale of the catenary running between the two shells of the dome.

His conclusion was that the shape of the Michelangelo's dome was satisfactory. So the structure was simply strengthened and even now we can admire the efficiency of that action based on the use of catenary as a mathematical model.

This was the very first example of conscious and documented use of catenary in Architecture. Indeed, many original drawings of catenaries referring to St. Peter's dome can be found in (Poleni, 1748).

28.4.2 St. Gaudenzio's Dome in Novara

The latest masonry dome in Italy was the St. Gaudenzio's Dome in Novara, built and designed by A. Antonelli between 1841 and 1878. It has a height from the floor level of the church to its top of 125 m, an internal diameter of 14 m and an external diameter of 22 m. Again we find two shells in the dome structure, but in this case the whole building exhibits a daring complex constructive system, astonishingly light. Unfortunately, the structure experienced many serious stability problems since the beginning of its life.

Nevertheless, investigations conducted on the structure of the dome had shown that the shape of thrust line is perfectly contained within the masonry section of

the dome, with minimal variations. In fact, the shape of the arch of the internal cross-section becomes very similar to that of a catenary, with the difference of an average quadratic deviation well below 1% (Corradi et al, 2009).

28.5 Conclusions

Firstly, within the context of mathematics, we investigated numerical and analytical relations between parabola and catenary and we have shown that, given a catenary, it is always possible to find a parabola very close to the catenary which inherits the stability property of catenary, point by point.

Then, within the context of building structures, the Brunelleschi's dome was investigated in some details, using just the mathematical concepts previously provided. At last, some dedicated comments were presented relating St. Peter's dome and San Gaudenzio's dome.

Our results enlighten how good were the ancient builders in managing mathematical concepts, both consciously and intuitively.

References

- Block P, DeJong M, Ochsendorf J (2006) As hangs the flexible line: Equilibrium of masonry arches. *Nexus Network Journal* 8:13–24
- Cazzani A, Malagu M, Turco E (2016a) Isogeometric analysis: a powerful numerical tool for the elastic analysis of historical masonry arches. *Continuum Mechanics and Thermodynamics* 28(1-2):139–156
- Cazzani A, Malagu M, Turco E, Stochino F (2016b) Constitutive models for strongly curved beams in the frame of isogeometric analysis. *Mathematics and Mechanics of Solids* 21(2):182–209
- Chant C, Goodman D (1999) *Pre-Industrial Cities and Technology*. Routledge, London
- Como M (2017) *Statics of Historic Masonry Constructions*. Springer
- Conti G (2014) *La matematica nella cupola di santa maria del fiore a firenze*. Itacha: *Viaggio nella Scienza* 4:5–11
- Corradi M, Filemio V, Trenetti M (2009) Antonelli's dome for san gaudenzio: Geometry and statics. *Nexus Network Journal* 11(2):243–56
- Ghione F (2009) *Una non parabola: la catenaria*. Quaderni di Laboratorio Università di Roma
- Lluís-i Ginovart J, Costa-Jover A, Coll-Pla S, Lopez-Piquer M (2017) Layout of catenary arches in the spanish enlightenment and modernism. *Nexus Network Journal* 19:85–99
- Gregory D (1697) *Catenaria*. *Philosophical Transactions of the Royal Society* 19:637–652
- Grillanda N, Chiozzi A, Bondi F, Tralli A, Manconi F, Stochino F, Cazzani A (2019) Numerical insights on the structural assessment of historical masonry stellar vaults: the case of santa maria del monte in cagliari. *Continuum Mechanics and Thermodynamics* pp 1–24
- Heyman J (1995) *The stone skeleton: structural engineering of masonry architecture*. Cambridge University Press
- Huylebrouck D (2007) Curve fitting in architecture. *Nexus Network Journal* 9:59–70
- Milankovitch M (1907) *Theorie der druckkurven*. *Zeitschrift für Mathematik und Physik* 55:1–27
- Poleni G (1748) *Memorie istoriche della gran cupola del tempio vaticano*. Stamperia del Seminario di Padova



Chapter 29

Innovative Voxel Approach for Homogenized Out-of-Plane Analysis of Non-Periodic Masonry Walls

Simone Tiberti & Gabriele Milani

Abstract This paper presents a MATLAB-based procedure for the derivation of out-of-plane homogenized failure surfaces for masonry elements. The procedure follows a so-called “voxel approach” that allows the creation of a 3D finite element mesh directly from the sketch of a masonry element. This approach is implemented into a dedicated MATLAB script. The validation of the procedure is performed by extracting homogenized out-of-plane failure surfaces for a stretcher bond masonry cell. These are compared to those available in literature for an analogous cell, obtained with a different model. The correspondence between the two models is satisfying, confirming the reliability of the presented procedure. Eventually, the behavior under out-of-plane actions is investigated for two single and one double curvature masonry cells. Homogenized out-of-plane failure surfaces and relevant failure modes are extracted for all the different cases and compared to those obtained for the flat case. The results for the curved masonry cells show an increase in out-of-plane resistance for one of the single curvature cases and for the double curvature case. Moreover, the deformed shapes at collapse are consistent with the expectations.

Keywords: Masonry curved elements · Homogenization · Upper bound limit analysis · Out-of-plane behavior

29.1 Introduction

Masonry is one of the most challenging materials to model. Its composite nature must be properly addressed in every mechanical model aiming at simulating its global behavior. For example, a dedicated failure criterion must be devised (Andreass, 1996), or its complexity can be reduced by considering it as a no tension

S. Tiberti, G. Milani

Technical University of Milan, Piazza Leonardo da Vinci 32, 20133 Milan
e-mail: simone.tiberti@polimi.it, gabriele.milani@polimi.it

© Springer Nature Switzerland AG 2020

B. E. Abali and I. Giorgio (eds.), *Developments and Novel Approaches in Nonlinear Solid Body Mechanics*, Advanced Structured Materials 130,
https://doi.org/10.1007/978-3-030-50460-1_29

481

material (Cuomo and Ventura, 2000). Also, specific models are to be conceived when considering curved masonry elements (Cazzani et al, 2016). In fact, the technique known as homogenization has been extensively used in the last three decades to obtain the global mechanical behavior and characteristics of masonry from its constituents (units and mortar). It is grounded on the possibility to identify a basic cell called Representative Element of Volume (REV), which recreates the original masonry pattern if translated. Homogenization is sometimes coupled with a limit analysis approach to assess the structural behavior at collapse of masonry elements. Common applications are devoted to assessing the behavior of in-plane loaded masonry bonds displaying a periodic arrangement of the units such as stretcher bond masonry: see in this regard Milani et al (2006a), Stefanou et al (2015), and Godio et al (2017). Some more works seek to investigate the behavior under out-of-plane loads, for instance Milani et al (2006b) and Cecchi et al (2007). Furthermore, only a few applications deal with curved masonry elements (Milani et al, 2009), leaving this field of application largely unexplored.

The application of homogenization in deriving the characteristics of masonry in historical buildings seems to be rather appealing. However, these structures often consist of masonry where the units (bricks and/or stones) are randomly arranged in the walls, forming the so-called “rubble masonry.” This apparently prevents the successful identification of a REV. A method to overcome this issue is described in Cavalagli et al (2018) that is based on the concept of SEPUC (Statistically Equivalent Periodic Unit Cell). Conversely, a multiscale approach employing mixed FEM analyses is introduced in Tedesco et al (2017).

This paper presents a procedure developed in MATLAB that aims at deriving out-of-plane homogenized failure surfaces of masonry elements. The code is based on a voxel approach that allows the generation of a 3D finite element mesh directly from the outline of a masonry panel. The validation of the procedure is performed on a flat stretcher bond masonry cell, and two different out-of-plane homogenized failure surfaces are extracted and compared to those resulting from a previous work (Milani and Taliercio, 2016). Eventually, the procedure here presented is applied to several curved masonry cells displaying distinct curvatures around their in-plane axes. Out-of-plane homogenized failure surfaces are extracted for different values of the curvature radius and compared to the flat case. Also, a double curvature case is investigated and critically commented.

29.2 Voxel Procedure for Homogenized Out-of-Plane Failure Surfaces

The 3D FE mesh is generated in MATLAB from the rasterized sketch of the considered masonry element. Each pixel of the picture is first turned into a tridimensional entity (called “voxel”), then is transformed into a single finite element. This is flagged as being part of either unit or mortar by extracting the RGB triplet of the original pixel. Specifically, the “red” value of the triplet is assessed and compared to a thresh-

old that determines the physical nature of the finite element. Each element is then given a centroid, whose coordinates belong to a reference system originated at the center of the test-window (Fig. 29.1). The overall dimensions of the cell are set as inputs by the user and exploited to create the eight nodes of each finite element, which is a solid brick. The transversal layout of the finite element mesh is simply obtained through extrusion of the in-plane configuration.

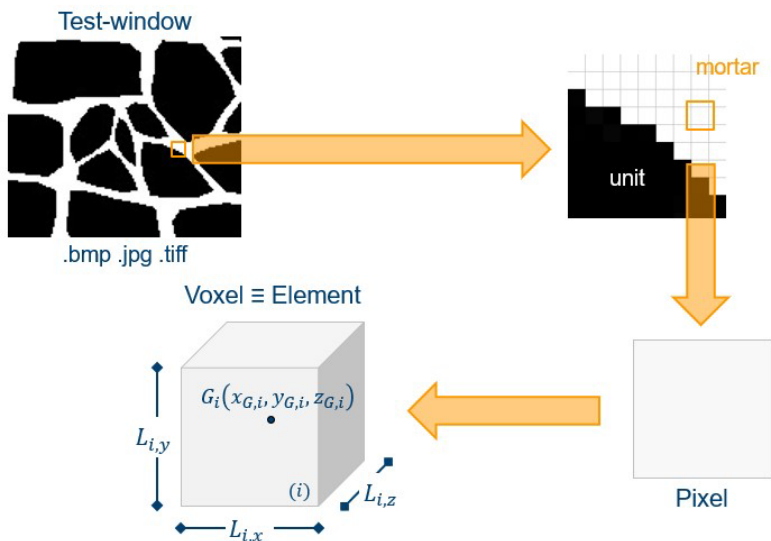


Fig. 29.1 Voxel procedure for the creation of the 3D finite element mesh of the considered masonry element.

The mesh obtained through this script represents the basis for calculating the out-of-plane homogenized failure surfaces of the considered masonry element. These are extracted as results coming from the solution of an upper bound limit analysis problem combined with a homogenization approach. This problem is written into another MATLAB script as a linear programming problem (specifically, a minimization one) formulated in standard form. The rotation rate of each finite element is neglected so that the unknowns of the problem are reduced. The out-of-plane kinematics of the finite elements is regulated via a Kirchhoff–Love plate model; also, they are considered as rigid elements, so that dissipation solely takes place on the interfaces of adjoining elements. The only active interfaces within the considered masonry elements are those between mortar finite elements and between one mortar and one unit finite element. A Mohr–Coulomb failure criterion is used to address the velocity jumps across the active interfaces. Eventually, the kinematics of unit finite elements is governed by that of the masonry unit to which they belong; this is achieved through ad-hoc master-slave relations that connect the velocities of each unit finite element to those of the centroid of its related master masonry unit. In the linear programming problem as formulated for this application, equality constraints

are to be enforced: they come from the velocity jumps due to dissipation, from the master-slave relations, from the periodicity conditions on the lateral boundaries of the considered masonry element (as required by the homogenization approach), and from the normalization of the dissipated external power (which is needed for finding a single solution in terms of deformed shape at collapse). Two different failure surfaces are extracted: one in the M_{xx} - M_{yy} plane and the other in the M_{xx} - M_{xy} plane, where M_{xx} is the vertical bending strength, M_{yy} the horizontal bending strength, and M_{xy} the torsional bending strength.

29.3 Numerical Validation of the Voxel Procedure

The validation of the proposed procedure is carried out by extracting out-of-plane homogenized failure surfaces for a stretcher bond masonry cell and comparing them with those obtained by Milani and Taliercio (2016) for the same cell. This stretcher bond masonry cell is made of standard Italian bricks whose dimensions are $25 \times 12 \times 5.5 \text{ cm}^3$, with mortar joints of 1 cm (Fig. 29.2a); two finite element meshes are created for this validation, a finer one with 260000 elements (48 over the thickness, Fig. 29.2b) and a coarser one with 17000 elements (12 over the thickness, Fig. 29.2c). The Mohr–Coulomb failure criterion in this application employs a cohesion of 0.132 MPa and a friction angle of 27° .

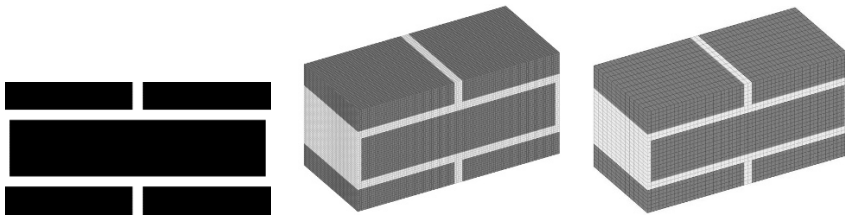


Fig. 29.2 (a) Stretcher bond masonry cell; (b) finer mesh; (c) coarser mesh.

Fig. 29.3 shows the homogenized out-of-plane failure surfaces obtained for the present model with the two meshes, compared against the ones resulting from Milani and Taliercio (2016). Both surfaces are in good agreement with the results coming from the aforementioned work, with only some negligible differences in the M_{xx} - M_{xy} plane that are likely due to the different kinematics assumed in the two models. Also, the use of a coarser mesh does not have a significant impact on the results, causing only a tiny reduction of the two failure surfaces (which moreover is on the safe side). Therefore, the coarser mesh will be used in all the following applications.

Fig. 29.4 shows the failure modes extracted for the finer mesh, which are associated to single out-of-plane load conditions - namely, the three moments M_{xx} , M_{yy} , M_{xy} . It can be seen that all of them are consistent with the expected deformed configurations at collapse for these three cases. In particular, the vertical overturning

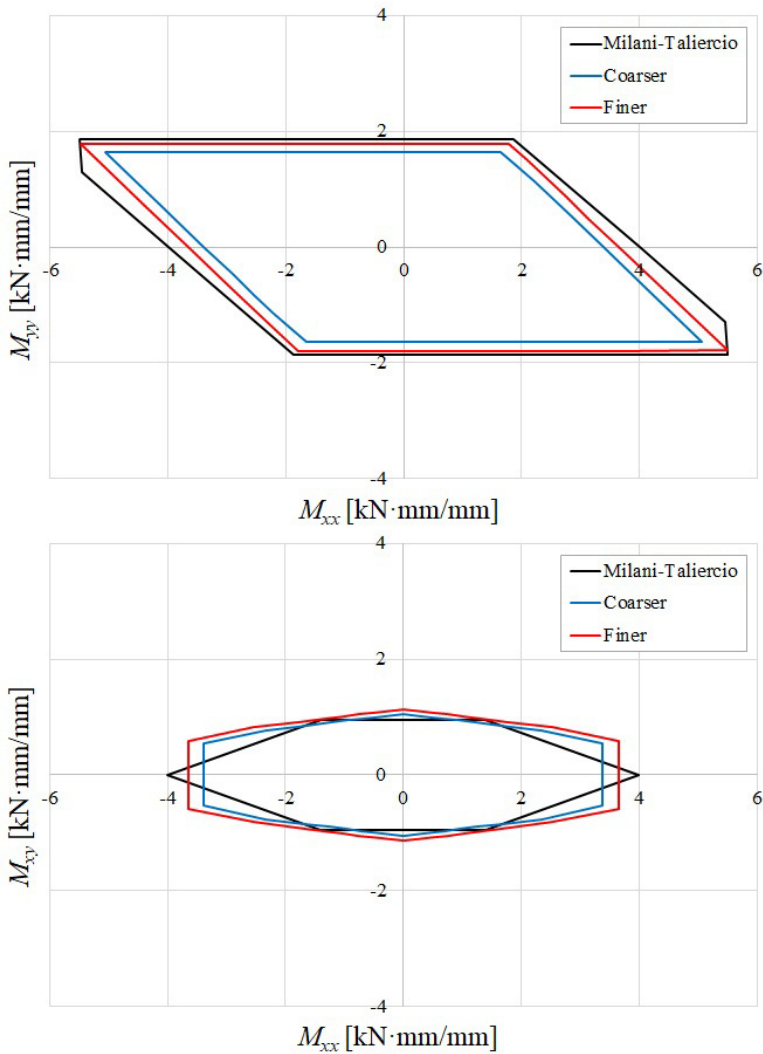


Fig. 29.3 Comparison of homogenized out-of-plane failure surfaces: (a) M_{xx} - M_{yy} plane; (b) M_{xx} - M_{xy} plane.

bending moment M_{xx} originates cracks in both the head and the bed joints, and the horizontal overturning bending moment M_{yy} causes only horizontal cracks in the bed joints.

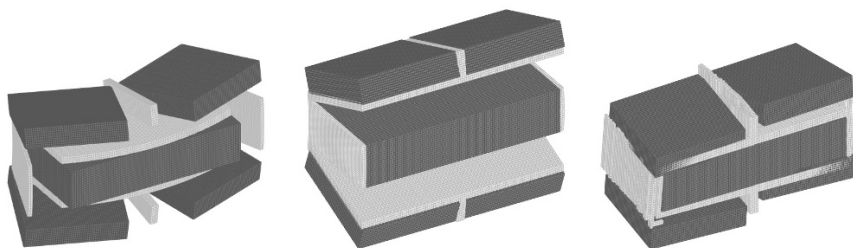


Fig. 29.4 Failure modes for relevant out-of-plane actions: (a) M_{xx} ; (b) M_{yy} ; (c) M_{xy} .

29.4 Application of the Voxel Procedure to Single Curvature Masonry Cells

In this section, the voxel procedure is applied to two single curvature masonry cells; specifically, the coarser mesh of the stretcher bond masonry cell presented in Fig. 29.2c is slightly modified to simulate a single curvature cell. Two meshes are then extracted: one displays a single curvature around axis X (Fig. 29.5a), the other

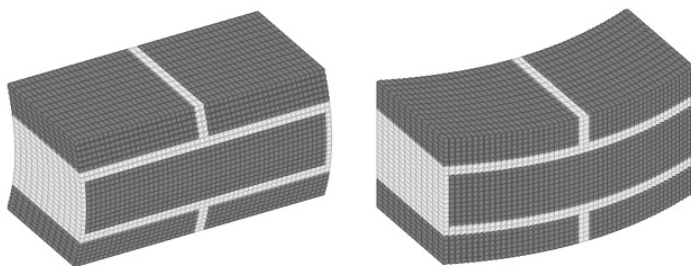


Fig. 29.5 Single curvature masonry cells: (a) curvature around axis X ; (b) curvature around axis Y .

a single curvature around axis Y (Fig. 29.5b), both with the same curvature radius of 1.5 m. It must be remarked that in Fig. 29.5 the curvature is visually enhanced for a better display of the curved configuration. Also here the Mohr–Coulomb failure criterion employs a cohesion of 0.132 MPa and a friction angle of 27° .

Figure 29.6 shows the homogenized out-of-plane failure surfaces obtained for the two single curvature cells, compared against the ones obtained in the previous section for the coarser mesh (from now on referred to as the “flat case”). It can be easily seen that the cell with single curvature around axis Y undergoes an increase of its out-of-plane strength, since both its failure surfaces are larger than those obtained for the flat case. Also, both the failure surfaces start losing their double symmetry in the M_{xx} - M_{xy} plane, which is to be expected due to the different behavior of the intrados and the extrados of the curved cell, as noted in Milani et al (2009).

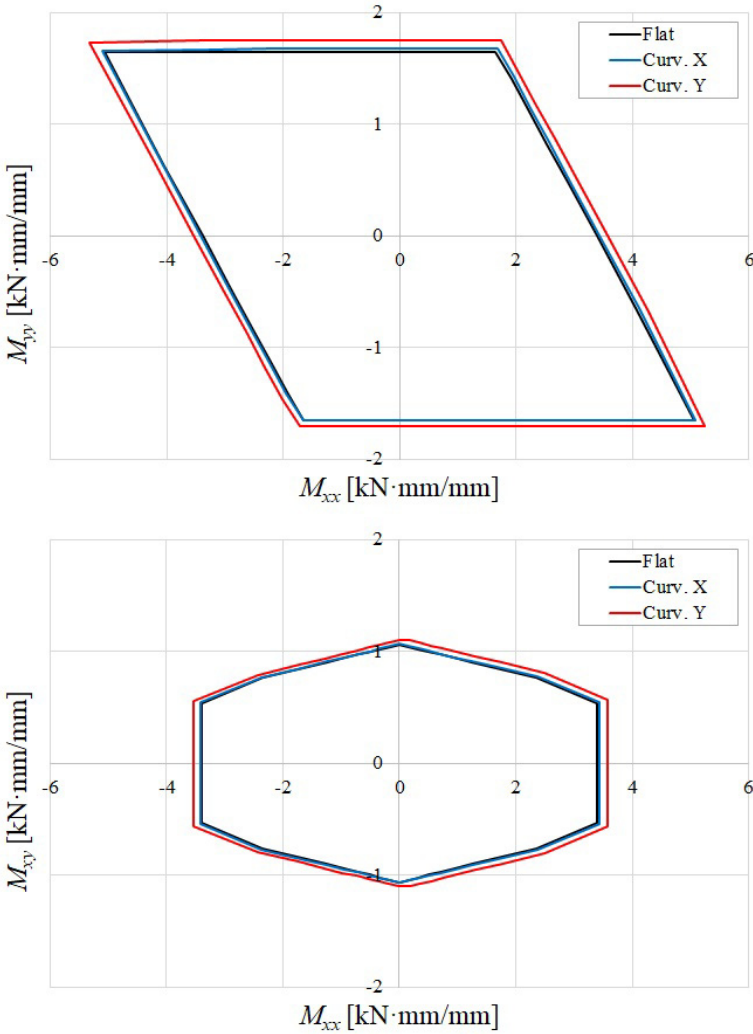


Fig. 29.6 Comparison of homogenized out-of-plane failure surfaces for curvature around axes X and Y: (a) M_{xx} - M_{yy} plane; (b) M_{xx} - M_{xy} plane.

Conversely, no discernible differences can be noted for the cell with single curvature around axis X.

Figure 29.7 shows three relevant failure modes for the two single curvature cells: those for the cell with curvature around axis X are displayed in Fig. 29.7a-c, while those for the cell with curvature around axis Y are displayed in Fig. 29.7d-f. While all the deformed configurations at collapse are consistent with the expectations, it must be remarked that those associated to M_{xx} are different for the two cases. In

fact, the failure mode for the curvature X cell displays splitting in correspondence of the interfaces between the bricks and the same head joint (Fig. 29.7a), whereas the one for curvature Y displays an in-between splitting of the head joints that lie above the central brick (Fig. 29.7d).

Eventually, a sensitive analysis is performed on the two curved cells to investigate the influence of the curvature radius on the dimension of the homogenized failure surfaces. Three different values of the curvature radius are investigated for each cell, respectively equal to 1 m, 1.5 m, and 2 m. Fig. 29.8 and Fig. 29.9 show the resulting out-of-plane homogenized failure surfaces for curvature around axis X and Y, respectively. Once again, no significant differences are observed for the two surfaces of the cell with curvature around axis X, whereas for decreasing values of the curvature radius the dimensions of both surfaces increase in the case of the cell with curvature around axis Y, which entails an increase of its out-of-plane strength.

29.5 Application of the Voxel Procedure to a Double Curvature Masonry Cell

As a final application, the voxel procedure is applied to a double curvature stretcher bond masonry cell, depicted in Fig. 29.10. The curvature radius around axis X is 1 m, while the one around axis Y is 1.5 m; again, both curvatures are visually enhanced in the figure for a better display of the curved configuration. Fig. 29.11 shows the out-of-plane homogenized failure surfaces for the double curvature cell compared against those obtained in the flat case. It is possible to notice that both surfaces are larger than those of the flat case, which means that a double curvature

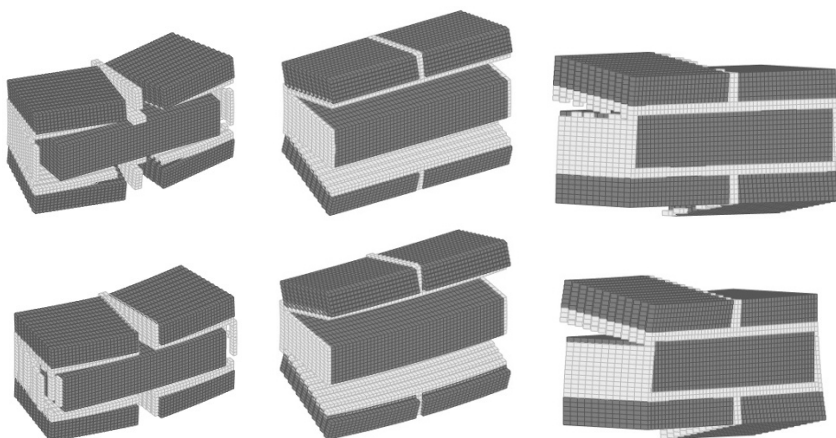


Fig. 29.7 Failure modes for relevant out-of-plane actions: (a) curvature X, M_{xx} ; (b) curvature X, M_{yy} ; (c) curvature X, M_{xy} ; (d) curvature Y, M_{xx} ; (e) curvature Y, M_{yy} ; (f) curvature Y, M_{xy} .

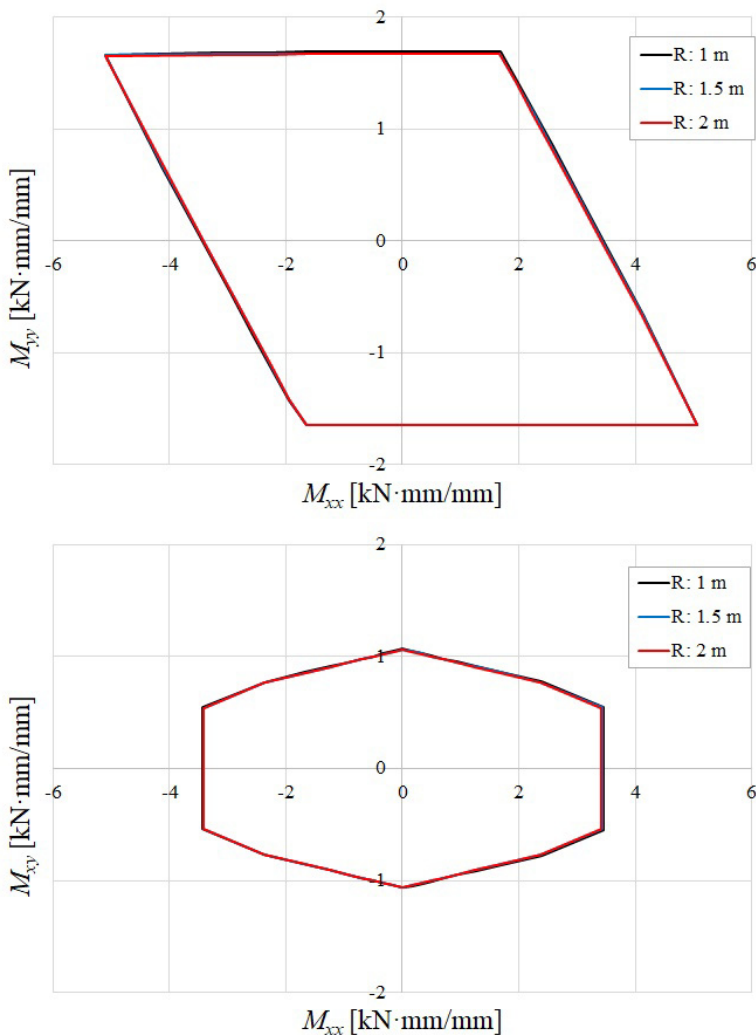


Fig. 29.8 Homogenized out-of-plane failure surfaces from sensitivity analysis for different curvature radii around X: (a) M_{xx} - M_{yy} plane; (b) M_{xx} - M_{xy} plane.

masonry structure displays a higher resistance to out-of-plane actions with respect to a flat one. Finally, Fig. 29.12 shows the three relevant failure modes for the double curvature cell; the deformed configurations at collapse more closely resemble those obtained for the single curvature cell with curvature around axis Y .

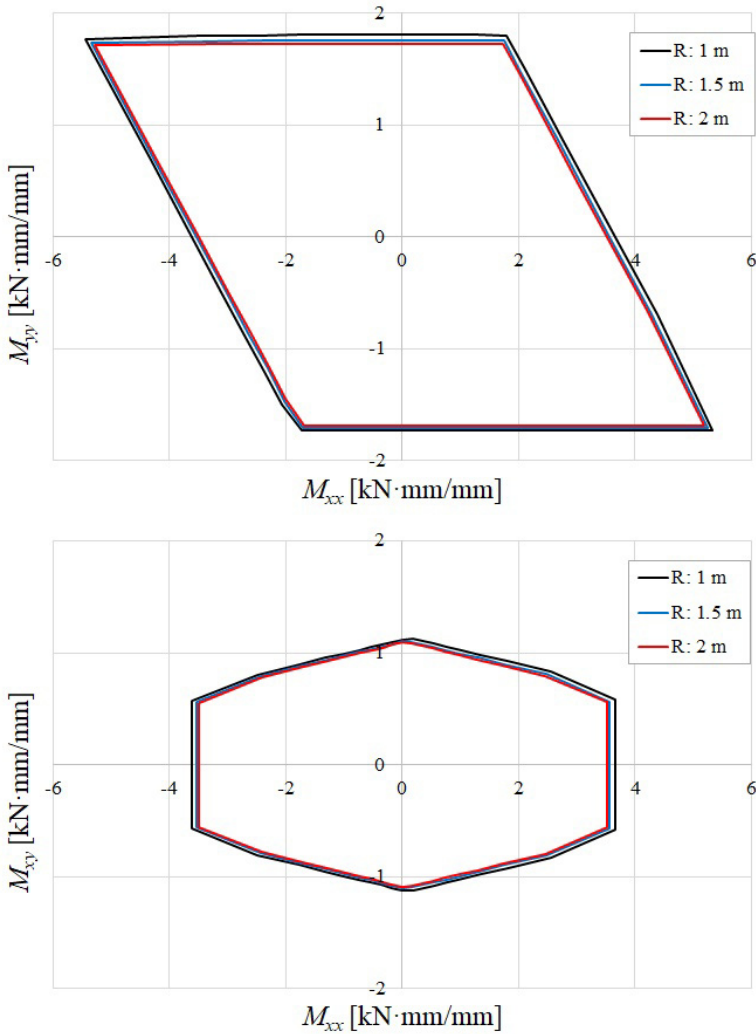


Fig. 29.9 Homogenized out-of-plane failure surfaces from sensitivity analysis for different curvature radii around Y: (a) M_{xx} - M_{yy} plane; (b) M_{xx} - M_{xy} plane.

29.6 Conclusion

A procedure set through a MATLAB code for deriving out-of-plane homogenized failure surfaces of masonry elements is presented. The outline of a masonry cell is transformed into a 3D FE mesh; then, an upper bound limit analysis problem employing a homogenization approach is solved to draw the homogenized failure surfaces. Two different out-of-plane homogenized failure surfaces are extracted for a

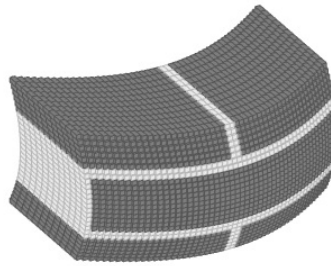


Fig. 29.10 Double curvature masonry cell.

single masonry element, exploring two sets of moment conditions. A stretcher bond masonry cell is investigated, for which the two failure surfaces and three relevant failure modes are extracted. The resulting failure surfaces for this sample cell are consistent with those obtained in a separate work using a different method; the failure modes are also consistent with the expectations, confirming the validity of the homogenized limit analysis problem as formulated in this application. Also, the procedure here presented is applied to two single curvature masonry cells, as well as to a double curvature masonry cell. It is found that, when the curvature radius is considered around the vertical axis of the curved cell, the out-of-plane strength domain increases more than in the opposite case (curvature around the horizontal axis). Also, smaller curvature radii imply an increase of the out-of-plane resistance. Eventually, some relevant failure modes are extracted for the investigated curved cells, all consistent with the expectations.

Future works will further refine the mesh generating procedure; namely, implementing a subroutine will be implemented to reduce the mesh size when dimensions of the source image are too big. In fact, this would result in a huge number of finite elements and, consequently, in an increase of the computational times needed for the numerical analysis. Moreover, the range of application of this MATLAB code will be expanded to investigate flat and curved cells of rubble masonry elements.

References

- Andreas U (1996) Failure criteria for masonry panels under in-plane loading. *Journal of Structural Engineering* 122(1):37–46
- Cavalagli N, Cluni F, Gusella V (2018) Failure surface of quasi-periodic masonry by means of Statistically Equivalent Periodic Unit Cell approach. *Meccanica* 53(7):1719–1736
- Cazzani A, Malagú M, Turco E (2016) Isogeometric analysis: a powerful numerical tool for the elastic analysis of historical masonry arches. *Continuum Mechanics and Thermodynamics* 28(1-2):139–156
- Cecchi A, Milani G, Tralli A (2007) A Reissner-Mindlin limit analysis model for out-of-plane loaded running bond masonry walls. *International Journal of Solids and Structures* 5(2):83–92
- Cuomo M, Ventura G (2000) A complementary energy formulation of no tension masonry-like solids. *Computer Methods in Applied Mechanics and Engineering* 189(1):313–339

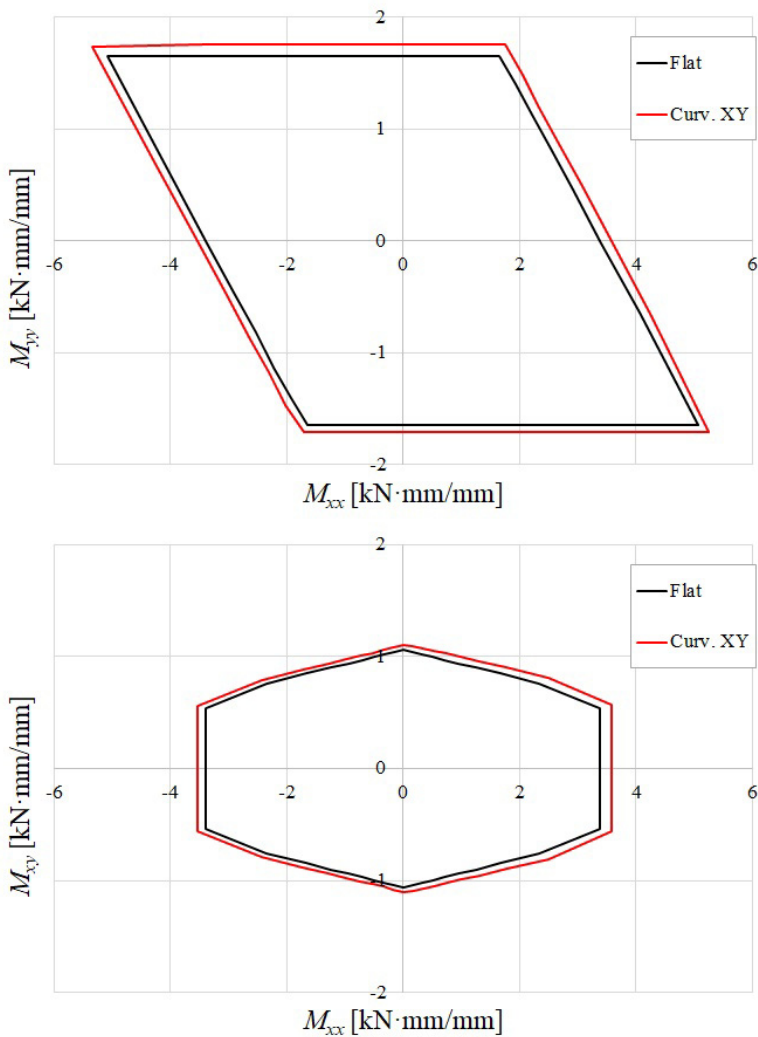


Fig. 29.11 Comparison of homogenized out-of-plane failure surfaces for double curvature cell: (a) M_{xx} - M_{yy} plane; (b) M_{xx} - M_{xy} plane.

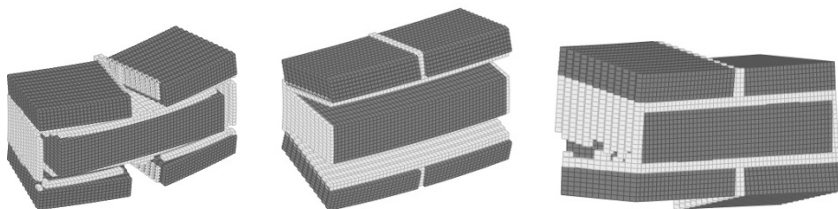


Fig. 29.12 Failure modes for relevant out-of-plane actions: (a) M_{xx} ; (b) M_{yy} ; (c) M_{xy} .

- Godio M, Stefanou I, Sab K, Sulem J, Sakji S (2017) A limit analysis approach based on Cosserat continuum for the evaluation of the in-plane strength of discrete media: Application to masonry. *European Journal of Mechanics - A/Solids* 66:168–192
- Milani G, Taliercio A (2016) Limit analysis of transversally loaded masonry walls using an innovative macroscopic strength criterion. *International Journal of Solids and Structures* 81:274–293
- Milani G, Lourenço PB, Tralli A (2006a) Homogenised limit analysis of masonry walls, Part I: Failure surfaces. *Computers and Structures* 84(3-4):166–180
- Milani G, Lourenço PB, Tralli A (2006b) Homogenization approach for the limit analysis of out-of-plane loaded masonry walls. *Journal of Structural Engineering* 132(10):1650–1663
- Milani G, Milani E, Tralli A (2009) Upper bound limit analysis model for FRP-reinforced masonry curved structures. Part I: Unreinforced masonry failure surfaces. *Computers and Structures* 87:1516–1533
- Stefanou I, Sab K, Heck JV (2015) Three dimensional homogenization of masonry structures with building blocks of finite strength: A closed form strength domain. *International Journal of Solids and Structures* 54:258–270
- Tedesco F, Bilotta A, Turco E (2017) Multiscale 3D mixed FEM analysis of historical masonry constructions. *European Journal of Environmental and Civil Engineering* 21(7-8):772–797